Exploring the application of N-heterocyclic organometallic complexes as potential therapeutics

Sarmishta Munuganti

Bachelor of Science, Bachelor of Science (Honours)

A thesis submitted for the degree of *Doctor of Philosophy* at

Monash University in December 2022

(*School of Chemistry*)

Copyright notice

© Sarmishta Munuganti (2022).

I certify that I have made all reasonable efforts to secure copyright permissions for third-party content included in this thesis and have not knowingly added copyright content to my work without the owner's permission.

Declaration

This thesis is an original work of my research and contains no material which has been accepted for the award of any other degree or diploma at any university or equivalent institution and that, to the best of my knowledge and belief, this thesis contains no material previously published or written by another person, except where due reference is made in the text of the thesis.

Print Name: SARMISHTA MUNUGANTI

Date: 21/12/2022

Abstract

This study explored the synthesis, characterisation, solution state stability and *in vitro* antimicrobial activity of a series of novel bismuth(III), rhenium(I), and gallium(III) N-heterocyclic complexes. These fundamental studies provide valuable insight into how structural modifications to a set of organic substrates can influence the overall chemical, photophysical and biological properties of the metal complexes.

Chapter 1 provides a summary of the current and emerging trends in antimicrobial resistance (AMR) which detail key mechanisms of resistance. Additionally, the role of metals in medicine and their target mechanisms within the fields of antibacterial, antifungal, and as cancer therapeutics is explored, with a particular focus on the role of bismuth, gallium, and rhenium. Furthermore, an introduction to the azole family of compounds and N-heterocyclic thione/thiols as biologically relevant substrates is discussed, with a specific focus on the substituted pyridyl 1,2,4-triazole scaffold.

Chapter 2 explores a series of seventeen novel homoleptic and heteroleptic bismuth(III) complexes bearing two general classes of N-heterocyclic thione ligands, pyridyl 1,2,4-triazole thiones (**2-1** to **2-12**) and 5-arylidene rhodanines (**2-13** to **2-17**). The synthetic routes to access the complexes of the forms $[Bi(SR)_3]$ (where SR = triazole thione) and $[BiPh_2(SR)]$ employ protolysis and salt metathesis methods. *In vitro* antimicrobial studies against five bacterial strains (Methicillin-resistant *Staphylococcus aureus* (MRSA), Vancomycin resistant *Enterococcus* (VRE), *Escherichia coli* (*E. coli)*, and *Pseudomonas aeruginosa* (*P. aeruginosa)*) and two fungal strains (*Candida albicans (C. albicans)* and *Candida auris (C. auris*)) showed that the degree of substitution around the metal centre markedly affects the overall biological output, with potent activity observed for the heteroleptic complexes (**2-7** to **2-12**) of the form $[BiPh_2(SR)]$.

Given the bioactive nature of organorhenium(I) complexes, chapter 3 sought to explore the synergistic relationship between the 1,2,4-triazole thione ligand class and the rhenium(I) tricarbonyl moiety, $[Re(CO)_3]^+$ via complexation. The synthesis, structural, photophysical and biological properties of twelve heteroleptic rhenium(I) complexes **3-1** to **3-12** of the form *fac*-$[Re(N^N)(CO)_3(L)]$, where N^N represents

either 1,10-phenanthroline (phen) or 2,2'-bipyridyl (bpy), were explored. Further modifications to the pyridyl 1,2,4-triazole substrate resulted in the synthesis, characterisation and photophysical activity of four additional complexes **3-13** to **3-16** of the form *fac*-[Re(L)$(CO)_3$Cl]. Although both series of complexes showed significantly less antimicrobial and photophysical activity when compared to the parent substituted pyridyl 1,2,4-triazole precursors, an important structure-activity relationship (SAR) was observed.

Chapter 4 details the attempted synthesis and isolation of gallium(III) triazole thiones. Despite numerous attempts, reactions between gallium(III) and substituted pyridyl 1,2,4-triazoles, ultimately culminated in the unsuccessful isolation of Ga(III) triazole thione-type complexes.

Publications and presentations

Publications

"Is Bismuth Really the "green" Metal? Exploring the Antimicrobial Activity and Cytotoxicity of Organobismuth Thiolate Complexes" L. J. Stephens, **S. Munuganti,** R. N. Duffin, M. V. Werrett and P. C. Andrews, Inorg. Chem., 2020, 59, 3494–3508.

"Modulating aryl substitution: Does it play a role in the anti-leishmanial activity of a series of tetra-aryl Sb(V) fluorinated carboxylates?" E. V. Artem'eva, R. N. Duffin, **S. Munuganti**, A. N. Efremov, P. C. Andrews, O. K. Sharutina and V. V. Sharutin, Polyhedron, 2022, 213, 115627.

"Investigations into a change of aryl group on the cytotoxicity and anti-leishmanial activity of a series of tris-aryl Sb(V) pentafluoropropionates" E. V. Artem'eva, R. N. Duffin, **S. Munuganti**, A. N. Efremov, P. C. Andrews, O. K. Sharutina and V. V. Sharutin, J. Inorg. Biochem., 2022, 234, 111864.

Presentations

Poster Presentation: An exploration into the antibacterial activity of N-heterocyclic Bi(III) thiolate complexes

RACI, Inorganic symposium, Monash University, Melbourne, Australia **2019**

Poster Presentation: An exploration into the antibacterial activity of N-heterocyclic Bi(III) thiolate complexes

ChemComm symposium, RMIT University, Melbourne, Australia, ***2019***

Oral presentation: The synthesis, characterization and antimicrobial studies of heterocyclic bismuth(III) complexes

OZOM12, University of Melbourne, Victoria, Australia **2019**

Poster Presentation: Answering the azole question, can we use bismuth(III) thiolates as antimicrobials?

RACI IC19, University of Wollongong, Wollongong, NSW, Australia **2019**

Acknowledgements

Achieving a PhD in the context of a global pandemic, this is something I will remember for the rest of my life. The last few years of my PhD were some of the most trying times, with Melbourne undergoing 245 days in lockdown, to the School of Chemistry shutting down 6 times; I would not have been able to complete this body of work without the support and guidance of my family, friends, supervisors, mentors and of course comrades.

First and foremost, I am so grateful to my main supervisor, Professor Phil Andrews for providing me with the opportunity to explore this wonderful area of chemistry. You always made time for me, especially in times of strife. I greatly appreciate the wisdom you have imparted. I came to your lab as a naïve and unsure undergraduate and I leave as a confident self-assured young woman. I look to you as an advisor and mentor both personally and professionally.

To my co-supervisor Dr Melissa Werrett, I am so grateful to have started my research journey under your tutelage. I still remember my first day in the lab and how you were so patient in teaching me the ropes. Your kindness, insights, and suggestions have helped me grow as a chemist and watching you make your mark in a new field has been inspiring. I have no doubt you will achieve great things in your career.

To Dr. Bekka Duffin, summarising our friendship in a paragraph wouldn't do it justice but I shall try! I look to you as a mentor and inspiration; Throughout the years you have been incredibly helpful, empathetic, and hard working. Your sheer determination and will to succeed is why you're a wonderful researcher. I cannot wait to see your career shine bright and for your dreams come into fruition, you're going to do wonders gal!

To my SoGs boy, IT support, Lab buddy and Guzy-fiend Nimrod Eren, we started and ended our PhD journeys together, I'm so grateful to have found a caring, conscientious, and encouraging writing buddy throughout COVID-19. You have been a pillar of strength for me, and I am so proud of what you have achieved.

To Dr. Dimuthu Seneviratha, I have never met anyone in my life so encouraging and compassionate. Every conversation that I would have with would leave me in a

position where I would feel a renewed sense of motivation. You've always been a source of positivity and the cheerful spirit that oozes out of you is incredibly infectious, you really know how to light up a room, friend.

Dr. Matt Flynn and Dr. Kirralee Burke words cannot express how grateful I am to you both for the countless number of hours spent sifting through my ramblings. Especially Kirralee, your words of encouragement near the end of my submission served as a beacon of hope and those coffee catchups sharing the exploits of our fur-children were a joy to look forward to.

To Dr. Megan Herdman, Dr. Michael Stevens and Dr. Liam Stephens, your constant encouragement, in-jokes, and general camaraderie helped me get through some trying days in the lab. I wish you all of the success in your endeavours. To Dr. Victoria Blair and the rest of the Andrews/Blair comrades past and present: Jamie Greer, Yih Ching Ong, Emily Lever, Max Teise, Bethan Beazley, Tania Sultana, Shazia Nawaz, Rupinder Dhamoon and Claudia Giarrusso, I could not have asked for a better team to work with and share my passion for science. You all got me through the many long days of experiments with such enjoyable conversations and laughs.

A special thanks goes to my obstacle removers, Dr. Alasdair Mackay, and Dr. Craig Forsyth, who took the time out of their busy schedules to run my experimental analyses in even the wee hours of the night. To Dr. Cory Smith, I was a bit of a madlad learning computational chemistry in the last 6 months of my PhD and you took me on board as your padawan, for that I will always appreciate.

Mum, dad, and Tej, no words can describe the love and support you have given me throughout my life and through this thesis. Matthew Ely, when we met, you didn't know what you were getting into, but I am so glad that you strapped yourself along for my wild and exciting ride. My pain, struggle, delirium, and craziness have all come to a satisfying end. Having you by my side, I wouldn't have it any other way.

Finally, I must acknowledge the use of the Monash X-ray Platform and Monash Analytical Platform, and the Faculty of Science Dean's Scholarship which made it possible for me to conduct this research.

List of Figures

Figure 1: Contributing factors to the increasing occurrence of AMR, created with BioRender.[2,4] 5

Figure 2: Summarised mechanisms of resistance observed in a microbial cell created on BioRender, whereby **A**: resistance of Linezolid via upregulation, **B**: resistance of ampicillin via chemical modification, **C**: resistance of Vancomycin via cell wall modification, and **D**: resistance of levofloxacin via efflux pump expression. 6

Figure 3: Generalised scheme for the degradation of penicillin via the use of a β-lactamase enzyme. β-lactam ring degradation highlighted in green, and liberation of CO_2 in orange.[43] 7

Figure 4: Mechanisms of resistance observed in a yeast cell whereby **A**: resistance of Terbinafine via squalene epoxidase point mutations, **B**: resistance of 5-Flucytosine via chemical modification, **C**: resistance of Amphotericin B via sterol site modification, **D**: resistance of caspofungin via FKS point mutations in 1,3-glucan synthase. **E:** resistance of fluconazole via efflux pump expression. 8

Figure 5: Simplified resistance mechanism of the antifungal drug flucytosine (5FC) and its metabolic by-product 5-fluoruracil (5FU) proposed by Billmyre and co-workers.[56] 9

Figure 6: Empirical structures of some landmark metal-based complexes used in early medicine. Au(I) derivative Auranofin (left), cisplatin (middle) and colloidal structure of the As-derivative salvarsan (right). 11

Figure 7: Simplified periodic table of elements highlighting the essential metals for life. 12

Figure 8: Empirical structures of **1-1:** silver sulfadiazine (**SSD**, A) and **1-2:** silver nanoparticles and **1-3:** 1,3-dibenzyl-4,5-diphenyl-imidazol-2-ylidene Ag(I) acetate (**SBC3**).[75] 13

Figure 9: Metal antimicrobial mechanisms of action, created in BioRender.[34,72,76] 14

Figure 10: Examples of two antifungal Cu(II)- and Zn(II)-based thiosemicarbazone complexes synthesized by Bajaj and co-workers.[104] 16

Figure 11: Antifungal Ni(II)-*S*-benzyldithiocarbazate complex synthesized by Malik *et al*.[105] 16

Figure 12: Examples of antifungal Co(II)- Schiff base complexes synthesized by Frei *et al*.[106] 17

Figure 13: Select antifungal Cu(II), Mn(II) and Ag(I) phenanthroline-based complexes synthesized by Gandra *et al*.[96] 18

Figure 14: Empirical structure of the commercially available platinum(II)-based anticancer drug, Oxaliplatin 20

Figure 15: Empirical structures of **1-12**, bismuth(III) subsalicylate **1-13,** bismuth(III) subgallate and **1-14,** [1,2-bis((1,3,2-dithiabismolan-2-yl)thio)ethane] Pravibismane. 20

Figure 16: Solid-state structure of colloidal bismuth(III) subcitrate detailing the dimeric unit $[Bi(cit)_2Bi]^{2-}$. Hydrogen atoms have been omitted for clarity and thermal ellipsoids are shown at 50%.[129] 22

Figure 17: Solid-state structure of colloidal bismuth(III) subsalicylate, hydrogen atoms have been omitted for clarity.[138] 23

Figure 18: The diverse applications of Re(I)-based chemistry as summarized by Dilworth.[156] 26

Figure 19: Structures of therapeutic compounds **1-15**: Gallium nitrate, **1-16**: tris(3-hydroxy-2-methyl-4H-pyran-4-onato) ^{67}gallium(III) **1-17**: gallium maltolate, and **1-18**: Tris-(8-quinolinolato)gallium(III) 28

Figure 20: Summary if alkylgallium(III) complexes prepared and evaluated for their therapeutic application.[205–208] 30

Figure 21: Key natural products containing N-heterocyclic scaffolds highlighted in purple 31

Figure 22: Examples of compounds within the azole sub-class of molecules. 32

Figure 23: Isomeric forms of triazole, **A**: 1H-1,2,3-triazole, 2H-1,2,3-triazole and **B**: 1H-1,2,4-triazole, 4H-1,2,4-triazole 32

Figure 24: Commercially available drugs based on the 1,2,4-triazole scaffold.[236]....34

Figure 25: Commercially available first generation, second generation and third generation triazole-based antifungal structures.[220] 35

Figure 26: Representative examples of select N-heterocyclic thiones which bear a thioamide functionality highlighted in purple. 36

Figure 27: Commercially available fungicide, Prothioconazole modelled from an N-heterocyclic thione scaffold.[247,248].....37

Figure 28: Examples of antimicrobial 1,2,4-triazole-3-thiones synthesized by Jalilan, Linciano *et al*.[249,250] 37

Figure 29: Anticancer 1,2,4-triazole-3-thiones developed by Mioc and Ghanaat *et al*.[251,252].....38

Figure 30: Tautomeric forms of 1H-1,2,4-triazolethione to 3-mercapto-1,2,4-triazole 39

Figure 31: Tautomeric forms of a 1,2,4-triazole with a Schiff base explored by Süleymanoğlu et al., with interactions highlighted in blue.[253] 40

Figure 32: potential binding modes for the n-heterocyclic thiol/thione moiety.....41

Figure 33: Solid-state structure of the biologically active Ru(II) complexes cis-[Ru(tzdt)$_2$(PPh$_3$)$_2$] (**Ru2**, **1-28^b** left) and trans-[Ru(tzdt)(PPh$_3$)$_2$(bipy)]PF$_6$ (**Ru3**, **1-28^c** right) synthesized by Corrêa, et al. Hydrogen atoms have been omitted for clarity and thermal ellipsoids are shown at 50%.[265] 43

Figure 34: Antifungal ruthenium(II) complexes **1-29^a =** *p*-cymene backbone with a coordinated L= clotrimazole (CTZ) **1-29^b =** ruthenium(II) cationic complex series based on the dithione moiety.....45

Figure 35: Schematic representation of the synthetic complexes of Cu(II), Au(I) and Pt(II) with the antifungal drugs ketoconazole (KTZ) and Clotrimazole (CTZ).[91] 46

Figure 36: Organometallic ferrocenyl 1,24-triazole and thiazole containing antifungal complexes where **1-31** = ferrocenyl vinyl 1,2,4-triazole derivatives **1-32** = N-substituted benzylidene-4-ferrocenyl-5-(1H-1,2,4-triazol-1-yl)-1,3-thiazol-2 amine

derivatives and **1-33** = ferrocene-containing 2-pyrazolyl-1,3-thiazolidin-4-ones.[274,276] 47

Figure 37: Asymmetric unit of the structure [Bi(Cys)$_3$] synthesized by Wong et al.[288] Hydrogen atoms have been omitted for clarity. 54

Figure 38: Molecular structures of some bioactive sulfur-based non-nutritive sweetener precursors employed by Andrews *et al.,* to synthesize bismuth(III) complexes.[294] 55

Figure 39: General structure of the homoleptic bismuth(III) β-thioxoketonate series of complexes synthesized by Andrews *et al*.[282] 55

Figure 40: A series of antibacterial homo- and heteroleptic bismuth(III) thiophosphinate complexes synthesized by Senevirathna *et al*.[284] 56

Figure 41: Early generation bismuth thiol (BT) precursors utilized by Domenico *et al*. 57

Figure 42: Molecular structures of some bioactive hypervalent organobismuthane complexes synthesized by Murafuji and co-workers.[309] 58

Figure 43: General structure of the heteroleptic phenylbismuth(III) *bis*-oxathiazolidine complexes synthesized by Luqman and co-workers.[283] 59

Figure 44: N-heterocyclic precursor molecules used in the synthesis of Bi(III) thiolate complexes by Luqman and co-workers.[315] 60

Figure 45: Chemical structures of the commercial thiazolidine-2,4-dione derivatives Rosiglitazone, Pioglitazone and Troglitazone.[319] 61

Figure 46: Empirical structure of the antidiabetic drug Epalrestat (right) and the 2-thioxothiazolidin-4-one ore (rhodanine; left). 62

Figure 47: DSC isotherm of the 1:1 mixture of $BiPh_3$ and triazole thione **3** taken from 50 °C to 250 °C. 76

Figure 48: Solution state ^{1}H spectral comparison of triazole precursor POTz, **3** and product, complex **2-3** [Bi(POTz)$_3$], taken in DMSO-d$_6$ at 25 °C 82

Figure 49: Solution state ^{13}C spectral comparison of triazole precursor POTz, **3** and product, complex [Bi(POTz)$_3$], **2-3** taken in DMSO-d$_6$ at 25 °C.....83

Figure 50: Comparative ^{1}H NMR spectra of **1:** Complex [BiPh$_2$(PFTz)], **2-11, 2:** BiPh$_3$ **3**: Sodium salt PFTz-Na, **5-Na** and **4:** precursor triazole thiolate PFTz, **5** all taken in DMSO-d$_6$ at 25 °C.....85

Figure 51: ^{1}H NMR spectrum of the solid recovered from protocol **VI** following solubilisation in DMSO-d$_6$, highlighting the rearrangement in solution to form complexes (from left to right) [Bi(POTz)$_3$] **2-3,** [BiPh$_2$(POTz)] **2-9**, [BiPh(POTz)$_2$] **2-9'** and BiPh$_3$ (methyl signals are not shown).....86

Figure 52: Asymmetric unit of the molecular structure of [BiPh$_2$(PTz)] **2-7.** Thermal ellipsoids are shown at the 50% probability level. Hydrogen atoms have been omitted for clarity.....88

Figure 53: Polymeric structure of [BiPh$_2$(PTz)] **2-7.** Thermal ellipsoids are shown at the 50% probability level. Hydrogen atoms have been omitted for clarity. Additional fragments generated are shown in wireframe form.....88

Figure 54: Asymmetric units of the molecular structure of [BiPh$_2$(PTTz)] **2-8**. Thermal ellipsoids are shown at the 50% probability level. Hydrogen atoms have been omitted for clarity.....89

Figure 55: Asymmetric units of the molecular structure of [BiPh$_2$(PFTz)], **2-11.** Thermal ellipsoids are shown at the 50% probability level. Hydrogen atoms have been omitted for clarity.....89

Figure 56: Asymmetric unit of the molecular structure of BiPh2(PDTz), **2-12**. Thermal ellipsoids are shown at the 50% probability level. Hydrogen atoms have been omitted for clarity.....90

Figure 57: Solid-state structure of the asymmetric unit of complex [BiPh(POTz)$_2$] **2-9'**. Thermal ellipsoids are given at 50% probability. Hydrogen atoms have been omitted for clarity.....92

Figure 58: Extended polymeric structure of **2-9'** Thermal ellipsoids given at 50% probability. Hydrogen atoms have been omitted for clarity. Extended fragments have been represented using a wireframe model. 93

Figure 59: Absorption spectra of [$BiPh_2$(POTz)] **2-9** at 30 μM in PBS over 48 hours. 94

Figure 60: Absorption spectra of [$BiPh_2$(POTz)] **2-9** at 30 μM in **a):** DMEM cell culture media, and in **b):** DMEM with 10 % FBS over 48 hours. 95

Figure 61: Changes to the absorption spectra of [$BiPh_2$(POTz)] **2-9** (30 μM) in the presence of 3 mM GSH (100 mol. equivalents) in ultrapure water over 24 h. The final DMSO concentration was 0.4 % (v/v). 97

Figure 62: Summary of heteroleptic diphenylbismuth(III) thiolato complexes **2-7** to **2-12**.....98

Figure 63: % cytotoxicity induced by the homoleptic *tris*-substituted bismuth(III) thiolate [$Bi(POTz)_3$] **2-3**, and heteroleptic phenylbismuth(III) thiolates [$BiPh_2$(POTz)] **2-9**, [$BiPh_2$(PDTz)] **2-12**, and $BiPh_3$ in 0.2 % v/v DMSO measured against a control of Triton-x-100 at 2 %..... 100

Figure 64: Cellular uptake of Bi(III) thiolate complexes [$Bi(POTz)_3$]**2-3**, [$BiPh_2$(POTz)] **2-9,** and $BiPh_3$ in MRSA and *E. coli* measured by ICP-MS. 102

Figure 65: Viability percentage of complexes of the form [$Bi(SR)_3$] **2-1** to **2-6**, against cos-7 cells. Dose response curves generated over a range of concentrations (24 nM – 50 μM) in the appropriate culture media from 10 mM DMSO stock solutions. Readings were compared spectroscopically to non-treated control and the percent growth inhibition calculated. Some data points missing due to viability exceeding 200 %. 103

Figure 66: Viability percentage of complexes of the form [$BiPh_2$(SR)] **2-7** to **2-12**, against cos-7 cells. Dose response curves generated over a range of concentrations (24 nM – 50 μM) in the appropriate culture media from 10 mM DMSO stock solutions. Readings were compared spectroscopically to non-treated control and the percent growth inhibition calculated. 104

Figure 67: % Hemolysis induced by the homoleptic tris-substituted bismuth(III) thiolato series of compounds of the form [$Bi(SR)_3$] **2-1** to **2-6** (left) and heteroleptic diphenylbismuth(III) thiolato series of compounds of the form [$BiPh_2$(SR)] **2-7** to **2-12** (right)..... 107

Figure 68: Solution state spectral comparison of MOBR*H* **8** (spectrum 2, top), and product, complex [$BiPh_2$(MOBR)], **2-14** (spectrum 1, bottom) taken in DMSO-d_6 at 25 °C. 114

Figure 69: Stacked ^{1}H NMR spectra of MOBR, **8** (2; top) and [$BiPh_2$(MOBR] (**2-14**; bottom) in DMSO-d_6 with select carbon atom signals labelled..... 115

Figure 70: Asymmetric unit and extended dimeric fragment of the molecular structure of [$BiPh_2$(BR)] **2-13**. Thermal ellipsoids are shown at the 50% probability level. Hydrogen atoms have been omitted for clarity. 118

Figure 71: Molecular structure of [$BiPh_2$(MOBR)] **2-14** showing thermal ellipsoids at 50% probability. Hydrogen atoms have been omitted for clarity. 118

Figure 72: Asymmetric unit of the molecular structure of [$BiPh_2$(InR)] **2-16.** Thermal ellipsoids are shown at the 50% probability level. Hydrogen atoms have been omitted for clarity. 119

Figure 73: Ground state orbital optimized structures of [$BiPh_2$(MOBR)] **2-14**. **A** = HOMO, **B** = LUMO structures. Isosurface values are taken at +/- 0.020..... 120

Figure 74: Changes to the absorption spectra of [$BiPh_2$(ThR)] **2-17** in PBS over 24 h. The complex concentrations were 30 μM with 0.4 % DMSO (v/v). 121

Figure 75: Changes to the absorption spectra of [$BiPh_2$(ThR)] **2-17** (30 μM) with 3 mM GSH (100 mol equivalent) in PBS over 24 h. 123

Figure 76: A representative example of a disc diffusion assay incorporating *C. glabrata.* R1 = BR*H*, **7;** R2 = [$BiPh_2$(BR)] **2-13;** R3 = MOBR*H*, **8;** R4 = [$BiPh_2$(MOBR)] **2-14;** R5 = [$Bi(BR)_3$]; and R6 = [$Bi(MOBR)_3$]. 124

Figure 77: Normalized MIC % growth curves of C. albicans treated with free rhodanines **7** to **9** and **12.** Dose response curves generated over a range of concentrations (0 – 15 μM) in the appropriate culture media from 10 mM DMSO stock solutions. Readings were compared spectroscopically to non-treated control and the percent growth inhibition calculated..... 125

Figure 78: Normalized MIC % growth curves of C. albicans treated with complexes **2-13** to **2-15** and **2-17.** Dose response curves generated over a range of concentrations

(0 – 15 μM) in the appropriate culture media from 10 mM DMSO stock solutions. Readings were compared spectroscopically to non-treated control and the percent growth inhibition calculated. 126

Figure 79: Viability percentage of complexes **2-13** to **2-15** and **2-17** against cos-7 cells. Dose response curves generated over a range of concentrations (48 nm – 100 μM) in the appropriate culture media from 10 mM DMSO stock solutions. Readings were compared spectroscopically to non-treated control and the percent growth inhibition calculated. 127

Figure 80: Structures of generational commercially available platinum-based anticancer drugs including cisplatin and its analogues. 137

Figure 81: General structure of the *fac*-Re(I) diimine tricarbonyl core. 138

Figure 82: A Re(I) anticancer complex, **Re-diSe** synthesized by Collery et al., for the purpose of treating triple-negative breast cancers.[391] 140

Figure 83: The general structure of the antibacterial triorganometallic complex with the general formula McPNA whereby the Ru(II) derivative = **RcPNA** and the Fe(II) derivative = **FcPNA.** 141

Figure 84: Structures of the free 1,10-phenanthroline derivative substrate and Re(I) complexes evaluated for antifungal activity.[400] 143

Figure 85: Selected structures of active antifungal Re(I) complexes **ReNN3Py** and **ReNN6Py**.[399] 144

Figure 86: Commercially available organic-based MitoTracker™ fluorophores used to stain cellular samples. 145

Figure 87: Examples of Re(I)-based fungal fluorophores developed by Carreño and co-workers.[402,406] 146

Figure 88: Typical molecular orbital (MO) diagram of a transition state metal complex 148

Figure 89: Simplified Jablonski diagram, created with BioRender. 149

Figure 90: Re(I) complexes incorporating N-heterocyclic ancillary ligands (from left to right): piperidine, morpholine, thiomorpholine and pyridine.[373] 152

Figure 91: Re(I) complexes incorporating an imidazole backbone and 1,2,3-triazole ancillary ligand.[414] 153

Figure 92: General structures of Re(I) tricarbonyl moieties bearing diimine and/or tetrazolato backbone ligands.[353,416,417,420] 153

Figure 93: Re(I) complexes incorporating a 2,2-bipyridyl backbone and thione/thiolate ancillary ligand.[432] 155

Figure 94: Structures of photoreactive Re(I) tricarbonyl complexes bearing the vicinal σ- or π-donating 1,2,3-triazole backbone ligands.[371,435,436] 156

Figure 95: Re(I) complexes featuring modified 1,2,4-triazoles as backbone ligands. 156

Figure 96: Complexes **3-1** to **3-12** of the general form *fac*-[Re(**phen**/**bipy**)$(CO)_3$(**L**)] (where **L** = pyta, pyta-t, pyta-Cl, pyta-2Me, futa, futa-Cl were synthesized according to the methods outlined in Scheme 10. 162

Figure 97: ^{1}H NMR spectra of complexes *fac*-[Re(phen)(CO_3)(DCM)]SO_3CF_3, **PS** (spectrum 3)**;** free triazole pyta-Cl, **3** (spectrum 2); and complex *fac*-[Re(phen)$(CO)_3$(pyta-Cl)], **3-9** (spectrum 1); taken in DMSO-d_6 at 25 °C. 164

Figure 98: ^{1}H NMR spectra of complexes *fac*-[Re(bpy)(CO_3)(DCM)]SO_3CF_3 **3-3** (spectrum 3), free triazole pyta-Cl **3** (spectrum 2); and complex *fac*-[Re(bpy)$(CO)_3$(pyta-Cl)], **3-3** (spectrum 1); taken in DMSO-d_6 at 25 °C..... 165

Figure 99: ^{1}H NMR spectra of complexes *fac*-[Re(bpy)$(CO)_3$(pyta-Cl)] **3-3** (spectrum 2); and complex *fac*-[Re(phen)$(CO)_3$(pyta-Cl)], **3-9** (spectrum 1); taken in DMSO-d_6 at 25 °C. 166

Figure 100: ^{13}C NMR of rhenium(I) tricarbonyl 1,10-phenanthroline solvato complex **RePS** (spectrum 3), triazole precursor pyta-t **2** (spectrum 2); and complex *fac*-[Re(phen)$(CO)_3$(pyta-t)] **3-8** taken in in DMSO-d_6 at 25 °C. 168

Figure 101: ^{13}C NMR of complex *fac*-[Re(bpy)$(CO)_3$(pyta-t)] **3-3** (spectrum 2); and complex *fac*-[Re(phen)$(CO)_3$(pyta-t)] **3-9** (spectrum 1); taken in DMSO-d_6 at 25 °C. 169

Figure 102: Comparative FT-IR spectra of Orange - Rhenium phen solvate complex; Blue - rhenium bipy solvate complex; Purple – complex **3-3** and Green –complex **3-9.** 173

Figure 103: Asymmetric unit of complex *fac*-[Re(bpy)(CO)$_3$(pyta)] **3-1.** Thermal ellipsoids are shown at the 50% probability level. Hydrogen atoms have been omitted for clarity. 174

Figure 104: Asymmetric unit of complex *fac*-[Re(bpy)(CO)$_3$(pyta-Cl)] **3-3.** Thermal ellipsoids are shown at the 50% probability level. Hydrogen atoms have been omitted for clarity. 175

Figure 105: Asymmetric unit of complex *fac*-[Re(bpy)(CO)$_3$(futa)] **3-5.** Thermal ellipsoids are shown at the 50% probability level. Hydrogen atoms have been omitted for clarity. 175

Figure 106: Asymmetric unit of complex *fac*-[Re(bpy)(CO)$_3$(futa-Cl)] **3-6.** Thermal ellipsoids are shown at the 50% probability level. Hydrogen atoms have been omitted for clarity. 175

Figure 107: Asymmetric unit of complex *fac*-[Re(phen)(CO)$_3$(pyta)] **3-7.** Thermal ellipsoids are shown at the 50% probability level. Hydrogen atoms have been omitted for clarity. 176

Figure 108: Asymmetric unit of complex *fac*-[Re(phen)(CO)$_3$(pyta-t)] **3-8**. Thermal ellipsoids are shown at the 50% probability level. Hydrogen atoms have been omitted for clarity. 176

Figure 109: Asymmetric unit of complex *fac*-[Re(phen)(CO)$_3$(pyta-Cl)] **3-9**. Thermal ellipsoids are shown at the 50% probability level. Hydrogen atoms have been omitted for clarity. 176

Figure 110: Asymmetric unit of complex *fac*-[Re(phen)(CO)$_3$(pyta-2Me)] **3-10**. Thermal ellipsoids are shown at the 50% probability level. Hydrogen atoms have been omitted for clarity. 177

Figure 111: Figure 112: Asymmetric unit of complex *fac*-[Re(phen)(CO)$_3$(futa)] **3-11**. Thermal ellipsoids are shown at the 50% probability level. Hydrogen atoms have been omitted for clarity. 177

Figure 113: Excitation profiles of **a)** fac-[Re(bpy)(CO)$_3$(L)] series of complexes **3-1** to **3-6** and **b)** fac-[Re(phen)(CO)$_3$(L)] series of complexes **3-7** to **3-12** taken at 10^{-4} in DCM at 298 K. 184

Figure 114: Emission profiles of **a)** fac-[Re(bpy)(CO)$_3$(L)] series of complexes **3-1** to **3-6** and **b)** fac-[Re(phen)(CO)$_3$(L)] series of complexes **3-7** to **3-12** taken at 10^{-4} in DCM. 185

Figure 115: Representative example ^{1}H NMR spectra of complex *fac*-[Re(phen)(CO)$_3$(pyta-t)] **3-9** over a period of 5 days taken in MeCN-*d$_3$* at 25 °C.... 188

Figure 116: ^{1}H NMR spectrum of complex *fac*-[Re(phen)(CO)$_3$(pyta-t)] **3-9** over a period of 5 days taken in DMSO-d$_6$ at 25 °C. 189

Figure 117: Changes to the absorption spectra of **a)** [Re(bpy)(CO)$_3$(pyta-Cl)] **3-3** and **b)** fac-[Re(phen)(CO)$_3$(pyta-Cl)] **3-9** in phosphate buffered saline (PBS) solution over 48 hours. The final DMSO concentration for both solutions were 0.4 % (v/v). 190

Figure 118: Changes to the absorption spectra of **a)** [Re(bpy)(CO)$_3$(pyta-Cl)] **3-3** and **b)** fac-[Re(phen)(CO)$_3$(pyta-Cl)] **3-9**, DMEM culture media supplemented with 10% FBS over 48 hours. The final DMSO concentration was 0.4 % (v/v). 192

Figure 119: Changes to the absorption spectra of **a)** [Re(bpy)(CO)$_3$(pyta-Cl)] **3-3** and **b)** fac-[Re(phen)(CO)$_3$(pyta-Cl)] **3-9**, in the presence of 3 mM GSH (100 mol. equivalents) in PBS over 24 h. The final DMSO concentration was 0.4 % (v/v)..... 194

Figure 120: MIC % growth against a control of complexes **3-1** to **3-6** against cos-7. Dose response curves generated over a range of concentrations (0 – 100 μM) in the appropriate culture media from 10 mM DMSO stock solutions. Readings were compared spectroscopically to non-treated control and the percent growth inhibition calculated. 195

Figure 121: Normalized MIC % growth curves of **a)** VRE **b)** MRSA and **c)** E. coli treated with complexes **3-7** to **3-12** of the form [Re(phen)(CO)$_3$(pyta)] Dose response curves generated over a range of concentrations (3.125 – 100 μM) in the appropriate culture media acquired from 10 mM DMSO stock solutions. Readings were compared spectroscopically to non-treated control and the percent growth inhibition calculated. 197

Figure 122: Normalized MIC % growth curves of C. albicans treated with the precursor rhenium(J) solvato-complex **RePS**, and complexes **3-7** to **3-10**. Dose response curves generated over a range of concentrations (0 – 50 μM) in the appropriate culture media acquired from 10 mM DMSO stock solutions. Readings were compared spectroscopically to non-treated control and the percent growth inhibition calculated. 198

Figure 123: ^{1}H NMR spectra of the *ortho*-pyridyl triazole py2ta-t*H* **15** (Spectrum 2); and complex *fac*-[Re(py2ta-t)(CO_3)Cl] **3-14,** (spectrum 1); taken in DMSO-d_6 at 25 °C. 205

Figure 124: ^{13}C NMR spectra of *ortho*-pyridyl triazole py2ta-t*H*, **15** (spectrum 2); and *fac*-[Re(py2ta-t)(CO_3)Cl], **3-14** (spectrum 1); and taken in DMSO-d_6 at 25 °C. 207

Figure 125: Dimeric unit of complex *fac*-[Re(py2ta)($CO)_3$Br] **3-13.** Thermal ellipsoids are shown at the 50% probability level. Hydrogen atoms have been omitted for clarity. Disorder of the terminal ends of the CO and Br atoms have been modelled over two positions. 210

Figure 126: Connective structure of complex *fac*-[Re(py2ta-Cl)($CO)_3$Br] **3-15.** Thermal ellipsoids are shown at the 50% probability level. Hydrogen atoms and solvent molecules have been omitted for clarity. Disorder of the terminal ends of the CO and Br atoms have been modelled over *P*-1 in two positions. 210

Figure 127: ^{1}H NMR spectra of complex *fac*-[Re($CO)_3$(py2ta-t)Cl] **3-14** over a period of 48 hours taken in DMSO-d_6 at 25 °C. 214

Figure 128: ^{1}H NMR spectra of complex *fac*-[Re($CO)_3$(py2ta-t)Cl] **3-14** over a period of 48 hours taken in D_2-DCM at 25 °C. 215

Figure 129: Changes to the absorption spectra of [Re($CO)_3$(py2ta-t)Cl] **3-14** (30 μM) in the presence of **a)** phosphate buffered saline (PBS) solution over 48 hours and **b)** 3 mM GSH (100 mol. equivalents) in ultrapure water over 24 h. The final DMSO concentration for both solutions were 0.4 % (v/v) 216

Figure 130: Changes in the **a)** excitation and **b)** emission profiles of *fac*-[Re(py2ta)($CO)_3$(Cl)] series of complexes **3-13** to **3-16** taken at 10^{-4} in DCM 218

Figure 131: TCSPC decay histograms and fitted mono-exponential decay functions (lex = 350 nm). Instrument response function (IRF) shown in light blue. 218

Figure 132: MIC % growth against a control of complexes **3-13** to **3-16** against cos-7. Dose response curves generated over a range of concentrations (0 – 100 μM) in the appropriate culture media from 10 mM DMSO stock solutions. Readings were compared spectroscopically to non-treated control and the percent growth inhibition calculated. 219

Figure 133: Siderophore structures incorporated by microbials with iron coordinating sites highlighted in orange.[483] 226

Figure 134: Triazole thiones **1,2,14** and **15** used in the attempted preparation of the Ga(III) homoleptic and heteroleptic complexes. 231

List of Schemes

Scheme 1: General structure of the Copper Catalyzed Azide Alkyne Cycloaddition, (CuAAC) 33

Scheme 2: Preparation of pyridyl substituted thiols **1** to **6** from isoniazid and substituted aryl isothiocyanates. 67

Scheme 3: Synthesis of the homoleptic *tris*- substituted bismuth(III) thiolato complexes **2-1** to **2-6** from the reaction of thiolates **1** to **6** with $[Bi(O^tBu)_3]$. 68

Scheme 4: Synthesis of heteroleptic Bi(III) thiolates **2-7** to **2-12** from the reaction of the sodium salt of **1** to **6** and $[BiPh_2Cl]$. 70

Scheme 5: Synthesis of heteroleptic Bi(III) thiolates from two equivalents of the sodium salt of **3** and $BiPhCl_2$ resulted in the formation of mixed species **2-9** and **2-9'.** 74

Scheme 6: Proposed solution-state thione-thiol tautomerization of PFTz, **5.** 84

Scheme 7: Preparation of arylrhodanine derivatives **7** to **11** from substituted aldehydes and rhodanine. 108

Scheme 8: Formation of heteroleptic diphenylbismuth(III) thiolates of the form $[BiPh_2(SR)]$ **2-13** to **2-17**, derived from rhodanine precursors **7** to **11.** 109

Scheme 9: Preparation of pyridyl and furan substituted thiones **1-6, 12** and **13** from acid hydrazides and substituted aryl isothiocyanates.[437] 158

Scheme 10: Synthesis of the neutral rhenium triazolato complexes and summarized general structure using an acetonitrile solvent system with the addition of an excess of triethylamine under microwave conditions. 159

Scheme 11: Preparation of 2-pyridyl substituted thiones **14-17** from picolinic acid, picolinohydrazide and substituted aryl isothiocyanates. 200

Scheme 12: Synthetic methods used to prepare rhenium(I) tricarbonyl complexes of the form *fac*-$[Re(N^N)(CO)_3X]$ **3-13** to **3-16** from triazoles **14-17** 202

Scheme 13: Synthetic route employed to synthesize $GaPh_3$ via the one-pot transmetallation of $HgPh_2$ and $Ga_{(m)}$. 232

Scheme 14: Synthetic pathway utilized for the preparation of a tris-substituted gallium(III) triazole thiolate from [$Ga(NO_3)_3.9H_2O$] and triazole **1**. 233

Scheme 15: Synthetic pathway utilized for the preparation of a tris-substituted gallium(III) triazole thiolate from $GaCl_3$ and triazole **1**. 234

Scheme 16: Synthetic pathway utilized for the preparation of a tris-substituted gallium(III) triazole thiolate from the direct metathesis of $GaCl_3$ and triazole **15**. . 234

Scheme 17: Synthetic pathway utilized for the preparation of a mono-substituted gallium(III) triazole thiolate from the telescopic isolation of $GaMe_3$ and triazole **1**. 235

List of Tables

Table 1: Chemical properties of gallium(III) and iron(III).[179,180] 27

Table 2: Summary of yields and appearances of homoleptic tris-substituted Bi(III) thiolato complexes **2-1** to **2-6**, (d.c. refers to decomposition) 69

Table 3: Summary of yields and appearances of heteroleptic diphenylbismuth(III) thiolato complexes **2-7** to **2-12** whereby PTz = **1**, PTTz = **2**, POTz = **3**, PCTz = **4**, PFTz = **5**, and PDTz = **6** 73

Table 4: Reactions and conditions employed for the attempted synthesis of phenylbismuth(III) bis-thiolate complex **2-9'.** 75

Table 5: Characteristic FT-IR assignments in precursors **1** to **6**. (br) = broad, (s) = strong (m) = moderate. **pyr**= pyridine, **tz**= triazole. 78

Table 6: Characteristic IR assignments in complexes **2-1** to **2-12** of the form $[Bi(SR)_3]$ and $[BiPh_2(SR)]$ 80

Table 7: Selected bond lengths (Å) and angles (°) of the solid-state structures of heteroleptic Bi(III) thiolate complexes **2-7, 2-8, 2-11** and **2-12** 91

Table 8: Antibacterial activities of complexes **2-7** to **2-12** and BiPh3 against MRSA, VRE, *E. coli, P. aeruginosa*, *C. albicans* and *C. auris*. The MICs of the *tris*-substituted complexes **2-1** to **2-6** were not included in the table as they showed no antibacterial activities up to 200 µM in disc diffusion assays. 98

Table 9: Selectivity index (SI) of complexes **2-7** to **2-12**. The SI is calculated using the MICs against bacterial and fungal strains and the IC_{50} against cos-7 cells. 105

Table 10: Summary of yields and appearances of heteroleptic diphenylbismuth(III) rhodanine complexes **2-13** to **2-17** whereby BR = benzylidene rhodanine **7**, MOBR = p-methoxybenzyl rhodanine **8**, 3MOBR = *tris-p*-methoxybenzylrhodanine **9**, InR = indole rhodanine **10**, and ThR = thiophene rhodanine **11**. 110

Table 11: Characteristic IR assignments in precursors **7** to **11** and complexes **2-13** to **2-17**. (br) = broad, (s) = strong (m) = moderate. 112

Table 12: Selected bond lengths (Å) and angles (°) of the solid-state structures of heteroleptic Bi(III) thiolate complexes of the form [$BiPh_2(SR)$], **2-13** to **2-16**. * Refers to bond lengths associated with dimerized structures. 117

Table 13: Selectivity index (SI) of complexes **2-13** to **2-15** and **2-17** the SI is calculated using the MICs against C. albicans and the IC_{50} against cos-7 cells. 128

Table 14: Summary of yields and appearances of Re(I) tricarbonyl bpy/phen ancillary triazole complexes **3-1** to **3-12**, (d.c. refers to decomposition). 160

Table 15: CO stretching frequency values in cm^{-1} of the prepared neutral rhenium complexes where A = symmetric in-phase stretching, B = total symmetric out-of-phase stretching and C = asymmetric stretching. 171

Table 17: Selected bond lengths (Å) and angles (°) of the solid-state structures of neutral Re(I) bipyridyl triazole thionate complexes **3-1, 3-3, 3-5** and **3-6.** 178

Table 18: Torsion angles (θ) in Re(I)-triazole complexes **3-7** to **3-11**. 180

Table 19: Selected bond lengths (Å) and angles (°) of the solid-state structures of neutral Re(I) phenanthroline triazole thionate complexes **3-7** to **3-11.** 181

Table 20: Summarised photophysical data obtained for complexes **3-1** to **3-12** of the general form *fac*-[Re(N^N)$(CO)_3$(**L**)] from diluted DCM solutions (*ca*. 10^{-5} M). 183

Table 21: Summary of yields and appearances of Re(I) tricarbonyl complexes of the form *fac*-[Re(N^N)$(CO)_3$Cl] (where N^N = *ortho*-pyridyl triazole thione) **3-13** to **3-16** (d.c. refers to decomposition). 203

Table 22: Characteristic FT-IR assignments in triazole thione precursors **14** to **17**. (br) = broad, (s) = strong (m) = moderate. **pyr**= pyridine, **tz**= triazole 208

Table 23: CO stretching frequency values in cm^{-1} of complexes **3-13** to **3-16** where A= symmetric in-phase stretching, B= total symmetric out-of-phase stretching and C = asymmetric stretching. 209

Table 24: Selected bond lengths (Å) and angles (°) of the solid-state structures of neutral Re(I) bipyridyl triazole thionate complexes **3-13.** 211

Table 25: Summarized photophysical properties of the Re(I) tricarbonyl complexes **3-13** to **3-16** of the form *fac*-[Re(N^N)(CO)$_3$Cl] (whereby = N^N = *ortho*-pyridyl triazole thione) from diluted DCM solutions (ca. 10^{-5} M)..... 217

Abbreviations

3DED	3D electron diffraction
4-MTT*H*	4-methyl- 4H-1,2,4-triazole-3-thiol
5-FC	5-fluorocytosine
5-FU	5-fluoruracil
Å	Angstrom
A549	Lung carcinoma epithelial cells
ABC	ATP-binding cassette
AMR	Antimicrobial resistance
aPDT	Antimicrobial Photodynamic therapy
API	Active pharmaceutical ingredient
AR	Antibiotic resistance
ATP	Adenosine triphosphate
B3LYP	Density functional theory basis set
BAL	2-3-dimercapto-1-propanol
BDI	Biomedical Discovery Institute
BHI	Brain Heart Infusion
BiOCl	Bismuth(III) oxychloride
BLI	B-lactamase inhibition
bpy	2,2'-bipyridine
BSA	Bovine serum albumin
BSS	Bismuth(III) subsalicylate
BT	Bismuth thiol
C_6D_6	Deuterated benzene
C auris	*Candida auris*
C. glabrata	*Candida glabrata*
C. haemulonii	*Candida. haemulonii*
CBS	Bismuth(III) subcitrate
CCDC	Cambridge crystallographic database
CDC	Centre for Disease control (USA)
CF_3SO_3	Triflate
CFU	Colony forming units
CH_3	Methyl
CH_3OH	Methanol

CO	Carbonyl
CO_2	Carbon dioxide
CORM	CO-releasing molecule
COSY	COrrelated SpectroscopY
COVID	Coronavirus Disease 2019
CTZ	Clotrimazole
CuAAC	Copper Catalysed Azide Alkyne Cycloaddition
CVD	Chemical vapour deposition
cys*H*	Cysteine
CYP	Cytochrome P450
CYP51	Cytochrome P450 14α-sterol demethylases
D_2O	Deuterated water
DCM	Dichloromethane
DFI	Diabetic foot infection
DFO	Desferrioxamine
DFT	Density Function Theory
DMEM	Dulbecco's Modified Eagle Medium
DMF	Dimethylformamide
DMSO	Dimethyl sulfoxide
DSC	Differential Scanning Calorimetry
EDG	Electron Donating group
EDT	1,2-ethanedithiol
EPS	Extracellular polysaccharide
ERG11	Lanestrol-14α-demethylase
ERG6,	Sterol methyltransferase gene
Escherichia coli	*E. coli*
ESI	Electrospray Ionization
ESKAPE	*Enterococcus faecium, Staphylococcus aureus, Klebsiella pneumoniae, Acinetobacter baumannii, Pseudomonas aeruginosa, and Enterobacter species*
ETC	Electron transport chains
EWG	Electron Withdrawing group
FBS	Foetal Bovine Serum
FCZ	Fluconazole
FDA	Food and Drug Administration

FT-IR	Fourier Transform Infrared spectroscopy
Galleria mellonella	*G. mellonella*
Ganite	Gallium nitrate
GM	General methodology
GM-MIC	Geometric mean of the Minimum Inhibitory Concentration
GP	General synthetic procedure
GSH	Glutathione
GSSG	Glutathione disulfide
H_2O_2	Hydrogen peroxide
HEK-293	Human embryonic kidney 293 cells
Helicobacter pylori	*H. pylori*
HGT	Horizontal gene transfer
HIV	Human immunodeficiency virus
HMBC	Heteronuclear Multiple Bond Correlation
HNO_3	Nitric acid
HOMO	Highest occupied molecular orbital
HPLC	High-performance liquid chromatography
HRMS	High resolution mass spectrometry
HSAB	Hard Acid Soft Base Theory
HSQC	Heteronuclear single quantum coherence spectroscopy
HT-29	Human colorectal adenocarcinoma cell line
HTS	High throughput screening
IC	Internal conversion (fluorescence)
IC_{50}	Inhibitory concentration at 50 % of a given population
ICP-MS	Inductively coupled plasma mass spectrometry
IFI	Invasive Fungal infection
IL	Intraligand
ILCT	Intraligand charge transfer
INH	Isonicotinohydrazide
IR	Infra-Red
IRF	Instrument response function
ISC	Intersystem Crossing
IUPAC	International Union of Pure and Applied Chemistry
KP46	*Tris*-(8-quinolinolato)gallium(III)
KTZ	Ketoconazole

L	Ligand
L929	Connective mouse tissue cells
LA	Lactic Acid
LANL2DZ	Density functional theory basis set
LB	Luria-Bertani
LC	Ligand-centred charge transfer
LD_{50}	Lethal dose to 50% of a large number of test animals of a particular species
LDH	Lactate dehydrogenase
LED	Light-emitting diode
LLCT	Ligand-to-Ligand Charge Transfer
LUMO	Lowest unoccupied molecular orbital
MBL	Metallo-β-lactamase
MBN-101	Pravibismane
MC	Metal-centred charge transfer
MCF-7	Breast cancer cell line
MCZ	Miconazole
MDR	Multidrug resistance
MeCN	Acetonitrile
MFC	Minimal fungal concentration
MIC	Minimum Inhibitory Concentration
MLCT	Metal-to-ligand charge transfer
MLLCT	Metal-ligand-to-ligand charge transfer
MO	Molecular orbital
MP	Melting point
MRSA	Methicillin resistant Staphylococcus aureus
ms	Millisecond
MT	Metallothionein
MW	Microwave
NCT	US national clinical trial identifier number
NDM-1	New Delhi metallo-ß-lactamase-1
NHC	N-heterocyclic carbene
NMR	Nuclear Magnetic Resonance
NSAID	Non-Steroidal Anti-Inflammatory Drugs
NTPase	Nucleoside triphosphate hydrolase

O_2.-	Reactive Oxygen Species
OH	Hydroxide
PAINS	Pan assay interference compound
PBI	Pyridylbenzimidazole
PBO	2-phenylbenzoxazole
PBS	Phosphate buffered saline solution
PCZ	Posaconazole
PDT	1,3-propanedithiol
PF_6	Hexafluorophosphate
PH	Picolinohydrazide
phen	1,10-phenanthroline
PhotoCORM	Photoinduced CO-Release Molecules
PMT1	Mannosyl transferase 1 enzyme
PNA	Peptide nucleic acid
Pseudomonas aeruginosa	*P. aeruginosa*
RBC	Bismuth(III) ranitidine subcitrate
Rhizoctonia bataticola	*R. bataticola*
ROS	Reactive Oxygen Species
RPMI	Roswell Park Memorial Institute Medium
RSD	Relative standard deviation
S_0	Ground state (fluorescence)
S1	Excited state (fluorescence)
SALP	Stereochemically active lone pair
SAR	Structure Activity Relationship
SEM	Scanning electron microscopy
SF	Solvent-free
SI	Selective index
SKOV3	Ovarian cancer cell line
SM	Solvent-mediated
SO_3CF_3	Triflate
SQLE	Squalene epoxidase
SSD	Silver sulfadiazine
Staphylococcus aureus	*S. aureus*
T_1	Singlet excited state
TD-DFT	Time Dependent-Density Functional Theory

Tg(fabp10a:EGFP)	Zebrafish embryo models
TGA	Thermogravimetric Analysis
THF	Tetrahydrofuran
TLC	Thin Layer Chromatography
TNBC	Triple negative breast cancer
TSC	Thiosemicarbazone
UDP	Uridine diphosphate
UV	Ultra-violet
VRE	Vancomycin-resistant Enterococcus
VSEPR	Valence shell electron pair repulsion
WHO	World Health Organisation
YNB	Yeast Nitrogen Base
YPD	Yeast Extract-Peptone-Dextrose

Contents

Copyright notice I

Declaration II

Abstract III

Publications and presentations V

Acknowledgements VI

List of Figures VIII

List of Schemes XXI

List of Tables XXIII

Abbreviations XXVI

Contents XXXII

1 Introduction 3

1.1 Antimicrobial resistance (AMR) 3

1.1.1 Modes of drug resistance 5

1.1.1.1 Antibacterial drug resistance 6

1.1.1.2 Antifungal drug resistance 7

1.2 Metals in medicine 11

1.2.1 Metal-based antibacterial agents 13

1.2.2 Metal-based antifungal agents 15

1.2.3 Metal-based anticancer agents 19

1.2.4 Bismuth in medicine 20

1.2.5 Rhenium in medicine 24

1.2.6 Gallium in medicine 26

1.3 Heterocyclic chemistry 30

1.3.1 N-heterocyclic azoles 31

1.3.1.1 Triazoles 32

1.3.1.2 Triazole thiones 36

1.4 Metal triazoles as therapeutic agents 42

1.4.1 Metal triazoles bearing antifungals 44

1.5 Research Significance 48

2 Bismuth(III) N-heterocyclic thiolates 53

2.1 Introduction 53

2.1.1 The biological action of bismuth(III) 53

2.1.2 Antibacterial bismuth(III) complexes 54

2.1.2.1 Antibacterial bismuth(III) thiolates 56

2.1.3 Antifungal bismuth(III) complexes 57

2.1.4 Bismuth(III) thiolates 59

2.1.5 Rhodanines: 5-substituted 2-thioxothiazolidin-4-ones 61

2.1.5.1 Rhodanine-based antimicrobials 62

2.2 Chapter objectives 64

2.3 Part 1: Results and discussion – triazoles 66

2.3.1 Synthesis and spectroscopic characterization of disubstituted 1,2,4-triazole-3-thiols 66

2.3.2 Synthesis of [$Bi(SR)_3$]: Homoleptic *tris*-substituted Bi(III) thiolates 67

2.3.3 Synthesis of [$BiPh_2(SR)$]: Heteroleptic diphenylbismuth(III) thiolates 70

2.3.4 Attempted synthesis of [$BiPh(SR)_2$]: Heteroleptic phenylbismuth(III) *bis*-thiolato complexes 74

2.3.5 Fourier Transform Infra-red (FT-IR) characterization 77

2.3.6 Nuclear Magnetic Resonance (NMR) studies 81

2.3.6.1 NMR spectroscopy of homoleptic tris-substituted bismuth(III) thiolates 81

2.3.6.2 NMR Spectroscopy of heteroleptic diphenylbismuth(III) thiolates 83

2.3.6.3 NMR Spectroscopy of the attempted heteroleptic phenylbismuth(III) bis-thiolates 85

2.3.7 High resolution mass spectrometry (HRMS) of Bi(III) thiolato complexes 86

2.3.8 X-ray crystallography 87

2.3.9 Solution-state stability studies 93

2.3.9.1 Stability in PBS 94

2.3.9.2 Stability in cell culture media 95

2.3.9.3 Stability in the presence of glutathione 96

2.3.10 Biological studies 97

2.3.10.1 Antimicrobial testing of heteroleptic diphenylbismuth(III) thiolates 97

2.3.10.2 Cytotoxicity assay 99

2.3.10.3 Bacterial cell uptake studies 101

2.3.10.4 Mammalian cell viability 102

2.3.10.5 Selectivity 105
2.3.10.6 Haemolysis assay 106
2.3.10.7 Summary of biological results 107
2.4 Part 2: Results and discussion – Rhodanines 108
2.4.1 Synthesis and spectroscopic characterization of a series of 5-substituted 2-thioxothiazolidin-4-ones (rhodanines) 108
2.4.2 Synthesis of heteroleptic phenylbismuth(III) rhodanines 109
2.4.3 FT-IR Characterization 110
2.4.4 HRMS and elemental analyses 112
2.4.5 NMR spectroscopy of heteroleptic phenylbismuth(III) rhodanines 113
2.4.5.1 ^{1}H NMR spectroscopy 113
2.4.5.2 ^{13}C NMR spectroscopy 114
2.4.6 X-ray crystallography 116
2.4.6.1 Computational analyses 119
2.4.7 Solution state stability studies 120
2.4.7.1 Stability in PBS 120
2.4.7.2 Stability in S-containing molecules 121
2.4.8 Biological Studies 123
2.4.8.1 Antifungal studies 123
2.4.8.2 Mammalian cell viability studies 126
2.5 Conclusions and future objectives 129
3 Rhenium(I) N-heterocyclic thiones 137
3.1 Introduction 137

3.1.1 Rhenium(I) in biological systems 139

3.1.2 Therapeutic applications of Re(I) complexes 140

3.1.3 Re(I) complexes as antibacterials 141

3.1.4 Re(I) complexes for fungal applications 143

3.1.5 Re(I) complexes as imaging agents 144

3.1.6 The photophysical properties of transition metal complexes 147

3.1.7 Tuning the photophysical properties of Re(I) complexes 150

3.1.8 Rhenium(I) N-heterocyclic chemistry 151

3.1.8.1 Rhenium(I) backbone triazoles 155

3.2 Chapter objectives 157

3.3 Part 1: Results and discussion –ancillary triazoles 158

3.3.1 Synthesis and spectroscopic characterization of disubstituted 1,2,4-triazole-3-thiones 158

3.3.2 Synthesis of neutral Re(I) p-triazole complexes 158

3.3.3 NMR spectroscopy 163

3.3.3.1 ^{1}H NMR studies 163

3.3.3.2 ^{13}C NMR studies 166

3.3.4 FT-IR spectroscopy 169

3.3.5 X-ray crystallography 174

3.3.6 Photophysical investigations 182

3.3.7 Stability studies 186

3.3.7.1 PBS stability studies 190

3.3.7.2 Media stability studies 191
3.3.7.3 Glutathione stability studies 193
3.3.8 Biological studies 194
3.3.8.1 Mammalian cell viability 195
3.3.8.2 Antibacterial testing 196
3.3.8.3 Antifungal testing 198
Part 2: Results and discussion – backbone triazoles 200
3.3.9 Synthesis and spectroscopic characterization of o-pyridyl-1,2,4-triazole-3-thiones 200
3.3.10 Synthesis of backbone Re(I) o-triazole complexes 201
3.3.11 NMR spectroscopy 204
3.3.11.1 ^{1}H NMR studies 204
3.3.11.2 ^{13}C NMR studies 205
3.3.12 FT-IR spectroscopy 207
3.3.13 X-ray crystallography 209
3.3.14 Stability studies 213
3.3.14.1 Glutathione stability studies 215
3.3.15 Photophysical investigations 216
3.3.16 Mammalian cell viability 219
3.4 Conclusions and future objectives 220
4 Gallium(III) N-heterocyclic thiones 225
4.1 Introduction 225

4.1.1 Iron acquisition in biological systems 225

4.1.1.1 The relationship between Fe(III) and Ga(III) 227

4.1.2 The biological properties of Gallium(III) 227

4.1.3 Gallium(III) antifungals 228

4.2 Chapter objectives 229

4.3 Statement of challenges 229

4.4 Results and discussion 230

4.4.1 Synthesis and spectroscopic characterization of precursor triazoles 230

4.4.2 Synthesis of Ga(III) precursors 231

4.4.3 Attempted synthesis of [$Ga(SR)_3$]: homoleptic *tris*-substituted Ga(III) thiolates 232

4.4.4 Attempted synthesis of [$Ga(Me)_2(SR)$]: Heteroleptic dimethylgallium(III) thiolates 235

4.4.5 Attempted synthesis of [$Ga(Ph)_2(SR)$]: heteroleptic diphenylgallium(III) thiolates 236

4.5 Conclusions and future objectives 237

5 General conclusions and future perspectives 241

6 Experimental 247

6.1 General Procedures 247

6.1.1 Biological testing 248

6.1.1.1 Bacterial testing 248

6.1.1.2 Zone of inhibition assay 249

6.1.1.3 Minimum inhibitory concentration (MIC) assay 249

6.1.1.4 Fungal testing 249

6.1.1.5 Fungal cell viability 250

6.1.1.6 Mammalian cell viability 250

6.2 Chapter 2 251

6.2.1.1 Bacterial cell uptake 251

6.2.1.2 ICP-MS 251

6.2.1.3 Bacterial membrane integrity assay 251

6.2.1.4 Haemolysis assay 252

6.2.2 Precursor syntheses 252

6.2.2.1 Synthesis of Bismuth(III) tert-butoxide, [$Bi(O^tBu)_3$] 252

6.2.2.2 Synthesis of triphenylbismuth(III) 253

6.2.2.3 Synthesis of diphenylbismuth(III) chloride, [$BiPh_2Cl$] 253

6.2.2.4 Synthesis of phenylbismuth(III) dichloride, [$BiPhCl_2$] 253

6.2.2.5 Synthesis of triazole thiolates 254

6.2.2.6 Synthesis of arylrhodanines 254

6.2.3 General synthetic procedures 254

6.2.3.1 GP1: Synthesis of [$Bi(SR)_3$]: Homoleptic tris-substituted bismuth(III) triazole thiolates. 254

6.2.3.2 GP2: Synthesis of [$BiPh_2SR$]: Heteroleptic diphenylbismuth(III) triazole thiolates. 254

6.2.3.3 GP3: Synthesis of [$BiPh_2SR$]: Heteroleptic diphenylbismuth(III) rhodanine thiolates. 255

6.2.4 [$Bi(SR)_3$]: *Tris*-substituted bismuth(III) triazole thiolato complexes 255

6.2.5 [$Bi(Ph)_2SR$]: Diphenylbismuth(III) triazole thiolato complexes 257

6.2.6 [Bi(Ph)$_2$SR]: Diphenylbismuth(III) rhodanine complexes 259

6.3 Chapter 3 261

6.3.1 Photophysical measurements 261

6.3.2 Precursor synthesis 262

6.3.2.1 Synthesis of rhenium(I) tricarbonyl diimine salts, [Re(N^N)(CO)$_3$Cl] 262

6.3.2.2 Synthesis of rhenium(I) solvate complexes, [Re(N^N)(CO)$_3$(solv)][SO$_3$CF$_3$] 263

6.3.3 General synthetic procedures 263

6.3.3.1 GP4: Synthesis of [Re(N^N)(CO)$_3$(L)]: phen/bpy-derived Re(I) tricarbonyl ancillary triazole complexes. 263

6.3.3.2 Synthesis of [Re(N^N)(CO)$_3$X]: Re(I) tricarbonyl backbone triazole complexes 264

6.3.4 [Re(N^N)(CO)$_3$(L)]: phen/bpy-derived Re(I) tricarbonyl ancillary triazole complexes 264

6.3.5 [Re(CO)$_3$(L)X]: Re(I) tricarbonyl backbone triazole complexes 270

6.4 Chapter 4 272

6.4.1 Precursor synthesis 272

6.4.1.1 In-situ synthesis of [GaMe$_3$]: trimethylgallium(III) 272

6.4.1.2 Synthesis of [GaPh$_3$]: triphenylgallium(III) 272

6.4.2 General synthetic procedures 272

6.4.2.1 Attempted synthesis of tris-substituted gallium(III) triazole thiolate complexes 272

6.4.2.2 Attempted synthesis of dimethylgallium(III) triazole thiolate complexes from $GaCl_3$ 272

7 References 275

CHAPTER 1: LITERATURE REVIEW

ANTIMICROBIAL RESISTANCE

METALS IN MEDICINE

N-HETEROCYCLICS

RESEARCH SIGNIFICANCE

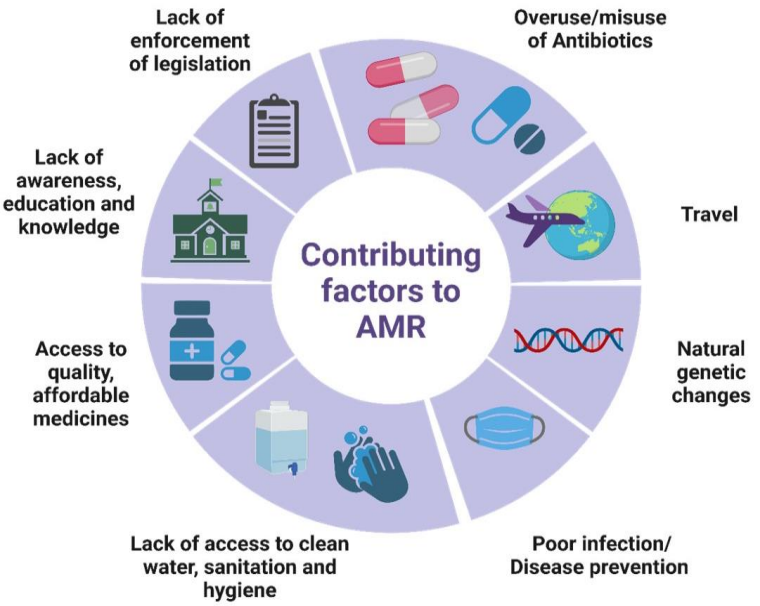

1 Introduction

1.1 Antimicrobial resistance (AMR)

"We are heading towards a post-antibiotic era which means, in effect, an end to modern medicine as we know it. Diseases as common as strep-throat or a child's scratched knee could once again kill."

- *Dr. Margaret Chan, 2013*

In 2013, the then Director-General of the World Health Organisation, Dr. Margaret Chan made this landmark statement,[1] placing considerable international attention on antimicrobial resistance (AMR, also known as antibiotic resistance, AR). Since then, the World Health Organization (WHO) has described AMR as one of the greatest threats we continue to face globally, now and into the future.[2–4]

AMR refers to the ability of microbes such as bacteria and fungi, to grow and proliferate in the presence of antibiotic treatments.[2,5,6] The issue of AMR continues to present itself through the overuse and misuse of therapeutics,[6,7] which has been exacerbated especially within the context of the current coronavirus COVID-19 pandemic.[8–12] As antibiotics have been deployed to treat secondary infections and comorbidities in COVID-19 patients,[10] this has aggravated the existing resistance selection pressures.[13–16] In a study conducted by Zhou and co-workers, two hospitals reported that 95 % of COVID-19 patients had been treated with antibiotics despite only 15 % of patients showing secondary bacterial infections.[17] Additionally, early reports indicated that of the patients who died from COVID-19, 50 % had presented with a secondary bacterial infection.[11,17]

In February 2019, the WHO published an extensive list of pathogens for which urgent antimicrobial stewardship is needed.[18–20] As part of this recent report, the list has encompassed six bacterial strains broadly referred to as the term "ESKAPE pathogens" (*Enterococcus faecium, Staphylococcus aureus, Klebsiella pneumoniae, Acinetobacter baumannii, Pseudomonas aeruginosa,* and *Enterobacter* species) for which growing multidrug resistance (MDR) and virulence have been detected. These pathogens are currently designated under the

"priority" status with the Gram-negative[1] bacteria *A. baumannii, P. aeruginosa* and *Enterobacteriaceae* elevated to a "Priority 1: critical" status.[18–21]

Over the last 20 years, the emergence of opportunistic fungal pathogens within hospital environments has increased the incidence of bloodstream infections, primarily in immunocompromised individuals.[22,23] Within the hospital setting, infection can occur through neonatal, surgical, haematological and burn unit environments.[23–26] The *Candida* genus represents a group of yeasts belonging to the fungal class *Ascomycota* and within this genus, over 20 different species have been identified and associated with human infection.[27,28] The *Candida* family of infections accounts for over 90% of invasive incidence attributed to the major strains: *Candida albicans (C. albicans), Candida glabrata (C. glabrata), Candida parapsilosis (C. parapsilosis), Candida tropicalis (C. tropicalis)* and *Candida krusei (C. krusei).* While *candida* generally remains dormant, the relationship between the species and host is altered in the presence of existing infection.

Extensive research has been employed into the social, economic, and medical impacts of AMR including the many strategies to mitigate its spread (Figure 1). A comprehensive review conducted by the WHO in 2019 detailed the estimated number of deaths due to AMR to top 10 million per year by 2050, in the instance where no action plan for antimicrobial stewardship is employed.[2,4,20,29–31] As frontline healthcare workers battle COVID-19, and the long-term public health issues like AMR are sidelined, the morbidity rate of AMR is expected to surpass this figure. The loss of life associated with routine invasive surgeries, and treatments like chemotherapy has allowed the rise of untreatable opportunistic microbes to place strain on healthcare systems.[8,11,14] There thus, is a great need for further research and the development of novel and improved treatments for AMR, particularly new chemical scaffolds.

[1] Species of bacteria can be broadly characterized as Gram-negative or Gram-positive. Gram-negative bacteria differ to Gram-positive by the thickness of the cell wall and membrane consisting of a "sandwiched" external phospholipid membrane, thick peptidoglycan layer and inner cell membrane).[503]

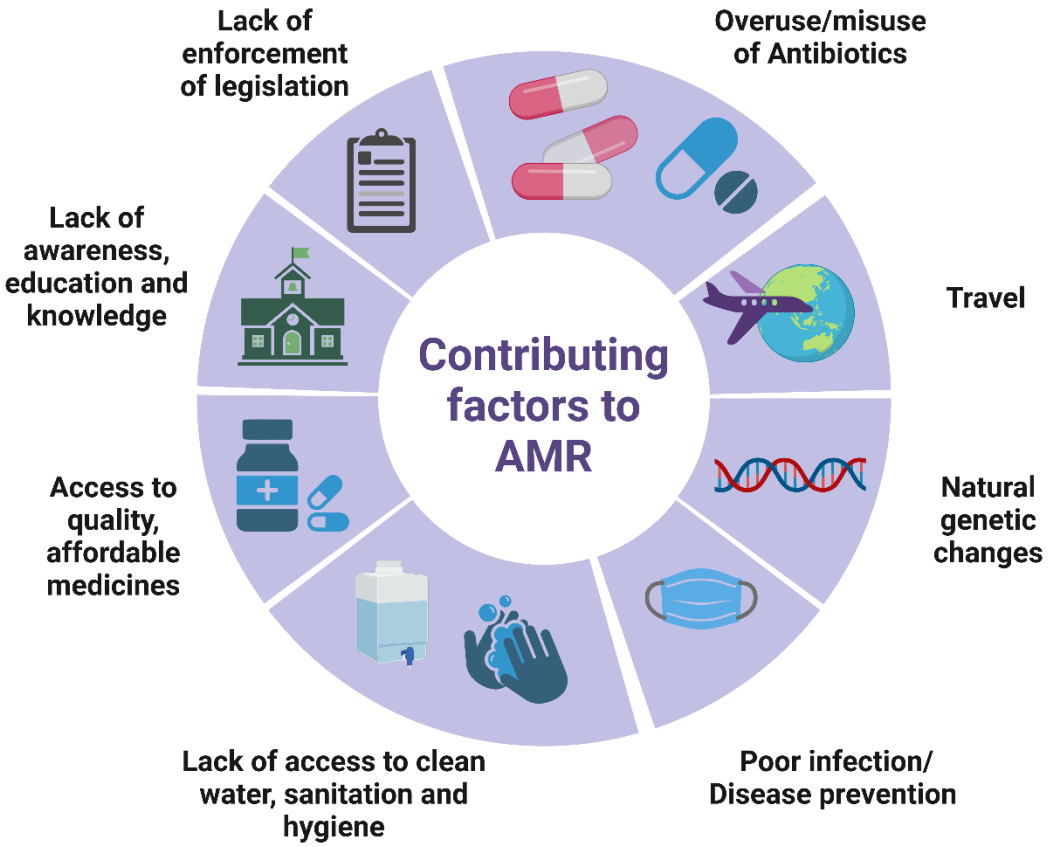

Figure 1: Contributing factors to the increasing occurrence of AMR, created with BioRender.[2,4]

1.1.1 Modes of drug resistance

The discovery of penicillin in 1928 by Sir Alexander Fleming served as a landmark event which created the boom in antibiotic discovery, also known as the 'golden era'. This period formed the basis of over half the antibiotics used today.[32,33] The pipeline for antibacterial drug development however, has since declined. The driving forces of molecular AMR processes which induce pressures on microbial populations within an environmental or organism (humans or animals) specific setting; these resistance mechanisms can be encoded through point mutations or horizontal gene transfer (HGT).[34,35] Specific examples of drug resistance can be summarized in the following section.

1.1.1.1 Antibacterial drug resistance

The most common resistance pathways generated by microbes include: enzyme modifications to target sites (Figure 2, antibiotic A: Linezolid), direct modification of the antibiotic (Figure 2, antibiotic B: Ampicillin), cell wall modifications (Figure 2, antibiotic C: Vancomycin) and via the expression of efflux pumps (Figure 2, antibiotic D: Levofloxacin).

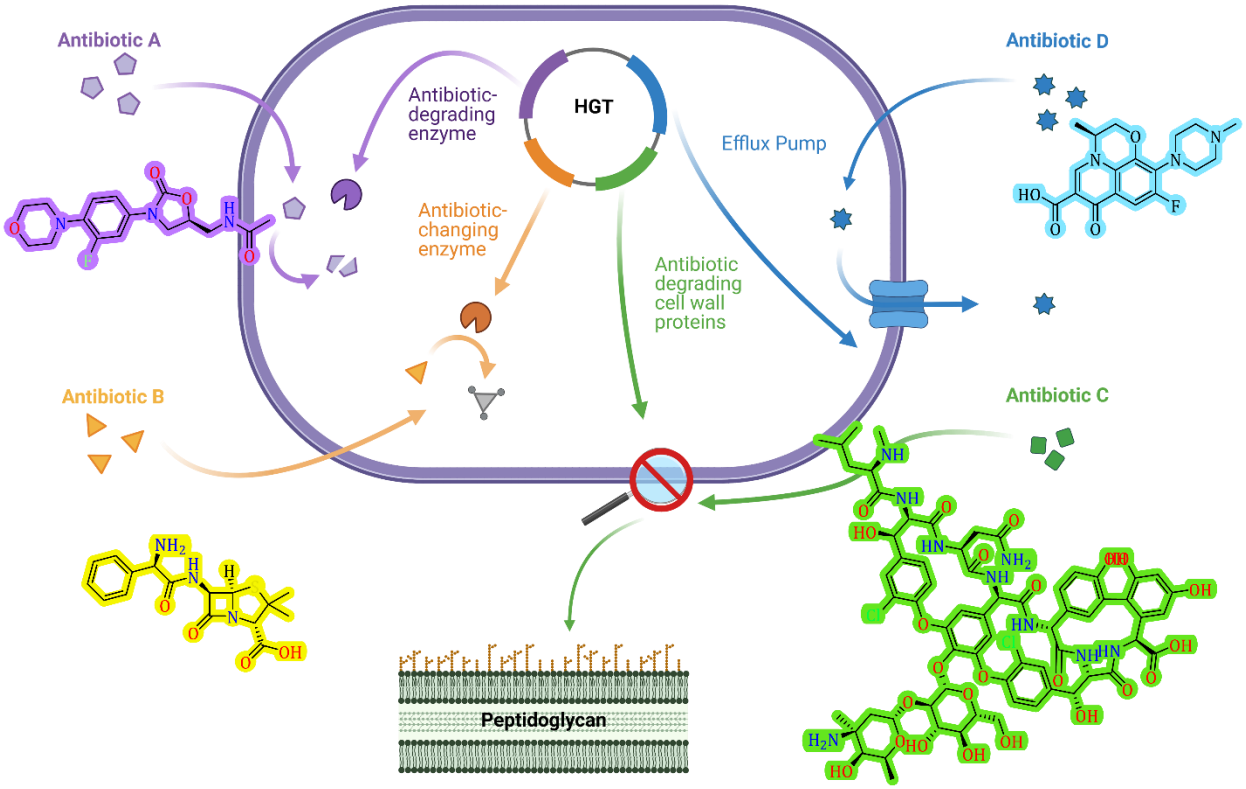

Figure 2: Summarised mechanisms of resistance observed in a microbial cell created on BioRender, whereby **A**: resistance of Linezolid via upregulation, **B**: resistance of ampicillin via chemical modification, **C**: resistance of Vancomycin via cell wall modification, and **D**: resistance of levofloxacin via efflux pump expression.

Bacteria can develop resistance to antibiotics by altering the structures of enzymes, receptors or target sites to reduce the binding affinity of the antibiotic; as a result, the antibiotic is unable to exert its effect.[36] Depicted as Antibiotic A in Figure 2, Linezolid was used to treat Gram-positive bacteria including Vancomycin resistant *Enterococcus* (VRE), Methicillin-resistant *Staphylococcus aureus* (MRSA) and

tuberculosis (Tb). Over time however, resistance was reported as a result of the structural modifications to the ribosomal target site.[36,37]

The most diverse mode of resistance deployed by bacteria involves the physical and chemical alteration of antibiotic compounds which results in the decreased binding affinity for their target sites.[38] Common chemical alteration pathways include: phosphorylation, glycosylation, thiol transfer, acyl transfer and nucleotidylation.[38] In 1940, after a strain of *E. coli* was shown to hydrolyze penicillin via metallo-β-lactamase (MBL) enzymes (Figure 3), this led to numerous studies into the inactivation of the β-lactam class of antibiotics.[39–43]

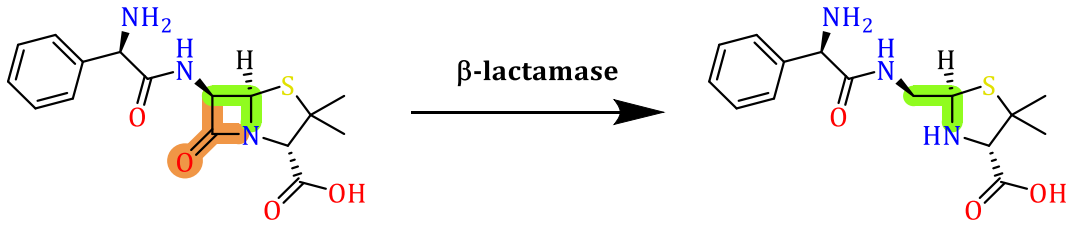

Figure 3: Generalised scheme for the degradation of penicillin via the use of a β-lactamase enzyme. β-lactam ring degradation highlighted in green, and liberation of CO_2 in orange.[43]

Bacterial cells can exhibit resistance to antibiotics by limiting the intracellular antibiotic concentrations inside a target cell.[34,44,45] The two pathways that this can be achieved by are reducing permeability of the cell wall (Figure 2, Antibiotic C), and via the overexpression of efflux pump systems to transport and expel the antibiotic (Figure 2, Antibiotic D). Gram-negative bacteria such as *K. pneumoniae* show innate resistance to large molecules such as vancomycin, as the molecule cannot penetrate the outer membrane of the cell due to its size and hydrophobicity.[34,35,38,46] Similarly, the overexpression of bacterial efflux pumps is an effective method to remove antibiotics from the cell, and this has been shown in certain species of *E. coli* through the removal of the fluoroquinolone, Levofloxacin.[47–49]

1.1.1.2 Antifungal drug resistance

Fungal cells are eukaryotic, which is a shared aspect with human cells.[22] Due to this, the development of antifungal drugs has been limited as it is difficult to establish specific metabolic and structural targets.[23,50,51] Specific modes of resistance among

the candida genus can be attributed to (but not limited to) site modification, abundance, overexpression, drug pump upregulation and biofilm formation, as summarised in Figure 4.[50,52] These mechanisms can occur either alone or concomitantly and can lead to cross-resistances across drugs.

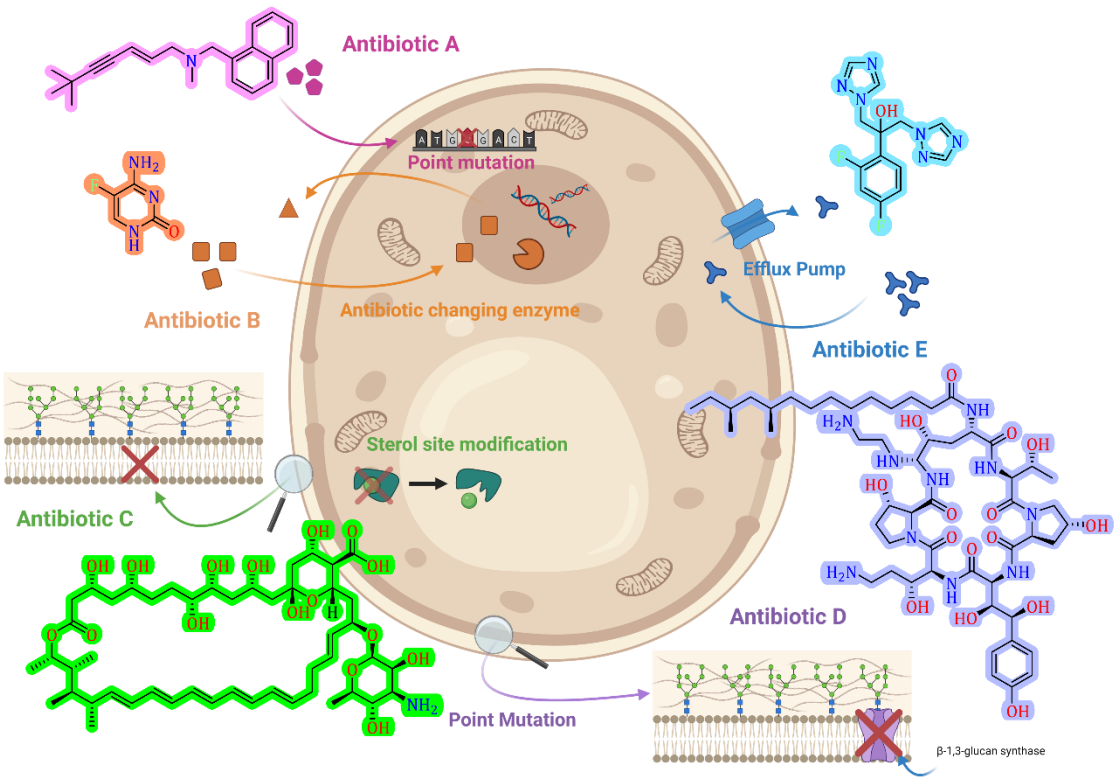

Figure 4: Mechanisms of resistance observed in a yeast cell whereby **A**: resistance of Terbinafine via squalene epoxidase point mutations, **B**: resistance of 5-Flucytosine via chemical modification, **C**: resistance of Amphotericin B via sterol site modification, **D**: resistance of caspofungin via FKS point mutations in 1,3-glucan synthase. **E:** resistance of fluconazole via efflux pump expression.

The use of allylamines such as Terbinafine (Figure 4, Antibiotic A) have been considered as the first-line therapeutic in dermatophyte infections.[53] Terbinafine predominantly targets the inhibition of squalene epoxidase (SQLE), which is a building block in the ergosterol biosynthetic pathway. In 2018 however, over 20 Terbinafine-resistant *Trichophyton interdigitale* isolates were identified through amino acid substitutions in SQLE, this was also observed in reports as early as 2016 for *C. albicans* species (Figure 4, Antibiotic A).[53–55]

One of the mechanisms by which fungal cells have developed resistance to conventional drugs include alteration to target sites via the point mutations in nucleobases. An example of this has been demonstrated with the drug Flucytosine (Figure 4, Antibiotic B). Developed in 1975, 5-fluorocytosine (5-FC) existed as a pro-drug which is taken up by fungal cells and converted to 5-flurouracil (5-FU), which is a toxic metabolite. However, resistance as recent as 2020 were identified by Billmyre and co-workers, whereby the accumulation of UDP-glucuronic acid in combination with alterations in nucleobase metabolic processes resulted in the suppression of both 5-FC and 5-FU (Figure 5) and thus, its use as an antifungal has declined.[56]

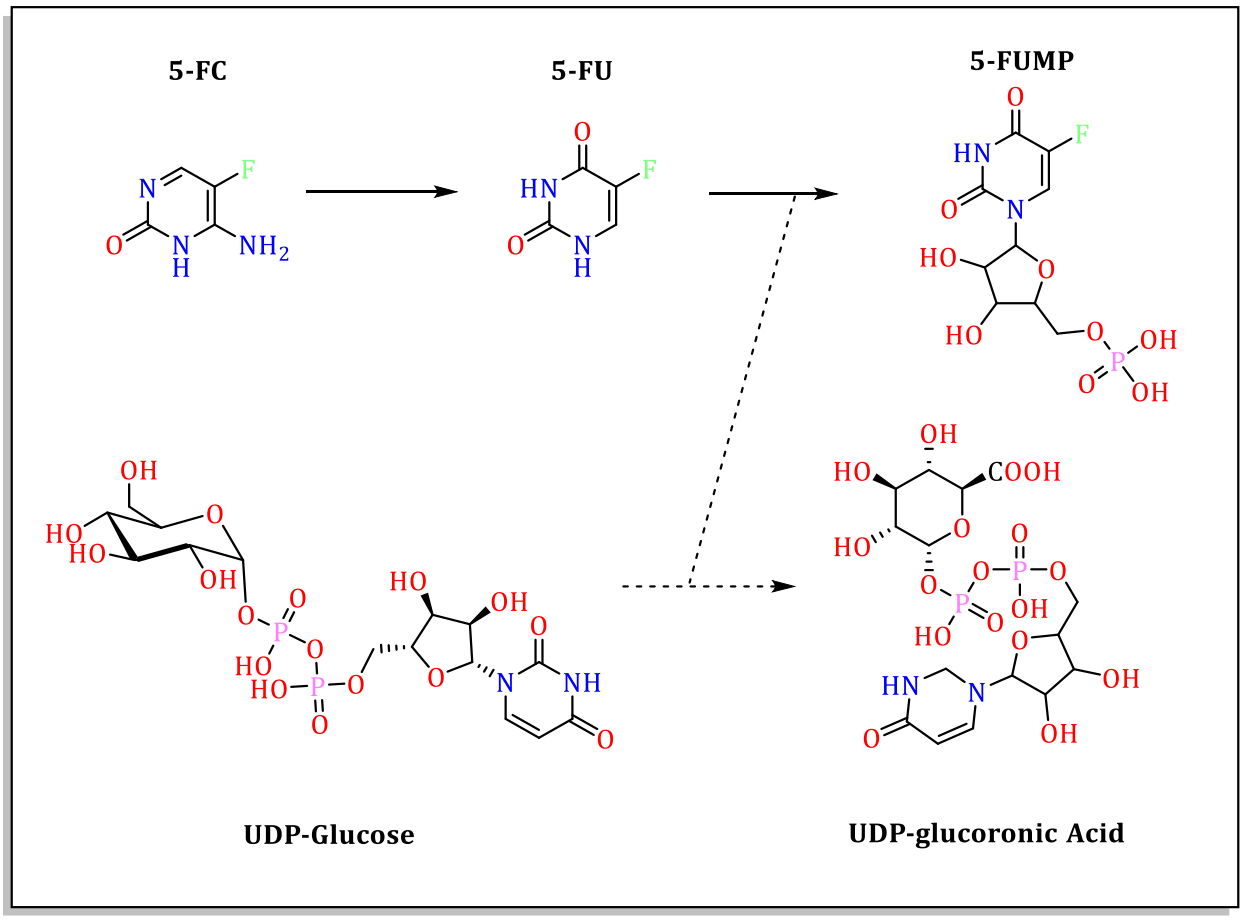

Figure 5: Simplified resistance mechanism of the antifungal drug flucytosine (5FC) and its metabolic by-product 5-fluoruracil (5FU) proposed by Billmyre and co-workers.[56]

First approved for treatment in 1957, conventional amphotericin B (Figure 4, Antibiotic C, AmpB) and other polyenes were the oldest commercially available drugs

which served as the gold-standard in antifungal therapy.[57] AmpB has been used in the treatment of Invasive Fungal Infections (IFIs) including Aspergillosis, Cryptococcosis, Blastomycosis, Candidemia and Coccidioidomycosis. However, due to its extreme renal toxicity, it has since been relegated to a second-line therapeutic.[24,50,52] The first known mechanism of AmpB resistance in a strain of *C. auris* was established in a 2021 study conducted by Rybak and co-workers whereby point mutations in the sterol methyltransferase gene, *ERG6,* synthetic pathway were identified.[58,59]

In recent times, the intrinsic resistance to echinocandin-based antifungals has been observed in *Candida* species. Micafungin, anidulafungin and caspofungin (Figure 4, Antibiotic D) represent the class of molecules which target the 1,3-β-D-glucan synthase component within the fungal cell wall.[60,61] There has been a steady emergence of echinocandin-resistant species through mutations in the *FKS1*and *FKS2* genes in 1,3-β-D-glucan synthase through amino acid substitutions resulting in the reduced susceptibility of the drug and consequent cross-resistance.[60–62]

Efflux pumps play a significant role in azole drug resistance as this mechanism involves the upregulation of plasma membrane and decreases the drug concentration within a cell.[52] In a representative example, the resistance to Fluconazole (Figure 4, Antibiotic E) can be attributed to two homologous ATP-binding cassette (ABC) transporters *Cdr1* and *Cdr2* especially with regards to patients suffering from chronic antifungal therapy.[51,60–62] Within the *Candida* species, the yeasts shown to display high genomic variability resulting in the total reduced susceptibility to azole antifungals.[23]

There is an urgent requirement for novel antibiotic drugs to combat AMR. Especially with regards to fungal resistance, all known efforts have narrowed outputs to just eight effective compounds listed in the World Health Organization Essential Medicines list.[63] Without effective treatments, microbes will continue to evolve survival mechanisms for overcoming existing antibiotics and evade therapies. Given the dramatic decrease in antimicrobial stewardship, this has emphasized the requirement for novel compounds with either a distinct mode of action (MoA) or multi-targeted therapy.[20,64] Attention has turned towards alternative avenues such

as repurposing existing drug candidates through the incorporation of metals to target different microbial pathways as well as open multiple modes of action.

1.2 Metals in medicine

The use of metals in medicine dates as far back as 2500 BC with the use of gold in Chinese medicine.[65,66] In the 16th century, copper was used in natural homeopathic treatments for illness and in the early 1900s, other metal compounds like auranofin and salvarsan (Figure 6) were used to treat conditions like rheumatoid arthritis and syphilis.[67] In modern medicine, Cisplatin has pioneered the field of metal-based anticancer therapeutics and led to the development of numerous analogues which continue to be used in chemotherapy.[68]

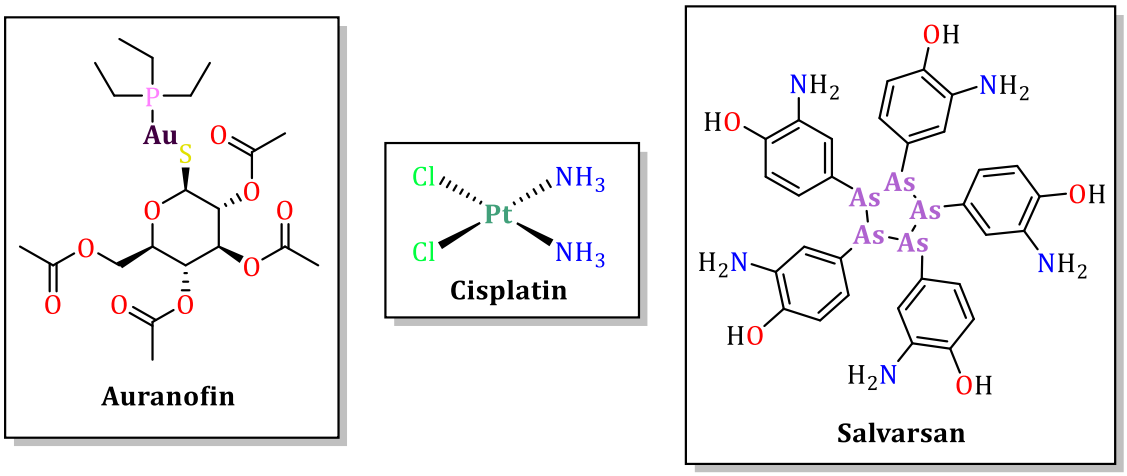

Figure 6: Empirical structures of some landmark metal-based complexes used in early medicine. Au(I) derivative Auranofin (left), cisplatin (middle) and colloidal structure of the As-derivative salvarsan (right).

The use of metals in biochemical processes has long been identified as innately therapeutic as metals have been used in essential cellular function. When reviewing the periodic table, the human body has been identified to require 20 essential elements to appropriately function, 10 of which are metals (Figure 7).[69] Following on from the '*golden era*' of antimicrobial discovery however, the use of metals as antibiotic agents had been overlooked by the boom in organic medicine.

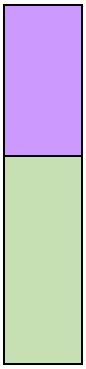

Bulk Biological elements

Trace elements essentials to humans

H																**He**
Li	**Be**											**B**	**C**	**N**	**O**	**F**	**Ne**
Na	**Mg**											**Al**	**Si**	**P**	**S**	**Cl**	**Ar**
K	**Ca**	**Sc**	**Ti**	**V**	**Cr**	**Mn**	**Fe**	**Co**	**Ni**	**Cu**	**Zn**	**Ga**	**Ge**	**As**	**Se**	**Br**	**Kr**
Rb	**Sr**	**Y**	**Zr**	**Nb**	**Mo**	**Tc**	**Ru**	**Rh**	**Pd**	**Ag**	**Cd**	**In**	**Sn**	**Sb**	**Te**	**I**	**Xe**
Cs	**Ba**	**La**	**Hf**	**Ta**	**W**	**Re**	**Os**	**Ir**	**Pt**	**Au**	**Hg**	**Tl**	**Pb**	**Bi**	**Po**	**At**	**Rn**
Fr	**Ra**	**Ac**	**Rf**	**Db**	**Sg**	**Bh**	**Hs**	**Mt**	**Ds**	**Rg**	**Cn**	**Nh**	**Fl**	**Mc**	**Lv**	**Ts**	**Og**

Ce	**Pr**	**Nd**	**Pm**	**Sm**	**Eu**	**Gd**	**Tb**	**Dy**	**Ho**	**Er**	**Tm**	**Yb**	**Lu**
Th	**Pa**	**U**	**Np**	**Pu**	**Am**	**Cm**	**Bk**	**Cf**	**Es**	**Fm**	**Md**	**No**	**Lr**

Figure 7: Simplified periodic table of elements highlighting the essential metals for life.

Today, metal nanoparticles, organometallic complexes (containing M-C bonds) and inorganic complexes have been incorporated in the treatment of many ailments including bacterial, fungal, cancer, viral and parasitic diseases.[67,70] As AMR continues to evade traditional organic-based drugs, metal complexes have been re-examined for their potential in combatting AMR due to their diverse modes of coordination spheres,

access to multiple oxidation states, redox chemistry, three-dimensionality, and the metal-to-ligand synergy which all play a significant part in therapeutic design.[71,72]

1.2.1 Metal-based antibacterial agents

Metals have been used as antibacterial agents for centuries with the most ubiquitous being silver (Ag).[72] Cationic silver, Ag(I) and nanoparticulate silver (AgNP) (Figure 8) are both topically applied antibacterials however, their MoA is still unknown.[73] It is unclear whether the MoA relies on the Ag(I) disrupting cellular processes, the nanoparticle producing an antibacterial response or whether a metal-to-ligand synergism is at play. Despite its use in metallotherapeutics, the associated cellular cytotoxicity, environmental accumulation and usage limitations pose as hurdles in the development of silver antimicrobials and thus, continues to be an area of improvement.[74]

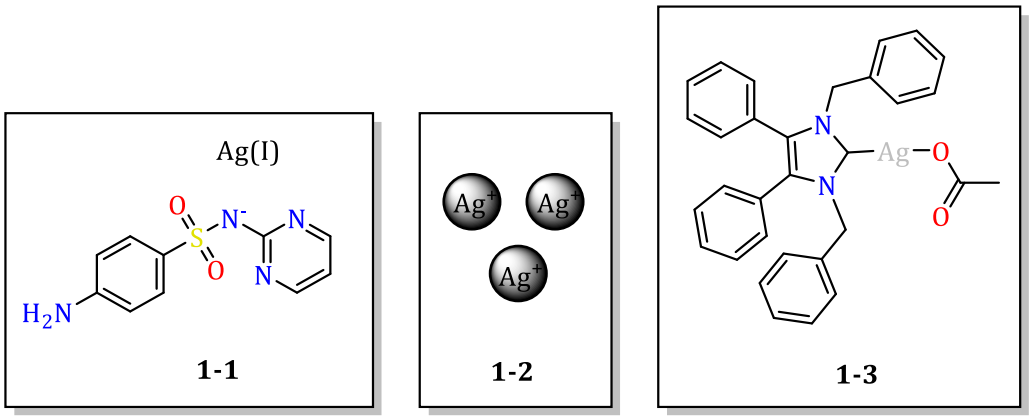

Figure 8: Empirical structures of **1-1:** silver sulfadiazine (**SSD**, A) and **1-2:** silver nanoparticles and **1-3:** 1,3-dibenzyl-4,5-diphenyl-imidazol-2-ylidene Ag(I) acetate (**SBC3**).[75]

The development of metal-based antibacterials primarily target metal homeostasis.[76] As iron plays an integral role in both bacterial and mammalian cell function to combat infection, the human body utilises '*nutritional immunity*' to prevent microbes from acquiring these nutrients.[76] Nutritional immunity refers to the sequestration of trace metals such as iron, manganese, copper and zinc by a host to limit microbial pathogenicity.[76,77] The primary mechanisms by which metals can be used to disrupt microbial function can be summarised in three processes: protein dysfunction, Reactive Oxygen Species (ROS) production, and membrane dysfunction.[74,78]

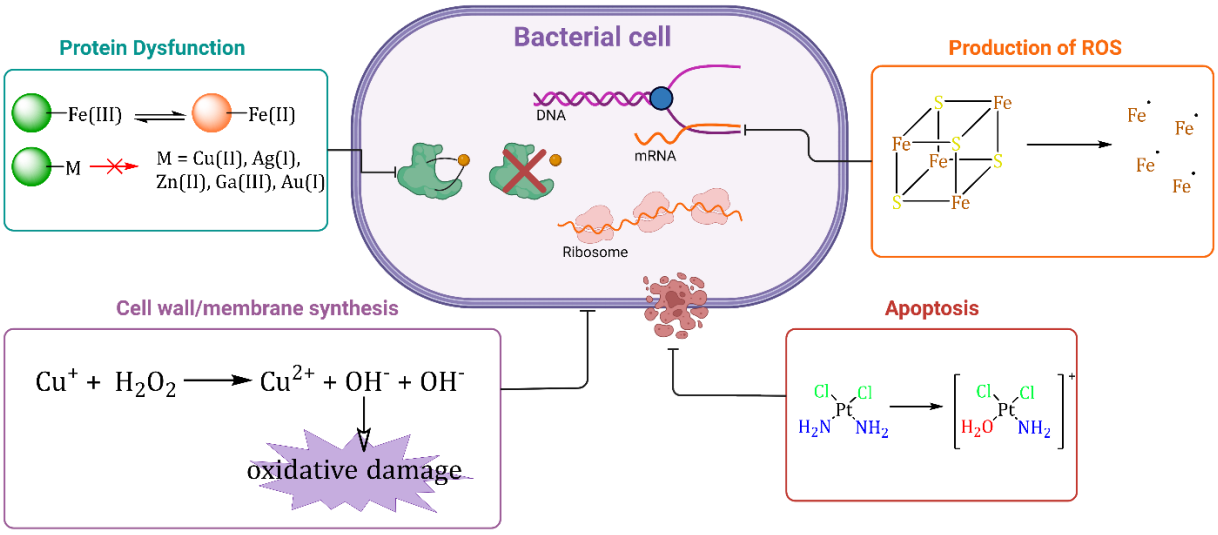

Figure 9: Metal antimicrobial mechanisms of action, created in BioRender.[34,72,76]

Metal antimicrobials are able to induce dysfunction in bacterial proteins through mismetallation.[79] Soft metals such as Cu(I), Ag(I), Hg(I), Cd(II), and Zn(II) can exchange with Fe(II), and disrupt enzymatic processes in a site-specific manner.[78,80] For example, the loss of protein function has been observed in *Mycobacterium tuberculosis (M. tuberculosis),* whereby Cu(I) ions disrupt the [4Fe-4S] dehydratase cluster resulting in the release of reactive Fe species causing ROS damage within the cell (Figure 9).[77,79,81–83]

The generation of Reactive Oxygen Species (ROS, singlet oxygen, $O_2^{\cdot-}$, H_2O_2) is known to cause damage to cellular contents such as DNA, proteins and membranes.[78,80] One of the forms of ROS generation is through the disruption of electron transport chains (ETC).[84] Although bacterial cells contain numerous electron rich sulfur scavengers to mitigate ROS such as cysteine, methionine, and glutathione (GSH), metal antimicrobials are able to evade these defences. Recently, the Au(I)-phosphine derivative Auranofin (Figure 6, Left) has shown promising antibacterial activity against *S. aureus* by targeting the redox enzyme thioredoxin reductase (TrxR).[85] The Au(I) species is able to irreversibly bind to TrxR and inhibit its activity resulting in cellular oxidative stress and ultimately intrinsic apoptosis.[86]

The degradation of cellular membranes is another primary target for metals. Morphological studies have identified Ag(I) to compromise the integrity of the

cytoplasmic membrane in *E. coli* cells. Similarly, Cu(II) ions have shown to attack respiratory enzymes within the cell membrane of *E. coli* by binding to sulfhydryl groups.[75,81,87,88]

Although there are significant challenges in the development of an appropriate metal-based antibacterial, their modes of action are both discrete and diverse. Through the induction of oxidative stress, protein dysfunction and membrane disruption, metal complexes have demonstrated the ability to damage pathogenic bacterial cells via multiple mechanisms.

1.2.2 Metal-based antifungal agents

At this time, the MoA of metal antifungals is largely underexplored and the rational design of molecules with improved antifungal activity is still empirical. Ribonucleotide reductase, mitochondria, lysosomes and mitogen-activated protein kinase cellular pathways are all known to be common between mammalian and fungal cells and have thus, been identified as potential target sites for metal-based antifungals.[59,89] However, specific to fungal cells is the disruption of metal homeostatic pathways involved in ergosterol synthesis, CYP51 generation, yeast-to-hyphal transitions, and adhesion.[23,59,90] Current MoA studies with metal-based agents however, have been limited to DNA interactions.[59]

The *in vitro* testing of metal antifungals has followed similar methodologies used for the assessment of metal antibacterials such as disc diffusion, zone of inhibition and broth dilution methods. Two recent expansive reviews conducted by Gasser *et al.,* and Frei *et al*., respectively, identified the rapidly expanding field of metal-based antifungals bearing a suite of organic ligand classes expanding beyond azoles,[15,91] Schiff bases,[92] thiosemicarbazones,[93] N-heterocyclics,[94,95] polypyridines,[96,97] amino acids,[98] and thiocarbamates.[59,99–103]

In 2021, Bajaj and co-workers explored the antifungal activity of a series of 155 thiosemicarbazone (TSC) derivatives and their metal complexes. The expansive study concluded the strongest candidates to be Cu(II) and Zn(II)-based complexes (Figure 10) which showed Minimum Inhibitory Concentration (MIC) values as low as 0.509 μM against *Rhizoctonia bataticola (R. bataticola*).[93,104] Overall, the general MoA of

these complexes were postulated to target the inhibition of ergosterol synthesis for fungal cell wall development.[93,104]

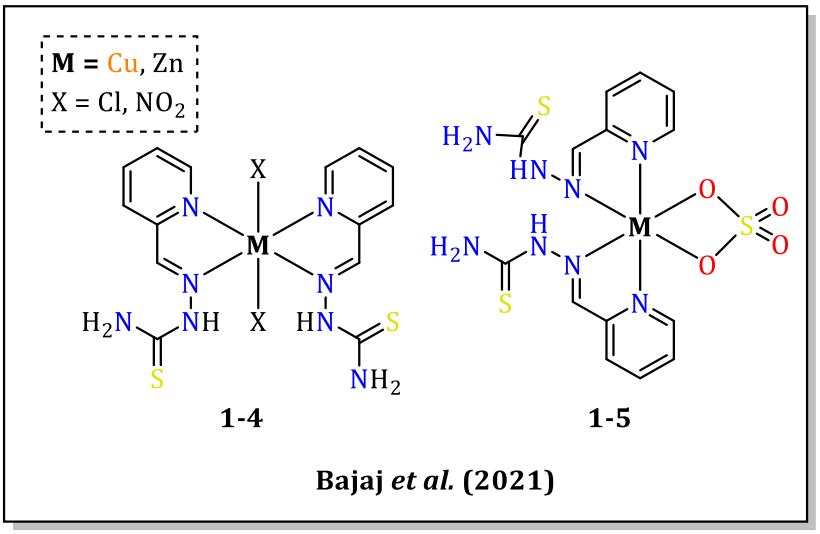

Figure 10: Examples of two antifungal Cu(II)- and Zn(II)-based thiosemicarbazone complexes synthesized by Bajaj and co-workers.[104]

In another study, Malik and co-workers identified a Ni(II) complex **1-6** (Figure 11) with appreciable antifungal activity (MIC values ranging from 1-32 µg/mL) against a selection of *C. albicans* isolates.[105] Flow cytometry studies revealed the MoA of these complexes to be via the ergosterol synthesis pathway, which was confirmed through the externalisation of cell phospholipids.[105]

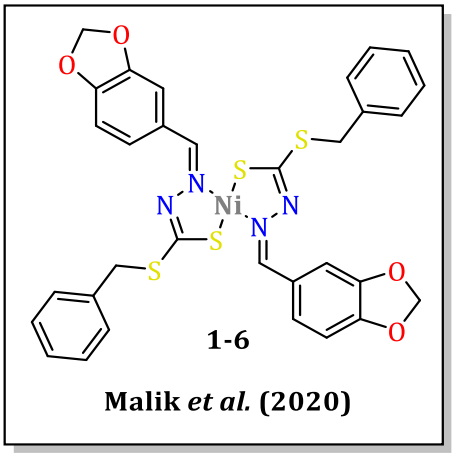

Figure 11: Antifungal Ni(II)-*S*-benzyldithiocarbazate complex synthesized by Malik *et al.*[105]

In other works, Frei *et al.* reported a series of Co(II) Schiff base complexes (**1-7** to **1-9**, Figure 12) which displayed MIC values as low as 0.39 µM against four selected

candida and cryptococcus yeasts.[106] Notably, the complexes demonstrated no cytotoxicity when tested *in vivo* against wax moth, *Galleria mellonella (G. mellonella)* animal models with a tolerance of up to 266 mg/kg.[106] To date, this study reports the first known *in vivo* toxicity report of a metal-based antifungal in the animal model, *G. mellonella.*

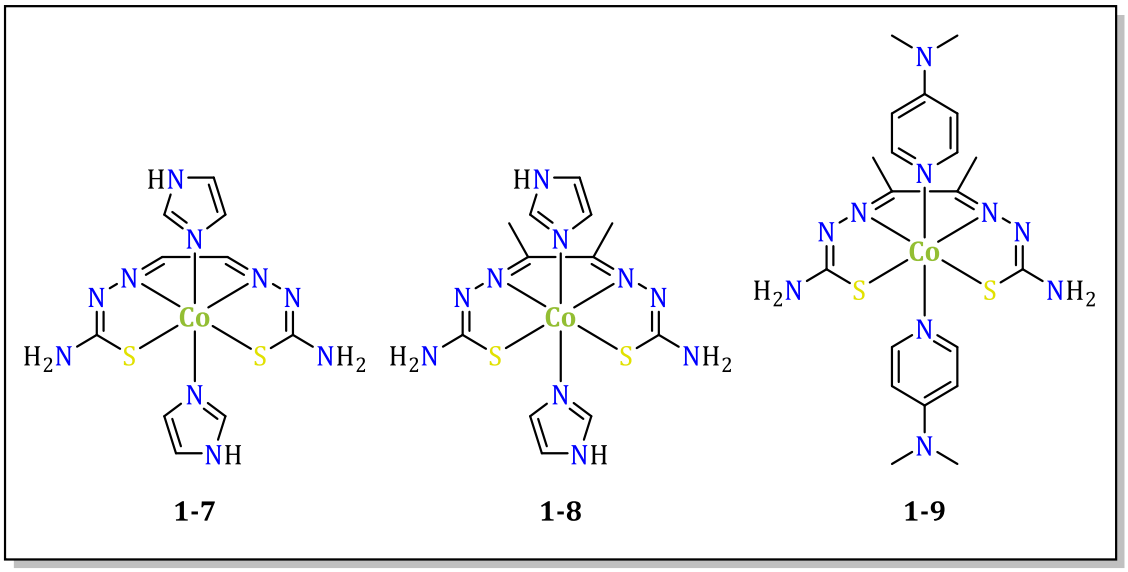

Figure 12: Examples of antifungal Co(II)- Schiff base complexes synthesized by Frei *et al.*[106]

Gandra *et al*. explored a series of eighteen Cu(II), Mn(II) and Ag(I) phenanthroline-based chelate complexes against the growth of a series of *Candida haemulonii (C. haemulonii)* strains whereby the overall geometric mean of the Minimum Inhibitory Concentration (GM-MIC) was used to calculate overall planktonic and biofilm growth.[96] Of the metal complexes evaluated, select Cu(II), Mn(II) and Ag(I) complexes showed appreciable inhibition on the growth of biofilm with GM-MIC values lower than 10 µM.[96] The key findings from this study uncovered more pronounced antifungal activity of the metal complexes when compared to their free ligand and metal salt counterparts.[96] This study formed the basis for a later, 2020 *in vivo* investigation against the *G. mellonella* larvae model whereby the Mn(II) complex **1-10^{b}** (Figure 13) showed the most promising results for further *in vivo* investigations.[107]

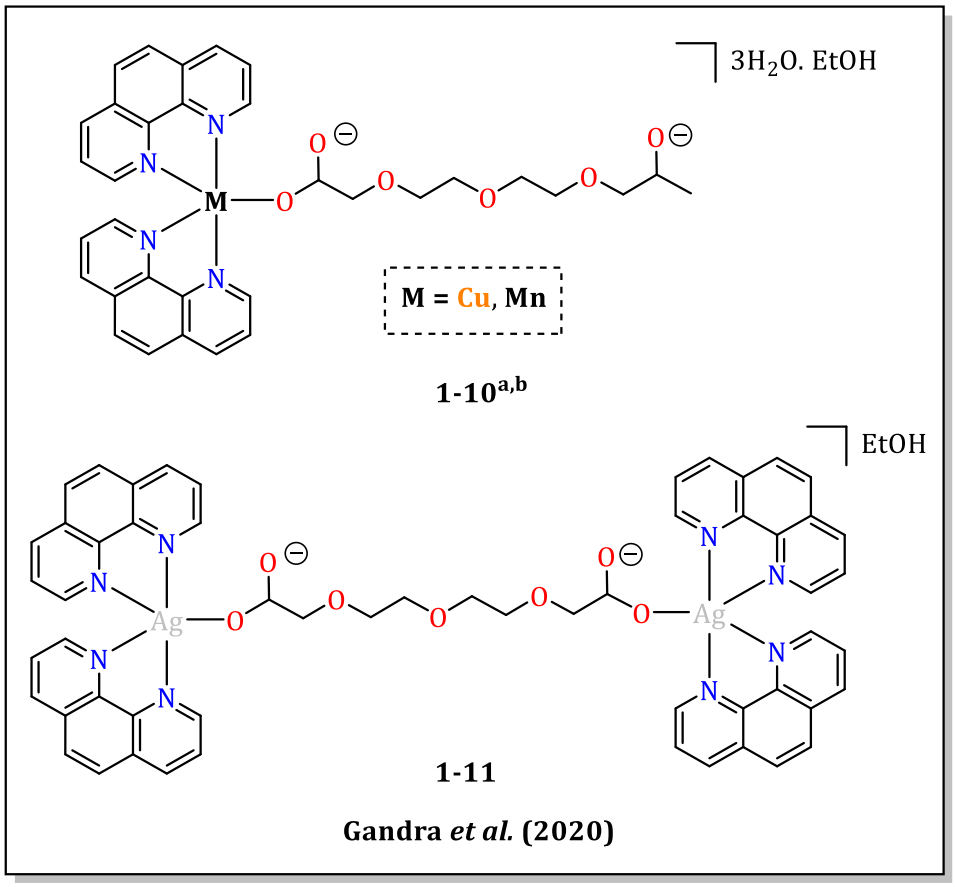

Figure 13: Select antifungal Cu(II), Mn(II) and Ag(I) phenanthroline-based complexes synthesized by Gandra *et al*.[96]

1.2.3 Metal-based anticancer agents

Cancer is the second leading cause of mortality worldwide.[108] Over the years, there have been multiple avenues explored for the treatment of cancer and cancer related illnesses, of which chemotherapy, radiotherapy and drug delivery have been the most common. However, with the employment of each therapeutic comes the undesirable side effects due to the lower selectivity between cancerous and healthy cells. This has necessitated the need to opt for alternative treatment regimens as well as alternative drugs. For years, platinum-based anticancer therapy had dominated the industry since the discovery of cisplatin.[68,109,110] However, the cytotoxicity coupled with the increased occurrence of resistance to platinum(II)-based drugs have directed research towards the exploration of alternative transition and non-transition metal complexes.[110–115]

The platinum-group of drugs have been used in cancer therapy for years and have solidified a presence in cancer therapy. Cisplatin, carboplatin and oxaliplatin target DNA through the formation of covalent adducts.[109] The desire to explore alternative metal-based cancer therapeutics has stemmed from the existing limitations arisen from the use of these drugs including the undesirable nephrotoxic side effects which have developed over their continual use. In a similar vein to AMR, recent research has uncovered the rise in resistance that cancer cells have developed towards these drugs and thus, their administration has been rendered ineffective against both particularly aggressive forms of cancer as well as patients who have relapsed forms of cancer.[113]

Despite the rise in resistance, the administration of platinum-based drugs continue to account for 50% of all treatments of cancer.[116] Although there have been concerted efforts to improve the selectivity, cytotoxicity, and efficacy of novel platinum anticancer agents, as of 2022, it has been almost 20 years since a new platinum(II)-based anticancer drug has been released on to the therapeutic market, with the last drug being oxaliplatin (Figure 14).[117]

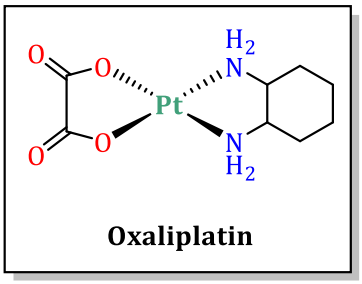

Figure 14: Empirical structure of the commercially available platinum(II)-based anticancer drug, Oxaliplatin.

1.2.4 Bismuth in medicine

In 1786, Louis Odier discovered the medicinal activity of bismuth for the treatment of dyspepsia.[118] Since then, bismuth has been used for over two centuries for the treatment of various ailments from cholera to syphilis.[119] In more recent times, the administration of the therapeutics Pepto-Bismol™ and De-nol™ based on the colloidal compounds of bismuth(III) subsalicylate (BSS) (Figure 15, **1-12**) and bismuth(III) subcitrate (CBS), respectively, have been used to target *Helicobacter pylori* (*H. pylori*) based infections.[119,120] The bismuth(III) salt of gallic acid in the form bismuth(III) subgallate (Figure 15, **1-13**), has been used in wound and gastrointestinal therapy as the active pharmaceutical ingredient (API) in the wound healing ointment, Sulbogin™ and has exhibited haemostatic effects suitable for patients using anti-platelet drugs.[121,122] Currently, the drug MBN-101, (Pravibismane, Figure 15, **1-14**) is being assessed for its pharmacokinetic safety and efficacy against patients with moderate to severe diabetic foot infection (DFI) with Phase I clinical trials underway (NCT: 02723539).[123]

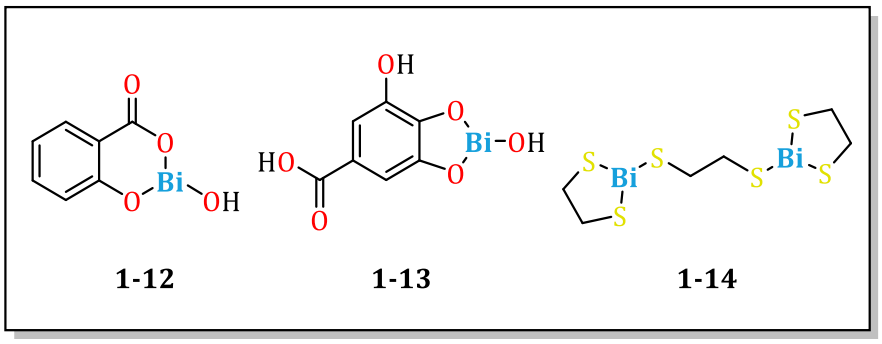

Figure 15: Empirical structures of **1-12**, bismuth(III) subsalicylate **1-13,** bismuth(III) subgallate and **1-14,** [1,2-bis((1,3,2-dithiabismolan-2-yl)thio)ethane] Pravibismane.

Despite their prevalent use, the molecular mechanism and structure of BSS is still widely debated. However, Sun and co-workers have presented a series of studies exploring the kinetic and thermodynamic properties of the drug under various physiological conditions.[124–131]

The utilisation of bismuth in medicinal chemistry stems from its unique chemical and physical properties. With a relatively large ionic radius of 1.16 Å, the metal can accommodate the formation of a variety of complexes ranging in coordination numbers from 3-10 however, majority of the biologically active bismuth-based complexes exist in the pentavalent, Bi(V) and trivalent, Bi(III) oxidation states; the latter being the most common and stable form.[124] Bismuth exists in its monoisotopic form (^{209}Bi) and although it has the heaviest stable nucleus in the periodic table, ^{209}Bi still undergoes α-decay at a rate of 1.9×10^{19} years.[132] Despite its heavy metal status as well as the close proximity more toxic elements in the periodic table (such as thallium, arsenic, and lead), elemental bismuth is considered safe and has earned its status as an environmentally friendly element.[133]

In aqueous media and under physiological conditions, bismuth exists in the form of Bi(III) salts, hydrated species, and oxides. Collectively, the species display low solubility and low oral bioavailability, and thus Bi(III) is perceived to have a low toxicity profile.[119,124,126,134] It is due to this low solubility that the consequent *in vivo* speciation of BSS, CBS and RBC are difficult to characterise. Despite their prevalent use, the molecular mechanisms by which CBS and BSS act are not fully understood. In 2003, Li *et al.,*[129] crystallised CBS under acidic conditions (pH ~3) which formed three different dimeric bismuth(III) structures of which formed two-dimensional negatively charged sheets comprised of a three-dimensional anionic framework of di-nuclear $[Bi(cit)_2Bi]^{2-}$ units (whereby cit = tetra-anionic citrate, Figure 16).[129] The researchers then hypothesised that the MoA of CBS follows the formation of a colloidal-type structure which can form a coating on ulcers and other internal growths within the gastrointestinal tract.[129]

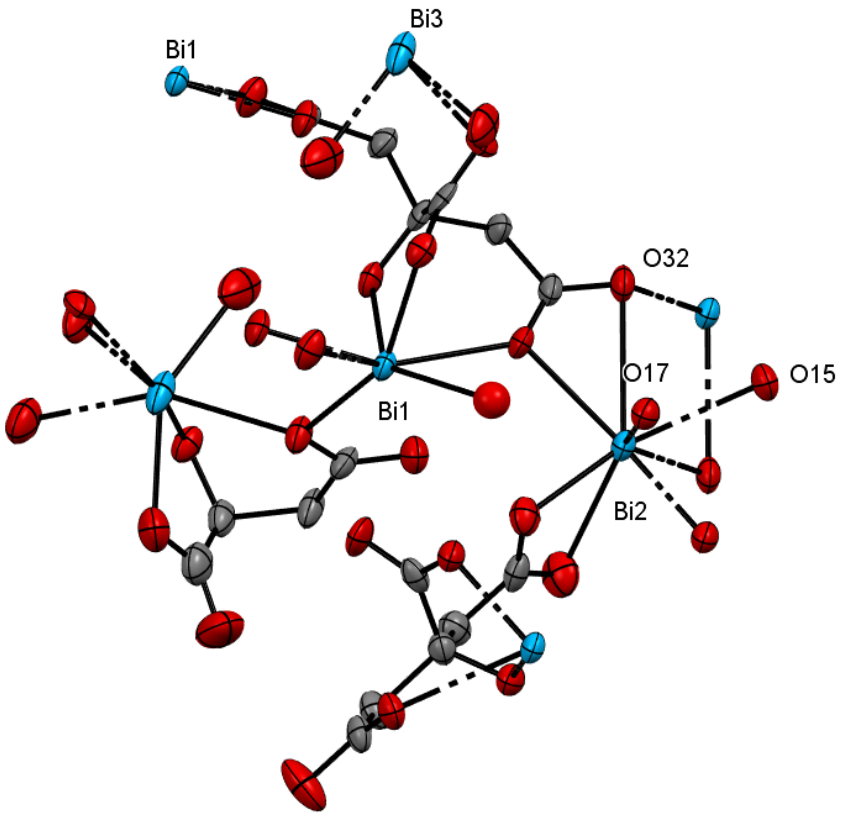

Figure 16: Solid-state structure of colloidal bismuth(III) subcitrate detailing the dimeric unit $[Bi(cit)_2Bi]^{2-}$. Hydrogen atoms have been omitted for clarity and thermal ellipsoids are shown at 50%.[129]

In a series of studies conducted by Sun and co-workers, the molecular mechanism of action for bismuth(III) drugs identified multiple targets for the disruption of cellular processes in *H. pylori.*[127] The primary mechanisms of which were associated with the synthesis of bacterial cell walls and membranes, adhesion processes, inhibition of ATP synthesis, oxidative stress, metal homeostatic and enzymatic disruption, and alterations to buffering pH.[120,127,135–137]

There have been numerous studies and postulations as to the structure of BSS. However, In 2022 a landmark discovery of the solid-state structure of BSS was elucidated through electron microscopy and three-dimensional electron diffraction (3DED) studies coupled with scanning electron microscopy (SEM) techniques.[138] The structure of BSS exhibits as a layered coordination polymer with the asymmetric unit $Bi_4O_4(HSal)_4$ supporting thermogravimetric analysis (TGA) and elemental analysis data.[138] The charge-balanced material was found to be in agreement with

similar reported protonated structures previously assigned by the Andrews and Whitmire groups, such as $[Bi_4O_2(HSal)_8].2MeCN/MeNO_2$ and $[Bi(HSal)_3(H_2O)]$.[139,140] Additionally, BSS was shown to exhibit a very high degree of stability in water and under acidic conditions. At a pH of 2 however, small proportions of the BSS were observed to convert to bismuth(III) oxychloride (BiOCl) with full conversion to the salt at a pH of 1.[141]

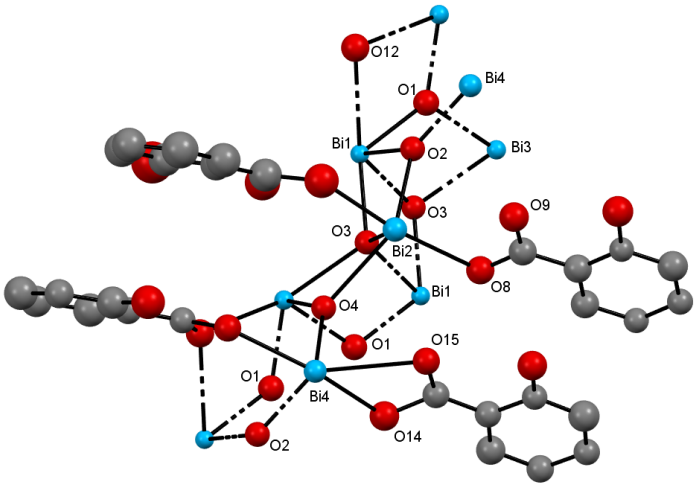

Figure 17: Solid-state structure of colloidal bismuth(III) subsalicylate, hydrogen atoms have been omitted for clarity.[138]

Since the discovery of the medicinal properties of Bi(III)-containing salts against *H. pylori* and the therapeutic success of the Bi(III)-based commercial drugs, the scope of bismuth(III)-based medicinal chemistry has expanded. In the last decade, many complexes have been pursued due to their attractive ability to form air stable compounds as well as their moderate to high Lewis acidity, which are both ideal attributes for an effective therapeutic.[142] The Andrews group have developed a library of organobismuth(III)- and bismuth(III)-based compounds bearing a variety of organic classes such as carboxylates, sulfonates, thiolates, Non-Steroidal Anti-Inflammatory Drugs (NSAIDs), phosphinates, phosphonates and N-heterocyclics and evaluated their antimicrobial activity, particularly towards *H. pylori* which will be explored in further detail in chapter 2.[143–146]

Following the outbreak of the novel coronavirus in late December 2019, the SARS-CoV-2 (coined COVID-19) rapidly spread across the globe and was declared as a

pandemic. In response to this pandemic, , Bi(III)-based therapeutics have expanded beyond AMR into the antiviral domain and pursued in combination therapy to overcome viral resistance. Shu *et al*., highlighted bismuth(III) ranitidine subcitrate (RBC) and CBS as inhibitors of nucleoside triphosphate hydrolase (NTPase) and RNA helicase activities.[147] Sun and co-workers supported this hypothesis and identified RBC as a potent broad spectrum inhibitor against COVID-19 via the mismetallation and displacement of Zn(II)-containing viral proteins. Both studies concluded the MoA of the bismuth(III) salts to be the enzymatic viral replication pathway.[148,149]

Over the last few decades, despite the repeated clinical use of bismuth(III)-based drugs against *H. pylori*, these compounds are one of the few antimicrobials in which no *in vitro* resistance has been observed.[150–152] To better understand the antimicrobial MoA of commercial bismuth(III)-based drugs, it is important to design novel bismuth(III) compounds of definite composition. Therefore, the field of organobismuth(III)-based medicinal chemistry continues to present as an area of key interest as more complexes show varied and unique antimicrobial activities. This will be explored in further detail in Chapter 2.

1.2.5 Rhenium in medicine

Rhenium exists as a highly refractory and corrosion-resistant metal however, given the scarcity (0.0007 ppm in the Earth's crust) and high cost ($1100/Kg), its elemental uses are relatively small in scale.[153–155] Elemental rhenium has been employed as a bimetallic catalyst for the production of petroleum products, alloys and as thermocouples.[153,156] The most stable and dominant feature of rhenium chemistry is the preference to form metallic bonding and clustered compounds with extensive M-M bonding.[153,154] A key feature of the mid-transition metal elements is the ability to accommodate a wide range of oxidation states, this arises from the number of available d electrons for bonding. Rhenium has been observed to exist in each of the oxidation numbers from -1 to +7 with the lower oxidation states typically associated with carbonyl ligands.[157] Unlike manganese, rhenium does not typically form a Re(II) ionic species in aqueous conditions and due to the greater number of d electrons, which have not migrated to the inert electron core, and the stability of higher

oxidation states is thus, maximised. The stabilisation of lower oxidation states can be attributed to the back donation of electron density from the rhenium to ligands.[153]

Rhenium-based compounds have been generally considered to be nontoxic. However, this prevailing viewpoint may be attributed to the scarce availability of elemental rhenium within the environment.[158] Toxicology studies have been conducted on the sodium perrhenate species (ReO_4^-) showing LD_{50} values in the range 1g/kg-1.8 g/kg, classing it as a low toxicity molecule.[158–160]

The biomedical applications of Re(I) complexes have been extensively explored I multiple reviews published between the years 1998 and 2019 with particular interest surrounding the rhenium carbonyl class of compounds.[161–168] The first known Re(I) carbonyl complex [$Re(CO)_3$(phen)Cl] (whereby phen = 1,10-phenanthroline) was discovered by Hieber and co-workers and was found to display luminescence when irradiated at 380 nm.[169] Since the discovery, Wrighton and Morse led extensive investigations into the photophysical and photochemical applications of these types of complexes and as a result, this field of chemistry has attracted significant attention.[170] The investigation of this family of compounds has extended into applications such as light-emitting diodes (LEDs),[171] photosensitisers,[172] confocal fluorescence microscopy,[173] cellular imaging,[163] chemotherapeutics,[165] photodynamic therapy,[172,174] and as Photoinduced CO-Release Molecules (PhotoCORMs) (Figure 18).[175]

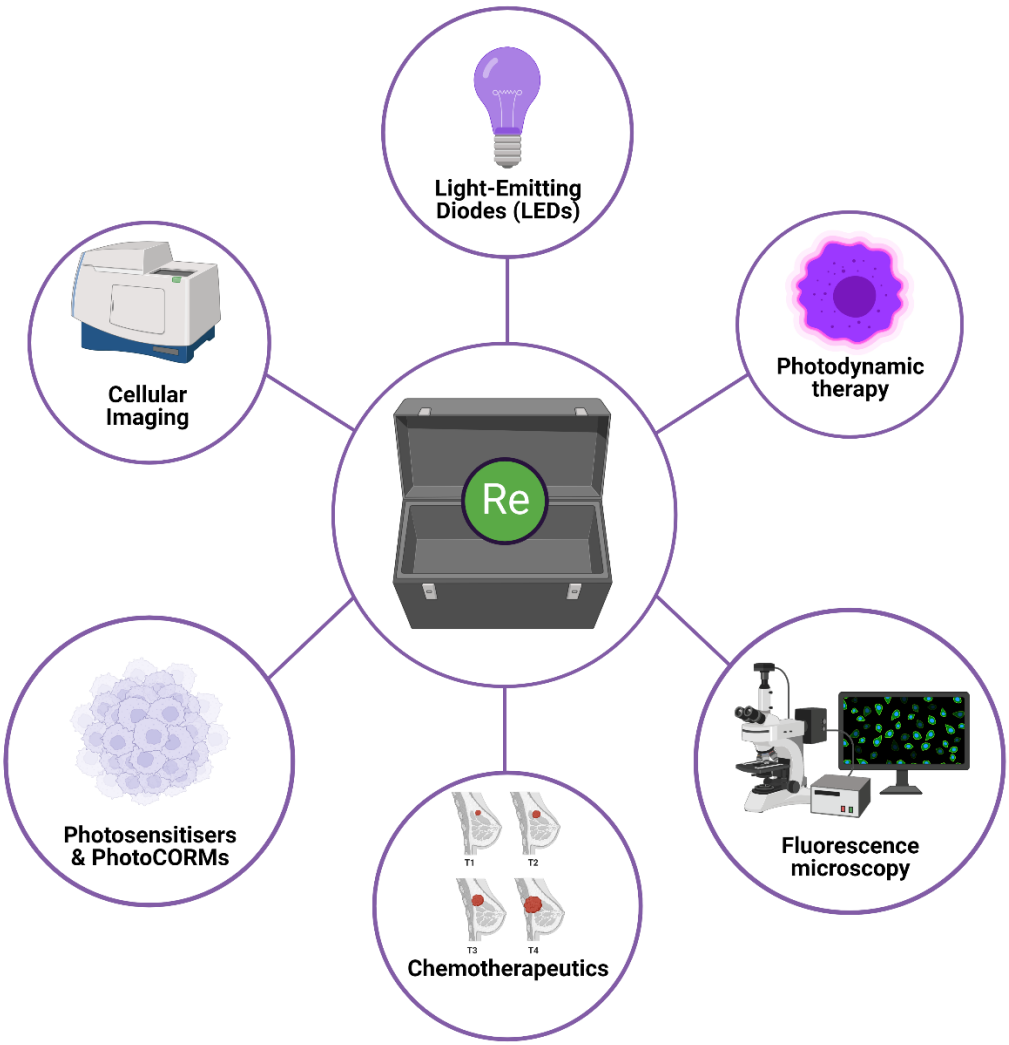

Figure 18: The diverse applications of Re(I)-based chemistry as summarized by Dilworth.[156]

As a third-row group 7a mid-transition metal, rhenium has demonstrated the propensity to bind to multiple donor atoms from oxygen, nitrogen, sulfur and phosphorus in the forms of oxides/oxido groups, sulfides, thiolates and nitrides.[158] Rhenium has also demonstrated the ability to bind to hard N- and O-donors which is reflected in the disruption of nucleobase DNA processes therefore, has been pursued as a potential metal of therapeutic interest.[176]

1.2.6 Gallium in medicine

As Gallium(III) is a hard Lewis acid and closely follows the chemistry of Aluminium(III), gallium-based compounds preferentially exist in the trivalent oxidation state.[177,178] Additionally, gallium species preferentially bind to electron-rich hard donors such as oxygen and nitrogen and form complexes with coordination

numbers of 4-6.[179] Biologically however, Ga(III) exhibits close similarities to the active ferric iron Fe(III) species, with regards to electron affinity, electronegativity, and ionic radius the two species are structurally similar (Table **1**).[174,179]

Table 1: Chemical properties of gallium(III) and iron(III).[179,180]

	Electronic Configuration	Electronic Affinity (kJ mol^{-1})	Ionic Radius (Å)	Preferred Coordination number	Reduction potential (V)	Electronegativity (Pauling Scale)
Ga(III)	[Ar]3d^{10}	1.81	28.9	6	0.620	-0.56
Fe(III)	[Ar]3d^{5}	1.83	15.7	6	0.645	+0.77

Although Ga(III) shares atomic similarities to Fe(III), they differ in other aspects. Biologically, the Fe(III) to Fe(II) reduction pathway is an essential process for cells to acquire exogenous iron. However, unlike Fe(III), Ga(III) cannot be reduced to a divalent state under physiological conditions.[181] Under acidic conditions (pH 3-7), hydrated Ga(III) cations are stable in the form of [Ga(OH)$_3$] if not stabilised by certain ligands.[182] Under basic conditions (pH >7), [Ga(OH)$_3$] undergoes further hydrolysis to the gallate species [Ga(OH)$_4$]$^{-1}$.[183–186] Under physiological conditions (pH 7.4), Ga(III) exists predominantly in the gallate form with a solubility of 1 μM; conversely, Fe(III) displays limited solubility (10^{-6}-10^{-12} μM).[184,186]

Some examples of gallium-based compounds which have been developed and explored in clinical trials include: gallium nitrate (GaN), ^{67}Ga citrate, tris(3-hydroxy-2-methyl-4H-pyran-4-onato) gallium (gallium maltolate, GaM), doxorubicin gallium transferrin conjugate, and *tris*-(8-quinolinolato)gallium(III) (KP46) (Figure 19).[187]

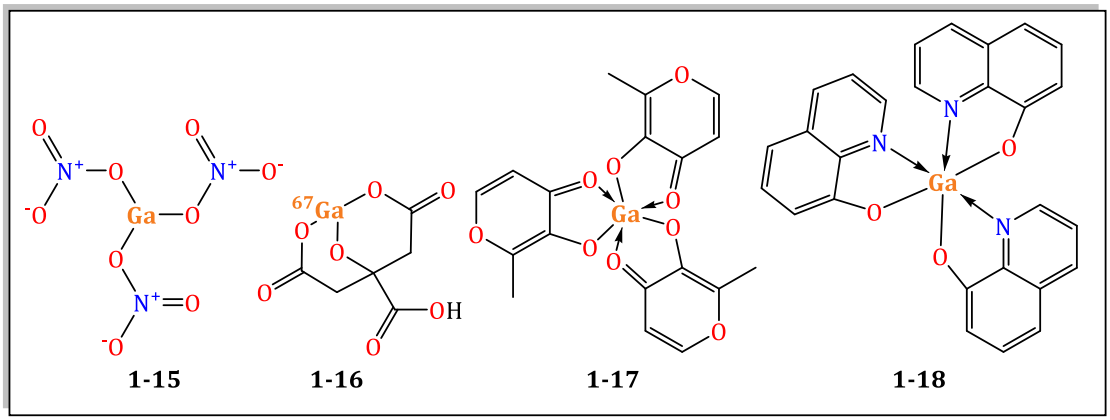

Figure 19: Structures of therapeutic compounds **1-15**: Gallium nitrate, **1-16**: tris(3-hydroxy-2-methyl-4H-pyran-4-onato) ^{67}gallium(III) **1-17**: gallium maltolate, and **1-18**: Tris-(8-quinolinolato)gallium(III).

As a radiopharmaceutical, ^{67}Ga-citrate has been used in the diagnostic imaging of cancers, inflammations, and infections.[180,188–190] Gallium nitrate (Ganite™) represents the first generation of gallium compounds to gain approval for clinical use by the Food and Drug Administration (FDA).[180,187] After a series of clinical trials, the compound was initially used in benign cancer-associated hypercalcaemia and later, its use extended to the treatment of malignancy-associated hypercalcaemia. The drug was later discontinued by the manufacturer in 2016 potentially due to adverse renal toxicity.[180] Recently, several studies have explored the efficacy of gallium nitrate against *Pseudomonas aeruginosa (P. aeruginosa)* and *Staphylococcus aureus* (*S. aureus*) all showing promising results, this will be explored in further detail in Chapter 4.[21,29,191–196]

In the sphere of cancer therapy, GaM and KP46 represent the second generation of nonradioactive gallium-based therapeutics.[194,197] GaM has been demonstrated to inhibit the proliferation of lymphoma and hepatocellular cancer cell lines *in vitro* at IC_{50} (Inhibitory concentration at 50 % of a given population) values that are significantly lower than those of Ganite™. Values range from 60-250 µM for Ganite™ and 25-35 µM for GaM suggesting that the latter has a greater therapeutic effect.[183,198,199] GaM is currently being explored in phase I clinical trials for the treatment of relapsed and refractory glioblastoma (US national clinical trial identifier number NCT:04319276).[200] Several studies have investigated the therapeutic

potential of KP46 against breast, ovarian, lung and colon cancer cell lines with IC_{50} values ranging between 0.85 μM and 10.4 μM.[181,194,197,201,202] Currently, KP46 is being investigated for its antitumor activity in phase I-II clinical trials (NCT: 04143789).[203,204]

While the therapeutic potential of Ganite™ and its second-generation derivatives has been well established, research into organogallium(III)-based compounds is limited to a few studies. To date, organogallium(III) complexes bearing carboxylato-, heterocyclic thiolato-, azole and quinolinolato-functional groups have been explored however, their antimicrobial potential was found to be limited (Figure 20).[205–208] As organogallium complexes have shown good selectivity towards parasites and cancer cells, with some exhibiting modes of action that are different from Ganite™,[206,209] further research is required to investigate their potential as antibacterial agents.

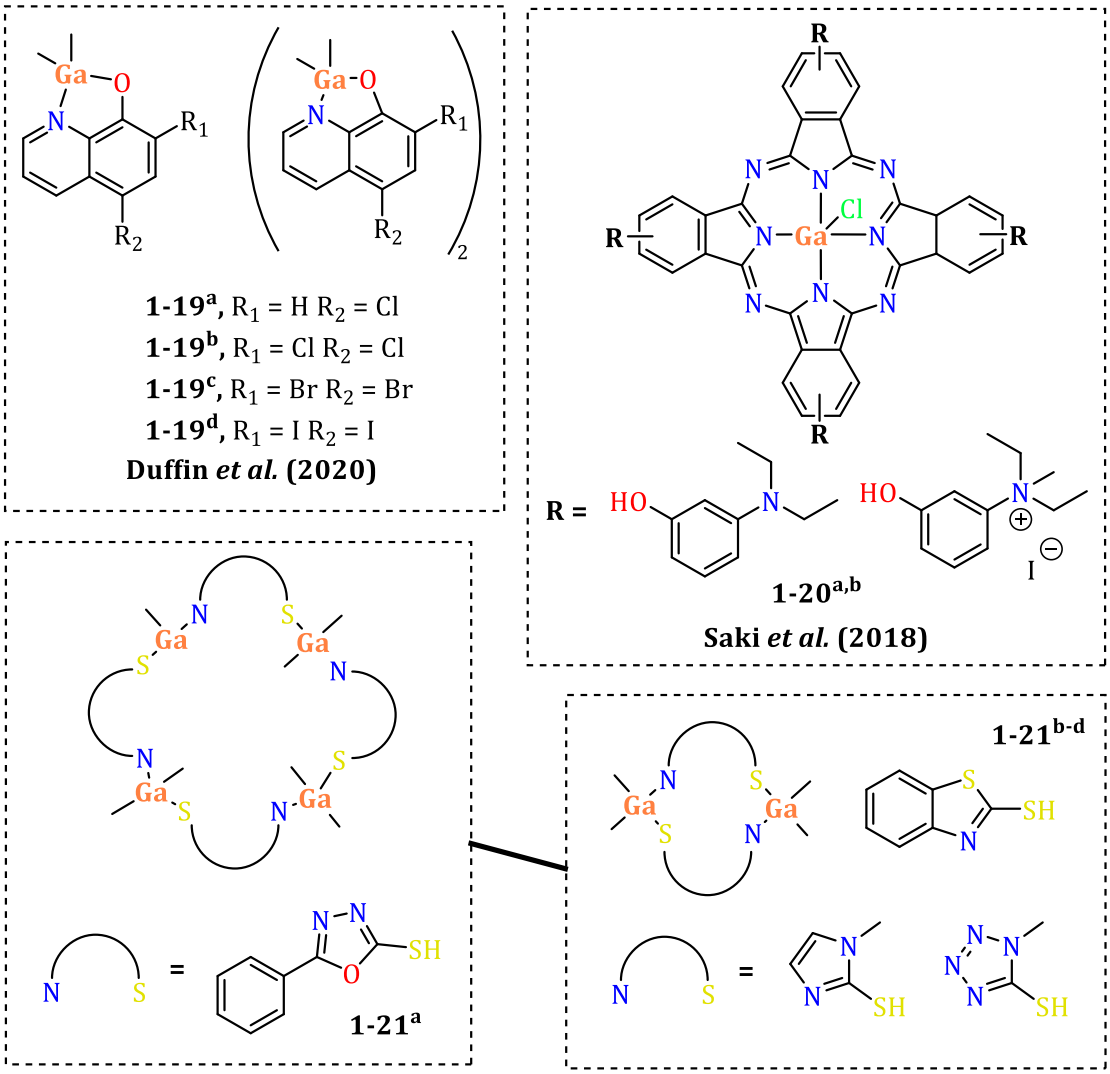

Figure 20: Summary if alkylgallium(III) complexes prepared and evaluated for their therapeutic application.[205–208]

1.3 Heterocyclic chemistry

Heterocyclic compounds are cyclic organic compounds which bear one, two or more heteroatoms; the most common heteroatoms found in heterocyclic molecules exist in combinations of C, N, O and S. However, other heteroatomic heterocyclics are also widely known.[210] Heterocyclic compounds are considered the most ubiquitous medicinal scaffolds in organic chemistry with molecular databases placing anywhere between 60-85 % of all unique small molecule drugs and biologically active chemical compounds to contain an N-heterocyclic core.[211,212] These scaffolds continue to play a dominant role across many fields given their abundance in nature, with prime

examples of natural products containing N-heterocyclic scaffolds including: nucleobases in which DNA and RNA synthesis occurs; hormones such as serotonin and histamine and vitamins such as Thiamine (Vitamin B1) and Riboflavin (vitamin B2) (Figure 21).[212–214]

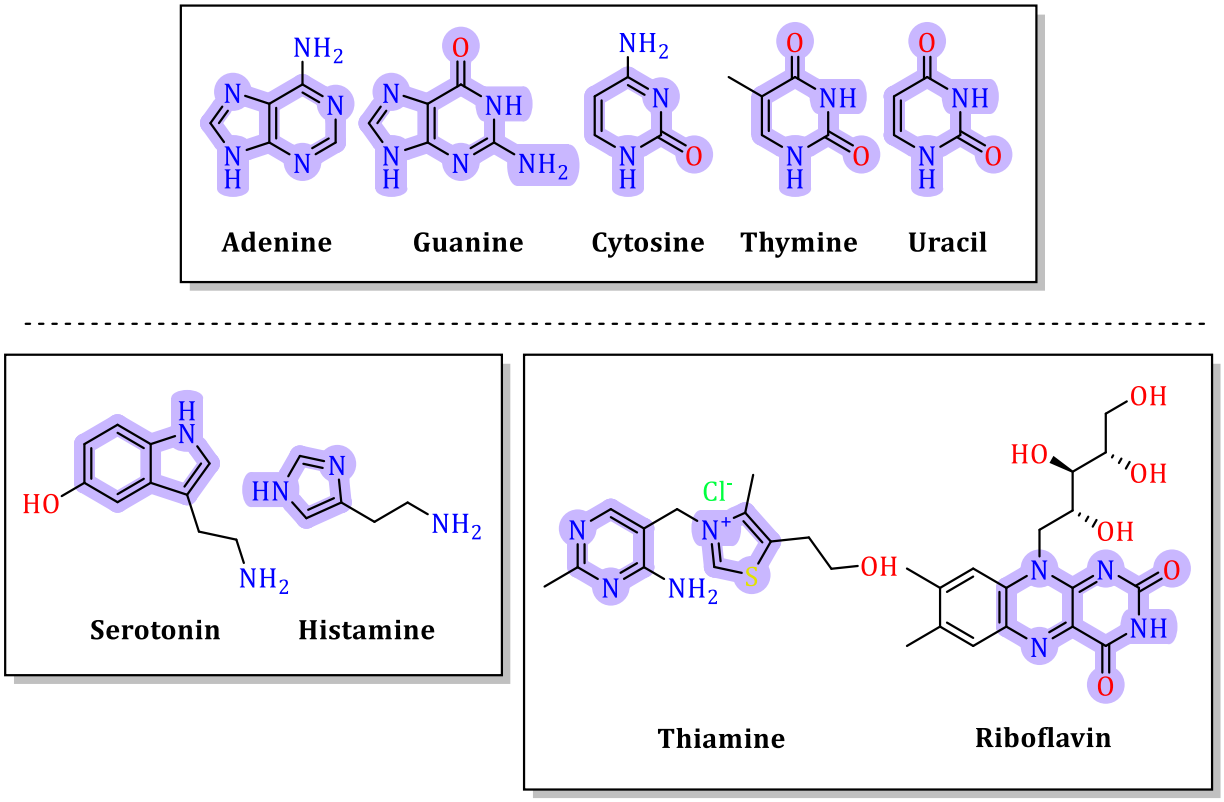

Figure 21: Key natural products containing N-heterocyclic scaffolds highlighted in purple.

N-heterocyclic molecules are utilised across a diverse array of applications as precursors, intermediates, and products and will continue to serve as building block for novel therapeutics to come. An important subset of N-heterocyclic compounds includes the diverse group of medicinally relevant molecules known as azoles.

1.3.1 N-heterocyclic azoles

Azoles are a group of organic molecules which comprise of one or more nitrogen and/or sulfur or oxygen molecules within an aromatic moiety. The azole class of compounds are comprised of the subclasses: pyrazole, indazole, imidazoles, triazoles, tetrazoles, oxazoles, thiazoles (Figure 22). These classes of compounds have been explored across a diverse range of applications including: anticancer agents,[215] antimicrobials,[216] antiparasitics,[217] corrosion inhibition[218] and agrochemicals.[219]

However, their use is ubiquitously associated with antifungal therapeutics.[220–223] Among the azole derivatives however, triazoles have predominantly been utilised in antifungal, antibacterial and anticancer therapy.[224]

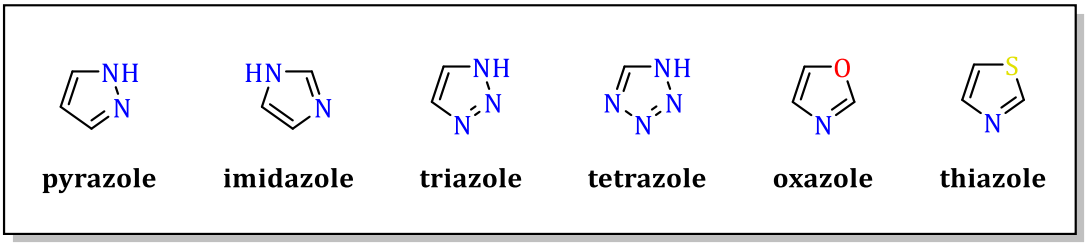

Figure 22: Examples of compounds within the azole sub-class of molecules.

1.3.1.1 Triazoles

The triazole class of compounds (also referred to as pyrrodiazoles) are five-membered heterocyclic ring systems which contains three nitrogen atoms. The arrangement of the nitrogen atoms can exist in two isomeric forms, the vicinal (1,2,3-triazole, **A**) and symmetrical (1,2,4-triazole, **B**) form, summarised in Figure 23. Both forms have been extensively explored in medicinal chemistry and have remarkably different therapeutic targets based on their structural design.

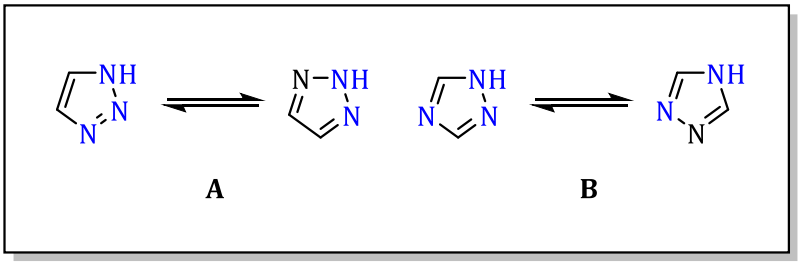

Figure 23: Isomeric forms of triazole, **A**: 1H-1,2,3-triazole, 2H-1,2,3-triazole and **B**: 1H-1,2,4-triazole, 4H-1,2,4-triazole

Triazoles have been identified as one of the key N-heterocyclics to exhibit impressive pharmacological activity and thus, have garnered extensive interest in a variety of sub-fields within the pharmacological design arena.[225–227] The 1,2,3-triazole scaffold and its derivatives have been popularly explored through the famous Azide-Alkyne Huisgen cycloaddition reaction (Scheme 1).[228] Popularly coined as the "Click Chemistry" reaction, the facile addition of an azide to an alkyne under mild conditions

has dramatically increased the scope of compounds that possess greater selectivity towards pathogens, higher yields, and large scope.[210]

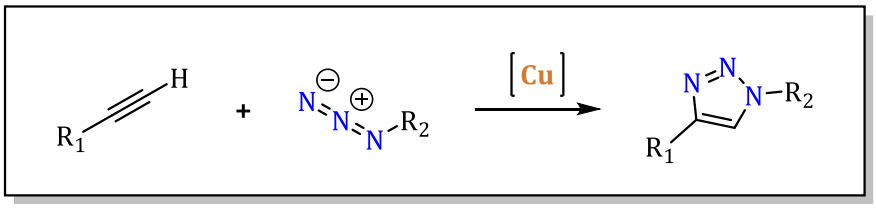

Scheme 1: General structure of the Copper Catalyzed Azide Alkyne Cycloaddition, (CuAAC)

Conversely, the symmetrical (1,2,4-) triazole form has attracted the attention of scientists across a broad range of fields including: antibacterials,[229] anticancer agents,[230] anticonvulsants,[231] anti-HIV agents,[232] antioxidants,[233,234] anti-inflammatories,[231] and antivirals (Figure 24).[232] These compounds however, are ubiquitous within the field of antifungal therapy.[235–238]

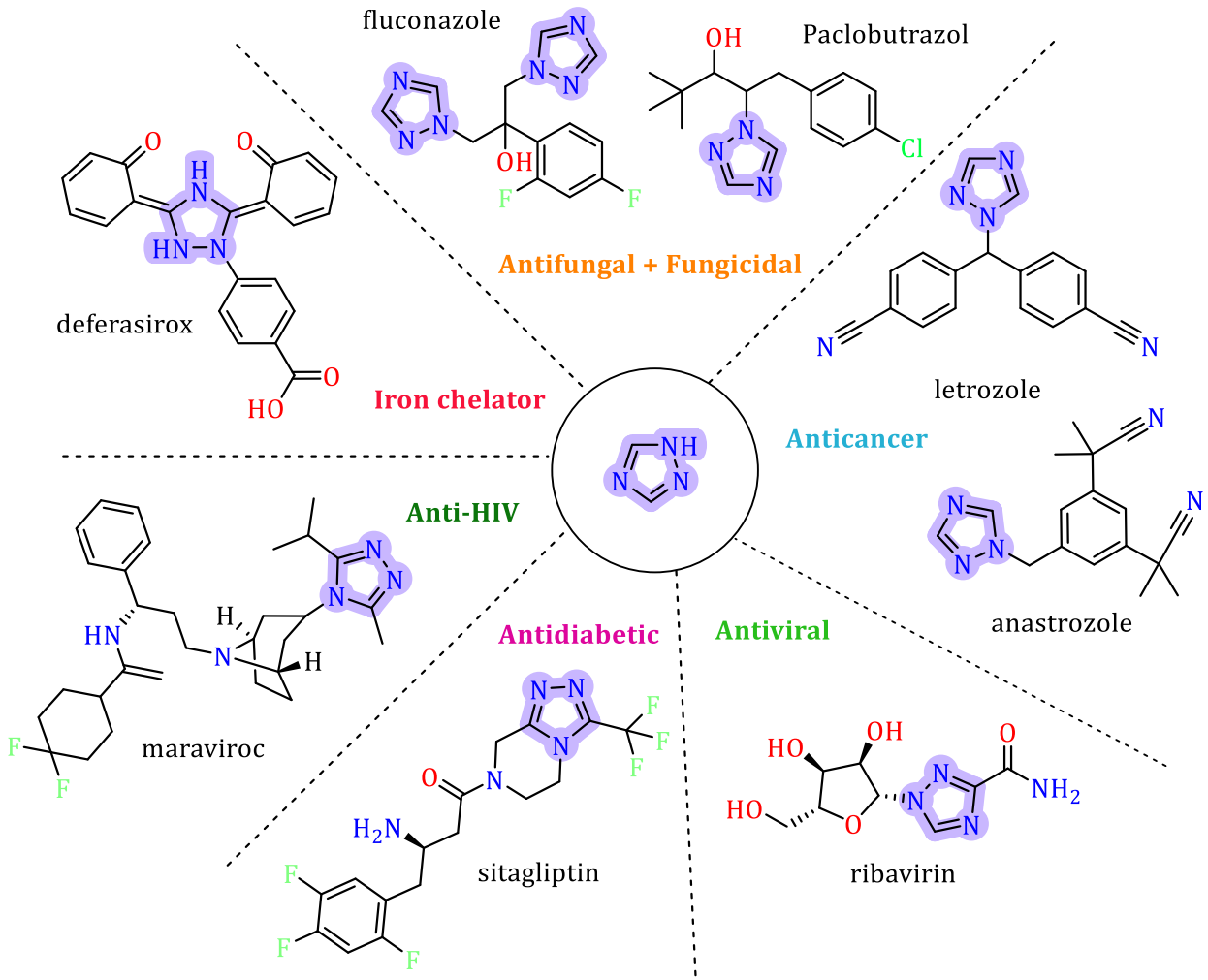

Figure 24: Commercially available drugs based on the 1,2,4-triazole scaffold.[235]

As discussed in section 1.3.1.1, 1,2,4-triazoles have been incorporated in therapeutic design as antifungal agents with the first commercially available drug, Fluconazole developed by Pfizer in 1989.[220] Fluconazole was designed to target the fungal biosynthetic ergosterol pathway, responsible for cellular proliferation through selectively targeting the iron-dependent fungal CYP51 (lanestrol-14α-demethylase, ERG11) enzyme.[220] Fluconazole showed lower toxicity profiles, higher bioavailability and increased specificity when compared to previously used imidazole antifungals. Since its discovery however, multiple second- and third-generation structures have been synthesised using the 1,2,4-triazole scaffold with enhanced pharmacokinetic profiles, these include: voriconazole, itraconazole and posaconazole (Figure 25).[239]

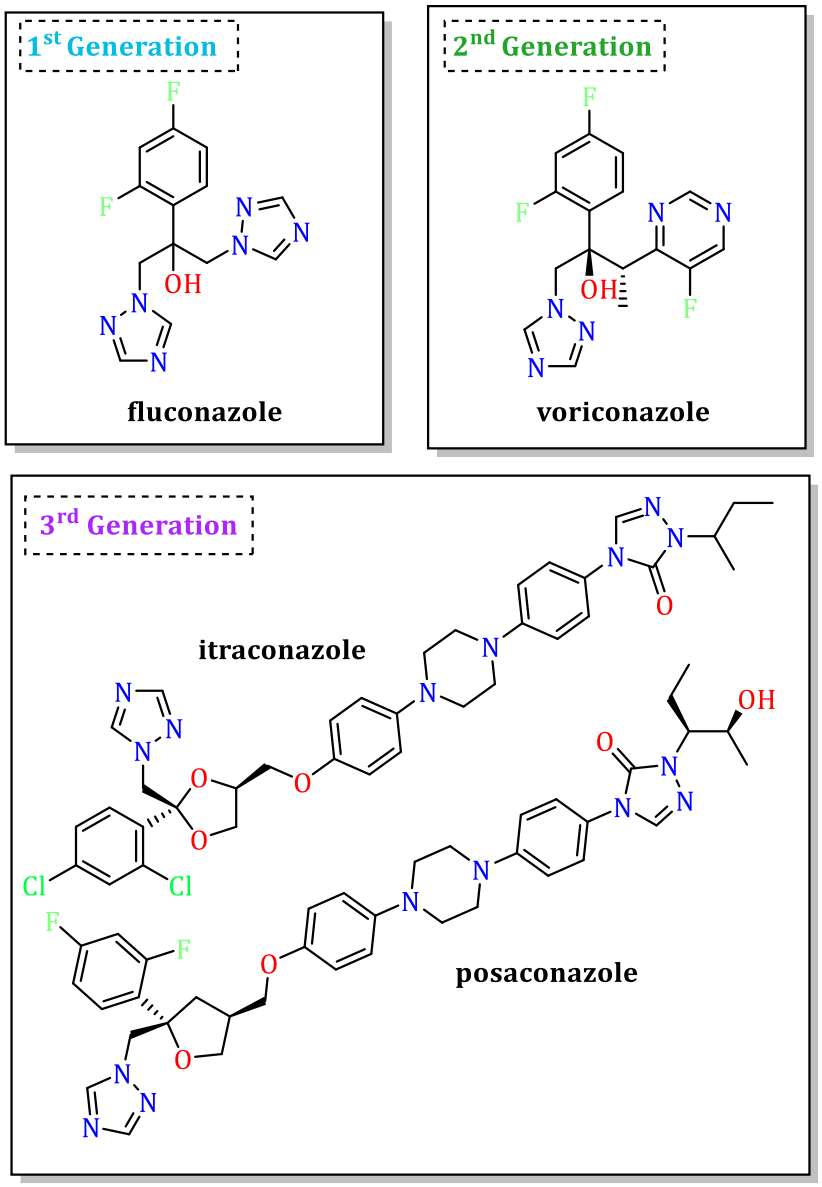

Figure 25: Commercially available first generation, second generation and third generation triazole-based antifungal structures.[220]

1,2,4-triazoles have shown remarkable versatility as stand-alone structures, building blocks, and synthetic intermediates for other bioactive compounds. Novel molecules containing the triazole scaffold continue to be designed in the field of medicinal chemistry as a result of their existing and tuneable biological activity against microbial, parasitic and tumour related infection. Many studies have identified these small molecules as ideal backbone candidates for further modification.[229,240–242]

1.3.1.2 Triazole thiones

The thione functional group (also referred to as thioketone and thiocarbonyl) represents a key synthetic intermediate in organosulfur chemistry. Over the last decade, this functional group has attracted significant interest in organic synthesis due to its facile incorporation into N-heterocyclics to produce the novel class of molecules known as the 'N-heterocyclic thiones' (Figure 26).[243] These sulfur-containing heterocyclics represent an important class of biologically active structures which are able to effectively interfere with enzymatic processes and produce enhanced biological activities than their precursor counterparts.[244,245]

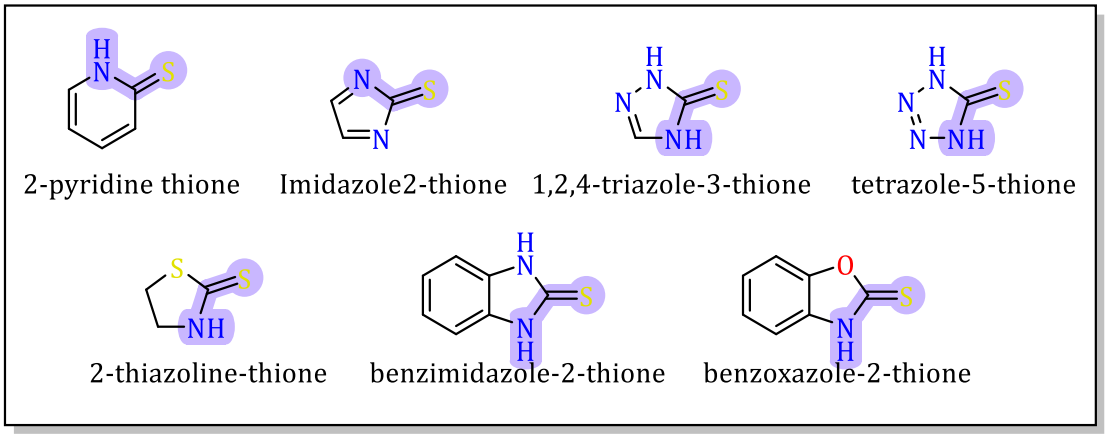

Figure 26: Representative examples of select N-heterocyclic thiones which bear a thioamide functionality highlighted in purple.

The incorporation of a thione group in either the 3- or 5- position of a 1,2,4-triazole results in the formation of a mercapto-1,2,4-triazole core (highlighted in Figure 27) which possesses enhanced biological and pharmacokinetic properties. Currently, of the commercially available drugs, Prothioconazole (Figure 27) has been available since 2004 under the brand name Proline™ as a broad-spectrum fungicide for the treatment of ascomycetes, basidiomycetes and deuteromycetes.[246,247] Like other azole antifungal drugs, the MoA involves inhibition of the fungal CYP51 enzyme involved in the biosynthesis of ergosterol.[246,247]

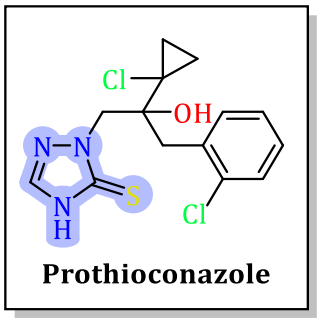

Figure 27: Commercially available fungicide, Prothioconazole modelled from an N-heterocyclic thione scaffold.[246,247]

Several examples of mercapto-triazole type molecules were synthesised by Jalilian and co-workers, and Luciano and co-workers whereby the derivatisation of the 1,2,3-thiadiazolo-1,2,4-triazoles with both alkyl and aryl substituted moieties (Figure 28, **1-22**$^{a.b}$) were evaluated against *C. neoformans* and *S. cerevisiae.*[248,249] The compounds displayed promising MIC values between 3.12 µg mL^{-1} and 6.25 µg mL^{-1}.[248] Additionally, Linciano and co-workers synthesised a small library of 1,2,4-triazolethione-based structures, the most promising of which showed cross-class micromolar bacterial inhibitory potential (Figure 28, **1-23**$^{a-d}$).[249] The MoA of these molecules were designed to target β-lactamase inhibition (BLI).[249]

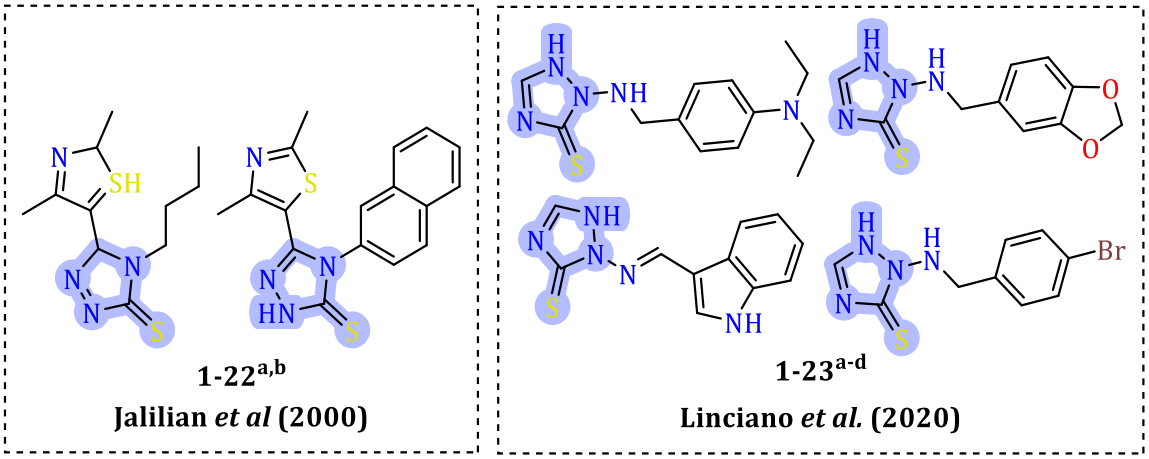

Figure 28: Examples of antimicrobial 1,2,4-triazole-3-thiones synthesized by Jalilan, Linciano *et al.*[248,249]

Mioc *et al.,* identified the 1,2,4-triazole ring as an effective bioisostere within the cancer domain due to its effective solubility, flexibility, and interaction with biological entities. The synthesis of a modified S-alkylated mercapto-1,2,4-triazole series of

molecules showed effective hydrogen bonding donor/acceptor efficacy which enhanced anticancer activity.[250] The MoA of the most active structure (Figure 29, **1-24**) was postulated to target the phospholipid-dependent kinase 1 receptor, which is responsible for the selective elimination of cancer stem cells responsible for the regeneration of tumours when tested against the HT-29 tumour cell line.[250]

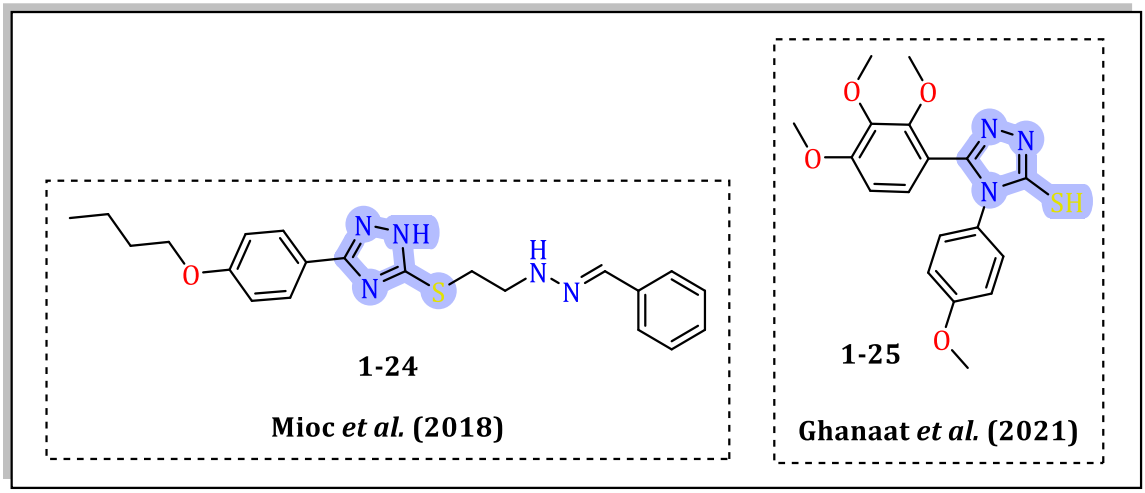

Figure 29: Anticancer 1,2,4-triazole-3-thiones developed by Mioc and Ghanaat *et al.*[250,251]

In another study conducted by Ghanaat and co-workers, a series of 3-mercapto-1,2,4-triazole derivatives were synthesised and displayed appreciable cytotoxic activity against A549 lung cancer, MCF-7 breast cancer and SKOV-3 ovarian cancer cell lines with the most active derivative showing an IC_{50} value of 15.37 µM against SKOV3 (Figure 29, **1-25**).[251] The derivative was shown to induce cellular apoptosis and cell cycle arrest at the G2/M phase with docking studies confirming binding to the colchine site, which leads to depolymerisation of microtubules and disruption of the cytoskeleton.[251]

A key feature of N-heterocyclic thiones is the tautomerisation between the thione and thiol forms (Figure 30). The additional coordination capability allows for greater structural diversity due to the ability to coordinate to a wider variety of biological substrates through the S- and/or N- terminus.

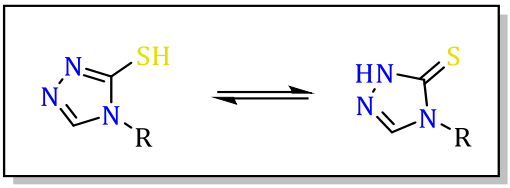

Figure 30: Tautomeric forms of 1H-1,2,4-triazolethione to 3-mercapto-1,2,4-triazole

Süleymanoğlu and co-workers confirmed the presence of both thiol and thione forms of a 1,2,4-triazole derivative modified with a Schiff base side arm using Density Functional Theory (DFT) techniques.[252] The study concluded that strong intermolecular hydrogen bonds may form between the S-H…O type interaction to result in the thiol form (Figure 31, top) and conversely, intramolecular chelation results in a -S…H-C- type interaction to give the thione form (Figure 31, bottom).[252]

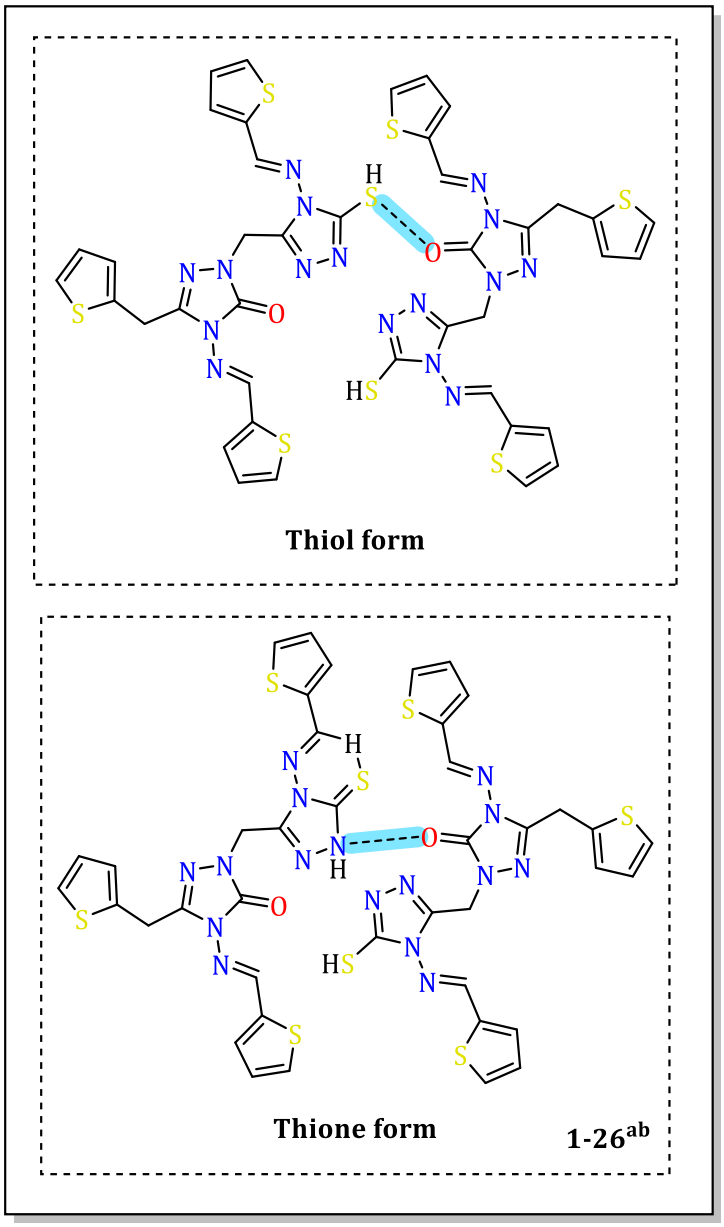

Figure 31: Tautomeric forms of a 1,2,4-triazole with a Schiff base explored by Süleymanoğlu et al., with interactions highlighted in blue.[252]

Ultimately, N-heterocyclic thiones are versatile molecules due to their electron rich nature and bridging capabilities.[243] The existence of both the thionate sulfur and thioamide nitrogen atoms allow for a greater degree of substitution, organic transformation, and coordination to metal centres and thus, are effective substrates for modification and application in therapeutics (Figure 32). For example, Sevaille and co-workers have demonstrated that molecules bearing the 1,2,4-triazole-3-thione moiety undergo metal ligation in the dizinc active sites of MBLs; in addition, these

molecules also show IC_{50} values within the micromolar range towards the tested MBLs.[253]

The deprotonation and metal coordination of the N-heterocyclic thionato moiety results in a negative charge which can be localised onto the exocyclic sulfur whereby the thioamide π-electron density can be concentrated between the C- and N-atoms (observed in **I,** Figure 32).[254] However, monodentate M-S bonding is often supported by secondary intramolecular dative interactions with the thioamido nitrogen atom (observed in **I-III,** Figure 32).[254] Additionally, four-membered planar chelates have been observed within the literature with strong N-M and relatively long M-S with small dihedral chelation angles (observed in **IV-VI,** Figure 32).[254]

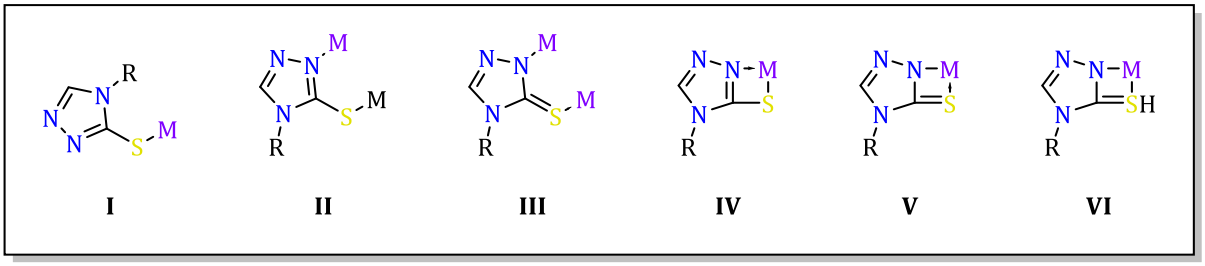

Figure 32: potential binding modes for the n-heterocyclic thiol/thione moiety.

It is postulated that taking 1,2,4-triazole thiones and binding them with metals may further enhance their biological activity by activating novel pathways and creating new modes of action, which in turn could mitigate resistant pathways.[255] Therefore, it is worth expanding upon the library of metal-triazoles with metals that have not been previously explored with these prospective ligands and evaluate their therapeutic efficacy both as antibacterial and antifungal agents.

1.4 Metal triazoles as therapeutic agents

As small molecules, azoles serve as a useful building block for organometallic complexes due to their capacity to bind to metals via multiple donor atoms. As broad-spectrum antibiotics they target multiple fungal pathways and thus, can be used as a starting point for further development. Many of the commercially available drugs and their second-generation derivatives such as Posaconazole (PCZ), Clotrimazole (CTZ), Ketoconazole (KTZ) and Miconazole (MCZ) have therefore, been utilised as antileishmanials, antiparasitics, and anticancer agents.[256,257]

In nature, certain metalloenzymes in bacteria and fungi contain *S,N* coordination sites, an example of this type of arrangement can be observed in plastocyanins, which are part of the blue copper protein family.[258] Coordination of the Cu(II) in a plastocyanin involves two histidine nitrogens, a cysteine sulfur and methionine sulfur to form an overall S,N-type coordination active site in the metallothionein (MT).[258,259] N-heterocyclic thionato *S,N* and S_2N_2 coordination compounds are effective mimetics for the active sites in these proteins as they provide similar electronic and structural properties.[254] An example of this follows the success of Auranofin whereby interest has been stimulated into N-heterocyclic thionates due to their sulfur-donating nature.[260]

N-heterocyclic thionate ligands complexed with various metals have produced a variety of biological outputs with the most recent studies exploring thionato ligand systems with Zn(II), Pd(II), Pt(II), Ag(I) Au(I) and Bi(III) ions.[261] Dennehy *et al.,* recently explored three Zn(II) complexes with N-donor azoles producing tetrahedral S_2N_2Zn environments, whereby the N-heterocyclic thionates of the thiosaccharinate form coordinate to the metal centre via the exocyclic sulfur atom.[262] Haemolytic studies of these complexes revealed no significant effects on erythrocyte sedimentation factors suggesting biocompatibility.[262] In another study conducted by Varna and co-workers, a series of Ag(I) N-heterocyclic thionates were observed to be particularly effective antibacterial agents especially towards the Gram-positive strains *B. subtilis, B. cereus* and *S. aureus* exhibiting MIC values between 1.6-4.5 μM.[263]

Of particular interest is the work of Corrêa, M. da Silva, Graminha and co-workers who explored the synergistic activity of ruthenium(II) and the 1,3-thiazolidine-2-thione (tzdtH) moiety as anticancer and antiparasitic agents.[264] The neutral tzdt*H* molecule shows thiol to thione tautomerism in solution however, in the solid-state preferentially forms the thione tautomer.[264] When coordinated however, the anionic tzdt ligand is shown to adopt a delocalised anionic state whereby both the *S*- terminus and *N*-terminus are coordinated to the Ru(II) metal centre forming a four-membered chelate.[264]

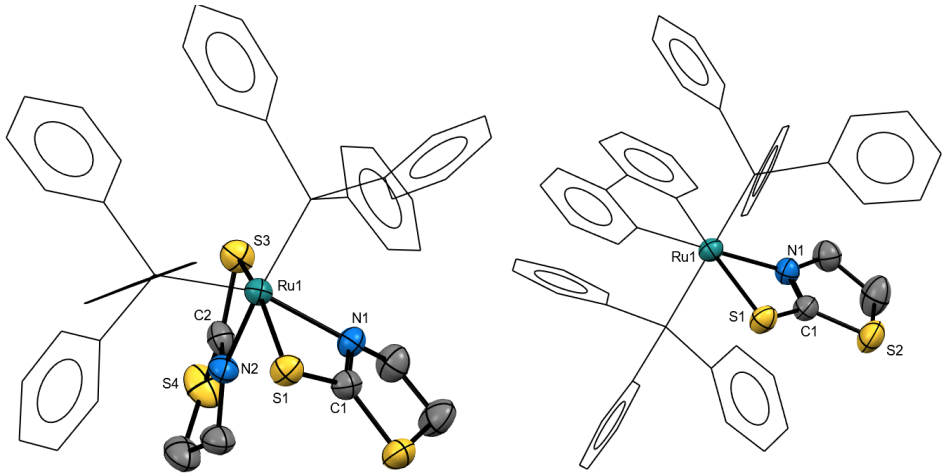

Figure 33: Solid-state structure of the biologically active Ru(II) complexes cis-[Ru(tzdt)$_2$(PPh$_3$)$_2$] (**Ru2**, **1-27^b** left) and trans-[Ru(tzdt)(PPh$_3$)$_2$(bipy)]PF$_6$ (**Ru3**, **1-27^c** right) synthesized by Corrêa, et al. Hydrogen atoms have been omitted for clarity and thermal ellipsoids are shown at 50%.[264]

The three novel complexes [Ru(tzdt)(bipy)(dppb)]PF$_6$ (**Ru1, 1-27^a**), *cis*-[Ru(tzdt)$_2$(PPh$_3$)$_2$] (**Ru2, 1-27^b**), and *trans*-[Ru(tzdt)(PPh$_3$)$_2$(bipy)]PF$_6$ (**Ru3, 1-27^c**) (where dppb = 1,4-bis(diphenylphosphino)butane and bipy = 2,2'-bipyridine), exhibited strong anticancer activity against MCF-7 breast cancer and DU-145 prostate cancer cells.[264] The most potent activity was shown by **1-27^b** with an LD$_{50}$ value 0.98 ± 0.2 (when compared to the drug control, cisplatin at 8.9 ± 2.6).[264] **1-27^c** also showed strong antiparasitic activity against *Trypanosoma cruzi* with an LD$_{50}$ of 0.010 ± 0.001 when compared to the drug control, benznidazole (LD$_{50}$ of 10.6 ± 0.8).[264]

In surveying the literature, the tendency of metals to form either a thionate/thioamide or thiolato-based complexes is dependent on the individual properties of the metal coordination environments. According to the Pearson HSAB principle, Ag(I), Cd(II), Ni(II), Cu(II) and Zn(II) ions all preferentially form M-S thiolate type arrangements however, in the presence of other bulky co-ligands such as triphenylphosphine (PPh_3) the reactivity of this bond may change to accommodate M-S thionate type arrangements as well.[261,265–267] Additionally, N-heterocyclic thiones impart biological activity within a Schiff-base system through the presence of both hard (N and O) and soft (S, C=N) donor atoms. The combination of these atoms influence the overall electronics of the system, as observed by Aboura *et al*.[268]

1.4.1 Metal triazoles bearing antifungals

Due to pathogenic fungi sharing characteristics with other eukaryotes such as parasites (leishmanial and trypanosomal), cancerous and tumour cells, the repurposing of drug classes used to target these groups has been explored as an alternative to mitigate resistance. The shared biosynthetic pathway has provided a useful basis for complex design, for example, many existing antifungal drugs have incorporated in metal complexes as anticancer and antiparasitic agents.

Efforts have been made to synthesise novel metal-based drugs using ruthenium(II)-based precursors with the known organic-based antifungal agents Clotrimazole (CTZ), fluconazole (FCZ) and ketoconazole (KTZ). Navarro *et al.,* synthesised a set of four complexes with the general formula {[Ru^{II}(η_6-arene)(Cl)(X)(Y)](Z)} (where X = CTZ, FCZ, KTZ Y = PPh_3 and counter ion Z = Cl^- or PF_6^-) and evaluated them against *Leishmania major (L. major)* and *trypanosoma cruzi (T. cruzi*).[269,270] The biological activity of these compounds confirmed the synergistic activity of the metal coordinating to the ligand with the most active compound of the series, [$Ru^{II}Cl_2$(η^6-CTZ)(η^6-*p*-cymene)] (Figure 34, **1-28[a]**) displaying selective indices (SIs) of 500 and 75 against *L. major* and *T. cruzi*.[269,271] In 2020, Kollipara and co-workers synthesised a series of cationic Ru(II) complexes (Figure 34, **1-28[b]**) which displayed appreciable activity against *C. albicans* isolates with inhibitory zones greater than fluconazole (FCZ) (>20 mm vs 18 mm).[272]

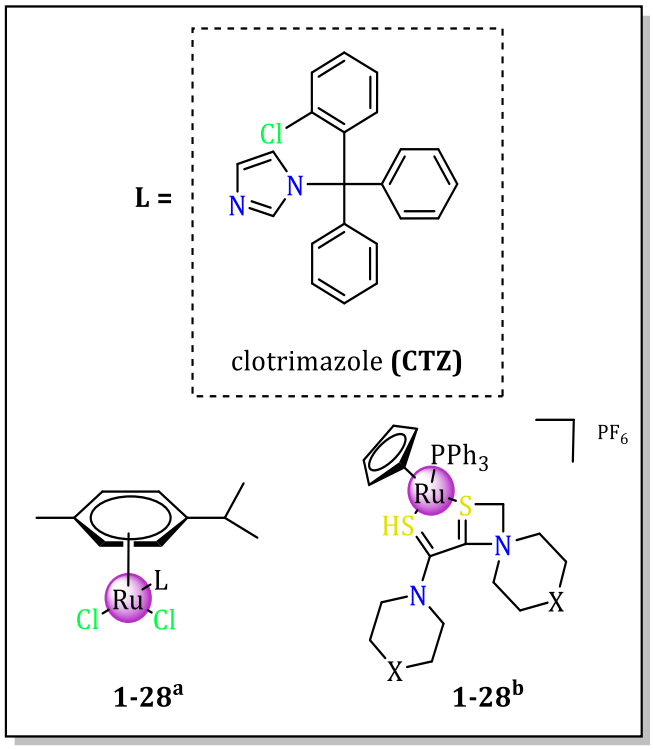

Figure 34: Antifungal ruthenium(II) complexes **1-28^{a}** = *p*-cymene backbone with a coordinated L= clotrimazole (CTZ) **1-28^{b}** = ruthenium(II) cationic complex series based on the dithione moiety.

In 2018 Gagini and Co-workers,[91] explored metal-drug synergistic interactions using eight complexes of the transition metals Cu(II), Au(I) and Pt(II) with the antifungals CTZ and ketoconazole (KTZ) (Figure 35, **1-29^{a-d}**).[91] The metal complexes were observed to display better minimal fungal concentration (MFC) values than their free ligand counterparts with values between 4 nM and 8 nM. It was found that the action of the phosphine ligand on the metal complex enhances the biological effect against *Sporothrix* spp.[91]

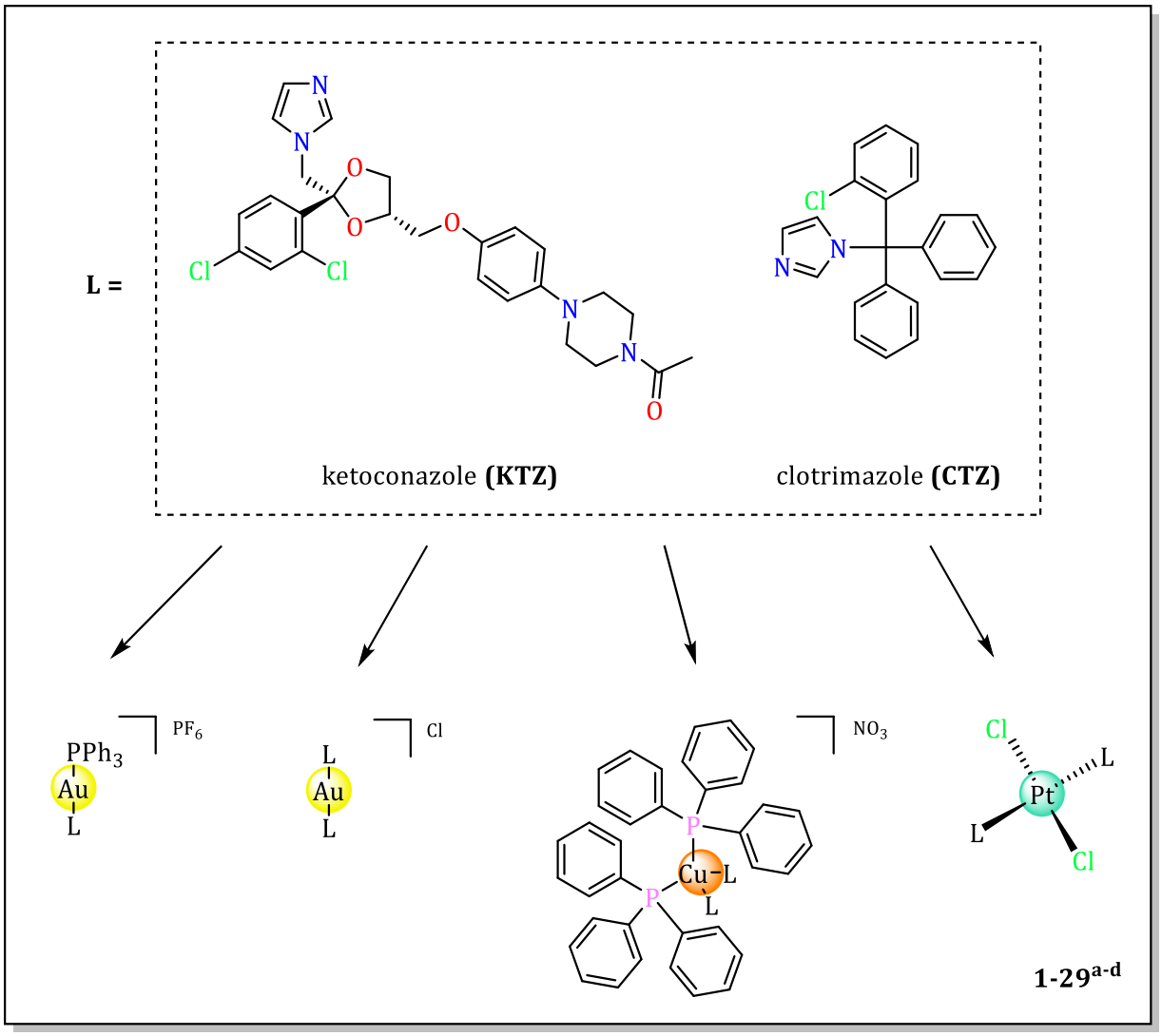

Figure 35: Schematic representation of the synthetic complexes of Cu(II), Au(I) and Pt(II) with the antifungal drugs ketoconazole (KTZ) and Clotrimazole (CTZ).[91]

The systematic evaluation of a library of organometallic ferrocene derivatives have been shown to exhibit significant antifungal activity. While the initial set of complexes synthesised by Fang *et al.,* containing 1,2,4-triazole and thiazole ligands complexes were tested against powdery mildews and brown rust (Figure 36, **1-30**) they showed no enhanced antifungal activity when compared to the precursor molecule, triadimefon.[273] In 2006, the second-generation library of *E,Z*-complexes (Figure 36, **1-31**) were evaluated against the fungal strains *P. zeae*, *A. solani, P. pircola,* and *C. ara*.[273] The *E*-isomers were shown to display higher inhibitory activity than the *Z*-isomers at 50 ppm and reported fungal inhibition up to 62%.[274] In a more recent 2018 study, Gabano and co-workers explored the ferrocenyl 2-pyrazolyl-1,3-

thiazolidin-4-ones against *C. albicans*; notably the methyl derivative (Figure 36, **1-33**) displayed MIC values of 1 mg/mL and by comparison, the antifungal drug control reported MIC values of 20 µg/mL.[256,269]

Over time, the structural modifications to the organometallic ferrocene library produced enhanced antifungal activity. Through these studies, the general MoA was concluded to target the ferrous cytochrome-P450 enzyme family and in turn, reduce virulence.[273,275,276]

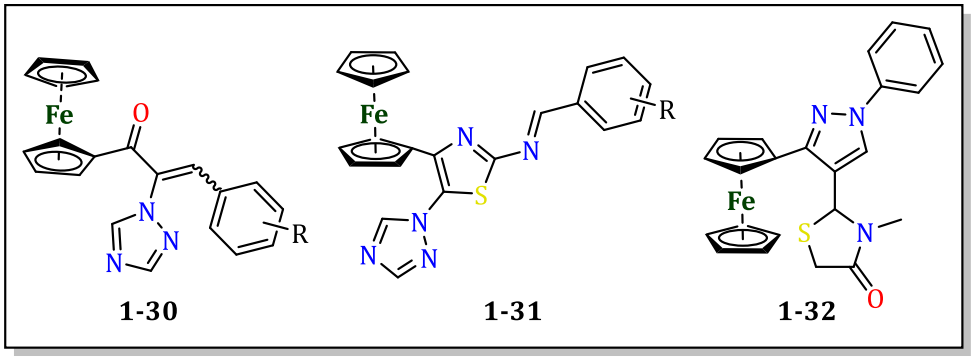

Figure 36: Organometallic ferrocenyl 1,24-triazole and thiazole containing antifungal complexes where **1-31** = ferrocenyl vinyl 1,2,4-triazole derivatives **1-32** = N-substituted benzylidene-4-ferrocenyl-5-(1H-1,2,4-triazol-1-yl)-1,3-thiazol-2 amine derivatives and **1-33** = ferrocene-containing 2-pyrazolyl-1,3-thiazolidin-4-ones.[273,275]

In 2021, FCZ derived Cu(II) and Zn(II) complexes synthesised by Stevanovic *et al.,* with the general formulae $\{[CuCl_2(FCZ)_2].5H_2O]\}_n$ and $\{[ZnCl_2(FCZ)_2].2C_2H_5OH\}_n$ showed 2.7-fold higher antifungal activity than the free FCZ drugs against clinical isolates of *C. albicans.*[277] The metal complexes were able to arrest hyphal formation and the Zn(II) complex reduced fungal cell adhesion.[277]

1.5 Research Significance

The underlying objective of this research seeks to address the requirement for novel drugs to provide an alternative route to combatting antimicrobial resistance. There has been a significant lag in commercial antimicrobial drug release and the need for new drugs to combat diseases eclipses the current rate of development.

The known impacts on metals in medicine continues to be an area of interest and the lack of knowledge concerning the MoA of metal-based complexes especially with respect to antimicrobial activity means that their potential for this application may be yet to be realised. Given that the antimicrobial and anticancer activity associated with bismuth, rhenium and gallium is well established, further research into the novel N-heterocyclic class of compounds complexed with bismuth(III), rhenium(I) and gallium(III) is required to expand upon the existing literature.

A range of biologically relevant metals: bismuth (Chapter 2), rhenium (Chapter 3) and gallium (Chapter 4), will be explored and reacted with a range of N-heterocyclic thione-based ligands namely 1,2,4-triazoles to produce novel complexes with antifungal and antibacterial activity. The triazole class of compounds has shown extensive therapeutic use especially within the fungal sphere however, resistance towards azole-based drugs has been widespread. Therefore, these ligands have been carefully chosen as they bear structural similarities with existing bioactive materials, additionally their synthetic protocols, reactivity, chemistry, and biological stability are known.

The synthetic strategies that will be employed involve variations in solvent, temperature, and time on the impacts of yield and purity of final products. All synthesised compounds intend to be characterised using a variety of analytical techniques such as: ^{1}H NMR and ^{13}C NMR spectroscopy, mass spectroscopy, FT-IR spectroscopy, melting point, and elemental analysis. Where possible, UV-Visible spectroscopy, X-ray diffraction and fluorescence spectroscopy will also be utilised.

For biological assessment, the solubility and stability of the synthesised complexes will be assessed in dimethyl sulfoxide (DMSO) via ^{1}H NMR spectroscopy in order to

determine their suitability for assay development. Additionally, their stability in biological media will also be assessed to establish their *in vitro* stability.

Although rhenium(I) tricarbonyl chemistry is well established in the literature, the biological stability of the N-heterocyclic class of compounds is yet to be explored and thus, will form as a supplement to this chapter. Additionally, their utility as backbone ligands will be assessed as to whether they are appropriate therapeutic agents.

The project summary and goals for this thesis include the synthesis, characterisation, biological and photophysical studies of a series of bismuth(III)-, rhenium(I)-, and gallium(III)-based complexes with a series of triazole thione-based ligands. Understanding the structural diversity and variation of this sub class of molecules and how they interact with different series of metals underpins this body of work. The complexation and metal-synergetic interactions play a significant role in the structural diversity as well as the biological activity.

CHAPTER 2: BISMUTH(III) N-HETEROCYCLIC THIOLATES

TRIS-SUBSTITUTED BISMUTH(III) TRIAZOLES

DIPHENYLBISMUTH(III) TRIAZOLES

TRIS-SUBSTITUTED BISMUTH(III) RHODANINES

DIPHENYLBISMUTH(III) RHODANINES

SYNTHESIS, CHARACTERISATION AND BIOLOGICAL STUDIES

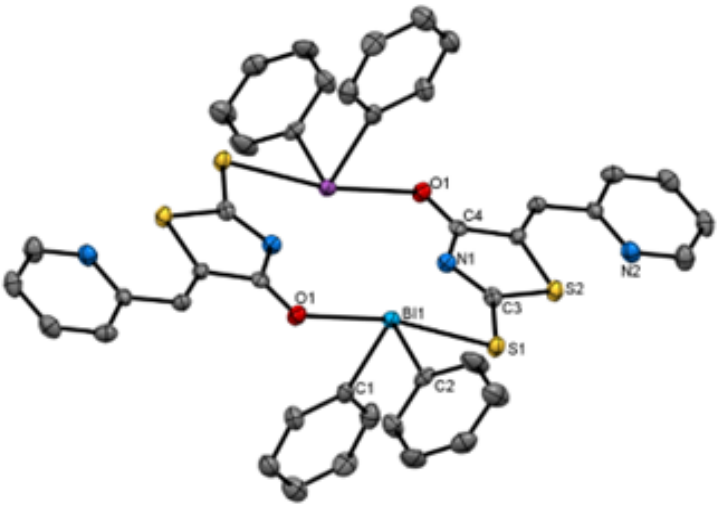

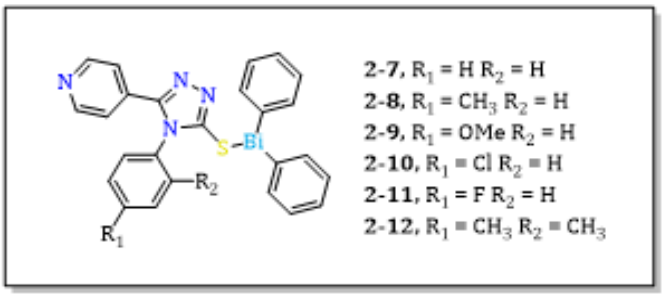

2 Bismuth(III) N-heterocyclic thiolates

2.1 Introduction

2.1.1 The biological action of bismuth(III)

Over the years, there has been extensive research surrounding the nature of the Bi-S bond. Bi(III) has been identified as a borderline Lewis acid according to the Pearson acid-base concept and thus, displays a high thiophilicity.[278] A variety of sulfur-bearing classes of compounds interact with bismuth through covalent or dative interactions in combination with other atoms such as oxygen or nitrogen e.g., S,N,[145,279] S,S,[280] S,O[281] or S[282,283]. The resulting complexes have displayed varying degrees of solution state stability.[279,281,283,284] Important structure-activity conclusions can be drawn through select factors namely, (1) the thermal and hydrolytic stability of the Bi-S bond in comparison to the Bi-O bond, (2) the kinetic lability of the Bi-S bond and (3) the propensity for the Bi-S bond to decompose and rapidly form Bi_2S_3 under certain conditions.[124,142,278,285,286]

Bismuth has been observed to form particularly unique biological interactions with sulfur containing proteins featuring cysteine residues namely, glutathione (GSH). Research conducted by Wong and co-workers has identified the structure of a *tris*-thiolato Bi(III) complex [$Bi(cys)_3$] comprising of three deprotonated cysteine (cys) ligands (Figure 37).[287,288] This supports the bio-coordination of Bi(III) with cysteine which also contributes to the interference in protein functions in *H. pylori*.[131] In a series of accumulative studies, Bi(III) was also demonstrated to interact with serum albumin and metallothionein, and postulated to cause the displacement of biological Zn(II) and Cd(II) causing an anti-ulcerative effect.[128,134,289,290]

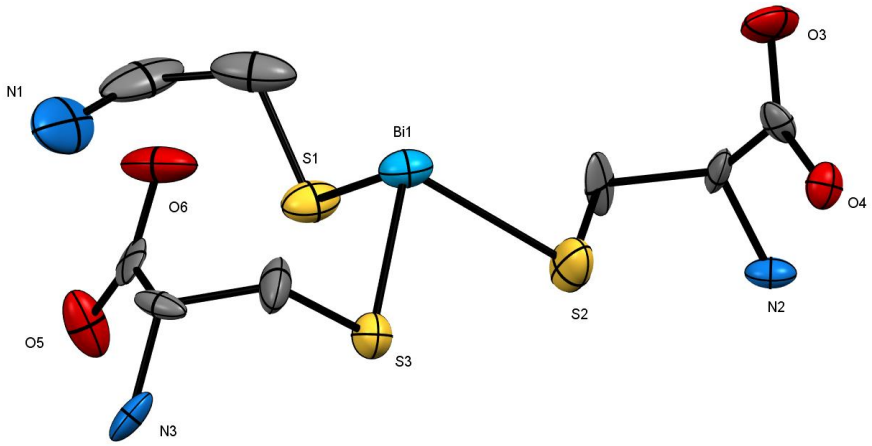

Figure 37: Asymmetric unit of the structure [Bi(Cys)$_3$] synthesized by Wong et al.[287] Hydrogen atoms have been omitted for clarity.

In another study conducted by Wang and co-workers,[291] a series of colloidal Bi(III) salts were shown to irreversibly inhibit the production of metallo-β-lactamases (MBLs) via metal displacement. Crystallographic studies showed Bi(III) binding to the NDM-1 active site resulting in the displacement of two Zn(II) cofactors.[291] The significant conformational changes observed as a result of the deactivation of MBL activity, followed by the confirmation of a Bi-S affinity was verified through the critical involvement of the cysteine Cys208 residue.[291]

2.1.2 Antibacterial bismuth(III) complexes

Touched upon in Chapter 1, bismuth-based metallodrugs have primarily gained traction in the treatment of *Helicobacter pylori (H. pylori)* related gastritis, ulceritis and gastric related cancers.[130] The derivatisation of bismuth-based compounds to include metal-organic and organometallic forms of bismuth, led to the expansion in library of Bi(III) alkoxides,[292] carboxylates,[144] sulfonates,[143] and thiolates,[145,279] for the treatment of *H. pylori*. Across each series, these bismuth(III) complexes displayed greater activity against *H. pylori* than their respective parent compounds.

Bismuth(III) has been explored with various organic ligand classes bearing sulfur atoms, by employing different modes of chelation and denticity which have impacted the overall therapeutic effect. For example, in a series of heteroleptic bismuth(III) sulfonate complexes of the form [BiPh$_2$(O$_3$SR)$_3$], minimum inhibitory concentration (MIC) values of ≥6.25 ug mL^{-1} were observed towards three strains of *H. pylori*. The

parent sulfonates showed no activity against the respective strains.[143] In another study conducted by Andrews *et al.*, complexation of bismuth(III) with a series of non-nutritive sulfamate sweeteners: saccharin (sac*H*), thiosaccharin (tsac*H*), acetosulfame (Ace*H*) and cyclamic acid (cycH_2) through either the N- or S- terminus (Figure 38) exhibited MIC values as low as 6.25 ug mL^{-1} which were comparable with the sulfonato series of complexes.[293] The sweeteners themselves displayed no bactericidal activity.[293,294]

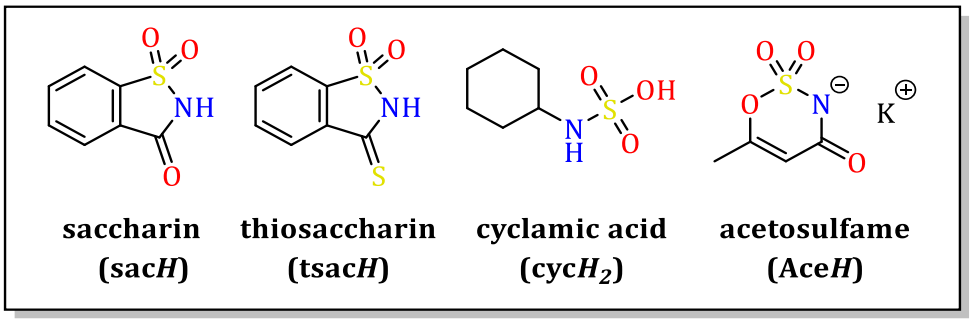

Figure 38: Molecular structures of some bioactive sulfur-based non-nutritive sweetener precursors employed by Andrews *et al.,* to synthesize bismuth(III) complexes.[293]

Later studies have explored chelation, with complexes incorporating both oxygen and sulfur donor atoms with the β-thioxoketonate series of compounds (Figure 39). Both homo- and heteroleptic bismuth(III) complexes of the form [BiL_3] complexed with the β-thioxoketones showed MIC values in the range 3.125-6.25 ug mL^{-1} in-line with MIC values obtained for other bismuth(III) carboxylate classes of compounds.[281]

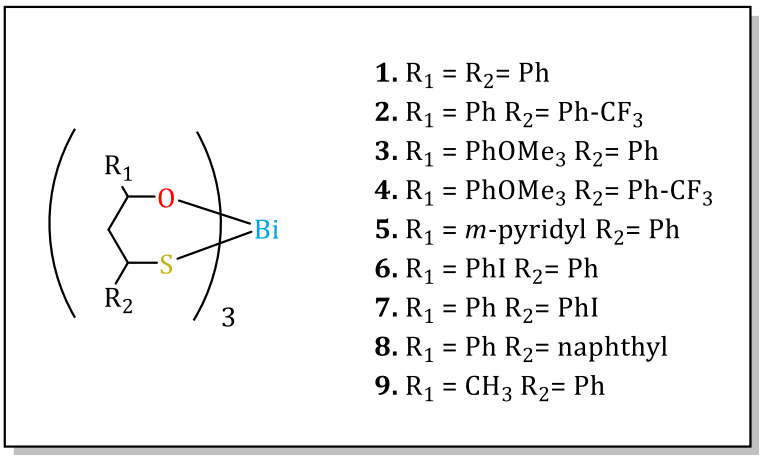

Figure 39: General structure of the homoleptic bismuth(III) β-thioxoketonate series of complexes synthesized by Andrews *et al.*[281]

Studies exploring the bismuth(III) thiophosphinate class of compounds (Figure 40) exhibited MIC values as low as 0.52 μM against the Gram-positive bacterial strains MRSA and VRE.[283] These complexes showed a general propensity to inhibit Gram-positive bacteria (e.g., MRSA, VRE) over Gram-negative bacteria (e.g., *E. coli, P. aeruginosa)*.[283]

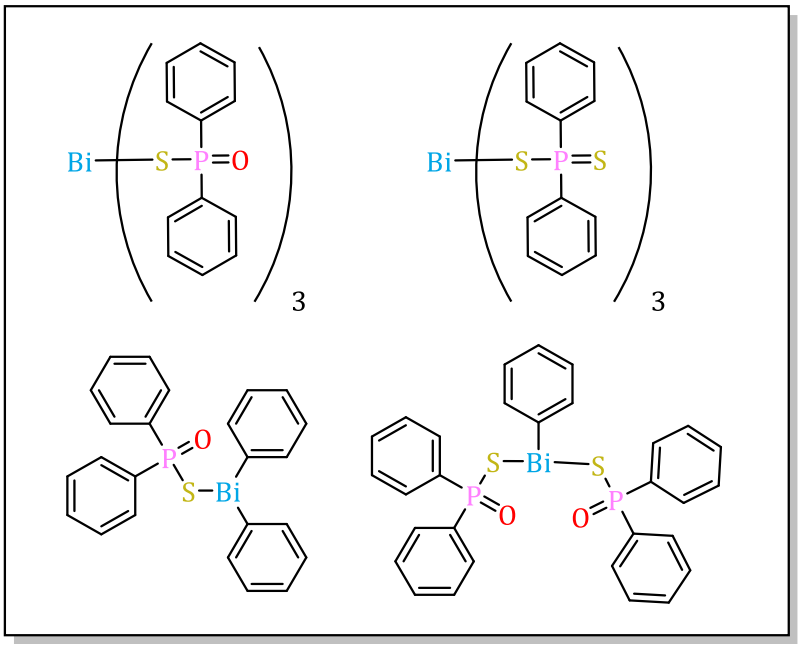

Figure 40: A series of antibacterial homo- and heteroleptic bismuth(III) thiophosphinate complexes synthesized by Senevirathna *et al.*[283]

2.1.2.1 Antibacterial bismuth(III) thiolates

Earlier studies of bismuth thiols (BTs) by Domenico and co-workers have explored the antimicrobial efficacy of a series of early generation bismuth(III) thiolates chelated with lipophilic thiol donors such as 1,2-ethanedithiol (EDT), 1,3-propanedithiol (PDT), or 2-3-dimercapto-1-propanol (BAL) (Figure 41).[295,296] The BTs were shown to be effective antimicrobials against biofilm formation with further studies conducted on the bismuth-2,3-dimercaptopropanol (BisBAL) complex.[297,298] BisBAL has shown to display antibiofilm and effective antibacterial activity against a variety of strains including: *Staphylococcus*, *K. pneumonia*, *Enterobacter*, MRSA and *P. aeruginosa.*[295,298–302]

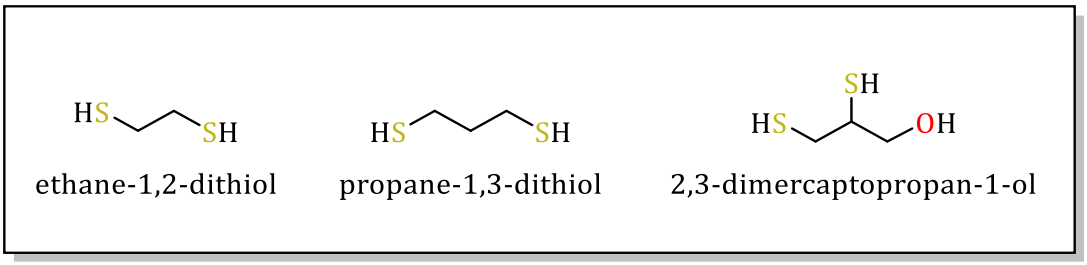

Figure 41: Early generation bismuth thiol (BT) precursors utilized by Domenico *et al*.

The derivative BisEDT synthesised by Domenico and co-workers,[299] was found to display antibacterial activity at subinhibitory concentrations; at higher concentrations, the complex was observed to show eukaryotic cell toxicity. This study suggested the application of these complexes is therefore suitable at low concentrations, due to the narrow therapeutic window.[296,299]

While the therapeutic MoA of BisBAL remains unclear, numerous studies have postulated it to be related to the interference of iron transport, delivery, and acquisition. In one study, the activity of BisBAL on redox enzymes was suggested to involve the thiol-exchange of Fe(III) in iron-sulfur clusters.[303,304] Additionally, the extracellular polysaccharide (EPS) production in bacterial biofilm has also been identified as a target site.[297,298,304,305] In a study exploring the formation of planktonic activated sludge flocs in the environment, Badireddy and Chellam, also postulated the disruption of the enzymatic carbohydrate acetylation pathway as active BisBAL target sites, one that shares an intrinsic link to the cellular action of BisBAL.[306,307]

2.1.3 Antifungal bismuth(III) complexes

While there has been considerable research in the antibacterial activity of bismuth, the antifungal activity of bismuth complexes have been limited to few derivatives and is therefore an expanding area of interest.[284] The antifungal activity of some organobismuthane compounds derived from alkyl ketones, aryl ketones (Figure 42) and carboxylates have been explored against the yeast *Saccharomyces cerevisiae* (*S. cerevisiae*).[308–310] Using a structure-activity relationship (SAR) study, a combination of modifying the lipophilicity-hydrophilicity relationship as well as the stabilisation of the metal complex produced zones of inhibition comparable to the clinical antifungal drug, Nystatin.[308] The mechanism of action was hypothesised to occur via

a Bi-Cl or Bi-O bond cleavage within the yeast cell; this results in the formation of a bismuth framework and preferential binding for a higher affinity thiol group.[308] Notably, the halobismuthanes explored in this study were reported as weak antibacterials, this could be indicative of the greater selectivity towards eukaryotic cells.

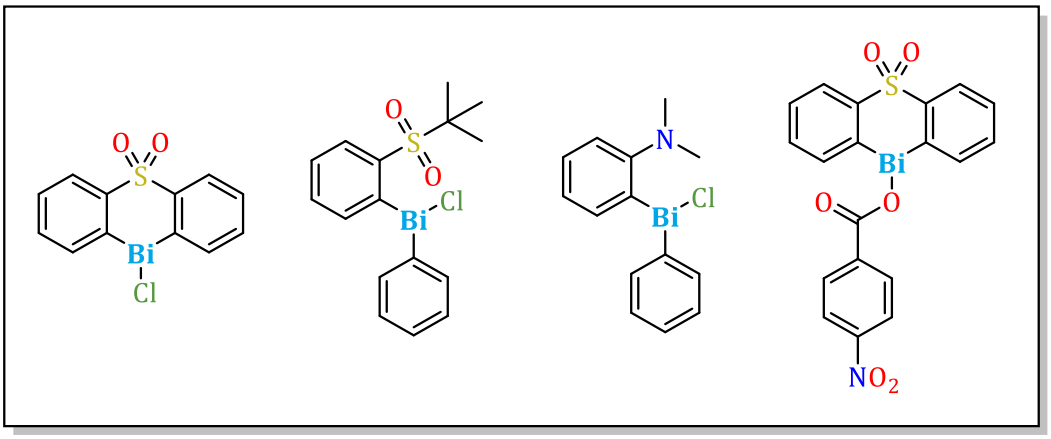

Figure 42: Molecular structures of some bioactive hypervalent organobismuthane complexes synthesized by Murafuji and co-workers.[308]

A separate study was conducted on the antifungal activity of bismuth sub-salicylate (BSS) showing a statistically significant increase in the biomass of *A. niger*.[311] A decrease in concentration of free solubilised bismuth(III) was observed in the aqueous medium, confirming intracellular uptake of the bismuth(III) species.[311] Solanki and co-workers reported some mixed bismuth(III) pyrazoline, acetate and salicylate complexes, tested against *A. niger* which showed zones of inhibition greater than the free pyrazolines.[312]

In another study conducted by Dawara and Singh, the synthesis of coumarin-based ligands with Bi(III) produced complexes with moderate antifungal activity when compared to the commercially available drug, Fluconazole (FCZ).[313] The antifungal activity of the Bi(III) complexes was higher than their corresponding free coumarins.[313]

2.1.4 Bismuth(III) thiolates

In the past decade, the Andrews group has explored several novel Bi(III) complexes derived from N-heterocyclic thiones, oxathiazolidines, and phenylthiazole displayed promising antibacterial activity with low toxicities to human cells.[279,280,282,314] Interestingly, all parent thiones were found to rearrange to their thiolate forms in the process of binding to the Bi(III) metal centre.

Several studies conducted by Luqman and co-workers explored the synthesis of various thiolato-based derivatives with bismuth(III) precursors.[279,282,314] In one study, seven phenyl-*bis*-thiolatobismuth(III) complexes of the form [$BiPhL_2$] (where L denotes the relevant substituted oxathiazolidine derivative, Figure 43) displayed MIC values of 1.1-1.2 μM against the Gram-positive bacteria: *S. aureus,* MRSA and VRE.[282] Microbial studies for these candidates revealed increased bactericidal activity of phenylbismuth(III) *bis*-thiolato derivatives when compared to the free oxathiazolidines as well as the *tris*-substituted bismuth(III) thiolato counterparts. These compounds were proven non-toxic to mammalian cos-7 cells rendering them ideal candidates for *in vitro* and *in vivo* studies.

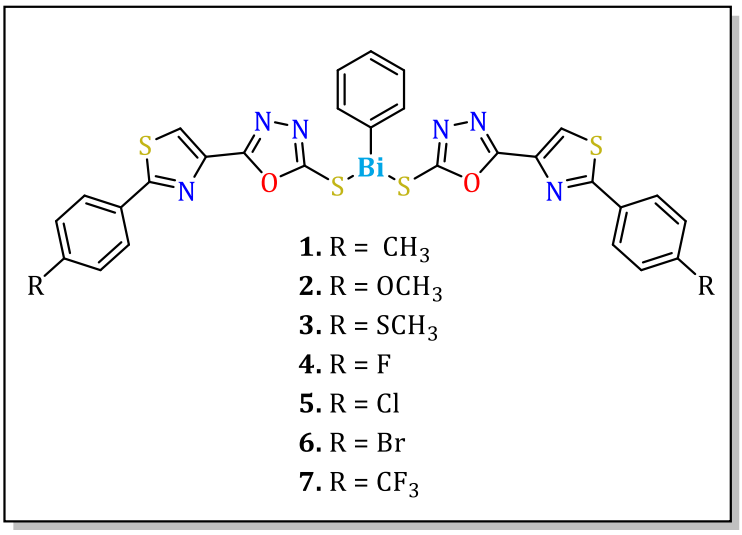

Figure 43: General structure of the heteroleptic phenylbismuth(III) *bis*-oxathiazolidine complexes synthesized by Luqman and co-workers.[282]

In another study conducted by Luqman and co-workers, the synthesis of bismuth(III) thiolato complexes derived from N-heterocyclic thione precursors were explored (Figure 44); in line with the previously observed trends, the bismuth(III) complexes

displayed enhanced bactericidal activity when compared to their free thione counterparts.[282,314] Some important conclusions drawn from this study included the apparent increase in antibacterial activity of the heteroleptic bismuth(III) thiolates of the form [BiPhL$_2$] when compared to the homoleptic *tris*-substituted bismuth(III) thiolates of the form [BiL$_3$] of other complexes. For example, the homoleptic *tris*-substituted bismuth(III) thiolate complex [Bi(4-MMT)$_3$] (where 4-MMT(H) = 4-methyl- 4H-1,2,4-triazole-3-thiol, Figure 44) showed MIC values of 180.13 μM towards MRSA, VRE, and *E. coli*, conversely the phenylbismuth(III) *bis*-thiolate analogue [BiPh(4-MMT)$_2$] showed MIC values in the range of 19.44-9.72 μM towards the same bacterial strains.[314] Notably within this study, Bi(V) analogues featuring both the dithiolato- and dithione type bonds formed [BiPh(L)$_2$(L*H*)$_2$] type structures. These complexes showed the most significant biological activity against VRE (MICs as low as 0.34 μM).[145]

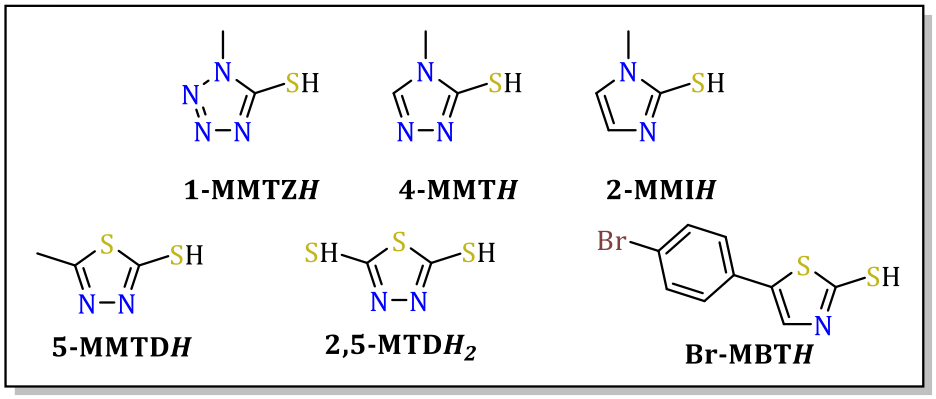

Figure 44: N-heterocyclic precursor molecules used in the synthesis of Bi(III) thiolate complexes by Luqman and co-workers.[314]

Following on from this research, the 1,2,4-triazole-thione system has been chosen as an attractive candidate for further study. Functionalisation of the triazoline-thione group through the addition of a pendant pyridyl group, as well as the addition of an aryl moiety in the 4-position afforded access to substrates of the general form: 5-(pyridin-4-yl)-4-phenyl-2H-1,2,4-triazole-3(4H)-thiol to react with bismuth(III) to form novel bismuth(III) thiolato complexes.

2.1.5 Rhodanines: 5-substituted 2-thioxothiazolidin-4-ones

N-heterocyclic compounds have cemented their status in drug discovery and design with over 60% of all organic-based therapeutics bearing a nitrogen heterocycle as of 2021.[212] The thiazolidinedione sub-class of compounds has gained traction in the scientific community as a promising building block for the design of novel therapeutic compounds.[315] Introduced in the late 1980s, the thiazolidine-2,4-dione (also referred to as 'glitazone') type heterocyclic compounds were exemplified by their use in the treatment of Mellitus diabetes type-II with the commercially available derivatives: Troglitazone, Rosiglitazone and Pioglitazone (Figure 45) currently in commercial use.[316] In a most recent clinical trial, rosiglitazone has been reassessed for its efficacy as a third line therapeutic (National Clinical Trial identifier: NCT02653209).[317]

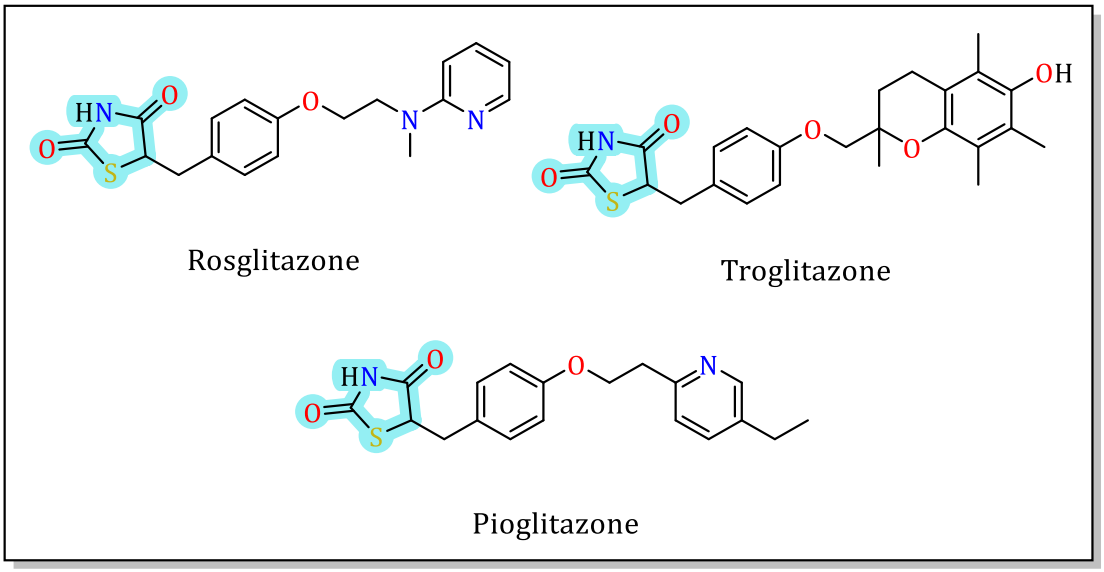

Figure 45: Chemical structures of the commercial thiazolidine-2,4-dione derivatives Rosiglitazone, Pioglitazone and Troglitazone.[318]

The rhodanine motif comprises of a five-membered heterocyclic ring bearing a thiazole core with a substituted thioxo- and carbonyl group at positions 1 and 3, respectively. While the motif is structurally related to the glitazone class (Figure 45, highlighted), the organic molecules bear different electronic characteristics and therapeutic activity.[318] Continual structural modifications of this series of compounds have resulted in a rich diversity of complexes bearing a broad

pharmacological profile from antibacterial,[316,319] antifungal,[320–322] antitumour,[323] and anticancer applications.[324] Commercially, the rhodanine scaffold is already present within the antidiabetic drug Epalrestat to treat diabetic neuropathy (Figure 46, left).[325] Approved by the Japanese FDA, Epalrestat is an aldose reductase inhibitor which acts on the receptors associated with abnormal heart function associated with diabetic peripheral neuropathy.[326] Epalrestat has been observed to reduce the accumulation of sorbitol (by product of glucose transformation) in the sciatic nerve and erythrocytes.[325,327]

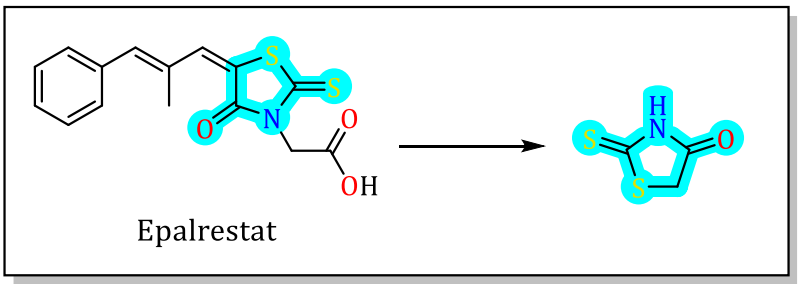

Figure 46: Empirical structure of the antidiabetic drug Epalrestat (right) and the 2-thioxothiazolidin-4-one ore (rhodanine; left).

While rhodanine is an important scaffold, the derivatization of this functional group has led to a wide array of pharmacologically important molecules. Namely, conjugation of this group to a aryl/alkyl moiety has resulted in appreciable antibacterial and antifungal activity.[320]

2.1.5.1 Rhodanine-based antimicrobials

The 5-arylmethylidenerhodanine derivatives containing a reactive exocyclic double bond have been identified as strong electrophiles, showing enhanced biological activity as identified in high throughput screening against microbes.[323,328,329] In a study conducted by Insuasty *et al*,[323] an alkylrhodanine derivative was found to display modest antifungal activity against *S. cerevisiae* with MIC values as low as 3.9 μg mL^{-1}.[320,323]

The reactivity of 5-benzylidinerhodanines have been identified as potential antifungals showing MIC values below 20 μg mL^{-1} against opportunistic fungal pathogens, yeasts, and dermatophytes.[329] Among some of the fungal resistant pathways, the 5-benzylidinerhodanine sub-class has been observed to encumber

fungal cell wall synthesis through the disruption of mannoproteins involved in cell wall adhesion. In a study conducted by Sortino and co-workers,[320] a series of rhodanine-3-acetic acid derivatives were identified to inhibit the growth of *C. albicans* in the nanomolar range (MICs as low as 0.002 μM) by targeting the mannosyl transferase 1 enzyme (PMT1).[321]

In terms of the MoA, rhodanines have been identified to target the inhibition of enzymes through various organic transformations. 5-benzylidinerhodanines for example, have been shown to undergo 1,4-conjugate addition reactions with nucleophilic cysteine side chains to form covalent adducts. Additionally, the rhodanine core itself can act as a diphosphate mimic and bind to metal centres like bacterial β-lactamases to disrupt protein function.[330,331] As these compounds have been found to interact with free cellular thiols and intracellular glutathione like metal complexes, further investigation into their antifungal activity would be an avenue of interest.[288,329]

Although rhodanines have been identified as privileged scaffolds in organic synthesis, their biological activity has been hypothesised to be unselective due to their ability to bind to multiple protein target sites. The moiety has been described as a 'pan assay interference compound' (PAINS) or frequent hitters.[332,333] Multiple high throughput screening (HTS) campaigns have postulated the moiety to be unselective due to the false positive hits or "promiscuity" of the molecule as a result of the consequent hydrogen/polar bonds associated with the exocyclic sulfur atom.[332,334] Despite this aspect, rhodanines should not be overlooked as building blocks for metal-based therapeutics, as explored in chapter 1, metal complexes offer three-dimensional diversity and potential for site-specific selectivity in addition to enhanced activity via metal-to-ligand synergy.

The rhodanine scaffold has presented as a potential target site for complexation with Bi(III) due to the multiple donor atoms present within the molecule (O,S,N) which allow for a different potential binding modes that may be present upon metal complexation. Additionally, as a small compound with low molecular complexity, there is an increased probability of binding to a biological target site.[335] Despite the rhodanine class being described as promiscuous binders, this study hopes to explore

whether an molecule with multiple binding atoms and modes can be "locked" into a particular conformation and thus, impart a therapeutic effect.

2.2 Chapter objectives

As highlighted in Chapter 1, many complexes have been developed with the intention to be used as antimicrobials and further therapeutics with several complexes showing desired properties. However, the optimisation of bismuth(III)-based therapeutics is still in its infancy with studies limited to synthesis, characterisation, and rudimentary biological evaluations. The biological targets of the Bi(III) ion are predominantly sulfur-based residues and hence, it is of interest to further expand upon the synthesis and biological evaluation of a series of Bi(III) thiolato-based complexes derived from the N-heterocyclic class of compounds.

Although there have been numerous studies pertaining to the synthesis and characterisation of bismuth(III)-based N-heterocyclic complexes, an in-depth expansion into the structure-activity relationship (SAR) of these complexes is yet to be explored and the solution state stability and toxicity are still an area of keen interest. Andrews *et al.,*[143] have also identified that a dramatic increase in the bactericidal properties of bismuth(III) could be attributed to heterolepticity of the metal species, with some compounds displaying activities greater than the commercial bismuth(III) sub-salicylate derivatives. Therefore, this will be explored upon in this chapter.

A series of both homoleptic and heteroleptic Bi(III) thiolates of the forms [$BiPh_2(SR)$] and [$Bi(SR)_3$] (where SR = triazole thione) will be explored for their therapeutic activity. The incorporated ligands include the substituted N-heterocyclic triazole and rhodanine classes in various substitutions. The complexes will be characterised via ^{1}H NMR and ^{13}C NMR spectroscopy, FT-IR spectroscopy, high resolution mass spectrometry (HRMS), elemental analysis, and melting point analysis. Where possible, the solid-state structures of the Bi(III)-thiolate complexes will be obtained via X-ray diffractometry and compared to relevant Bi(III) thiolates in the literature.

The solution stability of the heteroleptic bismuth(III) thiolates will be explored in the presence of wet DMSO-d_6, cell culture media and individual media components using

^{1}H NMR and UV-Visible spectroscopy. In order to gain insight into the intracellular complex stability, the bismuth(III) thiolates will be tested in the presence of glutathione and cysteine.

The activity of the Bi(III) thiolates will be assessed towards mammalian cos-7 cells using the CellTitre-Blue assay protocol.[336] Bacterial susceptibility testing will be conducted on the heteroleptic complexes against a series of Gram-positive and Gram-negative strains: methicillin resistant *Staphylococcus aureus* (MRSA), vancomycin-resistant *Enterococcus* (VRE), and Gram- *Escherichia coli* (*E. coli*) and *Pseudomonas aeruginosa* (*P. aeruginosa*) as well as the fungal strains *Candida auris (C. Auris)* and *Candida glabrata (C. glabrata).* The activity of these results will then be used to postulate the overall antimicrobial activity, toxicity, and selectivity of the Bi(III) thiolates towards cells.

To support the cellular assays, the relative Bi(III) uptake in bacterial cells (MRSA and *E. coli*) treated with select Bi(III) homoleptic and heteroleptic thiolates will be determined using ICP-MS to ascertain the correlation between cellular metal uptake and bioactivity. Similarly, the supporting haemolysis and membrane integrity assays intend to provide further insight into the potential mode of action of the Bi(III) heteroleptic and homoleptic thiolates.

2.3 Part 1: Results and discussion – triazoles

2.3.1 Synthesis and spectroscopic characterization of disubstituted 1,2,4-triazole-3-thiols

A series of disubstituted 1,2,4-triazole-3-thiols bearing a pyridyl moiety were synthesised following a facile, safe and high yielding microwave procedure.[337] As shown in Scheme 2, six pyridyl-substituted thiones were synthesised by the reaction of isonicotinic hydrazide with aryl isothiocyanate to form a hydrazine carbothioamide derivative. The corresponding derivative was oxidatively cyclised via the addition of 1 M sodium hydroxide upon heating under reflux conditions. The corresponding cyclised product was then treated with the addition of 1 M hydrochloric acid, resulting in the precipitation of a crude product. This was then recrystallised from hot ethanol to afford the desired compounds (Scheme 2). The final triazoles: 4-phenyl-5-(pyridin-4-yl)-2,4-dihydro-3H-1,2,4-triazole-3-thiol (PTz*H*, **1**), 5-(pyridin-4-yl)-4-(p-tolyl)-2,4-dihydro-3H-1,2,4-triazole-3-thiol (PTTz*H*, **2**), 4-(4-methoxyphenyl)-5-(1-phenylethyl)-2,4-dihydro-3H-1,2,4-triazole-3-thiol (POTz*H,* **3**), 4-(4-chlorophenyl)-5-(pyridin-4-yl)-2,4-dihydro-3H-1,2,4-triazole-3-thiol (PCTz*H,* **4**), 4-(4-fluorophenyl)-5-(pyridin-4-yl)-2,4-dihydro-3H-1,2,4-triazole-3-thiol (PFTz*H*, **5**), and 4-(2,4-dimethylphenyl)-5-(pyridin-4-yl)-2,4-dihydro-3H-1,2,4-triazole-3-thiol (PDTz*H*, **6**) were chosen as substrates for the formation of Bi(III) thiolate complexes.

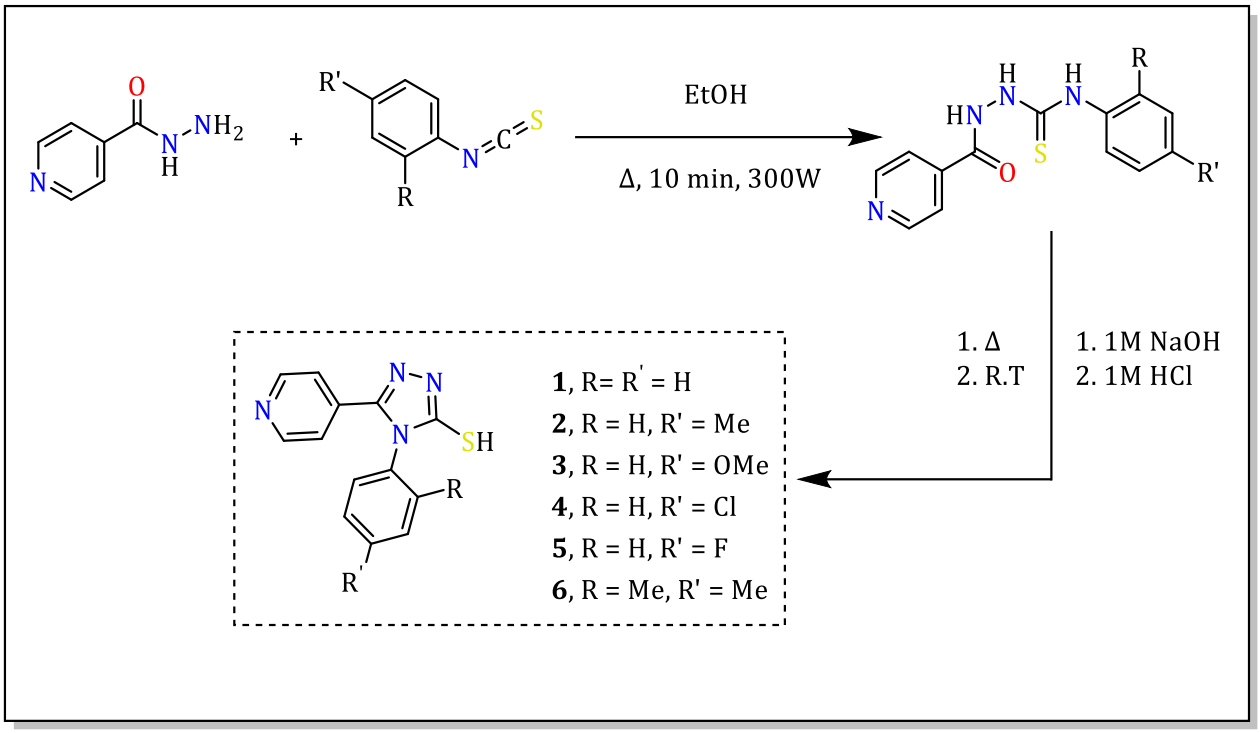

Scheme 2: Preparation of pyridyl substituted thiols **1** to **6** from isoniazid and substituted aryl isothiocyanates.

Varying substituents on the N2 triazole (aryl) ring provided insight into whether the effect of small structural changes impart a significant difference in the biological output of the respective Bi(III) thiolate complexes. The substrates **1** to **6** were characterised by ^{1}H NMR and ^{13}C NMR spectroscopy, high resolution mass spectrometry, FT-IR spectroscopy and melting point analysis in accordance with the literature values.[338] This reaction procedure was modelled from Youssef *et al.,*[338] and was further optimised using microwave irradiation, producing improved yields of the resulting substituted phenyl carbothioamide derivatives and final triazole thiols.

2.3.2 Synthesis of [Bi(SR)$_3$]: Homoleptic *tris*-substituted Bi(III) thiolates

A series of complexes were synthesised under standard Schlenk conditions, the homoleptic *tris*-substituted Bi(III) triazole thiolato complexes bearing a pyridyl moiety, **2-1** to **2-6.**

The general reaction scheme involved the cannula transfer of three equivalents of the parent triazole **1** to **6**, solubilised in dry tetrahydrofuran (THF) into an off-white THF

suspension of bismuth tert-butoxide [Bi(O^{t}Bu)$_3$] at room temperature (Scheme 3). This resulted in an immediate colour change of the solution to transparent yellow. The solution was left to stir under an atmosphere of nitrogen for four hours, resulting in bright yellow-orange opaque solutions in all cases. The removal of solvent *in vacuo* yielded brightly coloured orange-to-yellow solids.

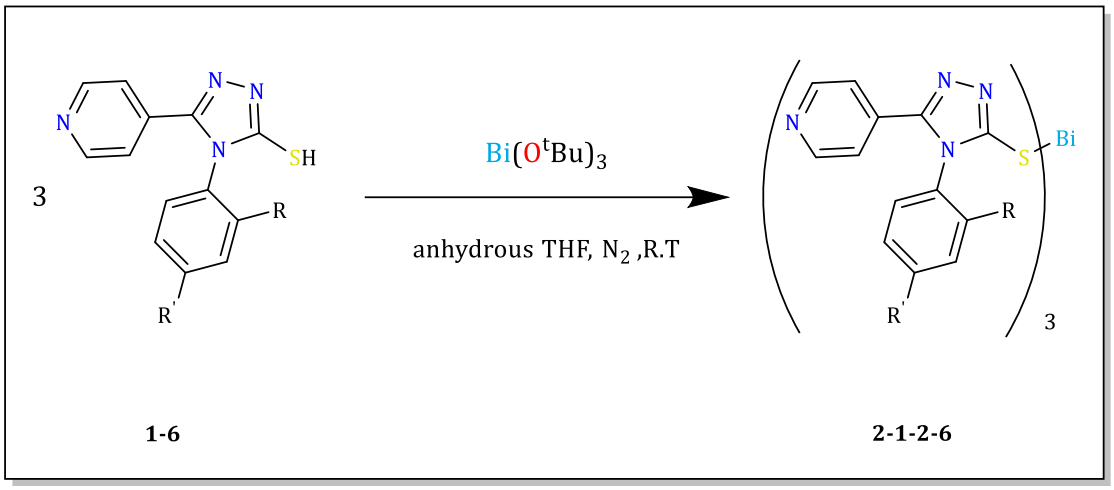

Scheme 3: Synthesis of the homoleptic *tris*- substituted bismuth(III) thiolato complexes **2-1** to **2-6** from the reaction of thiolates **1** to **6** with [Bi(O^{t}Bu)$_3$].

The obtained solids were washed with diethyl ether (Et$_2$O) and n-hexane to remove any unreacted starting materials and produced yields between 60-80 % of the *tris*-substituted Bi(III) triazole thiolato complexes **2-1** to **2-6** (Table 2). The complexes were characterised via ^{1}H NMR and ^{13}C NMR spectroscopy, FT-IR spectroscopy, HRMS and microanalysis. While crystal structures of the complexes have not yet been obtained, the ^{1}H NMR data of the compounds suggests binding to the Bi(III) metal centre occurs through the deprotonated thiol.

Table 2: Summary of yields and appearances of homoleptic tris-substituted Bi(III) thiolato complexes **2-1** to **2-6**, (d.c. refers to decomposition).

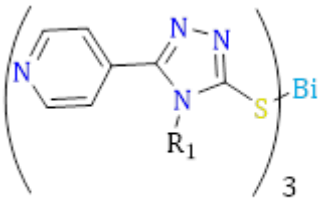

2-1 to **2-6**

Complex		Functional Group (R_1)	Yield (%)	Melting point (°C)	Appearance
2-1	[Bi(PTz)$_3$]	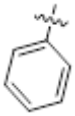	58	182 - 197 (d.c.)	Bright yellow powder
2-2	[Bi(PTTz)$_3$]	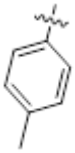	69	188 - 190 (d.c.)	Bright orange powder
2-3	[Bi(POTz)$_3$]	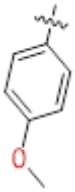	53	187 - 191 (d.c.)	Bright orange powder
2-4	[Bi(PCTzl)$_3$]	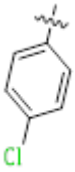	57	189 – 192 (d.c.)	Bright orange powder
2-5	[Bi(PFTz)$_3$]	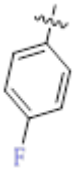	66	215 - 237 (d.c.)	Bright yellow powder
2-6	[Bi(PDTz,)$_3$]	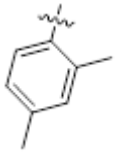	88	165 - 171 (d.c.)	Bright yellow powder

2.3.3 Synthesis of [BiPh$_2$(SR)]: Heteroleptic diphenylbismuth(III) thiolates

Heterocyclic thiolates are weakly acidic with pK_a values ranging between 5-11. Therefore, it has been demonstrated that in the presence of common organic solvents, metal salts (such as NaOH) may deprotonate these species.[243] To form the heteroleptic phenylbismuth(III) thiolato derivatives, the bismuth(III) salt diphenylbismuth(III) chloride [BiPh$_2$Cl] was utilised (Scheme 4).

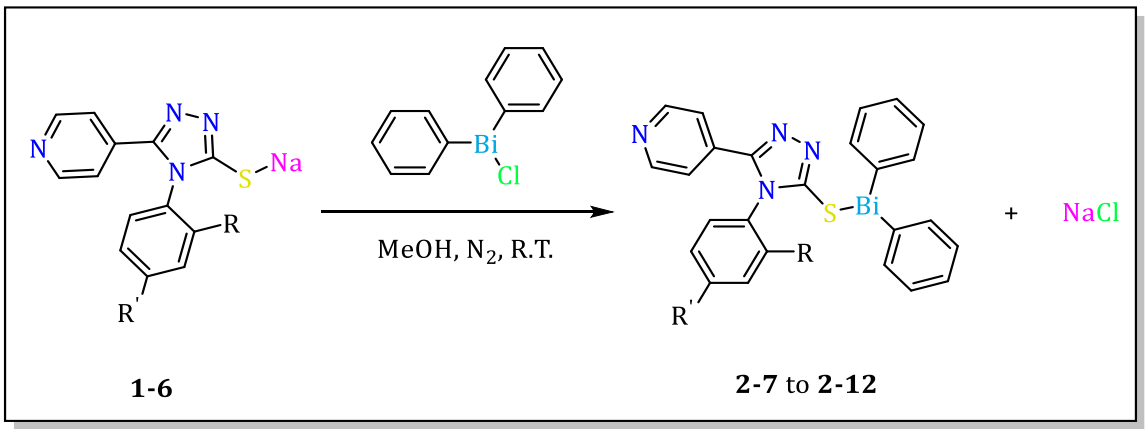

Scheme 4: Synthesis of heteroleptic Bi(III) thiolates **2-7** to **2-12** from the reaction of the sodium salt of **1** to **6** and [BiPh$_2$Cl].

The *para*-fluorophenyl triazole thiol PFTz, **5** was converted to a sodium salt when stirred with a solution of sodium hydroxide in methanol for two hours. The pale-yellow solution turned amber, and the solvent was removed *in vacuo* producing the salt in the form of a yellow powder in quantitative yield. Solution state studies revealed the upfield shift of all aromatic proton signals and absence of the thioamide proton signal, which was indicative of Na-binding.

As bismuth(III) salts have been demonstrated to decompose under ambient conditions, the [BiPh$_2$Cl] precursor and reaction were handled under inert air sensitive conditions.[143] [BiPh$_2$Cl] was added via a solid addition tube to a solution of the sodium thiolate in dry methanol at room temperature, resulting in an immediate colour change and precipitation from a transparent yellow to an opaque off-white suspension. The addition of distilled water to the reaction vessel allowed the desired crude complex to precipitate out of solution as an off-white solid. The precipitate was

collected via filtration, washed with water followed by Et_2O, and dried *in vacuo* to produce the complexes **2-7** to **2-12** with yields varying between 75-98 % (

Table 3).

The six synthesised complexes **2-7** to **2-12** (Figure 47) were characterised by ^{1}H and ^{13}C spectroscopy, FT-IR spectroscopy, HRMS, MP and (where possible) single crystal X-ray diffraction. The complexes displayed limited solubility in a selection of polar solvents such as ethanol, methanol, dimethyl sulfoxide, and acetonitrile (MeCN). ^{1}H and ^{13}C NMR spectra were able to be obtained in DMSO-d_6, however, over an extended period of time (>3 months) complexes appeared to rearrange in solution to form decomposition products.

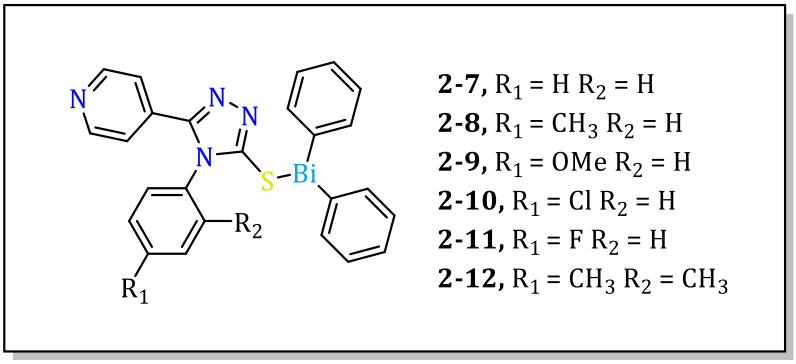

Figure 47: Summary of heteroleptic diphenylbismuth(III) thiolato complexes **2-7** to **2-12**

Table 3: Summary of yields and appearances of heteroleptic diphenylbismuth(III) thiolato complexes **2-7** to **2-12** whereby PTz = **1**, PTTz = **2**, POTz = **3**, PCTz = **4**, PFTz = **5**, and PDTz = **6**

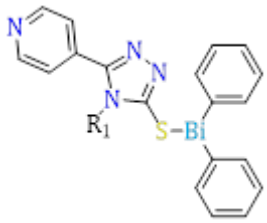

Complex		Functional Group (R_1)	Yield (%)	Melting point (°C)	Appearance
2-7	[$BiPh_2$(PTz)]	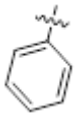	98	182 - 197 (d.c.)	Off white powder
2-8	[$BiPh_2$(PTTz)]	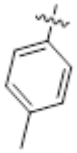	87	188 - 190 (d.c.)	Off white powder
2-9	[$BiPh_2$(POTz)]	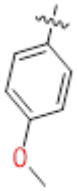	85	187 - 191 (d.c.)	Off white powder
2-10	[$BiPh_2$(PCTzl)]	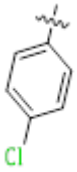	53	189 – 192 (d.c.)	Off white powder
2-11	[$BiPh_2$(PFTz)]	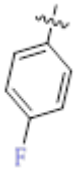	38	215 - 237 (d.c.)	Off white powder
2-12	[$BiPh_2$(PDTz,)]	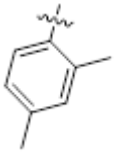	75	165 - 171 (d.c.)	Off white powder

2.3.4 Attempted synthesis of [BiPh(SR)$_2$]: Heteroleptic phenylbismuth(III) *bis*-thiolato complexes

Phenylbismuth(III) *bis*-thiolato complexes of the form [BiPh(SR)$_2$] were not accessible via the salt metathesis route. In a representative example, the reaction of two equivalents of **3** with one equivalent of the [BiPhCl$_2$] precursor resulted in the formation of mixed species with the major products obtained from these reactions being **2-9'** with a 15-30 % contamination of **2-9** (Scheme 5).

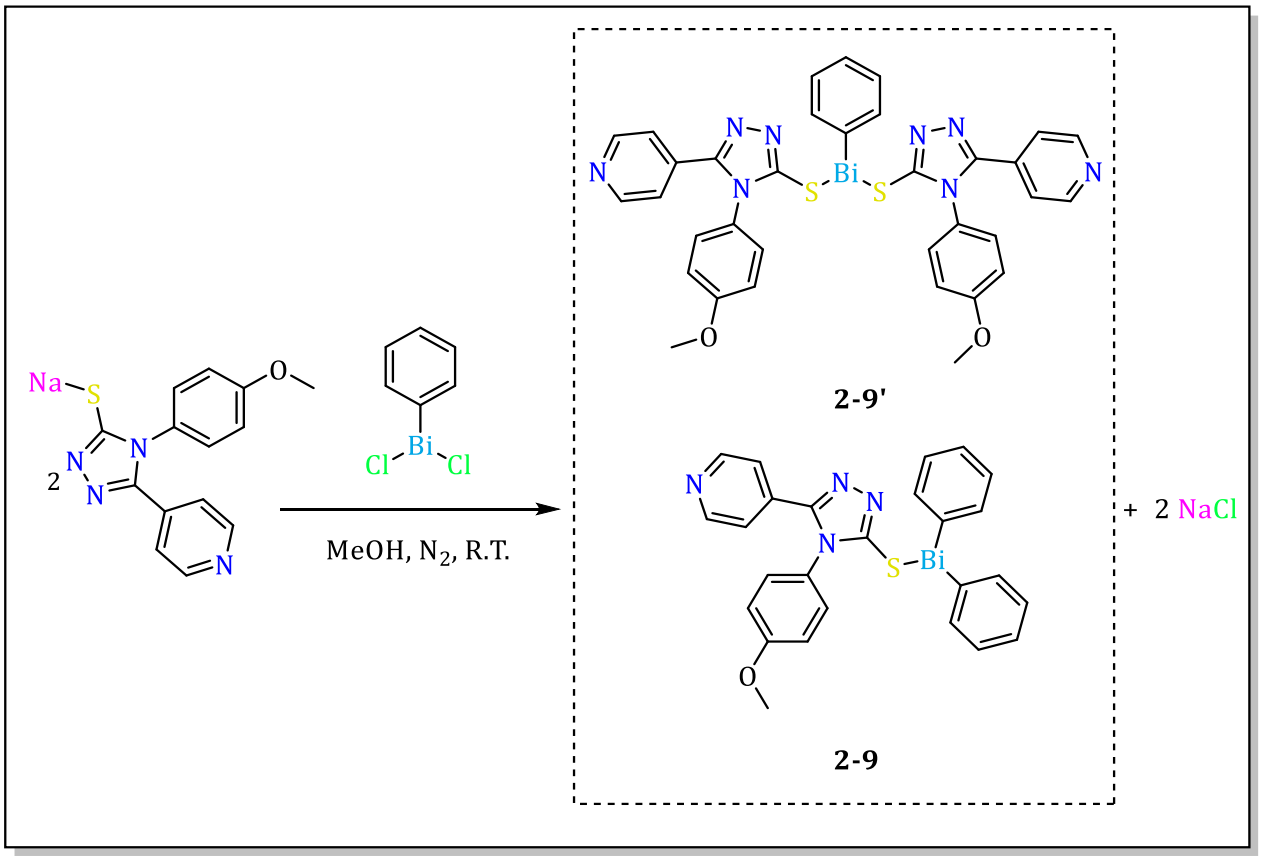

Scheme 5: Synthesis of heteroleptic Bi(III) thiolates from two equivalents of the sodium salt of **3** and BiPhCl$_2$ resulted in the formation of mixed species **2-9** and **2-9'.**

Using a series of established protocols,[2] the isolation of the heteroleptic phenylbismuth(III) *bis*-thiolato complexes proved to be challenging via standard

[2] These protocols have been used previously to synthesize bismuth(III) complexes of the form [BiPh$_2$L] and [BiPhL$_2$] with other substrates.[143,281,293]

protolysis, solvent-mediated and solvent-free methods using the thiol precursor **3** (POTz). In all reaction attempts, a solution-state flux was observed between the precursors and bismuth(III) species. Numerous attempts were made to drive reactions to completion by manipulating temperature, time, and solvent systems (EtOH, MeOH, toluene, THF, and n-hexane; solvent-free) however, this too resulted in the formation of multiple species (Table 4).

Table 4: Reactions and conditions employed for the attempted synthesis of phenylbismuth(III) bis-thiolate complex **2-9'.**

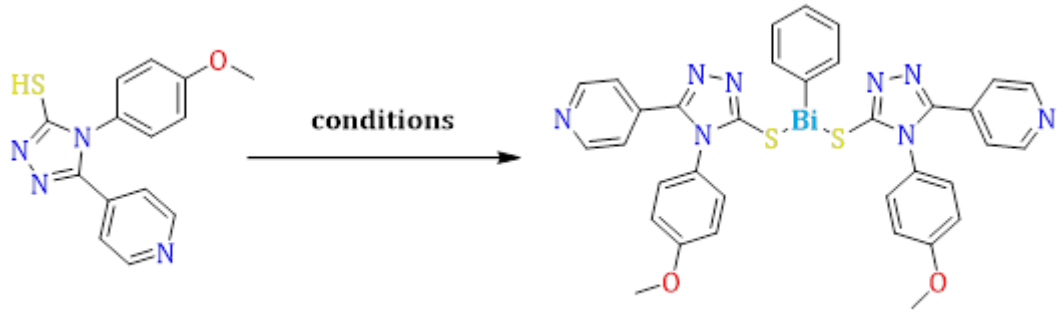

3 **2-9'**

Entry	Conditions	Result
1	$BiPh_3$ (1 equiv.), NaOH (2 equiv.), **3** (2 equiv.), MeOH, metathesis, 0 °C/R.T 4 hr	Mixture of **2-3** & **2-9'**
2	$BiPh_3$ (1 equiv.), Ag_2O (2 equiv.), **3** (2 equiv.), MeOH, metathesis, 0 °C, 4 hr	Mixture of **2-9** & **2-9'**
3	$BiPh_3$ (1 equiv.), NaOH (2 equiv.), **3** (2 equiv.), *n*-hexane, metathesis, 0 °C, 16 hr	N/R
4	$BiPh_3$, (1 equiv), **3** (2 equiv.), EtOH, Reflux, 4/16 hr	Decomp.
5	$BiPh_3$, (1 equiv), **3** (2 equiv.), EtOH/Toluene, Reflux, 4 hr	Decomp.
6	$BiPh_3$, (1 equiv), **3** (2 equiv.), EtOH, MW, 75 °C, 10 mins	Mixture of **3, 2-9** & $BiPh_3$
7	**2-9** (1 equiv.), **3** (1 equiv), Toluene, MW, 115 °C, 10 mins	Mixture of **3, 2-9** & **2-9'**
8	$BiPh_3$, (1 equiv), **2-3** (1 equiv.), Toluene, MW, 115 °C, 10 mins	Mixture of **2-3** & **2-9'**
9	$BiPh_3$, (1 equiv), **3** (2 equiv.), EtOH/THF, MW, 75 °C, 10 mins	Mixture of **2-3** & **2-9'**
10	$BiPh_3$, (1 equiv), **3** (2 equiv.), SF, 120 °C, 0.5/2/3 hr	Decomp.

Differential Scanning Calorimetry (DSC) was utilised as a qualitative technique to assess whether a reaction between the Bi(III) precursor and substrate would proceed via proton exchange. As the triazole thione substrate **3** exhibits a relatively moderate pK_a value, the equimolar and 2:1 reactions were initially assessed via the solvent-free method. Analysis of the equimolar reaction between triazole thione **3** and triphenylbismuth(III) ($BiPh_3$) revealed a mixture of thermal events within the thermochemical profile (Figure 48), which shows an endothermic maximum at 81.46 °C correlating to the melting of $BiPh_3$ followed by two exothermic minima at 140.34 °C and 174.53 °C. Although Thermogravimetric (TGA) analyses were not conducted in this study, these events correlate to the liberation of the first and second benzyl groups of the $BiPh_3$ molecule as observed with other Bi(III) complexes in the literature.[339]

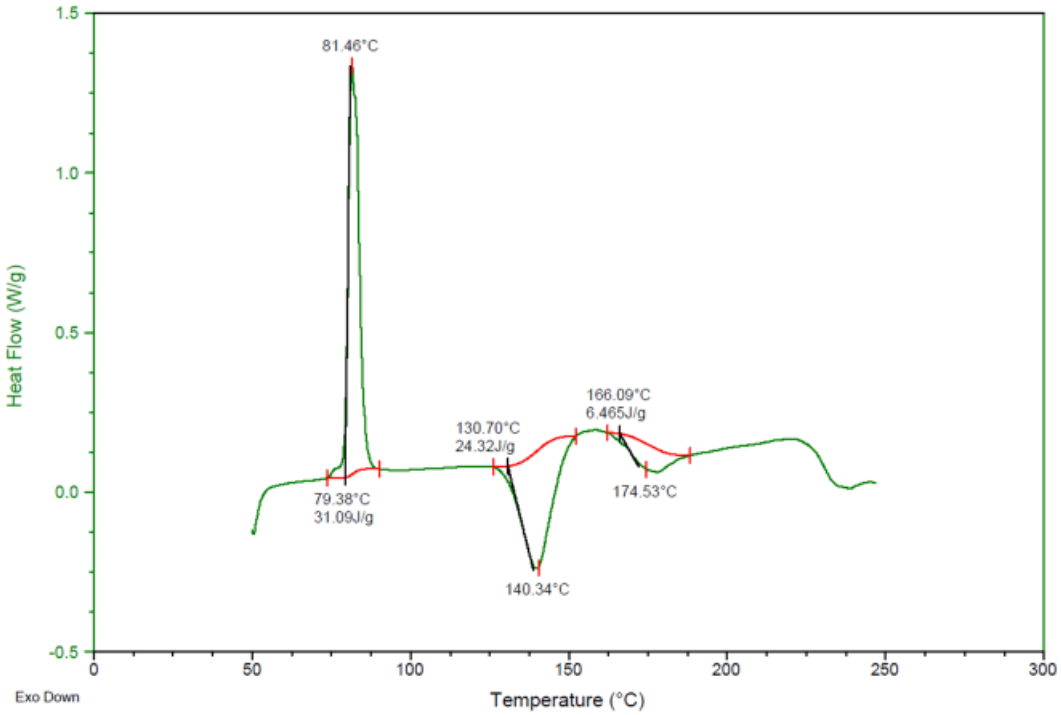

Figure 48: DSC isotherm of the 1:1 mixture of $BiPh_3$ and triazole thione **3** taken from 50 °C to 250 °C.

Following the DSC studies, using protocol **X**, solvent-free reactions were conducted using a Kugelrohr oven at 140 °C and 170 °C for four hours, resulting in the formation of pale-yellow solids. The solids were washed with hot ethanol and Et_2O, resulting in the same mixtures of species observed in protocol **XI.**

A number of purification techniques were employed to separate the species including vapour diffusion crystallisation, slow evaporation crystallisation, organic extraction, and chromatographic separation (column and HPLC). Under standard chromatographic conditions, the bismuth(III) species appeared to decompose over silica, so an alternative reverse-phase separation was trialled, utilising an alumina base in combination with the solvents: ethyl acetate, n-hexane, methanol, DCM, chloroform, and toluene. The poor resolution as a result of the solution-state flux between the phenylbismuth(III) *bis*-thiolate and diphenylbismuth(III) thiolate species deemed them to be inseparable.

Given the lack of purity and inconclusive nature of the reaction methodologies used, these mixtures were not considered for use in biological studies. However, one crystal of the complex [BiPh(POTz)$_2$], **2-9'** obtained from the solution of reaction **VI** was structurally elucidated via single crystal X-ray diffraction and the connectivity of the species will be discussed later in this chapter.

2.3.5 Fourier Transform Infra-red (FT-IR) characterization

FT-IR spectroscopy was utilised to provide insights into the binding nature of the free triazole thiolates **1** to **6** and the complexes **2-1** to **2-12** via analysing the changes in the thioamide v(C-N_{pyr}), v(C-N_{tz}) and proposed v(N-C=S) absorption bands (Table 6). Identifying the characteristic stretching vibrations proved to be difficult due to the coupling effects from neighbouring atoms.[340,341] Additionally, discriminating between pyridyl v(C-N) stretching and triazole v(C-N) stretching modes was difficult as mixed absorption bands were present in the region 3000-2500 cm^{-1} as well as 1500-1000 cm^{-1}.[340,342]

The precursors **1** to **6** were confirmed to be stable in the thione form through the absence of the *v*(S-H) between 2650-2550 cm^{-1} as well as the absence of the C-S-H-in plane bending modes between 850-918 cm^{-1}. However, there have been numerous instances in the literature where S-H stretching modes may not always be observed.[343–346] The precursor substrates were therefore, interpreted on the basis that v(C-N), v(N-H) and v(N-C=S) bands were present (Table 5).[340,342,344] Determining the general region of the *v*(C-S) vibrational band was difficult due to the

influence of heteroaromatic ring-stretching, ring-bending, in- and out of plane deformations, therefore requiring empirical correlation.[346]

Table 5: Characteristic FT-IR assignments in precursors **1** to **6**. (br) = broad, (s) = strong (m) = moderate. **pyr**= pyridine, **tz**= triazole.

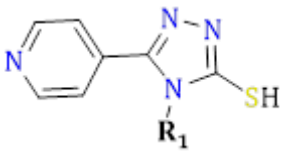

Triazole/R_1		ν(N-H)	ν(C=S)	ν(C-N)$_{pyr}$	ν(C-N)$_{tz}$	ν(NCS)	ν(CNN)
1	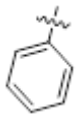	2846-2343	827	1283	1493	-	963
2	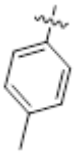	3024-2726	831	1319	1510	1602	969
3	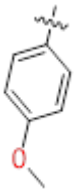	3400	831	1284	1513	1607	975
4	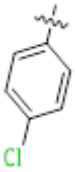	3036-2887	826	1274	1493	1622	973
5	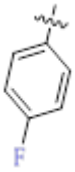	3102-2744	827	1266	1494	-	972
6	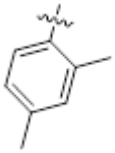	2618-2372	823	1295	-	1605	962

Interpretation of complexation was evaluated through the disappearance of the corresponding N-H broad signal, which is present in the 3400-2300 cm^{-1} region. While this suggests coordination to the Bi(III) metal centre, a conclusion could not be drawn whether it was through the sulfur or nitrogen terminus. The stretching absorption values of 824-839 cm^{-1} for the v(C-S) in complexes **2-1** to **2-12** were however, consistent with previously synthesised bismuth(III) thiolate complexes.[145,279,282] In previous studies, shifts in the triazole-thiol v(C-S) stretching frequency have been used as a primary indicator for Bi(III)-S complexation, however due to the complexity of this system, a conclusion could not be drawn. From the results obtained there appeared to be modest hypsochromic shift values of 2-12 cm^{-1} between the precursors **1** to **6** and complexes **2-1** to **2-12**.

Upon metal complexation, the propensity for thiocyanato-type ligands to shift to lower frequencies has been observed in the literature in-line with the results obtained in this study with some notable trends apparent when comparing the precursors **1** to **6** to the complexes **2-1** to **2-12.**[347] The FT-IR spectra of complexes **2-1** to **2-12** show the pyridyl v(C-N) stretching frequencies in the range 1427-1495 cm^{-1} (Table 6) which have shifted to a lower frequency than the respective precursor triazoles (1493-1510 cm^{-1}). Individual changes in the triazole v(C-N) stretching frequencies for the homoleptic *tris*-substituted bismuth(III) thiolates **2-1** to **2-6** however, were observed with stretching frequencies in the range of 1216-1298 cm^{-1} which have undergone a hypsochromic shift by 2-60 cm^{-1}.

In general, many strong and moderate intensity absorption bands were present in the regions of 1500-600 cm^{-1} due to the various functionalities present within the precursor triazole thiolates.[343,344] While the C-S, N-H and S-H vibrational and bending modes were used as a basis to ascertain the binding mode of the Bi(II) metal centre to the ligand, FT-IR spectroscopy alone could not determine the overall connectivity of the molecule. Other analytical techniques such as NMR spectroscopy and single crystal X-ray diffractometry were required to fully elucidated the connectivity and structure of the complexes.

Table 6: Characteristic IR assignments in complexes **2-1** to **2-12** of the form $[Bi(SR)_3]$ and $[BiPh_2(SR)]$

Complexes		ν(C-N)$_{pyr}$	ν(C-S)	ν(C-N)$_{tz}$
2-1	$[Bi(PTz)_3]$	1495	830	1285
2-2	$[Bi(PTTz)_3]$	1423	821	1259
2-3	$[Bi(POTz)_3]$	-	826	1251
2-4	$[Bi(PCTzl)_3]$	1492	826	-
2-5	$[Bi(PFTz)_3]$	1427	839	1216
2-6	$[Bi(PDTz,)_3]$	-	825	1298
2-7	$[BiPh_2(PTz)]$	1428	832	-
2-8	$[BiPh_2(PTTz)]$	1460	827	1390
2-9	$[BiPh_2(POTz)]$	1460	824	-
2-10	$[BiPh_2(PCTzl)]$	1460	824	-
2-11	$[BiPh_2(PFTz)]$	1460	826	
2-12	$[BiPh_2(PDTz)]$	1460	825	-

2.3.6 Nuclear Magnetic Resonance (NMR) studies

2.3.6.1 NMR spectroscopy of homoleptic tris-substituted bismuth(III) thiolates

Analysis of the ^{1}H NMR spectra of the *tris*-substituted Bi(III) complexes show a characteristic absence of the broad thiol proton signal observed in the parent triazole at approximately 14 ppm. This is indicative of deprotonation of the thiol and subsequent Bi(III)-S binding and is consistent with the literature.[145] Proton environments observed in the aromatic regions of complexes **2-1** to **2-6** all show an upfield shift of the *ortho*- and *meta*-pyridyl signals and *ortho-, meta*- and *para*-phenyl ligand signals relative to the parent substrates.

The reaction of triazole-thiolate **3** with bismuth *tert*-butoxide produced complex **2-3,** [Bi(POTz)$_3$]. Upon binding to the Bi(III) metal centre, an overall upfield shift and broadening of proton signals was observed for all aromatic signals, with respect to the starting material. Bi(II) complexes are known to aggregate and form polymeric structures, as observed by Herdman and co-workers.[146,348] Therefore, it is expected that a general broadening of signals is observed in the solution state. The *ortho*-pyridyl ligand signal (**1,2**) was observed to shift negligibly from 8.58 ppm to 8.55 ppm followed by shifts in the aromatic *para*-tolyl *ortho*- and *meta*-phenyl signals upfield from 7.32 ppm to 7.29 ppm (**10,13**) and 7.26 to 7.24 ppm (**9,14**) respectively (Figure 49).

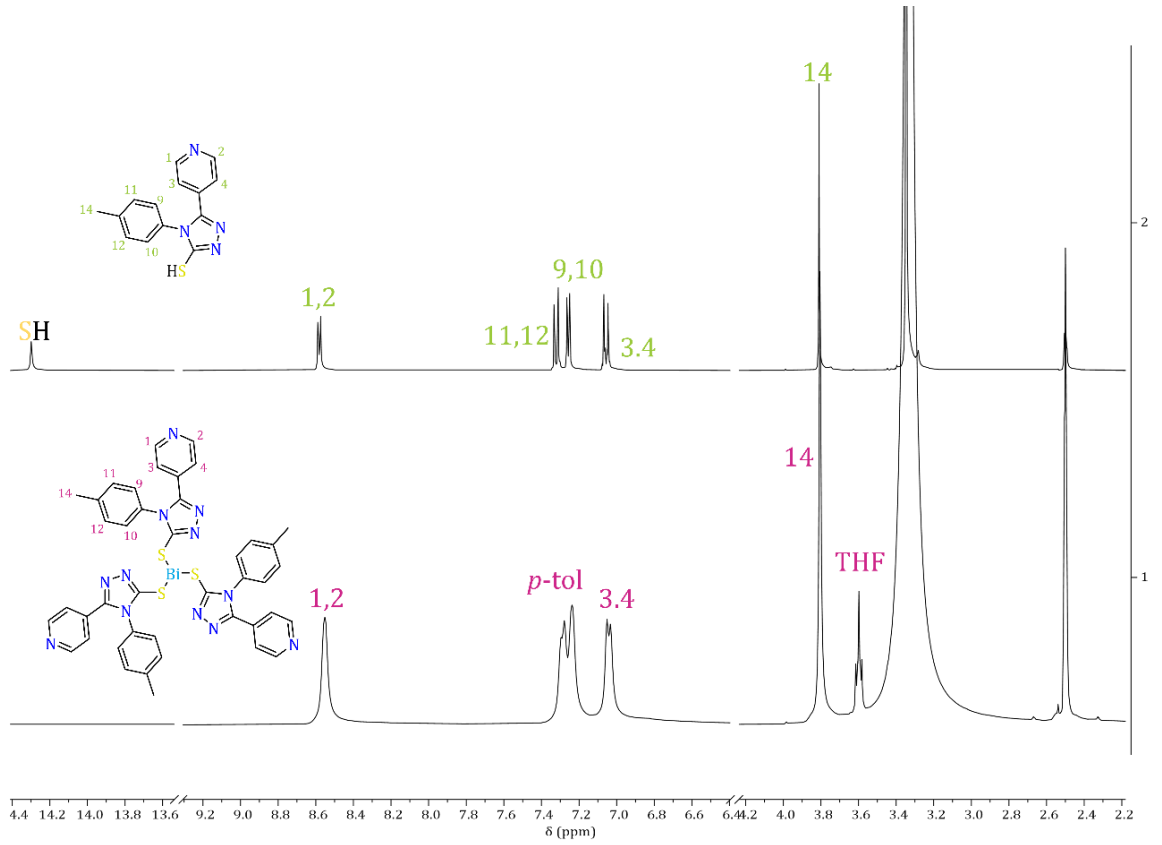

Figure 49: Solution state ^{1}H spectral comparison of triazole precursor POTz, **3** and product, complex **2-3** [$Bi(POTz)_3$], taken in DMSO-d_6 at 25 °C.

^{13}C NMR spectroscopy was used to determine whether the absence of the characteristic -SH signal was due to the Bi(III) metal centre binding to the S-terminus or the N-terminus of the N-heterocyclic thiol (thiol vs thione deprotonation). The ^{13}C NMR results were in-line with the ^{1}H NMR revealing little variation between the free triazole thiolate **3** and complex **2-3**. It is postulated that the notable absence of the thioamide C-S bond at 169.8 ppm (observed in spectrum 2, **7**, Figure 50) in the complex spectrum (spectrum 1, Figure 50) may be due to the shielding effects of the Bi(III) metal centre on the overall molecule. An overall decrease in signal intensity can also be attributed to the overall lower solubility of the *tris*-substituted bismuth(III) thiolate **2-3**, when compared to the precursor **3.** Similar to the ^{1}H NMR, the ^{13}C NMR shows a general upfield shift for all signals upon complexation of the free triazole thiolate to the bismuth(III) complex, this was evident for all of the homoleptic series, **2-1** to **2-6.**

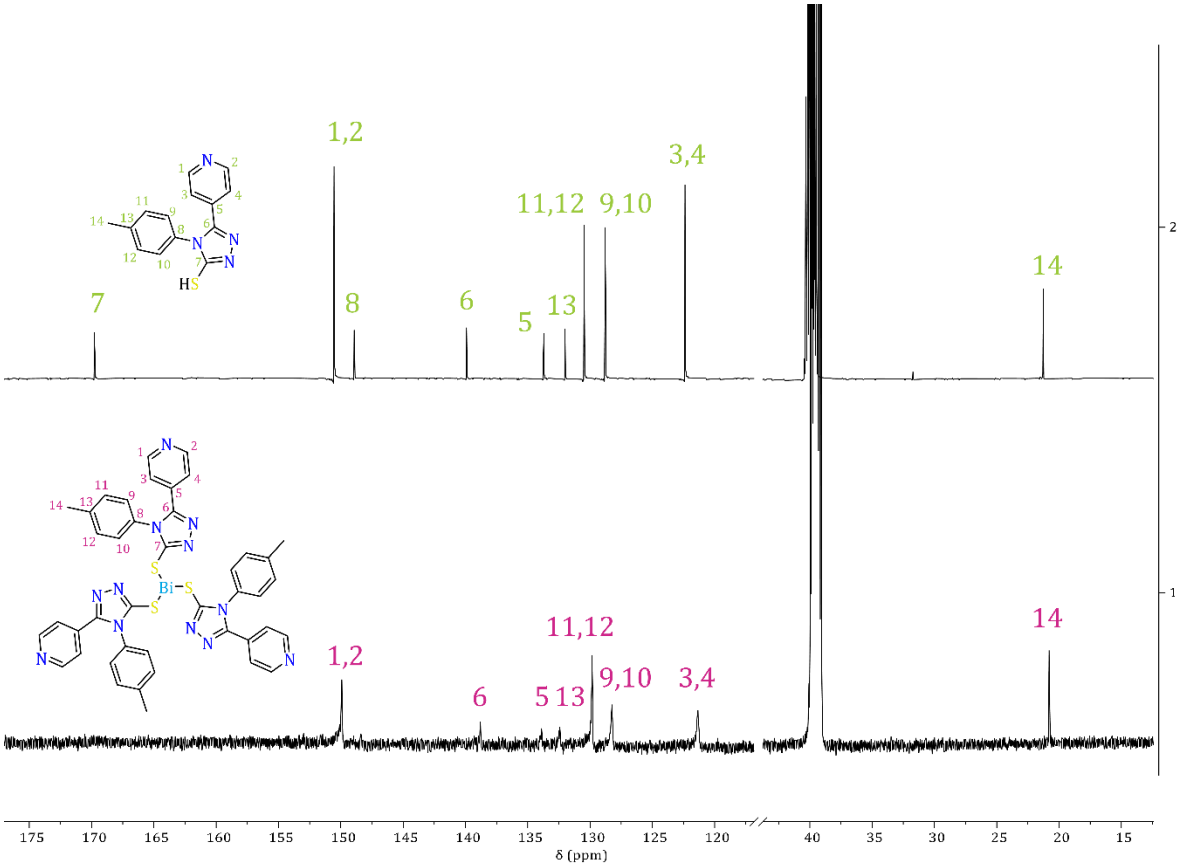

Figure 50: Solution state ^{13}C spectral comparison of triazole precursor POTz, **3** and product, complex [Bi(POTz)$_3$], **2-3** taken in DMSO-d$_6$ at 25 °C.

2.3.6.2 NMR Spectroscopy of heteroleptic diphenylbismuth(III) thiolates

In the spectrum of the free triazole PFTz **5**, the -SH group is shown as a broad signal at 14.34 ppm (Figure 51, spectrum 4). This is due to solution-state thione to thiol tautomerisation which has been described in the literature (Scheme 6).[314] Isolation of the precursor sodium salt (**5-Na**) derived from triazole **5**, can be confirmed via the total upfield shift of aromatic protons. The ligand *ortho*- and *meta*-pyridyl protons (Figure 51, **1,2** and **3,4** respectively) undergo a characteristic shift from 8.58 ppm (Figure 51, spectrum 4) to 8.43 ppm (Figure 51, spectrum 3). A coalescence of proton signals for the aryl ring is observed for the ligand aryl ring (Figure 51, **9-12** in spectrum 4 to **Ar** in spectrum 3).

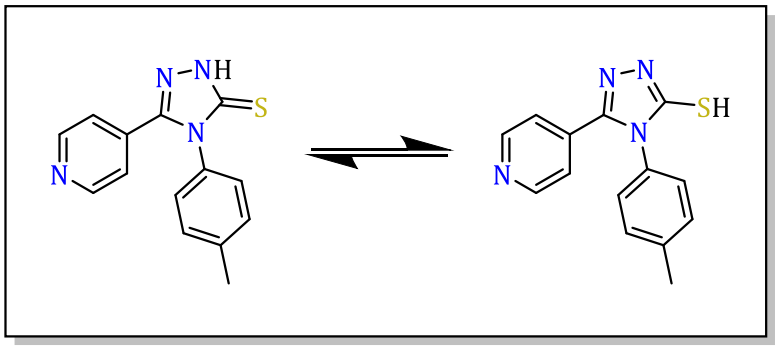

Scheme 6: Proposed solution-state thione-thiol tautomerization of PFTz, **5.**

The ^{1}H NMR spectrum of complex **2-11** [$BiPh_2$(PFTz)], reveals significant shifts of all aromatic signals with respect to the precursor materials indicating successful complexation. The most distinguishable feature of the heteroleptic diphenylbismuth(III) thiolate complex is the total upfield shifts of all aromatic signals with respect to both the free triazole precursor **5** and **5-Na**. A significant upfield shift of the *ortho*-pyridyl ligand signals from 8.58 ppm (Figure 51, Spectrum 4 **1,2**) to 7.69 ppm (Figure 51, Spectrum 1 **1,2**) is observed. Upfield shifts of the *ortho*- and *meta*-phenylbismuth(III) protons with respect to the precursor $BiPh_3$ were consistent with previously synthesised heteroleptic phenylbismuth(III) thiolato complexes.[279,314] The complexes **2-7** to **2-12** all contain shifted *ortho-, meta*- and *para*-phenylbismuth signals as well as thiolate signals.

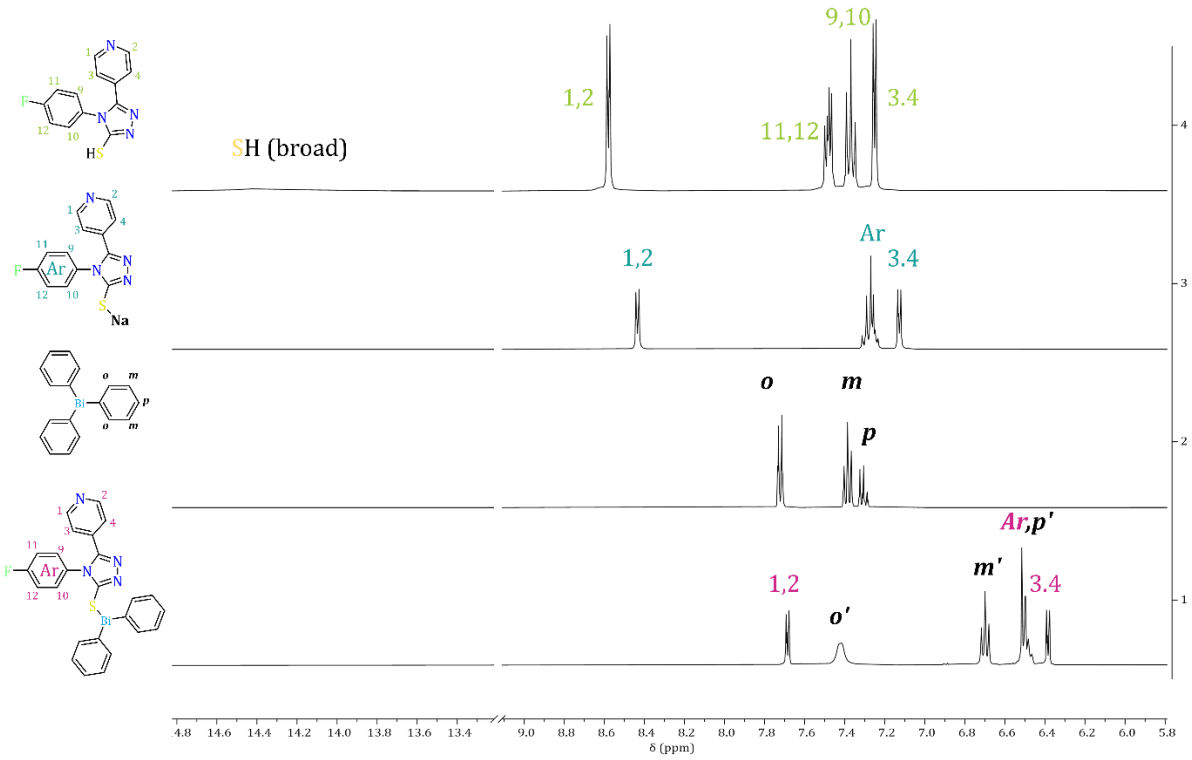

Figure 51: Comparative ^{1}H NMR spectra of **1:** Complex [$BiPh_2$(PFTz)], **2-11, 2:** $BiPh_3$ **3**: Sodium salt PFTz-Na, **5-Na** and **4:** precursor triazole thiolate PFTz, **5** all taken in DMSO-d_6 at 25 °C.

2.3.6.3 NMR Spectroscopy of the attempted heteroleptic phenylbismuth(III) bis-thiolates

The ^{1}H NMR spectrum obtained for the product obtained from protocol **VI** outlined in (section 2.3.4) revealed a mixture of species including: diphenylbismuth(III) thiolate [$BiPh_2$(POTz)], **2-9** phenylbismuth(III) *bis*-thiolate [$BiPh$(POTz)$_2$], **2-9'** precursor free thiol **3** and the homoleptic *tris*-substituted bismuth(III) thiolate complex [Bi(POTz)$_3$] **2-3** (Figure 52). The coalescence of aryl signals associated with the ligand $PoTz^-$ **3** moiety (indicated in purple) was observed due to the rapid exchange with $BiPh_3$. This phenomenon has been observed by Busse *et al.*, with a sulfonate-type ligand system whereby the integrations of the phenylbismuth(III)- moieties were used to quantify the presence of the redistributed Bi(III) sulfonate products.

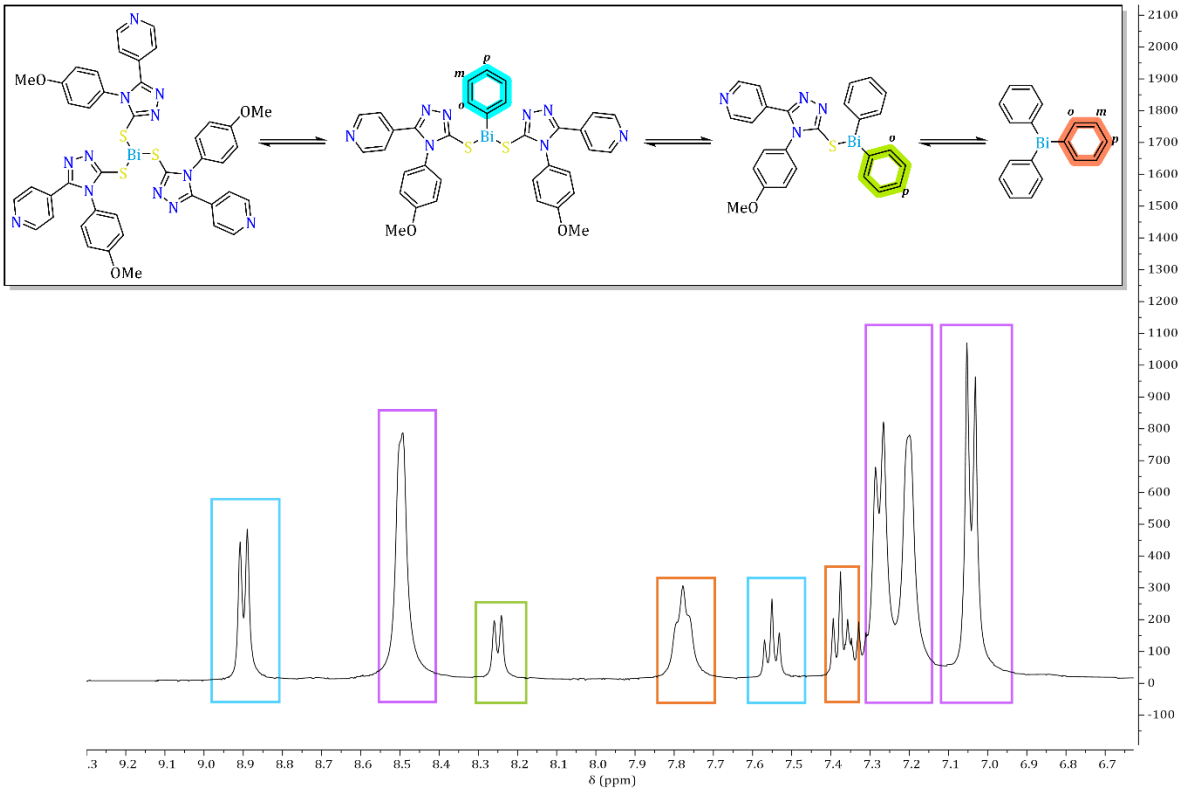

Figure 52: ^{1}H NMR spectrum of the solid recovered from protocol **VI** following solubilisation in DMSO-d_6, highlighting the rearrangement in solution to form complexes (from left to right) [Bi(POTz)$_3$] **2-3,** [BiPh$_2$(POTz)] **2-9**, [BiPh(POTz)$_2$] **2-9'** and BiPh$_3$ (methyl signals are not shown).

2.3.7 High resolution mass spectrometry (HRMS) of Bi(III) thiolato complexes

High resolution mass spectrometry was used to further support the formation of the homo- and heteroleptic bismuth(III) thiolates. Solid samples of each of the complexes **2-1** to **2-12** were solubilised in a mixture of DMSO and methanol and analysed via electrospray ionisation (ESI) techniques. Within the homoleptic series **2-1** to **2-6,** the parent ion was observed either in the positive ion mode as the protonated form with a solvent adduct [Bi(SR)$_3$ + Solvent], or as a fragment of the initial complex [Bi(SR)$_2$ + solvent]. While the heteroleptic series of complexes **2-7** to **2-12** showed the parent ion fragment in the positive ion mode as the protonated form [[BiPh$_2$(SR) + H]$^+$. All of the complexes showed the expected isotopic distribution patterns associated with Bi(III).

2.3.8 X-ray crystallography

Numerous attempts were made to obtain single crystals of the homoleptic *tris*-substituted bismuth(III) thiolate complexes **2-1** to **2-6** from the slow evaporation, layering and diffusion of solvents such as THF, ethanol, methanol, toluene, ethyl acetate, acetonitrile, DMF and DMSO. However, this proved to be unsuccessful. While the heteroleptic Bi(III) thiolato complexes **2-7** to **2-12** showed less solubility than the corresponding homoleptic *tris*-substituted counterparts in common organic solvents, solid-state crystallographic data was able to be obtained for some of the heteroleptic bismuth(III) thiolate complexes.

Solid-state structures were obtained for four out of the six novel heteroleptic diphenyl bismuth(III) thiolato complexes, **2-7**, **2-8**, **2-11** and **2-12**. The molecular structures are shown in Figure 53-Figure 57, and the selected bond lengths and angles are summarised in Table 7. Additionally, one phenylbismuth(III) *bis*-thiolato complex (**2-9'**) was also obtained from the slow evaporation of an impure reaction product from a DMSO/toluene solvent system, shown in Figure 58.

All of the heteroleptic bismuth(III) thiolato complexes show some structural similarities whereby the thiolato substrate binds to the bismuth(III) metal centre in a monodentate fashion however, their asymmetric units are not analogous. The Bi(III) metal centres adopt four and five coordinate geometries varying from distorted tetrahedral (complex **2-7**) to distorted disphenoidal/trigonal bipyramidal (complexes **2-8**, **2-11** and **2-12**) depending on the solvent system used to crystallise samples and thus, their extended fragments differ.

The asymmetric unit of complex **2-7** shows the central Bi(III) atom in a tetrahedral geometry and bound to two carbon atoms C1 and C2 corresponding to the two phenyl rings and one sulfur atom S1 corresponding to the deprotonated thiolate anion (Figure 53).

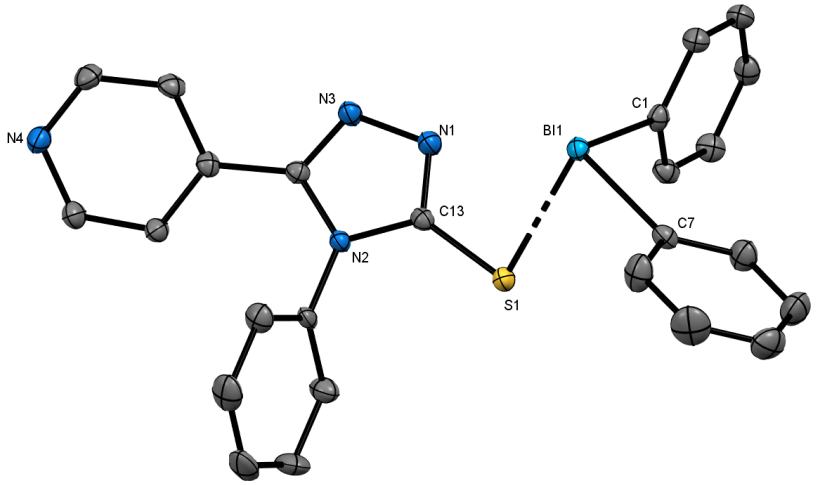

Figure 53: Asymmetric unit of the molecular structure of [$BiPh_2$(PTz)] **2-7.** Thermal ellipsoids are shown at the 50% probability level. Hydrogen atoms have been omitted for clarity.

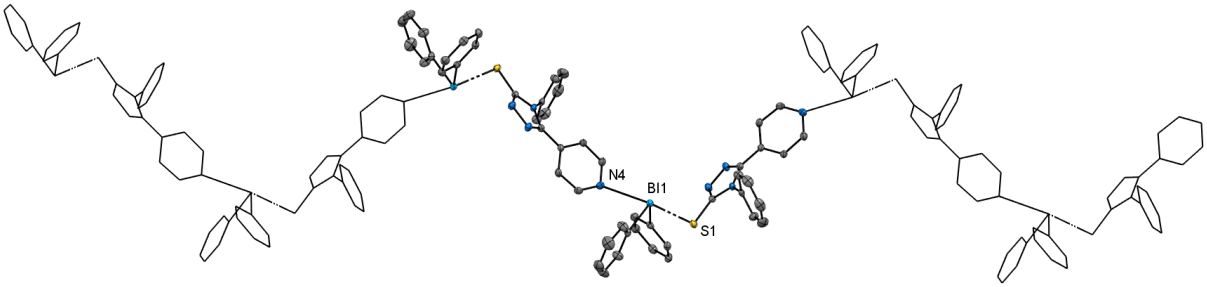

Figure 54: Polymeric structure of [$BiPh_2$(PTz)] **2-7.** Thermal ellipsoids are shown at the 50% probability level. Hydrogen atoms have been omitted for clarity. Additional fragments generated are shown in wireframe form.

The asymmetric units for structures **2-8, 2-11** and **2-12** all share similar coordination environments with the central bismuth(III) atom adopting a four-coordinate distorted disphenoidal motif. Whilst unusual, the large ionic radius of the central Bi(III) atom allows for different geometries and coordination numbers due to the presence of the 6s lone pair and consequently, the crystallisation of a wide variety of structures.[349]

The solid-state structures of this set of complexes adopt spatial arrangements similar to previously synthesised heteroleptic diphenylbismuth(III) sulfonate complexes.[143] The planes formed by the S1-Bi1-O1 and C1-Bi1-C7 interactions display angles of 158.100(5) ° and 99.000 °, leaving a large void across the S1-Bi1-O1 bond and *trans* to the two phenyl groups. The coordination of one water molecule in each of the **2-8**,

2-11 and **2-12** structures is presents as a result of the hydrolysis of the DMSO/toluene solvent matrix. This void is presumed to be occupied by the stereochemically active lone pair (SALP).[286] Similar to the previously synthesised heteroleptic bismuth(III) thiolates, binding of this triazole-thiolate system to the Bi(III) centre indicates the change in configuration of the stable free thiol to the more thermodynamically favourable anionic thiolate and in turn, a non-labile Bi-S bond.

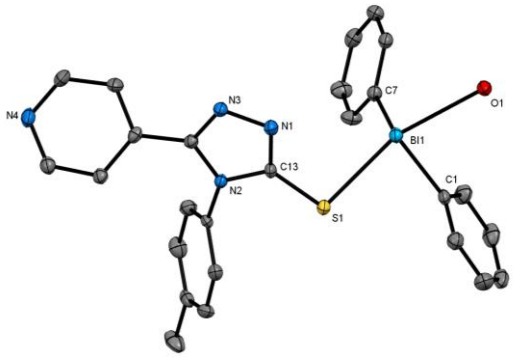

Figure 55: Asymmetric units of the molecular structure of [$BiPh_2$(PTTz)] **2-8**. Thermal ellipsoids are shown at the 50% probability level. Hydrogen atoms have been omitted for clarity.

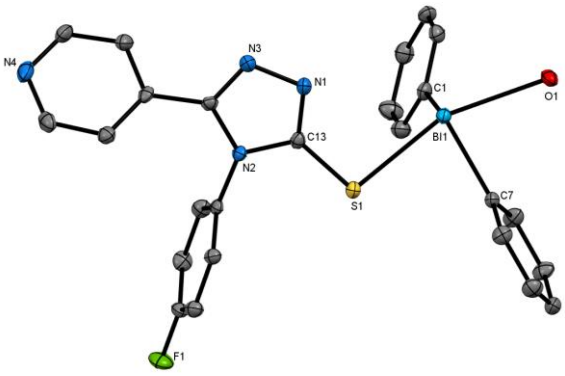

Figure 56: Asymmetric units of the molecular structure of [$BiPh_2$(PFTz)], **2-11.** Thermal ellipsoids are shown at the 50% probability level. Hydrogen atoms have been omitted for clarity.

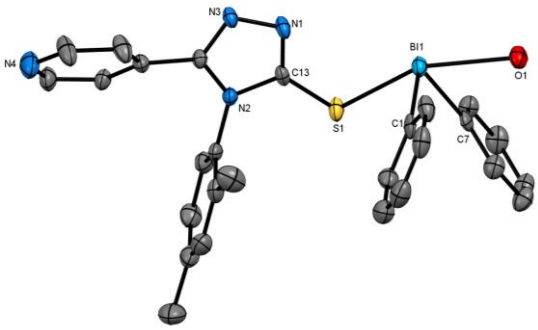

Figure 57: Asymmetric unit of the molecular structure of BiPh2(PDTz), **2-12**. Thermal ellipsoids are shown at the 50% probability level. Hydrogen atoms have been omitted for clarity.

Table 7: Selected bond lengths (Å) and angles (°) of the solid-state structures of heteroleptic Bi(III) thiolate complexes **2-7, 2-8, 2-11** and **2-12**.

Bond (Å)/Angle (°)	2-7	2-8	2-11	2-12
Bi(1)-S(1)	2.657(7)	2.666(8)	2.671(8)	2.660(13)
Bi(1)-C(1)	2.250(3)	2.241(3)	2.249(3)	2.263(6)
Bi(1)-C(7)	2.238(3)	2.250(3)	2.240(3)	2.238(6)
S(1)-C(13)	1.732(3)	1.732(3)	1.736(3)	1.733(6)
N(1)-C(13)	1.319(3)	1.320(4)	1.319(4)	1.322(7)
Bi(1)-O(1)	-	2.604(2)	2.634(2)	2.616(4)
Bi(1)-N(4)	2.792(2)	-	-	-
C(1)-Bi(1)-C(7)	97.90(10)	97.08(10)	99.00(11)	97.60(2)
C(1)-Bi(1)-S(1)	96.26(7)	80.46(8)	93.58(8)	92.83(14)
C(7)-Bi(1)-S(1)	88.10(6)	92.55(8)	81.38(8)	81.10(13)
C(13)-S(1)-Bi(1)	92.03(9)	97.84(10)	99.46(10)	100.05(18)
N(1)-C(13)-S(1)	124.90(2)	126.40(2)	127.30(2)	127.90(4)
O(1)-Bi(1)-S(1)	-	157.49(5)	158.01(5)	158.39(9)
O(1)-Bi(1)-C(1)	-	78.03(9)	82.65(9)	82.86(16)
S(1)-Bi(1)-N(4)	171.21(5)	-	-	-

Despite the protolysis and salt metathesis reactions of [$BiPhCl_2$] and thiolates **1** to **6** producing mixtures of compounds, single crystals of the phenylbismuth(III) *bis*-thiolato Bi(III) complex **2-9'** were obtained via slow evaporation from a crude crystal mixture (Figure 58). The asymmetric unit of this complex shows the bond length observed for the Bi(1) – C(15), Bi(1) – S(1) and Bi(1) – S(2) bonds to be representative of covalent interactions with bond lengths of 2.282 Å, 2.760 Å and 2.757 Å, respectively. The Bi(1) – N(4) and Bi(1) – N(5) bonds are dative with lengths of 2.827 Å and 2.564 Å. These lengths are comparable to similar bismuth(III) N-heterocyclic thiolato complexes synthesised by Luqman and co-workers (Bi – S average 2.640 Å, Bi – N: 2.865 Å).[314]

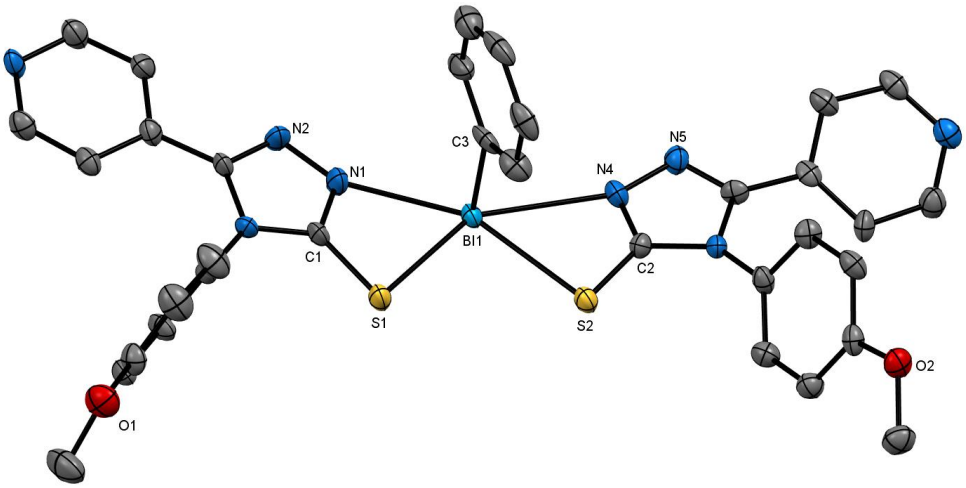

Figure 58: Solid-state structure of the asymmetric unit of complex [$BiPh(POTz)_2$] **2-9'**. Thermal ellipsoids are given at 50% probability. Hydrogen atoms have been omitted for clarity.

In the asymmetric unit of complex **2-9'** the Bi(III) centre is five-coordinate and monomeric in the solid-state however, when the structure is extended, a sixth interaction can be observed in an empty coordination site of the Bi(III) atom to an adjacent pyridyl-N. Similar to that seen in the heteroleptic diphenylbismuth(III)-*mono*-thiolato complexes **2-7** to **2-12,** an empty void can be observed and is presumed to be occupied by the SALP.

The length of this Bi(III) interaction is within the sum of the van der Waals radii of bismuth and nitrogen and thus the complex crystallises as a weakly-linked 1D

polymer with the Bi(III) centre adopting a six-coordinate, distorted octahedral geometry (Figure 59). The Bi-S bond distances Bi(1)–S(1) 2.760 Å and Bi(1)–S(2) 2.757 Å are typical of Bi(III) di-aryl thiolato complexes. Interestingly the asymmetric unit of the similar thiolate complex synthesised by Luqman and co-workers adopts a dimeric system similar to the polymeric network observed in structure **2-9'.**[282]

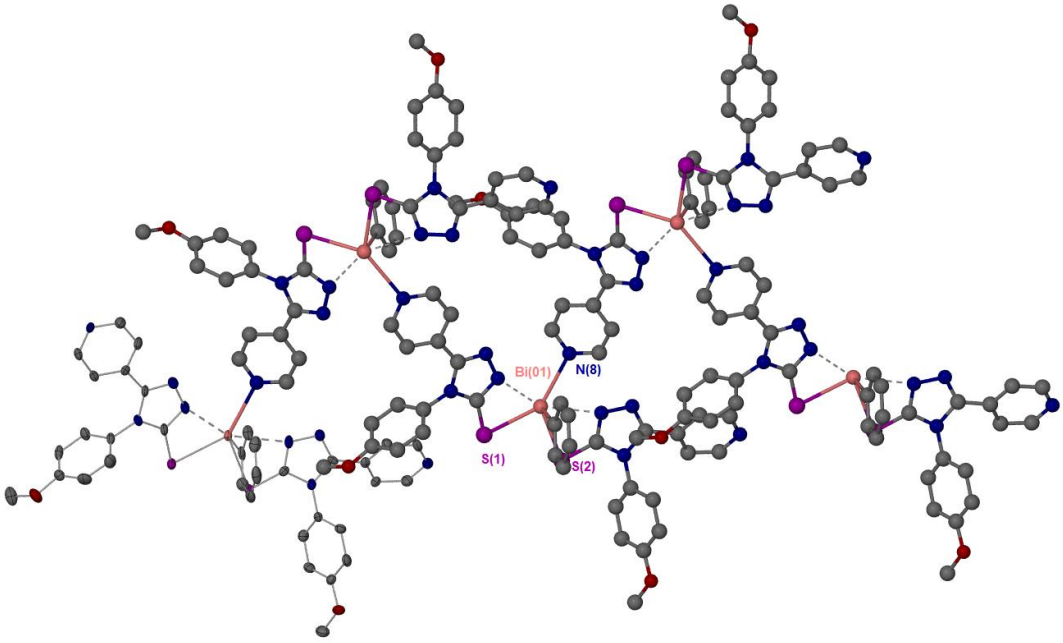

Figure 59: Extended polymeric structure of **2-9'** Thermal ellipsoids given at 50% probability. Hydrogen atoms have been omitted for clarity. Extended fragments have been represented using a wireframe model.

2.3.9 Solution-state stability studies

A key component of any potential therapeutic is the ability to remain stable across a variety of aqueous media, and under physiological conditions. Following their successful characterisation, the potential *in vivo* applications were addressed through the identification of any stability issues which may be encountered by the heteroleptic Bi(III) thiolato complexes. While the homoleptic *tris*-substituted Bi(III) thiolato complexes **2-1** to **2-6** demonstrated better solubility in aqueous solutions than the heteroleptic diphenylbismuth(III) thiolate complexes **2-7** to **2-12**, both sets of complexes displayed good solubility in the vehicle solvent DMSO. Overall, these results are consistent with previous observations in the literature.[146,283,350]

As DMSO is generally utilised as a carrier solvent for most biological assays, analysis of the heteroleptic diphenylbismuth(III) thiolates **2-1** to **2-12** were conducted using ^{1}H and ^{13}C NMR spectroscopy, whereby the solution-state stability was examined in wet DMSO-d_6 over a period of 48 hours. For each complex, the spectra were recorded at time intervals of 0, 24 and 48 hours and no significant changes in the chemical shifts and/or integrations of the complexes beyond the 48-hour time period were observed.

2.3.9.1 Stability in PBS

As orally administered drugs are typically absorbed in low pH gastric environments, these settings may additionally contain buffer salts such as NaCl, KCl and Na_3PO_4 therefore, the stability of the Bi(III) thiolates were initially evaluated in phosphate buffered saline (PBS) solutions at neutral pH (pH of 7.4) and room temperature conditions as an initial screen for potential *in* vivo application. Figure 60 shows the spectral changes of [$BiPh_2$(POTz)] **2-9**, assessed in PBS at 30-minute intervals over a period of 48 hours. Due to low aqueous solubility, **2-9** was initially solubilised in DMSO and diluted in PBS to give a final solution concentration of 30 μM.

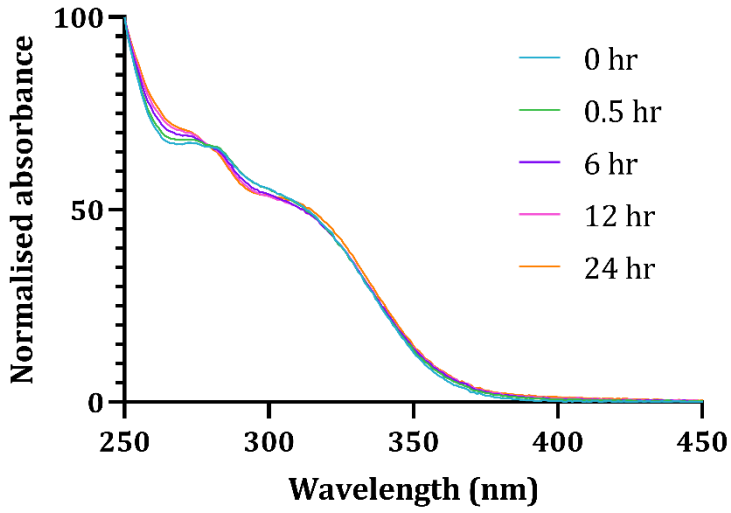

Figure 60: Absorption spectra of [$BiPh_2$(POTz)] **2-9** at 30 μM in PBS over 48 hours.

From these studies, it can be inferred that the heteroleptic diphenylbismuth(III) thiolate remains relatively stable in solution beyond 24 hours as evidenced by the minor spectral changes observed across the 30-minute time intervals.

2.3.9.2 Stability in cell culture media

Bismuth(III) carboxylato-based complexes have been observed to undergo hydrolytic decomposition to oxido-clusters however, Burke and Co-workers have identified the presence of certain serum proteins such as Foetal Bovine Serum (FBS) help to been incorporated to stabilise a series of phenylbismuth(III) *bis*-flavonolate compounds in solution.[350,351] It was worthwhile assessing the aqueous stability of the current series of heteroleptic diphenylbismuth(III) thiolates, therefore the model complex [$BiPh_2$(POTz)] **2-9** was chosen as a reference compound in the presence of cell culture media,. Figure 61 outlines two stability studies of complex **2-9** examined in Dulbecco's Modified Eagle Medium (DMEM, Figure 61, **a**) and DMEM supplemented with 10% FBS (Figure 61, **b**) over a period of 48 hours using UV-visible spectroscopy.

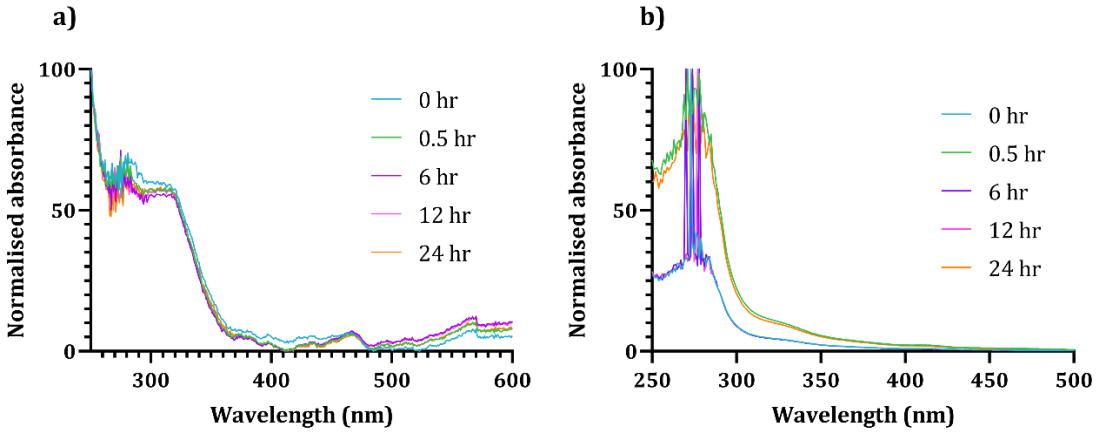

Figure 61: Absorption spectra of [$BiPh_2$(POTz)] **2-9** at 30 μM in **a):** DMEM cell culture media, and in **b):** DMEM with 10 % FBS over 48 hours.

Complex **2-3** in DMEM alone shows a modest decrease in absorption intensity over time which coincides with the deposition of a yellow precipitate within the quartz cuvette. However, when observing the spectrum of **2-9** in DMEM supplemented with FBS, all time points show poorly resolved signals between the region of 275 - 300 nm and a large variation in overall intensity between time intervals taken at 0-30 minutes and 6-24 hour. One of the major components responsible for drug binding in FBS is bovine serum albumin (BSA), which contains multiple discrete binding sites capable of hosting mononuclear and polynuclear complexes of Cu(II), Ni(III), Zn(II), Co(II) and

Pt(II).[72,352,353] Given this established metal binding capability, it is likely that complex **2-9** interacts with BSA as no precipitation was observed beyond the 48-hour period.

Overall, while these studies provide a rudimentary basis for the stability of complex **2-9** in biological media, further studies would be beneficial to explore the interaction of heteroleptic bismuth(III) thiolates with specific serum proteins. Topala *et al*., have identified serum albumins as one of the most important targets of organometallic drug pharmacodynamic and pharmacokinetic studies as these binding studies provide a useful inference on metal absorption and distribution.[352]

2.3.9.3 Stability in the presence of glutathione

As explored in section 2.1.1, bismuth has shown an affinity for glutathione molecules with the facile formation of the [$Bi(GSH)_3$] complex. Following studies incorporating the heteroleptic Bi(III) thiolate complexes in cell culture media, further analysis examined the interaction of complex **2-9** with glutathione (GSH) and specifically, whether the complexes were stable to ligand exchange with GSH.

The stability of complex **2-9** towards glutathione was studied using UV-visible spectroscopy as outlined in Figure 62. Under physiological conditions, intracellular glutathione levels have been observed to be in the millimolar scale, therefore, to replicate these conditions a 100-fold excess of GSH was used. The UV-visible spectra of **2-9** in the presence of GSH showed a general decrease in spectral intensity over time with broad characterless absorption bands. The deposition of a yellow precipitate supported the GSH-mediated release of the protonated triazole POTz*H* and concomitant binding of the GSH to the Bi(III) metal centre to form [$BiPh_2GS$] which remained in solution, and this was confirmed via ESI-MS.

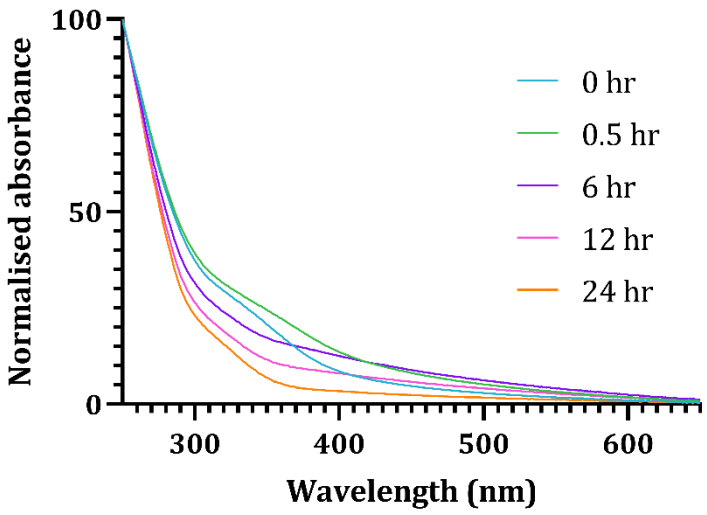

Figure 62: Changes to the absorption spectra of [$BiPh_2$(POTz)] **2-9** (30 μM) in the presence of 3 mM GSH (100 mol. equivalents) in ultrapure water over 24 h. The final DMSO concentration was 0.4 % (v/v).

2.3.10 Biological studies

2.3.10.1 Antimicrobial testing of heteroleptic diphenylbismuth(III) thiolates

Initially, all the parent triazole thiols and their corresponding Bi(III) complexes were screened against six clinically relevant microbial strains, four of which were bacterial and two fungal. Two Gram-positive (MRSA and VRE), two Gram-negative (E. coli and P. aeruginosa), and two fungal strains (*C. albicans* and *S. cerevisiae*) were chosen. The preliminary activity of the complexes against the microbes was assessed using a Kirby-Bauer disc diffusion assay, at a set concentration of 200 μg mL^{-1}.

The disc diffusion assays revealed bacterial activity for the heteroleptic phenylbismuth(III) thiolato complexes **2-7** to **2-12** (Figure 63), which showed clear zones of inhibition at 200 μg mL^{-1} against the four strains of bacteria. The parent thiols as well as the homoleptic *tris*-substituted Bi(III) thiolates did not show any antibacterial or antifungal activity as indicated by the confluent 'lawn' growth of all strains of bacteria and fungi. This trend is not unusual as the activity has been observed for other previously synthesised bismuth(III) complexes.[143,280,282]

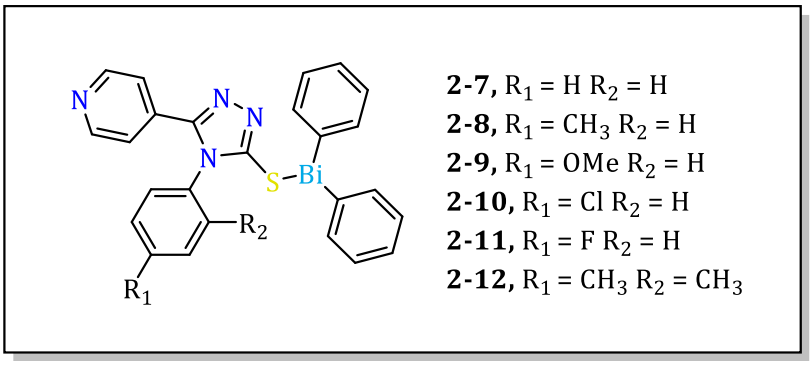

Figure 63: Summary of heteroleptic diphenylbismuth(III) thiolato complexes **2-7** to **2-12**.

Compounds that produced a clear zone of inhibition in the disc diffusion assay were then explored further with solution-based MIC testing against the four bacterial strains and two fungal strains (Table 8).

Table 8: Antibacterial activities of complexes **2-7** to **2-12** and $BiPh_3$ against MRSA, VRE, *E. coli, P. aeruginosa*, *C. albicans* and *C. auris*. The MICs of the complexes are given in μg mL^{-1} (μM) and the *tris*-substituted complexes **2-1** to **2-6** were not included in the table as they showed no antibacterial activities up to 200 μM in disc diffusion assays.

	MIC [μg mL^{-1} (μM)]					
	MRSA	**VRE**	***E. coli***	***P. aeruginosa***	***C. albicans***	***C. auris***
2-7	12.5 (9.90)	3.13 (2.47)	12.5 (9.90)	25 (19.80)	-	-
2-8	12.5 (10.25)	3.13 (2.56)	12.5 (10.25)	25 (20.50)	-	-
2-9	12.5 (10.65)	6.25 (5.33)	12.5 (10.65)	25 (21.30)	1.308	0.588
2-10	12.5 (21.50)	12.5 (10.75)	12.5 (21.50)	25 (21.50)	-	-
2-11	12.5 (10.35)	6.25 (5.18)	12.5 (10.35)	25 (10.35)	-	-
2-12	12.5 (10.60)	6.25 (5.30)	6.25 (5.30)	25 (21.20)	-	-
$BiPh_3$	28.40 (12.5)	14.20 (6.25)	(>50)	(>50)	(>50)	(>50)

The *in vitro* activity of the six heteroleptic diphenylbismuth(III) thiolato complexes suggested varied activities between Gram-positive and Gram-negative strains of bacteria. Overall, a small range of MICs was observed across the spectrum of complexes **2-7** to **2-12**, which suggested that within the series, minor changes in the 'R' groups had little effect in microbial activity. Complexes tested against MRSA, *E. coli* and *P. aeruginosa* had little internal variation within the series with all MIC values showing consistent results. Compounds generally exhibited half the MIC values when tested against MRSA and *E. coli* (12.5 μM), in contrast to *P. aeruginosa*, (25 μM). Interestingly, when tested against the Gram-positive strain VRE, the compounds showed the largest variation of activity within the series. Complexes [$BiPh_2$(PTz)] **2-7** (3.13 μM) and [$BiPh_2$(PTTz)] **2-8** (3.13 μM) show a twofold difference in activity when compared to complexes [$BiPh_2$(PFTz)] **2-11** (6.25 μM) and [$BiPh_2$(PDTz)] **2-12** (6.25 μM), this could indicate that small chemical modifications to the triazole thiolate ligand have impacted the results.

2.3.10.2 Cytotoxicity assay

While the mammalian cell viability studies are a useful probe to monitor the growth of a given cell population, the assay alone does not conclude whether the complexes are cytotoxic. From the conclusions drawn in the mammalian cell viability assay, it is undeterminable whether the concentration of the given heteroleptic bismuth(III) complex decreased the growth % due to cytotoxic effects (cell killing), cytostatic effects (inhibition of cell proliferation) or whether detachment occurred (adherent cells suspended in culture medium). Therefore, an additional CytoTox 96 assay was utilised to supplement the conclusions drawn from the mammalian viability assay and determine whether the heteroleptic bismuth(III) complexes impart a cytotoxic effect on the cos-7 cells.

The CytoTox 96 non-radioactive membrane integrity cytotoxicity assay shows that non-viable cells may undergo apoptosis through the loss of membrane integrity. The assay quantifies the release of lactate dehydrogenase (LDH), which is a stable cytosolic enzyme that is released upon the lysis of cells. While the assay itself determines the disruption in integrity of the membrane, it is unknown whether the

bismuth(III) heteroleptic complexes are interacting with the membrane itself, or rather causing an internal cascade reaction which leads to loss of membranal integrity. The membrane integrity assay for complexes **2-3**, **2-9**, **2-12** and $BiPh_3$ was performed at three approximate concentrations: MIC, 4 x MIC and MIC/2. From the data obtained, the lysis of cells remained consistent across the range of concentrations for each complex. Values obtained from the graphical data (Figure 64) are in agreement with the mammalian cell viability studies, whereby the heteroleptic diphenylbismuth(III) thiolato complex **2-9** in contrast to the bismuth(III) *tris*-substituted thiolato complex **2-3** shows over five times the activity. Notably, complex **2-12** which shows the lowest IC_{50} value in cell viability studies displayed relatively low cytotoxicity values at 11 % for the experiments conducted at 12 µM, 6 µM and 3 µM, respectively. The data obtained from both the cell viability studies and cytotoxicity studies intended to correlate in order to determine a trend; however, the cytotoxicity assay appeared to have significant inconsistencies when tested on a selection of compounds. Therefore, further studies are required to completely elucidate the cytotoxicity of these complexes.

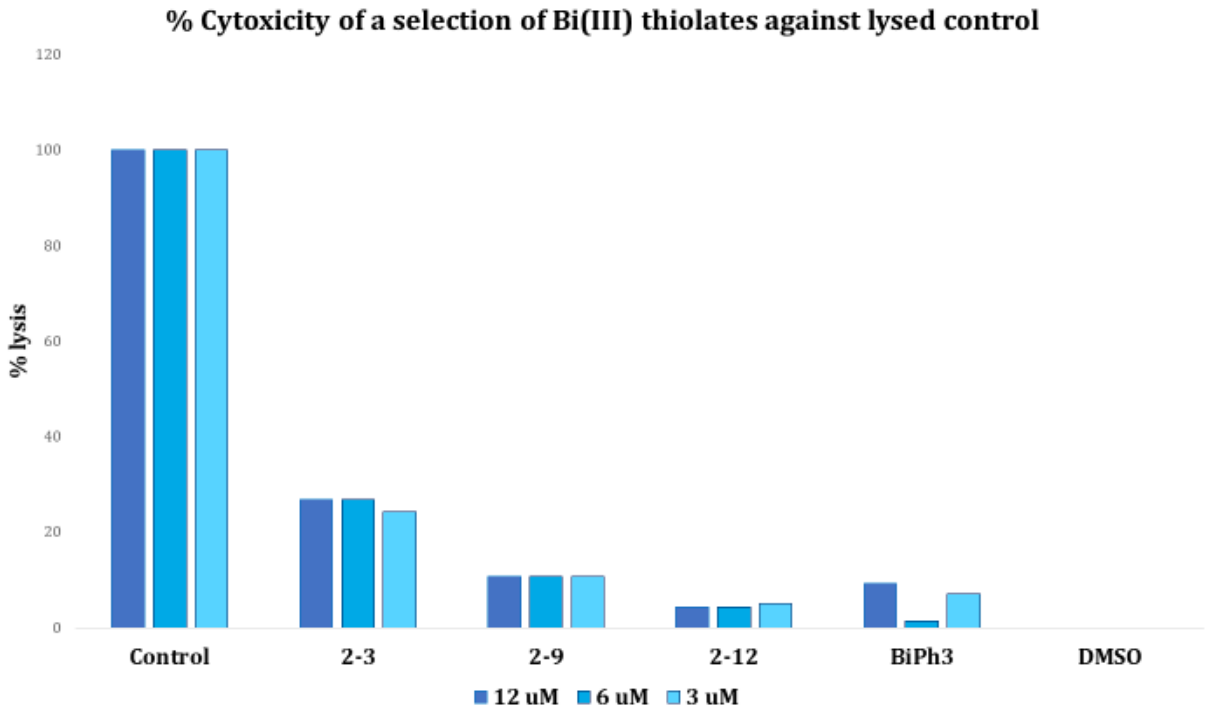

Figure 64: % cytotoxicity induced by the homoleptic *tris*-substituted bismuth(III) thiolate $[Bi(POTz)_3]$ **2-3**, and heteroleptic phenylbismuth(III) thiolates $[BiPh_2(POTz)]$ **2-9**,

[$BiPh_2$(PDTz)] **2-12**, and $BiPh_3$ in 0.2 % v/v DMSO measured against a control of Triton-x-100 at 2 %.

2.3.10.3 Bacterial cell uptake studies

Given the significant biological activity shown by the heteroleptic complexes when compared to their homoleptic counterparts, it was postulated this activity could be related to their cellular uptake. Further studies were conducted to probe the antibacterial activity of both the homoleptic *tris*-substituted bismuth(III) thiolates and heteroleptic diphenylbismuth(III) thiolates through the quantified cellular uptake using ICP-MS of Bi^{209} in MRSA and *E. coli.*

In the course of assessing cellular uptake, the homoleptic *tris*-substituted bismuth(III) thiolato complex [$Bi(POTz)_3$] **2-3,** and heteroleptic diphenylbismuth(III) thiolato complex [$BiPh_2$(POTz)] **2-9** were chosen as representative examples. Additionally, a control sample with no bismuth and precursor control ($BiPh_3$) was also included in the study.

The compounds were initially exposed to bacterial cells for 24 hours as per normal MIC testing protocol. Following exposure, the cells were then washed with PBS and prepared for Bi^{209} uptake analysis via ICP-MS through digestion and dilution in nitric acid.

The results obtained from ICP-MS revealed that there is a significant increase in the cellular uptake of Bi^{209} for the heteroleptic diphenylbismuth(III) thiolato complex **2-9** (34.1 ng/10^6 cells in *E. coli* and 39.1 ng/10^6 cells in MRSA) relative to the homoleptic *tris*-substituted thiolato complex **2-3** (1.49 ng/10^6 cells in *E. coli* and 0.18 ng/10^6 cells in MRSA). The results also show that there is a comparable uptake in both Gram-negative (*E. coli*) and Gram-positive (MRSA) bacteria for the heteroleptic complex. This trend is clearly evident from the uptake graphs shown in Figure 65.

In a comparable study conducted by Burke *et al.,*[350] the relative cellular uptake of bismuth was measured in Gram-positive VRE bacterial cells for a set of homo- and heteroleptic bismuth(III) flavonolate complexes of the forms [$Bi(L)_3$] and [$BiPh(L)_2$]. The homoleptic *tris*-substituted bismuth(III) flavonolates showed significantly lower

Bi accumulation relative to the heteroleptic bismuth(III) flavonolate counterparts.[350] Interestingly, the heteroleptic bismuth(III) flavonolate which showed the highest accumulation of Bi shared comparable antibacterial activity as complex **2-9** however, both complexes show vastly different accumulation values of ~250 Bi/10^6 cells in VRE for BiPh(flavonolate)$_2$ against 39.1 ng/10^6 cells in MRSA for **2-9**.[350]

A direct correlation between the cellular uptake and antibacterial activity of both complexes **2-3** and **2-9** can be observed with the most biologically active complexes producing higher uptake readings of bismuth(III) in bacterial cells. Despite these results, it will be pertinent to understand the complex cellular uptake in mammalian cos-7 cells as a comparative study.

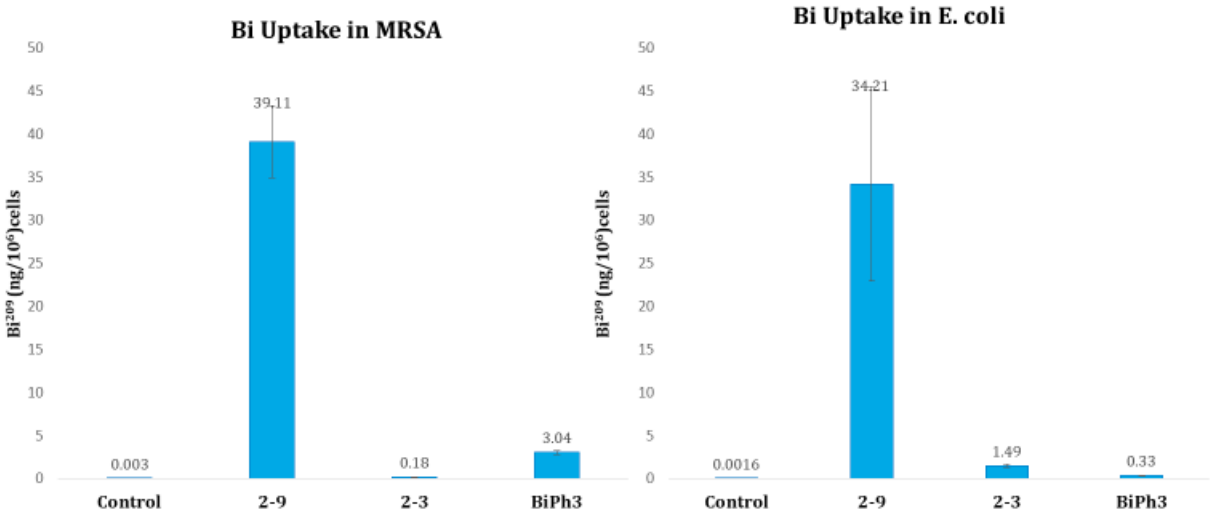

Figure 65: Cellular uptake of Bi(III) thiolate complexes [Bi(POTz)$_3$]**2-3**, [BiPh$_2$(POTz)] **2-9,** and BiPh$_3$ in MRSA and *E. coli* measured by ICP-MS.

2.3.10.4 Mammalian cell viability

In order to determine the feasibility of the bismuth(III) triazole thiolato complexes as drug candidates, it was necessary to probe the selectivity of these complexes through mammalian cell viability studies. As earlier reports presented preliminary cell viability studies of similar homo- and heteroleptic bismuth(III) triazole thiolates, the two series of complexes **2-1** to **2-6** and **2-7** to **2-12**, were tested for mammalian cell viability against the cos-7 primary monkey kidney cell line.

Observed in Figure 66, the homoleptic *tris*-substituted bismuth(III) thiolato complexes **2-1** to **2-6** exhibited no reasonable activity against the cos-7 cells with IC_{50} values exceeding 100 µM.

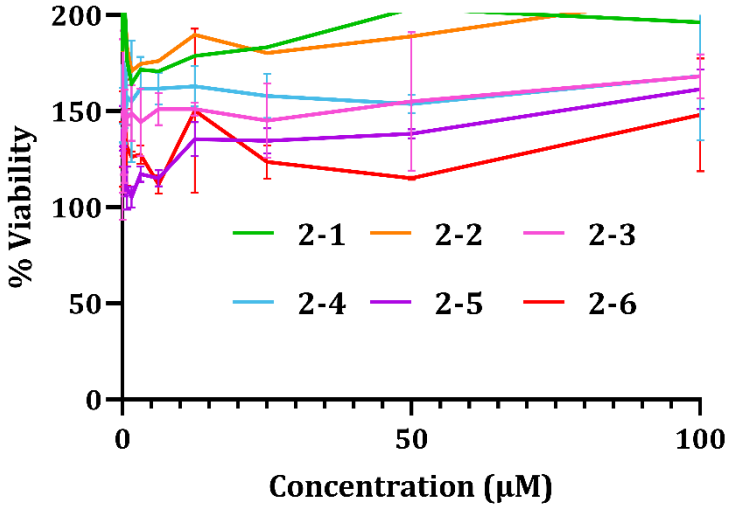

Figure 66: Viability percentage of complexes of the form $[Bi(SR)_3]$ **2-1** to **2-6**, against cos-7 cells. Dose response curves generated over a range of concentrations (24 nM – 50 µM) in the appropriate culture media from 10 mM DMSO stock solutions. Readings were compared spectroscopically to non-treated control and the percent growth inhibition calculated. Some data points missing due to viability exceeding 200 %.

The exposure of cos-7 cells to the heteroleptic Bi(III) thiolates resulted in a significant reduction in cell viability (Figure 67). This trend is consistent with the bacterial and fungal assays conducted with the heteroleptic diphenylbismuth(III) thiolate complexes exhibiting a higher degree of activity in contrast to the homoleptic *tris*-substituted bismuth(III) thiolato-complexes. Within the triazole thiolate series, there appeared to be minor variations between the derivatives. This is exhibited through the relatively tight IC_{50} range (0.280 µM – 10.08 µM). Interestingly, complex $[BiPh_2(PDTz)]$ **2-12** (IC_{50} 0.280 µM), bearing a dimethyl phenyl moiety, displayed the lowest viability values by an order of magnitude when compared to the rest of the series. The concept of 'magic methyl' groups has been explored in organic and medicinal chemistry before whereby the introduction of a single methyl group may change the activity of said molecule.[354,355] When comparing complex $[BiPh_2(PFTz)]$ **2-11** (IC_{50} 4.7 µM) and **2-12** (IC_{50} 0.280 µM), the addition of a single methyl group

produced a marked difference in potency, this could be due to a number of reasons including the change in rotational bonds due to sterics, conformational changes resulting in additional nonpolar interactions which can 'lock' the molecules to a particular configuration within the cellular binding site, as well as desolvation.[355] Further cellular studies are required to ascertain the specific mechanism of action for these complexes.

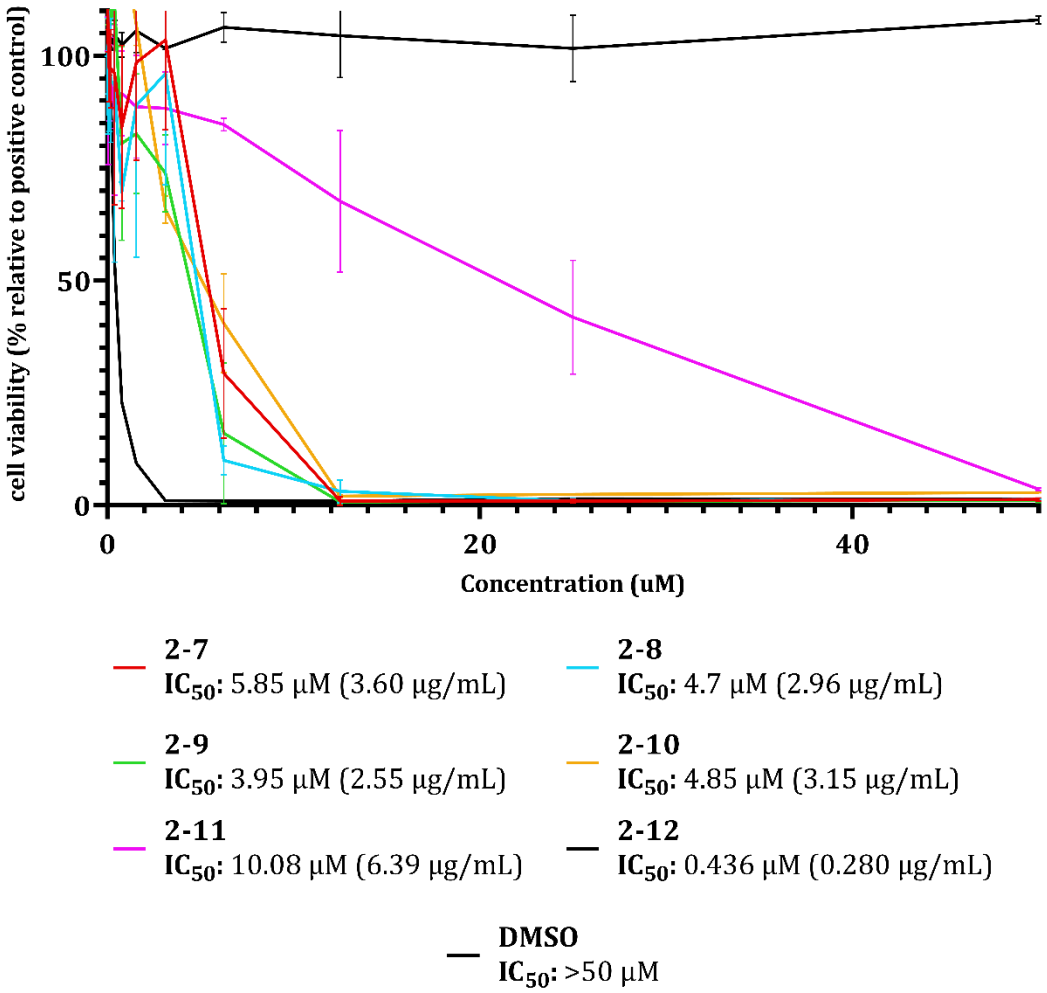

Figure 67: Viability percentage of complexes of the form [$BiPh_2$(SR)] **2-7** to **2-12**, against cos-7 cells. Dose response curves generated over a range of concentrations (24 nM – 50 µM) in the appropriate culture media from 10 mM DMSO stock solutions. Readings were compared spectroscopically to non-treated control and the percent growth inhibition calculated.

2.3.10.5 Selectivity

A key aspect that underpins drug discovery is identifying and optimising candidates to produce an optimal safety-efficacy profile, this can be achieved by utilising the selectivity (or therapeutic) index (SI) metric. The SI is defined by measuring the ratio between the highest exposure to the drug which results in no toxicity to the exposure that produces the desired efficacy.[356,357] In the context of this thesis, the SI has been measured using the ratio of antimicrobial activity (MIC) and the IC_{50} against cos-7 mammalian cells i.e., IC_{50} (cos-7)/MIC against each of the bacterial species (where possible). Generally, high SIs are favourable as they show a compounds propensity to have a safer *in vitro* profile.[358] The SI of complexes **2-7** to **2-12** using MRSA, VRE, *E. coli* and *P. aeruginosa* as reference bacterial strains, and *C. albicans* and *C. auris* as reference fungal strains are shown in Table 9.

Table 9: Selectivity index (SI) of complexes **2-7** to **2-12**. The SI is calculated using the MICs against bacterial and fungal strains and the IC_{50} against cos-7 cells.

	MRSA	**VRE**	***E. coli***	***P. aeruginosa***	***C. albicans***	***C. auris***
2-7	0.46	1.87	0.47	0.23	-	-
2-8	0.37	1.50	0.38	0.19	-	-
2-9	0.31	0.63	0.32	0.16	3.10	6.71
2-10	0.39	0.39	0.39	0.19	-	-
2-11	0.81	1.61	0.81	0.40	-	-
2-12	0.03	0.07	0.07	0.0017	-	-

The Bi(III) thiolate complexes display poor selectivity towards bacterial cells with all values against the Gram-positive strain MRSA below 1, this shows a non-significant affinity towards bacterial cells over mammalian cells. In the bacterial series, the Bi(III) thiolate complexes show greatest selectivity towards VRE however, complex **2-9** shows the highest SI for the pathogenic clinical isolate of *C. Auris*. In general,

complexes which were derived from the 2,5-dimethylphenyl derivative triazole (**2-12**) had the poorest SIs (0.0017-0.03), this could be due to the low antibacterial efficacy of these complexes.

Overall, the general trend of these complexes against the four strains of bacteria indicate that the bismuth(III) thiolate complexes possess poor SIs and therefore require further structural modification to consider them ideal candidates for drug development. Analysis of the one triazole complex **2-9** against the two *candida* strains suggests that Bi(III) thiolate complexes may have potential to be used as antifungal agents due to their greater selectivity towards fungal cells over mammalian cells.

2.3.10.6 Haemolysis assay

The results obtained from preliminary biological assays against the two heteroleptic complexes [$BiPh_2$(POTz)] **2-9**, and [$BiPh_2$(PDTz)] **2-12**, revealed a general selectivity towards mammalian cos-7 cells. To probe this selectivity, a selection of complexes **2-3**, **2-9** as well as $BiPh_3$ were evaluated for their haemolytic activity against red blood cells at a concentration of 25 μM. Trixton-x-100 at 2 % served as a positive control whilst DMSO at 2 % served as a negative control. In this assay, the release of haemoglobin, which was measured at 540 nm by UV-visible spectroscopy, was used to quantify the membrane damaging properties of the Bi(III) thiolates. The haemolytic activity of the homoleptic *tris*-substituted bismuth(III) thiolato series of complexes in contrast to the diphenylbismuth(III) thiolato series shows a lower lysis trend. In comparison to the positive control (100 % haemolysis), at 25 μg mL^{-1} all *mono* thiolates show lysis values higher than 100 % (Figure 68). Significantly, the *tris*-substituted bismuth(III) thiolates show 41 % haemolysis. This is particularly of interest as complexes **2-1** to **2-6** did not display any appreciable biological activity in both the bacterial and mammalian assays. The study at present is inconclusive regarding the selectivity of the bismuth(III) triazole thiolato complexes. Additionally, the haemolysis assay was both conducted on a much shorter timeframe of complex exposure to cells (2 hours) as well as completed only once and thus producing only a preliminary analysis and therefore, repeat testing is required.

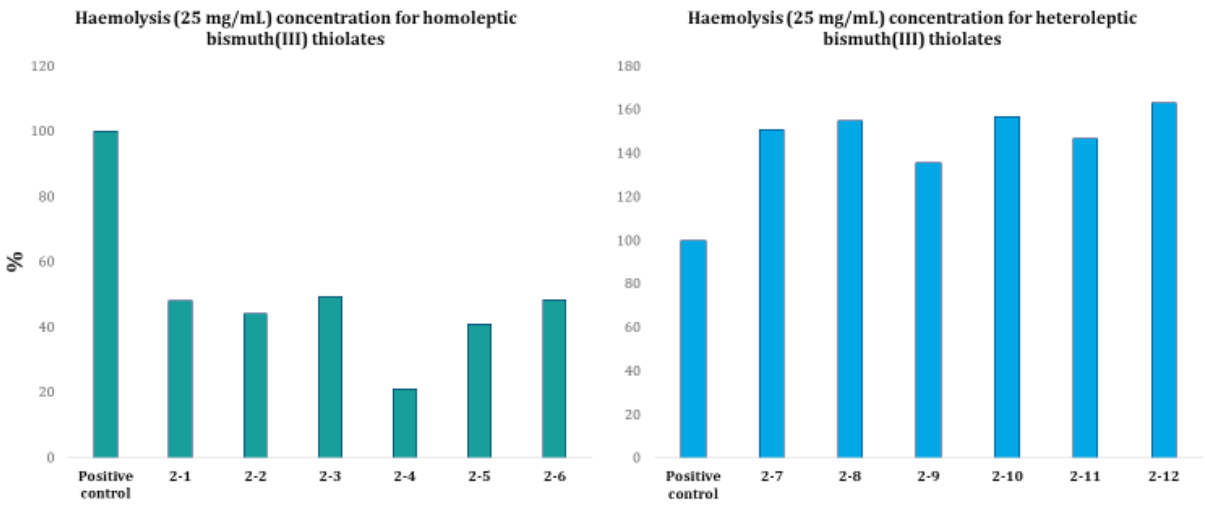

Figure 68: % Hemolysis induced by the homoleptic tris-substituted bismuth(III) thiolato series of compounds of the form [$Bi(SR)_3$] **2-1** to **2-6** (left) and heteroleptic diphenylbismuth(III) thiolato series of compounds of the form [$BiPh_2(SR)$] **2-7** to **2-12** (right).

2.3.10.7 Summary of biological results

Collectively, the biological studies conducted on the Bi(III) complexes show a marked effect between the homoleptic and heteroleptic thiolates. Initial disc diffusion results were consistent with other previously synthesised Bi(III) complexes whereby the homoleptic *tris*-substituted bismuth(III) thiolates showed no antibacterial or antifungal activity against the selected strains. Broth dilution assays conducted on the heteroleptic diphenylbismuth(III) thiolates **2-7** to **2-12** showed the most potent complexes to be **2-7** and **2-8** against VRE. Supporting this theory, cellular uptake studies taken in MRSA revealed a direct correlation of accumulation to antibacterial activity. However, further analysis via the cytotoxic membrane integrity assay revealed inconclusive results as to whether the heteroleptic Bi(III) complexes were cytotoxic. Although the heteroleptic Bi(III) thiolates showed antimicrobial activity, when exposed to mammalian cos-7 cells, the complexes showed a significant reduction in cellular viability. Further analyses revealed poor selectivity towards microbial cells over mammalian cells and thus, bringing into question whether these complexes may have a non-specific mode of action.

2.4 Part 2: Results and discussion – Rhodanines

In an effort to add to the structural diversity of the library of metal thiolates, the rhodanine sub-class of N-heterocyclic compounds were chosen as lead precursors for the development of a series of bismuth(III) thiolates due to their ability to form covalent and dative bonds. While the M-N and M-O type interactions are common in transition metal complexes, rhodanines show monodentate, bidentate or bridging type bonding modes across the S,N and O terminals in p-block metals. It is therefore, of interest to explore these precursors to further understand their interaction with bismuth(III) ions.

2.4.1 Synthesis and spectroscopic characterization of a series of 5-substituted 2-thioxothiazolidin-4-ones (rhodanines)

The synthesis of a series of rhodanine derivatives **2-13** to **2-17** proceeds via a simple aldol condensation in the presence of a catalyst, ammonium acetate and products can be formed mechanochemically through the grinding of rhodanine and an aldehyde in a 1:1 ratio (Scheme 7). The reaction is easily monitored via TLC and incorporates green chemistry principles, proving it to be an ideal substrate. To explore the structural diversity of the rhodanine class of compounds, five different rhodanine precursors were synthesised: benzylidene rhodanine (BR*H,* ***7****)* and *para*-methoxybenzyl rhodanine (MOBR*H,* ***8***), *tris-para*-methoxybenzylrhodanine (3MOBR*H,* ***9***), indole rhodanine (InR*H,* ***10***) and thiophene rhodanine (ThR*H,* ***11***).

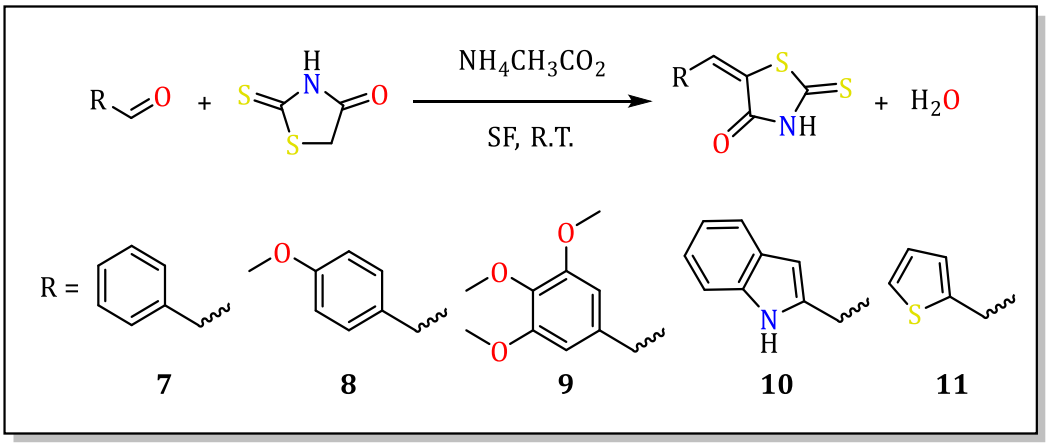

Scheme 7: Preparation of arylrhodanine derivatives **7** to **11** from substituted aldehydes and rhodanine.

2.4.2 Synthesis of heteroleptic phenylbismuth(III) rhodanines

Formation of the heteroleptic bismuth(III) rhodanines followed a more facile route with the implementation of microwave methods. In contrast to traditional reflux and solvent-free routes, initial reactions focused on the green chemical aspect of synthesis whereby the utilisation of a microwave irradiation greatly reduced reaction times, solvent use, and improved yields. The reaction proceeded via the microwave irradiation for twenty minutes of an equimolar reaction mixture of a rhodanine precursor with $BiPh_3$ in DMSO at 85 °C (Scheme 8). The resultant brightly coloured solution was then gravity filtered, and the complex was left to crystallise from the filtrate over a period of 2 days to 1 week. Crystals from each reaction were collected via filtration, washed with Et_2O, and dried *in vacuo* to produce the complexes **2-13** to **2-17** with yields varying between 25-83% (

Table 10).

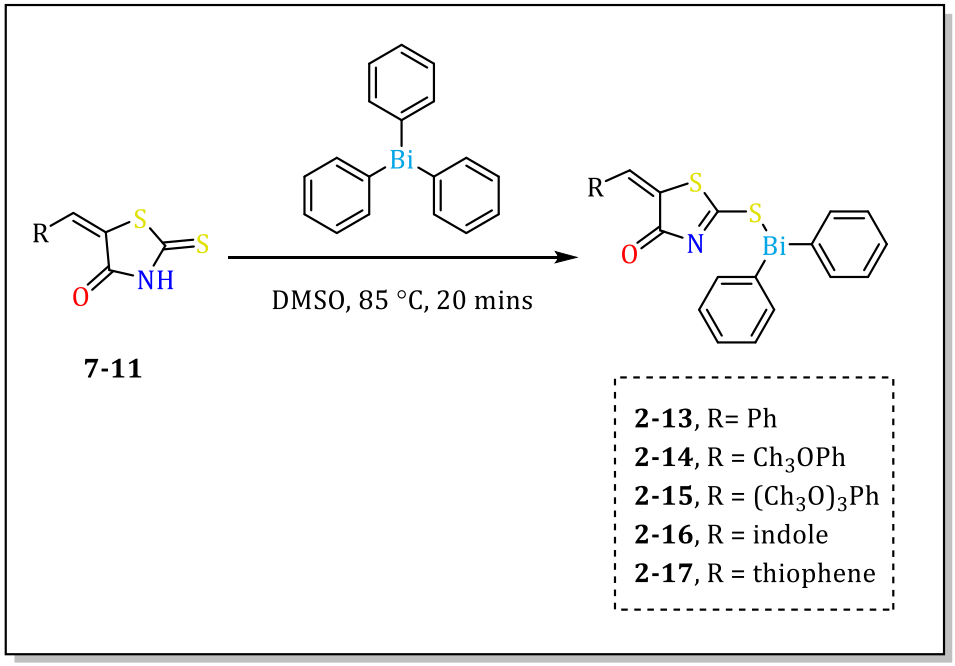

Scheme 8: Formation of heteroleptic diphenylbismuth(III) thiolates of the form $[BiPh_2(SR)]$ **2-13** to **2-17**, derived from rhodanine precursors **7** to **11.**

The five synthesised complexes **2-13** to **2-17** were characterised by ^{1}H and ^{13}C spectroscopy, FT-IR spectroscopy, HRMS, melting point and (where possible) single crystal X-ray diffraction. Similar to the heteroleptic Bi(III) triazole thiolates discussed

in section 2.3.1, these complexes also displayed limited solubility in the same suite of polar solvents.

Table 10: Summary of yields and appearances of heteroleptic diphenylbismuth(III) rhodanine complexes **2-13** to **2-17** whereby BR = benzylidene rhodanine **7**, MOBR = p-methoxybenzyl rhodanine **8**, 3MOBR = *tris-p*-methoxybenzylrhodanine **9**, InR = indole rhodanine **10**, and ThR = thiophene rhodanine **11**.

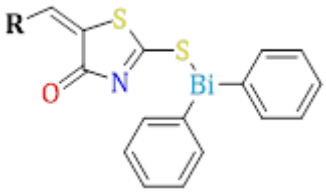

	Complex	Functional Group (R)	Yield (%)	Melting point (°C)	Appearance
2-13	[$BiPh_2$(BR)]	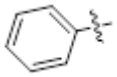	83	177 – 180	Yellow needles
2-14	[$BiPh_2$(MOBR)]	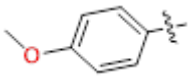	25	204 – 210	Orange needles
2-15	[$BiPh_2$(3MOBR)]	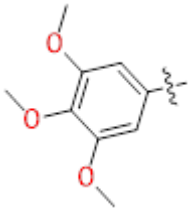	72	193 – 195	Red blocky crystals
2-16	[$BiPh_2$(InR)]	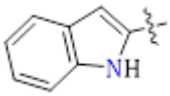	63	184 – 188	Orange blocky crystals
2-17	[$BiPh_2$(ThR)]	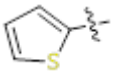	55	161 – 162	Bright yellow needles

2.4.3 FT-IR Characterization

Addressed in section 2.3.5, assigning vibrational absorption bands for thiocarbonyl-type functionalities within nitrogen-based heterocyclic systems proved to be challenging. Similar to the triazole thiolates, the rhodanine derivatives **7** to **11** exhibit a greater degree of molecular complexity due to the additional functional groups

present within the molecules, which consequently produce overlapping absorption bands. Exocyclic C=S and C=O type bonds influence the shift of the absorption bands therefore the accuracy of this interpreted data was empirically evaluated.

Molecules containing the rhodanine functionality have been observed to display three characteristic thioureide bands I, II and III which can be assigned to the mixed vibrations *ν*(C-N) + δ(N-H), *ν*(C-N-C) and *ν*(C=S) at three different absorption regions (Table 11).[341,359–361] In some cases, at lower frequencies, a fourth thioureide IV band can be observed corresponding to the *ν*(C-N) bending mode.[361]

The most prominent shift in stretching vibrations between the free rhodanines and the bismuth(III) complexes **2-13** to **2-17** was shown in the shift of the thioureide I band *ν*(C-N) + δ(N-H). The IR spectra for **2-13** to **2-17** show the band in the range of 1542-1580 cm^{-1} and a hypsochromic shift 8-20 cm^{-1} with respect to the parent rhodanines (1560-1586 cm^{-1}). A less prominent shift between 1-9 cm^{-1} is observed for the thioureide II *ν*(C-N-C) band between the precursor rhodanines and bismuth(III) complexes postulated to be due to vibrational coupling effects.

Due to the complex vibrational coupling FT-IR spectroscopy alone could not determine the overall connectivity and consequent binding mode of the Bi(III) therefore, other analytical techniques such as ^{1}H and ^{13}C NMR spectroscopy and single crystal X-ray diffractometry were required to fully elucidated the connectivity of the complexes **2-13** to **2-17.**

Table 11: Characteristic IR assignments in precursors **7** to **11** and complexes **2-13** to **2-17**. (br) = broad, (s) = strong (m) = moderate.

Compound		*ν*(C-N) + δ(N-H)	*ν*(C-N-C)	*ν*(C=S)	*ν*(C-N)
7	BR*H*	1586	1226	1182	758
2-13	[$BiPh_2$(BR)]	1580	1238	-	722
8	MOBR*H*	1560	1235	1165	819
2-14	[$BiPh_2$(MOBR)]	1579	1236	1167	821
9	3MOBR*H*	1571	1213	1125	822
2-15	[$BiPh_2$(3MOBR)]	1560	1222	1121	727
10	InR*H*	1562	1213	1139	739
2-16	[$BiPh_2$(InR)]	1542	1218	-	722
11	ThR*H*	1574	1221	1186	704
2-17	[$BiPh_2$(ThR)]	1561	-	1204	712

2.4.4 HRMS and elemental analyses

High resolution mass spectrometry was used to support the formation of the heteroleptic diphenylbismuth(III) rhodanines. Solid samples of each of the complexes **2-13** to **2-17** were solubilised in a mixture of DMSO and methanol and analysed via

ESI techniques. The parent ion was observed in the positive ion mode as the protonated form [[$BiPh_2$(SR) + H]$^+$. All of the complexes showed the expected isotopic distribution patterns associated with Bi(III).

2.4.5 NMR spectroscopy of heteroleptic phenylbismuth(III) rhodanines

2.4.5.1 ^{1}H NMR spectroscopy

Analysis of the ^{1}H NMR spectra of the heteroleptic Bi(III) complexes shows the absence of the thioamide proton signal occurring in the ^{1}H NMR spectrum of the respective parent thiol (observed as a very broad singlet at approximately 14 ppm). As bismuth is thiophilic, this is indicative of the tautomerisation to the thiol form, deprotonation of the thiol group and subsequent binding to the Bi(III) metal centre. Proton environments observed in the aromatic regions of complexes **2-13** to **2-17** all show a downfield shift of the *ortho*-phenylbismuth(III) signals. In a representative example of complex [$BiPh_2$(MOBR)] **2-14** in the stoichiometric reaction of MOBR **8,** with $BiPh_3$, the shift of *ortho*-phenylbismuth(III) signals can be observed as a doublet at 8.30 ppm. When compared to the spectrum of **8**, upfield shifts of all aromatic protons can be observed in the complex **2-14**. Notably, the benzylidene proton (4, Figure 69) has undergone an apparent shift from 7.63 ppm to 7.34 ppm upon binding to the Bi(III) centre (Figure 69).

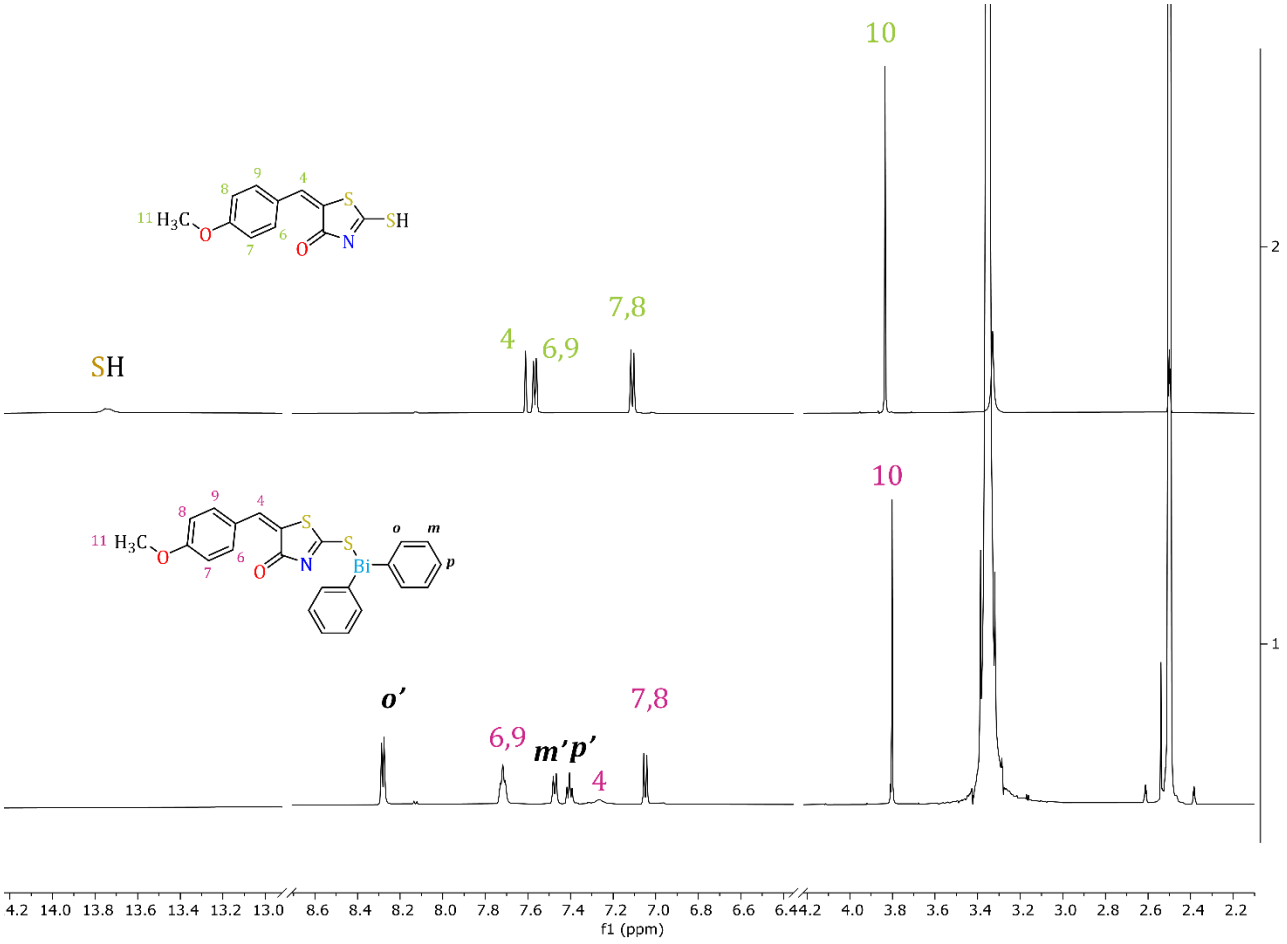

Figure 69: Solution state spectral comparison of MOBR*H* **8** (spectrum 2, top), and product, complex [$BiPh_2$(MOBR)], **2-14** (spectrum 1, bottom) taken in DMSO-d_6 at 25 °C.

2.4.5.2 ^{13}C NMR spectroscopy

The ^{13}C NMR spectra of complexes **2-13** to **2-17** in DMSO-d_6 show most of the expected rhodanine signals. The quaternary carbon signals associated with both the coordinated ligand and phenylbismuth(III) moieties were occasionally not observed due to the low solubility of the complexes. Analysis of the precursor MOBR*H* **8** indicates the typical signals observed in a substituted rhodanine (Figure 70). The molecule exists in the thione state as demonstrated by the characteristic presence of the C=S (C1) signal at δ = 169.9 ppm.[362,363] Additionally, the presence of more electronegative carbonyl (C1) and anisole-type (C10) signals at δ = 196.0 and δ = 161.9 ppm, respectively.

Upon complexation to the Bi(III), the absence of the C=S signal confirms the tautomerisation of precursor **8** from the thione form to the thiol form, the consequent

deprotonation of the thiol group results in the formation of a C-S bond. It is postulated that the C-S bond shifts beyond δ = 200 ppm due to the increased electronegative character of the dithioketimine C1 as a result of the polarised Bi-S bond.

In complex [$BiPh_2$(MOBR)] **2-14**, the ligand *ortho*- and *meta*-methoxyphenyl signals C6-C9 all undergo upfield shifting with signals in the range δ = 132.1-115.3 ppm compared to the respective precursor rhodanine **8** signals ($\delta_{(C6-C9)}$ = 133.2-115.6 ppm, Figure 70). Additionally, the *ortho-*, *meta*- and *para*- signals associated with the phenylbismuth(III) ligand lie at δ = 138.2, 130.8 and 128.5 ppm, respectively, these values are consistent with previously synthesised complexes within the literature.[314]

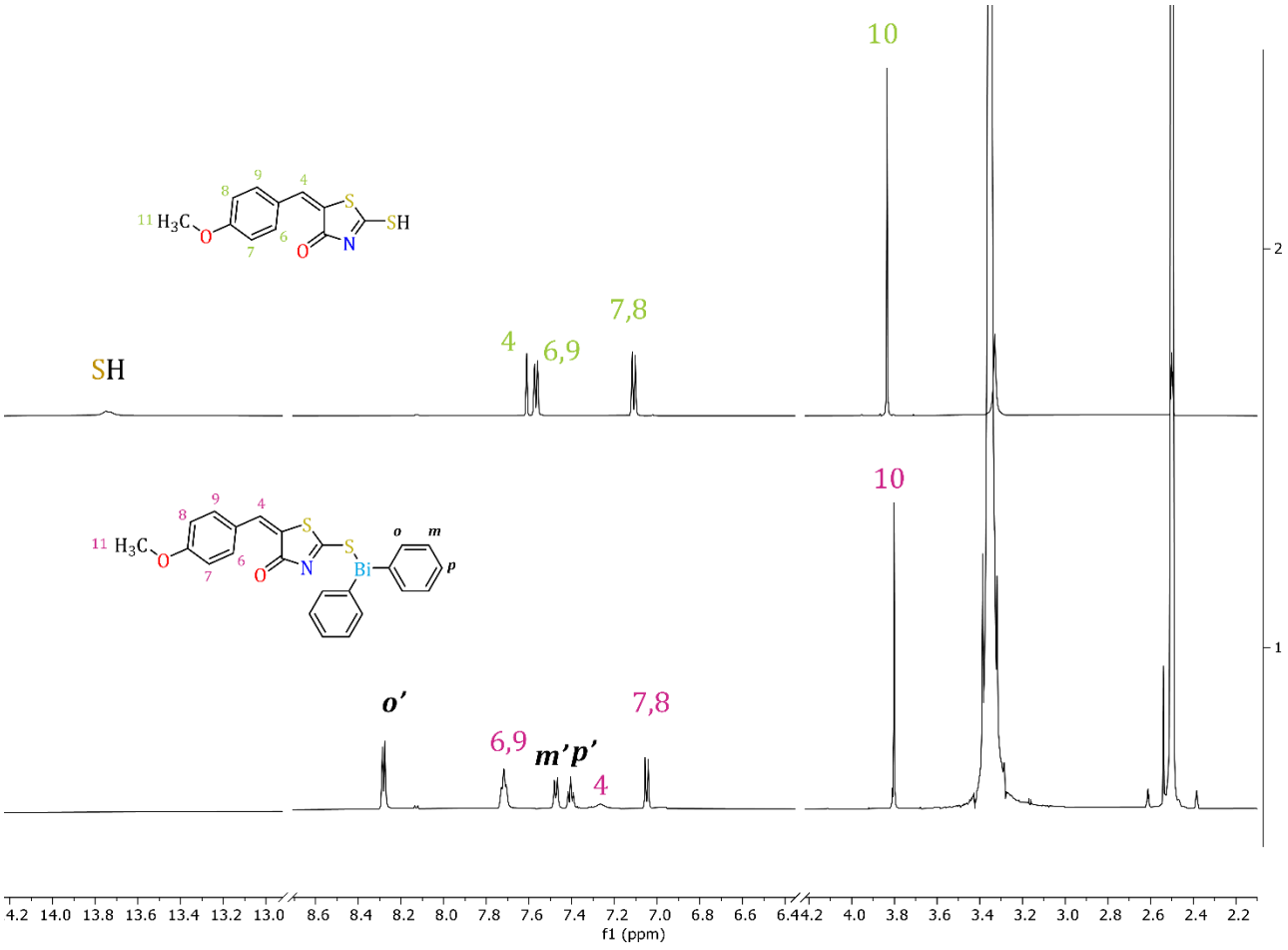

Figure 70: Stacked ^{1}H NMR spectra of MOBR, **8** (2; top) and [$BiPh_2$(MOBR] (**2-14**; bottom) in DMSO-d_6 with select carbon atom signals labelled.

2.4.6 X-ray crystallography

The solid-state structure of three of the five novel heteroleptic diphenylbismuth(III) rhodanine complexes [$BiPh_2$(BR)] **2-13**, [$BiPh_2$(MOBR)] **2-14** and [$BiPh_2$(InR)] **2-16** were obtained, analysed, and elucidated via single crystal X-ray diffraction. The molecular structures are shown in Figure 71-Figure 73 and the selected bond lengths and angles are summarised in Table 12. Crystals suitable for X-ray analysis were obtained from the reaction mixture through the slow evaporation of DMSO. All three complexes bear structural similarities with the asymmetric units of each being isostructural.

Table 12: Selected bond lengths (Å) and angles (°) of the solid-state structures of heteroleptic Bi(III) thiolate complexes of the form [$BiPh_2(SR)$], **2-13** to **2-16**. * Refers to bond lengths associated with dimerized structures.

Bond (Å)/Angle (°)	2-13	2-14	2-16
Bi(1)-S(1)	2.7431(10)	2.7821(12)	2.7936(17)
Bi(1)-C(1)	2.245(4)	2.257(5)	2.260(6)
Bi(1)-C(2)	2.245(5)	2.254(4)	2.258(6)
Bi(1)-O(1)*	2.567(3)	2.520(3)	2.7718(15)
S(1)-C(3)	1.683(4)	1.692(5)	1.703(7)
N(1)-C(3)	1.319(5)	1.317(6)	1.365(8)
C(1)-Bi(1)-C(2)	96.90(15)	94.98(17)	93.0(2)
C(1)-Bi(1)-S(1)	85.88(10)	90.19(12)	91.77(15)
C(2)-Bi(1)-S(1)	89.88(10)	86.97(13)	83.51(16)
O(1)-Bi(1)-S(1)*	164.72(7)	167.42(8)	165.96(10)
C(2)-Bi(1)-O(1)*	83.03(12)	81.35(14)	82.56(18)
C(1)-Bi(1)-O(1)*	81.57(12)	86.20(15)	87.18(18)
C(3)-S(1)-Bi(1)	95.43(13)	94.24(17)	96.7(2)
N(1)-C(3)-S(1)	124.9(3)	124.8(4)	124.7(5)

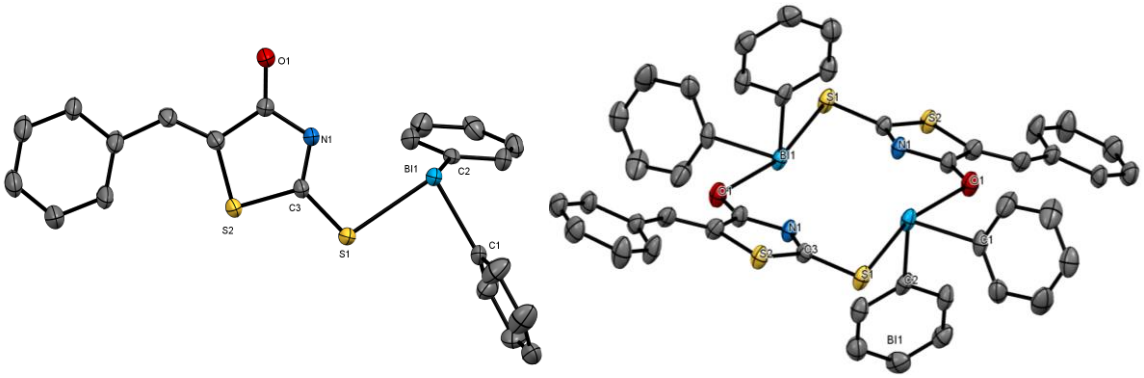

Figure 71: Asymmetric unit and extended dimeric fragment of the molecular structure of [$BiPh_2$(BR)] **2-13**. Thermal ellipsoids are shown at the 50% probability level. Hydrogen atoms have been omitted for clarity.

In a representative example of the diphenylbismuth(III) rhodanine complex [$BiPh_2$(MOBR)] **2-14**, the complex crystallises as a dimer with each Bi(III) metal centre adopting a five-coordinate geometry (Figure 72). The asymmetric unit shows the Bi(III) metal centre adopting a tetrahedral geometry whereby the bismuth core is covalently bound to two phenyl rings, a sulfur atom from the rhodanine core in addition to the stereochemically active lone pair (SALP) situated perpendicular to the three bonds. The length of the Bi core interaction for each complex is within the sum of the van der Waals radii of bismuth and nitrogen and the Bi-S bond distances listed are typical of Bi(III) aryl thiolate complexes.[145,280,282,364]

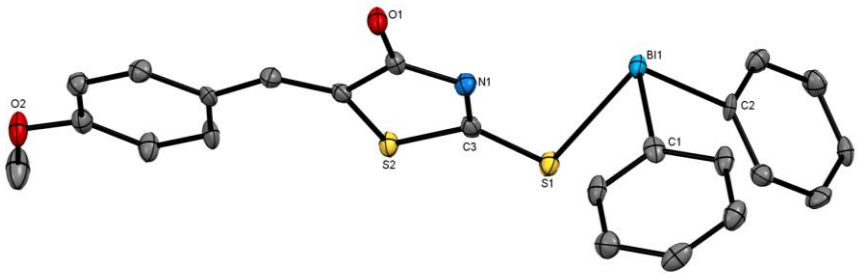

Figure 72: Molecular structure of [$BiPh_2$(MOBR)] **2-14** showing thermal ellipsoids at 50% probability. Hydrogen atoms have been omitted for clarity.

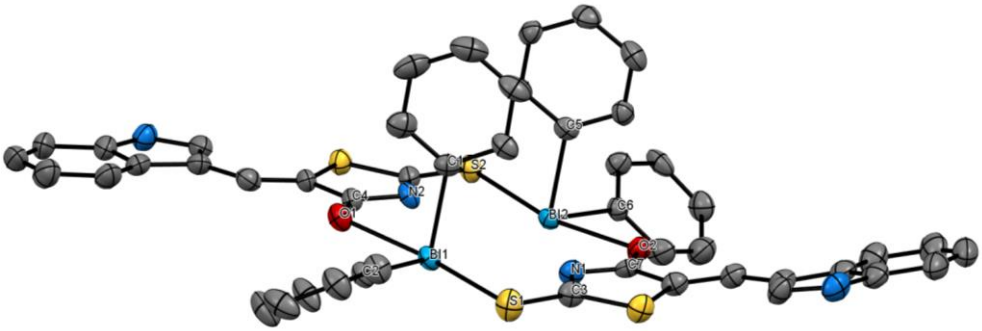

Figure 73: Asymmetric unit of the molecular structure of [$BiPh_2$(InR)] **2-16.** Thermal ellipsoids are shown at the 50% probability level. Hydrogen atoms have been omitted for clarity.

2.4.6.1 Computational analyses

To gain a greater understanding of the non-bonding effects of the theorised SALP in the expression of physical properties such as thermochromism, thermal conductivity in these molecules, Density Functional Theory (DFT) calculations were conducted on complex [$BiPh_2$(MOBR)] **2-14** (Figure 74). Analysis of the chemical bonding within the **2-14** structure shows that it is predominantly consistent of polar covalent interactions with significant contributions both from the charge accumulated on the Bi metal centre and through charge transfer.

DFT calculations were performed on **2-14** using the functional B3LYP and the LANL2DZ basis set to obtain a full potential all electron basis for Bi and an effective core potential for Bi. The full geometry, cell and atomic coordinates were optimised bearing symmetry. The geometry optimisation on the experimental product is in good agreement with the bond lengths displayed in the crystal structure and bond angles were used as a measure for the degree of lone pair expression in accordance with Valence Shell Electron Pair Repulsion (VSEPR) theory.

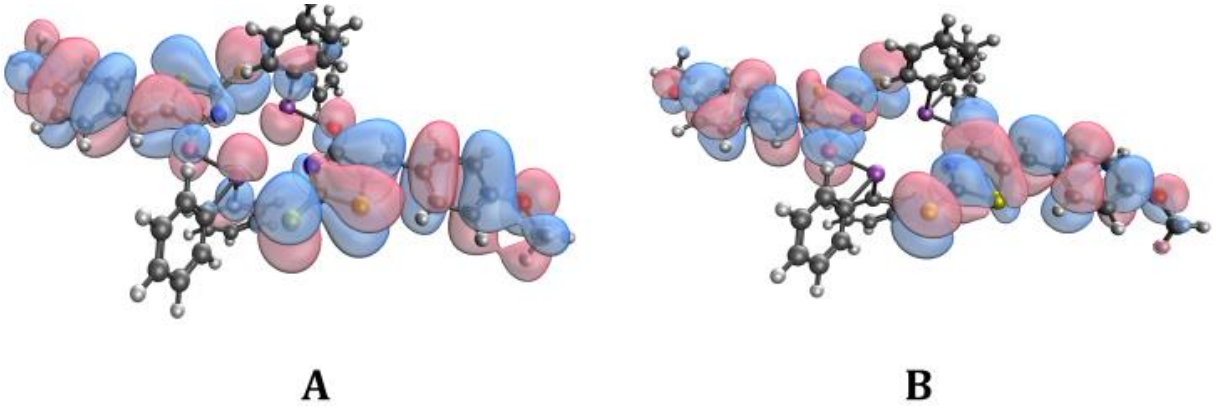

Figure 74: Ground state orbital optimized structures of [$BiPh_2$(MOBR)] **2-14**. **A** = HOMO, **B** = LUMO structures. Isosurface values are taken at +/- 0.020.

2.4.7 Solution state stability studies

Prior to evaluating the *in vitro* biological activity of the heteroleptic phenylbismuth(III) rhodanine complexes against bacterial, fungal and mammalian cells, it was important to determine the solution state stability of the complexes in the presence of aqueous media. As the complexes displayed low solubility in water, DMSO was chosen as a carrier solvent in which biological assays would be conducted. The ^{1}H and ^{13}C NMR spectra of complexes **2-13** to **2-17** were acquired in wet DMSO-d_6 over a period of 48 hours, accounting for the time duration relevant to the biological assays. After 48 hours, no spectral changes were observed when compared to initial readings and no precipitation of compound was observed in the NMR tubes, therefore, the Bi(III) rhodanine complexes were deemed to be hydrolytically stable in DMSO up to 48 hours.

A combination of both UV-visible spectroscopy and NMR spectroscopy were used to evaluate the solution-state stability of the Bi(III) rhodanine complexes. Using a representative example, [$BiPh_2$(ThR)] **2-17** was assessed in the presence of phosphate-buffered saline (PBS) and cell culture medium, glutathione (GSH) and cysteine (cys*H*). Changes in the absorption spectra and/or NMR spectra over time provided an insight into the stability of the complex within the given solution.

2.4.7.1 Stability in PBS

Initially, the solution-state stability of [$BiPh_2$(ThR)] **2-17**, was taken in PBS, which resulted in the immediate precipitation of ThR*H*, **11**. Figure 75 shows both changes in

spectral intensity as well as the shifting of absorption bands in line with these experimental observations. Additionally, as observed within the literature, heteroleptic bismuth(III) complexes have shown poor aqueous stability.[146]

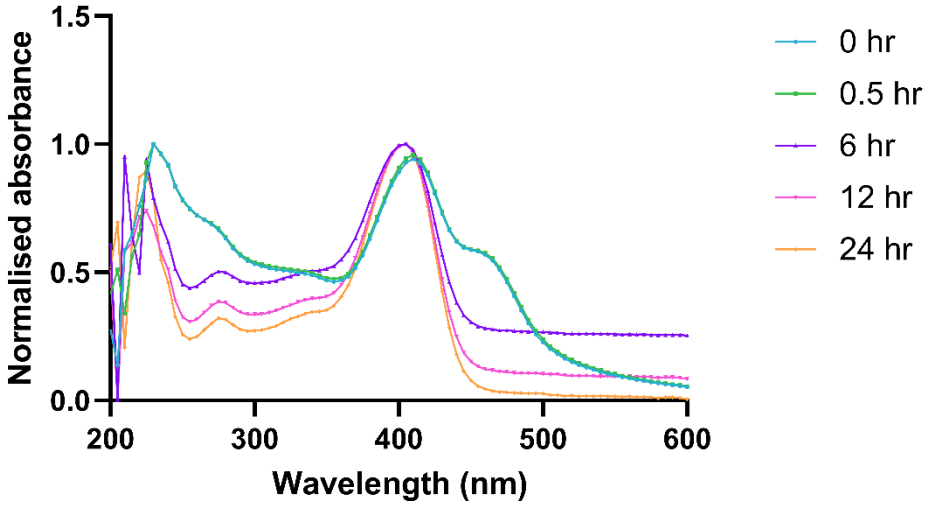

Figure 75: Changes to the absorption spectra of [$BiPh_2$(ThR)] **2-17** in PBS over 24 h. The complex concentrations were 30 µM with 0.4 % DMSO (v/v).

From the experimental data obtained, complex **2-17** is shown to be unstable in the presence of aqueous media as evidenced by the changes observed over time in the absorbance spectra. The decrease in absorbance maxima at *ca.* 250 nm and at *ca.* 400 nm is indicative of compound precipitation from solution. Analysis of the concomitant deposition of a yellow solid within the quartz cuvette revealed the liberation of the ThR*H* **11** molecule.

2.4.7.2 Stability in S-containing molecules

To validate the stability of the compounds in the presence of nucleophilic thiol containing compounds, a representative example of the diphenylbismuth(III) rhodanine complexes was tested in the presence of cysteine (Cys) and glutathione (GSH). Cysteine is an indispensable amino acid building block which is utilised in the synthesis of various proteins and regulations of intracellular redox processes in mammalian cells. Glutathione on the other hand, has numerous biological functions as an essential molecule. As a natural reservoir for cysteine, glutathione is a crucial antioxidant involved in protecting cellular components from the deleterious effects of

ROS and reactive nitrogen species. Literature studies have established the biological targets of Bi(III) containing compounds to be glutathione and cysteine containing molecules, therefore, the stability of a model diphenylbismuth(III) rhodanine, **2-17** was observed in the presence of these molecules using NMR and UV-Visible spectroscopic techniques.

Due to the poor water solubility of complex **2-17** and poor DMSO solubility of the glutathione (GSH) and cysteine (CysH) molecules, mixed solvent media of D_2O and DMSO in an 85:15 were used for both NMR experiments. The addition of **2-17** to the glutathione solvent mixture resulted in the immediate precipitation of a yellow solid within the NMR tube, and after the stability of the mixture was examined over a period of 48 hours, HRMS isotopic analysis revealed the yellow solid to be the [$BiPh_2GS$] species. Burke and co-workers observed a similar type of rearrangement whereby a phenylbismuth(III) *bis*-flavonolate complex [$BiPh(flav)_2$] in the presence of GSH resulted in the formation of the phenylbismuth(III) *bis*-glutathionate [$BiPh(GS)_2$] complex.[350] Although the ligand systems differ, the combination of the thiophilicity and binding affinity for Bi(III) appears to be stronger for the GSH and CysH molecules when compared to both the flavonolate and rhodanine ligands.[288]

UV-visible spectroscopy was utilised to establish the stability of complex **2-17** in the presence of glutathione. Figure 76 outlines the spectral changes which reflect the complex precipitation from solution. Due the rapid exchange of the rhodanine and glutathione, spectral intensities are observed to shift between zero and thirty minutes which align with the immediate precipitation of the [$BiPh_2GS$] product observed through NMR studies however, beyond thirty minutes, no major spectral changes were observed.

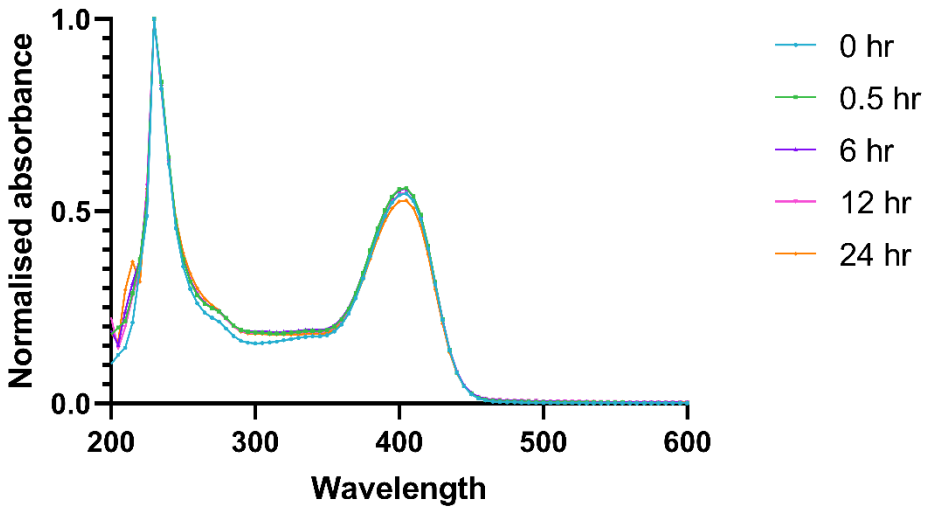

Figure 76: Changes to the absorption spectra of [$BiPh_2$(ThR)] **2-17** (30 μM) with 3 mM GSH (100 mol equivalent) in PBS over 24 h.

2.4.8 Biological Studies

Given the poor selectivity indices observed for the heteroleptic diphenylbismuth(III) triazole thiolates against the bacterial species, the diphenylbismuth(III) rhodanine complexes **2-13** to **2-17** were initially assessed for their antifungal activity towards the fungal strains *C. glabrata* and the yeast *S. cerevisiae* using a disc diffusion methodology. Following the disc diffusion results, the lead compounds were then taken forward to be assessed against *Candida albicans* (*C. albicans*) via the broth dilution method to determine their MIC values. The free rhodanines used for synthesis were also assessed for their antifungal activity via the broth dilution method and were found to be inactive.

Mammalian cellular viability assays were conducted for the free rhodanines **7** to **11,** and heteroleptic diphenylbismuth(III) rhodanine complexes **2-13** to **2-17** using cos-7 monkey kidney cells, to determine if the complexes affected the growth and viability of the cells. Following the assays, the consequent fungal selectivity of the complexes was examined.

2.4.8.1 Antifungal studies

Initial disc diffusion assays against *C. glabrata* and *S. cerevisiae* were performed concurrently with the rhodanido precursors BR*H* **7**, and MOBR*H* **8** (denoted by R1

and R3 in Figure 77) and complexes [$BiPh_2$(BR)] **2-13,** and [$BiPh_2$(MOBR)] **2-14** (denoted by R6 and R2 in Figure 77). The assay revealed microbial activity for the heteroleptic diphenylbismuth(III) rhodanine complex **2-14**, showing a clear zone of inhibition at 200 μg mL^{-1} against *C. albicans* (Figure 77, bottom left corner). The parent rhodanine precursors **7** and **8** as well as two homoleptic *tris*-substituted Bi(III) rhodanine complexes did not show any antifungal activity as indicated by the confluent 'lawn' growth of all strains of fungi.

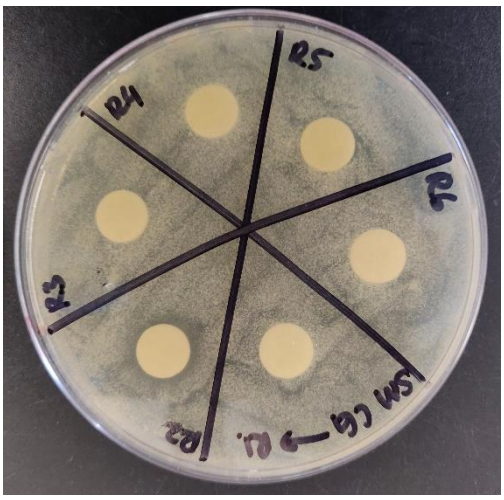

Figure 77: A representative example of a disc diffusion assay incorporating *C. glabrata.* R1 = BR*H*, **7;** R2 = [$BiPh_2$(BR)] **2-13;** R3 = MOBR*H*, **8;** R4 = [$BiPh_2$(MOBR)] **2-14;** R5 = [$Bi(BR)_3$]; and R6 = [$Bi(MOBR)_3$].

The disc diffusion assays provided results which were inconclusive in determining lead compounds to be taken to MIC broth testing. Therefore, the precursor rhodanines **7** to **11** were tested using the broth microdilution method and were found to have no effect on the growth of *C. albicans* in solution, as shown in Figure 78.

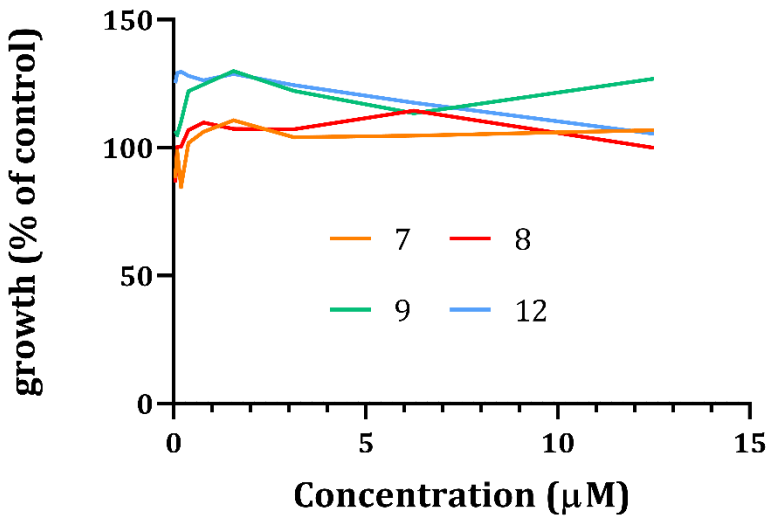

Figure 78: Normalized MIC % growth curves of C. albicans treated with free rhodanines **7** to **9** and **12.** Dose response curves generated over a range of concentrations (0 – 15 μM) in the appropriate culture media from 10 mM DMSO stock solutions. Readings were compared spectroscopically to non-treated control and the percent growth inhibition calculated.

Antifungal studies of the heteroleptic diphenylbismuth(III) rhodanine complexes were undertaken in conjunction with the Traven group within the Biomedical Discovery Institute (BDI) whereby the complexes were explored further with the solution-based broth microdilution method. Complexes **2-13** to **2-15** and **2-17** were tested against *C. albicans* (Figure 79) however, due to solubility concerns, complex **2-16** was not taken forward for solution-based testing.

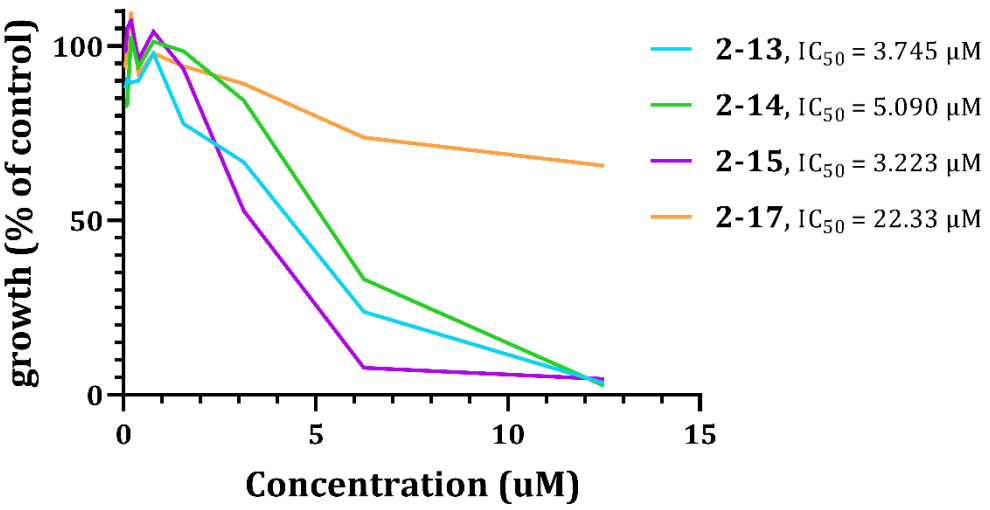

Figure 79: Normalized MIC % growth curves of C. albicans treated with complexes **2-13** to **2-15** and **2-17.** Dose response curves generated over a range of concentrations (0 – 15 µM) in the appropriate culture media from 10 mM DMSO stock solutions. Readings were compared spectroscopically to non-treated control and the percent growth inhibition calculated.

The growth curve of *C. albicans* upon exposure to the Bi(III) rhodanine series of complexes shows all complexes displaying a degree of biological activity (Figure 79). Low MIC values can be observed with the benzyl (**2-13**), methoxy (**2-14**) and tris-methoxy (**2-15**) rhodanido derivatives with the exception of the thiophene derivative **2-16**, showing a higher MIC value of 15 µM. Growth curves of *C. albicans* upon exposure to the rhodanine substrates did not show any inhibition of fungal growth. Therefore, it is evident that complexation to the Bi(III) metal centre has a marked influence on biological activity.

2.4.8.2 Mammalian cell viability studies

The CellTiter-Blue cell viability assay was utilised to determine the growth viability of complexes **2-13** to **2-15** and **2-17** towards cos-7 monkey kidney cells. The cells were initially seeded and adhered to 96 well plates for 24 hours, followed by the treatment of the complexes, which were diluted from an initial 20 mM DMSO solution to a working solution of 100 µM (for a final DMSO concentration to be at 0.5 %). After 20 hours of incubation at 37 °C with the complexes, the CellTiter-Blue dye was added and incubated for another 4 hours. The cell viability was then measured via fluorescence spectrophotometry.

The results obtained from the mammalian cell viability assay for the heteroleptic diphenylbismuth(III) rhodanine complexes show a reduced cell viability beyond a 4 µM concentration for complexes **2-13** to **2-17** whereby the viability falls below 50 % (Figure 80). The cell viability values for complex **2-17** show higher IC_{50} values at 15.23 µM.

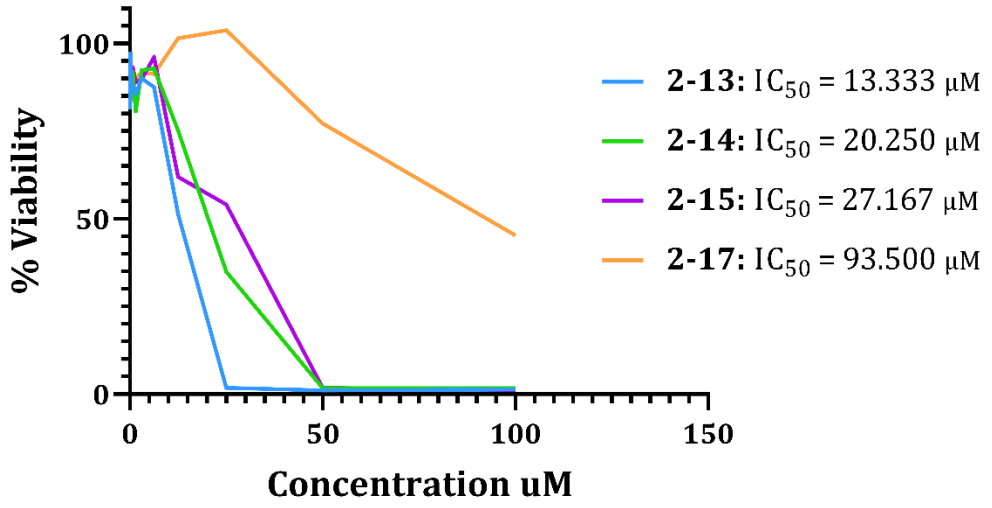

Figure 80: Viability percentage of complexes **2-13** to **2-15** and **2-17** against cos-7 cells. Dose response curves generated over a range of concentrations (48 nm – 100 µM) in the appropriate culture media from 10 mM DMSO stock solutions. Readings were compared spectroscopically to non-treated control and the percent growth inhibition calculated.

After the assessment of both antifungal activity and effect on cell viability against cos-7 cells, it is crucial to determine the ability of the complexes to selectivity inhibit pathogenic fungi in the presence of mammalian cells, especially given the structural similarities of each eukaryotic cell line. The selectivity index (SI) is defined as the ratio between antifungal activity (MIC) and the IC_{50} against cos-7 cells, calculated by the formula SI = IC_{50}/MIC (Table 13). Medicinally, higher SIs (at least >2) are most favourable as they show the potential of a complex to have a safe *in vitro* profile.[358]

Generally, for the heteroleptic diphenylbismuth(III) rhodanine series of complexes, the calculated SIs highlight the moderate selectivity for fungal cells (Table 13). The SIs of Bi(III) rhodanines show values ranging between 3.55-8.44, showing a moderate and non-significant affinity for fungal cells over mammalian cos-7 cells. The

complexes show greater activity towards mammalian cos-7 cells, with complex [$BiPh_2$(3MOBR)] **2-15** being the most selectively cytotoxic.

Table 13: Selectivity index (SI) of complexes **2-13** to **2-15** and **2-17** the SI is calculated using the MICs against C. albicans and the IC_{50} against cos-7 cells.

Complex	**$IC_{50(cos\text{-}7)}$**	**$MIC_{(C.\ albicans)}$**	**SI**
2-13	13.33	3.75	3.55
2-14	20.25	5.09	3.98
2-15	27.17	3.22	8.44
2-17	93.500	22.33	4.19

2.5 Conclusions and future objectives

Seventeen novel Bi(III) thiolates of the form [Bi(SR)$_3$] and [BiPh$_2$(SR)] have been synthesised, characterised via FT-IR spectroscopy, ^{1}H and ^{13}C NMR spectroscopy, HRMS spectroscopy, single crystal X-ray diffractometry and melting point analyses. Complexes **2-1** to **2-6** with the general formula [Bi(SR)$_3$] were prepared via the addition of three equivalents of triazole thiol substrates **1** to **6** to Bi(O^{t}Bu)$_3$. The heteroleptic diphenylbismuth(III) thiolates with the general formula [BiPh$_2$(SR)] were prepared via two reaction routes. Complexes **2-6** to **2-12** were prepared via a salt metathesis reaction of [BiPh$_2$Cl] and the sodium salts of precursors **1** to **6**, while complexes **2-13** to **2-17** were prepared via the equimolar addition of BiPh$_3$ and rhodanine derivatives **7** to **11**. Overall, both the triazole and rhodanine thiolato substrates were found to bind to the Bi(III) metal centre through the sulfur terminus, in line with previous investigations with similar type ligands.[145,282,293]

Attempts were made to synthesise Bi(III) complexes of the form [BiPh(SR)$_2$] via solvent mediated, solvent-free and salt metathesis methods however, these complexes were no longer pursued due to solution-state complex rearrangement, decomposition, poor yields, and difficult isolation.

Seven novel heteroleptic diphenylbismuth(III) thiolato complexes of the form [BiPh$_2$(SR)] were structurally characterised via single crystal X-ray diffraction. Four of the heteroleptic diphenylbismuth(III) thiolates derived from triazole thione precursors **2-7, 2-8, 2-11** and **2-12** adopt differing geometries. Complex **2-7** crystallised as a weakly polymeric 1D chain while complexes **2-8**, **2-11** and **2-12** were monomeric with five-coordinate distorted disphenoidal geometries. The three rhodanine derived heteroleptic diphenylbismuth(III) thiolates **2-13, 2-14** and **2-16** however, were isostructural and crystallised as dimers, adopting a five-coordinate disphenoidal geometry. The respective structures were consistent with previously reported Bi(III) structures in the literature and notably, the presence of a SALP is postulated to influence the overall geometries of the complexes.

Solution state stability studies were conducted with [BiPh$_2$POTz] **2-9** and [BiPh$_2$ThR] **2-17,** in phosphate buffered saline (PBS) solution, cell culture media (DMEM) supplemented with and without foetal bovine serum (FBS) as well as in the presence

of glutathione (GSH) via UV-visible spectroscopic techniques. Interestingly, complex [$BiPh_2$(PoTz)] **2-9** showed much better solution state stability in PBS in comparison to [$BiPh_2$(ThR)] **2-17**, however in the presence of glutathione, **2-17** appeared to be more stable in solution. Despite these solution-based results, both complexes were shown to deposit yellow solids which corresponded to their free ligand counterparts. Overall, from the limited studies conducted between the triazole and rhodanine ligands, the UV-visible spectra for **2-9** showed more changes in intensity when compared to **2-17**. Given the interesting cell culture media study results, it would be worthwhile exploring the solution state stability of the heteroleptic diphenylbismuth(III) thiolato complexes **2-7** to **2-12** in the presence of bovine serum albumin (BSA).

The antimicrobial activity for complexes **2-1** to **2-12** was assessed towards the Gram-negative and Gram-positive bacteria: Methicillin-resistant *Staphylococcus aureus* (MRSA), Vancomycin resistant *Enterococcus* (VRE), *Escherichia coli* (*E. coli)*, and *Pseudomonas aeruginosa* (*P. aeruginosa)* as well as two fungal strains: *Candida albicans (C. albicans)* and *Candida auris (C. auris)*. When tested against MRSA there was a two-fold difference in the MICs exhibited between the most active complexes **2-6**, **2-7, 2-10, 2-11** at 12.5 μM when compared to the least active complex **2-9** at 25 μM. In general, the antimicrobial activity of the triazole thiolato Bi(III) complexes was consistent with previous studies, whereby the degree of ligand substitution bore a marked variance. The heteroleptic Bi(III) thiolates showed antibacterial activity towards all of the bacterial species tested while the homoleptic Bi(III) thiolates did not. Based on the results obtained for the triazole thiolato-based Bi(III) complexes, biological testing for the heteroleptic diphenylbismuth(III) rhodanines **2-13** to **2-17** focused on the fungal strain *C. albicans* which exhibited antifungal activity with MIC values in the range of 3.3-15 μM.

Given the promising antimicrobial studies, complexes **2-1** to **2-17** were assessed against mammalian cos-7 monkey kidney cells. The heteroleptic Bi(III) thiolates **2-7** to **2-17** exhibited a decrease in mammalian cellular viability while the homoleptic Bi(III) thiolates **2-1** to **2-6** did not reduce the cellular viability of cos-7, with values > 100 μM. Across the heteroleptic Bi(III) series of complexes against *C. albicans*, **2-9** and **2-15** showed the best SI values of 6.71 and 8.44, respectively. Selectivity for bacterial species was poorer for the

heteroleptic bismuth(III) triazole thiolates **2-7** to **2-12** with the highest value being 1.87 against VRE (complex **2-7**).

Overall, some key findings addressed in this chapter highlight the medicinal relevance of heterocyclic compounds in organometallic chemistry. As substrates, these precursors continue to be an integral part of drug discovery and design, and N-heterocycles continue to be of use as lead structures. Between the rhodanine and triazole series of heteroleptic Bi(III) complexes, the structural, electronic, and biological activity significantly differed therefore, it is of interest to continue to explore other N-heterocyclic structures incorporating a thiolato-arm.

Biological testing was undertaken at low concentrations and due to the low solubility of the heteroleptic compounds, alternative testing regimes such as broth dilution and disc diffusion assays will need to be explored. Additionally, by decreasing the lipophilicity of the bismuth precursor through alteration of the phenyl groups, their solubility in aqueous media may be improved.

From the biological data results obtained, it can be deduced that the replacement of a single phenyl group by an ancillary thiolate ligand at the Bi(III) centre, has a large impact on the structural and electronic nature of the molecule, as previously observed in other heteroleptic Bi(III) complexes. This heterolepticity can be postulated to be intrinsically linked to the observed bioactivity. Electronically, the thiolate group decreases the overall covalent character of the complex, thereby promoting increased ligand lability and greater availability of Bi(III) ions. Lack of biological activity for the homoleptic *tris*-substituted Bi(III) thiolate complexes could therefore be attributed to the increased lability of the thiolato ligands when compared to the heteroleptic Bi(III) thiolates. It can be postulated that the additional stability of a chelating substrate, could decrease the availability of bismuth and hence decrease the activity. This has been demonstrated in a recent study conducted by Burke *et al*.[350]

Despite the non-toxic nature of bismuth, it should be noted that organobismuth(III) complexes should not be assumed to be safe due to the properties of the metal centre. As the cell membranes of mammalian and fungal cells share very similar characteristics, this has proven to be challenging to develop a complex that will selectively target pathogenic fungi rather than host cells. While the high toxicity

observed through the mammalian cos-7 cell viability studies precludes the heteroleptic Bi(III) thiolates from being useful as drug leads, these tests do not display a general trend against all cell lines. In a recent investigation conducted by Herdman *et al*, a series of heteroleptic Bi(III) phosphinates were explored as potential antibacterials, found the similar set of complexes to show an almost three-fold difference in activity for complexes tested against both cos-7 and human fibroblast mammalian cell lines.[146]

To further elucidate the properties of these Bi(III) thiolates, a number of *in vitro* tests could be explored for all the compounds synthesised including viability studies against a range of cell lines (human fibroblast, A549 and HEK-239 cells) to ascertain the cytotoxic effects on different cell types. Haemolysis and membrane integrity assays on these cell lines would provide useful information on the broad mammalian cell activity. While the fungal assays conducted provided a rudimentary understanding as to the potential therapeutic activity, an associative time-kill assay would provide more information as to whether the heteroleptic Bi(III) thiolates are fungistatic or fungicidal as well as the potential use of these complexes in preventing the formation of fungal biofilms.

Due to time constraints, the total bismuth uptake for mammalian cos-7 cells was unable to be obtained. To supplement the whole bacterial cell uptake results, these studies would provide further insight into whether the therapeutic activity correlates to the total bismuth entering prokaryotic and eukaryotic cells. Additionally, ICP-MS can be utilised for the novel phenylbismuth(III) thiolates to determine the whole cell uptake for yeast cells, as it has been previously performed for bacterial cells *E. coli* and MRSA.

Initial investigations into the cytotoxicity of the heteroleptic Bi(III) complexes was undertaken with the LDH CytotoxONE assay. To further supplement these studies, by taking a morphological approach and determining whether changes to the cellular integrity via confocal cellular imaging could be useful in determining the exact mechanism of action of these complexes.

While fungal testing on the phenylbismuth(III) rhodanine thiolato series of compounds has been completed, it would be useful to complete biological MIC tests

against Gram-positive and Gram-negative bacterial strains to investigate a full SAR between the triazole thiolate and rhodanine series of compounds. Due to the highly lipophilic nature of these complexes, it is also worthwhile analysing the binding modes of these complexes in the presence of serum albumins to observe whether these complexes will bind strongly and thus, decrease, or diminish their *in vivo* activity against microbial pathogens.

CHAPTER 3: RHENIUM(I) N-HETEROCYCLIC THIONES

RHENIUM(I) TRICARBONYL ANCILLARY TRIAZOLES

RHENIUM(I) TRICARBONYL BACKBONE TRIAZOLES

SYNTHESIS, CHARACTERISATION AND BIOLOGICAL STUDIES

PHOTOPHYSICAL STUDIES

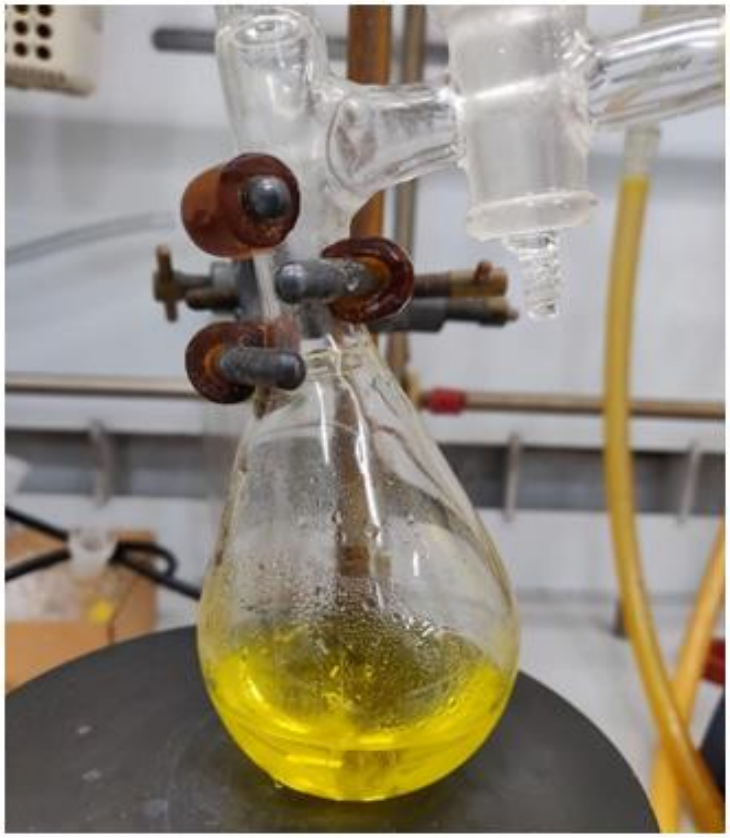

3 Rhenium(I) N-heterocyclic thiones

3.1 Introduction

Over the last 20 years, metal-based anticancer drugs have been limited to the use of platinum(II)-based complexes which exhibit a high degree of toxicity, resistance and limited efficacy (Figure 81).[176,365–368] Due to these limitations, the requirement of new therapeutics has come to the forefront of drug discovery.[269,368,369]

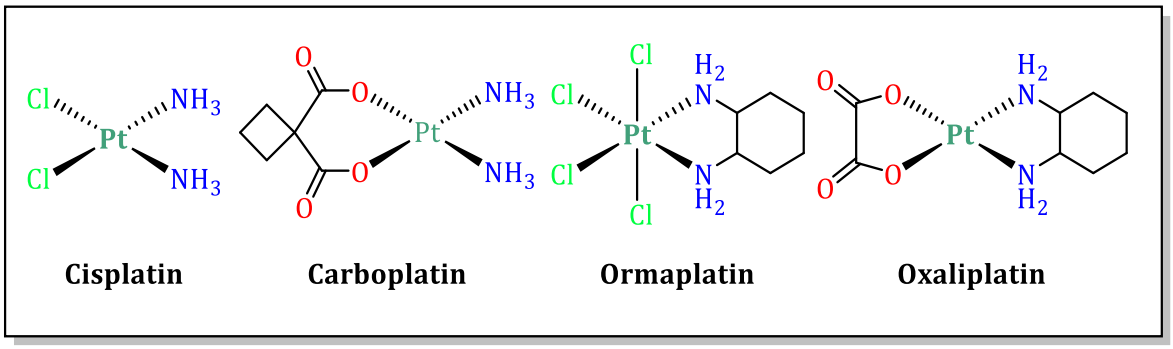

Figure 81: Structures of generational commercially available platinum-based anticancer drugs including cisplatin and its analogues.

The exploration into alternative metals to platinum has provided greater diversity in coordination modes and kinetic lability.[71] The interaction with ligands including the substitution, redox and electronic properties when compared to the characteristic commercially available four-coordinate Pt(II) drugs has widened the scope of therapeutic design.[70,71]

There has been a considerable amount of attention given to the exploration of rhenium complexes with regards to the fields of cellular imaging, anticancer, and antimicrobial drug discovery.[157] In 1974, Wrighton and Morse synthesised the diimine rhenium(I) tricarbonyl scaffold (Figure 82) and in turn, explored the phosphorescent nature of these molecules via fluorescence and vibrational spectroscopic techniques. Since then, these complexes have solidified their presence as strong photosensitisers with favourable properties such as: high photochemical stability, biological stability, and efficient luminescence. In addition, the excited state luminescence has shown effective tunability and selectivity within biological systems utilising a diverse range of ancillary and donor ligands.[370]

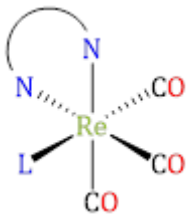

Figure 82: General structure of the *fac*-Re(I) diimine tricarbonyl core.

To date, over 150 rhenium(I) tricarbonyl-based complexes have been synthesised and continue to show varying photophysical, photochemical and biological properties.[164,371–373] The Re(I) tricarbonyl core interacts with various mammalian, bacterial and fungal biological processes, and previous studies have confirmed the interaction of rhenium(I)-based complexes with DNA via intercalation and groove binding processes.[31] Re(I) tricarbonyl complexes can also interact with histidine residues due to their affinity for harder nitrogen donor ligands.[162,374,375]

Previous studies have shown that rhenium(I) can be used as a potential antimicrobial agent due to its photoluminescence, cellular accumulation and potential to be used as a photoactivated CO releasing moiety (photoCORM).[161,175,376,377] The rationale behind using rhenium in this thesis follows on from previously derived heterocyclics that have been explored with the rhenium tricarbonyl set of compounds.

As shown in Chapter 2, the triazole class of compounds showed unique activity against a range of microbial and cell classes when synergistically explored with bismuth.[279,314,378] Coordination of the triazole thione to the bismuth(III) metal centre, enhanced biological activity was observed and in turn, a metal-ligand synergy was evident when explored with both microbial and mammalian cells. As detailed in Chapter **Error! Reference source not found.**, rhenium-based compounds have been extensively explored as potential imaging agents with a strong propensity to bind to N-type π-donors, such as the diimine class of compounds.

Mercapto-azole ligand systems have played an important part in therapeutic design and the propensity of these molecules to undergo tautomeric changes via the thiol-thione -NH-C=S and -N=C-SH to bind to a specific metal centre lends them as attractive candidates for a larger scale SAR study with multiple metals. The combination of the

exocyclic sulfur atom and cyclic nitrogen lends these types of molecules as ambidentate ligands.

The drive to use metals in medicine follows from the concept of nutritional immunity whereby we can alter the balance of nutrients available to a given pathogen versus the host. Nutritional immunity was touched upon in Chapter 2, whereby bismuth was explored as an alternative metal system for the uptake of iron. In this chapter, mismetallation and nutritional immunity has been explored with rhenium(I)-based systems and as a potential therapeutic.

3.1.1 Rhenium(I) in biological systems

Despite the numerous reports of Re(I) complexes bearing anticancer activity, discussions pertaining to the specific mode of action (MoA) of these complexes is sparse. The presumed intracellular target for many Re(I) complexes is assumed to be DNA therefore, many studies have explored these types of interactions.[31,379–384]

Early studies conducted by Zobi *et al.,*[385,386] showed *fac*-$[Re(CO)_3(OH_2)_3]^+$ moieties involved in the direct covalent binding, interactions with grooves in the helix and intercalation between base pairs in DNA functionality which were comparable to cisplatin.[176,384–386] Most of the interactions of Re(I) tricarbonyl polypyridine complexes with DNA is via intercalation through the use of a "spacer" ligand or through the planar diimine ligand. These studies have been supplemented by the hallmark hypochromism and high binding affinity studies utilising UV-Visible spectroscopy.[387]

Crystallisation of proteins incubated with Re(I) complexes have shown the Re(I) metal centre covalently binding to histidine residues through covalent modification.[176,388] Rhenium has also been demonstrated to accumulate in cells via a passive diffusion mechanism *in vivo* however, their predominant use as luminescent probes relies on a more active energy dependent pathway such as endocytosis. The presence of rhenium has been verified within the cytoplasm, mitochondria, and nucleus of various eukaryotic cells through flow cytometry techniques.[389] Re(I) has been shown to complex with both amine- and thiol- containing functional groups within biological systems to yield luminescent probes.[389,390] The Re(I) tricarbonyl

core has been complexed with amino acids, nucleosides, nucleobases, peptides and proteins.

3.1.2 Therapeutic applications of Re(I) complexes

Whilst Re(I) complexes have predominantly been explored in medical imaging, they have been shown to have promising *in vivo* antiproliferative results in the field of chemotherapeutics. Extensive examples of these biologically active complexes have been reviewed and discussed by Gasser and co-workers.[163]

As a transition metal, Re(I) can generate reactive oxygen species (ROS) such as singlet oxygen upon irradiation, which in turn disrupts cellular function. While the generation of ROS in cellular imaging is an undesirable property, within the field of metallotherapeutics it provides a useful basis for complex design when it can selectively target certain cell types. For example, Collery and co-workers synthesised a Re(I)-tricarbonyl diselenoether complex (**Re-diSe**, Figure 83) for the purpose of selectively targeting breast cancer.[391] In this study, the levels of ROS were statistically significant with values upwards of 2500 a.u. when compared to the mammalian control cells at 1500 a.u.

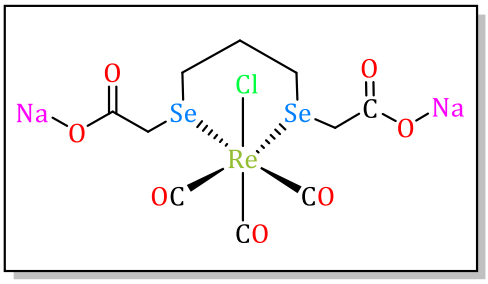

Figure 83: A Re(I) anticancer complex, **Re-diSe** synthesized by Collery et al., for the purpose of treating triple-negative breast cancers.[391]

The majority of therapeutic studies involving Re(I) complexes have been towards the treatment of cancer. In a recent study conducted by Mao and co-workers,[392] selectivity towards triple negative breast cancer (TNBC) cells was observed for complexes bearing the $Re(CO)_3^+$ core. Complexation of the Re(I) tricarbonyl motif with an ancillary desiferasirox ligand produced a potent complex which disrupted mitochondrial function through the accumulation of chelated cellular iron, eventually leading to the methylation of nucleic material and cellular apoptosis.[168,392]

3.1.3 Re(I) complexes as antibacterials

Although Re(I) complexes are well represented in the field of chemotherapeutics, their antimicrobial potential has not been explored as extensively. The earliest studies conducted by Mezler-Nolte and co-workers identified two particularly active hetero-tri-organometallic compounds **RcPNA** and **FcPNA** bearing the *fac*-$Re(CO)_3$ core (Figure 84), with inhibitory activity as low as 1.4 μM against the Gram-positive bacteria, MRSA.[376,393,394]

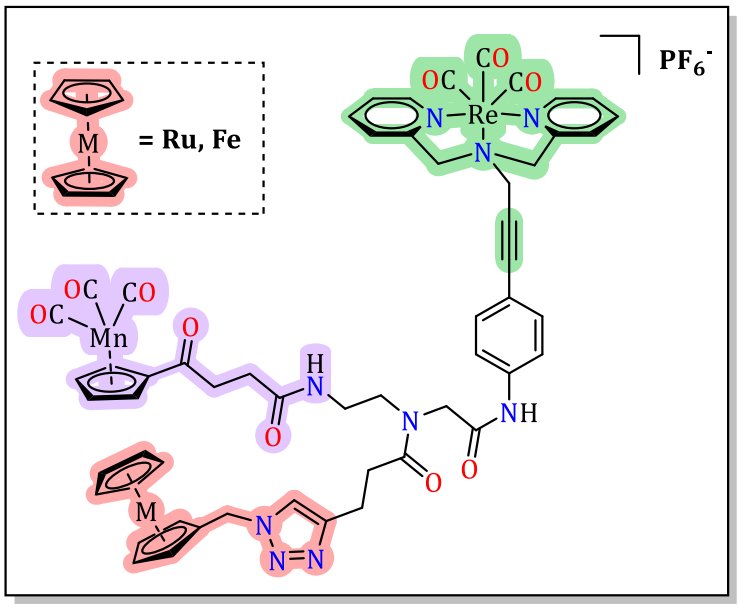

Figure 84: The general structure of the antibacterial triorganometallic complex with the general formula McPNA whereby the Ru(II) derivative = **RcPNA** and the Fe(II) derivative = **FcPNA.**

As lead structures, the charged complexes **FcPNA** and **RcPNA** feature three distinct parts: the peptide nucleic acid (PNA) backbone coupled with a cymantrene moiety, alkyne sidechain coupled with a Re(CO)(dipicolyl) group and a ferrocene/ruthenocene coupled to a 1,2,3-triazole ring.[168,393,394] In an extensive SAR study of the lead structures, Patra and co-workers attributed the antibacterial activity to the presence of both the $Re(CO)_3$ core with the PNA backbone.[376] The complexes were not active against the Gram-negative bacterial strains possibly due to the presence of an additional outer membrane. The hetero-tri-organometallic complexes have been postulated to disrupt essential cellular processes within the bacterial cell membrane. The organometallics were observed to affect respiration and cell wall

biosynthesis through membrane depolarisation in *B. subtilis* as well as the presence of marker proteins generated through ROS as a result of the redox-active ferrocene moiety in both organometallic compounds.[393]

In another study conducted by Metzler-Nolte, a series of benzannulated Re(I)-NHC complexes were synthesised and evaluated against the Gram-positive strains *B. subtilis, S. aureus* showing Minimum Inhibitory Concentration (MIC) values as low as 0.7 μM, although the mechanism of action is still unknown for these *fac*-$[Re(CO)_3]^+$ complexes.[395]

Photodynamic therapy (PDT) has been used as a mode of treatment for cancer where transition metal complexes generate ROS to selectively target and kill cancer cells. This success has led to the development of antimicrobial PDT (aPDT).[70,174,396] Using a bisquinoline scaffold, Blaskovic and Frei[397] synthesised a series of antimicrobial Re(I) bisquinoline analogues displaying light-induced antimicrobial activity against *S. aureus* and *E. coli* with MICs as low as 0.25-8 μg/mL (0.36-11.6 μM).[397] The complex was found to be 13-26 times more selective towards *S. aureus* and 1.5-3 times as active against *E. coli* when compared to the mammalian control human embryonic kidney (HEK) cells, respectively.[397] The authors suggested the MoA to be two distinct pathways, one mediated by the UV-light irradiation and the second possibly linked to the destabilisation of Fe-S clusters and increased aminoglycoside uptake as a result of the ROS production.[397]

Most recently, the *fac*-$[Re(CO)_3]^+$ scaffold has been explored with 3-arylcoumarin-based ligands against both bacteria (*S. aureus* and *E. faecium*) and fungi (*C. albicans, C. glabrata, C. krusei* and *C. parapsilosis)* with the most potent antibacterial complexes found to display inhibitory activity in the range 0.7-4.2 ug/mL (0.8-6.2 μM) against *S. aureus*.[398]

In a later study conducted by the same authors, a more comprehensive analysis of 57 *fac*-$[Re(CO)_3]^+$-based complexes were reviewed.[399] In this study a few key findings were addressed: of the 57 neutral and cationic Re(I) complexes tested, the *fac*-$[Re(CO)_3]^+$ showed mono- or dual antibacterial activity against *S. aureus* when coordinated to the inactive diimine ligands. Additionally, the complexes showed higher activity against *S. aureus* when coordinated to the free active diimine. each with

varying degrees of charge, ligand substitution, and lipophilicity suggested the most potent Re(I) complexes bore highly lipophilic diimine ligands with an overall positive charge.[399]

3.1.4 Re(I) complexes for fungal applications

Although the research surrounding the antimicrobial use of rhenium(I)-based complexes is scarce, some limited studies have been conducted in the recent years to evaluate their efficacy within the fungal domain.[173,399] Some postulations have been made as to why this field has not been pursued, the prevailing and predominant barrier to this research being the presence of the more robust fungal cell wall which prevents drug penetration.[400] Carreño and co-workers explored the first examples of cytotoxic Re(I) diimine tricarbonyl complexes, the results of which concluded the free 1,10-phenanthroline derivatives to be more potent antifungals than the complexes (Figure 85).[400]

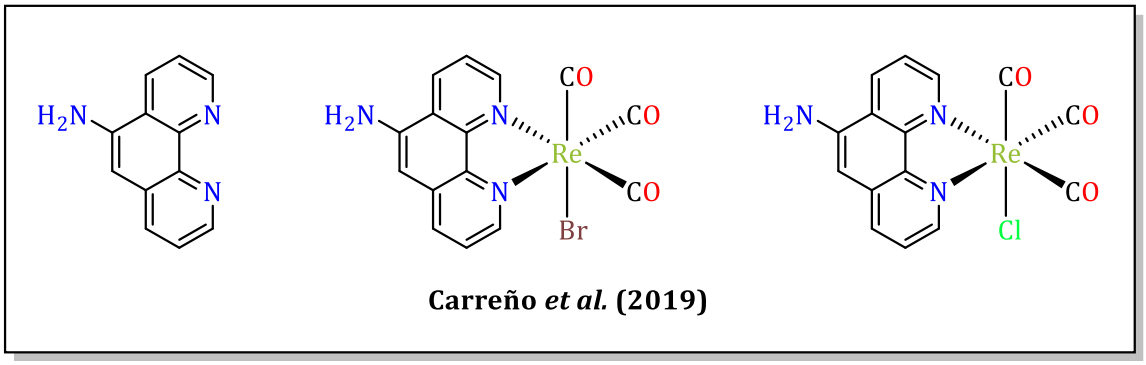

Figure 85: Structures of the free 1,10-phenanthroline derivative substrate and Re(I) complexes evaluated for antifungal activity.[400]

As mentioned in section 3.1.3, Sovari and co-workers explored the antifungal activity of a series of *fac*-$[Re(CO)_3]^+$ 3-arylcoumarin derivatives against four fungal *Candida* strains.[401] Although the complexes exhibited moderate to low MIC activity and selectivity towards all of the fungal strains, this study provided the basis for a later review of an extensive library of 57 Re(I) complexes to be evaluated for their antifungal activity.[399,401] Of the complexes studied, two were shown to suppress the morphological yeast-to-hyphal transition, an important virulence mechanism in pathogenic fungal strains, the complexes **ReNN3Py** and **ReNN6Py** (Figure 86) showed MIC values as low as 3.1 μM.[399] As a result of this inhibition, fungal-*S. aureus*

co-infection was eradicated. In addition, the complexes displayed no cardio-, hepato- or haematotoxicity or teratogenicity within the *in vivo* transgenic Tg(fabp10a:EGFP) zebrafish embryo models. In this comprehensive review, all of the tested complexes which showed antimicrobial activity were non-toxic and cationic in nature.[399] Interestingly to date, this is the first and only *in vivo* Re(I) antifungal study to be conducted.[399]

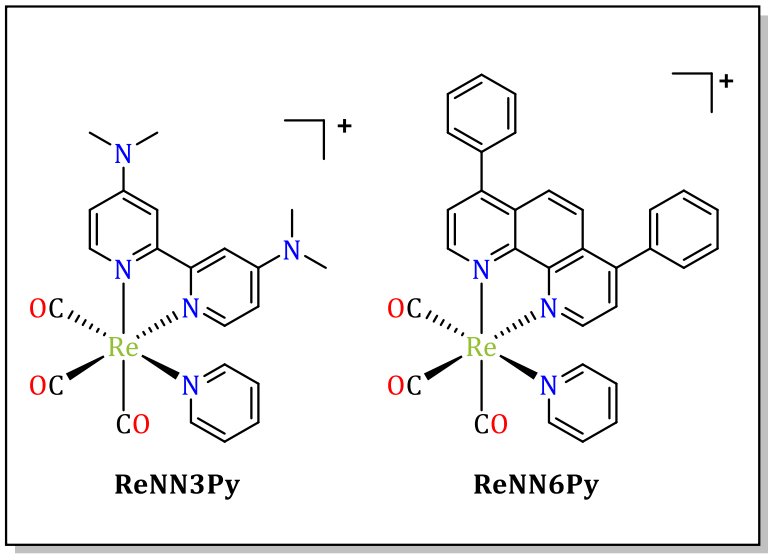

Figure 86: Selected structures of active antifungal Re(I) complexes **ReNN3Py** and **ReNN6Py**.[399]

Transition metal complexes which are d^6 display a high degree of versatility and Re(I) based complexes have exhibited desirable characteristics for antifungal therapy and fungal imaging. Although the aforementioned studies are promising, there is a distinct lack of data and dedicated systematic evaluations into Re(I)-based antifungal agents therefore, this provides a clear avenue for research. Additionally, combination therapies of rhenium and antibiotic substrates have been explored as a promising resource for the development of novel antimicrobial complexes capable of treating antibiotic resistant strains.[163]

3.1.5 Re(I) complexes as imaging agents

The introduction of fluorescence microscopy has widened the field of biomedical cellular imaging especially in structurally elucidating live cell processes and mechanisms. Research into the development of novel fluorescent indicators (denoted

by the broad term 'fluorophore') has predominantly focused on organic-based molecules such as the MitoTracker™ stains (Figure 87).[390] Over the last few years however, luminescent complexes bearing d^6 transition metals have gained traction.[377,389,390,402,403]

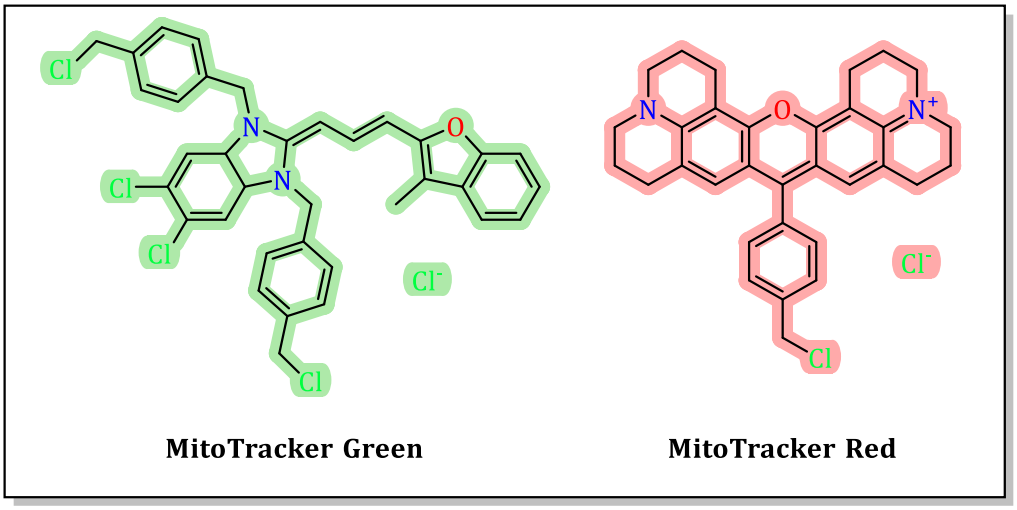

Figure 87: Commercially available organic-based MitoTracker™ fluorophores used to stain cellular samples.

The luminescent properties of rhenium have garnered interest for the use of Re(I)-based complexes as probes for walled cells, namely bacteria and fungi. While their use as antifungal agents has been limited to one to two studies, including yeasts *Candida albicans* and *saccharomyces cerevisiae,* confocal microscopic techniques have been used to image these live cells.[400,404–406]

Carreño and co-workers have explored a series of Re(I) complexes which were found to be suitable for soft staining of the walled cells and differentiation of the nucleus in *C. albicans* and *Cryptococcus spp* cells using confocal microscopy.[173,402,405] In one study, the complex **Re1** (Figure 88, top) presented desirable characteristics for use as a fluorophore and showed good emission in the visible range at 630 nm for tissue penetration and detection, a stokes shift greater than 200 nm for prevention of self-quenching and image dimming and low cytotoxicity.[402]

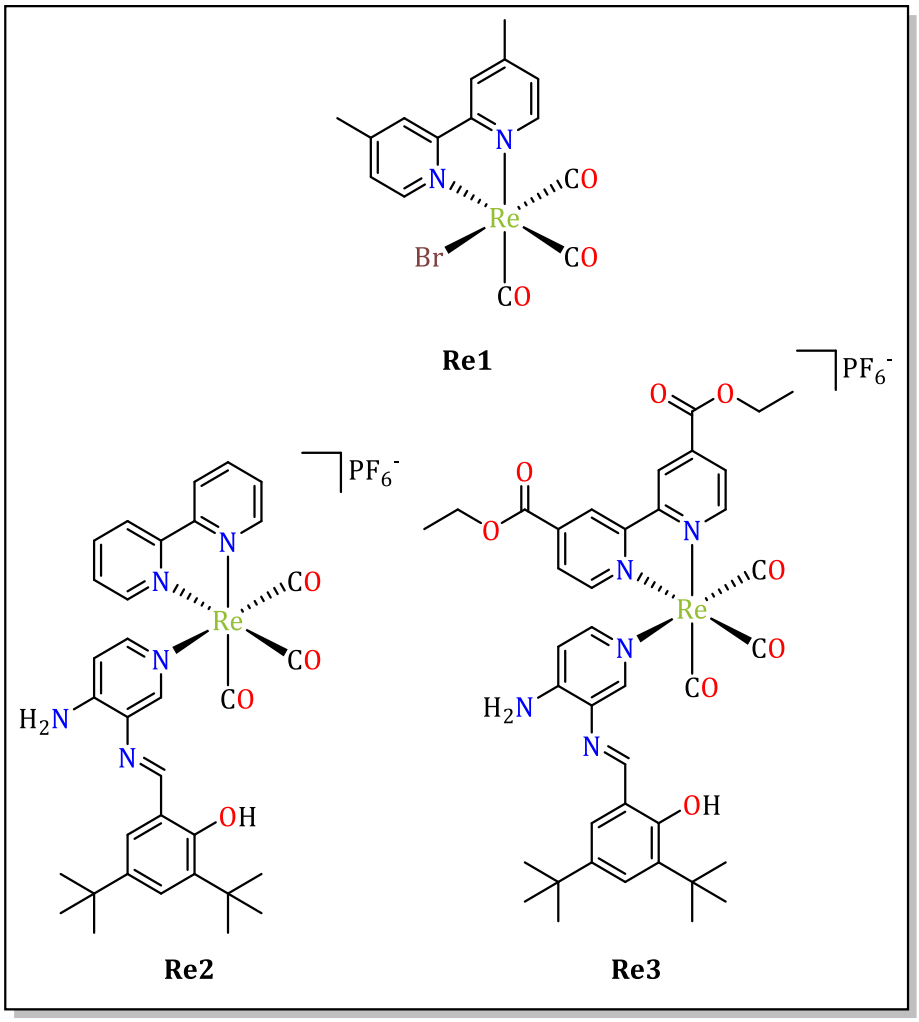

Figure 88: Examples of Re(I)-based fungal fluorophores developed by Carreño and co-workers.[402,406]

Another study identified the complex **Re2** (Figure 88, bottom left) as a useful stain and biomarker for the filamentous fungi *Botrytis cinerea (B. cinerea)* using live-cell fluorescence microscopy, the complex presented a similarly broad emission intensity greater than 600 nm and shift of 244 nm.[406] Another study conducted by the same research group confirmed the cellular localisation of **Re3** (Figure 88, bottom right) within the nucleus of *C. albicans*.[402] It was postulated that **Re3** interacts with DNA via the positive charge on the Re(I) metal centre through both electrostatic and covalent interactions between the heteroatomic groups within the ancillary Schiff base ligand and nucleobases.[379,402]

Modulation of the *fac*-$[Re(CO)_3]^+$ core has resulted in the development of a wide variety of complexes bearing photophysical and biological properties however, to

date, numerous studies have only tested Re(I) tricarbonyl complexes bearing a 2,2'-bipyridyl backbone as fluorescent markers for walled cells. The use of 1,10-phenanthroline-type backbones is limited.[402,404,406] In a review conducted by Otero and co-workers, the desirable characteristics of an efficient and suitable Re(I) based fungal fluorophore were postulated to contain: (a): a monocationic charge, (b) the presence of an (N'N) substituted backbone of either bpy or phen constitution, and (c) a relatively simple ancillary ligand which favours the formation of hydrogen bonding.[173]

Rhenium(I) complexes present as attractive candidates for therapeutic and diagnostic applications (also referred to as "theranostics"), such as the imaging of walled fungal cells. To date however, research is still being undertaken as to which specific cellular compartments can be stained by rhenium-based fluorophores and whether they are a function of charge or lipophilicity. Biomolecules have been targeted for bioconjugation with rhenium include hyaluronic acids, biotin, fructose and glucose; these complexes have shown use in the fields of tissue and anticancer therapy.[407–411]

3.1.6 The photophysical properties of transition metal complexes

When exploring the electronics of the rhenium(I) ion, multiple electronic transitions can be characterised and attributed to the arrangement of electrons. In a typical molecular orbital (MO) diagram of a d^6 transition metal, the interaction between the metal orbitals and ligand orbitals can give rise to a series of electronic states which in turn, can result in phosphorescence.

Figure 89 represents the MO diagram for a typical octahedral d^6 transition metal complex, for simplicity only the valence electrons (5d, 6s and 6p) have been taken into consideration for bonding and chemical equivalency has been assumed in the ligand orbitals. The 5d electrons are represented by the t_{2g} and e_g subset, the 6s electrons represented by the a_{1g} subset and the 6p electrons represented by the t_{1u}. When combined with the ligand t_{2g} π* orbital, the metal and ligand orbitals can contribute to the molecular orbitals with a_{1g}, e_g, and t_{1u} symmetry which sit at a higher level.

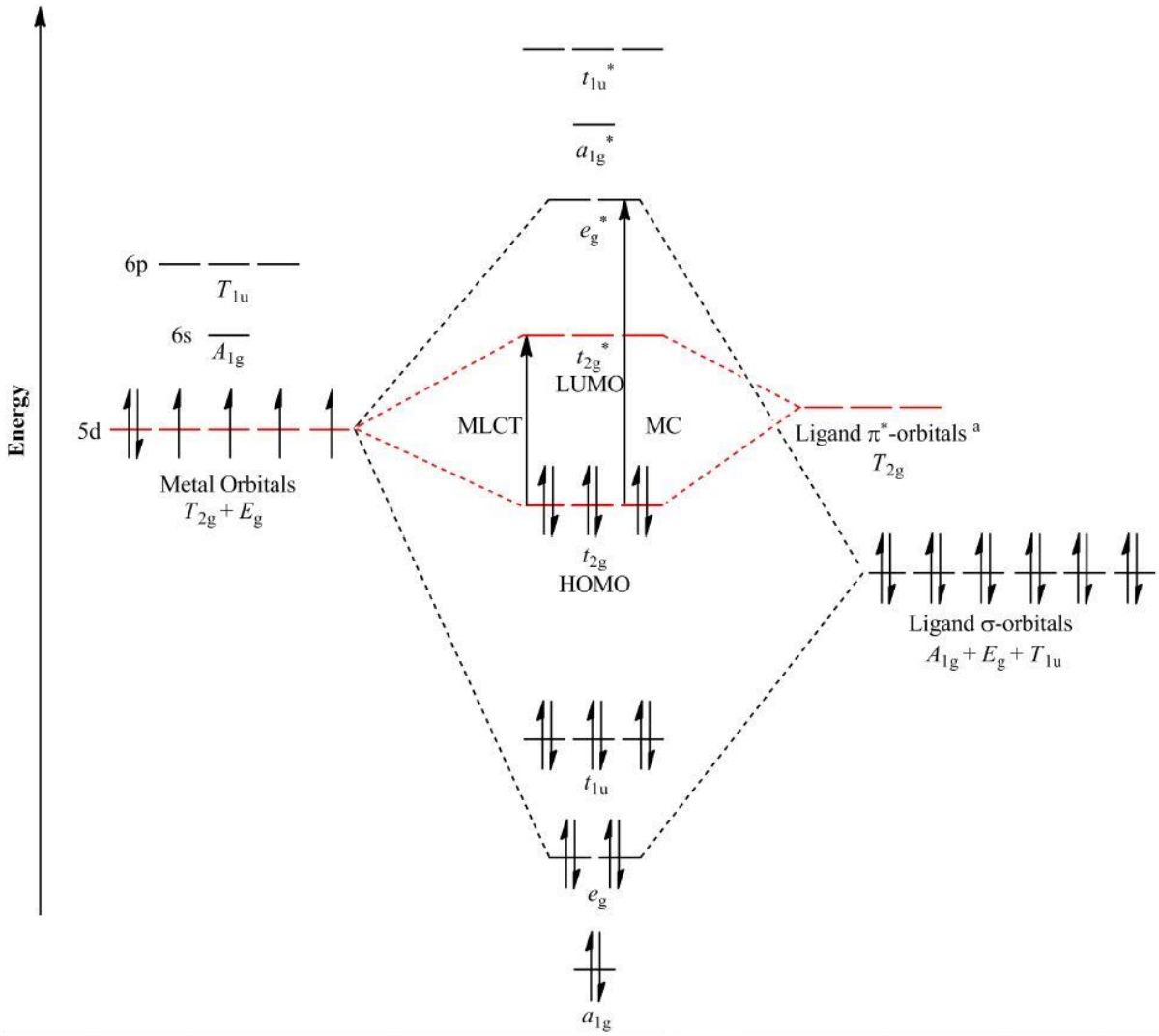

Figure 89: Typical molecular orbital (MO) diagram of a transition state metal complex

When a photon is absorbed by a Re(I) complex, this process can induce different types of electronic transitions within the complex such as: metal-centred (MC) charge transfer, ligand-centred (LC) charge transfer, ligand-to-ligand charge transfer (LLCT) and metal-to-ligand charge transfer (MLCT).

MLCT processes can be simplistically denoted by the transfer of an electron from the metal to the ligand. In a Re(I) complex, this often arises from the transition from the metal d orbital (HOMO) to the ligand antibonding π* orbitals (LUMO). LLCT transitions occur if the surrounding ligands around the metal centre are inequivalent, for example, in a heteroleptic system. The transferral of an electron from the π orbital to the π* orbital of a different ligand can occasionally mix with the MLCT to form a mixed MLLCT excited state in some cases. Ligand systems which incorporate

extended conjugation can also undergo intraligand (IL) transitions whereby an electron is transferred from the π to empty π* orbitals and often this occurs with aromatic systems.

The photophysical properties of rhenium(I) and every other atom/system can be attributed to the absorption and excitation of photons and can be simplistically represented by a Jablonski Diagram (Figure 90).

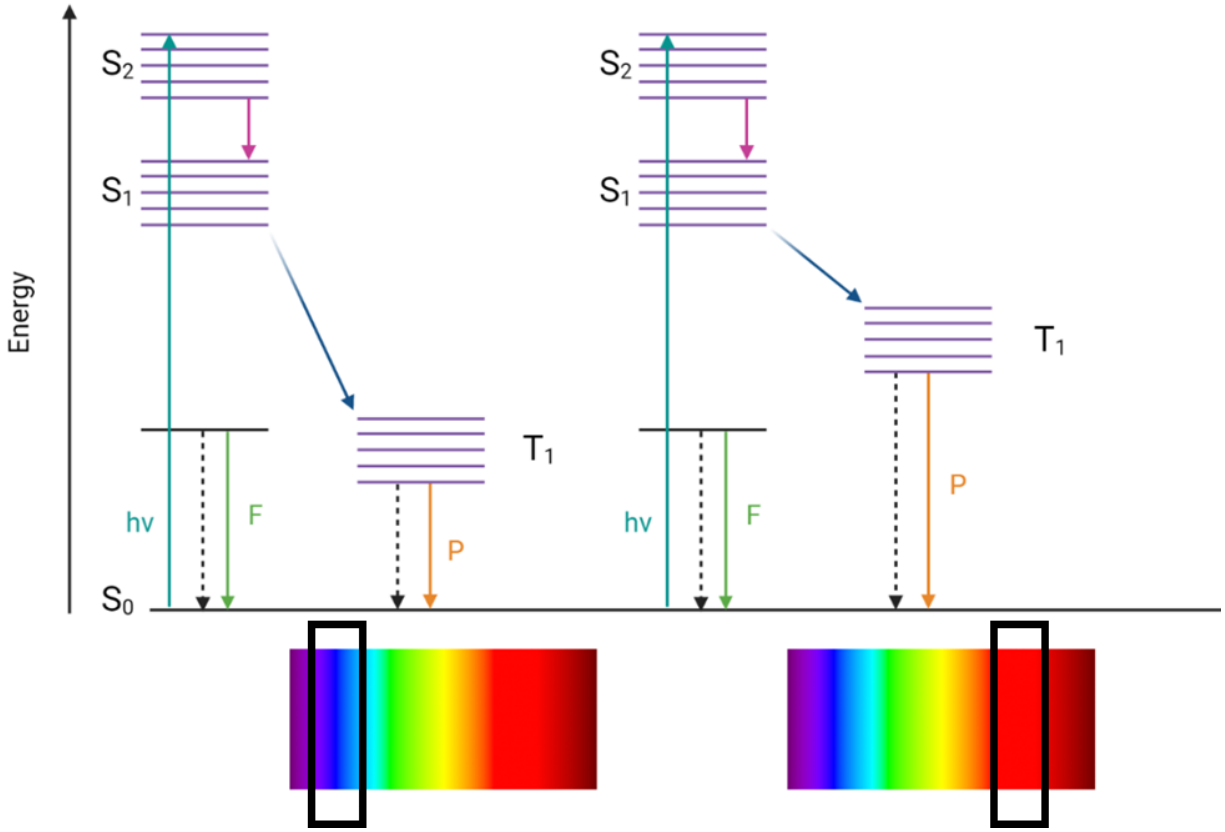

Figure 90: Simplified Jablonski diagram, created with BioRender.

The Jablonski diagram is used to represent the number of radiative and non-radiative process involved when a molecule interacts with an energy input (in the form of light, *hv*) and can be used to identify which processes contribute to the overall luminescent output of a molecule. When a given molecule in the ground state (denoted by S_0) is excited by a photon, the energy is absorbed by the molecule promotes an electron residing in the highest occupied molecular orbital (HOMO) to that of the lowest energy level within the excited singlet state, the lowest unoccupied molecular orbital (LUMO, generally S_n, denoted by S_1 in Figure 90). Often, electrons within the excited electronic configuration state will undergo a number of relaxation processes varying

in speed including vibrational relaxation which occurs between vibrational levels of the same excited state (purple bars, in Figure 90) and internal conversion (IC, denoted by the pink arrow in Figure 90) whereby the electron will vibrationally relax to a different electronic level, this process occurs in accordance with Kasha's rule.

Metal complexes can undergo shifts between the ^{1}MLCT and ^{3}MLCT allowing for the process of intersystem crossing (ISC, denoted by the blue arrow in Figure 90) due to the spin-orbital coupling properties. In this process, electrons can undergo transitions between the singlet and triplet excited states however, this transition is spin forbidden in accordance with Laporte's rules and does not obey the spin selection rule. The transformation of the singlet state to the triplet state (denoted by T_1 in Figure 90) allows electrons to occupy a longer excited state lifetime.

When a molecule undergoes decay from T_1, the process can occur through two processes, radiative and non-radiative pathways. Radiative decay from the triplet excited state is known as phosphorescence (Orange arrow, P, in Figure 90) while non radiative decay processes are consumed via vibrational relaxation processes (black dotted arrows). Collectively, fluorescence and phosphorescence can be coined under the umbrella of "luminescence" and in cases where the emissive properties of a molecule are unknown or unclear, this term is used.

3.1.7 Tuning the photophysical properties of Re(I) complexes

The electronic transitions that take place upon excitation can be modulated based on the ligands surrounding the metal centre. The MLCT transition is of interest in the scope of Re(I) tricarbonyl systems due to the combination of harnessing the low oxidation state of the metal centre and the low-lying π* diimine ligands such as bipyridine (bipy) and phenanthroline (phen) whereby the metal is readily oxidised and conversely the ligand is easily reduced. When exploring MLCT transitions, ligands which are readily reduced and contain low lying π* orbitals such as phen and bipy will arise. In rhenium(I)-diimine complexes, the most favourable transition occurs between the combined influence of the MLCT band and any chemical modifications to the complex will in turn, alter the effects of this transition.

Alterations to the general structure of the Re(I) tricarbonyl moiety can be made through three avenues, (i) changes made to the diimine backbone ligand N^N, (ii) the ancillary ligand and (iii) the overall charge of the Re(I) metal centre. Modifications to these groups, including their electron donating and withdrawing strength, will in turn affect the required energy for ligand reduction and photophysical output. Previous studies have identified a linear correlation between the electron donating strength of the ancillary ligand and overall emission output of the complex.[412] As ligands tend towards stabilisation of the HOMO, there is an increase in the energy of the MLCT, spectroscopically the emission wavelength is observed to decrease, and the quantum yield and lifetimes are observed to increase.[412]

Previous research has identified the effect of solvatochromism on the transfer states of rhenium(I) complexes.[413,414] Depending on the solvent in use, the effects of the dipole moments induced onto the excited and ground state energies of the molecule are altered. Thus, changing the solvent polarity has an effect on the luminescent output.

3.1.8 Rhenium(I) N-heterocyclic chemistry

It is well established that N-heterocyclic compounds can act as biological isosteres (referred to as 'bioisosteres').[211] The tunability of π-electronics within N-heterocyclic ligand systems such as pyrazoles, imidazoles, tetrazoles and triazoles allow for greater synthetic versatility and optimisation of fluorescence quantum yield.

The functionalisation of N^N bidentate diimine ligands (often of the form bpy or phen) within the *fac*-[$Re(CO)_3$(N^N)(X)] scaffold is often associated with the incorporation of multi-step synthetic pathway which requires difficult and low yielding purification methods.[415] Therefore, the integration of N-heterocyclic ligands as both ancillary L-type as well as bidentate (N^N) diimines has been explored as an alternative.[171,353,416–423] Although the incorporation of N-heterocyclics as ancillary ligands has shown modest enhancements to the overall photophysical and biological activity of Re(I) complexes, when compared to the derivatisation of traditional 2,2-bipyridyl and 1,10-phenathroline N^N diimines, these complexes provide valuable insights into the SAR studies of Re(I) tricarbonyl complexes as a whole.

Wilson and co-workers explored a comparative analysis of pyridine, piperidine, morpholine and thiomorpholine as ligands for Re(I) in terms of emission intensity and quantum yield, whereby increased outputs could be correlated to the increased acidity of the ligand (Figure 91).[373] Despite all of the complexes showing low cytotoxicity values in HeLa cells, only the Re(I) pyridyl derivative showed cellular luminescence, this was postulated to be due the complex rigidity resulting in higher energy and shorter wavelength emissions.[373]

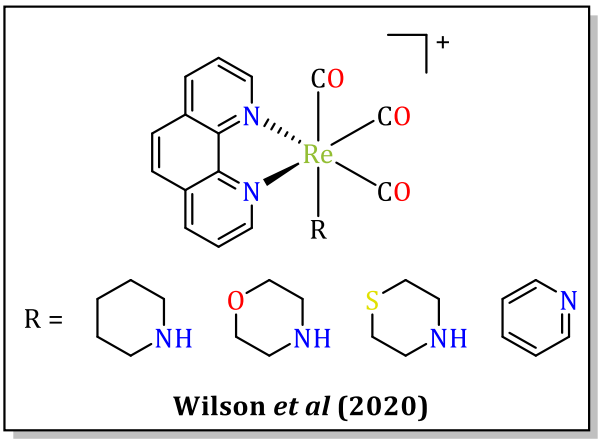

Figure 91: Re(I) complexes incorporating N-heterocyclic ancillary ligands (from left to right): piperidine, morpholine, thiomorpholine and pyridine.[373]

Explored in section 1.2.5, Re(I) tricarbonyl N-heterocyclic complexes have been predominantly explored as luminescent cellular probes and in Light Emitting Devices (LEDs).[414] For example, Mansour synthesised a series of mononuclear and binuclear Re(I) 1,2,3-triazolato-based complexes bearing a pyridylbenzimidazole (PBI) backbone.[414] The Re(I) triazolato complexes showed isomerisation from the N(1) position to the N(2) position and in addition, displayed diminished antifungal activity against *C. albicans* when compared to their PBI backbone derivatives.[414]

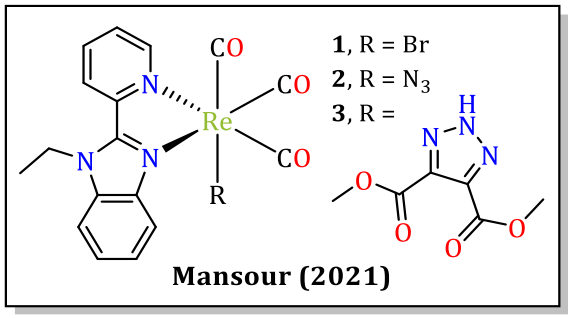

Figure 92: Re(I) complexes incorporating an imidazole backbone and 1,2,3-triazole ancillary ligand.[414]

There have been numerous studies featuring the rhenium(I) tetrazolato-based system as either backbone ligands or as ancillary ligands in conjunction with 1,10-phenathroline and 2,2-bipyridyl functionalised ligands (Figure 93). Overall, the complexes have shown good phosphorescence activity with excitation maxima over 600 nm, long excited state lifetime decay values of 200-300 ns, and quantum yield values between 4-6 % in degassed solutions.[416,417]

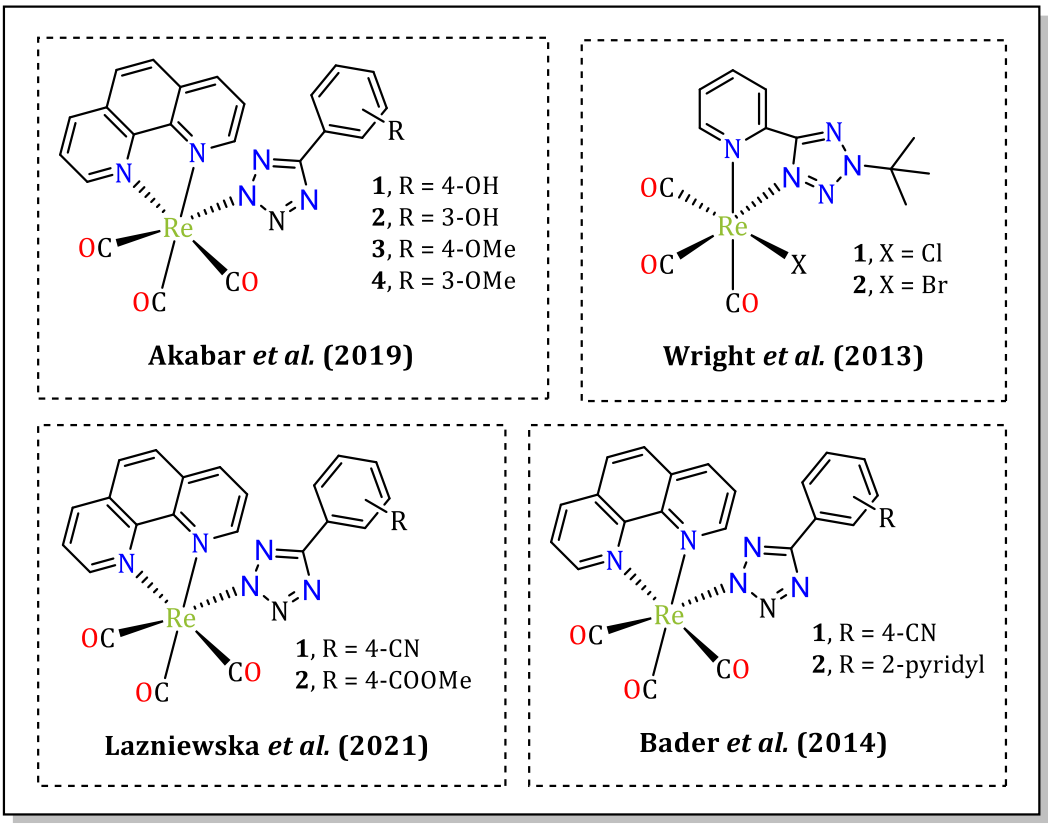

Figure 93: General structures of Re(I) tricarbonyl moieties bearing diimine and/or tetrazolato backbone ligands.[353,416,417,420]

Cellular imaging and photophysical studies have identified Re(I) tetrazolates to localise within the cytoplasm,[416] endoplasmic reticulum,[424] mitochondria,[425] and within lipid droplets.[420] Notably, since the release of the commercial Re(I) tetrazolato derivative, ReZolve-ER™ in 2016 for endoplasmic reticulum and plasma membrane cellular staining, these complexes continue to be of interest.[424,426]

The first known study of the coordination of a triazole-based anion to a rhenium(I) metal centre was conducted by Obata *et al.* with the discovery of the *fac*-Re(pyta-Bn)$(CO)_3(Cl)$ complex. However, this study explored the vicinal (1,2,3-) form of the triazole derivatised with a pyridyl ligand, to form a combined 'pyta' moiety.[427] In this study, the pyta diimine ligand showed an emission maxima of 333 nm when compared to the classical *fac*-Re(bpy)$(CO)_3(Cl)$ complex at 371 nm.[427] Since then, numerous other studies have highlighted the sensitivity of triazole-based ligands which have coordinated to Re(I) tricarbonyl systems impacting the chemical, and photophysical and biological activity.[371,428–431]

The vast majority of research surrounding Re(I) tricarbonyl-based complexes utilises a derivatised pyridine N-heterocyclics as axial donors, there have been few reports within the literature pertaining to the application of Re(I) tricarbonyl N-heterocyclic complexes bearing S-type donors as therapeutics.[371,389,432–434] For example, Fernandez-Moreira and co-workers synthesised a series of thiolato- and thione-based Re(I) tricarbonyl complexes with acceptable emission maxima within the yellow-to-red shifted region (572-675 nm, Figure 94).[82] Whilst the emission intensities for these complexes were observed to be lower than typical N-donor pyridyl-based axial ligands, it is postulated that this could be attributed to the presence of both electron donor and acceptor ligands causing internal competitive LLCT and MLCT processes. However, all of the complexes in this study presented low cytotoxicity when tested against A549 and HeLa cells with IC_{50} values <100 mM.[82]

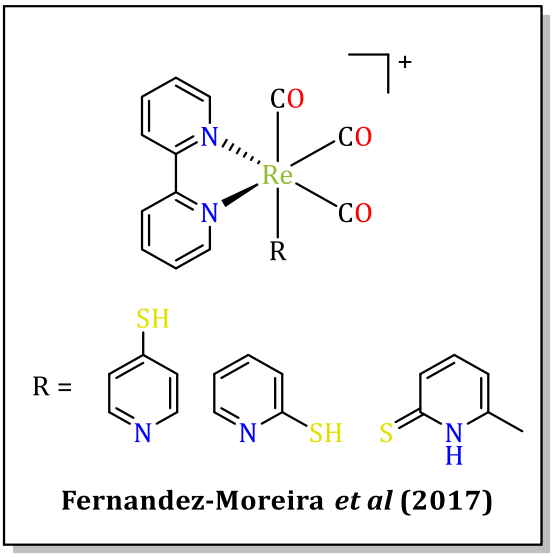

Figure 94: Re(I) complexes incorporating a 2,2-bipyridyl backbone and thione/thiolate ancillary ligand.[432]

The use of the tetrazole and imidazole moieties have been extensively explored by Coogan and co-workers however, explorative studies into alternative triazole-based scaffolds incorporating an exocyclic sulfur or that which incorporates a secondary thione moiety are limited.[377,389]

3.1.8.1 Rhenium(I) backbone triazoles

As demonstrated in Chapter 2, pyridyl-triazole (pyta) type ligands have demonstrated versatility in the synthetic chemistry sphere. The combined coordinative potential of the triazole heterocycle and pyridine ring provides enhanced conjugation, strong σ-donating capability, and enhanced functionality through the triazole ring. The direct isomerisation of pyridyl-triazole based ligands, impart a significant influence on the electronic properties of a molecule as the forms of triazole (vicinal and symmetrical) offer distinct functional features depending on the substitution and coordination to the metal centre.[175,382]

Numerous research groups including Lo and co-workers as well as Bertrand and Co-workers have explored the isomeric forms of Re(I) tricarbonyl complexes bearing a 2-pyta and aromatic group (Figure 95). Both research groups have uncovered some interesting trends pertaining to the 1,2,3-triazole-based fragments.[371,435,436]

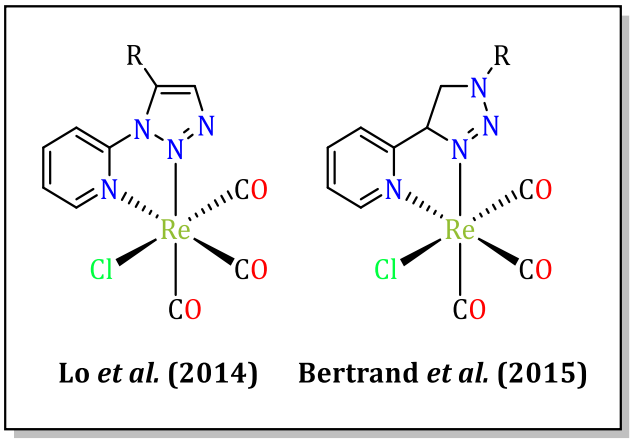

Figure 95: Structures of photoreactive Re(I) tricarbonyl complexes bearing the vicinal σ- or π-donating 1,2,3-triazole backbone ligands.[371,435,436]

Later, Wang *et al*. explored a 1,2,4-triazole-based ligand system with Re(I) which closely resembles the ligand system explored herein.[435] In this study, the conjugation of a 2-phenylbenzoxazole (PBO) moiety with a pyridyl-triazole moiety was found to enhance electron delocalisation and electronic distribution resulting in a smaller HOMO-LUMO gap. The results of this study showed the complexes luminesce in the solid-state presenting these complexes as potential light-emitting materials.[435] Building on this study, Hernández Mejías and co-workers published a Re(I) tricarbonyl complex incorporating a similar pyridyl-triazole backbone with PBO, and an ancillary triphenylphosphine which was shown to display photochemical reactivity towards the release of CO upon irradiation.[175]

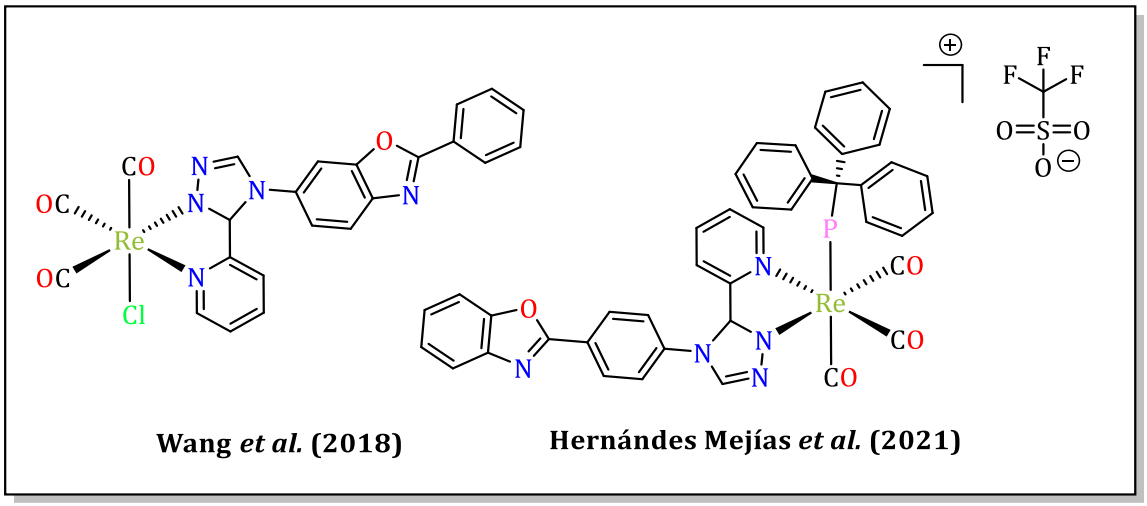

Figure 96: Re(I) complexes featuring modified 1,2,4-triazoles as backbone ligands.

3.2 Chapter objectives

The cytotoxicity of neutral Re(I) complexes is yet to be fully elucidated within the literature. While the luminescent output of these complexes has been well established, their therapeutic potential is an area of key interest. Studies exploring their stability in the presence of biological substrates, physiological conditions and in aqueous media have not been fully elucidated as yet. While many complexes bearing the diimine moiety have been synthesised, concerns regarding their solution-state stability may prevent them from progressing into *in vivo* studies.

The aims of this chapter are to capture the behaviour of three series of Re(I)-based complexes bearing the pyridyl-triazole ligand class. By comparing the solution-state, solid-state and theoretical behaviour of these sets of complexes we hope to understand the reactivity, stereochemistry and photophysical nature behind these systems and provide additional information to their binding modes. Previously, some 1,2,4-triazole based derivatives have been synthesised and structurally elucidated. By comparing the behaviour of the three sets of complexes we hope to understand and predict the nature of the Re(I) triazole system to contribute to the further development of a series of luminescent and biologically active Re(I)-based tricarbonyl triazole complexes.

Surprisingly, the coordination chemistry of the 1,2,4-triazolate anion with Re(I) is relatively underexplored with few examples reported. With the aim to expand upon the chemistry of Re(I) tricarbonyl 1,2,4-triazolato-based complexes, this chapter intends to prepare two series of complexes whereby the triazolato anion is coordinated to the fac-$[Re(N\hat{}N)(CO)_3]^+$ and fac-$[Re(CO)_3X]^+$ fragments.

The specific investigation explores the substituted 1,2,4-triazole thione moiety with the well-established Re(I) tricarbonyl core system, the substituted π-electron conjugated system on the substrate is not directly involved in the complexation to Re(I) however, in order to elucidate the nature of the Re(I)-ligand interaction. To our knowledge, the design of molecules bearing both a substituted pyridyl-triazole and dual N,S configuration are limited.

3.3 Part 1: Results and discussion –ancillary triazoles

3.3.1 Synthesis and spectroscopic characterization of disubstituted 1,2,4-triazole-3-thiones

The triazole thiolate substrates **1, 2, 4** and **6** used to form the Bi(III) homoleptic and heteroleptic thiolates (Chapter 2) were utilised as parent substrates for the formation of the proceeding Re(I) diimine complexes. To further add structural diversity, a further two disubstituted 1,2,4-triazole-3-thiones bearing a furan moiety (Scheme 9, **12** and **13**) were synthesised whereby the derivatives of the furan series followed a similar reaction procedure to the pyridyl series and were all adapted from a modified synthesis following Shaker and co-workers (Scheme 9).[437]

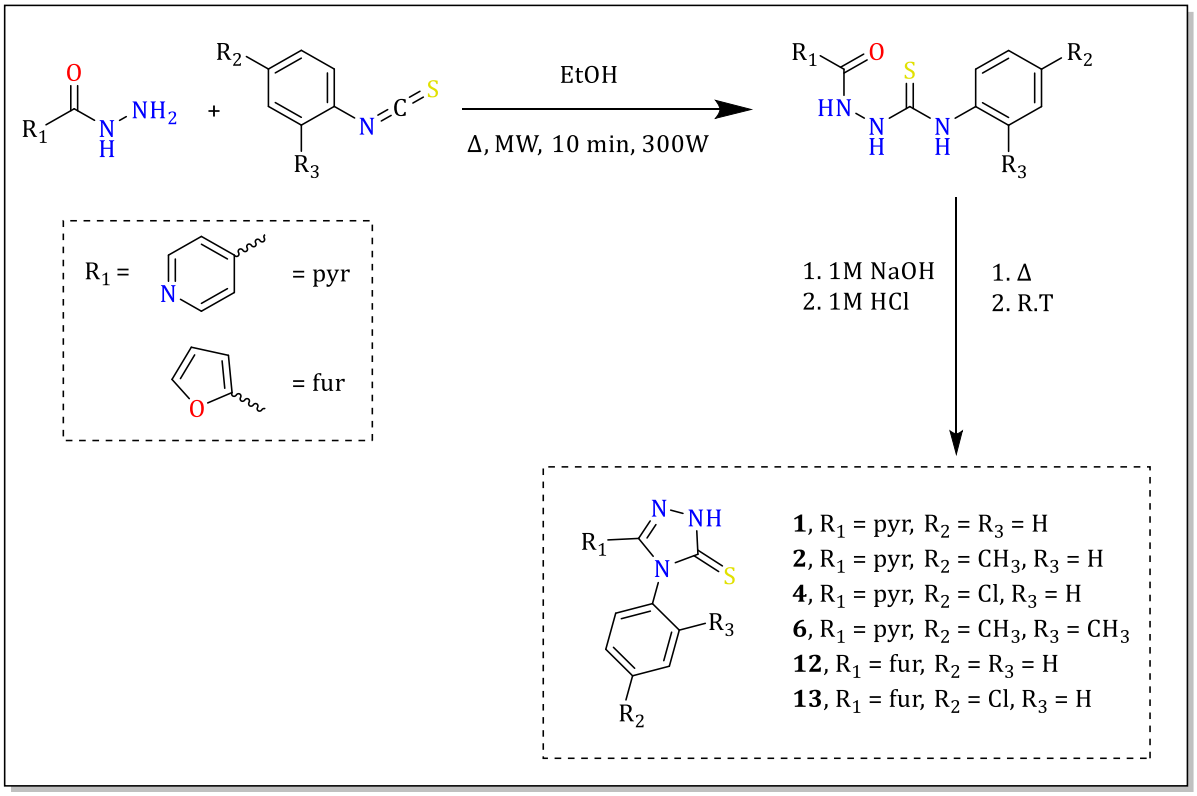

Scheme 9: Preparation of pyridyl and furan substituted thiones **1-6, 12** and **13** from acid hydrazides and substituted aryl isothiocyanates.[437]

3.3.2 Synthesis of neutral Re(I) p-triazole complexes

A series of six neutral Re(I) bipy and six neutral Re(I) phen complexes of the general form *fac*-[Re(N^N)(CO)$_3$L], where L refers to triazole thiolates **1-6** were synthesised via microwave irradiation. Following a previously reported procedure, the synthesis

of the Re(I) complexes were optimised under microwave conditions (Scheme 10) resulting in the crystallisation of the pure neutral complexes via filtration (in the filtrate) in moderate to high yields and without the need for further purification (Figure 97).

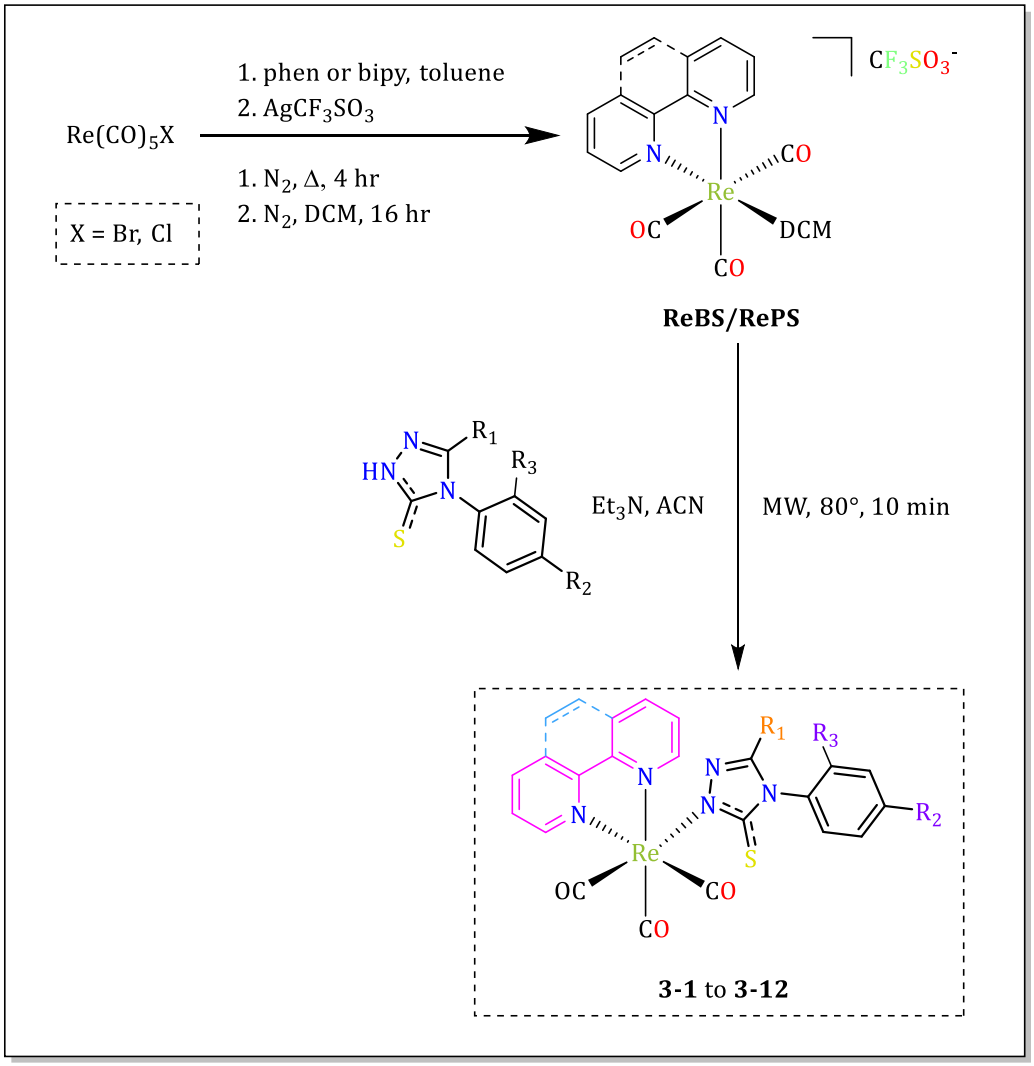

Scheme 10: Synthesis of the neutral rhenium triazolato complexes and summarized general structure using an acetonitrile solvent system with the addition of an excess of triethylamine under microwave conditions.

The general reaction proceeds via the equimolar reaction of either a Re(I) 1,10-phenanthroline (phen, **RePS**) or 2,2,-bipyridyl (bpy/bipy, **ReBS**) derived solvato precursor with a triazole substrate, within the presence of an excess of base, such as triethylamine (Et_3N). After the reaction was irradiated at 350 W at 80 °C for ten minutes, the resulting solutions produced a range of colours from transparent yellow

to orange-dark red, with immediate crystallisation of product, in some cases. In cases where no crystals immediately formed, within 24 hours the products precipitated from the reaction solutions as either fine, blocky, or needle-like orange to yellow crystals.

Using the solvato rhenium complexes, direct substitution by the deprotonated triazole was achieved in good yields ranging from 39 % to 74 % (Table 14). Previous methods have utilised heating of the reactants under reflux conditions followed by column chromatography for separation. However, this microwave method yielded pure crystalline solids of the general structure *fac*-[Re(N^N)(CO)$_3$(L)], individual complex structures can be summarised in Figure 97.

Table 14: Summary of yields and appearances of Re(I) tricarbonyl bpy/phen ancillary triazole complexes **3-1** to **3-12**, (d.c. refers to decomposition).

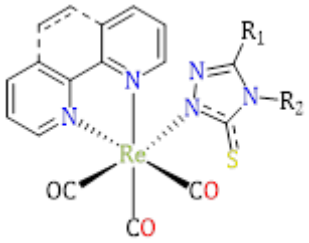

	Complex	Functional Group (R_1)	Functional group (R_2)	Yield (%)	Melting point	Appearance
3-1	*fac*-[Re(bpy)(CO)$_3$(pyta)]	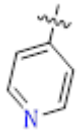	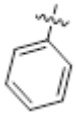	40	>300 (d.c.)	Orange needles
3-2	*fac*-[Re(bpy)(CO)$_3$(pyta-t)]	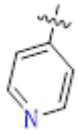	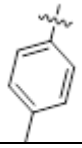	48	>300 (d.c.)	Yellow powder
3-3	*fac*-[Re(bpy)(CO)$_3$(pyta-Cl)]	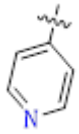	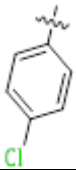	60	>300 (d.c.)	Yellow powder

3-4	*fac*-[Re(bpy)(CO)$_3$(pyta-2Me)]	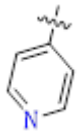	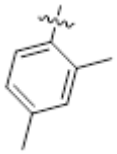	48	>300 (d.c.)	Yellow needles
3-5	*fac*-[Re(bpy)(CO)$_3$(futa)]	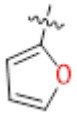	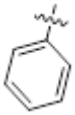	53	>300 (d.c.)	Orange blocks
3-6	*fac*-[Re(bpy)(CO)$_3$(futa-Cl)]	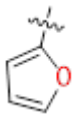	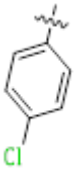	74	>300 (d.c.)	Orange blocks
3-7	*fac*-[Re(phen)(CO)$_3$(pyta)]	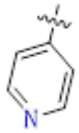	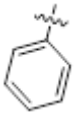	40	>300 (d.c.)	Orange blocks
3-8	*fac*-[Re(phen)(CO)$_3$(pyta-t)]	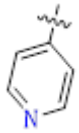	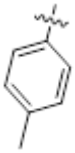	44	>300 (d.c.)	Orange blocks
3-9	*fac*-[Re(phen)(CO)$_3$(pyta-Cl)]	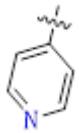	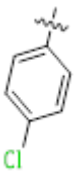	40	>300 (d.c.)	Orange blocks
3-10	*fac*-[Re(phen)(CO)$_3$(pyta-2Me)]	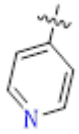	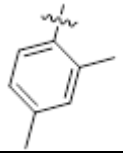	40	>300 (d.c.)	Orange blocks
3-11	*fac*-[Re(phen)(CO)$_3$(futa)]	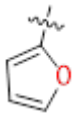	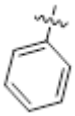	39	293-295	Orange blocks
3-12	*fac*-[Re(phen)(CO)$_3$(futa-Cl)]	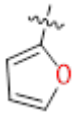	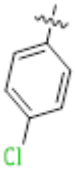	39	>300 (d.c.)	Orange blocks

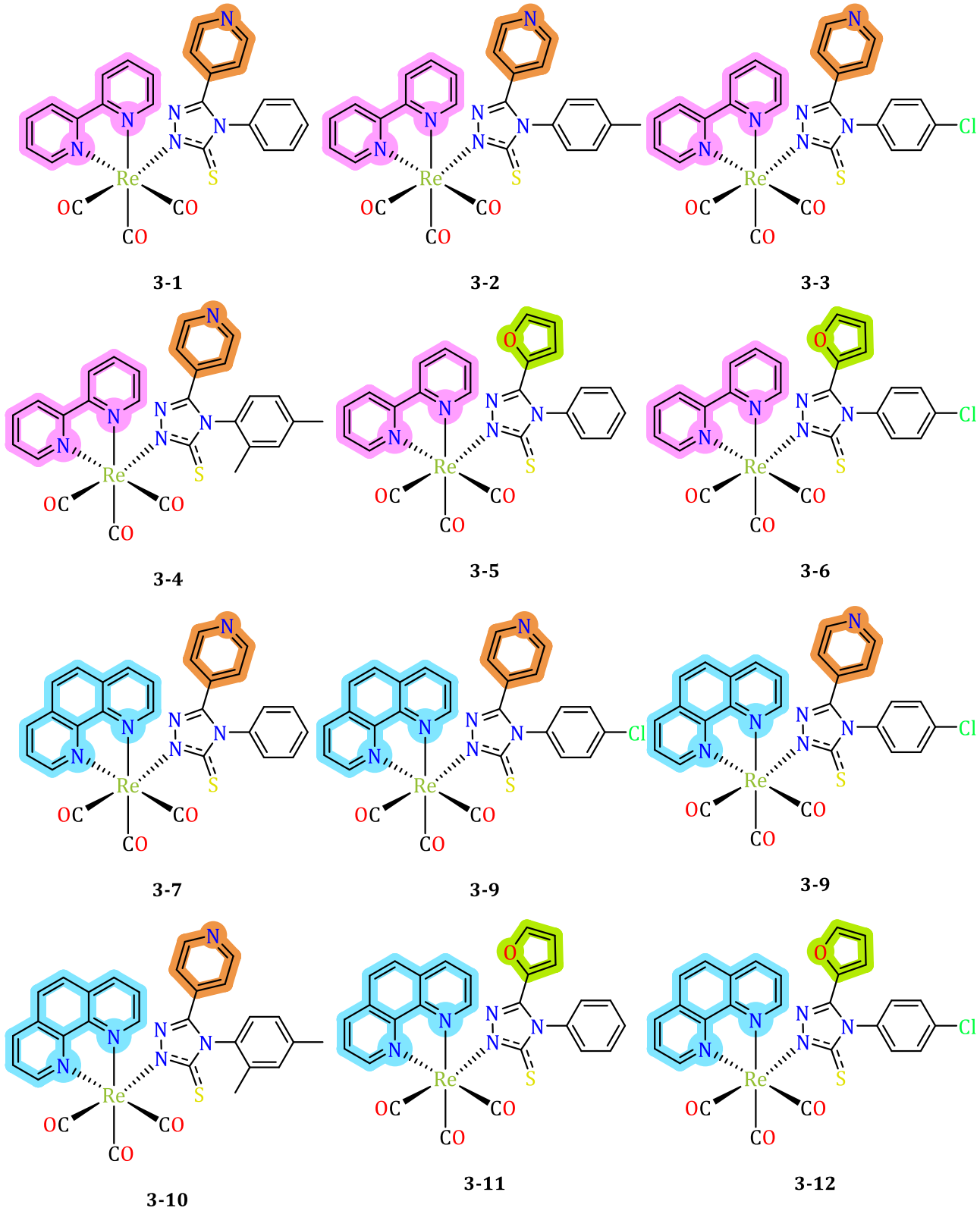

Figure 97: Complexes **3-1** to **3-12** of the general form *fac*-[Re(**phen**/**bipy**)$(CO)_3$(**L**)] (where **L** = pyta, pyta-t, pyta-Cl, pyta-2Me, futa, futa-Cl were synthesized according to the methods outlined in Scheme 10.

3.3.3 NMR spectroscopy

3.3.3.1 ^{1}H NMR studies

Analysis of the solution state structures of the rhenium(I) tricarbonyl triazole complexes were compared to their precursor counterparts and all spectra were observed to match with the desired complexes. Solution state analysis of the twelve complexes **3-1** to **3-12** synthesised via microwave irradiation was confirmed using 1D and 2D proton and carbon NMR studies. 2D HSQC and HMBC experimental methodology was utilised to differentiate between the assignments of the aryl triazole and diimine-based ligands.

In an illustrative example of the phenanthroline-based Re(I) triazolato complex *fac*-[Re(phen)(CO)$_3$(pyta-Cl)] **3-9**, the comparative ^{1}H NMR spectra shows consistent trends across the **3-7** to **3-10** series of compounds. Characteristic of all Re(I) phenanthroline tricarbonyl complexes is the marked downfield shift of the set of doublets from 9.55 ppm to 9.71, corresponding to the *ortho*-phenanthroline protons upon complexation. This is consistent across the series of complexes **3-7** to **3-10**. Additionally, there is an observed upfield shift of the *meta*- and *para*-phenanthroline proton signals from 9.07 ppm to 8.94 ppm, 8.39 ppm to 8.29 ppm and 8.19 ppm to 8.11 ppm, respectively. Within the ligand set of signals, like the bismuth(III) set of compounds (Chapter 2) complexation of the N2-triazole to the rhenium metal centre can be observed through a downfield shift of the *ortho*-pyridyl protons from 8.60 ppm to 8.94 ppm. The remaining *ortho*- and *meta*-chlorophenyl signals shift upfield from 7.61 ppm to 7.40 ppm and 7.47 ppm to 7.08 ppm, respectively. Markedly, an additional shift can be observed for the *meta*-pyridyl ligand protons from 7.26 ppm to 6.44 ppm. The overall trends observed for the phenanthroline backbone complexes can be observed the same for the bipyridyl set of complexes **3-1** to **3-4.** Overall, the signals attributed to the ancillary triazole ligand all experienced high field shifts due to the electron-withdrawing effect of the Re(I) core, as observed in the literature with similar types of complexes.[402,438,439]

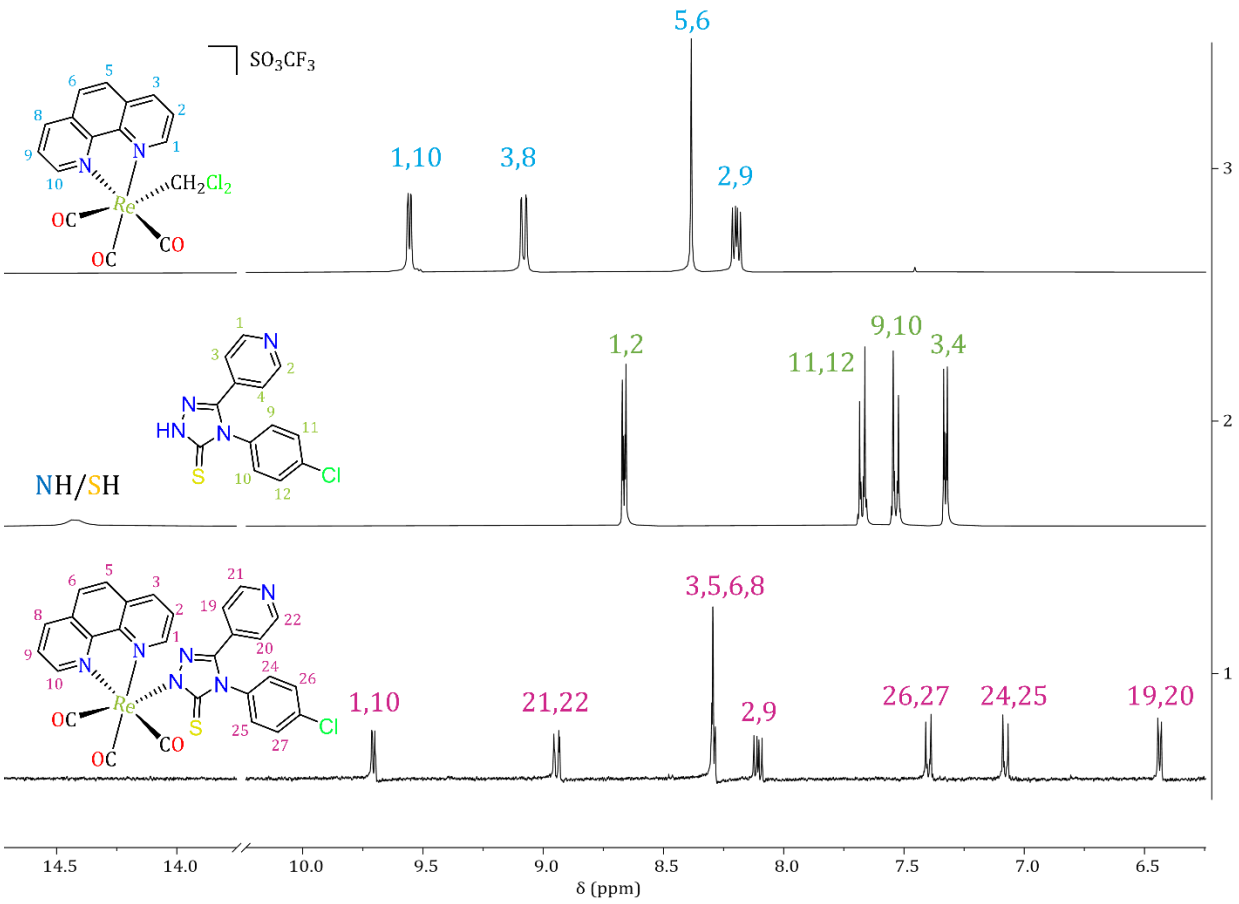

Figure 98: ^{1}H NMR spectra of complexes *fac*-[Re(phen)(CO_3)(DCM)]SO_3CF_3, **PS** (spectrum 3)**;** free triazole pyta-Cl, **3** (spectrum 2); and complex *fac*-[Re(phen)$(CO)_3$(pyta-Cl)], **3-9** (spectrum 1); taken in DMSO-d_6 at 25 °C.

In the same illustrative example of complex *fac*-[Re(bpy)$(CO)_3$(pyta-Cl)] **3-3** the bipyridyl derivative, a similar trend can be observed. Upon complexation to the triazole ligand, the ^{1}H NMR spectrum shows a downfield shift of the *ortho*-bipyridyl protons adjacent to the complexed N-donor from 9.12 ppm to 9.27 ppm. Like the phenanthroline counterpart, the meta- and para-bipyridyl protons undergo an upfield shift from 8.79 ppm to 8.38 ppm, 8.43 ppm to 8.32 ppm and 7.84 ppm to 7.75 ppm, respectively. The ligand proton environments show the same trends as observed in the phenanthroline backboned rhenium triazole complexes, with a downfield shift of the ligand *ortho*-pyridyl protons from 8.60 ppm to 8.73 ppm, and upfield shifts of the ligand corresponding *meta*-pyridyl, Chloro-phenyl *ortho*- and *meta*-phenyl protons from 7.26 ppm to 6.67 ppm, 7.61 ppm to 7.45 ppm and 7.47 ppm to 7.18 ppm, respectively.

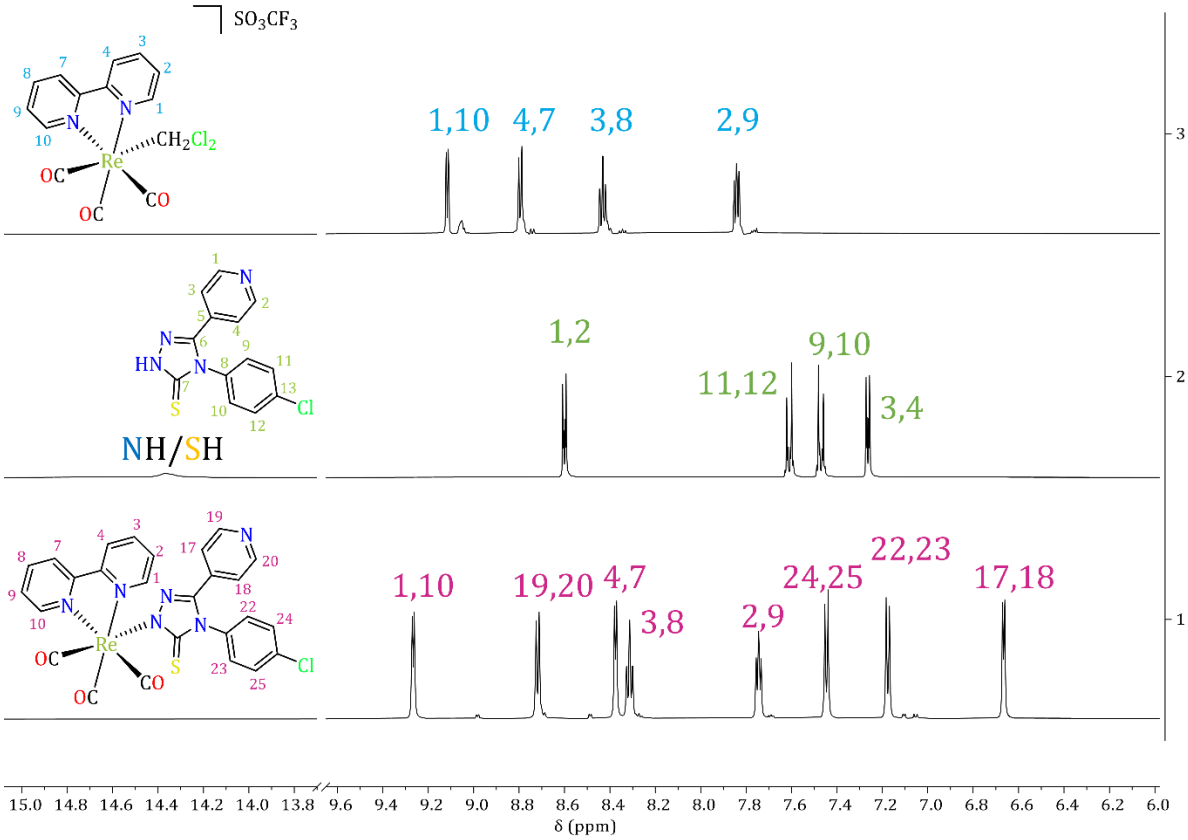

Figure 99: ^{1}H NMR spectra of complexes *fac*-[Re(bpy)(CO_3)(DCM)]SO_3CF_3 **ReBS** (spectrum 3), free triazole pyta-Cl **3** (spectrum 2); and complex *fac*-[Re(bpy)(CO)$_3$(pyta-Cl)], **3-3** (spectrum 1); taken in DMSO-d_6 at 25 °C.

When comparing the two sets of neutral rhenium(I) tricarbonyl triazolato complexes, phenanthroline against the bipyridyl counterpart, there are some identifiable differences that can be attributed to the overall electronic conjugation of the two systems. Generally, the phenanthroline set of complexes show broader and more marked shifts across the NMR spectrum. Additionally, the phenanthroline set of complexes are generally more downfield shifted than the bipyridyls. In Figure 99, the *ortho*-phenanthroline set of signals adjacent to the N- donor shifts further downfield at 9.71 ppm compared to the *ortho*-bipyridyl set of signals adjacent to the N-donor at 9.27 ppm. Additionally, the ligand *meta*-pyridyl signals are shifted further upfield for the phenanthroline complex at 6.44 ppm when compared to the bipyridyl complex at 6.67 ppm.

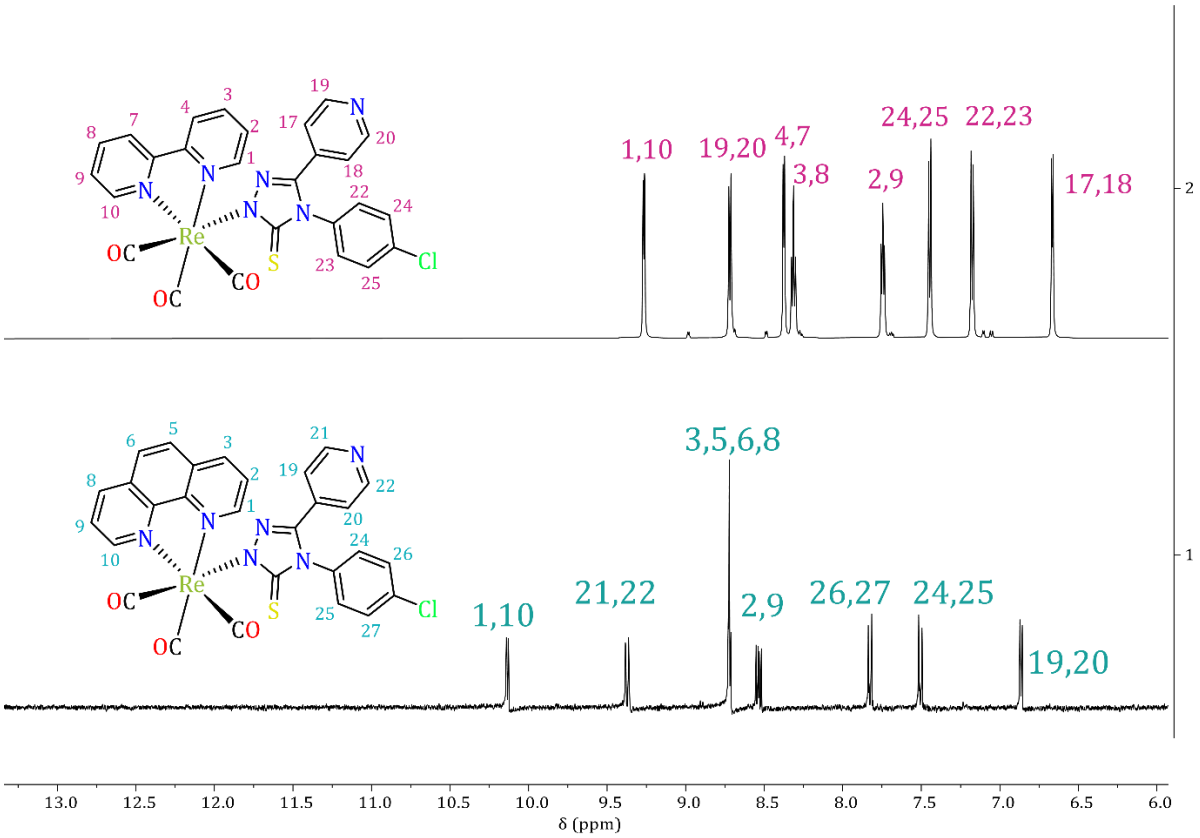

Figure 100: ^{1}H NMR spectra of complexes *fac*-[Re(bpy)(CO)$_3$(pyta-Cl)] **3-3** (spectrum 2); and complex *fac*-[Re(phen)(CO)$_3$(pyta-Cl)], **3-9** (spectrum 1); taken in DMSO-d$_6$ at 25 °C.

3.3.3.2 ^{13}C NMR studies

Due to poor solubility concerns, not all of the ^{13}C NMR spectra could be obtained for complexes **3-1** to **3-12** however, from the complexes that were able to be obtained, some noticeable signals were observed.

Analyses of the ^{13}C NMR spectra alluded to the isolation of one single and neutral product in all cases. This was further supported by a single set of ^{13}CO, and single set of signals within the aromatic region of each complex. The facial configuration of the CO ligands were validated through the presence of six sets of proton and carbon signals corresponding to the 1,10-phenanthroline, this could indicate the presence of a plane of symmetry within the molecules.[432] In a representative example of complex **3-8**, two low-intensity signals were identified corresponding to the Re(I)-CO environments at δ = 197.3 ppm and δ = 194.2 ppm, respectively (Figure 101, spectrum 1); confirmed through the utilisation of 2D HSQC experiments. This data fits in-line

with the literature, with the coalescence of two CO signals correlating well to the *facial* configuration as two of the signals exist in a *trans* arrangement to the diimine phen ligand while the remaining CO signal appears to be in a *trans* configuration to the triazolato ligand.[404,440]

In complex *fac*-[Re(phen)$(CO)_3$(pyta-t)] **3-8** upon coordination to the rhenium(I) metal centre, a downfield shift of the thioamide (N-C=S) signal is observed from δ = 169.4 ppm to δ = 176.5 ppm, this correlates well to the deshielding and mesomeric effects of the triazole ring to the metal centre. Additionally, the downfield shift of the thioamide signal could indicate an increase in π-electron density on the exocyclic C=S as a result of the regioselective coordination of the metal centre to the triazole N2 atom, this could be compensated by the decrease in bond order of the thioamide C-NH bond, as a result of this, a small shielding effect is observed for **C17** (Figure 101, spectrum 1 and Spectrum 2, **6** respectively).[441]

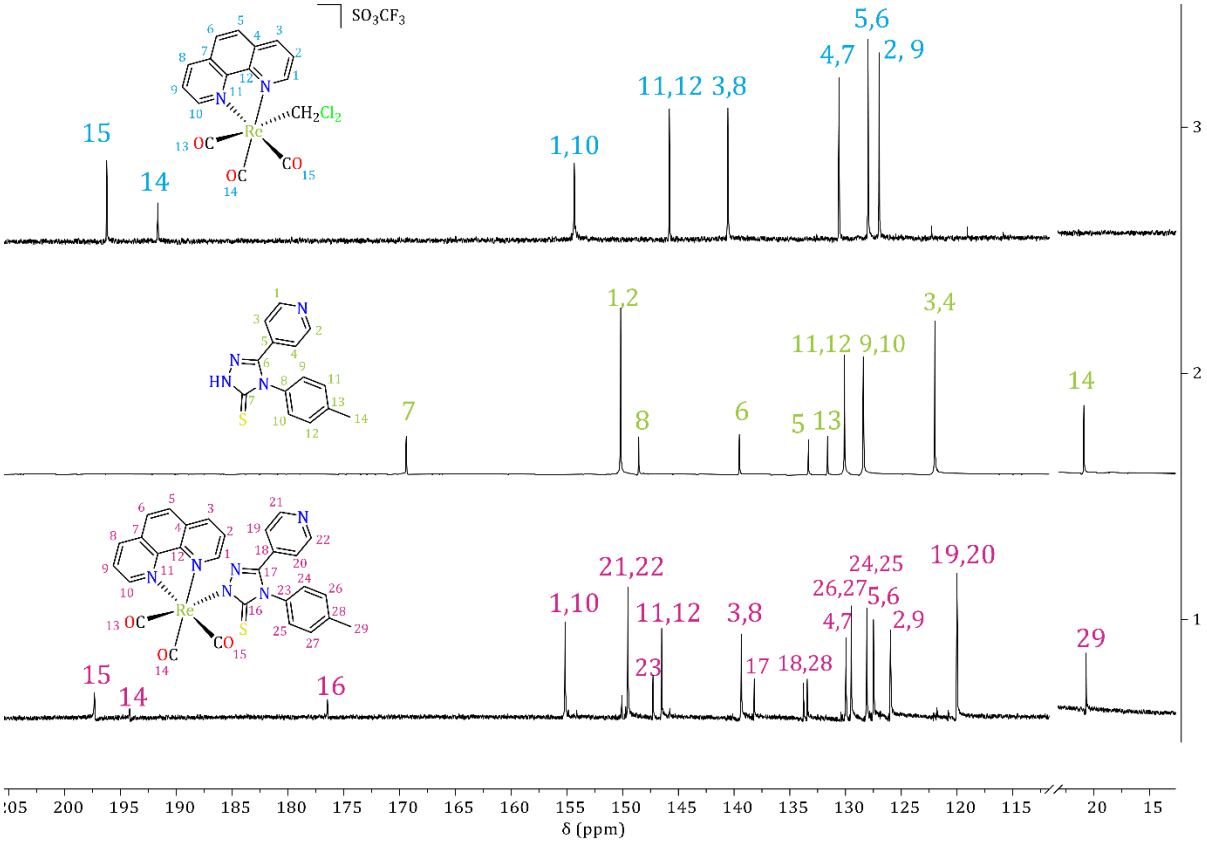

Figure 101: ^{13}C NMR of rhenium(I) tricarbonyl 1,10-phenanthroline solvato complex **RePS** (spectrum 3), triazole precursor pyta-t **2** (spectrum 2); and complex *fac*-[Re(phen)(CO)$_3$(pyta-t)] **3-8** taken in in DMSO-d$_6$ at 25 °C.

When comparing the ^{13}C NMR of the two sets of neutral rhenium(I) tricarbonyl triazolato complexes, **3-3** against the **3-9** (Figure 102), there is little variation between the characteristic CO signals as well as the general spectra. The bipyridyl set of complexes (**3-1 to 3-6**) appear to be marginally shifted downfield when compared to phenanthroline backbone complexes (**3-7 to 3-12**) with no other notable trends observed.

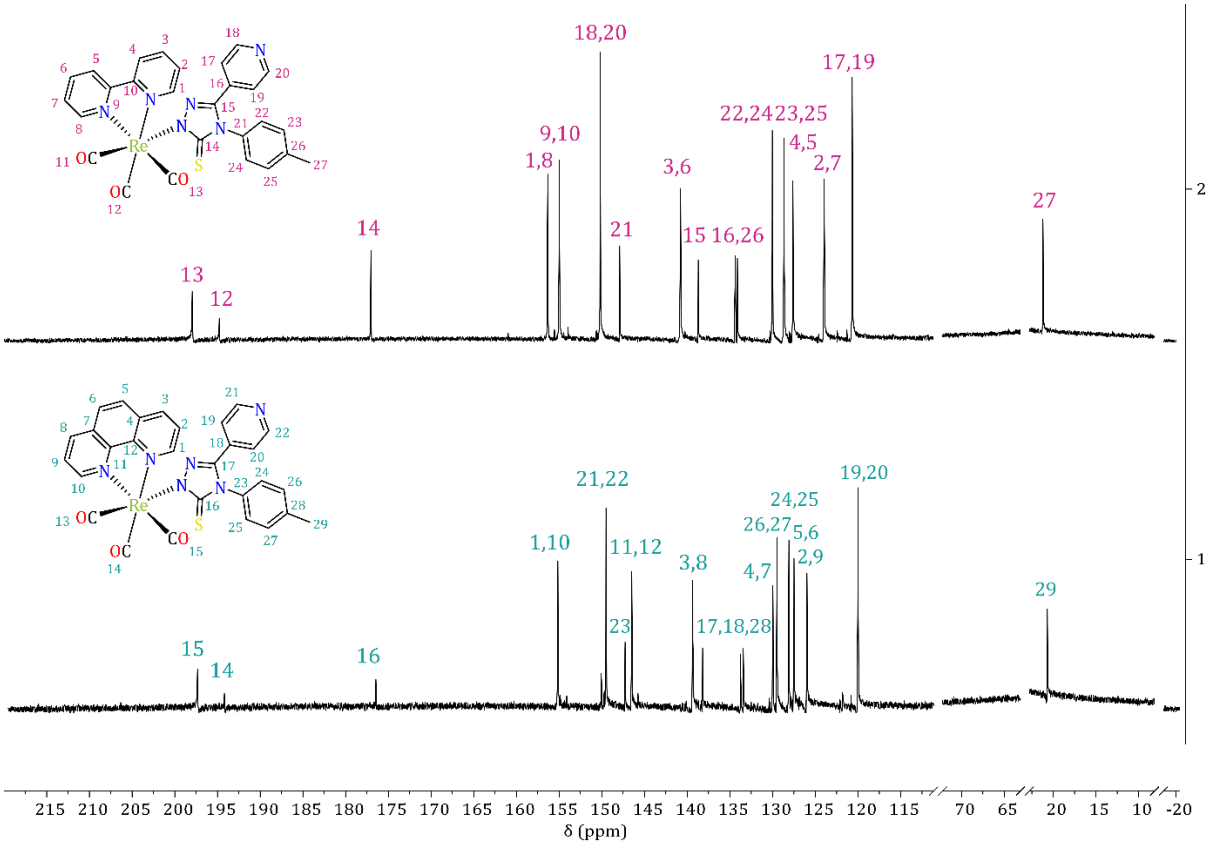

Figure 102: ^{13}C NMR of complex *fac*-[Re(bpy)$(CO)_3$(pyta-t)] **3-3** (spectrum 2); and complex *fac*-[Re(phen)$(CO)_3$(pyta-t)] **3-9** (spectrum 1); taken in DMSO-d_6 at 25 °C.

3.3.4 FT-IR spectroscopy

Crystalline materials of complexes **3-1** to **3-12** afforded the precipitation of the *facial* isomer systems of type [Re$(CO)_3$(N'N)(L)], which was supported by Infra-Red (IR) spectroscopy and solid-state crystallography. As observed in previously synthesised Re(I) tricarbonyl complexes, due to the trans effect of the CO ligands, the geometry of all complexes adopts a facial type of isomerism rather than a meridional system and this was supported via the characteristic absence of the very low symmetric CO signal in the FT-IR spectra which can be typically observed between the 2100-1800 cm^{-1} region, instead three distinct infrared modes were observed.[171,423]

Overall, the FT-IR stretching frequencies observed for all 12 complexes are consistent with the observed literature values for neutral rhenium complexes.[175,435,442] Characteristic strong vibrational stretches associated with the ν(CO) functional groups were observed beyond 1850 cm^{-1}. Analysis of the IR spectra revealed that all

complexes exhibit three characteristic carbonyl stretching bands between 2030 cm^{-1} and 1860 cm^{-1} which correspond to the totally C*s* symmetric in-phase (A), total symmetric out-of-phase stretching (B) and asymmetric stretching (C) frequencies.[416] Shifts in the CO symmetry show that the steric influence of the ancillary triazole ligand affects the d-π electron density of the carbonyl stretching frequencies. When comparing the symmetric in-phase stretching value of the precursor **RePS** (2029 cm^{-1}) to complex **3-9** (2019 cm^{-1})**,** the delocalisation of electron density from the Re(I) metal centre to the CO-π*-orbitals, results in a lowered CO stretching frequency of **3-9** compared to free CO (at 2143 cm^{-1}).[443] The values of the recorded stretching frequencies are summarised in Table 15. Changes observed between the reactant and product spectra of the rhenium precursors to rhenium(I) neutral triazole complexes was also monitored via IR spectroscopy.

Table 15: CO stretching frequency values in cm^{-1} of the prepared neutral rhenium complexes where A = symmetric in-phase stretching, B = total symmetric out-of-phase stretching and C = asymmetric stretching.

Neutral complexes		ν(CO) stretching frequency		
		A	B	C
ReBS	*fac*-[Re(bpy)(CO)$_3$(CH$_2$Cl$_2$)][CF$_3$SO$_3$]	2030	1907	1892
RePS	*fac*-[Re(phen)(CO)3(CH$_2$Cl$_2$)][CF$_3$SO$_3$]	2029	1920	1889
3-1	*fac*-[Re(bpy)(CO)$_3$(pyta)]	2008	1911	1864
3-2	*fac*-[Re(bpy)(CO)$_3$(pyta-t)]	2010	1912	1867
3-3	*fac*-[Re(bpy)(CO)$_3$(pyta-Cl)]	2010	1912	1869
3-4	*fac*-[Re(bpy)(CO)$_3$(pyta-2Me)]	2010	1913	1886
3-5	*fac*-[Re(bpy)(CO)$_3$(futa)]	2007	-	1881
3-6	*fac*-[Re(bpy)(CO)$_3$(futa-Cl)]	2007	-	1884
3-7	*fac*-[Re(phen)(CO)$_3$(pyta)]	2013	1914	1890
3-8	*fac*-[Re(phen)(CO)$_3$(pyta-t)]	2018	-	1894
3-9	*fac*-[Re(phen)(CO)$_3$(pyta-Cl)]	2019	1914	1890
3-10	*fac*-[Re(phen)(CO)$_3$(pyta-2Me)]	2019	1915	1887

3-11	*fac*-[Re(phen)(CO)$_3$(futa)]	2016	-	1891
3-12	*fac*-[Re(phen)(CO)$_3$(futa-Cl)]	2007	-	1882

The FT-IR spectra of the diimine rhenium(I) tricarbonyl triazolato complexes all show a decrease in intensity of the characteristic ν(CO) stretching modes when compared to the rhenium precursors. This is consistent with what is observed within the literature whereby the conjugated π-acid ancillary ligands destabilise the HOMO.[172,444] The phenanthroline-based systems show a less pronounced bathochromic shift with values ranging from 10-13 cm^{-1} in comparison to the bipyridine systems with a broader range from 3-22 cm^{-1} observed in Figure 103. Across the series of complexes, the coalescence of the symmetric out of phase stretching (column **B,** Table 15) and asymmetric stretching frequencies (**C,** Table 15) was observed for the furan-derived complexes (**3-5**, **3-6**, **3-11** and **3-12**) which was not observed in the pyridyl series.

Overall, alterations to the pyta aryl side groups (R_2 and R_3) appear to have no significant impact on the general connectivity of the Re(I) tricarbonyl ancillary triazole complexes however, alterations of the R_1 side group from a pyridyl to a furan functional moiety appear to have resulted in the disappearance/coalescence of the characteristic Re(I)-CO$_3$ bands.

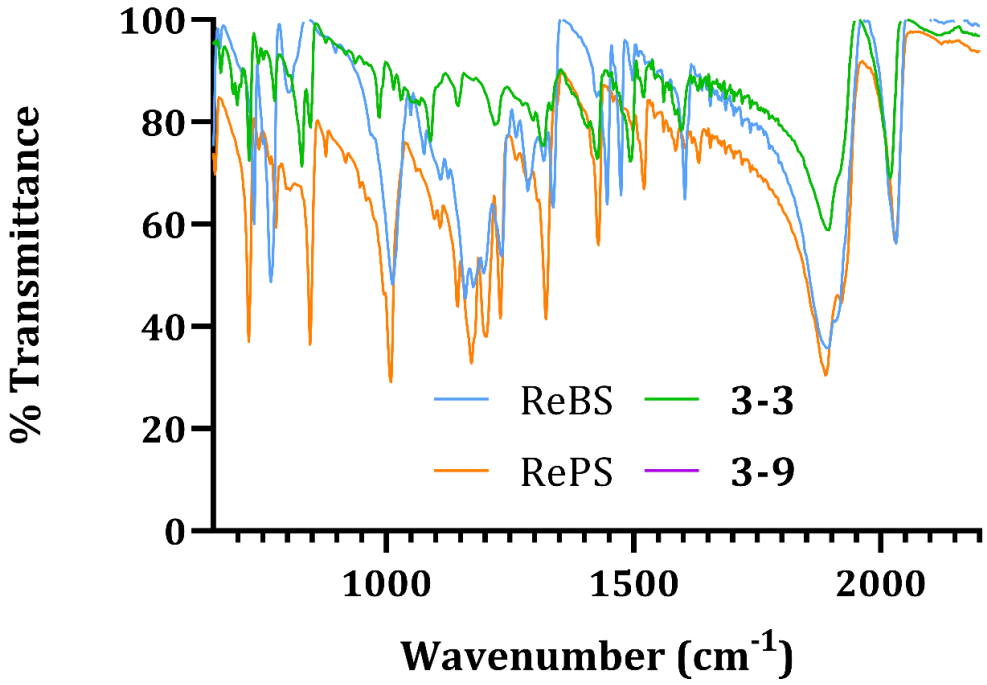

Figure 103: Comparative FT-IR spectra of Orange - Rhenium phen solvate complex; Blue - rhenium bipy solvate complex; Purple – complex **3-3** and Green –complex **3-9.**

Strong and moderate intensity absorption bands were present in the regions of 2030-600 cm^{-1} due to the various functionalities present within the precursor triazole thiolates however, FT-IR was used as a basis to identify changes to the rhenium(I) tricarbonyl core, via shifts in the *ν*(CO) vibrational mode and compared to the literature.[343,344] As described in Chapter 2 however, FT-IR spectroscopy alone could not be used to ascertain whether the triazole thione ligand was bound to the Re(I) metal centre through the *S*- or *N*- terminus, nor could it determine the overall connectivity of the molecule,. Other analytical techniques such as NMR spectroscopy and single crystal X-ray diffractometry were required to fully elucidate the connectivity and structure of the complexes.

3.3.5 X-ray crystallography

Single crystals were obtained for nine of the twelve neutral rhenium(I) triazolato complexes from the slow evaporation of acetonitrile solutions. Complexes **3-1**, **3-3** to **3-6,** and **3-7** to **3-11** were analysed and structurally elucidated via single crystal x-ray diffraction with the molecular structures shown in Figure 104-Figure 111 and the selected bond lengths and angles summarised in Table 16 and Table 18. All of the obtained solid-state structures illustrated the formation of one single and neutrally charged Re(I)-N2 linkage isomer which was in agreement with NMR spectroscopic data. The neutral complexes are all isostructural and adopt similar parent pseudo-octahedral to octahedral geometries with the Re(I)-CO ligands arranged in the *facial* conformation, this was in agreement with FT-IR spectroscopy and consistent with other Re(I) tricarbonyl diimine complexes observed within the literature.[373,423,445–447]

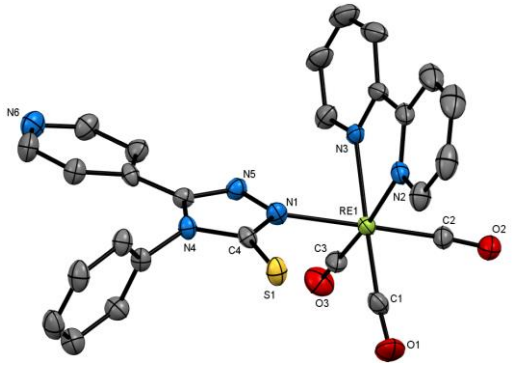

Figure 104: Asymmetric unit of complex *fac*-[Re(bpy)$(CO)_3$(pyta)] **3-1.** Thermal ellipsoids are shown at the 50% probability level. Hydrogen atoms have been omitted for clarity.

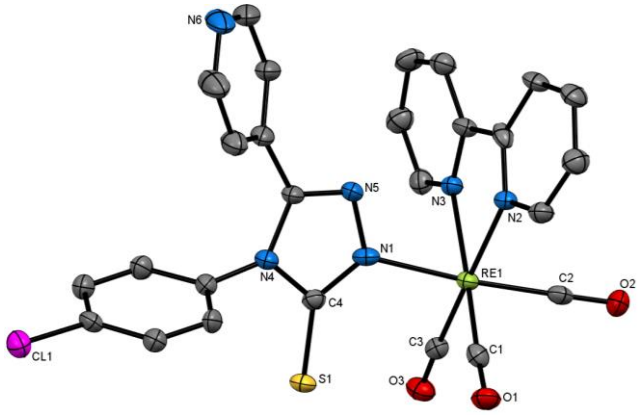

Figure 105: Asymmetric unit of complex *fac*-[Re(bpy)(CO)$_3$(pyta-Cl)] **3-3.** Thermal ellipsoids are shown at the 50% probability level. Hydrogen atoms have been omitted for clarity.

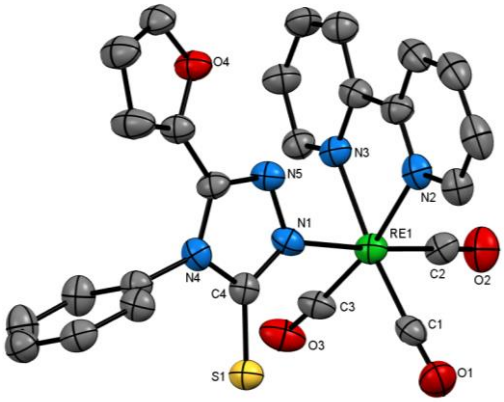

Figure 106: Asymmetric unit of complex *fac*-[Re(bpy)(CO)$_3$(futa)] **3-5.** Thermal ellipsoids are shown at the 50% probability level. Hydrogen atoms have been omitted for clarity.

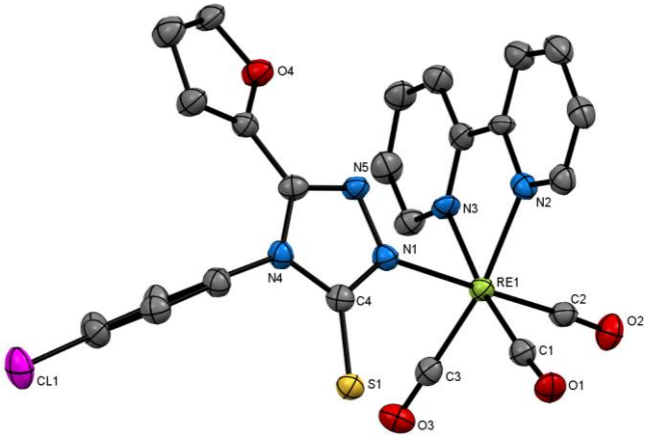

Figure 107: Asymmetric unit of complex *fac*-[Re(bpy)(CO)$_3$(futa-Cl)] **3-6.** Thermal ellipsoids are shown at the 50% probability level. Hydrogen atoms have been omitted for clarity.

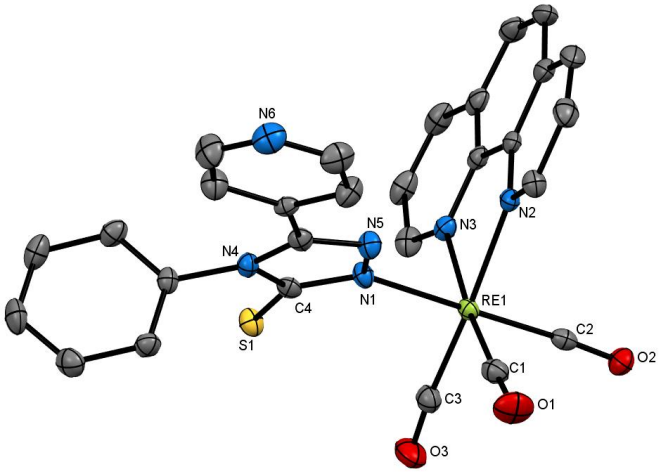

Figure 108: Asymmetric unit of complex *fac*-[Re(phen)(CO)$_3$(pyta)] **3-7.** Thermal ellipsoids are shown at the 50% probability level. Hydrogen atoms have been omitted for clarity.

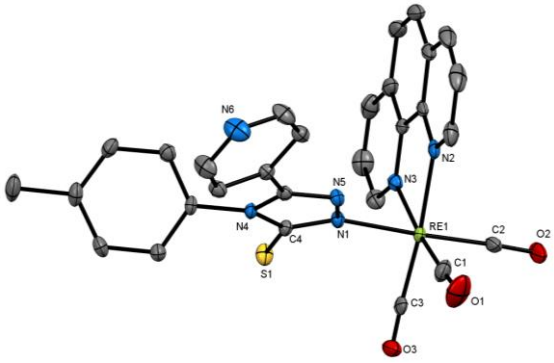

Figure 109: Asymmetric unit of complex *fac*-[Re(phen)(CO)$_3$(pyta-t)] **3-8**. Thermal ellipsoids are shown at the 50% probability level. Hydrogen atoms have been omitted for clarity.

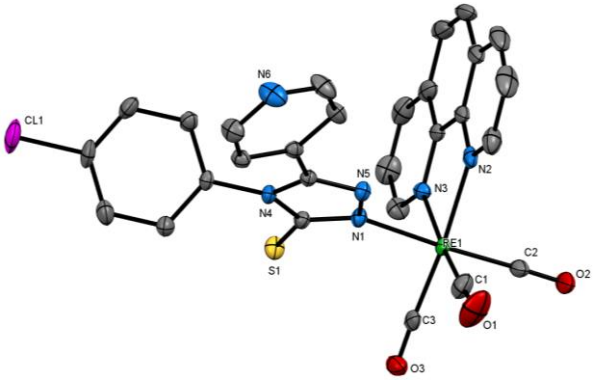

Figure 110: Asymmetric unit of complex *fac*-[Re(phen)(CO)$_3$(pyta-Cl)] **3-9**. Thermal ellipsoids are shown at the 50% probability level. Hydrogen atoms have been omitted for clarity.

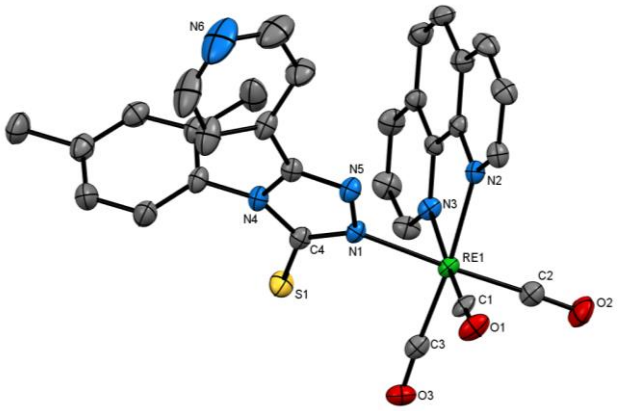

Figure 111: Asymmetric unit of complex *fac*-[Re(phen)(CO)$_3$(pyta-2Me)] **3-10**. Thermal ellipsoids are shown at the 50% probability level. Hydrogen atoms have been omitted for clarity.

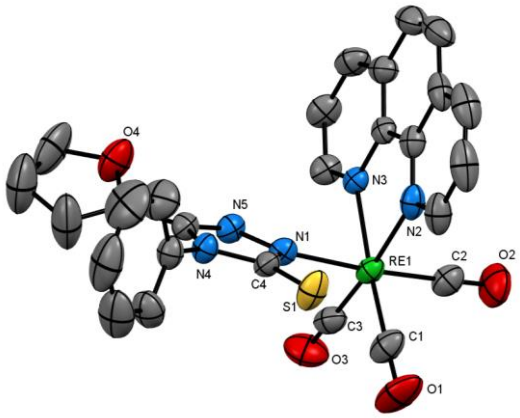

Figure 112: Figure 113: Asymmetric unit of complex *fac*-[Re(phen)(CO)$_3$(futa)] **3-11**. Thermal ellipsoids are shown at the 50% probability level. Hydrogen atoms have been omitted for clarity.

Table 16: Selected bond lengths (Å) and angles (°) of the solid-state structures of neutral Re(I) bipyridyl triazole thionate complexes **3-1, 3-3, 3-5** and **3-6.**

Bond (Å)/Angle (°)	**3-1**	**3-3**	**3-5**	**3-6**
Re(1)-N(1)	2.175(4)	2.164(5)	2.160(7)	2.170(5)
Re(1)-N(2)	2.169(4)	2.175(5)	2.172(7)	2.182(5)
Re(1)-N(3)	2.171(4)	2.180(5)	2.149(7)	2.169(5)
Re(1)-C(1)	1.916(5)	1.925(6)	1.922(10)	1.940(7)
Re(1)-C(2)	1.901(5)	1.903(6)	1.921(8)	1.930(7)
Re(1)-C(3)	1.912(5)	1.932(6)	1.899(8)	1.934(7)
N(1)-C(4)	1.350(6)	1.357(8)	1.341(10)	1.339(9)
S(1)-C(4)	1.690(5)	1.683(6)	1.691(8)	1.699(7)
O(2)-C(2)	1.167(6)	1.173(8)	1.144(10)	1.140(9)
O(3)-C(3)	1.158(7)	1.146(8)	1.166(11)	1.140(9)
O(1)-C(1)	1.168(7)	1.150(8)	1.159(12)	1.123(9)
C(2)-Re(1)-N(1)	176.81(19)	174.6(2)	175.1(3)	175.2(2)
N(3)-Re(1)-N(2)	74.21(17)	74.69(19)	74.9(3)	75.0(2)
N(1)-Re(1)-N(2)	90.00(16)	87.31(19)	82.3(2)	82.4(2)
N(1)-Re(1)-N(3)	82.11(15)	81.52(19)	86.0(3)	84.8(2)
Re(1)-N(1)-C(4)	131.8(3)	129.0(4)	131.8(6)	129.8(4)

Illustrated in Figure 104, *fac*-[Re(bpy)(CO)$_3$(pyta)] **3-1** crystallized in the *I2/a* monoclinic space groups with the Re(I) metal centre adopting an octahedral geometry and coordinated via the N2-atom of the pyta moiety. The bpy ligand occupies the equatorial plane *trans* to two corresponding CO ligands in an essentially co-planar configuration, whilst the heterocyclic pyta moiety sits in the axial plane of the crystal system. The bond distances of all Re(CO)$_3$ fragments remain consistent across the bpy series of complexes and within the structure of **3-1**, the Re(I)-CO bond *trans* to the pyta moiety, Re(1)-C(3) is 1.912(5) Å, which is in-line with other neutrally derived Re(I) tricarbonyl complexes.[353,416,418,448,449]

In an illustrative example, **3-7** (Figure 108) crystallised in the monoclinic space group C2/c whereby Re(I) metal centre conforms to a distorted octahedral geometry with a coordination number of six. The Re(1) metal centre is chelated by the phenanthroline at the N(2) and N(3) positions, as well as the triazole via the N(1) atom with bond distances of 2.184(2), 2.171(3), and 2.187(2) Å. Additionally, the triazole ancillary ligand does not sit in a single plane and is coordinated perpendicular to the backbone. Within the ancillary ligand, the pyridyl group at the substituted C(3) position sits perpendicular to the aryl group at the substituted N(3) position, this is presumably due to steric influences. The carbonyl ligands are in the *facial* arrangement which is consistent with the literature and in agreement with the ^{13}C NMR and FT-IR spectroscopic data.[389]

Within the Re(I) phenanthroline-type ligand system observed in **3-7**, the triazole core is essentially co-planar with one Re(I)-(CO) fragment whilst the associated ligand *p*-phenyl group is orthogonal to the triazole moiety. The triazole core deviates from co-planarity with a torsion angle of 78.3 ° which is in line with literature values with similar ligand systems, as observed by Bonello *et al*.[450,451] A summary of the characteristic torsion angles (θ) of the Re(I) tricarbonyl phen-based ancillary triazole complexes are summarised in Table 17.

Table 17: Torsion angles (θ) in Re(I)-triazole complexes **3-7** to **3-11**.

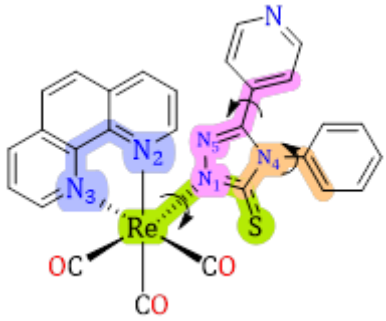

torsion angles (°)		3-7	3-8	3-9	3-10	3-11
3-7	N(2)-C(28)-C(27)-N(3)	1.1(4)	1.6(3)	1.9(3)	0.4(4)	3.5(5)
3-8	Re(1)-N(1)-C(4)-S(1)	-12.4(4)	-1.3(4)	-1.3(5)	10.9(4)	8.0(6)
3-9	C(4)-N(4)-C(11)-C(12)	-83.4(4)	71.4(3)	56.9(3)	94.8(4)	-78.8(5)
3-10	N(1)-N(5)-C(5)-C(6)	-177.6(3)	179.5(2)	179.8(19)	178.9(3)	-179.5(4)

Table 18: Selected bond lengths (Å) and angles (°) of the solid-state structures of neutral Re(I) phenanthroline triazole thionate complexes **3-7** to **3-11.**

Bond (Å)/Angle (°)	**3-7**	**3-8**	**3-9**	**3-10**	**3-11**
Re(1)-N(1)	2.171(3)	2.178(2)	2.1756(18)	2.178(2)	2.177(3)
Re(1)-N(2)	2.187(2)	2.180(2)	2.1794(19)	2.176(3)	2.193(3)
Re(1)-N(3)	2.184(2)	2.183(2)	2.1815(19)	2.190(3)	2.172(3)
Re(1)-C(1)	1.923(3)	1.922(3)	1.919(3)	1.904(3)	1.919(5)
Re(1)-C(2)	1.913(3)	1.915(3)	1.917(2)	1.922(3)	1.913(5)
Re(1)-C(3)	1.926(3)	1.925(3)	1.921(2)	1.937(3)	1.906(5)
N(1)-C(4)	1.347(4)	1.340(3)	1.345(3)	1.345(4)	1.349(5)
S(1)-C(4)	1.690(3)	1.694(2)	1.686(2)	1.680(3)	1.691(4)
O(2)-C(2)	1.156(4)	1.151(3)	1.148(3)	1.151(4)	1.150(5)
O(3)-C(3)	1.152(4)	1.144(3)	1.148(3)	1.155(4)	1.155(5)
O(1)-C(1)	1.147(4)	1.147(4)	1.149(3)	1.157(4)	1.161(6)
C(2)-Re(1)-N(1)	176.67(10)	176.59(9)	175.89(9)	177.22(11)	175.92(17)
N(2)-Re(1)-N(3)	75.30(9)	82.19(7)	75.51(7)	75.64(10)	75.26(13)
N(1)-Re(1)-N(2)	83.02(9)	82.19(7)	82.07(7)	81.00(9)	86.18(12)
N(1)-Re(1)-N(3)	89.72(9)	88.32(7)	87.99(7)	81.35(9)	85.95(12)
Re(1)-N(1)-C(4)	132.3(2)	133.41(16)	133.71(14)	129.2(2)	129.5(3)

3.3.6 Photophysical investigations

Photophysical experiments conducted for the neutral Re(I) tricarbonyl ancillary triazole complexes were measured in dilute deoxygenated DCM at 10^{-5} M at room temperature due to the observed decomposition in MeCN via ^{1}H NMR studies (to be discussed in section 3.3.7). The absorption and emission data for complexes **3-1** to **3-12** featuring 2,2-bipyridyl (bpy) and 1,10-phenanthroline (phen) diimines are summarised in Table 19. Due to time and instrumentation constraints, experiments were not conducted at low temperatures to investigate rigidochromic effects. Additionally, each sample was prepared with nitrogen degassed solvents however, due to the sensitive nature of organometallic Re(I) tricarbonyl complexes, it is possible that the presence of singlet oxygen may have presented some quenching effects.[412,449,452–454]

Across the series, the general absorption profiles of the complexes featuring a bpy (**3-1** to **3-6**) versus phen (**3-7** to **3-12**) were varied. Complexes **3-1** to **3-6** all show an intense high energy band in the range 273-278 nm with complex **3-4** (Figure 114, left) showing a high intensity band within this region corresponding to an intraligand $\pi\rightarrow\pi^*$ charge transfer (ILCT) transition. Additionally, complexes **3-1** to **3-3** show a secondary absorption band at *ca.* 360 nm postulated to be the characteristic metal-to-ligand charge transfer (MLCT) transition as previously observed for similar types of Re(I) tricarbonyl ancillary complexes.[428,435,453]

Table 19: Summarised photophysical data obtained for complexes **3-1** to **3-12** of the general form *fac*-[Re(N^N)(CO)$_3$(**L**)] from diluted DCM solutions (*ca*. 10^{-5} M).

Complex	λ_{abs} (nm) [10^4 ε, $M^{-1}cm^{-1}$]	λ_{exc} (nm)	Stokes shift (nm)	τ	ϕ
3-1	273 (0.757), 360 (0.293)	550	200	0.269 (0.85), 0.0189 (0.05)	0.0220
3-2	274 (0.668), 360 (0.302)	552	202	0.314 (0.92), 0.0297 (0.04)	0.00944
3-3	278 (0.636), 360 (0.307)	567	217	-	0.00659
3-4	278 (1.000) , 282 (1.000)	537	187	-	0.0102
3-5	275 (0.774)	553	203	0.477 (0.70), 0.193 (0.25)	0.0127
3-6	280 (0.633), 337 (0.273)	550	200	-	0.00290
3-7	257 (0.426), 357 (0.335)	600	250	-	0.0174
3-8	270 (0.192), 359 (0.227)	549	199	1.082 (0.90), 0.199 (0.07)	0.0622
3-9	256 (0.447), 354 (0.305)	580	230	1.258 (0.92), 0.203 (0.06)	0.0250
3-10	265 (1.000), 360 (0.242)	552	202	-	0.0503
3-11	266 (1.000), 327 (0.284)	539	189	0.625 (0.63), 0.143 (0.21)	0.0747
3-12	256 (0.251), 330 (0.315)	540	190	-	0.0216

Analysis of the six neutral Re(I) tricarbonyl ancillary triazoles featuring the phen diimine ligand (**3-7** to **3-12**) all showed similar absorption profiles. Illustrated in Figure 114 **b)**, a high intensity transition in the UV region between 250-260 nm is observed to correspond to the ILCT band followed by a secondary low intensity band between 315 – 380 nm, corresponding to the MLCT band with complex fac-[Re(phen)(CO)$_3$(futa-Cl)] **3-12** shown to display the most blue-shifted absorption maxima at λ_{abs} = 330 nm. When compared to other neutral Re(I) tricarbonyl phen-derived tetrazole complexes, the general absorption profiles appear to be more blue-shifted however, overall they are consistent with typical Re(I) tricarbonyl ancillary azole-based systems which show values ranging from 270-400 nm for the ILCT and MLCT bands.[404,445,448,450,455]

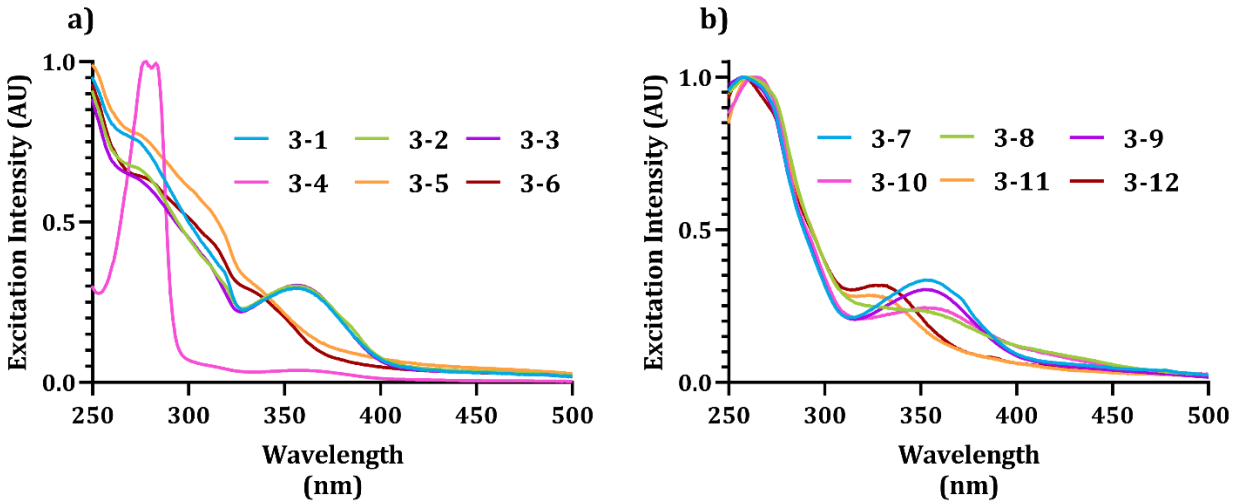

Figure 114: Excitation profiles of **a)** fac-[Re(bpy)(CO)$_3$(L)] series of complexes **3-1** to **3-6** and **b)** fac-[Re(phen)(CO)$_3$(L)] series of complexes **3-7** to **3-12** taken at 10^{-4} in DCM at 298 K.

Complexes **3-1** to **3-12** were all observed to exhibit phosphorescence in solution at room temperature (298 K) which was in line with the commonly observed Re(I) tricarbonyl complexes published in the literature.[175,375,416,446] However, the emission profiles across the bpy and phen series show noticeable differences in the dispersion of wavelengths. Following the excitation of each solution at 350 nm, each of the neutral Re(I) tricarbonyl ancillary triazole complexes exhibited a generally broad and characterless emission band beyond the 500 nm region at room temperature.

Complexes **3-1** to **3-6** (bpy series) were comparatively blue shifted and closer in range between 537 – 567 nm, whilst complexes **3-7** to **3-12** (phen series) were marginally red shifted between 539 – 580 nm. Interestingly, the bipyridine complexes show satellite-like emission signals between the 400-500 nm region, this could be potentially attributed to residual charge transfer states and other corresponding photochemical reactions occurring simultaneously.[373] Overall, the emission intensities for the phenanthroline backbone complexes (**3-7** to **3-12**) were generally higher than the bipyridine counterparts potentially attributed to the more conjugated and planar geometry.

With reference to the quantum yield measurements, complexes **3-1** to **3-6** (bpy series) showed values ranging from 3 – 22 %. However, complexes **3-7** to **3-12** (phen series) showed improved values ranging from 17 – 75 %, which is in line with other typical Re(I) tricarbonyl complexes found within the literature, with values ranging from 26-69 %.[353,373,416,449,455] These results are unsurprising given the more conjugated and planar nature of the phenanthroline diimine ligand influencing the overall photophysical output of the system.

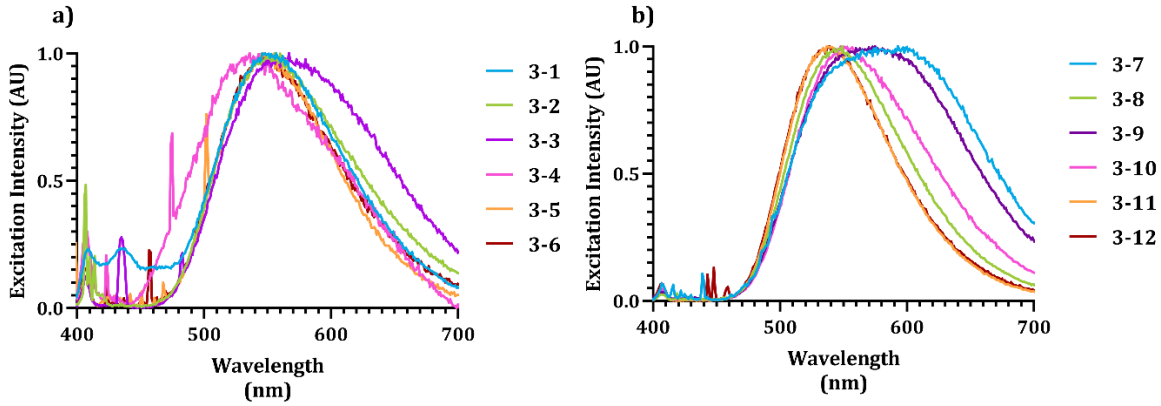

Figure 115: Emission profiles of **a)** fac-[Re(bpy)$(CO)_3$(L)] series of complexes **3-1** to **3-6** and **b)** fac-[Re(phen)$(CO)_3$(L)] series of complexes **3-7** to **3-12** taken at 10^{-4} in DCM.

Due to time constraints, not all complexes were chosen for emission lifetime studies however, complexes **3-1**, **3-2** and **3-5** from the bpy series and **3-8**, **3-9** and **3-11** from the phen series were chosen as representative examples. Whilst complexes **3-1, 3-2** and **3-5** show quick emission lifetime profiles at 0.269, 0.314 and 0.477 ms; complexes **3-8** and **3-9** showed the highest values beyond 1 microseconds (ms). The

emission values obtained for the tested complexes are comparable to the literature and thus, as simple fluorophores they fulfill the requirements for long lifetime.[420,425,456] Additionally, they overcome potential autofluorescence activity (at <<10 ns) which organic fluorophores are susceptible to within cells.[72,79]

Overall, the Re(I) tricarbonyl phen-derived triazole complexes **3-7** to **3-12** consistently produce better photophysical results. The moderate quantum yield values, long luminescence lifetimes and large stokes shifts to prevent self-quenching position these complexes as more desirable potential fluorophores.[425] It is evident that the ancillary N-heterocyclic ligand plays an important role in stabilising as well as delocalising the excited state and as a result, stabilising the overall complex. However, from these results it is clear that the diimine (N^N) ligand equally plays a more important role in overall luminescent output. While literature studies generally suggest the optic window of tissue penetration to be quite wide (reports are anywhere between 400 - 2000 nm),[457] the therapeutically relevant window has been identified to be anywhere between 600 – 950 nm.[456–458] Unfortunately, complexes **3-7** to **3-12** do not fit within the therapeutic range despite their modest emission outputs and thus, renders them unsuitable candidate for both further photophysical investigations, and tissue penetration studies for diagnostic imaging.

3.3.7 Stability studies

The rhenium triazolato complexes **3-1** to **3-12** display moderate solubility across a range of and polar aprotic solvents such as ethanol, methanol, acetonitrile, DCM, DMSO and acetone. The subtle structural and lipophilic changes to the complexes do not affect the overall solubility across the series within the DMSO solubilising medium. These observations are also consistent with other studies in the literature indicating the potential for these complexes to show excellent tuneable photophysical properties across a range of solvents.[371,442] To further expand on these studies and assess their ability to be used as potential therapeutic and/or contrasting agents, the triazole set of complexes **3-1** to **3-12** were tested for their solution state stability in a range of deuterated organic solvents across five days.

As photophysical experiments for rhenium(I)-based complexes are typically conducted in deoxygenated acetonitrile or dichloromethane, their deuterated

counterparts were chosen for stability assessment. However, complex **3-9** showed changes within the aromatic region in Acetonitrile-d_3 (MeCN-d_3) over a period of 48 hours. Figure 116 shows complex decomposition starting to occur at time 0 with the appearance of an additional set of signals corresponding to the acetonitrile solvato complex, [Re(phen)$(CO)_3$$(MeCN)^+$]. Simultaneously, the thiolato ligand is protonated and released from the Re(I) metal centre however, due to solution state equilibrium the free triazole is not observed within the spectrum, presumably due to either coalescence with the bound triazole signal, deuterated, or shown as a broad signal. Upon high resolution mass spectrometric analysis of the reaction mixture, isotopic patterns corresponding to the acetonitrile solvato complex, free triazole and bound triazole complexes were observed and over time. This ligand exchange process has been observed with other Re(I) tricarbonyl complexes and is a well-known occurrence.[436,452,455] Due to time constraints solution-state stability studies have not been explored for all twelve Re(I) tricarbonyl ancillary triazole complexes.

In a similar study, Massi *et al*., observed the back bonding of some methylated Re(I) tricarbonyl tetrazolate systems which were susceptible to exchange processes.[419,420] Given the fairly weak back bonding observed for the Re(I)-N tetrazole moiety, it is unsurprising that over time the Re(I)-triazole bond in *fac*-[Re(phen)$(CO)_3$(pyta-t)] **3-9** is reduced and weakened, as a result of the trans effect. Thus, allowing for the liberation of the pyta and concomitant solvent MeCN to coordinate as the ancillary ligand.

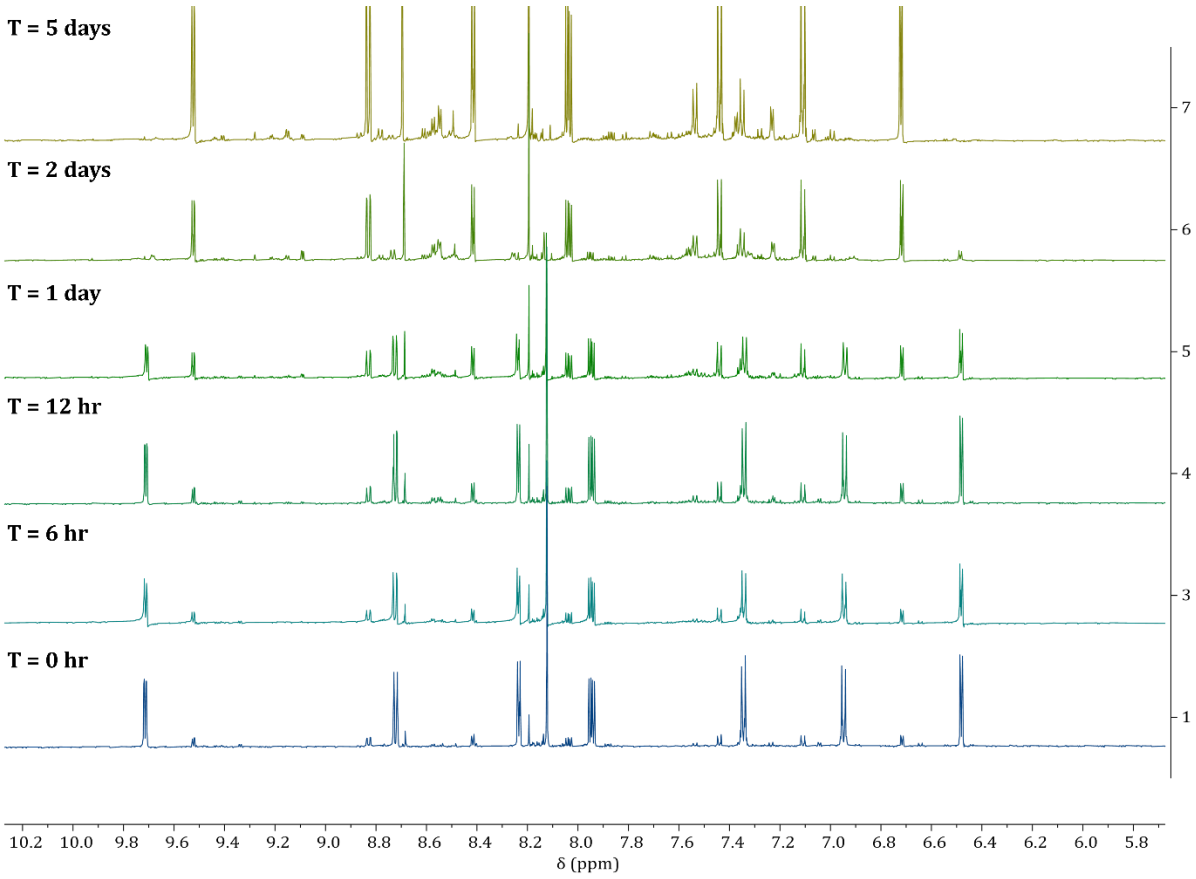

Figure 116: Representative example ^{1}H NMR spectra of complex *fac*-[Re(phen)(CO)$_3$(pyta-t)] **3-9** over a period of 5 days taken in MeCN-d_3 at 25 °C.

Deuterated DMSO-d$_6$ was chosen in proton stability studies due to the universal use of DMSO as a solubilising medium/carrier solvent for many biological experiments. Complex **3-9** showed good solubility and stability in DMSO, with no changes observed to the complex across a five-day period (Figure 117).

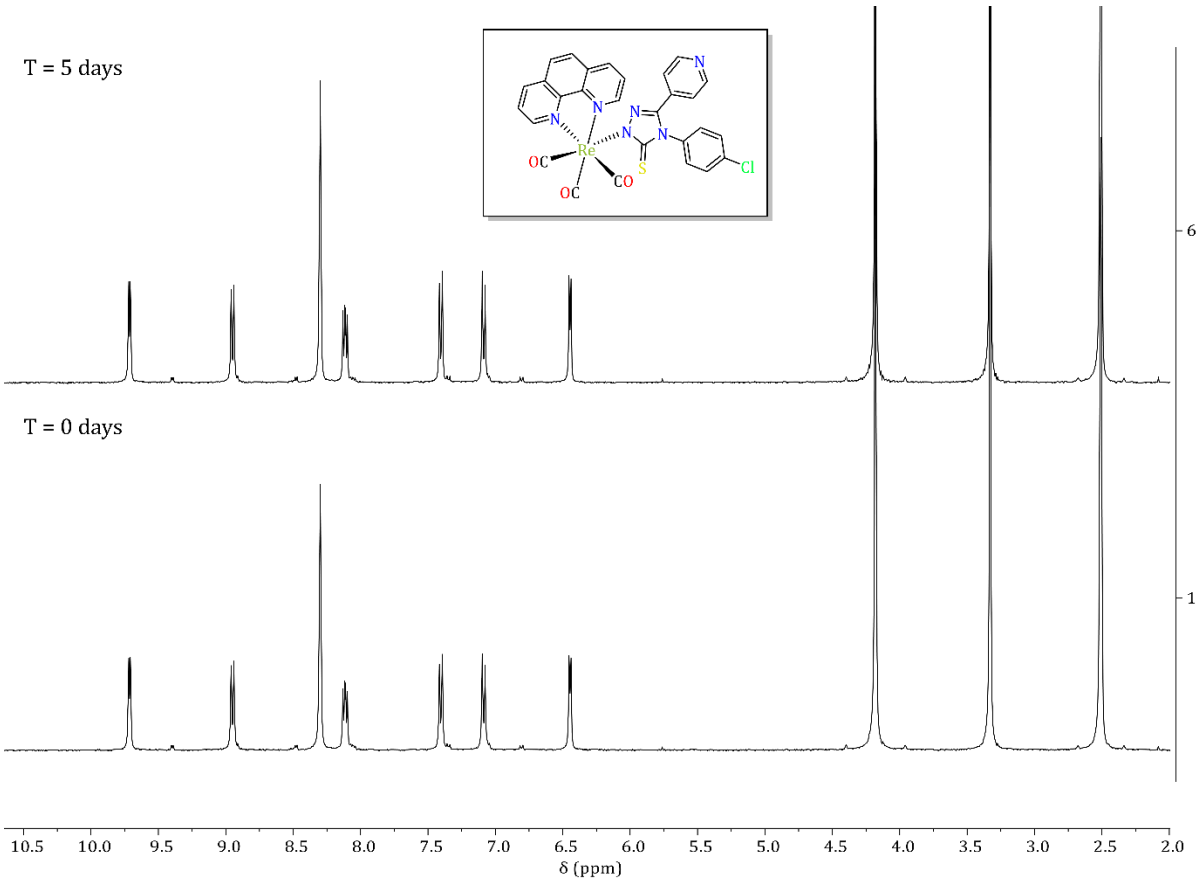

Figure 117: ^{1}H NMR spectrum of complex *fac*-[Re(phen)(CO)$_3$(pyta-t)] **3-9** over a period of 5 days taken in DMSO-d$_6$ at 25 °C.

Re(I) tricarbonyl complexes have been generally considered to be relatively photostable with moderate solubility in polar aprotic solvents. Through variations of the monodentate ancillary ligand, a degree of control can be administered to the uptake and intracellular accumulation.

Overall, from the stability studies conducted in DMSO-d$_6$, complexes **3-9** displays no spectral changes after a period of 48 hours (Figure 117); furthermore, the complexes were not observed to decompose in the presence of air. Therefore, the Re(I) tricarbonyl triazoles complexes can be deduced to have good hydrolytic stability and are thus, suitable candidates for biological testing.

In terms of photophysical investigation however, ^{1}H NMR studies reveal all complexes **3-1** to **3-12** to display poor solution stability in MeCN-*d$_3$* and thus, photophysical experiments were conducted in degassed dichloromethane (DCM).

3.3.7.1 PBS stability studies

Representative examples of the complexes [Re(bpy)(CO)$_3$(pyta-Cl)] **3-3** and fac-[Re(phen)(CO)$_3$(pyta-Cl)] **3-9** were evaluated for their stability in phosphate-buffered saline (PBS, pH = 7.4) solution, measured via UV-visible spectrometry. As discussed in Chapter 2, PBS represents a non-toxic neutral biological buffer which is used extensively in biological assays as a carrier solvent to mimic physiological conditions.

This study served to investigate whether the Re(I) tricarbonyl ancillary triazole complexes are inert to exchange processes with biologically relevant ions, and for reference the parent triazoles were also studied under the same conditions. Solutions containing complexes **3-3** and **3-9** were prepared from DMSO stocks and diluted into 1x PBS to produce final compound concentrations of 30 µM containing 0.4 % (v/v) DMSO and the absorption spectra of each respective solution was recorded in regular intervals over a period of 48 hours with the results summarised in Figure 118.

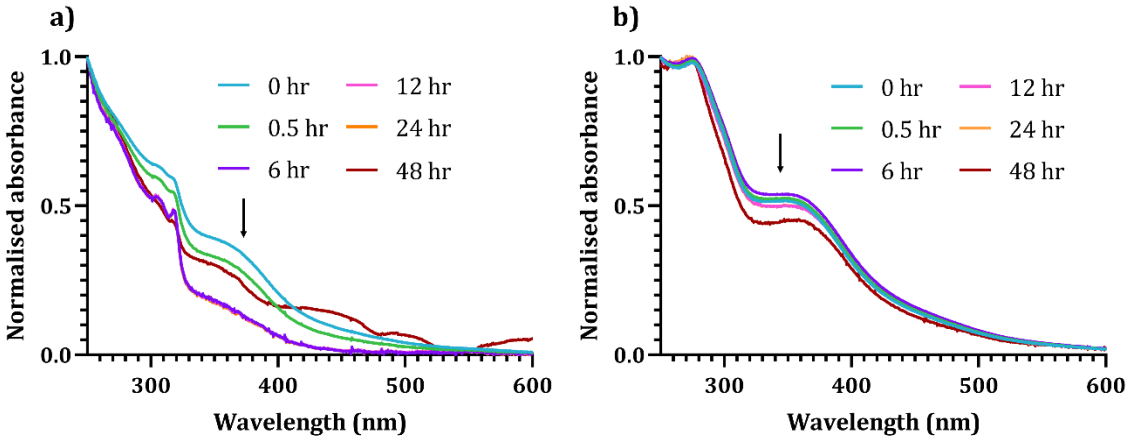

Figure 118: Changes to the absorption spectra of **a)** [Re(bpy)(CO)$_3$(pyta-Cl)] **3-3** and **b)** fac-[Re(phen)(CO)$_3$(pyta-Cl)] **3-9** in phosphate buffered saline (PBS) solution over 48 hours. The final DMSO concentration for both solutions were 0.4 % (v/v).

Between the two series of bpy (**3-3**, Figure 118, left) and phen (**3-3**, Figure 118, right) derived Re(I) tricarbonyl ancillary triazoles complexes, the absorption profiles show different patterns. However, both complexes show a decrease in absorption intensity over time with complex **3-9** stabilising after 24 hours. Additionally, both spectra show no associated red-or blue-shifted bands which could indicate the rapid precipitation

of the complex from solution over time, as evidenced by the appearance of a fine precipitate in which deposited within the quartz cuvette after the 48-hour studies were complete. Interestingly, the absorbance spectra of complex **3-3** at time 0 shows two major absorbance bands centred at *ca.* 320 and *ca.* 360 nm associated with the intraligand $\pi \rightarrow \pi^*$ transitions however, as time progresses, a more pronounced decrease in absorption intensity and general progression to a broad and characterless absorption profile is observed at 48 hours.

Overall, the absorption profiles for complexes **3-3** and **3-9** both appear to undergo changes over time indicating that the complexes are susceptible to ligand exchange processes in the presence of an aqueous medium. These complexes do not appear to be stable in PBS.

3.3.7.2 Media stability studies

To gain a better understanding of the stability of the Re(I) tricarbonyl ancillary triazole complexes, complexes **3-3** and **3-9** were evaluated in the presence of Dulbecco's Modified Eagle Medium (DMEM) cell culture media with the results illustrated in Figure 119. Using UV-visible spectrometry, the respective solutions were prepared from DMSO stocks and diluted into DMEM supplemented with foetal bovine serum (FBS) to produce final compound concentrations of 30 μM containing 0.4 % (v/v) DMSO. Spectral data for complexes **3-3** and **3-9** were collected and analysed at regular intervals over a period of 48 hours with the results summarised in Figure 119.

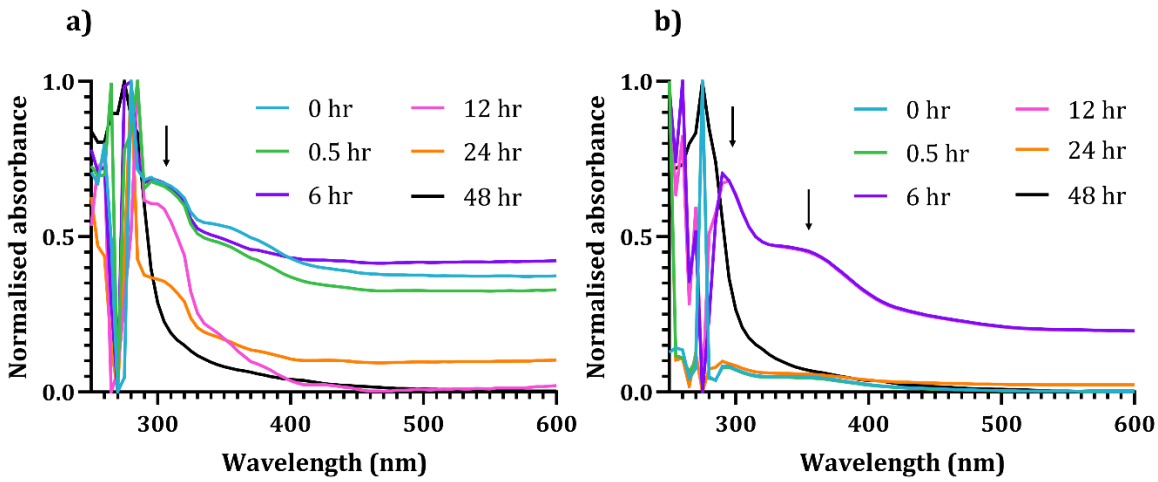

Figure 119: Changes to the absorption spectra of **a)** [Re(bpy)(CO)$_3$(pyta-Cl)] **3-3** and **b)** fac-[Re(phen)(CO)$_3$(pyta-Cl)] **3-9**, DMEM culture media supplemented with 10% FBS over 48 hours. The final DMSO concentration was 0.4 % (v/v).

From the spectral data obtained, an apparent decrease in absorption intensity is observed for complex **3-3** over time with the decrease in absorption maxima at *ca.* 320 nm (Figure 119, left). Although no precipitation was observed within the quartz cuvette at the completion of the 48-hour study, it is evident that the complex is significantly changing as the experiment progresses. The absorption spectrum of complex **3-9** (Figure 119, right) shows a strong band at *ca.* 275 nm at t = 30 minutes, however this signal appears to undergo a hypsochromic shift and is associated with the increase in spectrum intensity at 6 and 12 hours with apparent absorbance maxima at *ca.* 290 nm and *ca.* 360 nm, postulated to be associated with the intraligand $\pi \rightarrow \pi^*$ transitions of a new species. Beyond 24 hours, the spectra are observed to stabilise at *ca.* 275 nm.

From these preliminary experiments, it is clear that complexes *fac*-[Re(bpy)(CO)$_3$(pyta-Cl)] **3-3** and *fac*-[Re(phen)(CO)$_3$(pyta-Cl)] **3-9**, could be unstable in cell culture media under ambient conditions. It is postulated that the lability of the ligand could be causing structural alterations to the complexes upon exposure to serum albumins. Lazniewska *et al.,* have observed this activity with a series of neutral Re(I) tetrazolato complexes upon whereby a strong affinity for BSA was observed through the apparent changes in the fluorescent emission.[459]

3.3.7.3 Glutathione stability studies

In a reaction with the mixed N-S nucleophilic cysteine molecule, when undertaking ^{1}H NMR stability studies the resulting complexes were observed to precipitate over a period of 24 hours. High resolution mass spectrometry (HRMS) analyses of the residues were conducted and shown to be in agreement of the formation of a Re(I) diimine tricarbonyl complexes bearing a cysteine residue. This has been described within the literature before with a series of diimine chloromethyl analogues whereby a series of cationic Re(I) complexes were reacted with the cysteine methyl ester resulting in *S*-alkylation.[389] In the same study, the treatment of the Re(I) complex in the presence of reduced glutathione (GSH) resulted in the formation of a glutathione-rhenium(I) conjugate, also confirmed by HRMS.[389]

As discussed in chapter 2, the dissociation of the pyta ligands from the Bi(III) metal centre in the presence of glutathione can be observed therefore, it was worthwhile investigating whether the aforementioned ligands in the ancillary form, would dissociate from a Re(I) tricarbonyl system. The stability of the representative examples **3-3** [Re(bpy)$(CO)_3$(pyta-Cl)] and **3-9** [Re(phen)$(CO)_3$(pyta-Cl)] in the presence of GSH was evaluated using UV-Visible spectroscopy. The respective solutions were prepared using the methods outlined in chapter 2 and due to the low solubility of both complexes, DMSO stock solutions were prepared and diluted accordingly to give final Re(I) complex concentrations of 30 μM.

The UV-visible spectra of both **3-3** and **3-9** in the presence of GSH showed similar features over the 48-hour experiments with relatively simple profiles. Both spectra showed a general decrease in the intensity of major absorption bands. In Figure 120 spectrum **a)** corresponding to the Re(I) bpy complex **3-3** shows a 36% decrease in the intensity of absorption band at *ca.* 300 nm and complete diminishment of the band at *ca.* 360, both bands are associated with the π→π* IL transitions of the Re(I)-bound triazole. In Figure 120 spectrum **b)** corresponding to the Re(I) phen complex **3-9** however, a 75% decrease associated with the π→π* IL transitions of the Re(I)-bound triazole can be observed.

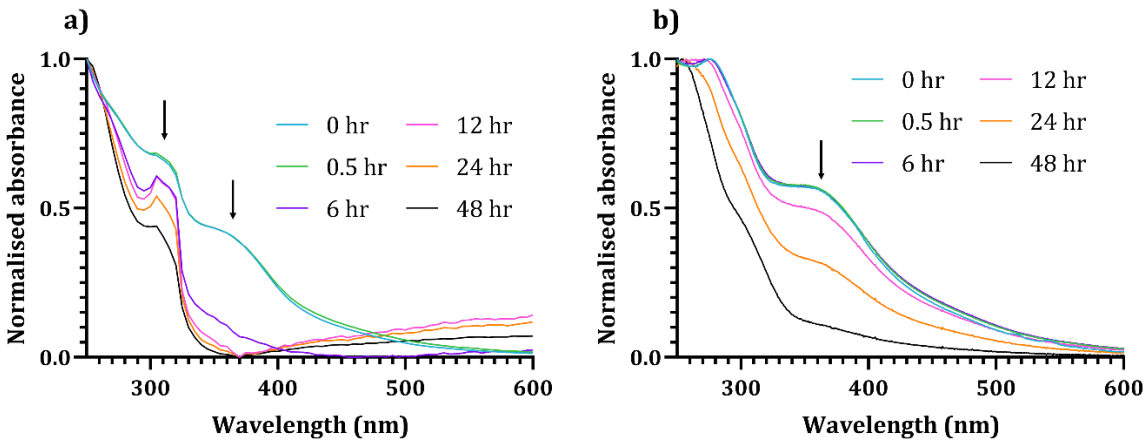

Figure 120: Changes to the absorption spectra of **a)** [Re(bpy)(CO)$_3$(pyta-Cl)] **3-3** and **b)** fac-[Re(phen)(CO)$_3$(pyta-Cl)] **3-9**, in the presence of 3 mM GSH (100 mol. equivalents) in PBS over 24 h. The final DMSO concentration was 0.4 % (v/v).

Overall, the results obtained by complexes **3-3** and **3-9** indicate that the heteroleptic Re(I) tricarbonyl ancillary triazole complexes react with GSH to form Re(I)-GSH species as confirmed through UV-visible spectroscopic. It may therefore be inferred that upon exposure to a glutathione-rich environment (such as a mammalian cell) that the triazole ligands do not remain coordinated to the Re(I) metal centre.

3.3.8 Biological studies

Given the successful release of the Re(I) tetrazolato-based staining agent ReZolve-ER™, biological investigations were pursued to evaluate the potential of Re(I) tricarbonyl triazole thiones as potential therapeutic agents, antibacterial agents or antifungal agents.[421,424] Initially, cellular viability experiments were conducted by incubating a selection of the prepared Re(I) complexes with cos-7 primary monkey kidney cells. These experiments were carried out to determine the behaviour of the complexes in a biological environment and assess how small structural changes may affect uptake, localisation and/or toxicity within cells.

Due to their superior photophysical performance, only the phen analogues **3-7** to **3-12** were investigated in addition, due to laboratory restrictions and time constraints, the bpy analogues were not explored. As the Re(I) tricarbonyl complexes were not water soluble, DMSO was used as a carrier solvent to solubilize them into aqueous cellular media.

3.3.8.1 Mammalian cell viability

The results obtained for the Re(I) triazole complexes show a reduced cell viability for complexes **3-1** to **3-6** whereby the viability falls below 80%. After the assessment of both antifungal activity and effect on cell viability against cos-7 cells, it is crucial to determine the ability of the complexes to selectivity inhibit pathogenic fungi in the presence of mammalian cells, especially given the structural similarities of each eukaryotic cell line. The selectivity index (SI) is defined as the ratio between antifungal activity (MIC) and the IC_{50} against cos-7 cells, calculated by the formula SI = IC_{50}/MIC. Medicinally, high SIs are most favourable as they show the potential of a complex to have a safe *in vivo* profile.[358]

Generally, for the rhenium(I) series of complexes, the calculated cellular viability shows that the viability tends to increase above >100%. This phenomenon has been observed in similar mammalian assay studies and can be attributed to the localisation of compound around the cellular membrane as well as the higher interaction of rhenium complex with membrane bound proteins. Due to time constrains, the cellular uptake of the diimine derivatives were not conducted.

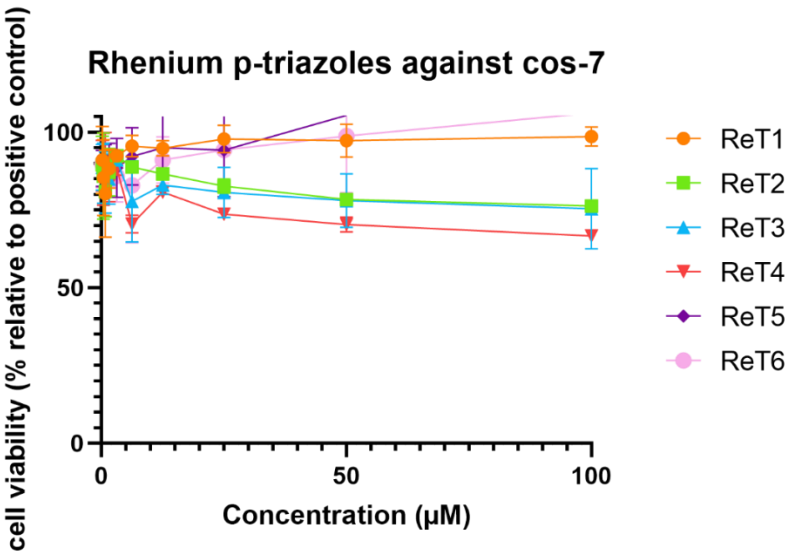

Figure 121: MIC % growth against a control of complexes **3-1** to **3-6** against cos-7. Dose response curves generated over a range of concentrations (0 – 100 μM) in the appropriate culture media from 10 mM DMSO stock solutions. Readings were compared spectroscopically to non-treated control and the percent growth inhibition calculated.

3.3.8.2 Antibacterial testing

In surveying the literature, the enhanced antimicrobial activity of the Re(I) complex over the free ligands has been postulated to be due to the high lipophilicity of the Re(I) metal. In reference to chelation theory, as π electrons become increasingly delocalized across the diimine backbone, this may cause the polarity of the ligand and central rhenium(I) ion to decrease. The reduced polarity may allow the complex to penetrate the lipid bilayer of the cell membrane where azole can prevent microbial cell growth therefore, the antibacterial activity of the Re(I) phenanthroline ancillary triazoles were tested against one Gram-negative bacterial strain; *Escherichia coli* (*E. coli*), and two Gram-positive bacterial strains; vancomycin resistant *enterococcus* (VRE), and methicillin resistant *staphylococcus aureus* (MRSA).

The antibacterial activity of the rhenium(I) triazole complexes **3-7** to **3-12** of the form [Re(phen)(CO)$_3$(L)] (where L = one of pyta, pyta-t, pyta-Cl, pyta-2Me, futa or futa-Cl) were evaluated via the solution-based broth microdilution assay. The complexes were initially solubilised in DMSO at concentrations of 10 mM, followed by the 1:100 dilution in the respective bacterial broths. The final maximum DMSO concentrations were calculated to be 1%. The complexes were added to 96 well plates followed by a two-fold dilution with the bacterial culture added to each well and incubated at 37 °C overnight. Absorbance data was acquired using a microplate reader set at 600 nm, whereby the broth alone was treated as a blank, solutions of the complexes with the respective BHI and LB broths were treated as the negative control and broths containing 100 % of bacterial growth were treated as the positive control. Figure 122 outlines the growth curves of three assays conducted against VRE, MRSA and *E. coli*.

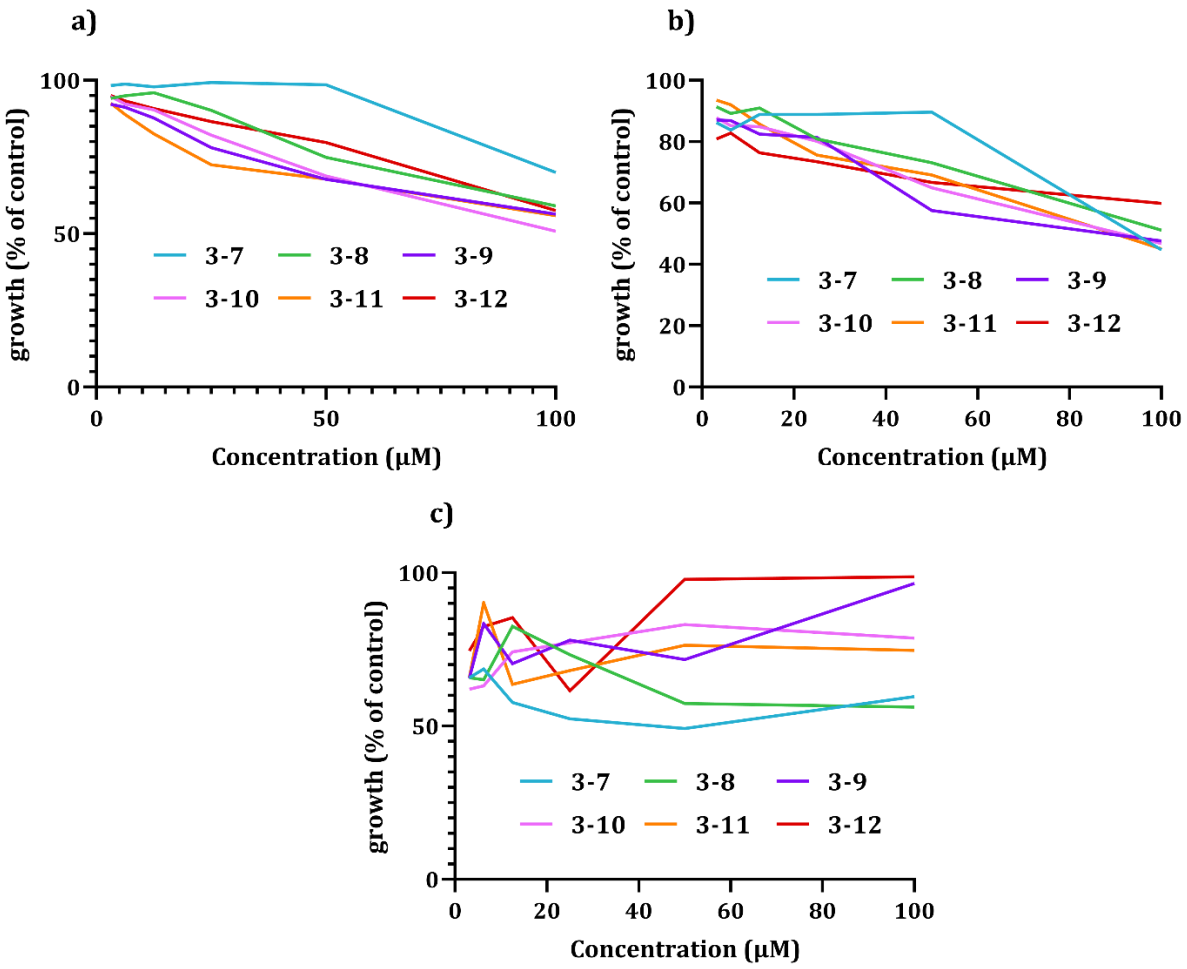

Figure 122: Normalized MIC % growth curves of **a)** VRE **b)** MRSA and **c)** E. coli treated with complexes **3-7** to **3-12** of the form [Re(phen)$(CO)_3$(pyta)] Dose response curves generated over a range of concentrations (3.125 – 100 μM) in the appropriate culture media acquired from 10 mM DMSO stock solutions. Readings were compared spectroscopically to non-treated control and the percent growth inhibition calculated.

From the preliminary MIC results obtained, all of the complexes appear to show a general decrease in bacterial cell viability with increasing concentration when tested against the Gram-positive bacteria, VRE and MRSA. As observed in chapter 2 with the heteroleptic Bi(III) triazoles, a small range of MICs was observed across the spectrum of the Re(I) phenanthroline triazoles which also suggests that minor changes in the 'R' groups had little change in microbial activity.

Interestingly, the growth curve observed for the set of complexes tested against *E. coli* shows more unpredictable results whereby the bacterial cell viability increases with

increasing concentration. This could potentially be due to solubility issues whereby the complex is precipitating out of solution over time.

Overall, the MIC of the complexes **3-7** to **3-12** do not appear to greatly affect the bacterial cellular viability however, the antibacterial assays appeared to have inconsistencies when tested on a selection of compounds. Further studies are required to completely elucidate the antibacterial activity of complexes **3-1** to **3-12**.

3.3.8.3 Antifungal testing

Antifungal studies of the heteroleptic phenanthroline-based rhenium(I) tricarbonyl ancillary triazole complexes (**3-7** to **3-10**) were undertaken in collaboration with Dr. Claudia Simm within the Biomedical Discovery Institute (BDI) whereby the complexes were assessed for their antifungal activity via solution-based broth microdilution methods as described in the Minimum Inhibitory Concentration (MIC) dilution Warwick protocol.[460,461] The precursor **RePS** along with complexes **3-7** to **3-10** were tested against *Candida albicans* (*C.* albicans) as outlined in Figure 123. Due to time constraints and COVID-19 restrictions however, not all complexes were taken forward for solution-based testing.

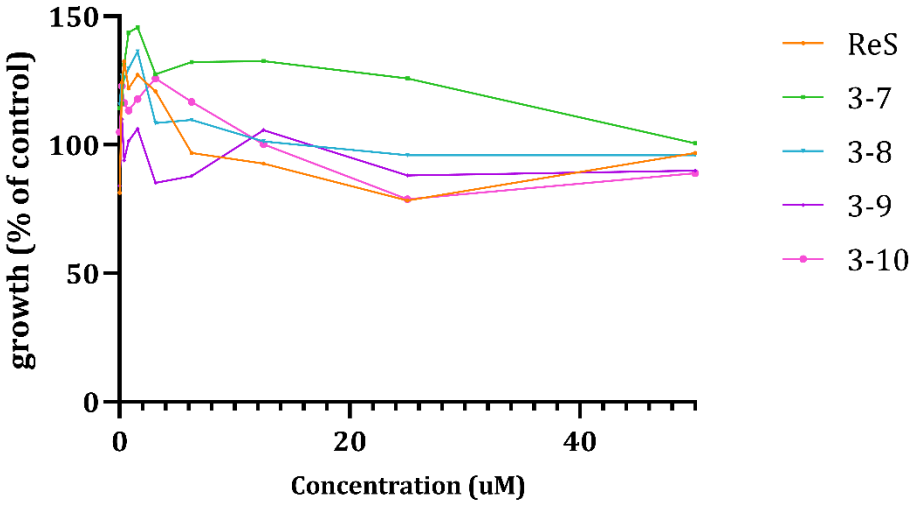

Figure 123: Normalized MIC % growth curves of C. albicans treated with the precursor rhenium(J) solvato-complex **RePS**, and complexes **3-7** to **3-10**. Dose response curves generated over a range of concentrations (0 – 50 µM) in the appropriate culture media

acquired from 10 mM DMSO stock solutions. Readings were compared spectroscopically to non-treated control and the percent growth inhibition calculated.

Observed in Figure 123, the growth curve of *C. albicans* upon exposure to the Re(I) ancillary triazole complexes **3-7** to **3-10** were shown to exhibit no reasonable activity against the fungal cells, with IC_{50} values exceeding 50 μM. In addition to the inactivity, complexes **3-7** and **3-8** were also observed to precipitate out of solution, indicating the low solubility in the growth medium. These results are unsurprising given the relatively high degree of lipophilicity detailed by similar types of Re(I) tricarbonyl-based complexes within the literature.[166,256,377,462]

Part 2: Results and discussion – backbone triazoles

3.3.9 Synthesis and spectroscopic characterization of o-pyridyl-1,2,4-triazole-3-thiones

The triazole thione precursors **14-17** were used as parent ligands for the formation of Re(I) backbone triazole complexes and followed the similar procedures outlined in Section 2.3.1 (Scheme 9), adapted from the modified synthesis by Youssef *et al.,* (Scheme 11).[338,437] In this section, picolinohydrazide (PH) was used in lieu of the isonicotinohydrazide (INH) as a precursor and the synthesis of the PH precursor involved a telescopic Fischer esterification followed by a solvent-free dehydration/condensation and organic work up in 78 % yield.

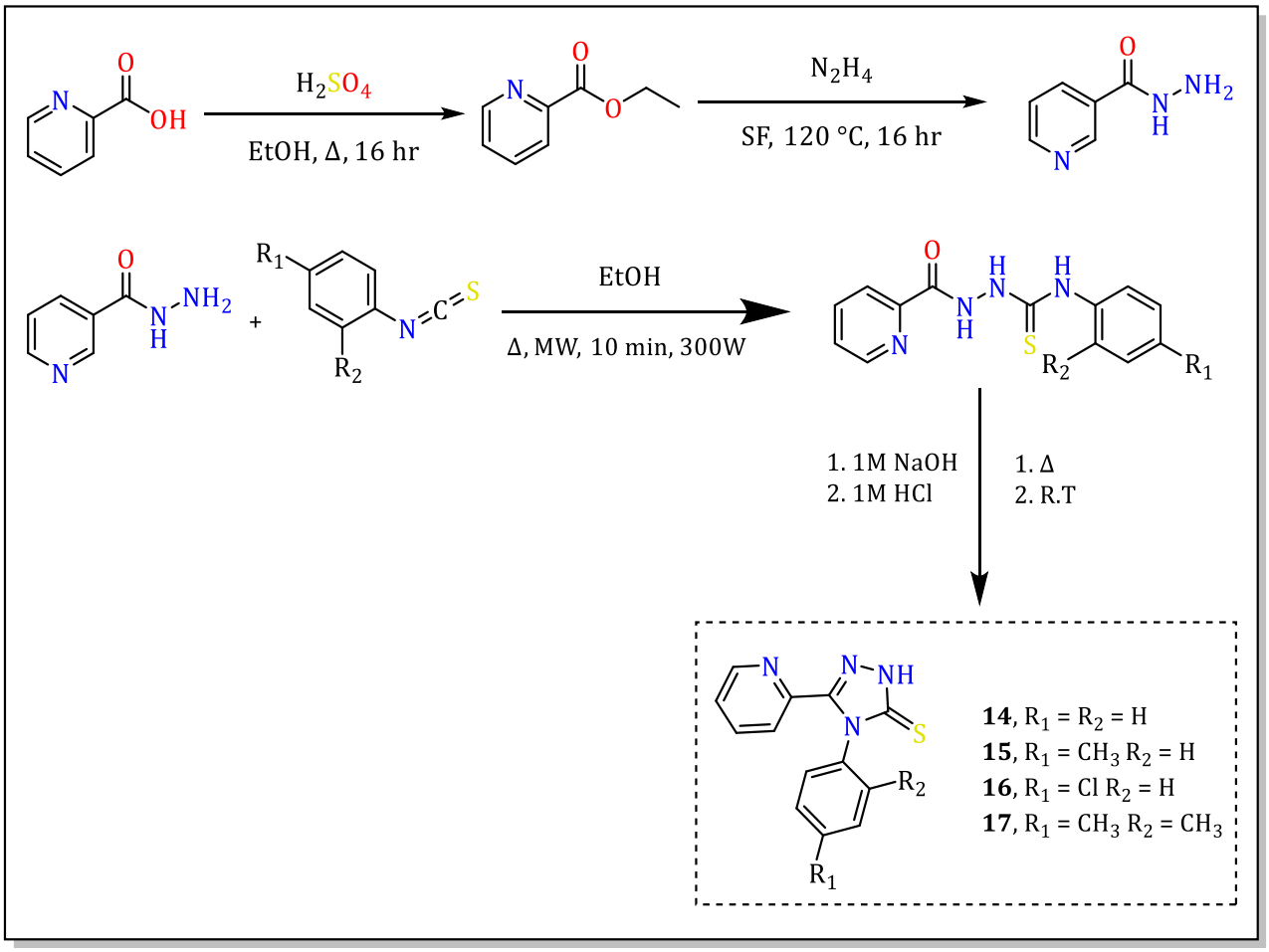

Scheme 11: Preparation of 2-pyridyl substituted thiones **14-17** from picolinic acid, picolinohydrazide and substituted aryl isothiocyanates.

The final triazoles: 4-phenyl-5-(pyridin-2-yl)-2,4-dihydro-3H-1,2,4-triazole-3-thiol (py2ta*H*, **14**), 5-(pyridin-2-yl)-4-(p-tolyl)-2,4-dihydro-3H-1,2,4-triazole-3-thiol (py2ta-t*H*, **15**), 4-(4-chlorophenyl)-5-(pyridin-2-yl)-2,4-dihydro-3H-1,2,4-triazole-3-thiol (py2ta-Cl*H,* **16**), and 4-(2,4-dimethylphenyl)-5-(pyridin-2-yl)-2,4-dihydro-3H-1,2,4-triazole-3-thiol (py2ta-2Me, **17**) were chosen as substrates for the formation of Re(I) complexes and were characterised by ^{1}H NMR and ^{13}C NMR spectroscopy, high resolution mass spectrometry, FT-IR spectroscopy and melting point analysis in accordance with the literature values.[338]

3.3.10 Synthesis of backbone Re(I) o-triazole complexes

Extensive studies have concluded that a chemical modification of the ancillary ligands coordinated to the rhenium(I) metal centre in turn changes the photophysical and biological effects of each complex.[427,428,442,453,454,463] Section 3.3 has introduced the triazole class of ligands acting as ancillary ligands however, to further expand on these investigations through chemical modifications to the chelate/diimine ligand. A design strategy was adopted whereby the synthesised *ortho*-pyridyl precursors **14-17** would coordinate to the Re(I) tricarbonyl core either through the monodentate N-pyridyl pendant arm or bidentate through the N-pyridyl and N-triazole moieties. Additionally, the synthesis of this new sub-class of triazole ligands would identify the function of the diimine chelate and ancillary triazole ligand in reference to photophysical and biological properties.

Four novel Re(I) tricarbonyl complexes **3-13** to **3-16** of the general form *fac*-[Re(N^N)(CO)$_3$X] (whereby N^N = *ortho*-pyridyl triazole thione) have been synthesised with varying substitutions on the triazole aryl ring following the reaction scheme outlined in Scheme 12.

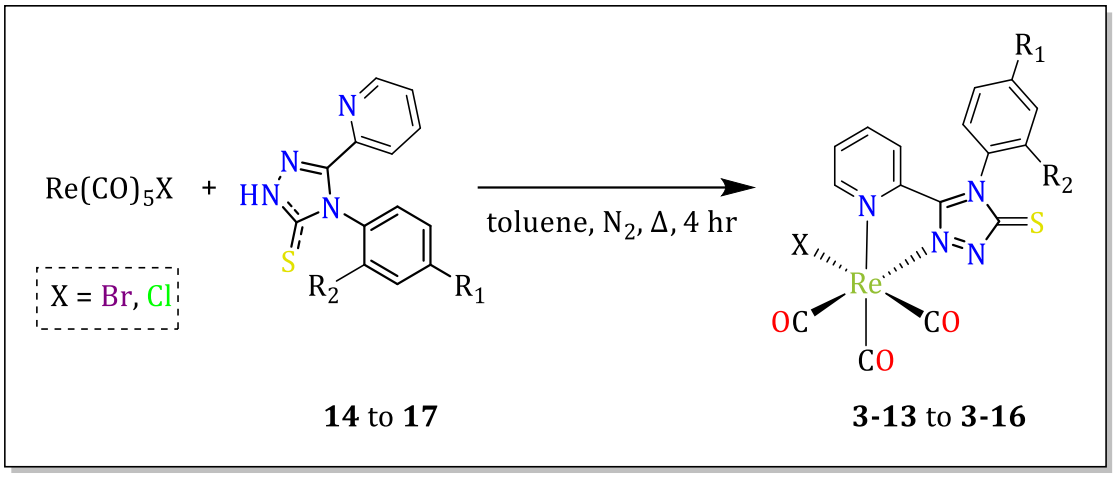

Scheme 12: Synthetic methods used to prepare rhenium(I) tricarbonyl complexes of the form *fac*-[Re(N^N)(CO)$_3$X] **3-13** to **3-16** from triazoles **14-17**.

Using Schlenk protocols, the reactions were carried out via a one-pot route whereby a pentacarbonyl rhenium(I) halide precursor and corresponding *ortho*-triazole thione substrate **14-17** were heated in toluene for four hours. The reaction mixtures were observed to change from opaque white to bright orange solutions, with the resulting complexes precipitating from the reaction solution as orange solids. Following isolation via gravity filtration, led to yields of 75-96 % (Table 20) after washing the product with small amounts of toluene, THF and Et$_2$O and drying *in vacuo.* The four complexes **3-13** to **3-16** are air and moisture stable and soluble in most polar organic solvents such as ethanol, methanol, THF, toluene, DMSO and DCM. The complexes display sparing solubility in water and non-polar solvents such as hexane and petroleum benzine. The novel complexes were characterised via ^{1}H NMR and ^{13}C NMR spectroscopy, FT-IR spectroscopy, HRMS, melting point and microanalysis. While one crystal structure has been isolated, the ^{1}H NMR data of the compounds suggests successful binding to the Re(I) metal centre occurs through the *ortho*-pyridyl N(4) and triazole N(2) atoms.

Table 20: Summary of yields and appearances of Re(I) tricarbonyl complexes of the form *fac*-[Re(N^N)(CO)$_3$Cl] (where N^N = *ortho*-pyridyl triazole thione) **3-13** to **3-16** (d.c. refers to decomposition).

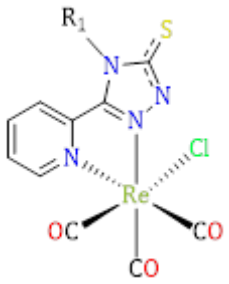

	Complex	Functional group (R_2)	Yield (%)	Melting point	Appearance
3-13	*fac*-[Re(py2ta)(CO)$_3$(Cl)]	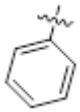	75	>300 (d.c.)	Orange solid
3-14	*fac*-[Re(py2ta-t)(CO)$_3$(Cl)]	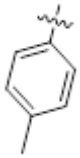	96	>300 (d.c.)	Orange solid
3-15	*fac*-[Re(py2ta-Cl)(CO)$_3$(Cl)]	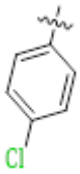	84	>300 (d.c.)	Orange solid
3-16	*fac*-[Re(py2ta-2Me)(CO)$_3$(Cl)]	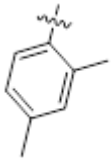	78	>300 (d.c.)	Orange solid

3.3.11 NMR spectroscopy

3.3.11.1 ^{1}H NMR studies

Analysis of the solution state structures of the rhenium(I) tricarbonyl complexes **3-13** to **3-16** were compared to their precursors and all spectra were observed to match with the desired complexes.

Figure 124 shows the comparative analysis of complex **3-14** (Spectrum 1) against the precursor triazole py2ta-t*H* **15,** whereby a series of consistent trends were observed across the series of complexes. Characteristic of all of the Re(I) tricarbonyl triazolato complexes was a marked absence of the sharp signal between 14-15 ppm corresponding to the protonated -NH upon complexation. Observing the pyridyl segment of the metal complex, upon coordination to the Re(I) metal centre, the ligand *ortho*-pyridyl signal closest to the N-donor shifts downfield from 8.37 ppm to 9.31 ppm (denoted by signal **1** in spectrum 1 and 2, Figure 124). Additionally, the *meta*- and *para*-pyridyl signals (**2** and **3**) also undergo modest downfield shifts from 7.39 ppm to 7.51 ppm, and 7.90 ppm to 8.10 ppm, respectively. However, presumably due to a shift in chemical equivalency of the phenyl-triazole segment of the molecule, aromatic coupling of the *ortho*-pyridyl signal **4** is observed to undergo a minor upfield shift as well as change in multiplicity.

Notably, the phenyl-triazole signals all undergo shifts upon metal complexation with the *ortho*-phenyl signal undergoing an appreciable shift to higher frequencies from 7.22 ppm to 6.86 ppm (**11**, **12**). Interestingly upon complexation, the *meta*-phenyl proton signals are non-equivalent due to the shift from a planar arrangement to a three-dimensional framework which in turn, changes the multiplicity and total number of chemical environments in the metal complex. The *meta*-phenyl triazole protons split from 7.15 ppm to 7.47 ppm and 7.32 ppm for protons **9** and **10**, respectively.

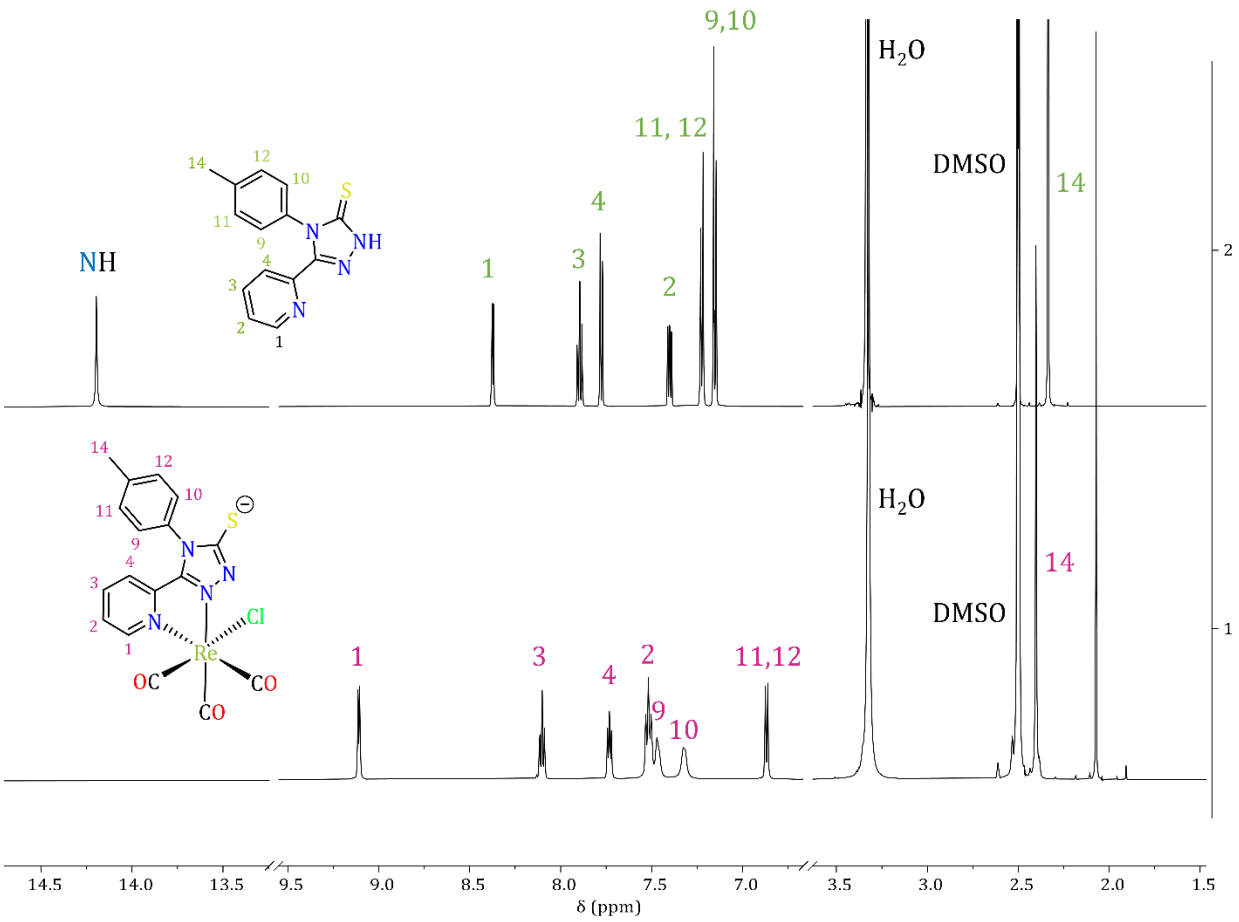

Figure 124: ^{1}H NMR spectra of the *ortho*-pyridyl triazole py2ta-t*H* **15** (Spectrum 2); and complex *fac*-[Re(py2ta-t)(CO_3)Cl] **3-14,** (spectrum 1); taken in DMSO-d_6 at 25 °C.

3.3.11.2 ^{13}C NMR studies

Similar to the twelve neutral Re(I) ancillary triazole complexes, not all of the ^{13}C NMR of the Re(I) backbone triazole complexes were obtained due to solubility issues however, comparative analysis of the ^{13}C NMR spectra of *fac*-[Re(py2ta-t)(CO_3)Cl] **3-14** and the precursor py2ta-t*H* **15** illustrated in Figure 125 shows all of the expected signals associated in a substituted triazole.

As observed in the neutral Re(I) tricarbonyl ancillary triazole complexes **3-1** to **3-12**, the ^{13}C NMR spectra suggests the formation of one neutral product in all cases. This is supported by the presence of a single set of CO and aromatic signals. In the spectrum of **3-14** (Figure 125, spectrum 1), three low intensity signals were identified and corresponded to the Re(I)-CO environments at δ = 197.4, δ = 197.0 and δ = 188.7. According to the C_s symmetry of the Re(I) triazole complexes, the two equatorial CO

ligands could be inequivalent due to the mesomeric effects of the *ortho*-pyridyl triazole situated *trans* to these environments forming a chelate ring/bidentate coordination environment. Although these signals are fairly weak and not well resolved, the presence of all three carbonyl environments fits well with the literature and correlating well to the *facial* configuration, as observed for the neutral Re(I) ancillary triazoles.[431,442]

The precursor py2ta-t*H* **15**, exists in the thione state evidenced by the downfield shifted signal present at δ = 174.3 correlating to the C(7)=S. However, upon complexation to the Re(I) metal centre, this signal undergoes an upfield shift to δ = 155.4 in addition to a general upfield shift of all other carbon atoms with the exception of the *ortho*-pyridyl C(1) and C(3). In this system, the same deshielding and mesomeric effects of the triazole ring are not observed, presumably due to the rigid coordination of the N(4) and N(1) atoms to the Re(I) metal centre. With the exception of the C(7)=S shift, no other notable trends are observed.

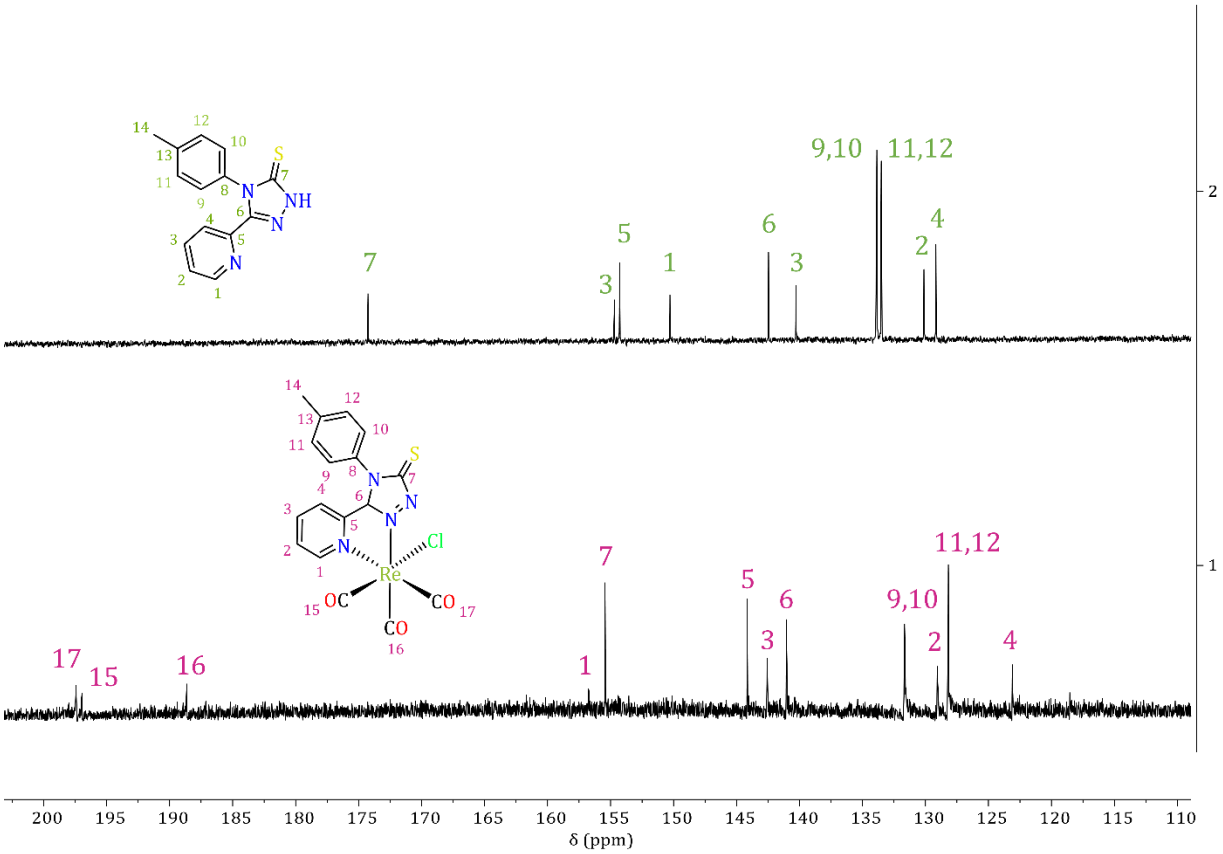

Figure 125: ^{13}C NMR spectra of *ortho*-pyridyl triazole py2ta-t*H*, **15** (spectrum 2); and *fac*-[Re(py2ta-t)(CO_3)Cl], **3-14** (spectrum 1); and taken in DMSO-d_6 at 25 °C.

3.3.12 FT-IR spectroscopy

FT-IR spectroscopy was utilised to provide insights into the binding nature of the free triazole thiolates **14** to **17** and the complexes **3-13** to **3-16** via analysing the changes in the Re(I)-CO absorption bands (Table 22) and confirm the synthesis of the novel Re(I) complexes. Similar to the precursors synthesised in section 2.3.5, identifying the characteristic stretching vibrations of the precursor triazole thiones **14** to **17** proved to be difficult due to the coupling effects from neighbouring atoms and mixed absorption bands present in the 1500-1000 cm^{-1} region.[340,342] In saying that, the *ortho*-pyridyl substrates **14** to **17** were also confirmed to be stable in the thione form through the absence of the *ν*(S-H) between 2650-2550 cm^{-1} as well as the absence of the C-S-H-in plane bending modes between 850-918 cm^{-1}.[340,342,344] The influence of heteroaromatic ring-stretching, ring-bending, in- and out of plane deformations were also postulated to be present for these precursors, as observed for precursors **1-6**.[346]

Table 21: Characteristic FT-IR assignments in triazole thione precursors **14** to **17**. (br) = broad, (s) = strong (m) = moderate. **pyr**= pyridine, **tz**= triazole.

Precursors		ν(N-H)	ν(C=S)	$\nu(C\text{-}N)_{pyr}$	$\nu(C\text{-}N)_{tz}$
14	**Py2ta*H***	2920	794	1327	1490
15	**Py2ta-T*H***	2921	793	1326	1492
16	**Py2ta-Cl*H***	2925	744	1327	1492
17	**Py2ta-2Me*H***	2907-2759	779	1274	1493

The successful coordination of the triazole thione ligand to the Re(I) tricarbonyl moiety is indicated through the appearance of three characteristic bands in the 2000-1850 cm^{-1} region of the FT-IR spectra. Analysis of the four complexes **3-13** to **3-16** show characteristic bands corresponding to the coordinated Re(I)-CO ligands, as observed in the literature (Table 22).[453] The characteristic ν(CO) stretching vibrations of complexes **3-13** to **3-16** are shown to have shifted to higher stretching frequencies by 10-13 cm^{-1} when compared to the reference **ReB** and **ReP** precursors (Table 22).[453] It is postulated that the shifting of these bands to longer wavelengths occurs as a result of the donor ability of the py2ta ligand.

Complexes *fac*-[Re(py2ta-Cl)$(CO)_3$Cl] **3-15**, and *fac*-[Re(py2ta-2Me)$(CO)_3$Cl] **3-16**, show an overlapping and coalescence of the total symmetric out-of-phase stretching, and asymmetric stretching frequencies associated with the v(CO) band (Table 22). This could potentially be due to the various functionalities present within the complexes.

Given the small sample size, a conclusion could not be drawn as to whether the coordination of the triazole thione to the Re(I) metal centre was occurring through the sulfur or nitrogen atom, as reported in Chapter 2. However, it appears that these

rhenium species exhibit similar stretching frequencies to other pyta-derived Re(I) tricarbonyl complexes featured in the literature.[431,442]

Table 22: CO stretching frequency values in cm^{-1} of complexes **3-13** to **3-16** where A= symmetric in-phase stretching, B= total symmetric out-of-phase stretching and C = asymmetric stretching.

	Neutral complexes	ν(CO) stretching frequency		
		A	B	C
ReB	*fac*-[Re(bpy)(CO)$_3$(Cl)]	2014	1923	1885
ReP	*fac*-[Re(phen)(CO)$_3$(Cl)]	2013	1891	1872
3-13	*fac*-[Re(py2ta)(CO)$_3$Cl]	2026	1915	-
3-14	*fac*-[Re(py2ta-t)(CO)$_3$Cl]	2024	1924	1884
3-15	*fac*-[Re(py2ta-Cl)(CO)$_3$Cl]	2023	1906	-
3-16	*fac*-[Re(py2ta-2Me)(CO)$_3$Cl]	2026	1912	-

3.3.13 X-ray crystallography

Single crystals of *fac*-[Re(py2ta)(CO)$_3$Br] **3-13** and *fac*-[Re(py2ta-Cl)(CO)$_3$Br] **3-15** were obtained from the slow evaporation of dichloromethane. However, both sets of crystals deemed unsuitable for solid-state structural elucidation. Nonetheless, the general connectivity of the complexes was determined. X-ray crystallographic analysis illustrates the formation of the Re(I)-N1 linkage isomer in the solid-state for complexes **3-13** and **3-15**, as depicted in Figure 126 and Figure 127. The solid-state data supports the conclusions which have been drawn from the analysis of the ^{13}C NMR whereby the formation of the N2 linkage isomer was not observed in both the

solid and solution states. A summary of selected bond lengths and angles for **3-13** is presented in Table 23.

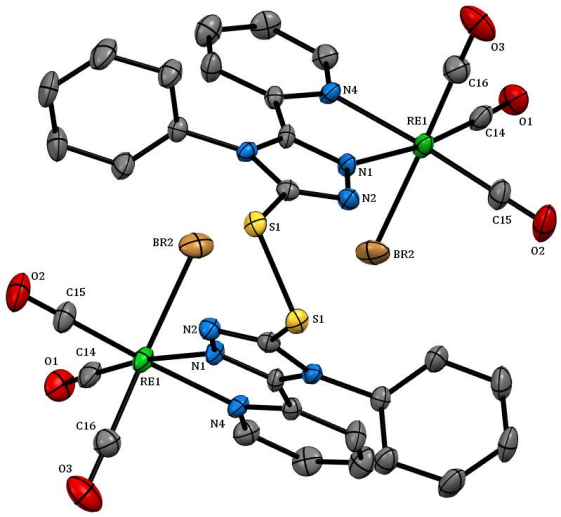

Figure 126: Asymmetric unit of complex *fac*-[Re(py2ta)$(CO)_3$Br] **3-13.** Thermal ellipsoids are shown at the 50% probability level. Hydrogen atoms have been omitted for clarity. Disorder of the terminal ends of the CO and Br atoms have been modelled over two positions.

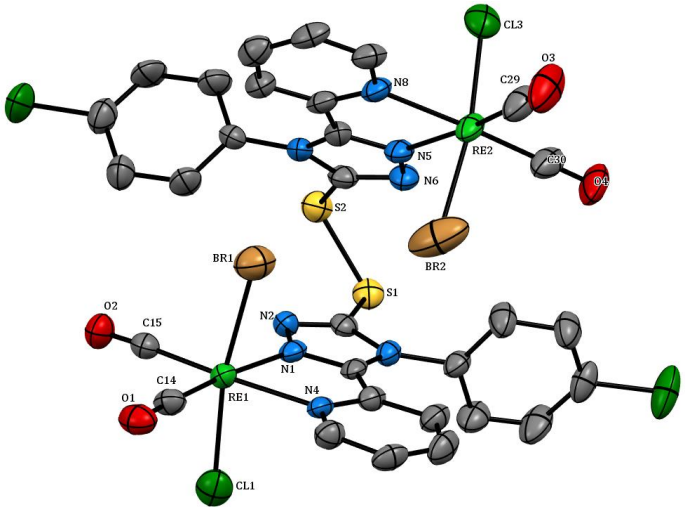

Figure 127: Connective structure of complex *fac*-[Re(py2ta-Cl)$(CO)_3$Br] **3-15.** Thermal ellipsoids are shown at the 50% probability level. Hydrogen atoms and solvent molecules have been omitted for clarity.

Table 23: Selected bond lengths (Å) and angles (°) of the solid-state structures of neutral Re(I) bipyridyl triazole thionate complexes **3-13.**

Bond length (Å)	3-13	Bond angle (°)	3-13
Re(1)-N(1)	2.147(5)	C(15)-Re(1)-N(1)	174.0(3)
Re(1)-N(4)	2.202(5)	N(4)-Re(1)-N(1)	73.9(2)
Re(1)-Br(2)	2.559(2)	N(16)-Re(1)-N(1)	90.3(5)
S(1)-S(1)	2.071(3)	C(16)-Re(1)-Br(2)	173.0(4)
Re(1)-C(16)	1.920(18)	N(4)-Re(1)-Br(2)	85.92(15)
Re(1)-C(15)	1.928(8)		
Re(1)-C(14)	1.935(8)		
N(2)-C(1)	1.308(9)		
S(1)-C(1)	1.754(7)		

Complex *fac*-[Re(py2ta)(CO)$_3$Br] **3-13,** shows many similarities with the earlier described neutral Re(I) tricarbonyl ancillary triazole complexes however, in relation to the overall structure, comparisons to the general diimine precursor *fac*-[Re(phen)(CO)$_3$(Cl)] will be made. The asymmetric unit of **3-13** shows the Re(I) metal centre present in an octahedral geometry, and as expected the Re(I) atom is coordinated to three carbonyl ligands in a facial configuration, this is consistent with the FT-IR data. In addition, the Re(I) metal centre is coordinated to one chlorine atom, and two nitrogen atoms of the py2ta moiety. Two carbonyl groups C(14)-O(1) and C(15)-O(2), and the ligand pyridine N(4) and triazole N(1) occupy the equatorial positions while the axial positions are occupied by the third carbonyl C(16)-O(3) and bromine Br(1) atom.

Formation of the Re(I)-N2 linkage isomer is not observed in the solution or solid-state, this is to be expected given the steric influence of the *fac*-[Re(N^N)(CO_3)]$^+$ fragment favouring coordination of the triazole ring at the N1 position, as observed with other Re(I)-triazole systems.[453] Additionally, as observed by similar types of ligand systems the nitrogen donor atoms of the chelate form an anti-conformation with the pyridyl and triazole segments adopting a coplanar system with the N-C-C-N dihedral angle of 3.4 ° in line with previously reported values.[464,465]

The asymmetric unit of **3-13** (Figure 126) shows the N(1) and N(4) donor atoms adopting the *anti*-conformation. Within the 1,2,4-triazole core, the N(1)-N(2) bond distance sits longer at 1.366(8) Å when compared to the N(2)-C(1) and N(1)-C(2) bonds at 1.319(8) and 1.308(9) Å, respectively. Changes to the thioamide (N(2)-C(1)=S(1)) functionality upon coordination to the Re(I) metal centre are apparent with the C(1)-S(1) bond lengthening at 1.754(7) Å to a delocalised state between a traditional C-S and C=S bond. Conversely, the associated N(2)-C(1) bond lies closer to the thionate N=C at 1.319(8) Å. The axial carbonyl group coordinates to the rhenium metal centre in a linear fashion with a dihedral angle of 178.1(14)°. All bond lengths and angles are in line with the typical rhenium complexes containing triazole-based ligands.[436,453,464–466]

Several differences can be observed for the crystallised complexes **3-13** and **3-15**. Complex **3-14** (Figure 126) crystallises in a monoclinic space group while **3-15** (Figure 127) has been modelled in the triclinic P1-bar space group. Due to the free rotation between the carbonyl groups and ancillary bromine atom, in both structures two components have been observed to occupy two distinct positions along the axial plane. In 38.3 % of the cases, the bromine atom Br(1), and the C(16)-O(3) groups in the coordination sphere occupy opposing positions. In the remaining 61.7 % the Br(2) and C(17)-O(4) groups lie in the axial positions. This occurrence was observed in the crystal structure of **3-15** as well.

Figure 127 illustrates the connective structure of complex *fac*-[Re(py2ta-Cl)($CO)_3$Br] **3-15**. Due to errors observed in the absorption as well as extensive residual electron density, the bond lengths and bond angle data has not been listed in Table 23

however, a disulfide S(1)-S(2) linkage can be observed in the extended dimerised fragment of **3-15** as observed in **3-13**.

The substitution of the py2ta ligand in the backbone position has a marked effect inducing strong steric hindrance and potential conjugation within these systems. When observing the organic ligand, the perpendicular aryl group suggests that the π-electron system of the py2ta and the aryl portion could have little interaction and thus, behave independently. In previous studies, there have been postulations that planarity and linearity have a marked influence on the electronics of the system as well as the overall photophysical output, this will be addressed in later sections.

3.3.14 Stability studies

As observed for the Re(I) ancillary triazoles complexes, the rhenium(I) backbone triazole complexes **3-13** to **3-16** also display moderate solubility across a range of polar solvents, unsurprisingly the structural changes to the backbone do not affect the overall solubility across the series within DMSO. ^{1}H NMR studies were conducted in two solvents, DMSO-d_6 and DCM-d_2 to be used as a direct comparison against the previously synthesised Re(I) ancillary triazoles. As a representative example of the Re(I) backbone triazole series, *fac*-[Re(CO)$_3$(py2ta-t)Cl] **3-14** was chosen as a model compound and showed good solubility and stability in DMSO, with minor changes observed to the complex across a five-day period (Figure 128).

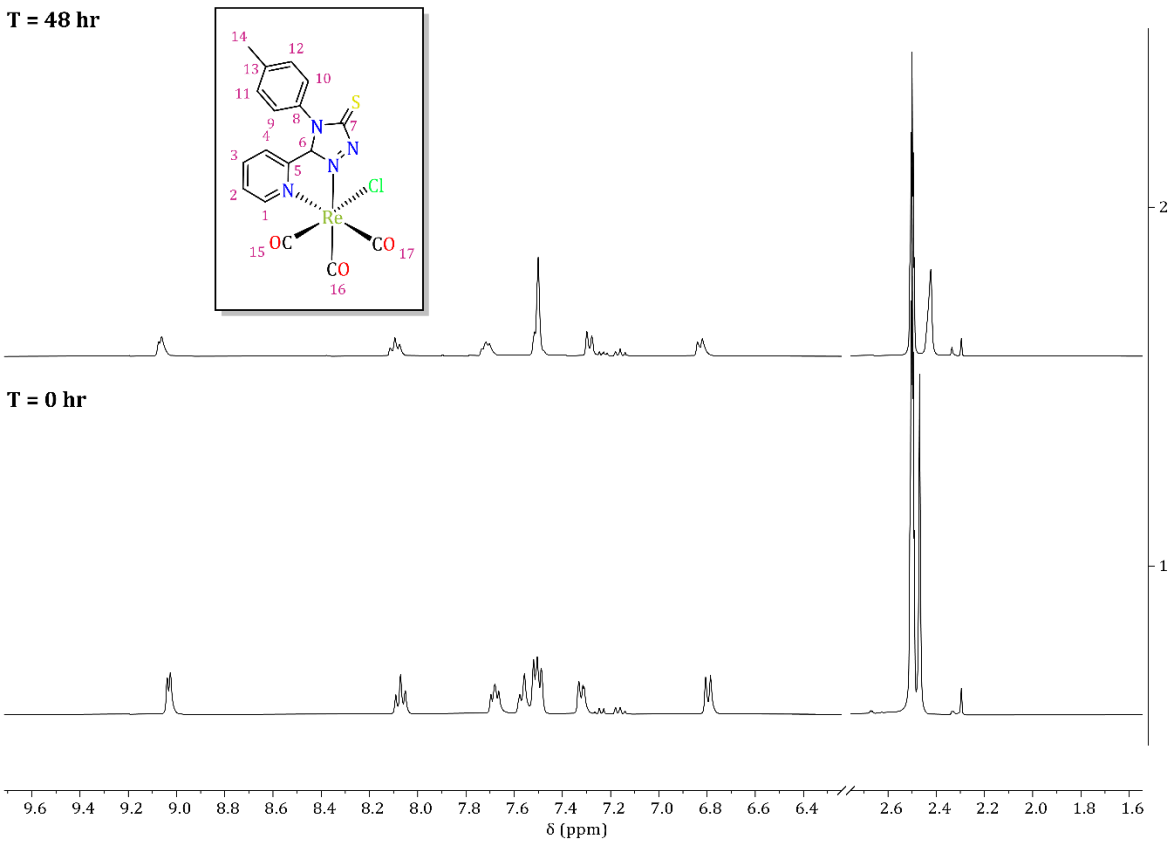

Figure 128: ^{1}H NMR spectra of complex *fac*-[Re(CO)$_3$(py2ta-t)Cl] **3-14** over a period of 48 hours taken in DMSO-d$_6$ at 25 °C.

In order to deduce whether the Re(I) tricarbonyl backbone complexes were susceptible towards ligand reactivity or exchange process, a time-dependent ^{1}H NMR study was conducted with complex **3-14** in deuterated DCM-*d*$_2$ and MeCN-*d*$_3$ as these two solvents are commonly used as carrier solvents for photophysical investigation. Furthermore, due to the unstable nature of the Re(I) tricarbonyl ancillary triazole complexes **3-1** to **3-12,** it was worthwhile investigating whether the Re(I) tricarbonyl backbone triazole counterparts would behave similarly in solution. Figure 129 shows that in the presence of DCM-d$_2$, **3-14** does not undergo any ligand exchange processed with the coordinating solvents.

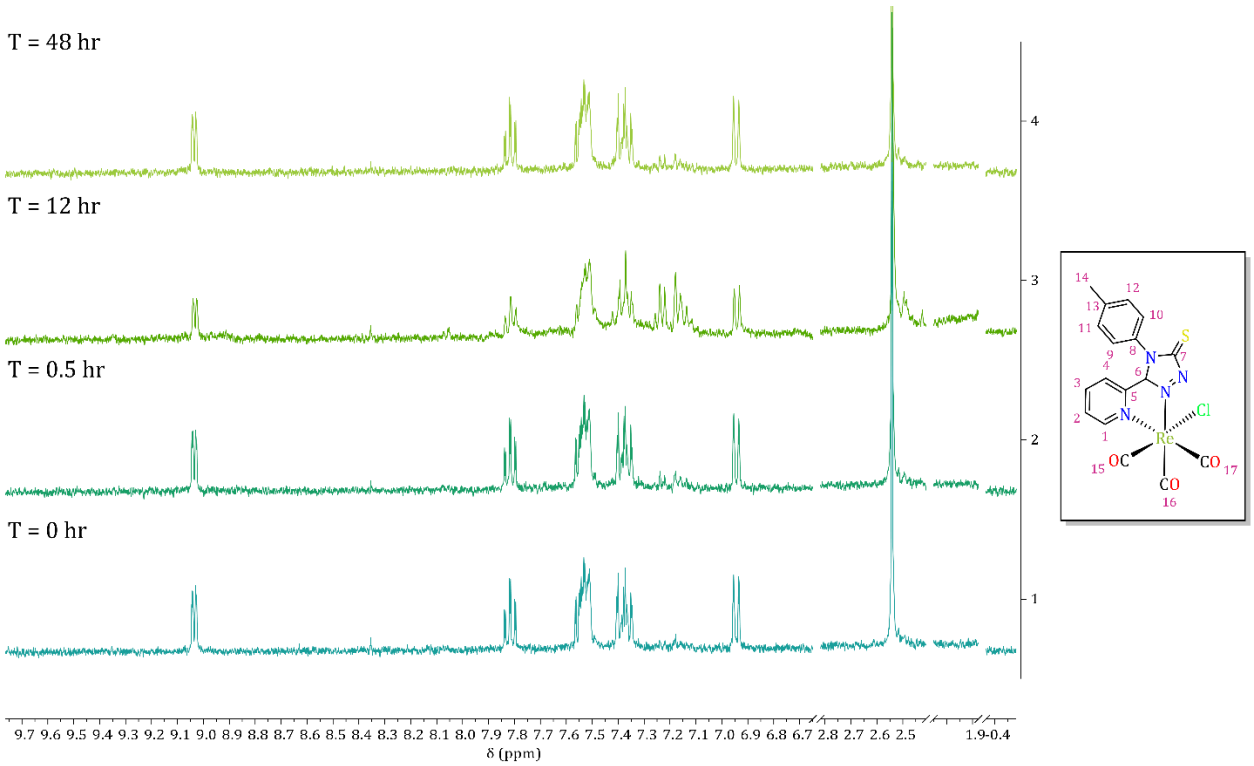

Figure 129: ^{1}H NMR spectra of complex *fac*-[Re(CO)$_3$(py2ta-t)Cl] **3-14** over a period of 48 hours taken in D$_2$-DCM at 25 °C.

Analysis of the time dependent ^{1}H NMR study in the presence of MeCN-*d*$_3$ however, resulted in changed spectra over a period of 48 hours. Upon reaching the 5-day experimental limit, the new system predominates with only minor traces of any other species observed. It is postulated that this exchange reaction could be occurring due to the labile nature of the substituted pyridyl-2-triazole ligand as observed in section 3.3.7.

3.3.14.1 Glutathione stability studies

Glutathione (GSH) is an important tripeptide found in large concentrations within mammalian cells. The redox-active molecule serves a predominant function in cellular detoxification via the oxidation of disulfide to form the GSSG species.[467–469] As several research studies have concluded the GSH molecule as a primary cellular target for rhenium(I) complexes, this study was performed to probe the reactivity in the presence of the neutral Re(I) backbone triazole complexes.[470–473]

The stability of the representative complex [Re(CO)$_3$(py2ta-t)Cl] **3-14** was initially explored in PBS using UV-Visible spectrometry. As shown in Figure 130 (left) changes

in the absorption intensities were observed over a period of 48 hours. Figure 130 (right) shows the response of **3-14** In the presence of GSH in PBS media whereby an increase and concomitant hypsochromic shift of the intraligand π→π* transition at *ca.* 325 nm which coincides with the deposition of a yellow precipitate in the quartz cuvette. These results could indicate that **3-14** can undergo ligand exchange processes in the presence of GSH. Supporting HRMS analysis of the reaction mixture beyond the 48-hour study revealed the isolation of a Re(I)-GSH conjugate, which is consistent with the literature.[470]

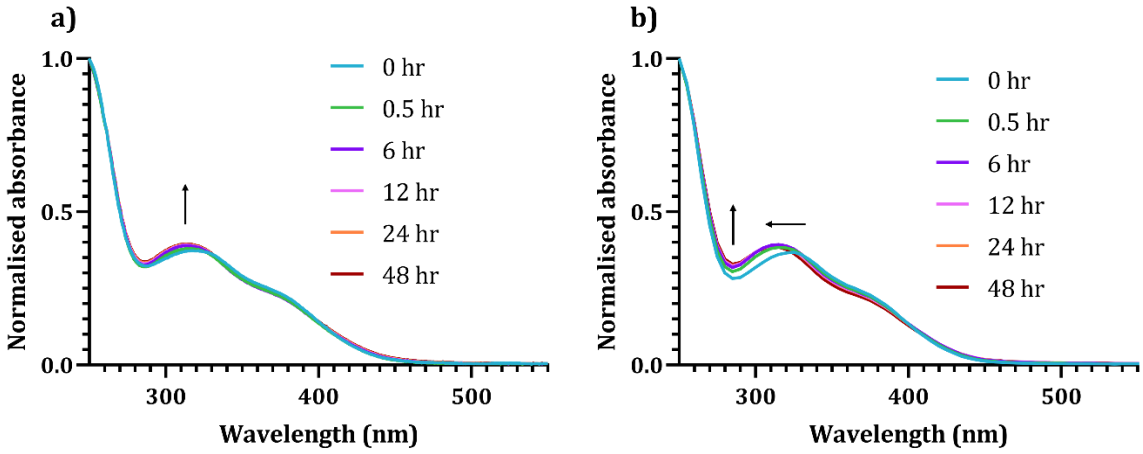

Figure 130: Changes to the absorption spectra of $[Re(CO)_3(py2ta\text{-}t)Cl]$ **3-14** (30 μM) in the presence of **a)** phosphate buffered saline (PBS) solution over 48 hours and **b)** 3 mM GSH (100 mol. equivalents) in ultrapure water over 24 h. The final DMSO concentration for both solutions were 0.4 % (v/v).

3.3.15 Photophysical investigations

The absorption spectra of the four backbone complexes were measured in DCM at room temperature at 10^{-5} M with the absorption data shown in Table 24. The complexes displayed the typical absorption and emission profile observed for a Re(I) tricarbonyl complex with a broad featureless emission maxima between 510-670 nm (Figure 131), this was consistent with complexes **3-1** to **3-12**. Additionally, all four complexes **3-13** to **3-16** showed intensities within the same region despite the structural variations with side groups.

Table 24: Summarized photophysical properties of the Re(I) tricarbonyl complexes **3-13** to **3-16** of the form *fac*-[Re(N^N)$(CO)_3$Cl] (whereby = N^N = *ortho*-pyridyl triazole thione) from diluted DCM solutions (ca. 10^{-5} M).

Complex	λ_{abs} (nm) [10^4 ε, $M^{-1}cm^{-1}$]	Λ_{exc} (nm)	τ	ϕ
3-13	260 (0.611), 350 (0.148), 440 (0.133)	570	>0.01	-
3-14	260 (0.628), 350 (0.160), 440 (0.140)	576	>0.01	167.1 (0.98), 0.05 (0.02)
3-15	260 (0.527), 350 (0.127), 440 (0.114)	570	>0.01	99.9 (0.98), 0.46 (0.02)
3-16	260 (0.639), 350 (0.160), 440 (0.141)	570	>0.01	188.4 (0.98), 0.35 (0.02)

The introduction of Electron Withdrawing Groups (EWG) and Electron Donating Groups (EDG) show no marked influence over the overall energy of the charge transitions within the complexes and thus, no marked emission shifts were observed between the complexes. In terms of emission intensity however, complex **3-14** bearing a *p*-tolyl substituted EDG showed the highest emission intensity. Modification to the aryl ring through the addition of an electron-donating methyl group produced diminishing returns as complex **3-15** showed the lowest emission intensity. Overall, complexes **3-13** to **3-16** showed generally poor emission profiles and would thus, be unsuitable agents to take forward for luminescent biological evaluation as biomarkers.

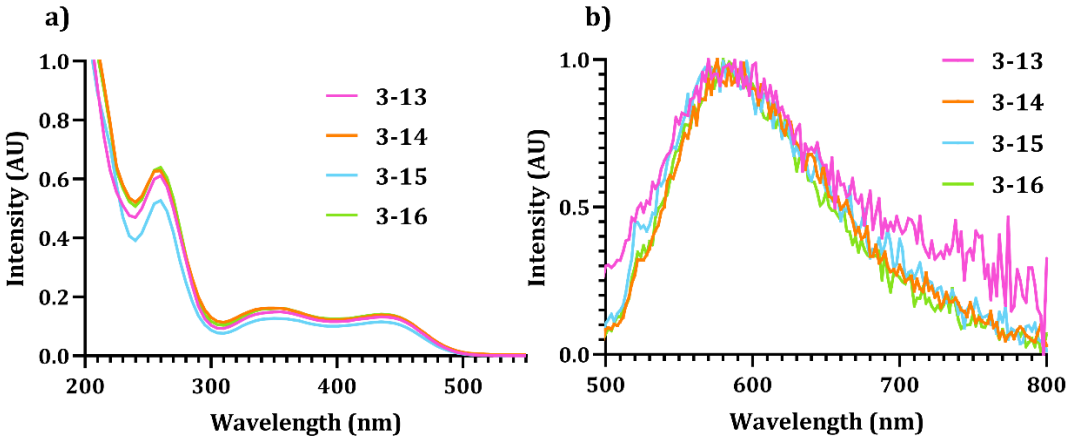

Figure 131: Changes in the **a)** excitation and **b)** emission profiles of *fac*-[Re(py2ta)(CO)$_3$(Cl)] series of complexes **3-13** to **3-16** taken at 10^{-4} in DCM.

Time resolved fluorescence studies of the Re(I) tricarbonyl backbone complex **3-14** identified long fluorescence lifetimes (167.1 ns) comprising of a single exponential component (Table 24 and Figure 132). The substitution pattern, or the effect of a *para*-phenyl chloride versus the dimethyl benzyl substituent, had little influence on emission wavelength.

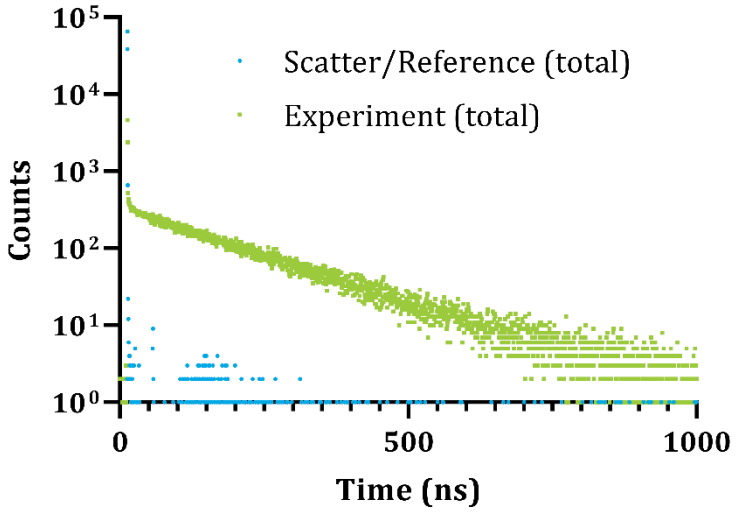

Figure 132: TCSPC decay histograms and fitted mono-exponential decay functions (lex = 350 nm). Instrument response function (IRF) shown in light blue.

3.3.16 Mammalian cell viability

The heteroleptic rhenium(I) tricarbonyl complexes *fac*-[Re(py2ta)(CO)$_3$Cl] **3-13,** *fac*-[Re(py2ta-t)(CO)$_3$Cl] **3-14**, *fac*-[Re(py2ta-Cl)(CO)$_3$Cl] **3-15**, and *fac*-[Re(py2ta-2Me)(CO)$_3$Cl] **3-16** were assessed for their cellular viability towards the L929 connective mouse tissue cell line utilising the methods outlined in both chapters 2 (2.3.10.4) and 3 (3.3.8.1), mammalian cell assays were conducted using L929 to determine if the complexes **3-13** to **3-16** effect cellular viability. Using the CellTiter-Blue viability assay the L929 cells were seeded into a 96 well plate and incubated for 24 hours to allow cell adherence. Working solutions of the rhenium complexes containing less than 1 % DMSO were added to the adhered cells and incubated overnight at 37 °C followed by the addition of the resazurin dye. The cells were incubated for a further 3-4 hours to allow for the conversion of the resazurin to resorufin by the metabolically active cells and the fluorescent output was measured via a plate reader. In all cases, the rhenium backbone complexes followed the similar trend found for **3-1** to **3-12** and showed no reduction in cellular viability.

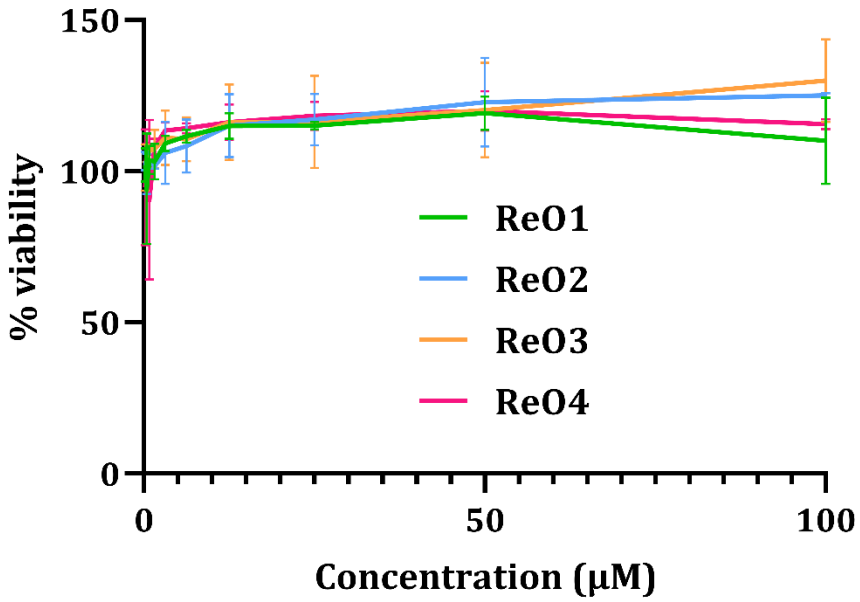

Figure 133: MIC % growth against a control of complexes **3-13** to **3-16** against cos-7. Dose response curves generated over a range of concentrations (0 – 100 µM) in the appropriate culture media from 10 mM DMSO stock solutions. Readings were compared spectroscopically to non-treated control and the percent growth inhibition calculated.

3.4 Conclusions and future objectives

A series of sixteen Re(I) tricarbonyl triazole-based complexes were synthesised and structurally characterised using a variety of spectroscopic techniques. The biological and photophysical properties of these complexes were explored in order to investigate whether small structural differences and chemical modifications between complexes could affect their properties. The synthesis of the precursor triazole thiolates follows and modifies the literature derived processes detailed in chapter 2, with the triazoles being used both as ancillary and diimine backbone ligands.

Part one of this chapter describes the synthesis of twelve neutral rhenium(I) tricarbonyl ancillary triazole complexes **3-1** to **3-12**, of the form *fac*-[Re(N'N)$(CO)_3$(**L**)] (where **L**= triazole thione), utilising the solvato-complexes *fac*-[Re(N^N)$(CO)_3(CH_2Cl_2)]SO_3CF_3$ (either **ReBS** or **RePS**) and triazole thiones **1-6** via microwave-assisted methods. Part two of this chapter describes the synthesis of a further four neutral rhenium(I) tricarbonyl backbone triazole complexes **3-13** to **3-16**, of the form *facial*-[Re(**L**)$(CO)_3$(Cl)] (where **L**= *ortho*-pyridyl triazole thione), utilising the $[Re(CO)_5Cl]$ salts and *ortho*-pyridyl triazole thiones **7**-**10** via solvent mediated reflux methods. All sixteen complexes were characterised via ^1H, ^{13}C, COSY and HSQC NMR spectroscopy, FT-IR, HRMS in addition to X-ray crystallography.

As indicated through FT-IR and X-ray crystallographic studies, complexes **3-1** to **3-12** showed good σ- and π- donor capabilities demonstrated by the changes in the electron density imparted on the Re(I) metal centre in comparison to the precursor **ReBS** and **RePS** complexes. Through X-ray crystallographic studies, all structures bound to the Re(I) metal centre via the N-atom over the S- atom with complexes **3-1** to **3-12** preferencing monodentate coordination, and **3-13** to **3-16** preferencing bidentate coordination. In all complexes, the triazole-aryl ring was not co-planar with the diimine bpy, phen, or *ortho*-pyridyl triazole N-donor rings and existed as separate aromatic systems which was presumed to influence the overall photophysical properties.

It is evident that metal to ligand synergism plays an integral role in both the biological and chemical activity. For complexes **3-1** to **3-12**, modifications to the axial ligand exhibits a minor influence on the overall photophysical properties of the complexes,

this could be attributed to the σ- and π-donor abilities of the triazole thione ligand which interact with the π-orbitals in the Re(I) metal centre. Complexes **3-13** to **3-16** however, show drastically diminished photophysical properties which could be attributed to the internal competitive electron donor- and acceptor-processes which are postulated to cause interferences with traditional MLCT and ILCT processes. Whilst the Re(I) ancillary triazoles show long-lived luminescence, these complexes were not tested under photoexcitation conditions, these results therefore suggest that alterations to the axial N-donor ligand would be a promising avenue for research.

Fluorophores that are suitable for live cell imaging require a set of key properties, good luminescent output, efficient cellular uptake, and low cytotoxicity. While these set of complexes exhibit low cytotoxicity their modest luminescent output renders them unsuitable candidates.

From the solution-state stability studies, complex **3-9** showed good stability under ambient and physiological conditions in deuterated DMSO and DCM. Interestingly, all of the Re(I) tricarbonyl ancillary complexes **3-1** to **3-12** and Re(I) tricarbonyl backbone complex **3-14** showed changes in the absorption spectra when exposed to cell culture media and glutathione, thus indicating a susceptibility towards ligand exchange. For future studies, the modification of these existing Re(I) systems to allow better aqueous solubility could result in increases of total uptake of the complexes.

To further support these studies, it is worthwhile exploring the stability of these complexes in the presence of bovine serum albumins (BSA) via either UV-visible spectrometry or time-dependent fluorometry. Serum albumins are the most abundant proteins present in blood and are often used as carrier molecules for the uptake of various drugs. As BSA shares very similar characteristics with human serum albumin, the solution state stability in the presence of both the ancillary and backbone Re(I) tricarbonyl triazole complexes may provide useful insight into the type of interaction, distribution and absorption for potential *in vivo* testing and future molecular docking studies.

Whilst complexes **3-7** to **3-12** were evaluated for their preliminary antimicrobial activity against three bacterial strains (MRSA, VRE and *E. coli*) and one fungal strain (*C. albicans*), they did not show appreciable MIC values presumably due to the highly

lipophilic nature. However, given the experimental inconsistencies further studies would be beneficial to verify the antimicrobial activity. Additionally, mammalian cell viability studies conducted for complexes **3-7** to **3-16** revealed no decrease in viability for both cos-7 and L929 cells tested.

In line with the literature, the natural progression of this body of work could be the modification of the existing Re(I) tricarbonyl complexes to their cationic forms. As charged Re(I)-based complexes have been found to effectively enter the cell and impart a therapeutic effect.[474,475]. Further studies into the modification of the existing set of triazole-thione ligands to bear more water-soluble groups may be a viable avenue to both improve photophysical output and applications in diagnostic imaging.

Understanding the electronic properties of the rhenium-based complexes allows the opportunity to explore and justify the absorption and emission character of the complexes. Computational calculations would be useful to identify whether the combination of ligand-metal interactions improved or diminished conjugation within the systems and in turn, the photophysical output. Using Density Functional Theory (DFT), HOMO-LUMO character and specific transition states involved in bonding can be assigned. For Re(I) systems the HOMO has been observed to comprise of over 50% metal d-orbital character.[172] TD-DFT calculations can predict the main contributor to the lowest energy band whether it is a mixed metal-to-ligand charge transfer (MLCT) or LLCT states. It is therefore worthwhile optimising geometric measurements from initial X-ray refinement data and verify whether the theoretical bond lengths and bond angles are generally in good agreement with the experimental data.

Collectively, these studies highlight how the diverse chemical, structural and photophysical properties can impact the biological activity with small alterations of the ligand moieties drastically impacting the overall efficacy of the molecule. Although the presented information provides a fundamental basis for complex design, this presents a challenge for future optimisation.

CHAPTER 4: GALLIUM(III) N-HETEROCYCLIC THIONES

HOMOLEPTIC GALLIUM(III) TRIAZOLES

HETEROLEPTIC GALLIUM(III) TRIAZOLES

SYNTHESIS, CHARACTERISATION AND BIOLOGICAL STUDIES

4 Gallium(III) N-heterocyclic thiones

4.1 Introduction

4.1.1 Iron acquisition in biological systems

One of the most important elements to life is iron, which is the central component of a majority of eukaryotic and prokaryotic systems. Although its abundance in nature is well documented, its bioavailability is generally considered to be low as it exists in the oxidised ferric form Fe(III).[476] Fe(III) can be consumed either endogenously or through dietary sources by mammalian organisms. However, microbes have developed complex biochemical pathways for the uptake of iron which involve the biotransformation to more useable and soluble form to maintain homeostatic function as well as more critically, virulence.[476–478] Modulation of the redox activity of ferrous iron Fe(II), balanced with the poor solubility and consequent bioavailability of ferric iron Fe(III), create opportunities for a microbial system to develop complex methods of acquisition.

Addressed in section 1.2.6, the human body has been shown to employ nutritional immunity to restrict the access of bioavailable iron to pathogenic microbes.[77,477] However, to overcome this, iron can be sequestered into specific storage systems by bacteria in the form of host proteins such as transferrin and lactoferrin, haem or alternatively, they may secrete small iron-coordinating molecules called siderophores (Figure 134).[193,479] These molecules bear hard donor atoms like oxygen and nitrogen and are capable of occupying two or more Fe-coordination sites.[480–482] Once the iron-bound siderophores have entered the cell through the outer membrane, via enzymatic process Fe(III) is able to reduce to Fe(II) within the cytoplasm whereby normal cellular functions are triggered, the small molecules may also trigger virulence factors.[481]

The structures of siderophores may be classified into four general groups, characterised by their Fe(III)-binding modes: hydroxamates, catecholates, carboxylates, and mixed-types (Figure 134).

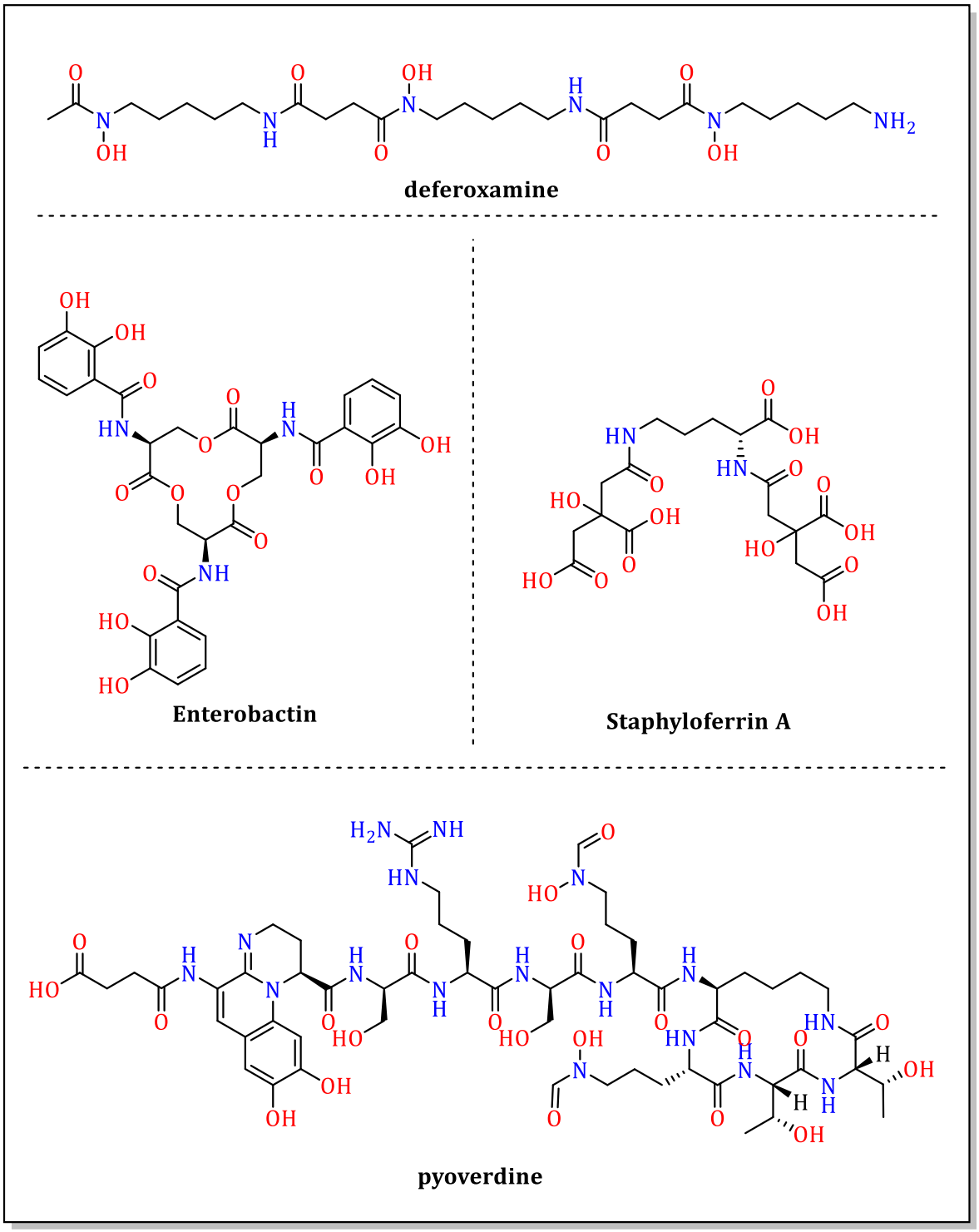

Figure 134: Siderophore structures incorporated by microbials with iron coordinating sites highlighted in orange.[483]

Hydroxamates are small molecules represent the largest class of fungal siderophores. These molecules form stable five-membered chelates with Fe(III). An example of this type can be demonstrated by deferoxamine (also referred to as desferrioxamine,

DFO) which is produced by *Streptomyces piloses*, a non-pathogenic bacterial siderophore (Figure 134, top).[477,484]

Catecholin-type siderophores such as Enterobactin (Figure 134, middle left) produced by Gram-negative type bacteria such as *E. coli* and *P. aeruginosa* have been shown to produce the highest Fe(III) affinity with a binding constant of $LogK_f$= 49.0, these types of molecules also forms stable five-membered chelates.[484,485]

While carboxylate-type siderophores such as staphyloferrin A (Figure 134, middle right) produced by Gram-positive *Staphylococcus* species are derived from citric acid, they contain both hydroxyl and carboxylate donor functionalities however, these types of small molecules are less effective at scavenging Fe(III). When compared to other siderophore types however, they are effective at low pH and thus, useful in acidic media.[484]

To evade inhibition, mixed-type siderophores have evolved over time, these small molecules contain two or more moieties to optimise function.[477,484] An example of this is Pyoverdine (Figure 134, bottom) which is produced by *P. aeruginosa* and contains both hydroxamate and catecholate groups. In addition to Fe(III), Pyoverdine has been shown to prevent oxidative stress by absorbing UV and radical scavenging.[476]

4.1.1.1 The relationship between Fe(III) and Ga(III)

While iron is redox active, gallium is not and thus through the use of the siderophores, gallium acts via a trojan horse mechanism to enter the cell and disrupt iron-redox involving processes. The FDA approved drug Ganite™ has recently been explored for its use as an antimicrobial. While the mechanism of action is not yet fully understood, the prevailing literature suggests the drug to enter cells through the iron-siderophore pathway and consequently, gallium-siderophore conjugates have been explored as a novel antimicrobial strategy.

4.1.2 The biological properties of Gallium(III)

The use of gallium in medical applications has been well established. Gallium undergoes d-block orbital contraction which allows the element to exist in the stable trivalent oxidation state. When observing the aqueous reactivity of Ga_2O_3, species

weak amphoteric character. However, the electropositive nature of gallium allows an effective formation of cations in aqueous media.

Within the biological context, the use of Ga(III) is strongly associated with the redox processes of Fe(III) via a 'Trojan Horse' mechanism. While iron can undergo physiological reduction from Fe(III) to Fe(II), gallium(III) cannot, through the process of mismetallation, gallium is able to replace iron and disrupt important processes and thus, overall cellular homeostasis.

Gallium(III) and Iron(III) both share very similar chemical characteristics and properties and in turn, follow similar biochemical transformations. While iron can enter the body through the means of various dietary sources, the transformations in which bioavailable Fe(III) is absorbed occurs through different pathways. Gallium(III), on the other hand cannot enter the body through dietary means.

In eukaryotic organisms, Ga(III) may interact with cells via multiple mechanisms and by employing various substrates in the process. Gallium can interfere with the structural integrity of transferrin and lactoferrin, the iron-binding proteins that transports iron in blood serum. Additionally, through the use of siderophores and ion channels, Ga(III) may enter cells and cause disruption. Another biological target of Ga(III) is the protein methionine, with its softer sulfur-bearing coordinating arms.

4.1.3 Gallium(III) antifungals

Gallium has been hypothesised to disrupt iron metabolic pathways via the Trojan horse mechanism in prokaryotic bacteria and some cancer cells. Recent research conducted on gallium nitrate [$Ga(NO_3)_3$] against two fungal strains Aspergillus and Candida have postulated the same mechanism in fungi by identifying a synergism between the metal salt and caspofungin, a current organic antifungal echinocandin.[486] It was postulated that the gallium salt produced an inhibitory effect under iron-limiting conditions.

4.2 Chapter objectives

1,2,4-triazole thiones have been shown to exhibit therapeutic potential when ligated with metals, therefore, the coordination chemistry of gallium(III) systems with these ligands will be explored herein.

A variety of synthetic strategies including solvent-mediated, solvent-free and metathesis type methodologies will be utilized whereby the purity, reaction times and yield will be compared to prepare a library of *tris*-substituted Ga(III) complexes with the general formula $[Ga(SR)_3]$ (SR = triazole thione). The synthesized complexes will be characterized via ^{1}H NMR and ^{13}C NMR spectroscopy, FT-IR spectroscopy, High-resolution mass spectrometry (HRMS), melting point analysis and where possible, the X-ray structures will be obtained and structurally elucidated.

In addition, this chapter aims to expand upon the library of heteroleptic organogallium(III) complexes through the attempted synthesis of a series of dimethylgallium n-heterocyclics of the form $[Ga(Me)_2SR]$ (SR = triazole thione).

4.3 Statement of challenges

In 2021, the School of Chemistry in Monash University had shut down 6 times due to the COVID-19 pandemic and resulted in the loss of 32 working days. These delays impacted both biological and stability studies as well as complex characterization in addition to the continued instrumentation problems arisen from 2020. Including the impacts of 2020, a total of twenty-one weeks of progress was lost.

These research interruptions occurred shortly after the commencement of the research described in Chapter 3 “Rhenium(I) N-heterocyclic thiones” and continued through the entirety of Chapter 4 “Gallium(III) N-heterocyclic thiones”. Consequently, the research conducted in this chapter was significantly affected.

Whilst the research impacts due to prolonged period of inaccessibility can be quantified through the total decrease in total research output, the intermittent loss of productivity was difficult to quantify and produced a more long-lasting impact on this body of work. Several cascade effects occurred to hinder research and can be summarized as follows:

- Planned experiments were reworked, shut down and repeated multiple times.
- Preparation for periods of shut down meant that additional time was lost to snap laboratory restart and shutdown procedures.
- Air sensitive, overnight reactions were avoided in accordance with OH&S policies due to the imposed curfews, limited laboratory staffing due to density limits and overall uncertainty.
- The loss of biological samples due to experiments being stopped prematurely meant that cells that took 4 weeks to grow and prepare had to be destroyed. 4 batches of cells were destroyed over each lockdown period resulting in the abandonment of biological studies for this body of work.
- Loss of fungal collaboration due to density limits imposed on laboratory spaces resulting in the reworking of Chapter 3 and 4 towards synthesis and characterization.
- A High-use auto-400 NMR machine was decommissioned for 34 weeks, due to a quenched magnet, and all long solution-state stability experiments were placed on hold for 13 weeks due to resulting in increased demand and strain on the NMR facility's remaining machines. The Interstate technician was unable to resolve this issue in a timely manner due to the imposed travel restrictions at the time.

All of these limitations served to impact the productivity of research over the affected years which continued well into 2022. This chapter is therefore intended to provide a preliminary analysis into the reactions described herein.

4.4 Results and discussion

4.4.1 Synthesis and spectroscopic characterization of precursor triazoles

A series of four triazole thiones were chosen as precursors for the attempted synthesis of the Ga(III) homoleptic and heteroleptic alkyl complexes: 5-(pyridin-4-yl)-4-(p-tolyl)-2,4-dihydro-3H-1,2,4-triazole-3-thione (pytz*H*) **1**, 5-(pyridin-4-yl)-4-(p-tolyl)-2,4-dihydro-3H-1,2,4-triazole-3-thione (pytz-t*H*) **2**, 4-phenyl-5-(pyridin-2-yl)-

2,4-dihydro-3H-1,2,4-triazole-3-thione (2pytz*H*) **14** and 5-(pyridin-2-yl)-4-(p-tolyl)-2,4-dihydro-3H-1,2,4-triazole-3-thione (2pytz-t*H*) **15**.

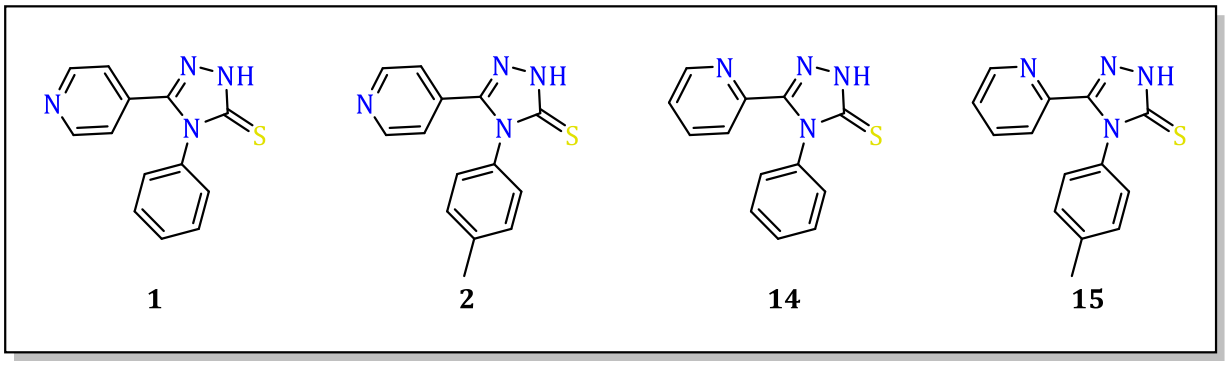

Figure 135: Triazole thiones **1,2,14** and **15** used in the attempted preparation of the Ga(III) homoleptic and heteroleptic complexes.

The triazole precursors were all prepared via the cyclisation of their picolino- and isonicotino-hydrazide precursors as described in sections 2.3.1 and 3.3.9 with the varying substitutions on the pyridyl- and aryl rings were chosen for structural diversity.

4.4.2 Synthesis of Ga(III) precursors

The choice of precursor for the synthesis of these heterocyclic gallium(III) complexes bears an important factor on their application as therapeutics. A series of alkyl and arylgallium(III) precursors were explored with the select few substrates. Following the synthesis of a series of alkylgallium(III) quinolinolates, the series of trialkyl gallium precursors $GaMe_3$, $GaEt_3$, $Ga(t\text{-butyl})_3$ were synthesised via one-pot in-situ metathesis either via the use of an organolithium precursor or Grignard methodology. To access triphenylgallium(III) ($GaPh_3$) required the in-situ transmetallation method with diphenylmercury ($HgPh_2$) as the metathesis method produces the solvent dependent metalated species $[Mg_3Br_3Cl_2(O(Et)_2)_6][GaPh_2Br_2]$.

The synthesis of $GaPh_3$ involved the one-pot solvent-free reaction of gallium metal and diphenylmercury(II) ($HgPh_2$) at 170 °C (Scheme 13). The resulting off white solid was crystallised from toluene, producing off-white needles in a 70 % yield. $GaPh_3$ is required to be handled and stored under inert conditions due to the hygroscopic

moisture sensitive nature of the compound. When exposed to moisture, the compound decomposes to $GaPh_2OH$ as confirmed by ^1H NMR studies.

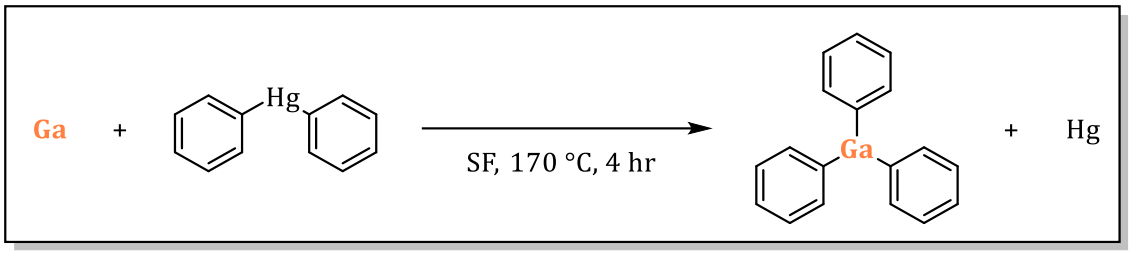

Scheme 13: Synthetic route employed to synthesize $GaPh_3$ via the one-pot transmetallation of $HgPh_2$ and $Ga_{(m)}$.

4.4.3 Attempted synthesis of $[Ga(SR)_3]$: homoleptic *tris*-substituted Ga(III) thiolates

Three separate synthetic routes were employed utilising $[Ga(NO)_3.9H_2O]$ and $GaCl_3$ as precursors in an attempt to produce the homoleptic tris-substituted gallium(III) triazoles. The first of which involved a well-established method within the Andrews group, the solvent-free reaction of gallium nitrate $[Ga(NO)_3.9H_2O]$ with the four triazole precursors **1-15.** This method has been previously established with carboxylic acid and sulfonic acid derivatives with the Bi(III) precursor $Bi(NO)_3$.[143]

To investigate whether a reaction would occur between the precursor molecules, differential scanning calorimetry (DSC) studies were employed to obtain a thermochemical profile which could then be correlated with experimental observations. DSC was used as a qualitative measure of reaction kinetics by allowing inferences to be made on the temperatures at which thermal events occur. An isotherm was obtained utilising a heating rate between 30 and 280 °C with a modulus of 10 °C per minute.

Established in Chapter 2, as the triazole thiolate display poor solubility in water, the second reaction route followed a salt metathesis route adapted from Orvig and co-workers whereby three equivalents of the triazole salt (**1-Na**) were reacted with one equivalent of the hydrated gallium nitrate precursor in methanol.[487]

Preliminary experiments detailed the heat-mediated solubilisation of the triazole **1** in ethanol, following complete dissolution, a solution of $[Ga(NO_3)_3.9H_2O]$ in water was

added dropwise to the warm triazole solution resulting in the solution changing from colourless to bright yellow indicating triazole deprotonation and metal complexation. The yellow reaction solution was then adjusted to neutral pH with the dropwise addition of 1M NaOH which resulted in the precipitation of a white solid. ^{1}H NMR spectrum analysis of the product revealed the complete recovery of triazole **1.**

Further attempts to isolate the homoleptic *tris*-substituted gallium(III) triazole species, involved the initial isolation of the triazole salt **1-Na** followed by the change in solvent to methanol and the addition of a weaker base, Na_2CO_3; this too resulted in the recovery of the starting material **1** (Scheme 14). Further modifications to the reaction procedure involved the addition of both the triazole **1** precursor and Ga(III) source and heating under reflux conditions, the bright yellow reaction mixture was then cooled to -25 °C resulting in the recovery and crystallisation of precursor triazole **1** from the reaction mixture.

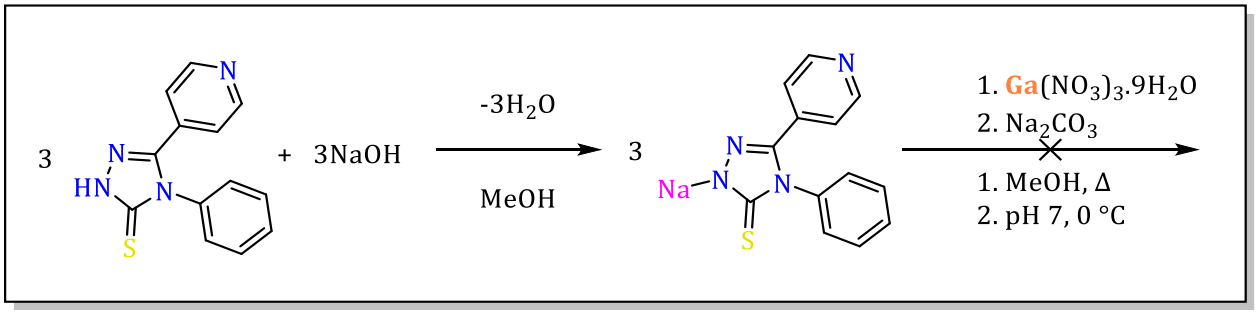

Scheme 14: Synthetic pathway utilized for the preparation of a tris-substituted gallium(III) triazole thiolate from $[Ga(NO_3)_3.9H_2O]$ and triazole **1**.

The third synthetic route followed a salt metathesis scheme utilising lithium as a base under Schlenk conditions (Scheme 15). The reaction proceeded via the equimolar addition of *n*-butyllithium to three equivalents of triazole **1** at -25 °C in THF. This resulted in changes to the reaction solution from transparent colourless to a transparent pale-yellow colour, indicating deprotonation and subsequent lithiation to form the *in-situ* **1-Li** species. In a separate vessel, $GaCl_3$ was solubilised in THF to form a colourless transparent solution, and cooled to -78 °C. The direct dropwise addition of the *in situ* **1-Li** species to the colourless $GaCl_3$ solution at -78 °C resulted in the immediate colour change to transparent green. The reaction was left to equilibrate to room temperature and the solvent was removed *in vacuo* to produce a pale-yellow

solid. ^{1}H NMR analysis of the crude product revealed a mixture of species however, triazole **1** was recovered following organic work up.

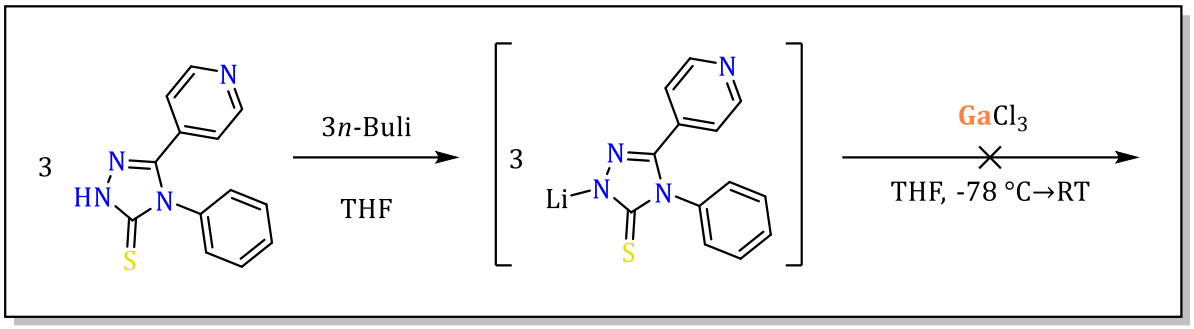

Scheme 15: Synthetic pathway utilized for the preparation of a tris-substituted gallium(III) triazole thiolate from $GaCl_3$ and triazole **1**.

Following the further modification made to the triazole thione precursors in Chapter 3, attempts were made to synthesise a *tris*-substituted gallium(III) 2-pyridyl 1,2,4-triazole complex using precursor **15** via a direct metathesis method (Scheme 16) under Schlenk conditions.

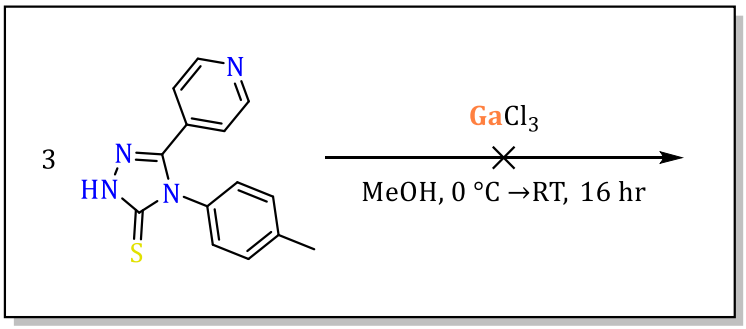

Scheme 16: Synthetic pathway utilized for the preparation of a tris-substituted gallium(III) triazole thiolate from the direct metathesis of $GaCl_3$ and triazole **15**.

$GaCl_3$ was solubilised in methanol and cooled to 0 °C, in a separate vessel, the triazole precursor **15** was dried and suspended in methanol resulting in the formation of a cloudy white solution. The cooled transparent colourless $GaCl_3$ solution was added dropwise to the cloudy white suspension of **15** resulting in the formation of a transparent pale-yellow solution which was stirred for a further 16 hours (overnight), concentrated *in vacuo* and cooled in an attempt to crystallise the product. ^{1}H NMR Analysis of the fine needle-like crystals showed them to be precursor **15**.

4.4.4 Attempted synthesis of [Ga(Me)$_2$(SR)]: Heteroleptic dimethylgallium(III) thiolates

Due to the air-sensitive nature of the precursors, all heteroleptic reactions proceeded under inert conditions following Scheme 17. Trimethylgallium ($GaMe_3$) was generated *in-situ* via the transmetallation of $GaCl_3$ with three equivalents of methyllithium (MeLi). care was taken to solubilise the $GaCl_3$ in cold *n*-hexane. The dropwise addition of MeLi into the gallium(III) chloride solution resulted in the immediate formation of a precipitate which corresponded to the deposition of LiCl. After the solution had equilibrated to room temperature, the *in situ* generated [$GaMe_3$] was added to a pre-cooled reaction vessel containing a solution of the triazole thione in either hexane, THF or diethyl ether (Et_2O). The resultant-coloured solution was left to stir for 2 hours, followed by the removal of solvent *in vacuo*.

Analysis of the residual precipitate/residue revealed a mixture of signals. The organic work up of the reaction resulted in the recovery of the precursor material, as observed during the attempted syntheses for the *tris*-substituted gallium(III) thiolates in section 4.4.3.

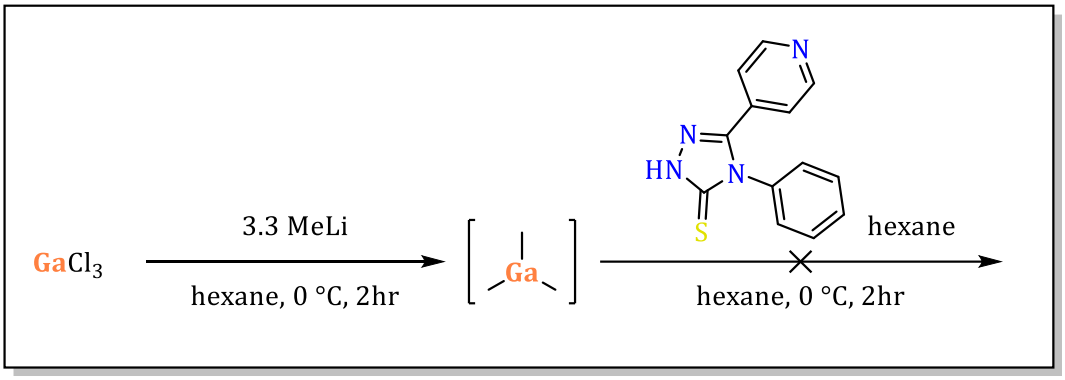

Scheme 17: Synthetic pathway utilized for the preparation of a mono-substituted gallium(III) triazole thiolate from the telescopic isolation of $GaMe_3$ and triazole **1**.

4.4.5 Attempted synthesis of [Ga(Ph)$_2$(SR)]: heteroleptic diphenylgallium(III) thiolates

The synthesis of the diphenylgallium(III) *mono*-substituted triazole complex was attempted, following the equimolar (1:1) addition of a toluene suspension of **1** to a transparent off-white $GaPh_3$ solution at room temperature. The resulting reaction mixture produced an opaque yellow solution and was left to stir overnight. Following overnight stirring, the opaque yellowy-green solution was kept aside to crystallise resulting in the formation of an oily residue with rhombohedral crystals, upon ^{1}H NMR analysis the crystals were identified as the precursor triazole thione/unreacted starting material.

In an effort to improve the stability of the complex, the alternative substrate explored in chapter 3, py2ta was utilised as a precursor. Utilising a substrate with the additional nitrogen donation with the intention to provide a better site for chelation with two nitrogen donor atoms. The reaction followed the addition of the two reagents added in an equimolar (1:1) ratio in THF. The $GaPh_3$ in THF produced a colourless transparent solution and was cooled to -78 °C. Following the dropwise addition of the py2ta resulted in a bright yellow solution which was allowed to equilibrate to room temperature overnight. The resulting solution was kept aside for crystals to form. However, analysis of the resultant crystals revealed them to be starting material.

There have been few examples identified within the literature of alkyl/arylgallium(III) heterocyclic thionato-based complexes with the most recent study being from 2007. Namely, gallium has been identified to produce more stable 4-or 5-membered chelation rings bearing oxygen-based donors such as carboxylato and alpha-hydroxy ketone-based organic substrates. The exploration of nitrogen and sulfur-based ligand systems is limited to the catalytic and chemical vapour deposition (CVD) studies with amido-based ligand systems being preferred.

4.5 Conclusions and future objectives

While multiple attempts were made to try and isolate the homoleptic *tris*-substituted gallium(III) triazoles, the reactions proceeded and produced the complex *in situ*, however upon organic workup and isolation, resulted in the hydrolysis of the reaction species and recovery of starting material. Upon analysis of the literature, Ga(III) preferentially forms five-membered chelates with substrates and although Ga(III) shows a preference towards hard nitrogen donors, the combination of the N-heterocyclic thione results in the formation of a strained four-membered chelate which is thus, an unfavourable configuration for the gallium(III) metal centre. Although four-membered Ga(III) chelates are rare, they exist with the addition of a stabilising Ga-O type interaction, the absence of which could explain the immediate hydrolysis of these types of complexes. For this reason, the *tris*-substituted gallium(III) triazole thione complexes were not pursued for further biological studies due to their instability in the solution state.

After multiple attempts were made to form Ga(III) complexes of the 4-pyridyl-1,2,4-triazole thione substrate, it was clear that a monodentate N-type donor interaction was unfavourable for complex formation, therefore a further attempt was made to pursue the formation of the substituted 2-pyridyl-1,2,4-triazole thione in the hopes that the additional N- donor from the co-ligand would stabilise the Ga(III) metal centre from hydrolysis. This reaction too, resulted in hydrolysis and recovery of starting material in all cases therefore, the pyridyl-1,2,4-triazole thione system was not pursued as a substrate of interest beyond this point.

Naturally, the progression of this body of work towards N-heterocyclic ligands with both hard and soft donor capabilities (e.g., N,O, O,S) may provide a viable alternative to complex to gallium(III). Perhaps the inclusion of an O-donor side arm or the addition of a carboxylate functionality may provide a stable chemical environment for chelation. However, it would be worthwhile to include a kinetic study in the presence of various coordinating solvents to confirm this. Additionally, it would be worthwhile to explore future complexes in the presence of Fe(III) and other biological components to probe the binding affinity and general solution-state stability of Ga(III) complexes

CHAPTER 5: CONCLUSION

GENERAL CONCLUSIONS

FURTHER WORK

FUTURE PERSPECTIVES

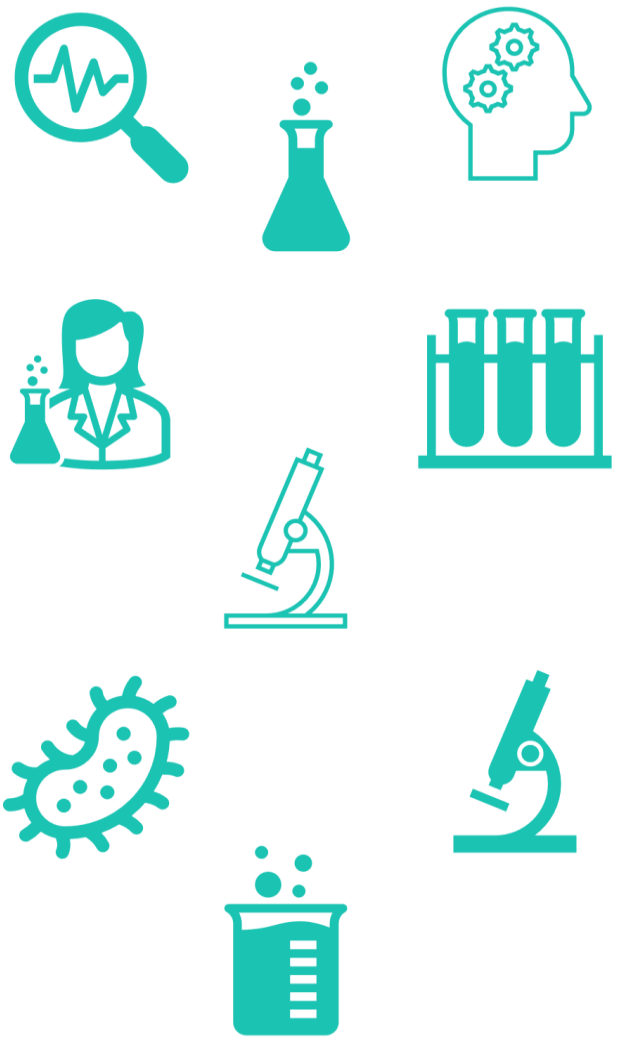

5 General conclusions and future perspectives

The global threat of AMR will persist beyond the COVID-19 crisis, and with the rise of infection rates will come the increased emergence of opportunistic infections. However, coordinated efforts to mitigate the adverse societal, economic, and medical effects will continue. Consequently, research into the various roles that metals, and organometallic complexes may play in medicine will proliferate.

Metal-based drug design is often overlooked, practically in its infancy when compared to the traditional organic-based drug design. This thesis therefore has explored the metal-to-ligand synergy that is exhibited by complexing an organic molecule to a metal, and whether this coupling imparts an enhanced therapeutic effect. The three metals that were explored, bismuth(III), rhenium(I) and gallium(III) each produced compounds with different physical, chemical, and biological characteristics.

Chapter 2 discussed the triazole thione and rhodanine classes of compounds as target ligands for complexation with bismuth(III). The development of an effective method for the synthesis of bismuth(III)-based N-heterocyclic thiolato-complexes proved to be a challenging pursuit, particularly with regards to the heteroleptic series of complexes. Numerous attempts were made to synthesise the phenylbismuth(III) *bis*-substituted thiolates under ambient conditions, through variations of the precursor materials, solvents, and parameters, all of which resulted in mixed products. Whilst the bismuth(III) triazole thione complexes showed antimicrobial activity, their subsequent mammalian activity rendered them unsuitable candidates for further development. Furthermore, stability studies indicated their susceptibility to undergo exchange processes in the presence of biological and media components.

As a class of biologically relevant thiolato-ligands, rhodanines provided valuable insights into the biological activity of PAINS (Pan Assay Interference) molecules. The phenylbismuth(III) rhodanines were synthesised using a facile one-pot microwave route. When coordinated to bismuth(III), the rhodanine ligands showed appreciable antifungal activity and thus, presenting them as potentially useful lead compounds as metal-based antifungals. However, as a PAINS molecules, it is uncertain whether the improved fungal response was attributed to the metal complex, or as an apparent

biological response as a result of the rhodanine complexing to the reference dye and producing improved photoluminescent output. While some medicinal chemists may argue that PAINS molecules should be avoided, these molecules provide an excellent starting point into understanding the metal-organic interactions at play in biological systems. Furthermore, they provide a basis for exploring protein-based studies and metal screening campaigns.

Chapter 3 explored the design, synthesis, and investigation into a library of Re(I) triazolato-based complexes for applications in therapeutics and imaging. The small structural changes made to the triazole substrates were then assessed on how the chemical, photophysical and biological properties of the metal complexes would be altered. Part one of this chapter discussed the synthesis, characterisation, and biological studies of the neutral complexes of the form: *fac*-[Re(N^N)$(CO)_3$(L)] where N^N represented either 1,10-phenanthroline (phen) or 2,2'-bipyridyl (bpy) and L represented one of a series of six 4-pyridyl-1,2,4-triazole thiones. Part two of this chapter also explored the backbone complexes of the form: *fac*-[Re(N^N)$(CO)_3$Cl] where (N^N) represented one of a series of four 2-pyridyl-1,2,4-triazole thiones. The first set of structural changes involved alterations to the backbone diimine ligand from bpy to phen as well as modification to the aryl moiety on the ancillary 1,2,4-triazole thione ligand. The second set of structural changes focused on alterations to the triazole thione ligand in the (N^N) backbone form. NMR, FT-IR, and single crystal X-ray crystallographic analyses revealed the structural similarities between the synthesised neutral complexes with each complex arranging in a *facial* configuration with the triazole thione ligand coordinated to the Re(I) metal centre via the N2 atom. While the photophysical output of the Re(I) phen-based complexes displayed longer lifetimes and more intense emission outputs compared to their bpy analogues, overall, the neutral complexes generally displayed poor luminescence. Similarly, biological assays conducted on the two sets of complexes revealed them to be poor *in vitro* agents with no appreciable antibacterial or antifungal activity. Furthermore, cellular viability assays conducted all of the Re(I) neutral complexes showed no apparent decrease in viability nor morphological changes to the cells when viewed under a microscope.

The exploration of these N-heterocyclic triazole thiolates with Ga(III) served to show that they were not suitable substrates. The hydrolysis of the complexes upon exposure to aqueous media rendered these complexes as unsuitable candidates for biological testing, however, their poor stability during synthesis provided a fundamental understanding as to the geometric and kinetic limitations of Ga(III) precursors. It is evident that a five-coordinate chelate ring is preferred for stable complexation and in this regard, ligands that form stable arrangements with the Ga(III) metal centre may not dissociate in biological and other aqueous media as easily.

The antimicrobial effect of Ga(III) is closely associate with the Fe(II) to Fe(III) redox system therefore, it is worthwhile exploring the thermodynamic and kinetic relationship between Ga(III) and Fe(III) species via spectroscopic titration-based studies. Upon the synthesis of Ga(III) homoleptic and heteroleptic complexes, it is worthwhile understanding the rate of dissociation in different types of aqueous media including single solvent systems, mixed solvent systems and biological growth media to gain a better understanding as to the biological mechanism of action and potential mode of dissociation.

Overall, while some organic and medicinal based researchers are able to ascertain whether a specific drug-class will impart a therapeutic effect via computational protein-based modelling, this is more difficult with metal-based complexes due to the unpredictability of each system. The design and synthesis of an appropriate metal-based therapeutic requires the careful application of skills as well as the knowledge and application of metal precursors before the optimisation can be considered.

The path of bioinorganic medicinal chemistry is still fraught with difficulties as molecules that show the strongest activity in screening may not be translatable in *in vivo* studies and thus, not an appropriate starting point. Despite the modest medicinal activity displayed by the complexes synthesised, the compounds shown in this thesis provide a theoretical basis for the design of superior bioinorganic molecules for application in therapeutics.

CHAPTER 6: EXPERIMENTAL

GENERAL PROCEDURES

CHAPTER 2

CHAPTER 3

CHAPTER 4

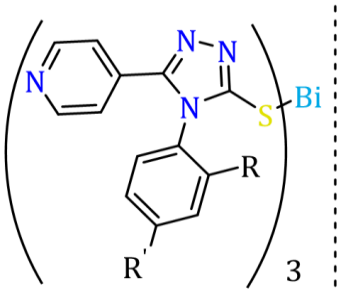

2-1 to **2-6**

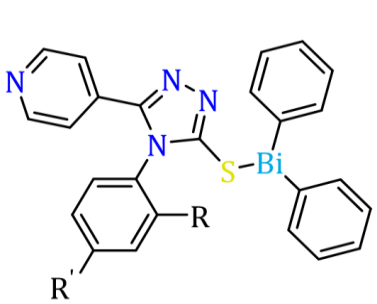

2-7 to **2-12**

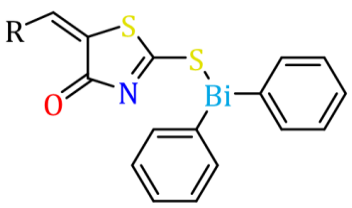

2-13 to **2-17**

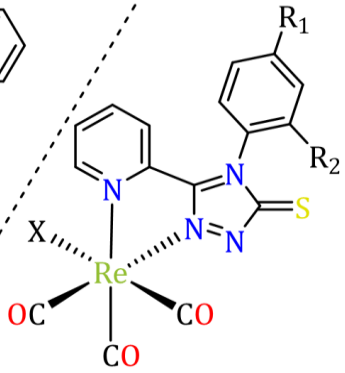

3-13 to **3-16**

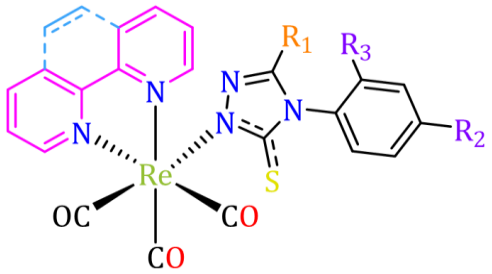

3-1 to **3-12**

6 Experimental

6.1 General Procedures

All compounds have been named using the IUPAC convention for nomenclature of organic and metal compounds. The appropriate numbering system classified in the schemes of each substance was not used in agreement with IUPAC convention, for practical reasons.

All reagents were purchased from Sigma Aldrich/Merck, Alfa Aesar or TCI Chemical and used as received, without further purification. All procedures involving rhenium complexes were carried out under nitrogen using standard Schlenk techniques.

Nuclear magnetic resonance spectra (consisting of ^{1}H, ^{13}C, 2D COSY, 2D HMBC and HSQC experiments) were recorded using Bruker Avance 400 and 600 spectrometers (400.1 MHz for ^{1}H, 100 MHz for ^{13}C) at room temperature. ^{1}H and ^{13}C chemical shifts were recorded on the δ scale in parts per million (ppm) and referenced to the appropriate deuterated solvent (chloroform-d_3 ($CDCl_3$) δ = 7.26 ppm, dimethyl sulfoxide-d_6 (DMSO-d_6) δ = 2.50 ppm, deuterium oxide (D_2O) δ = 4.79 ppm and d_6-benzene (C_6D_6) δ = 7.16 ppm). Signals were reported using the following format: chemical shift (δ ppm) (integration, multiplicity, and assignment). Multiplicities have been designated as singlet (s), doublet (d), doublet of doublets (dd), triplet (t) or multiplet (m).

Infra-red spectra were recorded in the solid-state with the frequencies recorded as wavenumbers (cm^{-1}) on an Agilent Technologies Cary 630 FT-IR spectrometer with a diamond stage. Compounds were scanned from 600 to 4000 cm^{-1} and the intensities of the IR bands were reported as strong (s), medium (m) or weak (w), with broad (br) bands and shoulders (sh) also indicated. Melting points of novel compounds were measured in open end capillary tubes on a digital Stuart Scientific SMP10 melting point apparatus.

Elemental microanalyses were performed on a Perkin Elmer 2400 Series II CHNS/O Elemental Analyser within the Department of Chemistry, Monash University (Clayton, Australia), or through The Campbell Microanalytical Laboratory, Department of

Chemistry, University of Otago (Dunedin, New Zealand). Melting points were determined using a BI Barnsted Electrothermal 9100 apparatus and are uncorrected.

High Resolution Mass Spectra (HRMS) analysis was carried out at the Monash Analytical Platform, Australia (School of Chemistry, Monash University). Test compound/s were infused directly into the MS via a kdScientific infusion pump at a static flow rate of 650 μL/h. MS setup was as follows: Agilent 6220 TOF MS system (Santa Clara, CA, USA) with a multimode dual nebuliser ESI/APCI source. The MS was operated in positive or negative mode using the following conditions: nebulizer pressure 35 psi, gas flow-rate 8 L/min, gas temperature 300°C, capillary voltage 2500/-2500 V, fragmentor 150 and skimmer 65 V. Instrument was operated in the extended dynamic range mode with data collected in m/z range 100–3200. DMSO, DCM, or acetonitrile was used at the matrix.

Crystallographic data was collected on one of the following: Bruker X8 APEXII CCD diffractometer equipped with an OXFORD Cryosystems 700 Cryostream and cooled to 123(1) K. Data was collected with monochromatic (graphite) MoKα radiation (λ = 0.71073 Å) and processed using the Bruker Apex2 v2014.7-1 software.[488] OXFORD Gemini Ultra equipped with an OXFORD Cryosystems 700 Cryostream and cooled to 123.00(13) K. Data was collected with monochromatic (graphite) CuKα (λ = 1.54184 Å) and processed using the CrysAlisPro v 1.171.34.36 software.[489] Lorentz, polarisation and absorption corrections (multi-scan – SADABS)[488] were applied. All compounds were solved and refined with SHELX-2016,[490] X-SEED,[491] Olex2,[492] and ShelXL.[267]

6.1.1 Biological testing

6.1.1.1 Bacterial testing

S. aureus (A134/ATCC6538), methicillin-resistant S. aureus (MRSA; M118797), vancomycin resistant E. faecalis (VRE; M846910), E. coli (G102) and P. aeruginosa (ATCC27853) were recovered from frozen (-80 °C) glycerol stocks (15% v/v) and streaked onto nutrient agar (MRSA, VRE, S. aureus) or Luria-Bertani (LB) agar (E. coli, P. aeruginosa) and incubated at 37 °C for 24 hours. Single colonies were then selected and incubated (37 °C) in 3 mL of Brain Heart Infusion (BHI) media (MRSA, VRE, S.

aureus) or LB media (E. coli, P. aeruginosa) for a further 18 hours with shaking (180 rpm) to obtain turbid overnight cultures.

6.1.1.2 Zone of inhibition assay

The antimicrobial activity of synthesized complexes was determined using a Kirby-Bauer disc diffusion method. Briefly, 200 µL of a 1 in 100 dilution of overnight cultured microbe for S. aureus, MRSA or VRE, *C. albicans* or *C. glabrata* were applied to either nutrient agar or LB agar plates in order to form the confluent microbial lawn. Sterile discs, inoculated with 80 µL of synthesized complexes, were then placed on the streaked agar plates before being incubated for 24 hr at 37 °C. After incubation, the zone of inhibition (if existed) was recorded and measured in mm. These tests were carried out in triplicate for each microbial cell line.

6.1.1.3 Minimum inhibitory concentration (MIC) assay

DMSO stocks were similarly prepared for complexes **2-1 – 2-16** and **3-1 – 3-16,** and bismuth(III) and rhenium(I) precursors at 10 mM. The working stocks were diluted in sterile water followed by either BHI or LB broth in 96 well plates, giving a maximum concentration range of 50 or 100 µM. This was serially diluted by a factor of two with a total of 100 µL/well. Overnight bacterial cultures were diluted to approximately 104 CFU/mL in broth before the addition of 5 µL to each well and incubation at 37 °C for 20 hours. Bacterial growth was determined by absorbance readings at 600 nm using a BMG-Labtech ClarioStar microplate reader. A positive control of no compound was treated as 100 % growth and the broth alone was the negative control. MIC values were determined as the concentration that inhibited ≥80 % growth (growth was ≤20 %) from a minimum of three independent experiments.

6.1.1.4 Fungal testing

The *Candida albicans* wildtype SC5314, *Candida auris* isolate LA MO YCAT1126 were recovered from frozen (-80 °C) glycerol stocks (15% v/v) and streaked onto nutrient agar or YPD medium, RPMI medium (with glutamine and without bicarbonate) or YNB medium agar and incubated at 37 °C for 24 hours. Single colonies were then selected and incubated (37 °C) in 3 mL RPMI (R6504), pH 7.0 (37 °C) without shaking for 20 hours to obtain turbid overnight cultures.

6.1.1.5 Fungal cell viability

The antimicrobial activity of synthesized complexes was determined using a MIC dilution Warwick protocol. DMSO stocks were similarly prepared for complexes **2-1 – 2-16** and **3-1 – 3-16,** and bismuth(III) and rhenium(I) precursors at 10 mM. The working stocks were diluted in RPMI (R6504) media in 96 well plates, giving a maximum concentration range of 50 or 100 µM. This was serially diluted by a factor of two with a total of 100 µL/well. Preparation of the fungal strains involved picking colonies of the YPD agar plate, preparing an inoculum followed by the serial microdilution solutions as described in the MIC dilution Warwick protocol. the metal complexes were added to the appropriate wells via two-fold dilution starting at 50 µM.

6.1.1.6 Mammalian cell viability

Cos-7 and human dermal fibroblasts were cultured and maintained in DMEM supplemented with 10% FBS, 1% Pen-Strep and 1% Glutamax (purchased from GibcoTM) at 37 °C in a 5 % CO2 incubator.[493] Cos-7 cultured for the CytoTox-ONE TM Homogeneous Membrane Integrity Assay were maintained in DMEM without pyruvate, supplemented with 5 % FBS, 1 % Pen-Strep and 1% Glutamax at 37 °C in a 5 % CO2 incubator.

CellTiter-Blue Cell Viability Assay was purchased from Promega™ and used for the determination of the percentage viability of cos-7 and L929 cells. Compounds and their respective precursors were solubilised in DMSO to make up a 10 mM working stock and sequentially diluted out in the appropriate culture media. Assays were set up in duplicate in Falcon 96 well plates. Volumes of 105 cos-7/mL and 105 L929/mL were seeded and adhered to 96 well plates 24 hours prior to compound addition. 20 hours after compound addition, 20 µL of CellTiter-Blue was added to each well in the 96 well plates, then incubated for a further 4 hours to total 24-hour incubation with compound. All cell assays were measured spectroscopically using fluorescence excitation at 544 nm and emission at 590 nm. The compounds were compared to a positive control of no drug and the percent inhibition calculated.[351] Fluorescence measurements were conducted on a BMG-Labtech ClarioStar microplate reader. Experiments were conducted independently at least three times, with values

averaged between the experiments. IC50 values were determined using GraphPad Prism 8.

6.2 Chapter 2

6.2.1.1 Bacterial cell uptake

Overnight cultures of MRSA and E. coli were first diluted to approximately 1 x 106 CFU/mL and added to falcon tubes containing the complexes diluted in BHI so that the overall concentration of the active components was 12.5 μM (for complexes **2-9** and **2-3**) in solution. After incubating for 20 hr (37 °C, 180 rpm), the falcon tubes were centrifuged for 15 minutes at 4000 rpm, with the resulting supernatant discarded. The pelleted cells left over were then washed 6 x with 1 mL PBS before being re-suspended in 3 mL BHI in order to determine the CFU/mL of bacteria present (serially diluted and overnight incubation of nutrient agar plates). The falcon tubes were then re-centrifuged (15 minutes, 4000 rpm) and the pelleted bacteria washed a further 6 x with 1 mL PBS, before 200 μL of concentrated HNO_3 was added and left to sit at 60 °C overnight. The solutions were then diluted with 4.8 mL of 2 % HNO_3 before the Bi209 composition was measured by ICP-MS.

6.2.1.2 ICP-MS

Determination of Bi content in bacterial cells following the uptake experiments was conducted using a PerkinElmer NexION 350 ICP-MS, measuring Bi at 208.98 amu. Raw count rates from the analyses were externally standardized by means of a calibration curve constructed using a commercially available Bi stock solution. An internal standard of 80 ppb Pb was used for Bi analysis. Precision is of the order of <5 % RSD from the single analyses. The final bismuth content was averaged from three independent bacterial experiments.

6.2.1.3 Bacterial membrane integrity assay

CytoTox-ONE TM Homogeneous Membrane Integrity Assay was purchased from Promega™ and used for the determination of % cytotoxicity of cos-7 cells. Complex **2-3**, **2-9** and **2-12** were solubilised in DMSO to make up 10 mM working stocks and diluted to 12, 6 and 3 μM. $BiPh_3$ and the reference complexes were solubilised in DMSO at 10 mM and diluted to give 100 μM, along with a DMSO control. Cos- 7 cells

were seeded at 104 cells/well and allowed to adhere overnight. Samples including the DMSO control were incubated for 24 hours, with negative control containing media with no cells and a positive control which was treated with Lysis Solution (0.18 % Triton) 4 hours prior to reading as the maximum LDH release control. CytoTox-ONE TM reagent was added after 24 hours and incubated at room temperature for 10 minutes before addition of the Stop Solution. The cells were measured spectroscopically using fluorescence excitation at 544 nm and emission at 590 nm on a BMG-Labtech ClarioStar microplate reader. The compounds were compared to a positive control of lysed cells and the percent cytotoxicity calculated. The experiment was independently run-in quadruplicate, with the cytotoxicity values averaged over the experiment.

6.2.1.4 Haemolysis assay

Haemolysis assays were performed as detailed by Ciornei *et al*.[494] Blood was first centrifuged at 800 x g for 10 minutes before the supernatant and buffy coat layer was discarded for use. This step was repeated a further 2 x before the resulting erythrocytes were resuspended in PBS (5 % v/v). Next, complexes (overall concentration - 25 μg/mL) were added to individual PCR tubes containing 1.5 mL of the erythrocytes and incubated for 2 hr at 37 °C with gentle end-over-end rotation. 2 % Trixton-X-100 served as a positive control whilst 2 % DMSO served as a negative control. After incubation, the samples were centrifuged at 800 x g for 10 mins. The % haemolysis was determined by measuring the absorbance of the supernatant (release of haemoglobin) at 540 nm and was expressed as a percentage of the positive control's induced haemolysis.

6.2.2 Precursor syntheses

6.2.2.1 Synthesis of Bismuth(III) tert-butoxide, [Bi(O^{t}Bu)$_3$]

To a solution of freshly sublimed $BiCl_3$ (30 mmol, 9.46 g) in 250 mL THF, a THF solution of potassium tert-butoxide (90 mmol, 10.10 g) was added at 0° C (cooled in an ice-water bath) and the resulting suspension was stirred for 24 h under the exclusion of light. The solvent was then removed *in vacuo* and [Bi(O^{t}Bu)$_3$] was extracted from the solid residue using dried n-pentane using a Soxhlet extractor.

Following removal of the n-pentane yielded the pure [Bi(O^{t}Bu)$_3$] (7.96 g, 62%) as a white precipitate, which was stored in an amber jar (in the absence of light) in a nitrogen-filled glovebox. ^{1}H NMR (400 MHz, C_6D_6): δ = 1.44 ppm (s; –CH_3).

6.2.2.2 Synthesis of triphenylbismuth(III)

All the manipulations were carried out under nitrogen until the reaction was quenched. Freshly sublimed anhydrous $BiCl_3$ (14. 073 g, 44.6 mmol) was stirred in approximately 250 mL of dry diethyl ether in a 500 mL three neck flask fitted with a 100 mL dropping funnel and a Schlenk tap. The reaction mixture was cooled to 0 °C and a solution of phenyl magnesium bromide (132 mL, 1M solution in ether or THF) was added drop wise via the dropping funnel. The reaction mixture was stirred overnight. The following day, the reaction mixture was poured over ice (approx. 200 g) and the slurry was allowed to melt to give a white precipitate. The precipitate was collected via filtration and was recrystallised from ethanol. (12.7894 g, 65%) MP: 78-80 °C (Lit. 78-80 °C); ^{1}H NMR (400 MHz, d_6-DMSO, 25 °C): δ = 7.73 (2H, d, ^{3}J = 6.56 Hz, Ha); 7.39 (2H, t, ^{3}J = 6.96 Hz, Hb); 7.31 (1H, t, ^{3}J = 7.36 Hz, Hc). FT-IR (Nujol, cm^{-1}): 3035 m, 1425 s, 994 s, 720 s.[495]

6.2.2.3 Synthesis of diphenylbismuth(III) chloride, [BiPh$_2$Cl]

A solution of $BiPh_3$ (2.94 g, 6.7 mmol) in ether (20 ml) was added to freshly sublimed $BiCl_3$ (1.05 g, 3.3 mmol) in ether (25 ml). A white precipitate immediately formed, and the reaction mixture was stirred for 1 h. The ether was decanted, the residue was washed with ether (2 x 10 ml) and dried to give $BiPh_2Cl$ (3.96 g, 99%). MP: 185-186 °C (Lit. 184-185 °C); 1H NMR (400 MHz, C_6D_6, 25 °C): δ = 8.98 (2H, d, J3 = 7.7, Ha); 7.97 – 7.87 (m, 2H); 7.44 – 7.33 (m, 1H).[495]

6.2.2.4 Synthesis of phenylbismuth(III) dichloride, [BiPhCl$_2$]

A solution of $BiPh_3$ (0.88 g, 2.0 mmol) in ether (10 ml) was added to freshly sublimed $BiCl_3$ (1.26 g, 4.0 mmol) in ether (15 ml). The initial unidentified white precipitate dissolved, and a pale-yellow precipitate gradually appeared. After stirring for 1 h, the solvent was filtered off with a filter cannula, the solid washed with ether (3 x 10 ml) and dried to yield $BiPhCl_2$ (1.86 g, 87%). MP: 242 °C (Lit. 242 °C) ^{1}H NMR (400 MHz,

DMSO-d_6, 25 °C): δ = 8.98 (2H, dd, J3 = 6.56, Ha); 7.91 (2H, t, J3 = 6.96, Hb); 7.39 (1H, t, J3 = 7.36, Hc).[495]

6.2.2.5 Synthesis of triazole thiolates

This reaction procedure was modelled from Youssef *et a*l.[338] and was further optimized using microwave irradiation producing improved yields of the resulting substituted phenyl carbothioamide derivatives and final thiols **1 – 6, 12**-**17**.

6.2.2.6 Synthesis of arylrhodanines

This reaction procedure was modelled from Nitsche *et al*. and further optimised using mechanochemical solvent-free methods.[496] Rhodanine (1 equiv) and the respective aldehyde (1 equiv) were ground together and reacted in a solvent-free reaction in the presence of a catalytic amount of ammonium acetate (0.1 equal) to form a sticky paste. The coloured paste was dissolved in hot ethanol and recrystallised to afford precursors **7-11**.

6.2.3 General synthetic procedures

6.2.3.1 GP1: Synthesis of [Bi(SR)$_3$]: Homoleptic tris-substituted bismuth(III) triazole thiolates.

All of the following manipulations were carried out under a nitrogen atmosphere using Schlenk techniques. Bi(O^{t}Bu)$_3$ (1 equiv.) was added to a solution of the tetrazole/triazole thiolate (3 equiv.) in dry THF at room temperature. The resulting solution was allowed to stir overnight before being concentrated under *vacuo*. The crude solid obtained was washed with cold diethyl ether and filtered to yield the desired compound.

6.2.3.2 GP2: Synthesis of [BiPh$_2$SR]: Heteroleptic diphenylbismuth(III) triazole thiolates.

All of the following manipulations were carried out under a nitrogen atmosphere using Schlenk techniques. BiPh$_2$Cl (1 equiv.) was added to a solution of the previously synthesized triazole (1 equiv.) with NaOH (1 equiv.) in dry methanol. The resulting solution was stirred at room temperature for 4 hr. After the elapsed time, the

precipitate that formed was filtered and washed with cold water and acetone to yield the desired complex.

6.2.3.3 GP3: Synthesis of [BiPh$_2$SR]: Heteroleptic diphenylbismuth(III) rhodanine thiolates.

All of the following manipulations were carried out using a CEM discover LabMate microwave as follows. $BiPh_3$ (1.2 equiv.) was first dissolved in 5 mL DMSO before the previously synthesized arylrhodanine (1 equiv.) was added. The resulting solution was reacted at 70 °C for 20 mins before being left to cool to room temperature. On cooling, the desired compound crystallised out of solution over a period of 12 hours – 1 week, which were filtered and collected without the need for further purification.

6.2.4 [Bi(SR)$_3$]: *Tris*-substituted bismuth(III) triazole thiolato complexes

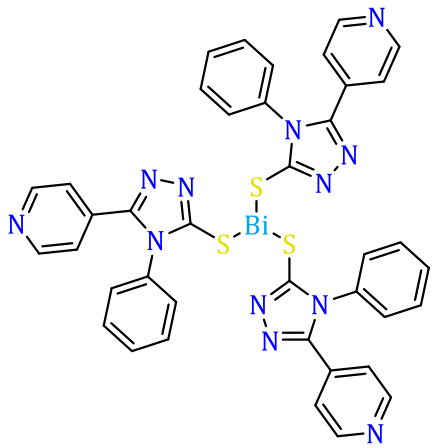

[Bi(PTz)$_3$] (2-1): Following GP4: Triazole thione **1** (380 mg, 1.5 mmol) and Bi(O^{t}Bu)$_3$ (215 mg, 0.5 mmol) were stirred in 10 mL THF. The title complex was isolated as a yellow solid (280 mg, 58%). ^{1}H NMR (400 MHz, DMSO-d_6, 25 °C) δ 8.53 (d, ^{3}J = 5.2 Hz, 2H), 7.51 (s, 3H), 7.37 (d, J = 6.2 Hz, 2H), 7.21 (d, J = 5.1 Hz, 2H). ^{13}C NMR (151 MHz, DMSO-d_6) δ 150.0, 134.7, 133.6, 129.4, 128.58, 121.6. FT-IR (film, cm^{-1}): 1495 (C-N), 1298 (C-C-N), 1285 (C-N), 830 (C-S). Melting Point: 197 °C (decomp.). MS (ESI) calculated for $C_{29}H_{36}BiCl_2N_8O_6S_3$: 935.4728 $[L_2Bi.CH_2Cl_2.6H_2O]^+$.

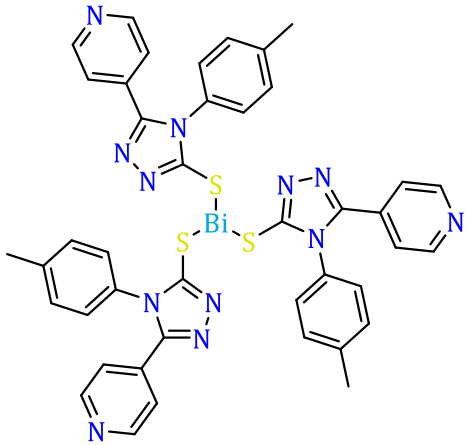

[Bi(PTTz)$_3$](2-2): Following GP4: Triazole thione **2** (400 mg, 1.5 mmol) and Bi(O^{t}Bu)$_3$ (215 mg, 0.5 mmol) were stirred in 10 mL THF. The title complex was isolated as a yellow solid (347 mg, 69%). ^{1}H NMR (400 MHz, DMSO-d_6, 25 °C) δ 8.52 (d, J = 6.2 Hz, 2H), 8.24 (d, J = 7.3 Hz, 4H), 7.54 (t, J = 7.6 Hz, 4H), 7.35 – 7.28 (m, 1H), 7.28 – 7.18 (m, 2H), 7.03 (d, J = 8.9 Hz, 1H). ^{13}C NMR (151 MHz, DMSO-d_6) δ 149.9, 138.8, 133.9, 129.8, 128.3, 121.4, 20.8. FT-IR (film, cm-

[1]): 1423 (C-N), 1259 (C-C-N), 821 (C-S). Melting Point: 190 °C (decomp.). (ESI) calculated for $C_{42}H_{33}BiN_{12}S_3$: 1033.9881 $(M - H)^-$.

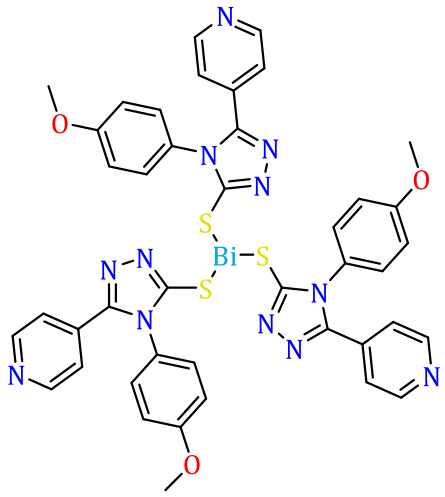

[Bi(POTz)$_3$] (2-3): Following GP4: Triazole thione **3** (425 mg, 1.5 mmol) and Bi(O^{t}Bu)$_3$ (215 mg, 0.5 mmol) were stirred in 10 mL THF. The title complex was isolated as an orange solid (280 mg, 53%). ^{1}H NMR (400 MHz, DMSO-d_6, 25 °C) δ 8.62 – 8.37 (m, 2H), 7.26 (dd, J = 20.5, 6.7 Hz, 4H), 7.04 (d, J = 8.4 Hz, 2H), 3.81 (s, 3H). ^{13}C NMR (151 MHz, DMSO-d_6) δ 159.6, 129.8, 121.6, 114.6, 55.4. FT-IR (film, cm^{-1}): 1251 (C-C-N), 826 (C-S). Melting Point: 191 °C (decomp.). MS (ESI) calculated for $C_{30}H_{42}BiN_8O_{10}S_2$: 947.4937 $[L_2Bi.2(CH_3OH).6H_2O]^+$.

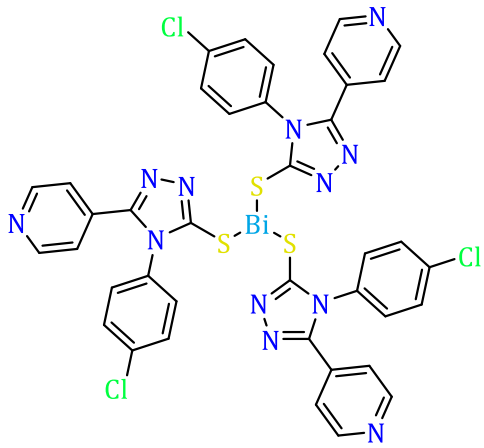

[Bi(PCTz)$_3$] (2-4): Following GP4: Triazole thiol **j** (408 mg, 1.5 mmol) and Bi(O^{t}Bu)$_3$ (215 mg, 0.5 mmol) were stirred in 10 mL THF. The title complex was isolated as a bright orange solid (303 mg, 57%). ^{1}H NMR (400 MHz, DMSO-d_6, 25 °C) δ 8.53 (d, J = 5.1 Hz, 2H), 7.56 (d, J = 8.3 Hz, 2H), 7.39 (d, J = 8.2 Hz, 2H), 7.21 (d, J = 5.1 Hz, 2H). ^{13}C NMR (151 MHz, DMSO-d_6) δ 113.0, 100.43, 96.07, 93.4, 92.3, 91.2, 84.4. FT-IR (film, cm^{-1}): 1492 (C-N), 1424 (C-N), 1091 (C-N), 826 (C-S). Melting Point: 192 °C (decomp.). MS (ESI) calculated for $C_{28}H_{20}BiCl_6N_8S_2$: 951.4693 $[L_2Bi.2(CH_2Cl_2)]^+$.

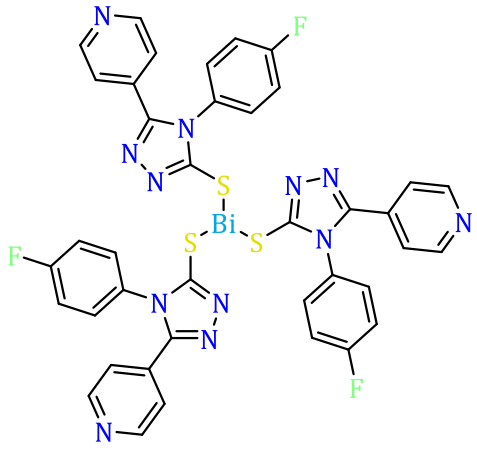

[Bi(PFTz)$_3$] (2-5): Following GP4: Triazole thione **4** (432 mg, 1.5 mmol) and Bi(O^{t}Bu)$_3$ (215 mg, 0.5 mmol) were stirred in 10 mL THF. The title complex was isolated as a yellow solid (336 mg, 66%). ^{1}H NMR (400 MHz, DMSO-d_6, 25 °C) δ 8.62 – 8.43 (m, 2H), 7.30 – 7.10 (m, 5H). ^{13}C NMR (151 MHz, DMSO-d_6) δ 162.9, 161.2, 150.0, 148.5, 133.6, 131.1, 131.0, 130.9, 121.6, 116.4, 116.3. FT-IR (film, cm^{-1}): 1602 (C-C), 1427 (C-N), 1216 (C-C-N), 839 (C-S), 827 (C-S). Melting Point: 237 °C (decomp.). MS (ESI) calculated for $C_{39}H_{24}BiF_3N_{12}S_3$: 1087.2122 (M + MeOH)$^-$.

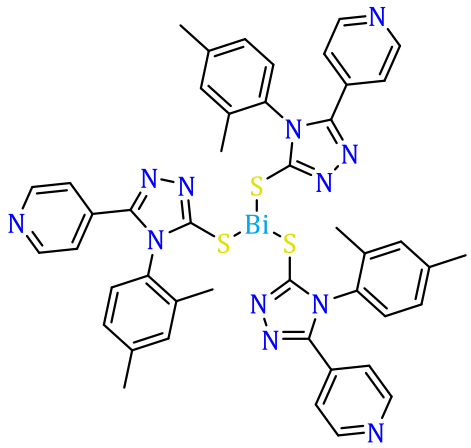

[Bi(PDTz)$_3$] (2-6): Following GP4: Triazole thione **5** (423 mg, 1.5 mmol) and Bi(O^{t}Bu)$_3$ (215 mg, 0.5 mmol) were stirred in 10 mL THF. The title complex was isolated as a yellow solid (463 mg, 88%). ^{1}H NMR (400 MHz, DMSO-d_6, 25 °C) δ 8.54 (d, J = 5.2 Hz, 2H), 7.49 – 6.90 (m, 5H), 2.35 (s, 3H), 1.97 (s, 3H). ^{13}C NMR (151 MHz, DMSO-d_6) δ 150.2, 139.6, 135.5, 133.5, 131.7, 131.2, 128.8, 127.9, 120.6, 20.8, 17.3. FT-IR (film, cm^{-1}): 1298 (C-N), 825 (C-S). Melting Point: 171 °C (decomp.). MS (ESI) calculated for $C_{45}H_{39}BiN_{12}S_3$: 1129.2619 (M + DMSO)$^-$.

6.2.5 [Bi(Ph)$_2$SR]: Diphenylbismuth(III) triazole thiolato complexes

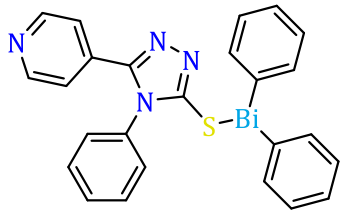

[Bi(Ph)$_2$(PTz)] (2-7): Following GP2, BiPh$_2$Cl (200 mg, 0.5 mmol) was reacted with triazole thione **1** (138 mg, 0.5 mmol) in methanol. The title complex was isolated as an off-white solid (302 mg, 98%). ^{1}H NMR (400 MHz, DMSO-d_6, 25 °C) δ 8.52 (d, J = 6.2 Hz, 2H), 8.24 (d, J = 7.3 Hz, 4H), 7.54 (t, J = 7.6 Hz, 4H), 7.35 – 7.28 (m, 1H), 7.28 – 7.18 (m, 2H), 7.03 (d, J = 8.9 Hz, 1H). ^{13}C NMR (151 MHz, DMSO-d_6) δ 149.9, 137.9, 135.2, 134.7, 131.1, 129.7, 129.5, 127.9, 127.5, 121.0. FT-IR (film, cm^{-1}): 1599 (C=C), 1428 (C-N), 1342 (C-N), 832 (C-S), 722 (C-C). Melting Point: 214 - 219 °C. MS (ESI) calculated for $C_{25}H_{19}BiN_4S$: 645.1505 (M + H)$^+$. CCDC 1968621.

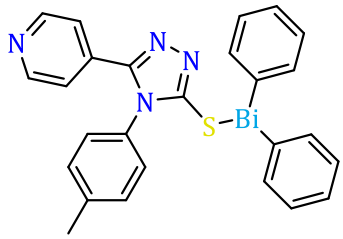

[Bi(Ph)$_2$(PTTz)] (2-8): Following GP2: $BiPh_2Cl$ (200 mg, 0.5 mmol) was reacted with triazole thione **2** (145 mg, 0.5 mmol) in methanol. The title complex was isolated as an off-white solid (274 mg, 87%). ^{1}H NMR (400 MHz, DMSO-*d*$_6$, 25 °C) δ 8.52 (d, *J* = 6.2 Hz, 2H), 8.24 (d, *J* = 7.3 Hz, 4H), 7.54 (t, *J* = 7.6 Hz, 4H), 7.35 – 7.28 (m, 1H), 7.28 – 7.18 (m, 2H), 7.03 (d, *J* = 8.9 Hz, 1H). ^{13}C NMR (151 MHz, DMSO-d_6) δ 150.0, 137.8, 137.3, 131.1, 130.3, 130.2, 127.6, 127.6, 121.0. FT-IR (film, cm^{-1}): 1575 (C=C), 1460 (C-N), 1390 (C-N), (C-S), 735 (C-H). Melting Point: 161 - 162 °C. MS (ESI) calculated for $C_{25}H_{19}BiN_4S$: 645.1507 $(M + H)^+$. CCDC 1968619.

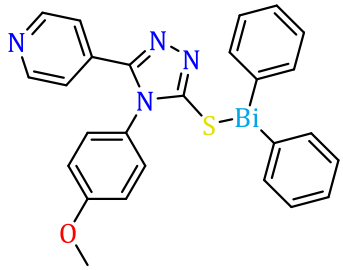

[Bi(Ph)$_2$(POTz)] (2-9): Following GP2**:** $BiPh_2Cl$ (200 mg, 0.5 mmol) was reacted with triazole thione **3** (153 mg, 0.5 mmol) in methanol. The title complex was isolated as an off-white solid (273 mg, 85%). ^{1}H NMR (400 MHz, DMSO-*d*$_6$, 25 °C) δ 8.59 – 8.45 (m, 2H), 8.24 (d, *J* = 7.3 Hz, 4H), 7.54 (t, *J* = 7.6 Hz, 4H), 7.41 – 7.28 (m, 2H), 7.29 – 7.17 (m, 4H), 7.03 (d, *J* = 8.9 Hz, 2H), 3.80 (s, 3H). ^{13}C NMR (151 MHz, DMSO-*d*$_6$) δ 150.0, 137.8, 131.1, 128.3 (d, *J* = 236.8 Hz), 121.0, 114.8, 55.5. FT-IR (film, cm $^{-1}$): 1575 (C=C), 1460 (C-N), 1390 (C-N), 824 (C-S), (C-H). Melting Point: 119 - 123 °C. Elemental analysis, calc. C, 48.30; H, 3.27; N, 8.67; found C, 48.95; H, 3.33; N, 8.69; MS (ESI) calculated for $C_{25}H_{19}BiN_4S$: 647.1302 $(M + H)^+$.

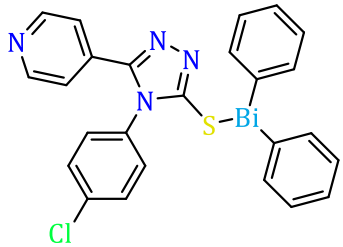

[Bi(Ph)$_2$(PCTz)] (2-10): Following GP2: $BiPh_2Cl$ (200 mg, 0.5 mmol) was reacted with triazole thione **4**(155 mg, 0.5 mmol) in methanol. The title complex was isolated as an off-white solid (173 mg, 53%). ^{1}H NMR (400 MHz, DMSO-*d*$_6$, 25 °C) δ 8.52 (d, *J* = 6.2 Hz, 4H), 8.26 (d, *J* = 7.3 Hz, 2H), 7.55 (dd, *J* = 8.2, 6.1 Hz, 5H), 7.33 (dd, *J* = 8.1, 6.0 Hz, 3H), 7.29 – 7.15 (m, 2H). ^{13}C NMR (151 MHz, DMSO-*d*$_6$) δ 131.7, 130.3, 114.8. FT-IR (film, cm^{-1}): 1575 (C=C), 824 (C-S), 735 (C-H). Melting Point: 119 - 123 °C (decomp.). MS (ESI) calculated for $C_{25}H_{19}BiClN_4S$: 650.0735 $(M + Na)^+$. Elemental analysis, calc. C 46.13 H, 2.79 N, 8.61; found C, 44.95; H, 2.64; N, 8.47.

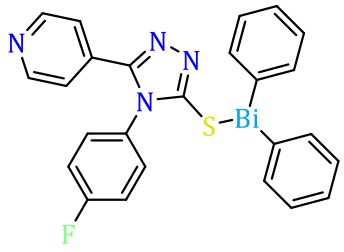

[Bi(Ph)$_2$(PFTz)] (2-11): Following GP2: $BiPh_2Cl$ (200 mg, 0.5 mmol) was reacted with triazole thione **5** (148 mg, 0.5 mmol) in methanol. The title complex was isolated as an off-white solid (121 mg, 38%). ^{1}H NMR (600 MHz, DMSO-d_6, 25 °C) δ 8.56 – 8.46 (m, 1H), 8.25 (dd, J = 7.8, 1.4 Hz, 2H), 7.56 (t, J = 7.6 Hz, 2H), 7.42 – 7.30 (m, 2H), 7.25 – 7.15 (m, 1H). ^{13}C NMR (151 MHz, DMSO-d_6) δ 150.0, 137.8, 131.2, 127.6, 121.2, 116.7, 116.6. FT-IR (film, cm^{-1}): 1575 (C=C), 1460 (C-N), 824 (C-S), 735 (C-H). Melting Point: 121 °C (decomp.). MS (ESI) calculated for $C_{25}H_{19}BiFN_4S$: 635.10782 $(M + H)^+$. CCDC 1968620.

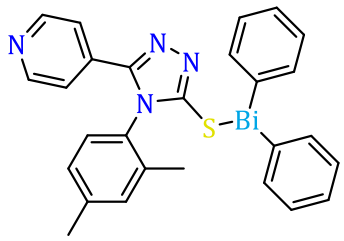

[Bi(Ph)$_2$(PDTz)] (2-12): Following GP2: $BiPh_2Cl$ (200 mg, 0.5 mmol) was reacted with triazole thione **6** (152 mg, 0.5 mmol) in methanol. The title complex was isolated as an off-white solid (242 g, 75%). ^{1}H NMR (600 MHz, DMSO-d_6, 25 °C) δ 8.49 (d, J = 6.2 Hz, 1H), 8.35 – 8.18 (m, 3H), 7.52 (t, J = 7.5 Hz, 3H), 7.36 – 7.26 (m, 2H), 7.21 (dd, J = 4.4, 1.8 Hz, 2H), 7.19 – 7.13 (m, 1H), 7.10 (d, J = 7.9 Hz, 1H), 2.34 (s, 2H), 1.83 (s, 2H). ^{13}C NMR (151 MHz, DMSO-d_6) δ 150.1, 137.9, 134.8 (d, J = 40.2 Hz), 131.9, 128.2 (d, J = 38.6 Hz), 127.5, 120.0. FT-IR (film, cm^{-1}): 1575 (C=C), 1460 (C-N), 824 (C-S), (C-H). Melting Point: 161 - 162 °C. MS (ESI) calculated for $C_{27}H_{23}BiN_4S$: 645.1507 $(M + H)^+$. CCDC 1968623.

6.2.6 [Bi(Ph)$_2$SR]: Diphenylbismuth(III) rhodanine complexes

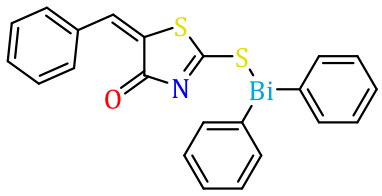

[Bi(Ph)$_2$(BR)] (BR1: 2-13): Following GP3: $BiPh_3$ (220 mg, 0.5 mmol) was reacted with rhodanine **1** (111 mg, 0.5 mmol) in DMSO. The title complex was isolated from the reaction filtrate as needle-like crystals (242 g, 83 %). ^{1}H NMR (600 MHz, DMSO-d_6, 25 °C) δ 8.29 (dd, J = 7.7, 1.4 Hz, 4H), 7.72 (t, J = 7.5 Hz, 4H), 7.56 – 7.45 (m, 5H), 7.44 – 7.36 (m, 3H), 7.34 (s, 1H). ^{13}C NMR (151 MHz, DMSO) δ 138.33, 137.78, 134.32, 132.04, 130.77, 130.60, 130.42, 129.74, 128.80, 128.43, 127.96. FT-IR (film, cm^{-1}): 1586 ((C-N)+δ(N-H)), 1226 (C-N-C), 1182 (C=S), 758 (C-N). Melting Point: 180 °C (decomp.). MS (ESI) calculated for $C_{22}H_{16}BiNOS_2$: 582.8206 $(M - H)^+$.

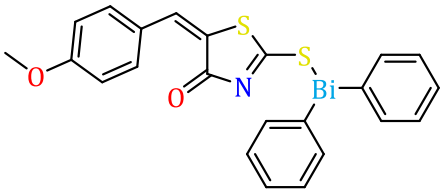

[Bi(Ph)$_2$(MOBR)] (2-14): Following **GP3**: $BiPh_3$ (200 mg, 0.5 mmol) was reacted with rhodanine **2** (80 mg, 0.32 mmol) in DMSO. The title complex was isolated from the reaction filtrate as orange needles (55 mg, 25 %). ^{1}H NMR (600 MHz, DMSO-d_6, 25 °C) δ 8.31 – 8.26 (m, 4H), 7.72 (t, J = 7.2 Hz, 4H), 7.47 (d, J = 8.4 Hz, 2H), 7.41 (t, J = 7.4 Hz, 2H), 7.27 (s, 1H), 7.07 – 7.03 (m, 2H), 3.80 (s, 3H).^{13}C NMR (151 MHz, DMSO-d_6) δ 160.96, 138.15, 137.77, 132.04, 130.75, 128.46, 115.30, 55.91 FT-IR (film, cm^{-1}): 1579 ((C-N)+δ(N-H)), 1236 (C-N-C), 821 (C-N). Melting Point: 210 °C (decomp.). MS (ESI) calculated for $C_{23}H_{18}BiNO_2S_2$: 636.0489 $(M + Na)^+$. CCDC 2207467.

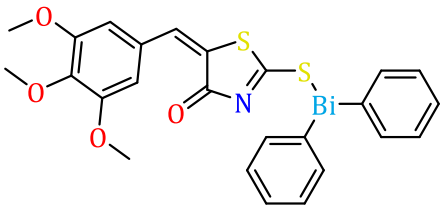

[Bi(Ph)$_2$(3MOBR)] (2-15): Following **GP3**: $BiPh_3$ (140 mg, 0.32 mmol) was reacted with rhodanine **3** (80 mg, 0.32 mmol) in DMSO. The title complex was isolated from the reaction filtrate as red block crystals (55 mg, 72 %). δ ^{1}H NMR (600 MHz, DMSO) δ 8.31 – 8.27 (m, 2H), 7.70 (t, J = 7.3 Hz, 2H), 7.53 (s, 2H), 7.43 – 7.36 (m, 1H), 6.90 (s, 4H). ^{13}C NMR (151 MHz, DMSO) δ 153.71, 139.88, 137.85, 137.78, 132.12, 129.41, 128.59, 108.24, 60.69, 56.49. FT-IR (film, cm-1): 1560 ((C-N)+δ(N-H)), 1222 (C-N-C), 727 (C-N). Melting Point: 210 °C (decomp.). Melting Point: 195 °C (decomp.). MS (ESI) calculated for $C_{25}H_{22}BiNO_4S_2$: 696.0715 $(M + Na)^+$.

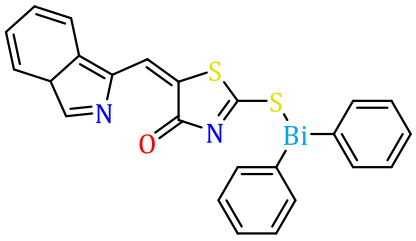

[Bi(Ph)$_2$(InR)] (2-16): Following **GP3**, $BiPh_3$ (200 mg, 0.5 mmol) was reacted with rhodanine **4** (152 mg, 0.5 mmol) in DMSO. The title complex was isolated from the reaction filtrate as orange blocky crystals (242 g, 63 %). ^{1}H NMR (600 MHz, DMSO-d_6, 25 °C) δ 11.91 (s, 1H), 8.30 (d, J = 7.3 Hz, 4H), 7.83 (d, J = 7.9 Hz, 1H), 7.69 (s, 4H), 7.58 (s, 1H), 7.46 (dt, J = 8.1, 0.9 Hz, 1H), 7.40 (t, J = 7.4 Hz, 2H), 7.21 (ddd, J = 8.2, 7.0, 1.2 Hz, 1H), 7.16 (dd, J = 14.9, 1.1 Hz, 1H), 7.16 (s, 1H). FT-IR (film, cm-1): 1542 ((C-N)+δ(N-H)), 1218 (C-N-C), 722 (C-N). Melting Point: 188 °C (decomp.). MS (ESI) calculated for $C_{24}H_{19}BiN_2OS_2$: 667.0460 $(M + FA-H)^-$. CCDC 2207535.

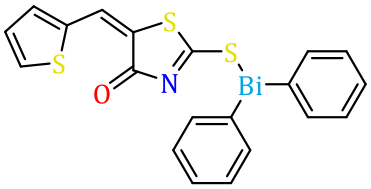

[Bi(Ph)$_2$(ThR)] (2-17): Following **GP3**, $BiPh_3$ (200 mg, 0.5 mmol) was reacted with rhodanine **5** (113 mg, 0.5 mmol) in DMSO. The title complex was isolated from the reaction filtrate as yellow needle-like crystals (161 g, 55 %). ^{1}H NMR (400 MHz, DMSO-d_6, 25 °C) δ 8.28 (d, *J* = 7.2 Hz, 4H), 8.02 (d, *J* = 4.8 Hz, 4H), 7.81 (s, 5H), 7.73 (t, *J* = 7.7 Hz, 5H), 7.65 (d, *J* = 3.6 Hz, 5H), 7.40 (q, *J* = 7.8 Hz, 2H), 7.28 (dd, *J* = 5.1, 3.7 Hz, 4H). ^{13}C NMR (101 MHz, DMSO) δ 139.29, 137.69, 133.24, 132.14, 131.57, 130.28, 128.89, 128.31, 127.99. FT-IR (film, cm-1): 1561((C-N)+δ(N-H)), 1186 (C=S), 704 (C-N). Melting Point: 161 - 162 °C. MS (ESI) calculated for $C_{20}H_{14}BiNOS_3$: 611.9956 $(M + Na)^+$.

6.3 Chapter 3

6.3.1 Photophysical measurements

Emission and excitation spectra were collected using an Agilent Technologies Cary Eclipse Fluorescence Spectrometer, using standard quartz fluorescence cuvettes of 1 cm path length. Emission and excitation spectra were corrected for source intensity (lamp and grating) and emission spectral response (detector and grating) by a calibration curve supplied with the instrument.

UV-visible absorption spectra were collected at room temperature using a Cary 60 UV-Visible (Agilent Technologies, USA) scanning the range 200–750 nm. Fluorescence and excitation spectra were recorded on a Cary Eclipse Fluorescence Spectrophotometer (Agilent Technologies, USA) using an excitation slit width of 5 nm and emission slit width of 5 nm for all measurements. The photomultiplier tube (PMT) voltage of the fluorescence spectrophotometer was varied depending on the fluorescence intensity of the sample. All UV-visible and fluorescence measurements were performed using type 41FL UV Quartz macro fluorescence cuvettes from FireflySci (USA) with a 10 mm path length.

According to the approach described by Demas and Crosby,[497] luminescence quantum yields (f) were measured in optically dilute solutions (O.D. < 0.1) at the excitation wavelength (nm) obtained from absorption spectra and compared to the reference emitter by the following equation:

$$\Phi_x = \Phi_r \left[\frac{A_r(\lambda_r)}{A_x(\lambda_x)}\right]\left[\frac{I_r(\lambda_r)}{I_x(\lambda_x)}\right]\left[\frac{n_x^2}{n_r^2}\right]\left[\frac{D_x}{D_r}\right]$$

where A is the absorbance at the excitation wavelength (l), I is the intensity of the excitation light at the excitation wavelength (l), n is the refractive index of the solvent,

D is the integrated intensity of the luminescence and f is the quantum yield. The subscripts r and x refer to the reference and the sample, respectively. The quantum yield determinations were performed at identical excitation wavelengths, for the sample and the reference, therefore cancelling out the FT-IR (lr)/Ix(lx) term in the above equation. The quantum yields of the complexes were either measured against an air-equilibrated 0.1 M solution of Coumarin 153 in ethanol (Φ_r = 0.53).

Time-resolved fluorescence decays were measured on a previously described home-built set-up using the method of time correlated single photon counting (TCSPC).[498] Data were fitted by an exponential decay convolved with the instrument response function (IRF, typically ,90–100 ps). Goodness-of-fit of the data by the fitting function was determined from the x2 fitting parameter and the distribution of the residuals. Emission times were recorded using a photon counting device (Picoquant, PicoHarp 300) through a router (Picoquant, PHR 800) with a trigger diode assembly (PicoQuant, TDA 200) to provide the start signal.[499] Data collection was performed using the SymPhoTime (Picoquant) and WinSpec (Princeton) software suites. The photon stream from the APD was collected in t3r mode where both macro times (time from start of measurement) and micro times (time from previous laser pulse) are recorded for every photon. SM trajectories (from macro times) and decay profiles (from micro times) were constructed and analysed using the BIFL software package (Scientific Software Technologies Center).[500]

Degassed solutions were prepared by gently bubbling nitrogen gas into the prepared sample for 15 min before measurement.

6.3.2 Precursor synthesis

6.3.2.1 Synthesis of rhenium(I) tricarbonyl diimine salts, [Re(N^N)(CO)$_3$Cl]

The preparation of fac-[Re(N^N)(CO)$_3$Cl] (N^N= 1,10-phenanthroline or 2,2'-bipyridine) was carried out following procedures adapted from previously published

work. Rhenium pentacarbonyl chloride (1 eq) and the corresponding diimine (bipy or phen) (1.1 eq) were added to toluene and heated at reflux for 4 hours. A yellow solid was filtered off and washed with cold toluene to yield the final complex.[501]

Yield of [Re(phen)(CO)$_3$Cl]: 0.643 g (98%). MP 330 °C (dec.). νmax (FT-IR)/cm-1: 3749 w, 3085 w, 2013 s (CO, A´(1)), 1891 s (CO, A´(2)), 1872 s br (CO, A´´), 1601 m, 1571 w, 1491 w, 1470 m, 1443 m, 1314 w, 1246 w, 1162 w, 1122 w, 1105 w, 1070 w, 967 w, 764 m, 732 m.

Yield of [Re(bpy)(CO)$_3$Cl]: 0.651 g, 90%. M.p. 300 °C (dec.). νmax (FT-IR)/cm^{-1}: 3897 w, 3749 w, 3088 w, 2014 s (CO, A´(1)), 1923 s (CO, A´(2)), 1885 s br (CO, A´´), 1629 w, 1602 w, 1584 w, 1518 w, 1492 w, 1425 m, 1409 m, 1340 w, 1315 w, 1302 w, 1210 w, 1196 w, 1143 w, 1108 w, 1098 w, 1063 w, 961 w, 850 m, 782 w, 722 m.

6.3.2.2 Synthesis of rhenium(I) solvate complexes, [Re(N^N)(CO)$_3$(solv)][SO$_3$CF$_3$]

fac-Re(N^N)(CO)$_3$Cl (0.5 g, 1.02 mmol) and silver triflate (0.264 g, 1.02 mmol) were added to a Schlenk flask and the vessel evacuated. Dry DCM (50 mL) was added, and the solution was refluxed under N_2 with the exclusion of light for 5 hours, after which a white precipitate was observed. After cooling to room temperature, this was removed by filtration through a Celite pad. The solvent was removed by evaporation to leave a yellow powder.[502]

6.3.3 General synthetic procedures

6.3.3.1 GP4: Synthesis of [Re(N^N)(CO)$_3$(L)]: phen/bpy-derived Re(I) tricarbonyl ancillary triazole complexes.

To an acetonitrile solution of the precursor [*fac*-[Re(phen)(CO)$_3$DCM]SO$_3$CF$_3$] solvato complex, 1.3 equivalents of the corresponding triazole and 1.4 equivalents of triethylamine were added in a microwave vial. This mixture was heated in a CEM microwave reactor for 10 minutes reaching maximum of 80 °C affording the desired complexes. The resulting products were collected as is after removal of solvent and did not require any further purification.

6.3.3.2 Synthesis of [Re(N^N)(CO)$_3$X]: Re(I) tricarbonyl backbone triazole complexes

The preparation of *fac*-[Re(N^N)(CO)$_3$Cl] (N^N= *ortho*-pyridyl triazole thione) was carried out following procedures adapted from previously published work. Rhenium pentacarbonyl chloride (1 eq) and the corresponding *ortho*-pyridyl triazole thione **14- 17** (1 eq) were added to toluene and heated at reflux for 4 hours. A yellow solid was filtered off and washed with cold toluene to yield the final complex.[501]

6.3.4 [Re(N^N)(CO)$_3$(L)]: phen/bpy-derived Re(I) tricarbonyl ancillary triazole complexes

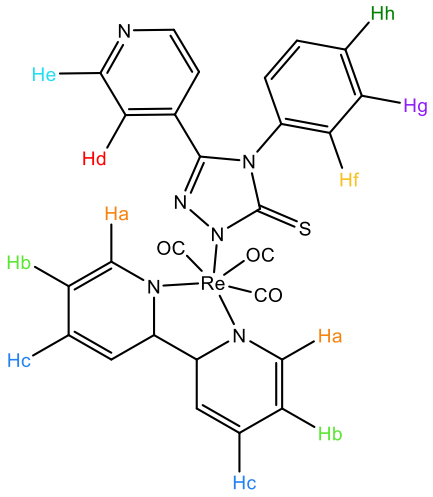

[Re(bpy)(CO)$_3$(pyta)] (3-1): Following **GM3** [Re(bpy)(CO)$_3$(DCM)]SO_3CF_3 (52 mg, 0.079 mmol) was reacted with triazole thiol **1** (20 mg, 0.079 mmol) in acetonitrile. The title complex was crystallised from the reaction mixture as orange needles (21.4 mg, 40 %). ^{1}H NMR (600 MHz, DMSO-d_6) δ 9.28 (ddd, J = 5.5, 1.6, 0.7 Hz, 2H), 8.73 (dt, J = 8.2, 1.0 Hz, 2H), 8.37 – 8.28 (m, 4H), 7.75 (ddd, J = 7.6, 5.5, 1.3 Hz, 2H), 7.44 – 7.35 (m, 3H), 7.15 – 7.08 (m, 2H), 6.64 – 6.58 (m, 2H).^{13}C NMR (151 MHz, DMSO-d_6) δ 176.43, 155.89, 154.55, 149.71, 140.35, 136.21, 133.87, 129.08, 128.81, 128.50, 127.17, 123.52, 120.25. FT-IR (film, cm $^{-1}$): 2008s (CO, A) 1911s (CO, B), 1864s (CO, C), 1596m, 1421m, 1326m, 763s, 689m. Melting Point: >300 °C (decomp.). MS (ESI) calculated for $C_{26}H_{19}N_6O_3ReS$: 682.0733 $(M + H)^+$. Elemental analysis: calculated: C: 45.81, H: 2.81, N: 12.33, Found : C: 45.99, H: 2.56, N: 12.28. CCDC: 2220942

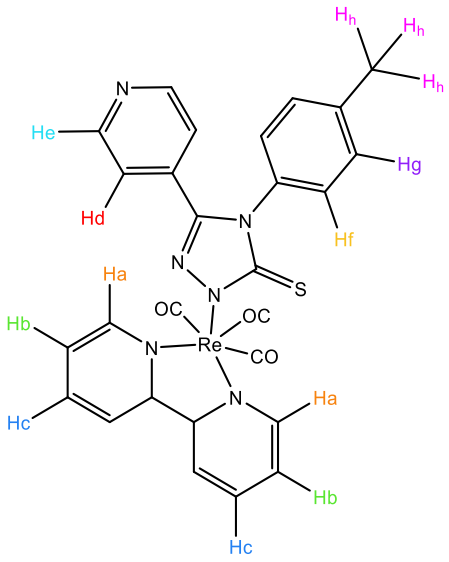

[Re(bpy)(CO)$_3$(pyta-t)] (3-2): Following **GM3** [Re(bpy)(CO)$_3$(DCM)]SO$_3$CF$_3$ (53.2 mg, 0.081 mmol) was reacted with triazole thiol **2** (26 mg, 0.081 mmol) in acetonitrile. The title complex was precipitated from the reaction mixture as a yellow powder (27 mg, 48 %). ^{1}H NMR (600 MHz, DMSO-d_6) δ 9.31 – 9.24 (m, 2H), 8.74 – 8.66 (m, 2H), 8.37 – 8.23 (m, 4H), 7.74 (ddt, J = 7.7, 5.5, 1.1 Hz, 2H), 7.18 (d, J = 8.0 Hz, 2H), 6.97 (d, J = 8.0 Hz, 2H), 6.66 – 6.62 (m, 2H), 2.31 (s, 3H). ^{13}C NMR (151 MHz, DMSO-d_6) δ 197.96, 194.79, 177.03, 156.34, 154.99, 150.29, 150.18, 147.91, 140.78, 138.71, 134.38, 134.12, 130.03, 128.65, 127.62, 123.97, 120.67. δ FT-IR (film, cm $^{-1}$): 2010s (CO, A), 1912s (CO, B), 1867s (CO, C), 1328s, 764s. Melting Point: >300 °C (decomp.). MS (ESI) calculated $C_{27}H_{21}N_6O_3ReS$: 696.0890 $(M + H)^+$. Elemental analysis calculated: C: 46.61, H: 3.04, N: 12.08, Found.

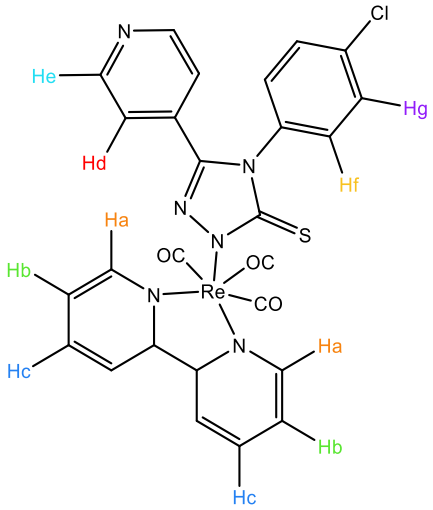

[Re(bpy)(CO)$_3$(pyta-Cl)] (3-3): Following **GM3**: [Re(bpy)(CO)$_3$(DCM)]$^+$ (52.7 mg, 0.080 mmol) was reacted with triazole thiol **3** (23 mg, 0.080 mmol) in acetonitrile. The title complex was precipitated from the reaction mixture as a yellow powder (34.2 mg, 60 %). ^{1}H NMR (600 MHz, DMSO-d_6) δ 9.29 – 9.24 (m, 2H), 8.72 (dq, J = 8.3, 1.1 Hz, 2H), 8.38 (dq, J = 5.4, 3.5, 2.7 Hz, 2H), 8.32 (tt, J = 7.9, 1.8 Hz, 2H), 7.75 (dddd, J = 6.7, 5.5, 2.2, 1.2 Hz, 2H), 7.48 – 7.41 (m, 2H), 7.21 – 7.13 (m, 2H), 6.69 – 6.62 (m, 2H). ^{13}C NMR (151 MHz, DMSO-d_6) δ 197.45, 176.29, 155.90, 154.54, 149.85, 149.83, 147.43, 140.36, 135.07, 133.73, 133.33, 130.46, 129.08, 127.19, 123.54, 120.45. δ FT-IR (film, cm $^{-1}$): 2010s (CO, A), 1912s (CO, B), 1869s (CO, C), 1325m, 764s. Melting Point: >300 °C (decomp.). MS (ESI) calculated for $C_{26}H_{18}ClN_6O_3ReS$: 717.0302 $(M + H)^+$. Elemental analysis: calculated: C: 43.60, H: 2.53, N: 11.73, Found. CCDC 2220943.

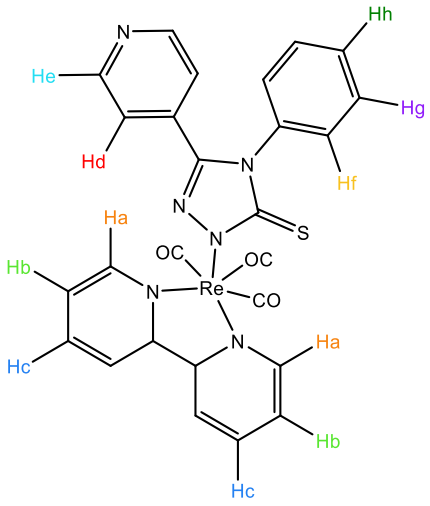

[Re(bpy)(CO)$_3$(pyta-2Me)] (3-4): Following **GM3:** [Re(bpy)(CO)$_3$(DCM)]$^+$ (59 mg, 0.089 mmol) was reacted with triazole thiol **4** (25.5 mg, 0.089 mmol) in acetonitrile. The title complex was crystallised from the reaction mixture as yellow needles (30.3 mg, 48 %). ^{1}H NMR (400 MHz, DMSO-d_6) δ 9.32 (dd, J = 22.9, 5.7 Hz, 2H), 8.79 – 8.56 (m, 2H), 8.30 (dd, J = 21.7, 6.6 Hz, 4H), 7.80 (t, J = 6.6 Hz, 1H), 7.69 (t, J = 6.7 Hz, 1H), 7.09 – 6.95 (m, 3H), 6.62 (d, J = 5.2 Hz, 2H), 2.28 (s, 3H), 1.39 (s, 3H).^{13}C NMR (151 MHz, DMSO-d_6) δ 149.9, 137.9, 135.2, 134.7, 131.1, 129.7, 129.5, 127.9, 127.5, 121.0. FT-IR (film, cm $^{-1}$): 2010s (CO, A), 1913s (CO, B), 1866s (CO, C), 1599, 1323, 765. Melting Point: >300 °C (decomp.). MS (ESI) calculated for $C_{28}H_{23}N_6O_3ReS$: (M + H)$^+$. Elemental analysis: calculated: C: 47.38, H: 3.27, N: 11.84, Found.

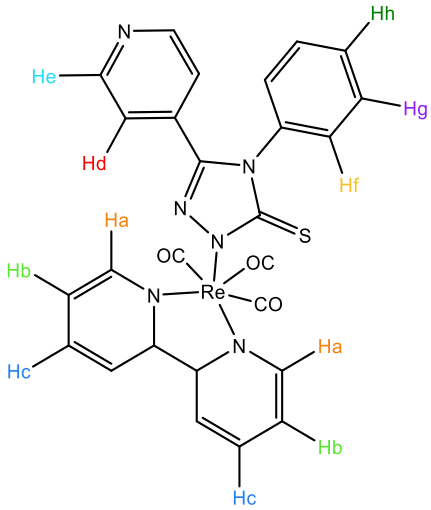

[Re(bpy)(CO)$_3$(futa)] (3-5): Following **GM3:** [Re(bpy)(CO)$_3$(DCM)]$^+$ (50 mg, 0.076 mmol) was reacted with triazole thiol **5** (21.7 mg, 0.076 mmol) in acetonitrile. The title complex was crystallised from the reaction mixture as orange blocks (26.7 mg, 53 %). ^{1}H NMR (600 MHz, DMSO-d_6) δ 9.30 (dd, J = 5.6, 1.5 Hz, 4H), 8.68 (d, J = 8.1 Hz, 5H), 8.29 (td, J = 7.9, 1.6 Hz, 5H), 7.74 (ddd, J = 7.2, 5.5, 1.2 Hz, 4H), 7.51 (d, J = 1.7 Hz, 2H), 7.40 (p, J = 3.5, 3.1 Hz, 7H), 7.12 – 7.05 (m, 4H), 6.30 (dd, J = 3.5, 1.8 Hz, 2H), 5.53 (d, J = 3.4 Hz, 2H), 3.51 (s, 4H), 3.48 – 3.39 (m, 4H), 3.43 (s, 4H), 3.36 (s, 14H), 3.35 (s, 1H), 2.69 (s, 1H), 2.57 – 2.51 (m, 0H), 2.50 – 2.44 (m, 1H), 1.02 (s, 1H).^{13}C NMR (151 MHz, DMSO-d_6) δ 174.92, 155.72, 154.76, 143.95, 142.98, 141.12, 140.33, 136.24, 129.02, 128.54, 127.12, 123.53, 111.23, 109.93. FT-IR (film, cm $^{-1}$): 2013s (CO, A), 1914s (CO, B), 1890 (CO, C), 1592, 1422, 1320, 721, 690. Melting Point: >300 °C (decomp.). MS (ESI) calculated for $C_{25}H_{18}N_5O_4ReS$: 670.0555 (M + H)$^+$. Elemental analysis: calculated: C: 44.77, H: 2.71, N: 10.44, Found. CCDC 2220944.

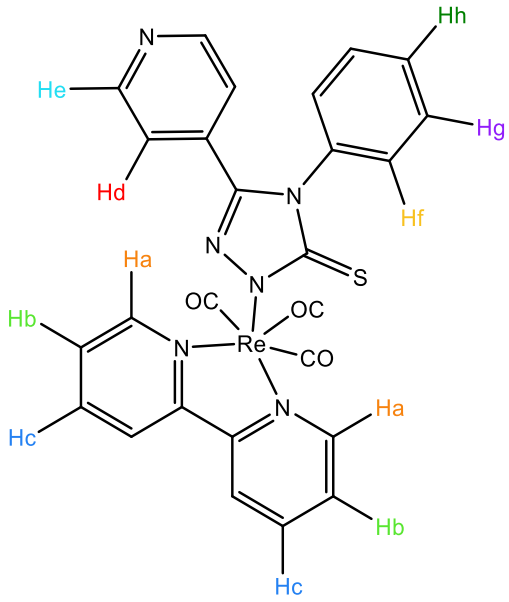

[Re(bpy)(CO)$_3$(futa-Cl)] (3-6): Following **GM3**: [Re(bpy)(CO)$_3$(DCM)]$^+$ (53.7 mg, 0.081 mmol) was reacted with triazole thiol **6** (22.8 mg, 0.081 mmol) in acetonitrile. The title complex was crystallised from the reaction mixture as orange blocks (42.3 mg, 74 %). ^{1}H NMR (600 MHz, DMSO-d$_6$) δ 9.71 (dd, J = 5.1, 1.4 Hz, 2H, Ha), 8.94 (dd, J = 8.3, 1.4 Hz, 2H, Hb), 8.30 (s, 2H, Hd), 8.27 – 8.22 (m, 2H, Hc), 8.11 (dd, J = 8.2, 5.1 Hz, 2H, Hf), 7.40 – 7.30 (m, 3H, Hi+Hj), 7.04 – 6.97 (m, 2H, He), 6.40 – 6.36 (m, 2H, Hg). ^{13}C NMR (151 MHz, DMSO-*d*$_6$) δ 155.71, 154.69, 142.74, 133.34, 130.47, 128.97, 123.52, 99.50. FT-IR (film, cm $^{-1}$): 2013s (CO, A), 1914s (CO, B), 1890s (CO, C), 1592, 1422, 1320, 721, 690. Melting Point: >300 °C (decomp.). MS (ESI) calculated for $C_{25}H_{17}ClN_5O_4ReS$: 704.0154 (M + H)$^+$. Elemental analysis: calculated: C: 42.58, H: 2.43, N: 5.03, Found. CCDC 2220947.

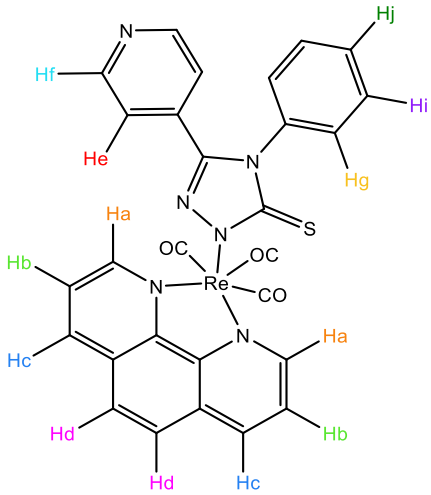

[Re(phen)(CO)$_3$(pyta)] (3-7): Following **GM3**: [Re(phen)(CO)$_3$(DCM)]$^+$ (50 mg, 0.073 mmol) was reacted with triazole thiol **1** (20.5 mg, 0.073 mmol) in acetonitrile. The title complex was crystalised from the reaction mixture as orange blocks (20 mg, 40 %). ^{1}H NMR (600 MHz, DMSO-d$_6$) δ 9.71 (dd, J = 5.1, 1.4 Hz, 2H, Ha), 8.94 (dd, J = 8.3, 1.4 Hz, 2H, Hb), 8.30 (s, 2H, Hd), 8.27 – 8.22 (m, 2H, Hc), 8.11 (dd, J = 8.2, 5.1 Hz, 2H, Hf), 7.40 – 7.30 (m, 3H, Hi+Hj), 7.04 – 6.97 (m, 2H, He), 6.40 – 6.36 (m, 2H, Hg). ^{13}C NMR (151 MHz, DMSO-*d*$_6$) δ 149.9, 137.9, 135.2, 134.7, 131.1, 129.7, 129.5, 127.9, 127.5, 121.0. FT-IR (film, cm $^{-1}$): 2013s (CO, A), 1914s (CO, B), 1890s (CO, C), 1592, 1422, 1320, 721, 690. Melting Point: >300 °C (decomp.). MS (ESI) calculated for $C_{28}H_{17}N_6O_3ReS$ (M + H)$^+$. Elemental analysis: calculated: C: 47.79, H: 2.43, N: 11.94 Found. C: 47.93, H: 2.43, N: 11.90. CCDC 2220952.

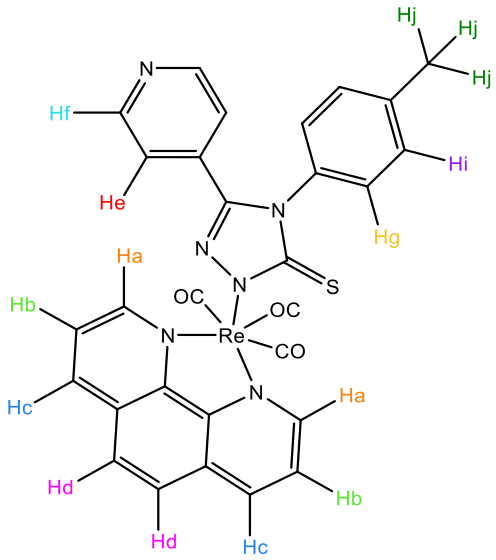

[Re(phen)(CO)$_3$(pyta-t)] (3-8): Following **GM3:** [Re(phen)(CO)$_3$(DCM)]$^+$ (50 mg, 0.073 mmol) was reacted with triazole thiol **2** (31 mg, 0.073 mmol) in acetonitrile. The title complex was crystallised from the reaction mixture as orange blocks (23 mg, 44 %). ^{1}H NMR (600 MHz, DMSO-d_6) δ 9.71 (dt, J = 5.1, 1.7 Hz, 2H), 8.94 (dt, J = 8.3, 1.6 Hz, 2H), 8.31 – 8.23 (m, 4H), 8.14 – 8.08 (m, 2H), 7.16 – 7.11 (m, 2H), 6.88 (dd, J = 8.4, 2.1 Hz, 2H), 6.43 – 6.38 (m, 2H), 2.29 (d, J = 1.8 Hz, 3H).^{13}C NMR (151 MHz, DMSO-d$_6$) δ 197.34, 194.19, 176.45, 155.14, 150.06, 149.51, 147.27, 146.49, 139.35, 138.19, 133.76, 133.44, 129.96, 129.49, 128.10, 127.49, 125.97, 120.01, 20.68. δ FT-IR (film, cm^{-1}): 2018 (CO, A), 1894 (CO, B), 1516, 1427, 1323, 847, 723. Melting Point: >300 °C (decomp.). MS (ESI) calculated for $C_{29}H_{19}ReN_6O_3ReS$: 717.0996 $(M)^+$, 719.1023 $(M+H)^+$ Elemental analysis: calculated: C: 48.53, H: 2.67, N: 11.71, Found. CCDC 2220948.

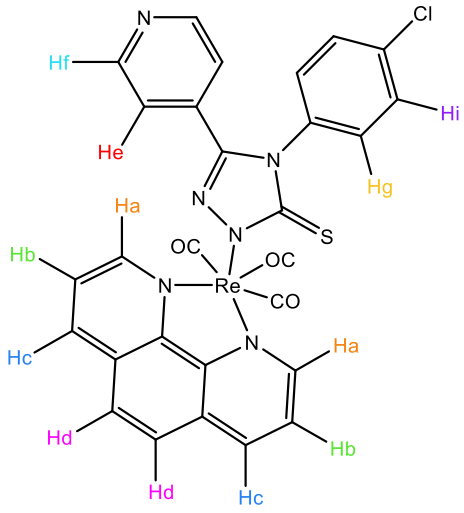

[Re(phen)(CO)$_3$(pyta-Cl)] (3-9): Following **GM3** [Re(phen)(CO)$_3$(DCM)]$^+$ (50 mg, 0.073 mmol) was reacted with triazole thiol **3** (21 mg, 0.073 mmol) in acetonitrile. The title complex was crystallised from the reaction mixture as orange blocks (21.5 mg, 40 %). ^{1}H NMR (400 MHz, DMSO-d$_6$) δ 9.70 (dd, J = 5.1, 1.4 Hz, 2H, Ha), 8.94 (dd, J = 8.3, 1.4 Hz, 2H, Hf), 8.32 – 8.26 (m, 4H, Hd+Hc), 8.11 (dd, J = 8.2, 5.1 Hz, 2H, Hb), 7.43 – 7.35 (m, 2H, Hi), 7.08 (d, J = 8.7 Hz, 2H, Hg), 6.47 – 6.40 (m, 2H, He). ^{13}C NMR (151 MHz, DMSO-d_6) δ 131.7, 130.3, 114.8. FT-IR (film, cm^{-1}): 2019 (CO, A), 1893s (CO, B), 1494s 1427, 1318, 1089, 829, 723. Melting Point: >300 °C (decomp.). MS (ESI) calculated for $C_{28}H_{16}ClN_6O_3ReS$: $(M + Na)^+$. Elemental analysis: calculated: C: 45.56, H: 2.18, N: 11.38, Found. CCDC 2220949.

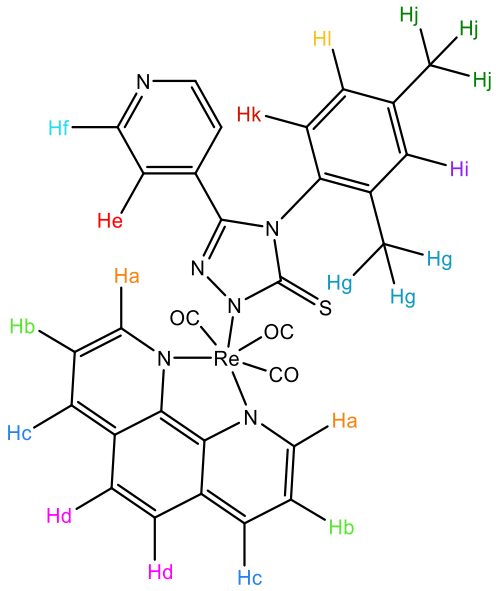

[Re(phen)(CO)$_3$(pyta-2Me)] (3-10): Following **GM3**, [Re(phen)(CO)$_3$(DCM)]$^+$ (50 mg, 0.073 mmol) was reacted with triazole thiol **4** (18 mg, 0.073 mmol) in acetonitrile. The title complex was crystallised from the reaction mixture as orange blocks (20.3 mg, 40%). ^{1}H NMR (600 MHz, DMSO-d$_6$) δ 9.82 – 9.77 (m, 1H, Ha), 9.73 – 9.69 (m, 1H, Ha), 8.91 (ddd, J = 43.2, 8.3, 1.3 Hz, 2H, Hb), 8.31 – 8.20 (m, 5H, Hc+Hd+Hi), 8.17 (dd, J = 8.3, 5.1 Hz, 1H, Hl), 8.04 (dd, J = 8.3, 5.1 Hz, 1H, Hk), 7.00 (d, J = 7.6 Hz, 1H,), 6.91 (d, J = 7.9 Hz, 2H, Hf), 6.43 – 6.38 (m, 2H, He), 2.23 (s, 3H, Hj), 0.91 (s, 2H, Hg). ^{13}C NMR (151 MHz, DMSO-*d*$_6$) δ 174.06, 154.23, 153.41, 148.13, 145.42, 144.40, 144.35, 137.62, 137.50, 137.03, 133.18, 131.91, 130.97, 129.68, 128.30, 128.22, 127.09, 125.82, 125.72, 125.59, 124.41, 123.91, 117.63, 18.99, -0.49. FT-IR (film, cm^{-}1): 2019s (CO, A), 1915s (CO, B), 1887s (CO, C), 1422, 845, 722. Melting Point: 186.1 – 189.0 °C. MS (ESI) calculated for C$_{30}$H$_{21}$N$_6$O$_3$ReS:(M + H)$^+$. Elemental analysis: calculated: C: 49.24, H: 2.89, N: 11.48, Found.

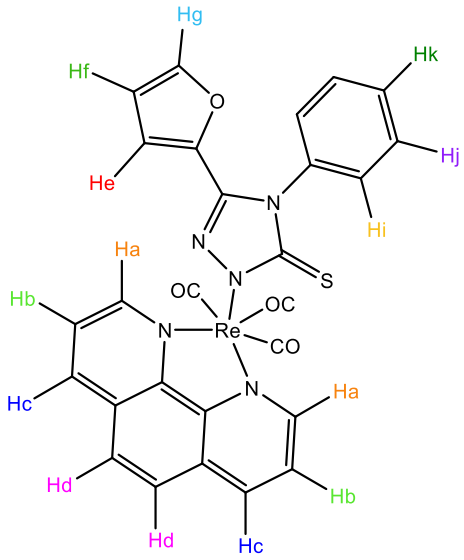

[Re(phen)(CO)$_3$(futa)] (3-11): Following **GM3**: [Re(phen)(CO)$_3$(DCM)]$^+$ (50 mg, 0.073 mmol) was reacted with triazole thiol **5** (17.7 mg, 0.073 mmol) in acetonitrile. The title complex was crystallised from the reaction mixture as orange blocks (19.5 mg, 39%). ^{1}H NMR (400 MHz, DMSO-*d*$_6$) δ 9.73 (dd, J = 5.1, 1.4 Hz, 2H, Ha), 8.93 (dd, J = 8.3, 1.4 Hz, 2H, Hb), 8.28 (s, 2H, Hd), 8.10 (dd, J = 8.3, 5.1 Hz, 2H, Hc), 7.47 (d, J = 1.8 Hz, 1H, Hg), 7.51 – 7.22 (m, 2H, Hj), 6.97 (d, J = 7.4 Hz, 2H, Hl), 6.26 (dd, J = 3.5, 1.9 Hz, 1H, Hf), 5.36 (d, J = 3.5 Hz, 1H, He). ^{13}C NMR (151 MHz, DMSO-*d*$_6$) δ 197.36, 194.04, 174.77, 155.35, 146.21, 143.77, 142.83, 140.86, 139.31, 135.97, 129.92, 128.86, 128.73, 128.42, 127.48, 125.88, 111.07, 109.68. δ FT-IR (film, cm^{-1}): 2015s (CO, A), 1890s (CO, C), 1500, 1427, 1327, 725, 692. Melting Point: >300 °C

(decomp.). MS (ESI) calculated for $C_{27}H_{16}N_5O_4ReS$: $(M + H)^+$. Elemental analysis: calculated: C: 46.81, H: 2.33, N: 10.11, Found. CCDC 2220950.

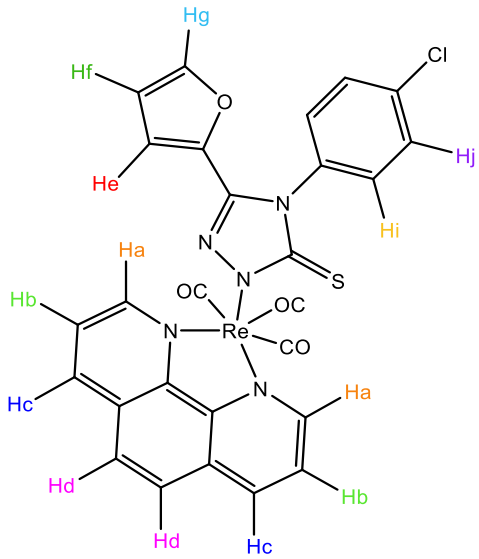

[Re(phen)(CO)$_3$(futa-Cl)] (3-12): Following **GM3**: $[Re(phen)(CO)_3(DCM)]^+$ (50 mg, 0.073 mmol) was reacted with triazole thiol **6** (20 mg, 0.073 mmol) in acetonitrile. The title complex was crystallised from the reaction mixture as orange blocks (19.3 mg, 39%). ^{1}H NMR (600 MHz, DMSO-d_6) δ 9.74 (dd, J = 5.1, 1.5 Hz, 2H), 8.92 (dd, J = 8.4, 1.5 Hz, 2H), 8.27 (d, J = 1.7 Hz, 2H), 8.10 (dd, J = 8.2, 5.2 Hz, 2H), 7.45 – 7.38 (m, 2H), 7.05 (dd, J = 9.0, 2.2 Hz, 2H), 6.33 – 6.25 (m, 1H), 5.57 – 5.50 (m, 1H). ^{13}C NMR (151 MHz, DMSO-d_6) δ 197.31, 174.68, 155.32, 146.24, 143.94, 142.62, 140.69, 139.34, 134.87, 133.26, 130.39, 129.94, 128.86, 127.49, 125.89, 111.19, 109.96. FT-IR = 2008, 1882, 1493, 1425, 1330, 998, 837, 738, 722, 1313. Melting Point: 293-295 °C. MS (ESI) calculated for $C_{27}H_{15}ClN_5O_4ReS$: 728.01527 $(M + H)^+$. Elemental analysis: calculated: C: 44.60, H: 2.08, N: 9.63, Found. CCDC 2220951.

6.3.5 [Re(CO)$_3$(L)X]: Re(I) tricarbonyl backbone triazole complexes

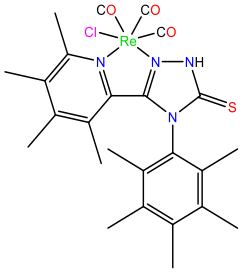

[Re(py2ta)(CO)$_3$Cl] (3-13) Following **GM2**: $[Re(CO)_5(Cl)]$ (103.2 mg, 0.255 mmol) was reacted with *ortho*-pyridyl triazole thione **14** (65 mg, 0.255 mmol) in toluene. The title complex was precipitated from the reaction mixture as an orange solid (100.2 mg, 75 %). ^{1}H NMR (400 MHz, DMSO) δ 8.39 (d, J = 4.8 Hz, 1H), 7.96 (td, J = 7.6, 1.7 Hz, 1H), 7.87 (d, J = 7.9 Hz, 1H), 7.47 (tq, J = 7.3, 3.2 Hz, 4H), 7.34 (dd, J = 6.7, 2.6 Hz, 2H). ^{13}C NMR (101 MHz, C_6D_6) δ 174.26, 154.69, 154.28, 150.29, 142.46, 140.28, 133.91, 133.86, 133.51, 130.12, 129.17.FT-IR (film, cm $^{-1}$): 2026s (CO, A) 1915s (CO, C), 1479m, 691m. MS (ESI) calculated for $C_{16}H_{10}ClN_4O_3ReS$: 591.0537 $[(M + MeOH]^+$. CCDC: 2221270

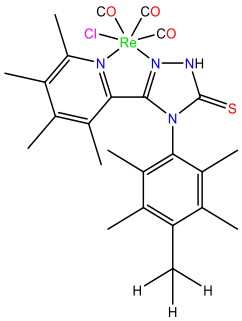

[Re(py2ta-t)(CO)$_3$Cl] (3-14) Following **GM2**: [Re(CO)$_5$(Cl)] (98 mg, 0.227 mmol) was reacted with *ortho*-pyridyl triazole thione **15** (65 mg, 0.227 mmol) in toluene. The title complex was precipitated from the reaction mixture as an orange solid (125 mg, 96 %). FT-IR (film, cm^{-1}): 2024s (CO, A), 1924s (CO, B), 1884s (CO, C), 1479s, 737m. ^{1}H NMR (600 MHz, DMSO) δ 9.11 (dt, *J* = 5.5, 1.1 Hz, 1H), 8.27 – 8.09 (m, 1H), 7.73 (ddd, *J* = 7.8, 5.5, 1.3 Hz, 1H), 7.52 (t, *J* = 8.9 Hz, 2H), 7.47 (s, 1H), 7.32 (s, 1H), 7.02 – 6.79 (m, 1H), 2.07 (s, 2H). ^{13}C NMR (151 MHz, DMSO) δ 155.43, 144.16, 142.56, 141.05, 131.70, 131.66, 131.60, 129.06, 128.22, 128.18, 123.11, 21.39. MS (ESI) calculated for $C_{17}H_{12}ClN_4O_3ReS$: 671.0228 [M + DMSO + H_2O]$^+$.

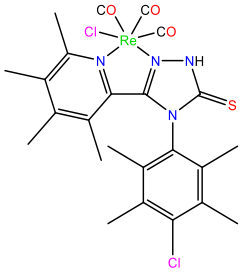

[Re(py2ta-Cl)(CO)$_3$Cl] (3-15) Following **GM2**: [Re(CO)$_5$(Cl)] (92 mg, 0.227 mmol) was reacted with *ortho*-pyridyl triazole thione **16** (65 mg, 0.227 mmol) in toluene. The title complex was precipitated from the reaction mixture as an orange solid (106.2 mg, 84 %). ^{1}H NMR (600 MHz, DMSO) δ 8.36 (ddd, *J* = 4.8, 1.7, 1.0 Hz, 1H), 7.94 (td, *J* = 7.7, 1.7 Hz, 1H), 7.55 – 7.48 (m, 2H), 7.42 (ddd, *J* = 7.5, 4.8, 1.3 Hz, 1H), 7.39 – 7.32 (m, 2H). FT-IR (film, cm^{-1}): 2023s (CO, A), 1906s (CO, B), 1464s, 730m. MS (ESI) calculated for $C_{18}H_{14}ClN_4O_3ReS$: 617.0335 [M + Na]$^+$.

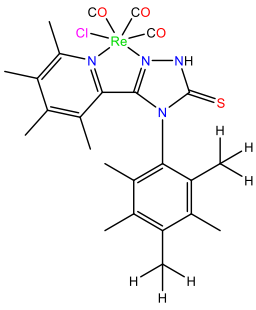

[Re(py2ta-2Me)(CO)$_3$Cl] (3-16) Following **GM2**: [Re(CO)$_5$(Cl)] (94 mg, 0.227 mmol) was reacted with *ortho*-pyridyl triazole thione **17** (65 mg, 0.227 mmol) in toluene. The title complex was precipitated from the reaction mixture as an orange solid (100 mg, 78 %). ^{1}H NMR (400 MHz, DMSO) δ 8.36 (d, *J* = 5.0 Hz, 1H), 7.91 (t, *J* = 7.5 Hz, 1H), 7.82 (d, *J* = 7.9 Hz, 1H), 7.44 – 7.37 (m, 1H), 7.16 (s, 1H), 7.07 – 6.98 (m, 2H). FT-IR (film, cm-1): 2026s (CO, A), 1912s (CO, B), 1483w, 1278w, 748w. MS (ESI) calculated for $C_{16}H_9Cl_2N_4O_3ReS$: 1279.9118 [2M + MeCN + 2Na]$^+$.

6.4 Chapter 4

6.4.1 Precursor synthesis

6.4.1.1 In-situ synthesis of [$GaMe_3$]: trimethylgallium(III)

Caution: Trimethylgallium(III) [Ga(CH3)3] is an extremely pyrophoric liquid. To reduce the presence of pyrophoric vapours when manipulating the liquid, the flask containing [Ga(CH3)3] was placed in an ice-water bath for 10 minutes prior to use, which allowed for significantly safer handling.

6.4.1.2 Synthesis of [$GaPh_3$]: triphenylgallium(III)

Ga metal (1.31 g, 18.8 mmol) and HgPh2 (9.52 g, 26.8 mmol) were combined under inert conditions and heated at 170 °C for 5 hours with stirring. The resulting solid was washed with toluene and cannulated to a fresh Schlenk to remove Hg, then concentrated in vacuo to afford an off-white solid in 60 % yield (3.23 g). 1H NMR (400 MHz, DMSO-d_6): δ = 7.58 (6H, m, Ha), 7.27 (9H, m, Hb,c).

6.4.2 General synthetic procedures

6.4.2.1 Attempted synthesis of tris-substituted gallium(III) triazole thiolate complexes

To a methanolic solution (20 mL) of Ga(III) nitrate nonahydrate $[Ga(NO_3)_3]\cdot 9H_2O$ (0.2 mmol, 0.083 g), a hot methanolic solution (20mL) containing the appropriate triazole thione (0.6 mmol) was added; resulting in an immediate colour change. After cooling to room temperature, the pH of the transparent reaction solution was slowly adjusted to neutral using *ca.* 1.0 M Na_2CO_3 solution resulting in the precipitation of a Ga(III) complex. The precipitate was collected on a Büchner funnel and washed with distilled water (5 x 2 mL) and diethyl ether (2 x 2 mL), and then dried *in vacuo.*

6.4.2.2 Attempted synthesis of dimethylgallium(III) triazole thiolate complexes from $GaCl_3$

$[Ga(CH_3)_3]$ (1 mmol, ρ = 1.132 g mL-1, 0.11 mL) produced in situ as per 6.4.1.1, was added to a solution of triazole thione (1 mmol) in THF (6-10 mL) cooled to -78 °C; producing an immediate bright colour change to the solution. The reaction solution was stirred overnight and then filtered, and the volatiles were removed under

reduced pressure to obtain a coloured solid. The solid was recrystallised from hot hexane to yield the corresponding triazole thione.

7 References

[1] K. Moisse, "Antibiotic Resistance Could Bring 'End of Modern Medicine,'" can be found under https://abcnews.go.com/blogs/health/2012/03/16/antibiotic-resistance-could-bring-end-of-modern-medicine, **2012**.

[2] WHO, *World Heal. Organ.* **2014**, *61*, 383–394.

[3] Seventy-first session of the United Nations General Assembly, **2016**.

[4] M. Mendelson, M. P. Matsoso, *South African Med. J.* **2015**, *105*, 325.

[5] World Health Organization, "Antimicrobial resistance in Western Pacific," can be found under https://www.who.int/westernpacific/health-topics/antimicrobial-resistance, **2021**.

[6] H. O. Ukuhor, *J. Infect. Public Health* **2021**, *14*, 53–60.

[7] B. Aslam, W. Wang, M. I. Arshad, M. Khurshid, S. Muzammil, M. H. Rasool, M. A. Nisar, R. F. Alvi, M. A. Aslam, M. U. Qamar, M. K. F. Salamat, Z. Baloch, *Infect. Drug Resist.* **2018**, *11*, 1645–1658.

[8] G. M. Knight, R. E. Glover, C. F. McQuaid, I. D. Olaru, K. Gallandat, Q. J. Leclerc, N. M. Fuller, S. J. Willcocks, R. Hasan, E. van Kleef, C. I. R. Chandler, *Elife* **2021**, *10*, 1–27.

[9] F. Micoli, F. Bagnoli, R. Rappuoli, D. Serruto, *Nat. Rev. Microbiol.* **2021**, *19*, 287–302.

[10] T. M. Rawson, D. Ming, R. Ahmad, L. S. P. Moore, A. H. Holmes, *Nat. Rev. Microbiol.* **2020**, *18*, 409–410.

[11] M. A. B. Lucien, M. F. Canarie, P. E. Kilgore, G. Jean-Denis, N. Fénélon, M. Pierre, M. Cerpa, G. A. Joseph, G. Maki, M. J. Zervos, P. Dely, J. Boncy, H. Sati, A. del Rio, P. Ramon-Pardo, *Int. J. Infect. Dis.* **2021**, *104*, 250–254.

[12] C. C. Lai, S. Y. Chen, W. C. Ko, P. R. Hsueh, *Int. J. Antimicrob. Agents* **2021**, *57*, 106324.

[13] T. M. Rawson, L. S. P. Moore, N. Zhu, N. Ranganathan, K. Skolimowska, M.

Gilchrist, G. Satta, G. Cooke, A. Holmes, *Clin. Infect. Dis.* **2020**, *71*, 2459–2468.

[14] S. Ghosh, C. Bornman, M. M. Zafer, *J. Infect. Public Health* **2021**, *14*, 555–560.

[15] P. Kumar Bhaumik, K. Ghosh, S. Chattopadhyay, *Polyhedron* **2021**, *200*, 115093.

[16] J. Rodríguez-Baño, G. M. Rossolini, C. Schultsz, E. Tacconelli, S. Murthy, N. Ohmagari, A. Holmes, T. Bachmann, H. Goossens, R. Canton, A. P. Roberts, B. Henriques-Normark, C. J. Clancy, B. Huttner, P. Fagerstedt, S. Lahiri, C. Kaushic, S. J. Hoffman, M. Warren, G. Zoubiane, S. Essack, R. Laxminarayan, L. Plant, *J. Glob. Antimicrob. Resist.* **2021**, *25*, 5–7.

[17] F. Zhou, T. Yu, R. Du, G. Fan, Y. Liu, Z. Liu, J. Xiang, Y. Wang, B. Song, X. Gu, L. Guan, Y. Wei, H. Li, X. Wu, J. Xu, S. Tu, Y. Zhang, H. Chen, B. Cao, *Lancet* **2020**, *395*, 1054–1062.

[18] L. C. De Freitas, *Cad. Pesqui.* **2017**, *43*, 348–365.

[19] V. V. Mogasale, P. Saldanha, V. Pai, P. D. Rekha, V. Mogasale, *Sci. Rep.* **2021**, *11*, 1–7.

[20] World Health Organization (WHO), *2019 Antibacterial Agents in Clinical Development: An Analysis of the Antibacterial Clinical Development Pipeline*, Geneva, **2019**.

[21] D. M. P. De Oliveira, B. M. Forde, T. J. Kidd, P. N. A. Harris, M. A. Schembri, S. A. Beatson, D. L. Paterson, M. J. Walker, *Clin. Microbiol. Rev.* **2020**, *33*, DOI 10.1128/CMR.00181-19.

[22] M. K. Kathiravan, A. B. Salake, A. S. Chothe, P. B. Dudhe, R. P. Watode, M. S. Mukta, S. Gadhwe, *Bioorganic Med. Chem.* **2012**, *20*, 5678–5698.

[23] G. Morace, F. Perdoni, E. Borghi, *J. Glob. Antimicrob. Resist.* **2014**, *2*, 254–259.

[24] D. S. Thompson, P. L. Carlisle, D. Kadosh, *Eukaryot. Cell* **2011**, *10*, 1173–1182.

[25] M. E. Brandt, K. C. Hazen, S. A. Howell, in *Man. Clin. Microbiol. 11th Ed.*, American Society Of Microbiology, **2015**, pp. 1984–2014.

[26] J. F. Ha, C. M. Italiano, C. H. Heath, S. Shih, S. Rea, F. M. Wood, *Burns* **2010**, *37*, 181–195.

[27] S. Chen, M. Slavin, Q. Nguyen, D. Marriott, E. G. Playford, D. Ellis, T. Sorrell, the A. C. Australian Candidemia Study, *Emerg. Infect. Dis.* **2006**, *12*, 1508–16.

[28] P. Uppuluri, A. Khan, J. E. Edwards, in *Candida Albicans Cell. Mol. Biol.*, Springer International Publishing, Cham, **2017**, pp. 5–23.

[29] A. Miró-Canturri, R. Ayerbe-Algaba, Y. Smani, *Front. Microbiol.* **2019**, *10*, 41.

[30] J. R. Perfect, *Nat. Rev. Drug Discov.* **2017**, *16*, 603–616.

[31] R. R. Varma, B. H. Pursuwani, E. Suresh, B. S. Bhatt, M. N. Patel, *J. Mol. Struct.* **2020**, *1200*, 127068.

[32] D. Lyddiard, G. L. Jones, B. W. Greatrex, *FEMS Microbiol. Lett.* **2016**, *363*, 84.

[33] J. Davies, in *Can. J. Infect. Dis. Med. Microbiol.*, Hindawi Limited, **2006**, pp. 287–290.

[34] J. M. A. Blair, M. A. Webber, A. J. Baylay, D. O. Ogbolu, L. J. V. Piddock, *Nat. Rev. Microbiol.* **2015**, *13*, 42–51.

[35] I. Yelin, R. Kishony, *Cell* **2018**, *172*, 1136-1136.e1.

[36] B. G. Spratt, *Science (80-.).* **1994**, *264*, 388–393.

[37] F. Guerin, M. Sassi, L. Dejoies, A. Zouari, S. Schutz, S. Potrel, M. Auzou, A. Collet, D. Lecointe, G. Auger, V. Cattoir, *J. Antimicrob. Chemother.* **2020**, *75*, 1699–1703.

[38] G. D. Wright, *Adv. Drug Deliv. Rev.* **2005**, *57*, 1451–1470.

[39] L. A. Dever, T. S. Dermody, *Arch. Intern. Med.* **1991**, *151*, 886–895.

[40] L. E. Bryan, *J. Antimicrob. Chemother.* **1988**, *22*, 1–15.

[41] R. R. Yocum, J. R. Rasmussen, J. L. Strominger, *J. Biol. Chem.* **1980**, *255*, 3977–3986.

[42] T. A. Mukhtar, K. P. Koteva, D. W. Hughes, G. D. Wright, *Biochemistry* **2001**, *40*, 8877–8886.

[43] J. R. Knowles, A. Houghton Professor, *Philos. Trans. R. Soc., Ser. B* **1985**, *18*, 403–408.

[44] M. W. McCarthy, D. P. Kontoyiannis, O. A. Cornely, J. R. Perfect, T. J. Walsh, *J. Infect. Dis.* **2017**, *216*, S474–S483.

[45] S. B. Hoffman, *Compend. Contin. Educ. Pract. Vet.* **2001**, *23*, 464–472.

[46] S. I. Miller, *MBio* **2016**, *7*, DOI 10.1128/mBio.01541-16.

[47] D. C. Hooper, in *Emerg. Infect. Dis.*, Centers For Disease Control And Prevention, **2001**, pp. 337–341.

[48] J. Rajowar, S. D. Akoijam, A. Sen, K. Akhter, S. Singh, *J. Evol. Med. Dent. Sci.* **2021**, *10*, 583+.

[49] S. K. Morgan-Linnell, L. B. Boyd, D. Steffen, L. Zechiedrich, *Antimicrob. Agents Chemother.* **2009**, *53*, 235–241.

[50] D. S. Perlin, in *Candida Albicans Cell. Mol. Biol.*, Springer International Publishing, Cham, **2017**, pp. 471–489.

[51] S. Campoy, J. L. Adrio, *Biochem. Pharmacol.* **2017**, *133*, 86–96.

[52] D. S. Perlin, R. Rautemaa-Richardson, A. Alastruey-Izquierdo, *www.thelancet.com/infection* **2017**, *17*, e383–e392.

[53] A. Singh, A. Masih, A. Khurana, P. K. Singh, M. Gupta, F. Hagen, J. F. Meis, A. Chowdhary, *Mycoses* **2018**, *61*, 477–484.

[54] I. S. Sharafutdinov, G. D. Ozhegov, A. E. Sabirova, V. V. Novikova, S. A. Lisovskaya, A. M. Khabibrakhmanova, A. R. Kurbangalieva, M. I. Bogachev, A. R. Kayumov, *Molecules* **2020**, *25*, 642.

[55] Y. Hu, Y. Hu, Y. Lu, S. Huang, K. Liu, X. Han, Z. Mao, Z. Wu, X. Zhou, *Mycopathologia* **2017**, *182*, 397–402.

[56] R. B. Billmyre, S. Applen Clancey, L. X. Li, T. L. Doering, J. Heitman, *Nat. Commun.* **2020**, *11*, 1–9.

[57] T. M. Anderson, M. C. Clay, A. G. Cioffi, K. A. Diaz, G. S. Hisao, M. D. Tuttle, A. J. Nieuwkoop, G. Comellas, N. Maryum, S. Wang, B. E. Uno, E. L. Wildeman, T. Gonen, C. M. Rienstra and M. D. Burke, *Nat. Chem. Biol.*, 2014, **10**, 400–406.

[58] J. M. Rybak, K. S. Barker, J. F. Muñoz, J. E. Parker, S. Ahmad, E. Mokaddas, A. Abdullah, R. S. Elhagracy, S. L. Kelly, C. A. Cuomo, P. D. Rogers, *Clin. Microbiol. Infect.* **2022**, *28*, 838–843.

[59] Y. Lin, H. Betts, S. Keller, K. Cariou, G. Gasser, *Chem. Soc. Rev.* **2021**, *50*, 10346–10402.

[60] Y. Lee, E. Puumala, N. Robbins, L. E. Cowen, *Chem. Rev.* **2021**, *121*, 3390–3411.

[61] A. Logan, A. Wolfe, J. C. Williamson, *Curr. Infect. Dis. Rep.* **2022**, *1*, 1–12.

[62] J. Houšť, J. Spížek, V. Havlíček, *Metabolites* **2020**, *10*, 106.

[63] World Health Organization, *WHO Model List of Essential Medicines*, **2017**.

[64] U. Theuretzbacher, K. Outterson, A. Engel, A. Karlén, *Nat. Rev. Microbiol.* **2020**, *18*, 275–285.

[65] P. J. Sadler, *Adv. Inorg. Chem.* **1991**, *36*, 1–48.

[66] S. Medici, M. Peana, V. M. Nurchi, J. I. Lachowicz, G. Crisponi, M. A. Zoroddu, *Coord. Chem. Rev.* **2015**, *284*, 329–350.

[67] Z. Guo, P. J. Sadler, *Angew. Chemie Int. Ed.* **1999**, *38*, 1512–1531.

[68] E. E. Trimmer, J. M. Essigmann, *Essays Biochem.* **1999**, *34*, 191–211.

[69] M. A. Zoroddu, J. Aaseth, G. Crisponi, S. Medici, M. Peana, V. M. Nurchi, *J. Inorg. Biochem.* **2019**, *195*, 120–129.

[70] K. J. Franz, N. Metzler-Nolte, *Chem. Rev.* **2019**, *119*, 727–729.

[71] J. Karges, R. W. Stokes, S. M. Cohen, *Trends Chem.* **2021**, *3*, 523–534.

[72] E. J. Anthony, E. M. Bolitho, H. E. Bridgewater, O. W. L. Carter, J. M. Donnelly, C. Imberti, E. C. Lant, F. Lermyte, R. J. Needham, M. Palau, P. J. Sadler, H. Shi, F. X. Wang, W. Y. Zhang, Z. Zhang, *Chem. Sci.* **2020**, *11*, 12888–12917.

[73] S. Eckhardt, P. S. Brunetto, J. Gagnon, M. Priebe, B. Giese, K. M. Fromm, *Chem. Rev.* **2013**, *113*, 4708–4754.

[74] J. L. Hobman, L. C. Crossman, *J. Med. Microbiol.* **2015**, *64*, 471–497.

[75] A. Evans, K. A. Kavanagh, *J. Med. Microbiol.* **2021**, *70*, 001363.

[76] M. I. Hood, E. P. Skaar, *Nat. Rev. Microbiol.* **2012**, *10*, 525–537.

[77] C. Healy, N. Munoz-Wolf, J. Strydom, L. Faherty, N. C. Williams, S. Kenny, S. C. Donnelly, S. M. Cloonan, *Respir. Res.* **2021**, *22*, 1–44.

[78] J. A. Lemire, J. J. Harrison, R. J. Turner, *Nat. Rev. | Microbiol.* **2013**, *11*, DOI 10.1038/nrmicro3028.

[79] N. Gugala, J. A. Lemire, R. J. Turner, *J. Antibiot. (Tokyo).* **2017**, *70*, 775–780.

[80] L. Macomber, J. A. Imlay, *Proc. Natl. Acad. Sci.* **2009**, *106*, 8344–8349.

[81] M. T. Maung, A. Carlson, M. Olea-Flores, L. Elkhadragy, K. M. Schachtschneider, N. Navarro-Tito, T. Padilla-Benavides, *FASEB J.* **2021**, *35*, e21810.

[82] F. F. Xu, J. A. Imlay, *Appl. Environ. Microbiol.* **2012**, *78*, 3614–21.

[83] C. Maxim, M. Badea, A. M. Rostas, M. C. Chifiriuc, G. G. Pircalabioru, S. Avram, R. Olar, *Appl. Organomet. Chem.* **2022**, *36*, DOI 10.1002/aoc.6471.

[84] R. Z. Zhao, S. Jiang, L. Zhang, Z. Bin Yu, *Int. J. Mol. Med.* **2019**, *44*, 3–15.

[85] Y. Hokai, B. Jurkowicz, J. Fernández-Gallardo, N. Zakirkhodjaev, M. Sanaú, T. R. Muth, M. Contel, *J. Inorg. Biochem.* **2014**, *138*, 81–88.

[86] C. Roder, M. J. Thomson, *Drugs R D* **2015**, *15*, 13–20.

[87] R. B. Thurman and C. P. Gerba, *Crit. Rev. Environ. Control*, 1989, **18**, 295–315.

[88] J. B. Fein, Q. Yu, J. Nam, N. Yee, *Chem. Geol.* **2019**, *521*, 28–38.

[89] D. Martínez-Soto, J. Ruiz-Herrera, *Rev. Iberoam. Micol.* **2017**, *34*, 192–202.

[90] F. Gerwien, V. Skrahina, L. Kasper, B. Hube, S. Brunke, *FEMS Microbiol. Rev.* **2018**, *050*, 1–21.

[91] T. Gagini, L. Colina-Vegas, W. Villarreal, L. Pereira Borba-Santos, C. de Souza Pereira, A. Azevedo Batista, M. Kneip Fleury, W. de Souza, S. Rozental, L. S. Antô nio Costa, M. Navarro, *New J. Chem* **2018**, *42*, 13641.

[92] Z. H. Chohan, M. Hanif, *J. Enzyme Inhib. Med. Chem.* **2013**, *28*, 944–953.

[93] K. Bajaj, R. M. Buchanan, C. A. Grapperhaus, *J. Inorg. Biochem.* **2021**, *225*, 111620.

[94] A. M. Mansour, *Eur. J. Inorg. Chem.* **2018**, *2018*, 852–860.

[95] A. Pejović, A. Minić, J. Jovanović, M. Pešić, D. I. Komatina, I. Damljanović, D. Stevanović, V. Mihailović, J. Katanić, G. A. Bogdanović, *J. Organomet. Chem.* **2018**, *869*, 1–10.

[96] R. M. Gandra, P. M. Carron, M. F. Fernandes, L. S. Ramos, T. P. Mello, A. C. Aor, M. H. Branquinha, M. McCann, M. Devereux, A. L. S. S. Santos, P. Mc Carron, M. F. Fernandes, L. S. Ramos, T. P. Mello, A. C. Aor, M. H. Branquinha, M. McCann, M. Devereux, A. L. S. S. Santos, *Front. Microbiol.* **2017**, *8*, 1257.

[97] T. Dimitrijević, I. Novaković, D. Radanović, S. B. Novaković, M. V. Rodić, K. Anđelković, M. Šumar-Ristović, *J. Coord. Chem.* **2020**, *73*, 702–716.

[98] M. Daniluk, W. Buchowicz, M. Koszytkowska-Stawińska, K. Jarząbek, K. N. Jarzembska, R. Kamiński, M. Piszcz, A. E. Laudy, S. Tyski, *ChemistrySelect* **2019**, *4*, 11130–11135.

[99] Y. T. Liu, G. D. Lian, D. W. Yin, B. J. Su, *Res. Chem. Intermed.* **2012**, *38*, 1043–1053.

[100] Y. T. Liu, G. D. Lian, D. W. Yin, B. J. Su, in *Spectrochim. Acta - Part A Mol. Biomol. Spectrosc.*, Elsevier, **2013**, pp. 131–137.

[101] X. Hu, S. Li, G. Yang, H. Liu, G. Boden, L. Li, *PLoS One* **2014**, *9*, DOI 10.1371/journal.pone.0087096.

[102] Y. Liu, L. Yang, D. Yin, Y. Dang, L. Yang, Q. Zou, J. Li, J. Sun, *J. Organomet. Chem.* **2019**, *899*, 120903.

[103] A. Frei, A. G. Elliott, A. Kan, H. Dinh, S. Braese, A. E. Bruce, M. R. Bruce, F. Chen, D. Humaidy, N. Jung, A. P. King, P. G. Lye, H. K. Maliszewska, A. M. Mansour, D. Matiadis, M. P. Muñoz, T.-Y. Pai, S. Pokhrel, P. J. Sadler, M. Sagnou, M. Taylor, J. J. Wilson, D. Woods, J. Zuegg, W. Meyer, A. K. Cain, M. A. Cooper, M. A. T. Blaskovich, **2022**, DOI 10.26434/CHEMRXIV-2022-LDMBM.

[104] S. Chandra, S. Raizada, M. Tyagi, P. K. Sharma, *Spectrochim. Acta - Part A Mol.*

Biomol. Spectrosc. **2008**, *69*, 816–821.

[105] M. A. Malik, S. A. Lone, M. Y. Wani, M. I. A. Talukdar, O. A. Dar, A. Ahmad, A. A. Hashmi, *Bioorg. Chem.* **2020**, *98*, 103771.

[106] A. Frei, A. P. King, G. J. Lowe, A. K. Cain, F. L. Short, H. Dinh, A. G. Elliott, J. Zuegg, J. J. Wilson, M. A. T. Blaskovich, *Chem. - A Eur. J.* **2021**, *27*, 2021–2029.

[107] R. M. Gandra, P. McCarron, L. Viganor, M. F. Fernandes, K. Kavanagh, M. McCann, M. H. Branquinha, A. L. S. Santos, O. Howe, M. Devereux, *Front. Microbiol.* **2020**, *11*, 470.

[108] M. & G. 2016 C. of D. C. Naghavi, *Lancet* **2017**, *390*, 1151–1210.

[109] S. Ghosh, *Bioorg. Chem.* **2019**, *88*, 102925.

[110] P. C. Bruijnincx, P. J. Sadler, *Curr. Opin. Chem. Biol.* **2008**, *12*, 197–206.

[111] B. Englinger, C. Pirker, P. Heffeter, A. Terenzi, C. R. Kowol, B. K. Keppler, W. Berger, *Chem. Rev.* **2019**, *119*, 1519–1624.

[112] N. Muhammad, Z. Guo, *Curr. Opin. Chem. Biol.* **2014**, *19*, 144–153.

[113] P. Heffeter, U. Jungwirth, M. Jakupec, C. Hartinger, M. Galanski, L. Elbling, M. Micksche, B. Keppler, W. Berger, *Drug Resist. Updat.* **2008**, *11*, 1–16.

[114] R. Paprocka, M. Wiese-Szadkowska, S. Janciauskiene, T. Kosmalski, M. Kulik, A. Helmin-Basa, *Coord. Chem. Rev.* **2022**, *452*, 214307.

[115] P. Jia, R. Ouyang, P. Cao, X. Tong, X. Zhou, T. Lei, Y. Zhao, N. Guo, H. Chang, Y. Miao, S. Zhou, *J. Coord. Chem.* **2017**, *70*, 2175–2201.

[116] E. Miyawaki, H. Kenmotsu, Y. Shintani, I. Sekine, T. Shukuya, K. Takayama, A. Inoue, I. Okamoto, K. Kiura, K. Takahashi, N. Yamamoto, T. Kawaguchi, E. Miyaoka, I. Yoshino, H. Date, *BMC Cancer* **2022**, *22*, 1–10.

[117] W. H. Organization, *WHO Model List of Essential Medicines*, **2013**.

[118] J. A. Salvador, S. A. Figueiredo, R. M. Pinto, S. M. Silvestre, *Future Med. Chem.* **2012**, *4*, 1495–1523.

[119] H. Li, H. Sun, *Curr. Opin. Chem. Biol.* **2012**, *16*, 74–83.

[120] P. Soetji Rahajoe, C. Yustisia Hasan, A. Elizabeth Pranoto, *Sci. Rep.* **2021**, DOI 10.21203/rs.3.rs-1105357/v1.

[121] L. M. Mai, C. Y. Lin, C. Y. Chen, Y. C. Tsai, *Biomaterials* **2003**, *24*, 3005–3012.

[122] NCT02723539, *https://clinicaltrials.gov/show/NCT02723539* **2016**.

[123] D. M. Griffith, H. Li, M. V. Werrett, P. C. Andrews, H. Sun, *Chem. Soc. Rev.* **2021**, *50*, 12037–12069.

[124] L. Jin, K. Y. Szeto, L. Zhang, W. Du, H. Sun, *J. Inorg. Biochem.* **2004**, *98*, 1331–1337.

[125] H. Li, R. Wang, H. Sun, *Acc. Chem. Res.* **2019**, *52*, 216–227.

[126] R. Wang, H. Li, T. K. Y. Ip, H. Sun, in *Adv. Inorg. Chem.*, Academic Press Inc., **2020**, pp. 183–205.

[127] H. Sun, K. Y. Szeto, *J. Inorg. Biochem.* **2003**, *94*, 114–120.

[128] W. Li, L. Jin, N. Zhu, X. Hou, F. Deng, H. Sun, *J. Am. Chem. Soc.* **2003**, *125*, 12408–12409.

[129] R. Ge, H. Sun, *Acc. Chem. Res.* **2007**, *40*, 267–274.

[130] Y. Wang, C.-N. Tsang, F. Xu, P.-W. Kong, L. Hu, J. Wang, I. K. Chu, H. Li, H. Sun, *Chem. Commun.* **2015**, *51*, 16479–16482.

[131] P. De Marcillac, N. Coron, G. Dambier, J. Leblanc, J. P. Moalic, *Nature* **2003**, *422*, 876–878.

[132] R. Mohan, *Nat. Chem.* **2010**, *2*, 336–336.

[133] A. Slikkerveer, F. A. de Wolff, *Med. Toxicol. Adverse Drug Exp.* **1989**, *4*, 303–323.

[134] Y. Wang, L. Hu, F. Xu, Q. Quan, Y. T. Lai, W. Xia, Y. Yang, Y. Y. Chang, X. Yang, Z. Chai, J. Wang, I. K. Chu, H. Li, H. Sun, *Chem. Sci.* **2017**, *8*, 4626–4633.

[135] B. Han, Z. Zhang, Y. Xie, X. Hu, H. Wang, W. Xia, Y. Wang, H. Li, Y. Wang, H. Sun, *Chem. Sci.* **2018**, *9*, 7488–7497.

[136] P. Malfertheiner, A. Link, M. Selgrad, *Nat. Rev. Gastroenterol. Hepatol.* **2014**, *11*, 628–638.

[137] E. Svensson Grape, V. Rooth, M. Nero, T. Willhammar, A. K. Inge, *Nat. Commun.* **2022**, *13*, DOI 10.1038/s41467-022-29566-0.

[138] T. D. Boyd, I. Kumar, E. E. Wagner, K. H. Whitmire, *Chem. Commun.* **2014**, *50*, 3556–3559.

[139] I. Kumar, P. Andrews, K. H. Whitmire, *Eur. J. Inorg. Chem.* **2015**, *2015*, 605–608.

[140] H. L. DuPont, *Drug Intell. Clin. Pharm.* **1987**, *21*, 687–693.

[141] A. Toma, C. I. Raţ, A. Silvestru, T. Rüffer, H. Lang, M. Mehring, *J. Organomet. Chem.* **2016**, *806*, 5–11.

[142] T. Shu, M. Huang, D. Wu, Y. Ren, X. Zhang, Y. Han, J. Mu, R. Wang, Y. Qiu, D. Y. Zhang, X. Zhou, *Virol. Sin.* **2020**, *35*, 321–329.

[143] R. Wang, J. F. W. Chan, S. Wang, H. Li, J. Zhao, T. K. Y. Ip, Z. Zuo, K. Y. Yuen, S. Yuan, H. Sun, *Chem. Sci.* **2022**, *13*, 2238–2248.

[144] S. Yuan, R. Wang, J. F. W. Chan, A. J. Zhang, T. Cheng, K. K. H. Chik, Z. W. Ye, S. Wang, A. C. Y. Lee, L. Jin, H. Li, D. Y. Jin, K. Y. Yuen, H. Sun, *Nat. Microbiol.* **2020**, *5*, 1439–1448.

[145] J. P. Gisbert, M. Romano, A. G. Gravina, P. Solís-Muñoz, F. Bermejo, J. Molina-Infante, M. Castro-Fernández, J. Ortuño, A. J. Lucendo, M. Herranz, I. Modolell, F. Del Castillo, J. Gõmez, J. Barrio, B. Velayos, B. Gõmez, J. L. Domínguez, A. Miranda, M. Martorano, A. Algaba, M. Pabõn, T. Angueira, L. Fernández-Salazar, A. Federico, A. C. Marín, A. G. McNicholl, *Aliment. Pharmacol. Ther.* **2015**, *41*, 768–775.

[146] M. M. Gerrits, A. H. M. Van Vliet, E. J. Kuipers, J. G. Kusters, *Helicobacter Pylori and Antimicrobial Resistance: Molecular Mechanisms and Clinical Implications*, **2006**.

[147] W. G. Veloira, P. Domenico, J. J. LiPuma, J. M. Davis, E. Gurzenda, J. A. Kazzaz, *J. Antimicrob. Chemother.* **2003**, *52*, 915–919.

[148] A. M. W. C. Thompson, *Annu. Reports Prog. Chem. - Sect. A* **1997**, *93*, 189–198.

[149] N. N. Greenwood, A. Earnshaw, *Chemistry of the Elements*, Elsevier, **1997**.

[150] U.S. Geological Survey, *Miner. Commod. Summ.* **2020**.

[151] J. R. Dilworth, *Coord. Chem. Rev.* **2021**, *436*, DOI 10.1016/j.ccr.2021.213822.

[152] H. J. Lunk, D. V. Drobot, H. Hartl, *ChemTexts* **2021**, *7*, 6.

[153] A. A. Haase, E. B. Bauer, F. E. Kühn, D. C. Crans, *Coord. Chem. Rev.* **2019**, *394*, 135–161.

[154] G. F. Nordberg, B. A. Fowler, M. Nordberg, L. T. Friberg, *Handbook on the Toxicology of Metals*, **2007**.

[155] F. Maresh, M. J. Lustok, P. P. Cohen, *Proc. Soc. Exp. Biol. Med.* **1940**, *45*, 576–579.

[156] K. K. W. Lo, *Acc. Chem. Res.* **2015**, *48*, 2985–2995.

[157] K. K. W. Lo, *Top. Organomet. Chem.* **2010**, *29*, 115–158.

[158] A. Leonidova, G. Gasser, *ACS Chem. Biol.* **2014**, *9*, 2180–2193.

[159] L. C. C. Lee, K. K. Leung, K. K. W. Lo, *Dalt. Trans.* **2017**, *46*, 16357–16380.

[160] M. S. Capper, H. Packman, M. Rehkämper, *ChemBioChem* **2020**, *21*, 2111–2115.

[161] E. B. Bauer, A. A. Haase, R. M. Reich, D. C. Crans, F. E. Kühn, *Coord. Chem. Rev.* **2019**, *393*, 79–117.

[162] S. Sato, O. Ishitani, *Coord. Chem. Rev.* **2015**, *282–283*, 50–59.

[163] K. Schindler, F. Zobi, *Molecules* **2022**, *27*, 539.

[164] W. Hieber, H. Fuchs, *Zeitschrift für Anorg. und Allg. Chemie* **1941**, *248*, 256–268.

[165] M. Wrighton, L. David, *J. Am. Chem. Soc.* **1974**, *96*, 998–1003.

[166] P. V. Simpson, M. Falasca, M. Massi, *Chem. Commun.* **2018**, *54*, 12429–12438.

[167] K. Schindler, F. Zobi, *Chimia (Aarau).* **2021**, *75*, 837–844.

[168] C. Otero, A. Carreño, R. Polanco, F. M. Llancalahuen, R. Arratia-Pérez, M. Gacitúa, J. A. Fuentes, *Front. Chem.* **2019**, *7*, 454.

[169] I. Yousuf, M. Bashir, F. Arjmand, S. Tabassum, *Coord. Chem. Rev.* **2021**, *445*, 214104.

[170] Á. D. Hernández Mejías, A. Poirot, M. Rmili, N. Leygue, M. Wolff, N. Saffon-Merceron, E. Benoist, S. Fery-Forgues, *Dalt. Trans.* **2021**, *50*, 1313–1323.

[171] C. C. Konkankit, S. C. Marker, K. M. Knopf, J. J. Wilson, *Dalt. Trans.* **2018**, *47*, 9934–9974.

[172] S. C. Gad, in *Encycl. Toxicol. Third Ed.*, Academic Press, **2014**, pp. 691–692.

[173] J. P. Maher, *Annu. Reports Prog. Chem. - Sect. A* **1997**, *93*, 45–58.

[174] A. J. Downs, *Chemistry of Aluminium, Gallium, Indium, and Thallium*, Blackie Academic & Professional, London; New York, **1993**.

[175] A. Sigel, N. P. Farrell, H. Sigel, E. Freisinger, R. K. O. Sigel, I. Riddell, S. J. Lippard, V. Brabec, J. Kasparkova, V. Menon, *Metallo-Drugs: Development and Action of Anticancer Agents : Development and Action of Anticancer and Antitumor Agents*, Walter De Gruyter GmbH, Berlin/Boston, GERMANY, **2018**.

[176] C. R. Chitambar, W. E. Antholine, *Antioxidants Redox Signal.* **2013**, *18*, 956–972.

[177] M. D. Bartholomä, A. S. Louie, J. F. Valliant, J. Zubieta, *Chem. Rev.* **2010**, *110*, 2903–2920.

[178] L. R. Bernstein, T. Tanner, C. Godfrey, B. Noll, *Met. Based. Drugs* **2000**, *7*, 33–47.

[179] R. E. Weiner, *Nucl. Med. Biol.* **1996**, *23*, 745–751.

[180] W. R. Harris, L. Messori, *Coord. Chem. Rev.* **2002**, *228*, 237–262.

[181] L. R. Bernstein, *Pharmacol. Rev.* **1998**, *50*, 665 LP – 682.

[182] *Meyler's Side Eff. Drugs* **2016**, 506–507.

[183] D. L. Bailey, D. Sabanathan, A. Aslani, D. H. Campbell, B. J. Walsh, N. A. Lengkeek, *Asia Ocean. J. Nucl. Med. Biol.* **2021**, *9*, 1.

[184] J. P. Lavender, J. Lowe, J. R. Barker, J. I. Burn and M. A. Chaudhri, *Br. J. Radiol.*, 1971, **44**, 361–366.

[185] E. V. Staab, W. H. McCartney, *Semin. Nucl. Med.* **1978**, *8*, 219–234.

[186] F. Minandri, C. Bonchi, E. Frangipani, F. Imperi, P. Visca, *Future Microbiol.* **2014**, *9*, 379–397.

[187] G. Centola, F. Xue, A. Wilks, *Metallomics* **2020**, *12*, 1863–1877.

[188] C. R. Chitambar, *Int. J. Environ. Res. Public Heal.* **2010**, *7*, 2337–2361.

[189] N. Gugala, R. J. Turner, in *Biomed. Appl. Met.*, Springer International Publishing, Cham, **2018**, pp. 129–150.

[190] F. Kurtuldu, N. Mutlu, A. R. Boccaccini, D. Galusek, *Bioact. Mater.* **2022**, DOI 10.1016/j.bioactmat.2021.12.034.

[191] E. López-Jácome, R. Franco-Cendejas, H. Quezada, R. Morales-Espinosa, I. Castillo-Juárez, B. González-Pedrajo, A. M. Fernández-Presas, A. Tovar-García, V. Angarita-Zapata, P. Licona-Limón, M. Martínez-Vázquez, R. García-Contreras, *Curr. Opin. Pharmacol.* **2019**, *48*, 48–56.

[192] D. Denoyer, S. A. S. Clatworthy, M. A. Cater, *Met. Ions Life Sci.* **2018**, *18*, 469–506.

[193] M. S. Chua, L. R. Bernstein, R. Li, S. K. S. So, *Anticancer Res.* **2006**, *26*, 1739–1743.

[194] L. R. Bernstein, J. J.M. van der Hoeven, R. O. Boer, *Anticancer. Agents Med. Chem.* **2012**, *11*, 585–590.

[195] "Oral Gallium Maltolate for the Treatment of Relapsed and Refractory Glioblastoma - Full Text View - ClinicalTrials.gov," can be found under https://clinicaltrials.gov/ct2/show/NCT04319276?term=gallium+maltolate&draw=2&rank=1, **n.d.**

[196] A. R. Timerbaev, *Metallomics* **2009**, *1*, 193–198.

[197] J. A. Lessa, G. L. Parrilha, H. Beraldo, *Inorganica Chim. Acta* **2012**, *393*, 53–63.

[198] "Evaluation of AP-002 in Patients With Solid Tumors - Full Text View - ClinicalTrials.gov," can be found under https://clinicaltrials.gov/ct2/show/NCT04143789, **n.d.**

[199] Y. Wang, Y. Mei, Y. Song, C. Bachus, C. Sun, H. Sheshbaradaran, M. Glogauer, *Eur. J. Pharmacol.* **2020**, *889*, 173613.

[200] N. Saki, M. Akin, A. Atsay, H. R. Pekbelgin Karaoglu, M. B. Kocak, *Inorg. Chem. Commun.* **2018**, *95*, 122–129.

[201] R. N. Duffin, V. L. Blair, L. Kedzierski, P. C. Andrews, *Eur. J. Med. Chem.* **2020**, *186*, DOI 10.1016/j.ejmech.2019.111895.

[202] K. Kowolik, M. Shanmugam, T. W. Myers, C. D. Cates, L. A. Berben, *Dalt. Trans.* **2012**, *41*, 7969.

[203] S. Suh, J. H. Hardesty, T. A. Albright and D. M. Hoffman, *Inorg. Chem.*, 1999, **38**, 1627–1633.

[204] M. R. Kaluäerović, G. N. Kaluäerović, S. Gómez-Ruiz, R. Paschke, A. Hemprich, J. Kühling, T. W. Remmerbach, *J. Inorg. Biochem.* **2011**, *105*, 164–170.

[205] K. Hemming, *Chem. Educ.* **2001**, *6*, 396–398.

[206] J. Jampilek, *Molecules* **2019**, *24*, 3839.

[207] M. M. Heravi, V. Zadsirjan, *RSC Adv.* **2020**, *10*, 44247–44311.

[208] N. N. Makhova, L. I. Belen'kii, G. A. Gazieva, I. L. Dalinger, L. S. Konstantinova, V. V. Kuznetsov, A. N. Kravchenko, M. M. Krayushkin, O. A. Rakitin, A. M. Starosotnikov, L. L. Fershtat, S. A. Shevelev, V. Z. Shirinian, V. N. Yarovenko, *Russ. Chem. Rev.* **2020**, *89*, 55–124.

[209] A. Mermer, T. Keles, Y. Sirin, *Bioorg. Chem.* **2021**, *114*, 105076.

[210] P. Prasher, M. Sharma, F. Zacconi, G. Gupta, A. A. A. Aljabali, V. Mishra, M. M. Tambuwala, D. N. Kapoor, P. Negi, T. de J. Andreoli Pinto, I. Singh, D. K. Chellappan, K. Dua, *Curr. Org. Chem.* **2020**, *25*, 654–668.

[211] H.-Z. Zhang, L.-L. Gan, H. Wang, C.-H. Zhou, *Mini-Reviews Med. Chem.* **2016**, *17*, 122–166.

[212] A. Anwar, M. R. Mungroo, S. Khan, I. Fatima, R. Rafique, Kanwal, K. M. Khan, R. Siddiqui, N. A. Khan, *Antibiotics* **2020**, *9*, 188.

[213] B. El Ibrahimi, L. Guo, in *Azoles - Synth. Prop. Appl. Perspect.*, IntechOpen, **2021**.

[214] C. L. Price, J. E. Parker, A. G. Warrilow, D. E. Kelly, S. L. Kelly, *Pest Manag. Sci.* **2015**, *71*, 1054–1058.

[215] M. Shafiei, L. Peyton, M. Hashemzadeh, A. Foroumadi, *History of the*

Development of Antifungal Azoles: A Review on Structures, SAR, and Mechanism of Action, Academic Press, **2020**.

[216] P. M. Gurubasavaraj, J. S. Charantimath, *Lett. Drug Des. Discov.* **2018**, *16*, 492–501.

[217] C. Girmenia, *Expert Opin. Investig. Drugs* **2009**, *18*, 1279–1295.

[218] D. Allen, D. Wilson, R. Drew, J. Perfect, *Expert Rev. Anti. Infect. Ther.* **2015**, *13*, 787–798.

[219] C. -H. Zhou, Y. Wang, *Curr. Med. Chem.* **2012**, *19*, 239–280.

[220] G. Aromí, L. A. Barrios, O. Roubeau, P. Gamez, *Coord. Chem. Rev.* **2011**, *255*, 485–546.

[221] K. Bozorov, J. Zhao, H. A. Aisa, *Bioorganic Med. Chem.* **2019**, *27*, 3511–3531.

[222] A. Jain, P. Piplani, *Mini-Reviews Med. Chem.* **2019**, *19*, 1298–1368.

[223] R. Valiulin, *Org. Chem. 100 Must-Know Mech.* **2020**, DOI 10.1515/9783110608373/HTML.

[224] F. Gao, T. Wang, J. Xiao, G. Huang, *Antibacterial Activity Study of 1,2,4-Triazole Derivatives*, Elsevier Masson, **2019**.

[225] R. Kaur, A. R. Dwivedi, B. Kumar, V. Kumar, *Recent Developments on 1,2,4-Triazole Nucleus in Anticancer Compounds: A Review*, **2016**.

[226] J. K. Shneine, Y. H. Alaraji, *Chemistry of 1, 2, 4-Triazole: A Review Article*, **2016**.

[227] S. A. El-Sebaey, *ChemistrySelect* **2020**, *5*, 11654–11680.

[228] A. Cetin, I. H. Geçibesler, *J. Appl. Pharm. Sci.* **2015**, *5*, 120–126.

[229] Z. Peng, G. Wang, Q. H. Zeng, Y. Li, Y. Wu, H. Liu, J. J. Wang, Y. Zhao, *Food Chem.* **2021**, *341*, 128265.

[230] J. K. Shneine, Y. H. Alaraji, *Int. J. Sci. Res. ISSN (Online Index Copernicus Value Impact Factor* **2013**, *14611*, 2319–7064.

[231] R. Aggarwal, G. Sumran, *Eur. J. Med. Chem.* **2020**, *205*, DOI 10.1016/j.ejmech.2020.112652.

[232] C. Tratrat, *Curr. Top. Med. Chem.* **2020**, *20*, 2235–2258.

[233] Z. Kazeminejad, M. Marzi, A. Shiroudi, S. A. Kouhpayeh, M. Farjam, E. Zarenezhad, *Biomed Res. Int.* **2022**, *2022*, DOI 10.1155/2022/4584846.

[234] Z. Jin, Y. Hu, A. Huo, W. Tao, L. Shao, J. Liu, J. Fang, *J. Organomet. Chem.* **2006**, *691*, 2340–2345.

[235] M. Strzelecka, P. Świątek, *Pharmaceuticals* **2021**, *14*, 224.

[236] H. A. M. El-Sherief, B. G. M. Youssif, S. N. Abbas Bukhari, A. H. Abdelazeem, M. Abdel-Aziz, H. M. Abdel-Rahman, *Eur. J. Med. Chem.* **2018**, *156*, 774–789.

[237] S. Bitla, A. A. Gayatri, M. R. Puchakayala, V. Kumar Bhukya, J. Vannada, R. Dhanavath, B. Kuthati, D. Kothula, S. R. Sagurthi, K. R. Atcha, *Bioorg. Med. Chem. Lett.* **2021**, *41*, 128004.

[238] E. Stingaci, M. Zveaghinteva, S. Pogrebnoi, L. Lupascu, V. Valica, L. Uncu, A. Smetanscaia, M. Drumea, A. Petrou, A. Ciric, J. Glamoclija, M. Sokovic, V. Kravtsov, A. Geronikaki, F. Macaev, *Bioorganic Med. Chem. Lett.* **2020**, *30*, 127368.

[239] E. S. Raper, *Coord. Chem. Rev.* **1997**, *165*, 475–567.

[240] A. Das, M. W. Ashraf, B. K. Banik, *ChemistrySelect* **2021**, *6*, 9069–9100.

[241] G. Küçükgüzel, P. Çıkla-Süzgün, *Eur. J. Med. Chem.* **2015**, *97*, 830–870.

[242] A. A. Al, A. A. Hassa, M. M. Makhlou, S. Bräse, *Molecules* **2020**, *25*, 3036.

[243] J. E. Parker, A. G. S. Warrilow, H. J. Cools, C. M. Martel, W. David Nes, B. A. Fraaije, J. A. Lucas, D. E. Kelly, S. L. Kelly, *Appl. Environ. Microbiol.* **2011**, *77*, 1460–1465.

[244] A. R. Jalilian, S. Sattari, M. Bineshmarvasti, A. Shafiee, M. Daneshtalab, *Arch. Pharm. (Weinheim).* **2000**, *333*, 347–354.

[245] P. Linciano, E. Gianquinto, M. Montanari, L. Maso, P. Bellio, E. Cebrián-Sastre, G. Celenza, J. Blázquez, L. Cendron, F. Spyrakis, D. Tondi, *Pharmaceuticals* **2020**, *13*, 52.

[246] M. Mioc, S. Avram, V. Bercean, L. Kurunczi, R. M. Ghiulai, C. Oprean, D. E.

Coricovac, C. Dehelean, A. Mioc, M. Balan-Porcarasu, C. Tatu, C. Soica, *Front. Chem.* **2018**, *6*, 373.

[247] J. Ghanaat, M. A. Khalilzadeh, D. Zareyee, *Mol. Divers.* **2021**, *25*, 223–232.

[248] N. Süleymanoğlu, R. Ustabaş, Ş. Direkel, Y. B. Alpaslan, Y. Ünver, *J. Mol. Struct.* **2017**, *1150*, 82–87.

[249] L. Sevaille, L. Gavara, C. Bebrone, F. De Luca, L. Nauton, M. Achard, P. Mercuri, S. Tanfoni, L. Borgianni, C. Guyon, P. Lonjon, G. Turan-Zitouni, J. Dzieciolowski, K. Becker, L. Bénard, C. Condon, L. Maillard, J. Martinez, J. M. Frère, O. Dideberg, M. Galleni, J. D. Docquier, J. F. Hernandez, *ChemMedChem* **2017**, *12*, 972–985.

[250] E. S. Raper, *Coord. Chem. Rev.* **1996**, *153*, 199–255.

[251] T. S. Lobana, *Coord. Chem. Rev.* **2021**, *441*, 213884.

[252] M. Ravera, E. Gabano, M. Sardi, G. Ermondi, G. Caron, M. J. McGlinchey, H. Müller-Bunz, E. Monti, M. B. Gariboldi, D. Osella, *J. Inorg. Biochem.* **2011**, *105*, 400–409.

[253] L. Colina-Vegas, K. M. Oliveira, B. N. Cunha, M. R. Cominetti, M. Navarro, A. A. Batista, *Inorganics* **2018**, *6*, DOI 10.3390/inorganics6040132.

[254] F. De Rienzo, R. R. Gabdoulline, M. C. Menziani, R. C. Wade, *Protein Sci.* **2000**, *9*, 1439–1454.

[255] P. A. Vigato, S. Tamburini, D. E. Fenton, *Coord. Chem. Rev.* **1990**, *106*, 25–170.

[256] M. Dennehy, O. V. Quinzani, R. M. Ferullo, A. Granados, R. A. Burrow, *Inorganica Chim. Acta* **2011**, *377*, 77–83.

[257] K. P. Kepp, *Inorg. Chem.* **2016**, *55*, 9461–9470.

[258] M. Dennehy, F. Delgado, M. Agotegaray, A. Campelo, E. Freire, R. Baggio, *J. Mol. Struct.* **2022**, *1253*, DOI 10.1016/j.molstruc.2021.132241.

[259] D. Varna, E. Geromichalou, E. Papachristou, R. Papi, A. G. Hatzidimitriou, E. Panteris, G. Psomas, G. D. Geromichalos, P. Aslanidis, T. Choli-Papadopoulou, P. A. Angaridis, *J. Inorg. Biochem.* **2022**, *228*, DOI 10.1016/j.jinorgbio.2021.111695.

[260] R. S. Corrêa, M. M. Da Silva, A. E. Graminha, C. S. Meira, J. A. F. Dos Santos, D. R. M. Moreira, M. B. P. Soares, G. Von Poelhsitz, E. E. Castellano, C. Bloch, M. R. Cominetti, A. A. Batista, *J. Inorg. Biochem.* **2016**, *156*, 153–163.

[261] B. Shirinkam, M. Tabatabaee, B. M. Kukovec, C. L. Oliver, M. Ghassemzadeh, *Monatshefte fur Chemie* **2014**, *145*, 1753–1757.

[262] M. Ghassemzadeh, L. Fallahnedjad, M. M. Heravi, B. Neumüller, *Polyhedron* **2008**, *27*, 1655–1664.

[263] R. K. Dani, M. K. Bharty, S. Paswan, S. Singh, N. K. Singh, *Inorganica Chim. Acta* **2014**, *421*, 519–530.

[264] W. Aboura, T. Benabdallah, F. Zhang, B. Therrien, *Inorganica Chim. Acta* **2018**, *483*, 93–97.

[265] M. Ravera, E. Moreno-Viguri, R. Paucar, S. P Erez-Silanes, E. Gabano, **2018**, DOI 10.1016/j.ejmech.2018.05.044.

[266] M. Navarro, C. Gabbiani, L. Messori, D. Gambino, *Drug Discov. Today* **2010**, *15*, 1070–1078.

[267] A. Martínez, T. Carreon, E. Iniguez, A. Anzellotti, A. Sánchez, M. Tyan, A. Sattler, L. Herrera, R. A. Maldonado, R. A. Sánchez-Delgado, *J. Med. Chem.* **2012**, *55*, 3867–3877.

[268] L. Dkhar, M. Sawkmie, A. L. Ka-Ot, S. R. Joshi, W. Kaminsky, M. R. Kollipara, *J. Organomet. Chem.* **2020**, *923*, DOI 10.1016/j.jorganchem.2020.121418.

[269] J. X. Fang, Z. Jin, Z. M. Li, W. Liu, *Appl. Organomet. Chem.* **2003**, *17*, 145–153.

[270] H. Yu, L. Shao, J. Fang, *J. Organomet. Chem.* **2007**, *692*, 991–996.

[271] J. Fang, Z. Jin, Y. Hu, W. Tao, L. Shao, *Appl. Organomet. Chem.* **2006**, *20*, 813–818.

[272] J. Shin, J. E. Kim, Y. W. Lee, H. Son, *Toxins (Basel).* **2018**, *10*, DOI 10.3390/toxins10030112.

[273] N. L. Stevanović, I. Aleksic, J. Kljun, S. S. Bogojevic, A. Veselinovic, J. Nikodinovic-Runic, I. Turel, M. I. Djuran, B. Glišić, *Pharmaceuticals* **2021**, *14*, 1–20.

[274] N. C. Norman, *Chemistry of Arsenic, Antimony and Bismuth, Springer Press*, Blackie Academic & Professional, **1997**.

[275] A. Luqman, V. L. Blair, R. Brammananth, P. K. Crellin, R. L. Coppel, P. C. Andrews, *Chem. Eur. J* **2014**, *20*, 14362–14377.

[276] A. Luqman, V. L. Blair, R. Brammananth, P. K. Crellin, R. L. Coppel, L. Kedzierski, P. C. Andrews, *Eur. J. Inorg. Chem.* **2015**, *2015*, 725–733.

[277] A. Luqman, V. L. Blair, A. M. Bond, P. C. Andrews, *Angew. Chemie Int. Ed.* **2013**, *52*, 7247–7251.

[278] P. C. Andrews, V. L. Blair, R. L. Ferrero, P. C. Junk, L. Kedzierski, R. M. Peiris, *Dalt. Trans.* **2014**, *43*, 1279–1291.

[279] A. Luqman, V. L. Blair, R. Brammananth, P. K. Crellin, R. L. Coppel, P. C. Andrews, *Eur. J. Inorg. Chem.* **2015**, *2015*, 4935–4945.

[280] D. C. Senevirathna, R. N. Duffin, L. J. Stephens, M. E. Herdman, M. V. Werrett, P. C. Andrews, *Aust. J. Chem.* **2020**, *73*, 1226–1236.

[281] T. Klapötke, *J. Organomet. Chem.* **1987**, *331*, 299–307.

[282] P. J. Sadler, H. Li, H. Sun, *Coord. Chem. Rev.* **1999**, *185–186*, 689–709.

[283] G. G. Briand and N. B. T.-A. in I. C. Burford, Academic Press, 2000, vol. 50, pp. 285–357.

[284] Y.-J. Wang and L. Xu, *J. Inorg. Biochem.*, 2008, **102**, 988–991.

[285] S. A. Shetu, L. M. Sanchez-Palestino, G. Rivera, D. Bandyopadhyay, *Tetrahedron* **2022**, 133117.

[286] H. Sun, H. Li, I. Harvey, P. J. Sadler, *J. Biol. Chem.* **1999**, *274*, 29094–101.

[287] L. Zhang, Ka Yee Szeto, Wai Biu Wong, Tat Tuck Loh, P. J. Sadler, H. Sun, *Biochemistry* **2001**, *40*, 13281–13287.

[288] R. Wang, T. P. Lai, P. Gao, H. Zhang, P. L. Ho, P. C. Y. Woo, G. Ma, R. Y. T. Kao, H. Li, H. Sun, *Nat. Commun.* **2018**, *9*, 1–12.

[289] P. C. Andrews, V. L. Blair, P. C. Junk, I. Kumar, *Chem. Commun.* **2013**, *49*, 2870–

2872.

[290] P. C. Andrews, R. L. Ferrero, P. C. Junk, I. Kumar, Q. Luu, K. Nguyen, J. W. Taylor, *Dalt. Trans.* **2010**, *39*, 2861–2868.

[291] P. C. Andrews, M. Busse, G. B. Deacon, R. L. Ferrero, P. C. Junk, K. K. Huynh, I. Kumar, J. G. MacLellan, *Dalt. Trans.* **2010**, *39*, 9633.

[292] P. C. Andrews, R. L. Ferrero, C. M. Forsyth, P. C. Junk, J. G. MacLellan, R. M. Peiris, *Organometallics* **2011**, *30*, 6283–6291.

[293] P. C. Andrews, R. L. Ferrero, P. C. Junk, R. M. Peiris, *J. Organomet. Chem.* **2013**, *724*, 88–94.

[294] P. Domenico, L. Baldassarri, P. E. Schoch, K. Kaehler, M. Sasatsu, B. A. Cunha, *Antimicrob. Agents Chemother.* **2001**, *45*, 1417–1421.

[295] C. L. Wu, P. Domenico, D. J. Hassett, T. J. Beveridge, A. R. Hauser, J. A. Kazzaz, *Am. J. Respir. Cell Mol. Biol.* **2002**, *26*, 731–738.

[296] J. P. P. Folsom, B. Baker, P. S. S. Stewart, *J. Appl. Microbiol.* **2011**, *111*, 989–996.

[297] A. R. Badireddy, B. R. Korpol, S. Chellam, P. L. Gassman, M. H. Engelhard, A. S. Lea, K. M. Rosso, *Biomacromolecules* **2008**, *9*, 3079–3089.

[298] P. Domenico, R. J. Salo, S. G. Novick, P. E. Schoch, K. Van Horn, B. A. Cunha, *Antimicrob. Agents Chemother.* **1997**, *41*, 1697–1703.

[299] H. Zhang, J. Tang, X. Meng, J. Tsang, T. K. Tsang, *Dig. Dis. Sci.* **2005**, *50*, 1046–1051.

[300] P. Domenico, J. M. Tomas, S. Merino, X. Rubires, B. A. Cunha, *Infect. Immun.* **1999**, *67*, 664–669.

[301] C. T. Huang, P. S. Stewart, *J. Antimicrob. Chemother.* **1999**, *44*, 601–605.

[302] P. Domenico, E. Gurzenda, A. Giacometti, O. Cirioni, R. Ghiselli, F. Orlando, M. Korem, V. Saba, G. Scalise, N. Balaban, *Peptides* **2004**, *25*, 2047–2053.

[303] P. Domenico, J. Reich, W. Madonia, B. A. Cunha, *J. Antimicrob. Chemother.* **1996**, *38*, 1031–1040.

[304] P. Domenico, *J. Microbiol. Exp.* **2015**, *2*, DOI 10.15406/jmen.2015.02.00049.

[305] A. R. Badireddy, S. Chellam, *J. Appl. Microbiol.* **2011**, *110*, 1426–1437.

[306] A. R. Badireddy, S. Chellam, S. Yanina, P. Gassman, K. M. Rosso, *Biotechnol. Bioeng.* **2008**, *99*, 634–643.

[307] T. Murafuji, M. Tomura, K. Ishiguro, I. Miyakawa, *Molecules* **2014**, *19*, 11077–11095.

[308] T. Murafuji, K. Kitagawa, D. Yoshimatsu, K. Kondo, K. Ishiguro, R. Tsunashima, I. Miyakawa, Y. Mikata, *Eur. J. Med. Chem.* **2013**, *63*, 531–535.

[309] T. Murafuji, Y. Miyoshi, M. Ishibashi, A. F. M. M. Rahman, Y. Sugihara, I. Miyakawa, H. Uno, **n.d.**, DOI 10.1016/j.jinorgbio.2003.12.024.

[310] S. A. Alharbi, B. H. Mashat, N. A. Al-Harbi, M. Wainwright, A. S. Aloufi, S. Alnaimat, *Saudi J. Biol. Sci.* **2012**, *19*, 147–150.

[311] J. S. Solanki, T. R. Thapak, A. Bhardwaj, U. N. Tripathi, *J. Coord. Chem.* **2011**, *64*, 369–376.

[312] L. Dawara, R. V. Singh, *J. Coord. Chem.* **2011**, *64*, 931–941.

[313] A. Luqman, V. L. Blair, R. Brammananth, P. K. Crellin, R. L. Coppel, P. C. Andrews, *Chem. - A Eur. J.* **2014**, *20*, 14362–14377.

[314] S. M. Mousavi, M. Zarei, S. A. Hashemi, A. Babapoor, A. M. Amani, *Artif. Cells, Nanomedicine Biotechnol.* **2019**, *47*, 1132–1148.

[315] S. Maddila, S. Gorle, S. B. Jonnalagadda, *Drug Screening of Rhodanine Derivatives for Antibacterial Activity*, Taylor & Francis, **2020**.

[316] C. Angwin, C. Jenkinson, A. Jones, C. Jennison, W. Henley, A. Farmer, N. Sattar, R. R. Holman, E. Pearson, B. Shields, A. Hattersley, *BMJ Open* **2020**, *10*, e042784.

[317] S. L. Mueller, P. K. Chrysanthopoulos, M. A. Halili, C. Hepburn, T. Nebl, C. T. Supuran, A. Nocentini, T. S. Peat, S. A. Poulsen, *Molecules* **2021**, *26*, 3010.

[318] M. Mori, D. Deodato, M. Kasula, D. M. Ferraris, A. Sanna, A. De Logu, M. Rizzi, M. Botta, *Bioorg. Med. Chem. Lett.* **2018**, *28*, 637–641.

[319] M. Sortino, P. Delgado, S. Juárez, J. Quiroga, R. Abonía, B. Insuasty, M. Nogueras, L. Rodero, F. M. Garibotto, R. D. Enriz, S. A. Zacchino, *Bioorg. Med. Chem.* **2007**, *15*, 484–494.

[320] M. G. Orchard, J. C. Neuss, C. M. S. Galley, A. Carr, D. W. Porter, P. Smith, D. I. C. Scopes, D. Haydon, K. Vousden, C. R. Stubberfield, K. Young, M. Page, *Bioorganic Med. Chem. Lett.* **2004**, *14*, 3975–3978.

[321] Z.-H. H. Chen, C.-J. J. Zheng, L.-P. P. Sun, H.-R. R. Piao, *Eur. J. Med. Chem.* **2010**, *45*, 5739–5743.

[322] A. Insuasty, J. Ramírez, M. Raimondi, C. Echeverry, J. Quiroga, R. Abonia, M. Nogueras, J. Cobo, M. Rodríguez, S. Zacchino, B. Insuasty, A. Insuasty, J. Ramírez, M. Raimondi, C. Echeverry, J. Quiroga, R. Abonia, M. Nogueras, J. Cobo, M. V. Rodríguez, S. A. Zacchino, B. Insuasty, *Molecules* **2013**, *18*, 5482–5497.

[323] L. J. Yin, A. K. D. bin Ahmad Kamar, G. T. Fung, C. T. Liang, V. R. Avupati, *Biomed. Pharmacother.* **2022**, *145*, 112406.

[324] J. W. Steele, D. Faulds, K. L. Goa, *Drugs Aging* **1993**, *3*, 532–555.

[325] M. A. Ramirez, N. L. Borja, *Pharmacotherapy* **2008**, *28*, 646–655.

[326] N. Hotta, Y. Akanuma, R. Kawamori, K. Matsuoka, Y. Oka, M. Shichiri, T. Toyota, M. Nakashima, I. Yoshimura, N. Sakamoto, Y. Shigeta, *Diabetes Care* **2006**, *29*, 1538–1544.

[327] A. B. Patel and P. Kumari, ed. R. Varala, IntechOpen, Rijeka, 2016, p. Ch. 2.

[328] T. Tomasic, L. Masic, *Curr. Med. Chem.* **2009**, *16*, 1596–1629.

[329] Y. Xiang, C. Chen, W. M. Wang, L. W. Xu, K. W. Yang, P. Oelschlaeger, Y. He, *ACS Med. Chem. Lett.* **2018**, *9*, 359–364.

[330] J. Brem, S. S. Van Berkel, W. Aik, A. M. Rydzik, M. B. Avison, I. Pettinati, K. D. Umland, A. Kawamura, J. Spencer, T. D. W. Claridge, M. A. McDonough, C. J. Schofield, *Nat. Chem.* **2014**, *6*, 1084–1090.

[331] D. Kaminskyy, A. Kryshchyshyn, R. Lesyk, *Expert Opin. Drug Discov.* **2017**, *12*, 1233–1252.

[332] J. Baell, M. A. Walters, *Nature* **2014**, *513*, 481–483.

[333] T. Mendgen, C. Steuer, C. D. Klein, **2011**, DOI 10.1021/jm201243p.

[334] A. L. Hopkins, C. R. Groom, A. Alex, *Drug Discov. Today* **2004**, *9*, 430–431.

[335] E. M. Czekanska, *Methods Mol. Biol.* **2011**, *740*, 27–32.

[336] N. Y. Megally Abdo, M. M. Kamel, *Chem. Pharm. Bull.* **2015**, *63*, 369–376.

[337] N. Y. Megally Abdo, M. M. Kamel, N. Youssef, M. Abdo, M. M. Kamel, *Chem. Pharm. Bull* **2015**, *63*, 369–376.

[338] P. C. Andrews, G. B. Deacon, P. C. Junk, N. F. Spiccia, *Green Chem.* **2007**, *9*, 1319–1327.

[339] C. N. R. Rao, R. Venkataraghavan, *Spectrochim. Acta* **1962**, *18*, 541–547.

[340] C. Cogrossi, *Spectrochim. Acta Part A Mol. Spectrosc.* **1972**, *28*, 855–870.

[341] C. N. R. Rao, R. Venkataraghavan, *Can. J. Chem.* **1964**, *42*, 43–49.

[342] E. Romano, N. A. J. Soria, R. Rudyk, S. A. Brandán, *Mol. Simul.* **2012**, *38*, 561–566.

[343] H. Gökce, N. Öztürk, Ü. Ceylan, Y. B. Alpaslan, G. Alpaslan, *Spectrochim. Acta - Part A Mol. Biomol. Spectrosc.* **2016**, *163*, 170–180.

[344] R. J. Xavier, E. Gobinath, *Spectrochim. Acta - Part A Mol. Biomol. Spectrosc.* **2012**, *86*, 242–251.

[345] S. Bandyopadhyay, A. Dey, *Analyst* **2014**, *139*, 2118–2121.

[346] I. Sabatini, A, Bertini, *Inorg. Chem.* **1965**, *4*, 959–961.

[347] R. A. Wheeler, P. N. V. P. Kumar, *J. Am. Chem. Soc.* **1992**, *114*, 4776–4784.

[348] K. J. Burke, L. J. Stephens, M. V. Werrett, P. C. Andrews, *Chem. - A Eur. J.* **2020**, *26*, 7657–7671.

[349] M. E. Herdman, M. V Werrett, R. N. Duffin, L. J. Stephens, R. Brammananth, R. L. Coppel, W. Batchelor, P. C. Andrews, *Dalt. Trans.* **2020**, *49*, 7341–7354.

[350] A. Pathak, V. L. Blair, R. L. Ferrero, M. Mehring, P. C. Andrews, *Chem. Commun.* **2014**, *50*, 15232–15234.

[351] T. Topală, A. Bodoki, L. Oprean, R. Oprean, *Clujul Med.* **2014**, *87*, 5.

[352] N. Monti, V. Longo, S. Zacchini, G. Vigarani, L. Giorgini, E. Bonora, M. Massi, V. Fiorini, S. Stagni, *Inorganica Chim. Acta* **2021**, *518*, 120244.

[353] C. S. F. Leung, S. S. F. Leung, J. Tirado-Rives, W. L. Jorgensen, *J. Med. Chem.* **2012**, *55*, 4489–4500.

[354] H. Schönherr, T. Cernak, *Angew. Chemie - Int. Ed.* **2013**, *52*, 12256–12267.

[355] R. D. Abughazaleh, T. S. Tracy, in *Wiley StatsRef Stat. Ref. Online*, John Wiley & Sons, Ltd, Chichester, UK, **2014**.

[356] P. Y. Muller, M. N. Milton, *Nat. Rev. Drug Discov.* **2012**, *11*, 751–761.

[357] J. C. Pritchett, L. Naesens, J. Montoya, in *Hum. Herpesviruses HHV-6A, HHV-6B, HHV-7, Third Ed.*, Elsevier B.V., **2014**, pp. 311–331.

[358] D. T. Elmore, *J. Chem. Soc.* **1958**, *77*, 3489–3492.

[359] M. Von Rolf, M. Reinhard, A. Lüttringhaus, *Zeitschrift fur Naturforsch. - Sect. B J. Chem. Sci.* **1955**, *10*, 367–370.

[360] R. Mecke, R. Mecke, A. Lüttringhaus, *Chem. Ber.* **1957**, *90*, 975–986.

[361] T. Mroczek, T. Plech, M. Wujec, *J. Chromatogr. Sci.* **2017**, *55*, 117–129.

[362] O. D. Cretu, S. F. Barbuceanu, G. Saramet, C. Draghici, *J. Serbian Chem. Soc.* **2010**, *75*, 1463–1471.

[363] N. Burford, M. D. Eelman, D. E. Mahony, M. Morash, *Chem. Commun.* **2003**, 146–147.

[364] E. C. Sutton, C. E. McDevitt, M. V. Yglesias, R. M. Cunningham, V. J. DeRose, *Inorganica Chim. Acta* **2019**, *498*, 118984.

[365] B. A. J. Jansen, J. Brouwer, J. Reedijk, *J. Inorg. Biochem.* **2002**, *89*, 197–202.

[366] N. J. Wheate, S. Walker, G. E. Craig, R. Oun, *Dalt. Trans.* **2010**, *39*, 8113–8127.

[367] U. Das, B. Kar, S. Pete, P. Paira, *Dalt. Trans.* **2021**, *50*, 11259–11290.

[368] A. Frei, J. Zuegg, A. G. A. G. Elliott, M. Baker, S. Braese, C. Brown, F. Chen, C. G.

Dowson, G. Dujardin, N. Jung, A. P. P. King, A. M. Mansour, M. Massi, J. Moat, H. A. H. A. Mohamed, A. K. A. K. Renfrew, P. J. P. J. Rutledge, P. J. P. J. Sadler, M. H. M. H. M. H. Todd, C. E. C. E. C. E. Willans, J. J. J. Wilson, M. A. M. A. Cooper, M. A. T. M. A. T. Blaskovich, C. G.Dowson, G. Dujardin, N. Jung, A. P. P. King, A. M. Mansour, M. Massi, J. Moat, H. A. H. A. Mohamed, A. K. A. K. Renfrew, P. J. P. J. Rutledge, P. J. P. J. Sadler, M. H. M. H. M. H. Todd, C. E. C. E. C. E. Willans, J. J. J. Wilson, M. A. M. A. Cooper, M. A. T. M. A. T. Blaskovich, *Chem. Sci.* **2020**, *11*, 2627–2639.

[369] Z. Asbai, A. Bonfiglio, P. Mercandelli, F. Polo, M. Mauro, *Polyhedron* **2021**, *197*, DOI 10.1016/j.poly.2021.115025.

[370] H. C. Bertrand, S. Clède, R. Guillot, F. Lambert, C. Policar, *Inorg. Chem.* **2014**, *53*, 6204–6223.

[371] J. Skiba, A. Kowalczyk, P. Stączek, T. Bernas, D. Trzybiński, K. Woźniak, U. Schatzschneider, R. Czerwieniec, K. Kowalski, *New J. Chem.* **2019**, *43*, 573–583.

[372] B. L. Murphy, S. C. Marker, V. J. Lambert, J. J. Woods, S. N. MacMillan, J. J. Wilson, *J. Organomet. Chem.* **2020**, *907*, 121064.

[373] K. Potgieter, P. Mayer, T. Gerber, N. Yumata, E. Hosten, I. Booysen, R. Betz, M. Ismail, B. Van Brecht, *Polyhedron* **2013**, *49*, 67–73.

[374] B. Merillas, E. Cuéllar, A. Diez-Varga, T. Torroba, G. García-Herbosa, S. Fernández, J. Lloret-Fillol, J. M. Martín-Alvarez, D. Miguel, F. Villafañe, *Inorg. Chem.* **2020**, *59*, 11152–11165.

[375] M. Patra, M. Wenzel, P. Prochnow, V. Pierroz, G. Gasser, J. E. Bandow, N. Metzler-Nolte, *Chem. Sci.* **2015**, *6*, 214–224.

[376] A. J. Amoroso, M. P. Coogan, J. E. Dunne, V. Fernández-Moreira, J. B. Hess, A. J. Hayes, D. Lloyd, C. Millet, S. J. A. Pope, C. Williams, *Chem. Commun.* **2007**, 3066–3068.

[377] L. J. Stephens, S. Munuganti, R. N. Duffin, M. V. Werrett, P. C. Andrews, *Inorg. Chem.* **2020**, *59*, 3494–3508.

[378] V. W. W. Yam, K. K. W. Lo, K. K. Cheung, R. Y. C. Kong, *J. Chem. Soc. Chem. Commun.* **1995**, 1191–1193.

[379] L. A. Mullice, R. H. Laye, L. P. Harding, N. J. Buurma, S. J. A. Pope, *New J. Chem.* **2008**, *32*, 2140–2149.

[380] R. F. Vitor, I. Correia, M. Videira, F. Marques, A. Paulo, J. Costa Pessoa, G. Viola, G. G. Martins, I. Santos, *ChemBioChem* **2008**, *9*, 131–142.

[381] D. I. Konovalov, A. A. Ivanov, T. S. Frolova, I. V. Eltsov, Y. M. Gayfulin, L. Plunkett, M. Bazzar, A. M. Adawi, J. S. G. Bouillard, S. I. Baiborodin, O. I. Sinitsyna, N. V. Kuratieva, V. V. Yanshole, O. A. Efremova, M. A. Shestopalov, *Chem. - A Eur. J.* **2020**, *26*, 13904–13914.

[382] B. Gallego, M. R. Kaluderovic, H. Kommera, R. Paschke, E. Hey-Hawkins, T. W. Remmerbach, G. N. Kaluderovic, S. Gómez-Ruiz, *Invest. New Drugs* **2011**, *29*, 932–944.

[383] D. L. Ma, C. M. Che, F. M. Siu, M. Yang, K. Y. Wong, *Inorg. Chem.* **2007**, *46*, 740–749.

[384] F. Zobi, B. Spingler, T. Fox, R. Alberto, *Inorg. Chem.* **2003**, *42*, 2818–2820.

[385] F. Zobi, O. Blacque, R. K. O. Sigel, R. Alberto, *Inorg. Chem.* **2007**, *46*, 10458–10460.

[386] K. K. W. Lo, K. Y. Zhang, S. P. Y. Li, *Eur. J. Inorg. Chem.* **2011**, 3551–3568.

[387] B. R. Crane, A. J. Di Bilio, J. R. Winkler, H. B. Gray, *J. Am. Chem. Soc.* **2001**, *123*, 11623–11631.

[388] A. J. Amoroso, R. J. Arthur, M. P. Coogan, J. B. Court, V. Fernández-Moreira, A. J. Hayes, D. Lloyd, C. Millet, S. J. A. Pope, *New J. Chem.* **2008**, *32*, 1097–1102.

[389] K. L. Haas, K. J. Franz, *Chem. Rev.* **2009**, *109*, 4921–4960.

[390] P. Collery, V. Veena, A. Harikrishnan, D. Desmaele, *Invest. New Drugs* **2019**, *37*, 973–983.

[391] Z. Y. Pan, C. P. Tan, L. S. Rao, H. Zhang, Y. Zheng, L. Hao, L. N. Ji, Z. W. Mao, *Angew. Chemie - Int. Ed.* **2020**, *59*, 18755–18762.

[392] M. Wenzel, M. Patra, C. H. R. Senges, I. Ott, J. J. Stepanek, A. Pinto, P. Prochnow, C. Vuong, S. Langklotz, N. Metzler-Nolte, J. E. Bandow, *ACS Chem. Biol.* **2013**, *8*,

1442–1450.

[393] M. Patra, G. Gasser, D. Bobukhov, K. Merz, A. V. Shtemenko, N. Metzler-Nolte, *Dalt. Trans.* **2010**, *39*, 5617–5619.

[394] D. Siegmund, N. Lorenz, Y. Gothe, C. Spies, B. Geissler, P. Prochnow, P. Nuernberger, J. E. Bandow, N. Metzler-Nolte, *Dalt. Trans.* **2017**, *46*, 15269–15279.

[395] H. S. Liew, C. W. Mai, M. Zulkefeli, T. Madheswaran, L. V. Kiew, N. Delsuc, M. Lee Low, *Molecules* **2020**, *25*, 4176.

[396] A. Frei, M. Amado, M. A. Cooper, M. A. T. Blaskovich, *Chem. - A Eur. J.* **2020**, *26*, 2852–2858.

[397] S. N. Sovari, I. Kolly, K. Schindler, Y. Cortat, S. C. Liu, A. Crochet, A. Pavic, F. Zobi, *Molecules* **2021**, *26*, DOI 10.3390/molecules26175302.

[398] S. N. Sovari, N. Radakovic, P. Roch, A. Crochet, A. Pavic, F. Zobi, *Eur. J. Med. Chem.* **2021**, *226*, 113858.

[399] A. Carreño, E. Solís-Céspedes, C. Zúñiga, J. Nevermann, M. M. Rivera-Zaldívar, M. Gacitúa, A. Ramírez-Osorio, D. Páez-Hernández, R. Arratia-Pérez, J. A. Fuentes, *Chem. Phys. Lett.* **2019**, *715*, 231–238.

[400] S. N. Sovari, S. Vojnovic, S. S. Bogojevic, A. Crochet, A. Pavic, J. Nikodinovic-Runic, F. Zobi, *Eur. J. Med. Chem.* **2020**, *205*, 112533.

[401] A. Carreño, A. E. Aros, C. Otero, R. Polanco, M. Gacitúa, R. Arratia-Pérez, J. A. Fuentes, *New J. Chem.* **2017**, *41*, 2140–2147.

[402] M. Patra, G. Gasser, *ChemBioChem* **2012**, *13*, 1232–1252.

[403] A. Carreño, D. Páez-Hernández, C. Zúñiga, A. Ramírez-Osorio, N. Pizarro, A. Vega, E. Solis-Céspedes, M. M. Rivera-Zaldívar, A. Silva, J. A. Fuentes, *Dye. Pigment.* **2021**, *184*, 108876.

[404] A. Carreño, M. Gacitúa, D. Páez-Hernández, R. Polanco, M. Preite, J. A. Fuentes, G. C. Mora, I. Chávez, R. Arratia-Pérez, *New J. Chem.* **2015**, *39*, 7822–7831.

[405] A. Carreño, K. Fernández, F. Sáez-Cortez, C. Otero, R. Arratia-Pérez, J. A. Fuentes,

R. Polanco, *J. Chil. Chem. Soc.* **2019**, *64*, 4428–4431.

[406] L. Henry, N. Delsuc, C. Laugel, F. Lambert, C. Sandt, S. Hostachy, A. S. Bernard, H. C. Bertrand, L. Grimaud, A. Baillet-Guffroy, C. Policar, *Bioconjug. Chem.* **2018**, *29*, 987–991.

[407] K. Yin Zhang, K. Ka-Shun Tso, M. W. Louie, H. W. Liu, K. Kam-Wing Lo, *Organometallics* **2013**, *32*, 5098–5102.

[408] M. W. Louie, M. H. C. Lam, K. K. W. Lo, *Eur. J. Inorg. Chem.* **2009**, *2009*, 4265–4273.

[409] K. K. W. Lo, M. W. Louie, K. S. Sze, J. S. Y. Lau, *Inorg. Chem.* **2008**, *47*, 602–611.

[410] L. Raszeja, A. Maghnouj, S. Hahn, N. Metzler-Nolte, *ChemBioChem* **2011**, *12*, 371–376.

[411] L. A. Sacksteder, J. N. Demas, M. Lee, B. A. DeGraff, *J. Am. Chem. Soc.* **1993**, *115*, 8230–8238.

[412] S. Clède, C. Policar, *Chem. - A Eur. J.* **2015**, *21*, 942–958.

[413] N. Akabar, V. Chaturvedi, G. E. Shillito, B. J. Schwehr, K. C. Gordon, G. S. Huff, J. J. Sutton, B. W. Skelton, A. N. Sobolev, S. Stagni, D. J. Nelson, M. Massi, *Dalt. Trans.* **2019**, *48*, 15613–15624.

[414] P. J. Wright, M. G. Affleck, S. Muzzioli, B. W. Skelton, P. Raiteri, D. S. Silvester, S. Stagni, M. Massi, *Organometallics* **2013**, *32*, 3728–3737.

[415] P. J. Wright, S. Muzzioli, M. V. Werrett, P. Raiteri, B. W. Skelton, D. S. Silvester, S. Stagni, M. Massi, *Organometallics* **2012**, *31*, 7566–7578.

[416] M. V. Werrett, D. Chartrand, J. D. Gale, G. S. Hanan, J. G. MacLellan, M. Massi, S. Muzzioli, P. Raiteri, B. W. Skelton, M. Silberstein, S. Stagni, *Inorg. Chem.* **2011**, *50*, 1229–1241.

[417] C. A. Bader, R. D. Brooks, Y. S. Ng, A. Sorvina, M. V. Werrett, P. J. Wright, A. G. Anwer, D. A. Brooks, S. Stagni, S. Muzzioli, M. Silberstein, B. W. Skelton, E. M. Goldys, S. E. Plush, T. Shandala, M. Massi, *RSC Adv.* **2014**, *4*, 16345–16351.

[418] C. A. Bader, T. Shandala, E. A. Carter, A. Ivask, T. Guinan, S. M. Hickey, M. V.

Werrett, P. J. Wright, P. V. Simpson, S. Stagni, N. H. Voelcker, P. A. Lay, M. Massi, S. E. Plush, D. A. Brooks, *PLoS One* **2016**, *11*, e0161557.

[419] R. R. Varma, F. U. Vaidya, C. Pathak, M. P. Dhaduk, R. A. Dabhi, B. S. Bhatt, M. N. Patel, *Inorg. Chem. Commun.* **2021**, *134*, 109005.

[420] J. G. Vaughan, B. L. Reid, S. Ramchandani, P. J. Wright, S. Muzzioli, B. W. Skelton, P. Raiteri, D. H. Brown, S. Stagni, M. Massi, *Dalt. Trans.* **2013**, *42*, 14100–14114.

[421] A. M. Mansour, *RSC Adv.* **2021**, *11*, 22715–22722.

[422] C. A. Bader, A. Sorvina, P. V. Simpson, P. J. Wright, S. Stagni, S. E. Plush, M. Massi, D. A. Brooks, *FEBS Lett.* **2016**, *590*, 3051–3060.

[423] V. Fernández-Moreira, F. L. Thorp-Greenwood, M. P. Coogan, *Chem. Commun.* **2010**, *46*, 186–202.

[424] A. Sorvina, C. A. Bader, C. Caporale, E. A. Carter, I. R. D. Johnson, E. J. Parkinson-Lawrence, P. V. Simpson, P. J. Wright, S. Stagni, P. A. Lay, M. Massi, D. A. Brooks, S. E. Plush, *Oncotarget* **2018**, *9*, 35541–35552.

[425] M. Obata, A. Kitamura, A. Mori, C. Kameyama, J. A. Czaplewska, R. Tanaka, I. Kinoshita, T. Kusumoto, H. Hashimoto, M. Harada, Y. Mikata, T. Funabiki, S. Yano, *Dalt. Trans.* **2008**, 3292–3300.

[426] A. Boulay, A. Seridi, C. Zedde, S. Ladeira, C. Picard, L. Maron, E. Benoist, *Eur. J. Inorg. Chem.* **2010**, *2010*, 5058–5062.

[427] A. Comia, L. Charalambou, S. A. E. Omar, P. A. Scattergood, P. I. P. Elliott, A. Sinopoli, *Inorganics* **2020**, *8*, 22.

[428] C. B. Anderson, A. B. S. Elliott, J. E. M. Lewis, C. J. McAdam, K. C. Gordon, J. D. Crowley, *Dalt. Trans.* **2012**, *41*, 14625–14632.

[429] K. O. Piletska, K. V. Domasevitch, A. N. Gusev, V. F. Shul'Gin, A. V. Shtemenko, *Polyhedron* **2015**, *102*, 699–704.

[430] V. Fernández-Moreira, H. Sastre-Martín, *Inorganica Chim. Acta* **2017**, *460*, 127–133.

[431] A. Gómez, G. Jara, E. Flores, T. Maldonado, F. Godoy, M. Muñoz-Osses, A. Vega, R.

Mera, C. Silva, J. Pavez, *New J. Chem.* **2020**, *44*, 14171–14179.

[432] M. He, H. Y. V. Ching, C. Policar, H. C. Bertrand, *New J. Chem.* **2018**, *42*, 11312–11323.

[433] J. Wang, B. Delavaux-Nicot, M. Wolff, S. Mallet-Ladeira, R. Métivier, E. Benoist, S. Fery-Forgues, *Dalt. Trans.* **2018**, *47*, 8087–8099.

[434] W. K. C. Lo, G. S. Huff, J. R. Cubanski, A. D. W. Kennedy, C. J. McAdam, D. A. McMorran, K. C. Gordon, J. D. Crowley, *Inorg. Chem.* **2015**, *54*, 1572–1587.

[435] R. M. Shaker, *Arkivoc*, 2006, **9**, 59–112.

[436] T. U. Connell, D. J. Hayne, U. Ackermann, H. J. Tochon-Danguy, J. M. White, P. S. Donnelly, *J. Label. Compd. Radiopharm.* **2014**, *57*, 262–269.

[437] G. Bistoni, S. Rampino, N. Scafuri, G. Ciancaleoni, D. Zuccaccia, L. Belpassi, F. Tarantelli, *Chem. Sci.* **2016**, *7*, 1174–1184.

[438] T. Morimoto, O. Ishitani, *Acc. Chem. Res.* **2017**, *50*, 2673–2683.

[439] L. Maria, C. Moura, A. Paulo, I. C. Santos, I. Santos, *J. Organomet. Chem.* **2006**, *691*, 4773–4778.

[440] H. D. Stoeffler, N. B. Thorntor, S. L. Temkin, K. S. Schanze, *J. Am. Chem. Soc.* **1995**, *117*, 7119–7128.

[441] T. Das, K. K. Rajak, *J. Organomet. Chem.* **2020**, *908*, 121098.

[442] N. Pizarro, M. Saldí, N. Guzmán, C. Sandoval-Altamirano, S. Kahlal, J. Y. Saillard, J. R. Hamon, A. Vega, *New J. Chem.* **2019**, *43*, 2449–2457.

[443] V. Fiorini, A. M. Ranieri, S. Muzzioli, K. D. M. Magee, S. Zacchini, N. Akabar, A. Stefan, M. I. Ogden, M. Massi, S. Stagni, *Dalt. Trans.* **2015**, *44*, 20597–20608.

[444] R. O. Bonello, I. R. Morgan, B. R. Yeo, L. E. J. Jones, B. M. Kariuki, I. A. Fallis, S. J. A. Pope, *J. Organomet. Chem.* **2014**, *749*, 150–156.

[445] S. Ranjan, S. Y. Lin, K. C. Hwang, Y. Chi, W. L. Ching, C. S. Liu, Y. T. Tao, C. H. Chien, S. M. Peng, G. H. Lee, *Inorg. Chem.* **2003**, *42*, 1248–1255.

[446] A. Carreño, M. Gacitúa, J. A. Fuentes, D. Páez-Hernández, J. P. Peñaloza, C. Otero,

M. Preite, E. Molins, W. B. Swords, G. J. Meyer, J. M. Manríquez, R. Polanco, I. Chávez, R. Arratia-Pérez, *New J. Chem.* **2016**, *40*, 7687–7700.

[447] A. Carreño, M. Gacitua, E. Schott, X. Zarate, J. M. Manriquez, M. Preite, S. Ladeira, A. Castel, N. Pizarro, A. Vega, I. Chavez, R. Arratia-Perez, *New J. Chem.* **2015**, *39*, 5725–5734.

[448] T. Auvray, A. K. Pal, G. S. Hanan, *Eur. J. Inorg. Chem.* **2021**, *2021*, 2570–2577.

[449] S. Ali, M. R. Malik, A. A. Isab, S. Ahmad, *J. Coord. Chem.* **2009**, *62*, 475–480.

[450] M. J. Stout, B. W. Skelton, A. N. Sobolev, P. Raiteri, M. Massi, P. V. Simpson, *Organometallics* **2020**, *39*, 3202–3211.

[451] J. L. Wedding, H. H. Harris, C. A. Bader, S. E. Plush, R. Mak, M. Massi, D. A. Brooks, B. Lai, S. Vogt, M. V. Werrett, P. V. Simpson, B. W. Skelton, S. Stagni, *Metallomics* **2017**, *9*, 382–390.

[452] J. Lazniewska, M. Agostino, S. M. Hickey, E. Parkinson-Lawrence, S. Stagni, M. Massi, D. A. Brooks, S. E. Plush, *Chem. - A Eur. J.* **2021**, *27*, 11406–11417.

[453] M. Wolff, L. Munoz, A. François, C. Carrayon, A. Seridi, N. Saffon, C. Picard, B. Machura, E. Benoist, *Dalt. Trans.* **2013**, *42*, 7019–7031.

[454] N. M. Shavaleev, Z. R. Bell, T. L. Easun, R. Rutkaite, L. Swanson, M. D. Ward, *Dalt. Trans.* **2004**, 3678–3688.

[455] K. Welsher, S. P. Sherlock, H. Dai, *Proc. Natl. Acad. Sci. U. S. A.* **2011**, *108*, 8943–8948.

[456] A. N. Bashkatov, E. A. Genina, V. I. Kochubey, V. V. Tuchin, *J. Phys. D. Appl. Phys.* **2005**, *38*, 2543–2555.

[457] J. F. Algorri, M. Ochoa, P. Roldán-Varona, L. Rodríguez-Cobo, J. M. López-Higuera, *Cancers (Basel).* **2021**, *13*, 3484.

[458] B. Kowalska-Krochmal, R. Dudek-Wicher, *Pathogens* **2021**, *10*, 1–21.

[459] J. Moat, A. Rizoulis, G. Fox, M. Upton, *J. Water Health* **2016**, *14*, 727–737.

[460] M. P. Coogan, P. J. Dyson, M. Bochmann, *Organometallics* **2012**, *31*, 5671–5672.

[461] K. Schindler, Y. Cortat, M. Nedyalkova, A. Crochet, M. Lattuada, A. Pavic, F. Zobi, *Pharmaceuticals* **2022**, *15*, DOI 10.3390/ph15091107.

[462] J. D. Crowley, P. H. Bandeen, *Dalt. Trans.* **2010**, *39*, 612–623.

[463] J. D. Crowley, P. H. Bandeen, L. R. Hanton, *Polyhedron* **2010**, *29*, 70–83.

[464] J. D. Crowley, D. A. McMorran, Springer, Berlin, Heidelberg, **2012**, pp. 31–83.

[465] M. She, Z. Wang, T. Luo, B. Yin, P. Liu, J. Liu, F. Chen, S. Zhang, J. Li, *Chem. Sci.* **2018**, *9*, 8065–8070.

[466] L. Y. Niu, Y. S. Guan, Y. Z. Chen, L. Z. Wu, C. H. Tung, Q. Z. Yang, *J. Am. Chem. Soc.* **2012**, *134*, 18928–18931.

[467] Y. Mao, Y. Xu, Z. Li, Y. Wang, H. Du, L. Liu, R. Ding, G. Liu, *Sensors (Switzerland)* **2019**, *19*, DOI 10.3390/s19245348.

[468] M. W. Louie, T. T. H. Fong, K. K. W. Lo, *Inorg. Chem.* **2011**, *50*, 9465–9471.

[469] R. R. Ye, B. C. Chen, J. J. Lu, X. R. Ma, R. T. Li, *J. Inorg. Biochem.* **2021**, *223*, 111537.

[470] J. Yang, J. X. Zhao, Q. Cao, L. Hao, D. Zhou, Z. Gan, L. N. Ji, Z. W. Mao, *ACS Appl. Mater. Interfaces* **2017**, *9*, 13900–13912.

[471] F. X. Wang, J. H. Liang, H. Zhang, Z. H. Wang, Q. Wan, C. P. Tan, L. N. Ji, Z. W. Mao, *ACS Appl. Mater. Interfaces* **2019**, *11*, 13123–13133.

[472] S. C. Marker, S. N. MacMillan, W. R. Zipfel, Z. Li, P. C. Ford, J. J. Wilson, *Inorg. Chem.* **2018**, *57*, 1311–1331.

[473] B. S. McGhie, J. R. Aldrich-Wright, *Biomedicines* **2022**, *10*, 578.

[474] S. R. Stoyanov, J. M. Villegas, A. J. Cruz, L. L. Lockyear, J. H. Reibenspies, D. P. Rillema, *J. Chem. Theory Comput.* **2005**, *1*, 95–106.

[475] J. Kramer, Ö. Özkaya, R. Kümmerli, *Nat. Rev. Microbiol.* **2020**, *18*, 152–163.

[476] R. Golonka, B. S. Yeoh, M. Vijay-Kumar, *J. Innate Immun.* **2019**, *11*, 249–262.

[477] G. Bairwa, W. Hee Jung, J. W. Kronstad, *Metallomics* **2017**, *9*, 215.

[478] C. C. Philpott, *Biochim. Biophys. Acta - Mol. Cell Res.* **2006**, *1763*, 636–645.

[479] D. H. Howard, *Clin. Microbiol. Rev.* **1999**, *12*, 394–404.

[480] S. J. Post, J. A. Shapiro, W. M. Wuest, *Medchemcomm* **2019**, *10*, 505–512.

[481] H. Haas, *Appl Microbiol Biotechnol* **2003**, *62*, 316–330.

[482] M. Albelda-Berenguer, M. Monachon, E. Joseph, in *Adv. Appl. Microbiol.*, Academic Press, **2019**, pp. 193–225.

[483] K. H. Negash, J. K. S. Norris, J. T. Hodgkinson, *Molecules* **2019**, *24*, 3314.

[484] R. W. Bastos, L. Rossato, C. Valero, K. Lagrou, A. L. Colombo, G. H. Goldman, *Front. Cell. Infect. Microbiol.* **2019**, *9*, DOI 10.3389/fcimb.2019.00414.

[485] U. Sheldrick, G. M. Sheldrick, Bruker AXS Inc, Madison, **n.d.**

[486] CrysAlisPro, **2010**.

[487] G. M. Sheldrick, *ACTA Crystallogr.* **2015**, *C71*, 3–8.

[488] L. J. Barbour, *J. Supramol. Chem.* **2001**, *1*, 189–191.

[489] O. V Dolomanov, R. J. Gildea, **2014**, DOI 10.1107/S0021889808042726.

[490] V. V Sharutin, A. I. Poddel'sky, O. K. Sharutina, *Russ. J. Coord. Chem. Khimiya* **2021**, *47*, 791–860.

[491] C. Nitsche, C. D. Klein, *Tetrahedron Lett.* **2012**, *53*, 5197–5201.

[492] J. M. Willey, L. M. Sherwood, C. J. Woolverton, H. Prescott, *New York McGraw-Hill* **2008**, *577*, 978–982.